The Structural Evolution of the Faroe Islands, NE Atlantic Margin

WALKER, RICHARD,JAMES

DEPARTMENT OF EARTH SCIENCES, UNIVERSITY OF DURHAM

The Structural Evolution of the Faroe Islands, NE Atlantic Margin

A thesis submitted to the University of Durham
for the degree of Doctor of Philosophy in the
Faculty of Science

Richard Walker

2010

Abstract

The NE Atlantic margin plays host to numerous basins, developed in phases from the Devono-Carboniferous through to the Cenozoic, which record the build up to plate separation and formation of the North Atlantic Ocean. Existing models for this invoke broadly NW-SE extension within the basins, which are segmented by regional-scale NW-SE trending strike-slip lineaments, which are commonly termed ‘transfer zones’. However, there is a general paucity of information concerning the true kinematics of the so-called transfer zones. In this study, the Palaeogene and later structural evolution of the NE Atlantic margin is investigated using abundant field data collected on the Faroe Islands, and systematic observations that characterise the related deformation structures developed in the Faroe Islands Basalt Group (FIBG).

Structures in the Faroe Islands provide evidence for a 6-stage tectonic evolution, here split into 3 broad phases: (*1a*) E-W to NE-SW extension, accommodated by dip-slip N-S and NW-SE trending faults. Continued NE-SW extension (*1b*) was then accommodated by the emplacement of a regionally significant NW-SE- and NNE-SSW-oriented dyke swarm. Event 1 affects the majority of the FIBG stratigraphy, resulting in thickness variations, most notably across the Judd, Brynhild and Westray (‘transfer’) fault-zones. Continued magmatism and anticlockwise rotation of the extension vector led to (*2a*) the emplacement of ENE-WSW and ESE-WNW conjugate dykes, followed by intrusion of the large, saucer-shaped sills on the islands. Their intrusion heralded the onset of N-S crustal extension and was followed by (*2b*) crustal extrusion involving both E-W shortening and further N-S extension facilitated primarily by slip on ENE-WSW (dextral) and ESE-WNW (sinistral) conjugate strike-slip faults, interlinked with minor NE and SW dipping thrust faults. During the final stages of this event (*2c*), the regional extension vector rotated into a NW-SE orientation that was accommodated predominantly by slip along NE-SW oriented dextral-oblique-slip faults. Event 2 began towards the end of magmatism associated with the FIBG, and most likely continued through to the onset of oceanic-spreading on the Aegir ridge (ca. 55 Ma). Finally, (3) Event 1 and 2 structures were reactivated as extension and extensional-hybrid features, characterised best by the entrainment of clastic material along fault planes. Relative timings of Event 3 structures suggest they formed during a period of compression and uplift following the formation of a through-going mid-ocean ridge system (i.e. on the Reykjanes, Kolbeinsey and Mohns ridges).

The progressive anticlockwise rotation of the extension vector identified here is broadly consistent with the most recent NE Atlantic continental break-up reconstructions. Importantly, this model does **not** require basin-scale transfer zones during the Palaeogene, suggesting instead that these NW-SE faults formed as normal faults during a pre-cursor margin-parallel extension episode (Event 1) prior to the onset of oceanic spreading in the Faroe-Iceland sector. This study emphasises the importance of carrying out detailed field studies in addition to the

more usual regional-scale modelling studies, in order to validate and add further detail to basin kinematic histories.

Mineralised syn- to post-magmatic fault sets display a recurring zeolite-calcite-zeolite trend in mineralisation products, which precipitate during successive phases of fault development during each individual event. Fault style and damage zone width appear to be related to the stage of fault development, with early fault/vein meshes linking to form through-going structures with associated damage zones. Dykes and sills are found to form their own fractures, rather than exploiting pre-existing sets. Dyke propagation appears to be buoyancy-driven, with magmatic pressure overcoming the minimum compressive stress. Sills, however, most likely seeded at an interface in the stratigraphy between a weak, more ductile material (i.e. a sedimentary horizon), and a rigid material (i.e. basalt lavas) above. Following this initial development, sill growth and propagation would likely be controlled by viscous dissipation, leading to the complex ramp and flat architecture, with rapid intrusion resulting in upward ramping of the sill. The alternation from fault events, to dyke events and back again corresponds to a switch from faulting with mineralisation along extensional hybrid veins, to magmatic intrusions into extension fractures followed by extensional hybrids (conjugates), and back to extensional and shear hybrid faults (again as conjugates). This alternation reflects variations in the differential regional stress, as well as the magmatic evolution of the margin, and most likely relates to the migration of lithospheric thinning northwestwards across the area, towards the eventual axis of break-up.

We find that, in particular, faults in basalts are in many ways comparable to faults formed at shallow crustal depths in carbonate rocks and crystalline basement, most likely reflecting the similarities in their mechanical properties under near-surface pressures and temperatures. The nature and style of the post-magmatic fault infills provides compelling evidence to suggest that subterranean cavities associated with faults were persistent open features within the FIBG. Structures equivalent to these late, clastic-filled faults of the Faroes may occur in other parts of the NE Atlantic margin, particularly along the axes of gentle regional-scale folds that are widely developed in the region. The late fault displacements observed are all well below seismic resolution, and such structures may be more widespread across the region than previously anticipated. Importantly, the probable unsealed nature of the clastic infills makes them potential fluid-migration pathways, both up- and across-faults within the Cenozoic volcanic sequences of the NE Atlantic region.

Table of Contents

Chapter 1.

Introduction

Chapter 2.

The Faroe Islands Basalt Group: North Atlantic Igneous Province, NE Atlantic margin

Chapter 3.

Onshore evidence for progressive changes in rifting directions during continental break-up in the NE Atlantic and the role of NW-SE trending structures in the Faroe-Shetland basin

Chapter 4.

The nature and significance of post-magmatic faults and associated clastic infills on the NE Atlantic margin: evidence from the Faroe Islands

Chapter 5.

Faults, fault-rocks and fractures in basalts: Faroe Islands, NE Atlantic Margin

Chapter 6.

Discussion, conclusions and future research

List of Figures

Chapter 1:

Chapter 2:

Chapter 3:

Chapter 4:

Chapter 5:

Chapter 6:

Acknowledgements

Firstly I'd like to thank all of the people who have influenced me (to my benefit that is) during my time at Durham: My supervisors, Bob Holdsworth and Jonny Imber for their support guidance and encouragement, and also for their honest criticisms, as well as verbal and even physical abuse over the past few years – without them I would never have developed the sense of flare and style that I now possess. A special mention to Dave Ellis at StatoilHydro, for his support, not only during this project, but with future endeavours. I feel our numerous discussions have led to a definite progression in ideas. Also at StatoilHydro: many thanks to Gareth and Adam again for their support, and some great memories.

Thanks of course to my friends and colleagues at Durham – Chris Mallows, Alan Rooney (colleague only), Jude Coggon, Fabio Domingos, Dave Selby, Steve Smith, Dougal Jerram, Mike Mawby, Nic De Paola, Dave Healy, Leanne Wake, Jaqs Malarkey, My Boy, Dave Stevenson, Gary Wilkinson, and of course ***not*** forgetting Dave Moy, and all of the other people I have met in the department. These people really were the anchor that gave my soul license to soar.

I'd also like to extend my thanks to Thomas Varming at Jardfeingi, for all of his help, especially during field seasons. On the matter of field seasons, many thanks to Simon Passey, and my various field assistants, well, the good ones that is… Nick Roberts, Matthew Felgate, James Glover and Lucy McGee. Maybe a couple of others but I doubt anyone will read this far, so here is a list of popular baby names I found on a website dedicated to the subject. Please feel free to put your surname after the appropriate forename and I shall accredit your contribution: Jack, Oliver, Thomas, Harry, Joshua, Alfie, Charlie, Daniel, James, William, Olivia, Ruby, Emily, Grace, Jessica, Chloe, Sophie, Lily Amelia, Evie. Frankly I find it hard to believe that these are all that popular, considering I don't know anyone by the majority of the listed names – or maybe I've just failed to make the distinction between popular and common. I guess they're a reflection of popular-culture reference. Alfie is a clear giveaway, as terrible a film as that was, and as unconvincing an actor Jude Law has been in everything he's done.

Three years is a long time to remember everyone who has helped, through data support or discussion (e.g. Laurent Geoffroy, Knud Simonsen, Carmen Gaina, Phil Ball, the Føroya Dátusavn Durham's RRG members, conference delegates etc.), so I do apologize if I have missed you.

Finally, a big thank you to Mum, Chris and Sian – they didn't really do anything that they wouldn't have done in any other circumstance, but thanks anyway.

In all seriousness, I would like to say a big thank you to all of the above – they have certainly helped in getting me to this position, and I am sincerely indebted to them all. (And incase there is any doubt, Bob and Jonny have been nothing but kind to me, and I was never the subject of any verbal or physical abuse).

Declaration

No part of this thesis has previously been submitted for a degree at this or any other university. The work described in this thesis is entirely that of the author, except where reference is made to previously published or unpublished work.

Richard J. Walker

University of Durham

Department of Earth Sciences

January 2010

1

Introduction

1.1 Introduction

Existing interpretations of seismic reflection data and potential field modelling studies have proposed that faults and fractures in the Faroe Islands are related to a series of NW-SE trending lineaments, interpreted as broad 'transfer-zones' (Rumph et al., 1993; Ellis et al., 2009) that lie parallel to the regional extension direction during the Palaeogene. Along strike and to the NE on the Norwegian shelf, transfer-zones appear to segment Jurassic and later basins, and a similar model is applied in the Faroe-Shetland Basin (FSB; Doré et al., 1999), although this region now lies buried by a significant thickness (up to 6km locally) of Tertiary basalts. Several 'transfer zone' lineaments identified offshore in the FSB project through the Faroe Islands and any structures related to these inferred fault zones should therefore be exposed on land. In particular, structures and offsets relating to the Judd, Westray and Brynhild lineaments (Ellis et al., 2002; Ellis et al., 2009) should be evident. The kinematics and surface expression of these 'transfer zones' are important if they are equivalent to transfer zones recognised in other basins worldwide (e.g. Gibbs, 1984; Rosendahl, 1987; Doré et al., 1997; Brekke, 2000). If they are analogous to these structures they should significantly influence or control the provenance and distribution of sediments into the

FSB through time. However, an alternative model has suggested that these NW-SE structures are related instead to changes in Palaeocene rift orientation immediately prior to and during continental break-up (Doré et al., 1999). In this model, variations in rift orientation would result in distinct successive fault and fracture sets, within which, the 'transfer zones' would simply relate to a single phase or event.

The primary focus of this thesis is the documentation of the structural evolution of the Faroe Islands based on the observed geometric and kinematic development of deformation structures exposed on the islands. The main aim of this thesis is to create a four-dimensional (4-D) model for the development of structures on the Faroe Islands, as a critical test of the existing models. An ancillary aim (though equally important) is to characterise the hitherto poorly understood geological characteristics of faults in extrusive basaltic lava sequences.

1.2 Methodology

Datasets in this thesis have been collected at multiple scales, including: (1) large-scale remote-sensing mapping using high-resolution aerial imagery and topography; (2) meso-scale field-mapping; and (3) microstructural analysis of thin sections.

1.2.1 Remote sensing

A more detailed methodology for remote sensing analysis is presented in *Chapter 2*; a synopsis is given here. Remote-sensing analyses were conducted using ArcGIS software, incorporating topographic (10m resolution; *Munin*) and bathymetric data (30m resolution; courtesy of *the University of the Faroe Islands*), and 2D aerial and satellite images (0.5m resolution; courtesy of *Føroya Dátusavn*). Contour datasets were processed to create topographic surfaces, from which derivatives such as hillshades, slope, break-in-slope and aspect maps could be made. Combined, these datasets were used to pick surfaces (independent of scale) and lineaments at 1:5,000, 1:50,000 and 1:250,000 scales. All remote-sensed analyses have been conducted within the WGS 1984, 29°N (projected) coordinate system. Lineament orientations were calculated within ArcGIS and verified using Global Mapper, and have been collated into rose-plots using the EZ-rose software (Baas, 2000). Lines picked in the field and remotely have also been used to create 3-D surfaces within Gocad, whilst orientation data gathered in the field was collated using stereographic projection software, MyFault™ (version 1.03; of Pangea Scientific).

1.2.2 Outcrop and hand specimen data

Detailed structural mapping and data collection were carried out at 406 localities on 10 of the main islands (see *Chapter 3* for full details). Field measurements were primarily concerned with outcrop-scale brittle-feature geometries, since large-scale features such as strike and dip variations in lava flow layering could be mapped remotely.

Orientation data have been collected in a standard compass-bearing system. At the time of study, magnetic deviation was calculated to the nearest ½ degree as 7°W (source: National Oceanic and Atmospheric Administration (NOAA)). Planar data were collected as dip-azimuth and dip; within the thesis text, this is converted to strike, dip, dip direction (e.g. 045.85° NW; where the strike is found at bearing 45° and dip is 85° from horizontal towards the NW). All locality coordinates are geo-referenced in UTM zone 29°N on the WGS 1984 geoid. Field data have been plotted using the MyFault™ software (version 1.03). This software can be used to display both orientation and kinematic data and has numerous calculation methods for stress inversions (detailed in the following section). Data collection in the field was based around reducing error for this style of analysis; plane measurements were collected as either: 1) strike azimuth, dip and downward-dip direction; or 2) dip azimuth and dip. Fault plane striations and slickenlines were taken as a rake upon that plane, thereby removing the possibility of an angular mismatch between the plane and the lineation.

Oriented hand specimens were also collected from key localities in order to assess the meso- to micro-scale characteristics of the exhumed Faroese fault rocks, associated features (e.g. veins) and wall-rock characteristics.

1.3 Stress inversion techniques

Palaeostress orientations have been calculated using standard inversion methods in MyFault™ (v. 1.03) stereonet software, produced by Pangaea Scientific Limited. The program offers five inversion methods, which are detailed below. This allows a quick and easy comparison between different methodologies (**Fig. 1.1**), each of which is based on different assumptions. Every dataset has been run through each methodology (provided data numbers are sufficient) in order to assess any mismatches in the resulting palaeostress orientation calculations. For all datasets, the methodology chosen has been based on the result that is most consistent with fault rock characterisation. For instance, where available, tensile veins are used to verify the orientation of σ3. Using the data set example in Figure 1, we would choose the simple shear tensor average, on the basis that: (1) σ3 is oriented within the densest pole cluster (not shown) of the tensile veins; (2) σ1 is horizontal and oriented within the acute angle between a mean ENE and a mean ESE conjugate strike-slip set; (2) the horizontal extension and shortening directions fit well with the observed fault rocks; and (4) calculation errors are minor, unlike other methods in which the program has attempted to switch σ2 and σ3 (though with no evidence for this in the field). Sceptics may question whether comparison between the different methods is valid, and in fact there is no generally accepted approach to deciding which method is used. Palaeostress calculations are based on varying assumptions (the most significant and widespread being that strain is equal to stress), and as such we used them simply as a guide. However, as strain in the Faroes appears to be reasonably minor (<<10%), thus the degree of rotational strain is likely to be negligible, we feel this approach is suitable for the present study.

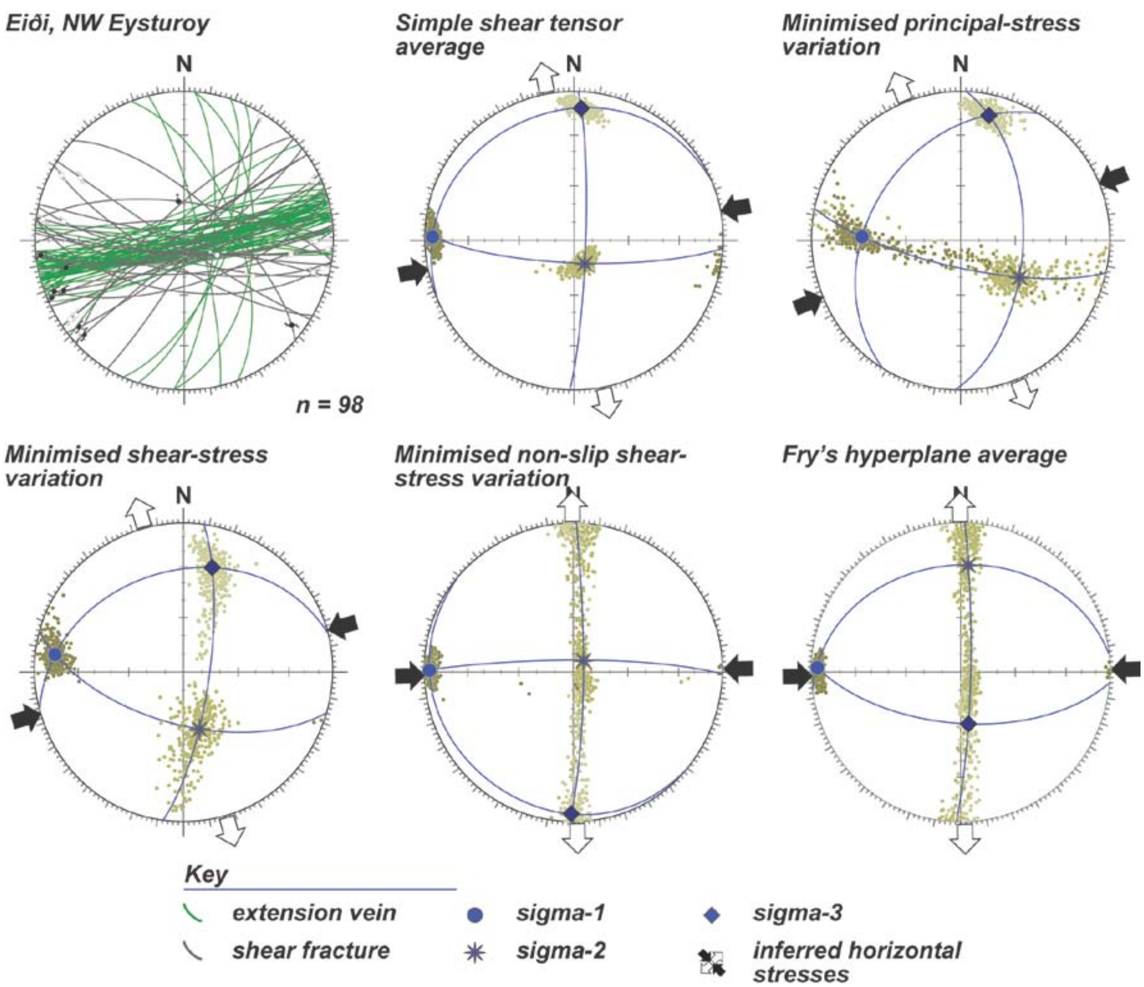

Fig. 1.1. Palaeostress calculations for faults and extension fractures at Eiði, NW Eysturoy. Typical variation in Principal stress orientations is ~10-15°, though in some cases ranges from 20-30° (for instance between the Fry's hyperplane average, and the other methods). In this example set, the *simple shear tensor average* gives the least spread during recalculation (i.e. it has the tightest clusters), and is therefore used to represent the palaeostress calculation. Other methods for this data set appear to switch the maximum and intermediate principal stresses ($\sigma 1$ and $\sigma 2$ respectively) during recalculations resulting in the observed point-spread along the $\sigma 1$-$\sigma 2$ plane. The horizontal extension direction is within 15-20° across the different methodologies, and fits with a N-S extension as indicated by extension fractures in the data set. As such, this result is viewed as reliable.

1.3.1 Simple shear tensor average (Sperner et. al., 1993)

In this method, a simple shear stress state is assumed for each fault, with the intermediate principal stress lying in the fault plane perpendicular to the slip direction. The individual stress tensors can then be averaged together to give an estimate of the collective stress tensor. The angle between the maximum principal stress and the fault plane can be varied to search for the minimum deviation between the faults in the set; MyFault™ automatically scans between 0 and 45°.

The method assumes that slip occurs in the same direction as when the fault was first formed, and it does not allow for an estimate of the intermediate principal stress. Its average value will tend to lie close to 0.5, where the maximum and minimum principal stresses are normalised to 1 and 0, respectively. As such, in all the inversion methods detailed here, the stress ratio: (intermediate-minimum) / (maximum-minimum) is equal to the intermediate stress.

The uncertainties in these quantities are estimated using the bootstrap resampling method (as is the case for all the methods described herein). For each calculation, MyFault randomly samples the record set, choosing the same number of records for the new set as were in the original. Since the sampling is random, there will necessarily be duplication of one or more of the original records. It then computes the principal stress tensor for each resampled set and computes its tensor distance from the principal stress tensor of the full original record set (Michael, 1987a).

1.3.2 Minimised Principal-stress variation (Reches, 1987)

This method assumes that the stress resulting in fault slip obeys a Coulomb yield criterion, $\tau = C + \mu\sigma$, where τ is the shear stress resulting in slip, C is the cohesion stress, μ is the friction coefficient and σ is the normal stress acting on the fault. Assuming that all faults in the set were subject to the same regional stress state, then the principal stresses should be the same for all faults. It should be noted, however, that local effects, such as variations in material properties, will cause the actual stress state to vary between faults.

To estimate the regional stress, it is assumed that the best value is found by minimising the variations of the computed principal stresses within the fault set, using the same cohesion and friction coefficient for all faults. This assumption leads to determination of a set of linear equations in C, μ and six principal stress components. C represents the hydrostatic or lithostatic component, and is therefore unknown; It is assumed to be zero because the mean stress (and hence the absolute normal stress) is unknown. All stresses are normalised so that the maximum principal stress equals 1 and the minimum equals 0. To find the value of μ, MyFault™ solves the equations using a range of friction angles from 0 to 45°, choosing the value that gives the minimum variation in principal stresses for all faults.

1.3.3 Minimised shear-stress variation (Michael, 1984, 1987a, 1987b, 1991)

Slip on a fault surface occurs when the resolved shear stress on that surface exceeds the frictional resistance to slip. For a uniform regional state of stress, the direction of slip will depend on the orientation of the fault and local factors such as frictional anisotropy. Thus the actual slip direction may not coincide with the maximum resolved shear stress. To estimate the regional stresses, this method applies the assumption that the magnitude of the slip stress on the fault is similar for all faults in the set at the time of slip. Thus, minimising the variations in slip stress among the faults leads to determination of a set of linear equations, which are solved by the standard eigenvector method, giving the three principal stresses and their direction.

1.3.4 Minimised non-slip shear-stress (Angelier, 1984)

The deviations between the maximum resolved shear stress on the fault plane and the actual slip direction lead to a non-linear minimisation problem. A set of linear equations can be derived instead by minimising the variations in the non-slip stress (the shear stress component in the fault plane normal to the slip direction) among the faults. These equations are solved by the standard least squares technique, giving the three principal stresses and their direction. Again, because the mean stress during slip is generally unknown, the principal stresses are normalised such that the maximum stress equals 1 and the minimum equals 0.

1.3.5 Fry's hyperplane average (Fry, 1999, 2001)

In order to estimate the regional stresses, this method transforms the data to a 5-component reduced stress space. In such coordinates, idealised slip on all possible faults occurs on a hyperplane, whose normal is the stress tensor giving rise to the slip. Thus the problem is reduced to finding the hyperplane best fitting the measured fault slip data (Shan et al., 2003, 2004; Li et al., 2005). Using the eigenvectors of the measurements in the 5-component space, the minimum eigenvector gives the best-fitting stress components. Converting back to normal space gives the stress tensor.

1.4 Definitions

1.4.1 Faults, fractures and kinematic indicators

1.4.1.1 Fault classification

A fracture can be defined as a brittle discontinuity or rupture within a material (e.g. rock) and can form on all scales, from micro-fractures to plate-scale faults. In terms of fracture mechanics, meso-scale fractures are subdivided into 3 subsets, based on the relative displacement of the wall rock materials across the fracture (**Fig. 1.2**; e.g. Atkinson, 1987): (1) *Mode I*, tensile opening with no shear, (2) *Mode II*, in-plane shear, and (3) *Mode III*, anti-plane shear. Joints and extension veins are examples of Mode I fractures, whereas shear fractures, faults and slickenfibre veins are examples of Mode II and III fractures.

Typically, tension fractures will form perpendicular to the minimum principal stress, $\sigma 3$, and parallel to the maximum principal stress, $\sigma 1$, resulting in uniaxial strain. Shear fractures on the other hand will typically form in confined compression at angles <45° to $\sigma 1$. In biaxial stress states, shear fractures are oriented parallel to the intermediate stress, $\sigma 2$, and will form a conjugate pair at an angle <45° to the $\sigma 1$-$\sigma 2$ plane (Hancock, 1985).

Faults are classed based on their geometry and direction of slip, which has led to the formation of two classification schemes: (1) *Anderson's dynamic classification*, and (2) simple geometric classifications. Anderson's dynamic classification of faults (**Fig. 1.2b**; Anderson, 1951) is based on the assumption that one principal stress ($\sigma 1/\sigma 2/\sigma 3$) will be oriented normal to the Earth's surface (i.e. vertical). Fault terminology arising from this classification includes: normal faults (where $\sigma 1$ is vertical); Wrench or strike-slip faults (where $\sigma 2$ is vertical); and reverse faults (where $\sigma 3$ is vertical).

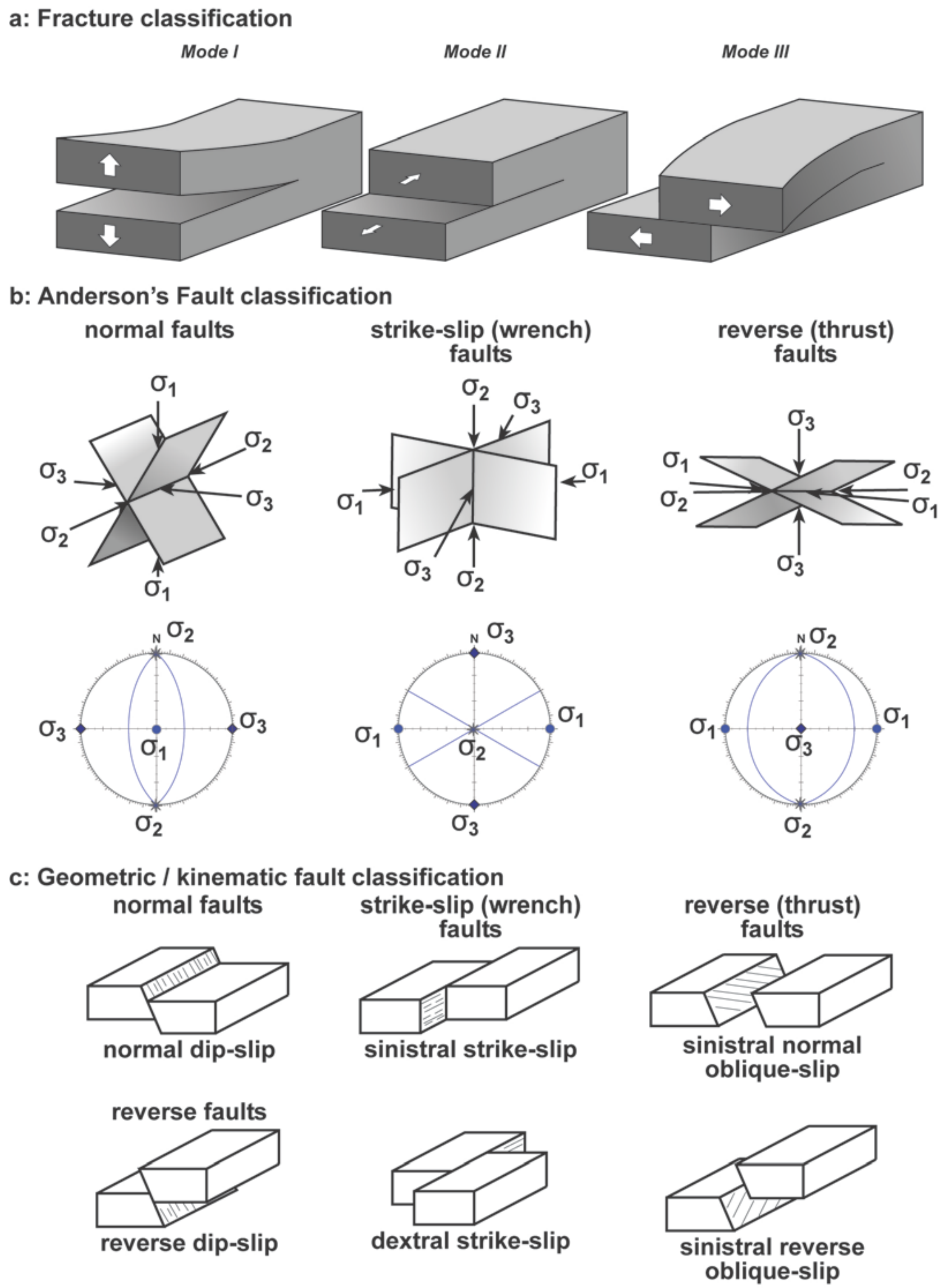

Fig. 1.2. (**a**) Fracture types (*Mode I*, *II*, and *III*) based on the relative displacement of material on either side of a fracture. (See text for explanation). (**b**) Andersonian and (c) geometric fault classification schemes (from McClay, 1987).

Geometric and kinematic fault classifications (**Fig. 1.2c**; e.g. McClay, 1987) are based on the relative direction of slip across a fault plane, and are split into five divisions: (1) Normal faults (extension of horizontal datum surfaces); (2) Reverse faults (shortening of horizontal datum surfaces); (3) Strike-slip faults (horizontal motion, with no change in length of horizontal datum surfaces); (4) Oblique-slip faults (combining strike- and dip-slip motion); and (5) Rotational faults. References to fault classes in the present thesis use the geometric/kinematic classification, with the exception of rotational faults, of which none were identified during the study.

1.4.1.2 Kinematic indicators

The sense of slip can be determined simply by the presence of offset geological structures. However, in instances where these are not available, brittle shear-sense indicators can be used (**Fig. 1.3**). These include: (1) fault plane striations; (2) fault plane undulations; and (3) secondary fracture systems.

Fault plane striations can take two general forms (**Fig. 1.3a**): (a) *striae*, where fragments or asperities scratch against the fault surface during movement; or (b) *slickenfibres*, which are syn-kinematic, elongate crystals that grow on the shear plane as fault movement occurs. In the case of fault striae, the end of the indentation points in the direction of the missing counterpart surface. Slickenfibres grow at low angles to the fault wall, and will tend to break along or across the fibres, resulting in a roughly stepped surface. These steps indicate the direction of motion, with the missing block travelling in the down-step direction (**Fig. 1.3a**).

Fault plane undulations (i.e. bends along the plane) can result in the formation of localised tensile jogs, or zones of compression, depending on the relative kinematics of the fault, and are commonly used in conjunction with striae and/or secondary fractures in order to determine the sense of displacement.

Secondary fractures developed during shear along a main fault form a reproducible set of structures observed in numerous types of material under a wide range of confining pressures and strain rates (Cloos, 1955; Byerlee et al., 1978; **Fig. 1.3b**). The most abundant elements are *R*, *R'*, *P* and *T* fractures. The synthetic *R* (Riedel) fractures are extensional, and form at a low angle (10-20°) to the mean fault plane, whereas *R'* fractures are antithetic and conjugate to R, and form at a high angle to the mean fault plane (70-90°). Contractional *P* fractures are synthetic and form at an angle of 10-20° to the mean fault plane. *T* fractures are tensile, and develop at an angle of 30-90°. The various morphologies of these secondary fractures are shown in **Figure 1.3b**.

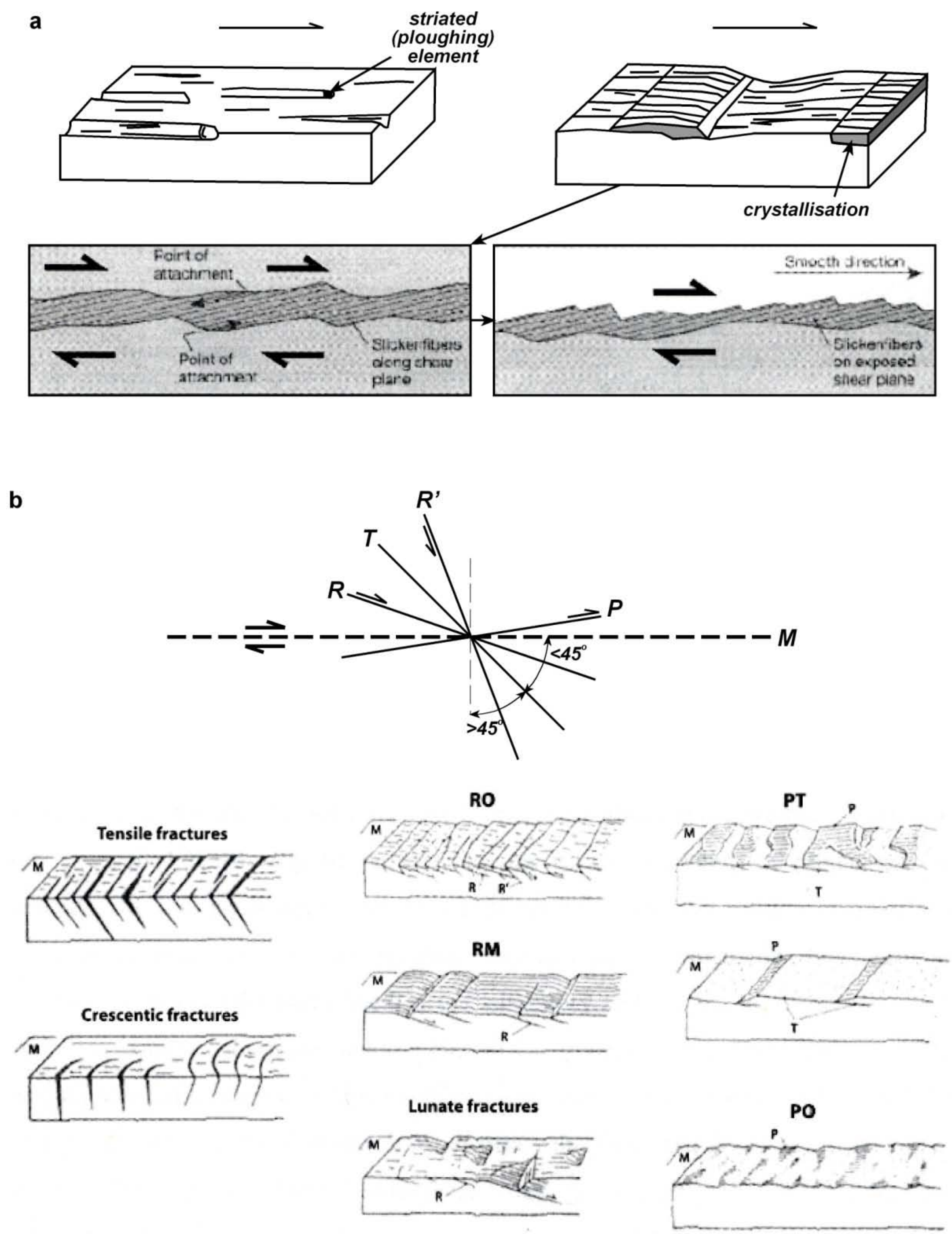

Fig. 1.3. Forms of kinematic indicators resulting from brittle deformation: (**a**) fault plane striae (grooves) and slickensides (mineral fibres) (From Petit, 1987; Twiss and Moores, 1992). (**b**) Shear sense criteria from secondary fractures: ***M***, main fracture; ***R*** and ***R'***, synthetic and antithetic Riedel shears respectively; ***T***, tensile fractures; ***P***, synthetic shears associated with dextral shear (in this example) (After Petit, 1987).

1.4.1.3 Hydrofractures

Anderson's theory of faulting assumes that faulting is controlled by a Mohr-Coulomb type failure criterion (Anderson, 1951; **Fig. 1.4a**). Slip will occur when the applied stresses equal the rock strength. Brittle faulting of intact rock can therefore be described by the Coulomb Criterion for shear failure:

$$\tau = C + \mu_i \sigma'_n \quad \text{or} \quad \tau = C + \mu_i (\sigma_n - P_f)$$

where, τ is the shear stress at failure (shearing resistance), σ_n is the normal stress (σ'_n is the effective normal stress, σ_n-P_f,), C is the cohesive strength, μ is the coefficient of internal friction, and P_f is the pore fluid pressure. Pore fluid is important when considering the formation of fractures, as it decreases the normal stress required for failure by an amount equal to the pore fluid pressure (i.e. the second part of the equation above; **Fig. 1.4b**). Therefore we can define tensile *hydrofractures* here as fluid-assisted mode I fractures that form planes perpendicular to the minimum compressive stress (σ_3; Sibson, 1985; e.g. **Fig. 1.4a**). As such, hydrofractures are commonly used to infer the orientation of the regional stress field. The principal effective stresses in order of decreasing magnitude are denoted $\sigma'_1 = \sigma_1 - Pf$, $\sigma'_2 = \sigma_2 - Pf$, $\sigma'_3 = \sigma_3 - P_f$. Under low values for differential stress (i.e. $\sigma_1 - \sigma_3 < 4T$, where T is the tensile strength of the rock) hydrofractures will form when the condition $\sigma'_3 = -T$ is achieved (Hubbert and Rubey, 1959).

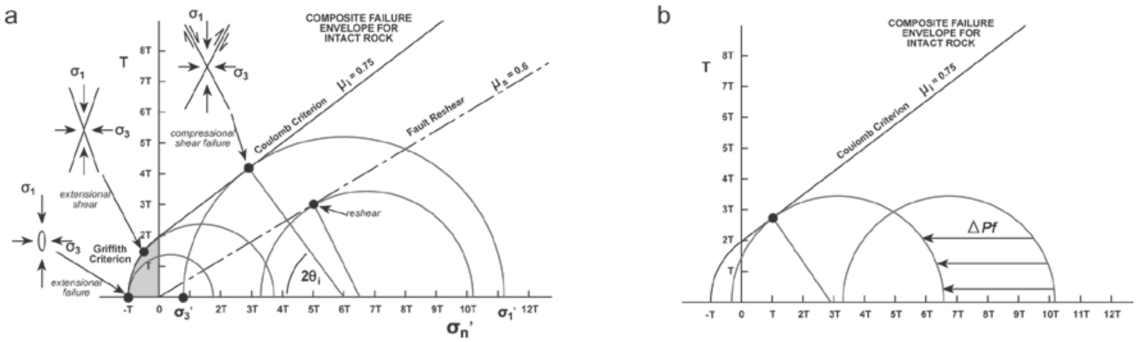

Fig. 1.4. (**a**) Mohr diagram (shear stress (*T*) against effective normal stress (σ'_n)) with composite failure envelope for intact rock (bold black line) and reshear condition for a cohesionless fault (dash-dot line). Critical stress circles are shown for 3 modes of brittle failure and for reshear on an optimally oriented cohesionless fault. Expected orientations with respect to the principal stress axes of newly-formed compressional shear, extensional shear and extension fractures are shown in the attached cartoons (Sibson, 2004). (**b**) Effect of fluid pore pressure on the formation of a fault.

Complex hydrofracture systems with orthogonal sets of tensile hydrofractures related to a single tectonic phase are common in nature. This requires local permutations in the relative magnitudes of the principal stresses (e.g. Colletini et al., 2006 and references therein), for which there are several proposed mechanisms depending on the specific geological conditions. Of particular note with reference to the present study is the effect of pore pressure charge, release and recharge following fracture events (as detailed by Colletini et al. 2006 for the Zuccale Fault Zone on Elba, Italy). In their study, a complex system of mutually cross-cutting vertical and horizontal hydrofractures was interpreted as being the result of local stress permutations induced by the cyclic build-up and subsequent release of overpressure below the low-permeability Zuccale Fault Zone (**Fig. 1.5**). In this model, fluid pressure release results in the formation of a fluid filled crack, and a drop in the normal effective stress to zero. Since the fluid filled crack has a tensile strength of zero, it cannot decrease further with

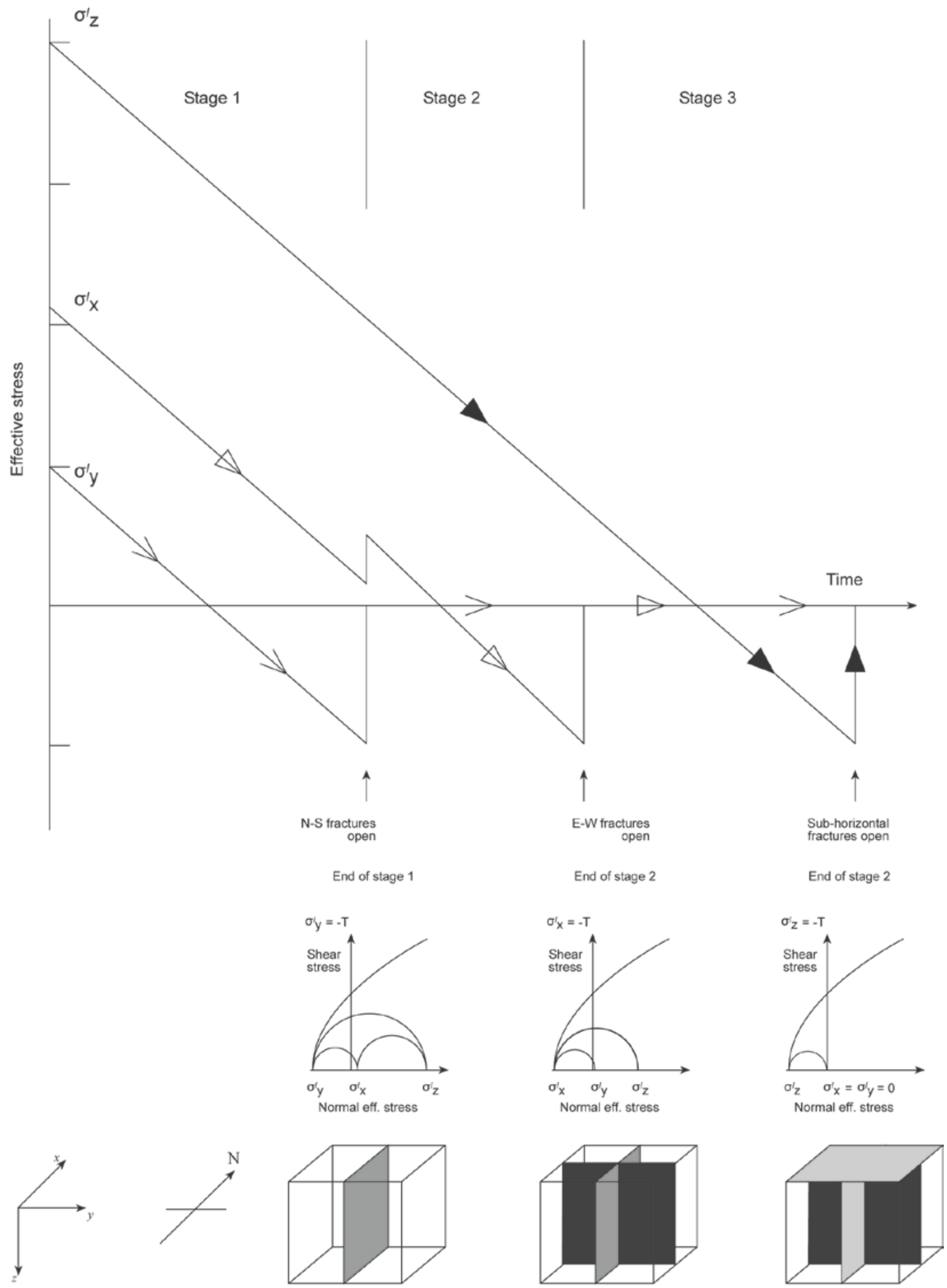

Fig. 1.5. Model for the development of 3 orthogonal vein sets: (**a**) During overpressure build-up, the principal effective stresses are reduced. As each principal effective stress reaches –*T*, fractures open in perpendicular planes and that same principal effective stress jumps up to zero. (**b**) The stress states plotted as Mohr circles when each set of hydrofractures is about to open. The Cartesian axes system, north direction and the orientations of the 3 fracture sets are shown below.

increasing fluid pressure, provided that this increase exceeds the cementation (healing) rate (otherwise the fracture would regain tensile strength and future deformation would occur along it). A constant supply of fluids would result in lowering of σ’1 and σ’2, until the point that σ’2 and σ’3 were switched (at zero) (**Fig. 1.5**). Failure would therefore occur perpendicular to the previous σ2 orientation. With further recharge (which again has to be faster than the healing rate), σ’1 would continue to drop until failure when the normal effective stress reached –*T*, forming a fracture perpendicular to the original orientation of σ1 (**Fig. 1.5**).

1.4.1.4 Fault rocks

The fault rock terminology used in this thesis follows the nomenclature and definitions of Schmid and Handy (1991) for cohesive rocks (i.e. *cataclasites* and *foliated cataclasites*). For breccias, of which there are numerous examples in the Faroes, we use the classifications of Woodcock and Mort (2008) (**Fig. 1.6a**), which is based on grain size, rather than the lack of cohesion during faulting. Breccias are therefore split into: (1) *crackle breccias*, (2) *mosaic breccias*, and (3) *chaotic breccias*; terms that simply describe how well the clasts fit together (**Fig. 1.6b-d**).

Cataclasites are composed predominantly of mechanically disaggregated minerals, the clasts of which have undergone subsequent frictional grain-boundary sliding, rotation and disaggregation. In some cases, cataclasites contain a foliation (i.e. *foliated cataclasite*), which is defined by either bands of fine and coarse comminuted clasts, fine grained material localised along parallel fractures, or bands of syn-tectonic alteration products (Chester et al., 1985). Cataclasites can be segregated depending on the relative proportion of matrix (Schmid and Handy, 1991), into: *microbreccia* (0-10%), *protocataclasite* (10-50%), *cataclasite* (50-90%) and *ultracataclasite* (90-100%).

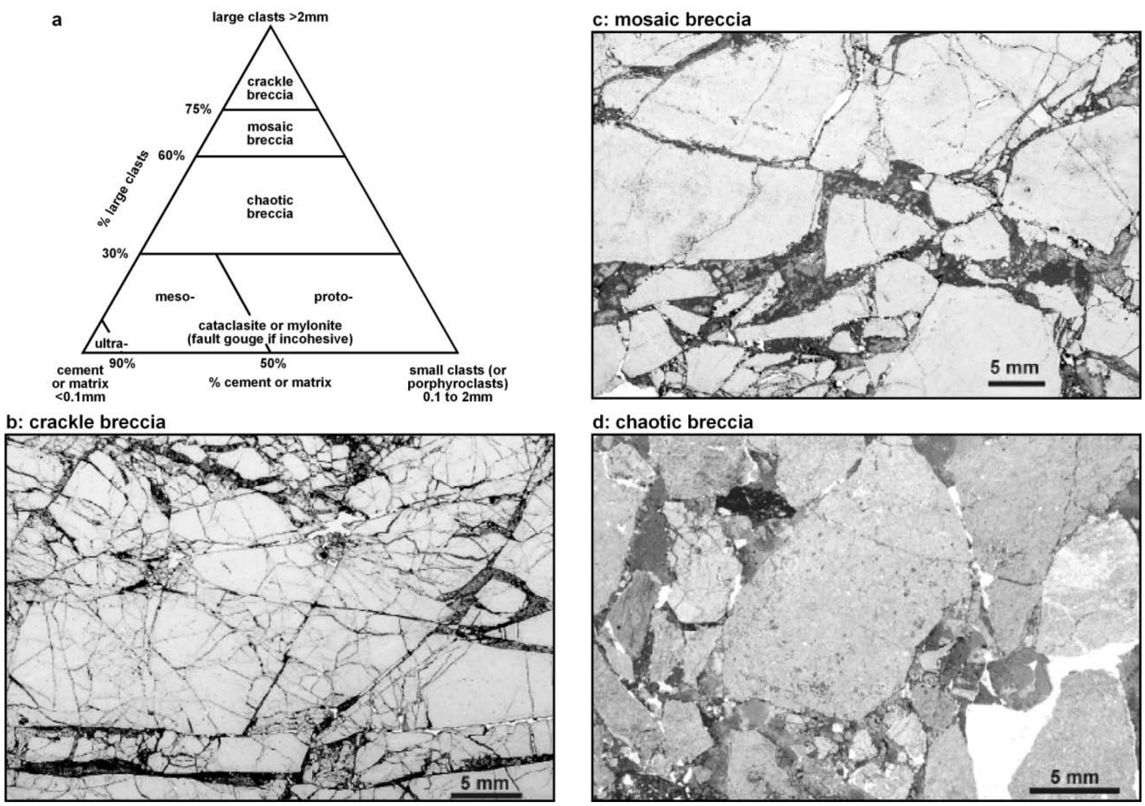

Fig. 1.6. (**a**) Ternary diagram for a brecciated fault rock classification, and examples of (**b**) crackle breccia, (**c**) mosaic breccia, and (**d**) chaotic breccia from the Dent Fault Zone, NW England. (From Woodcock and Mort, 2008)

1.4.1.5 Fault damage zones and fault cores

The nomenclature referring to fault zones in this thesis is based on the definitions detailed in Caine et al. (1996). Depending on its stage of development, a fault zone in an upper crustal protolith may comprise wall rocks, a fault core and damage zone (**Fig. 1.7**). The terminology is not dependant on the presence of all three components (i.e. fault core; damage zone; wall rocks), nor is any scaling relationship implied. Hence, a fault core is defined here as '*the structural, lithological, and morphological part of a fault zone where most of the displacement is accommodated*' and the damage zone as '*a network of subsidiary structures that bound the fault core*' (Caine et al., 1996).

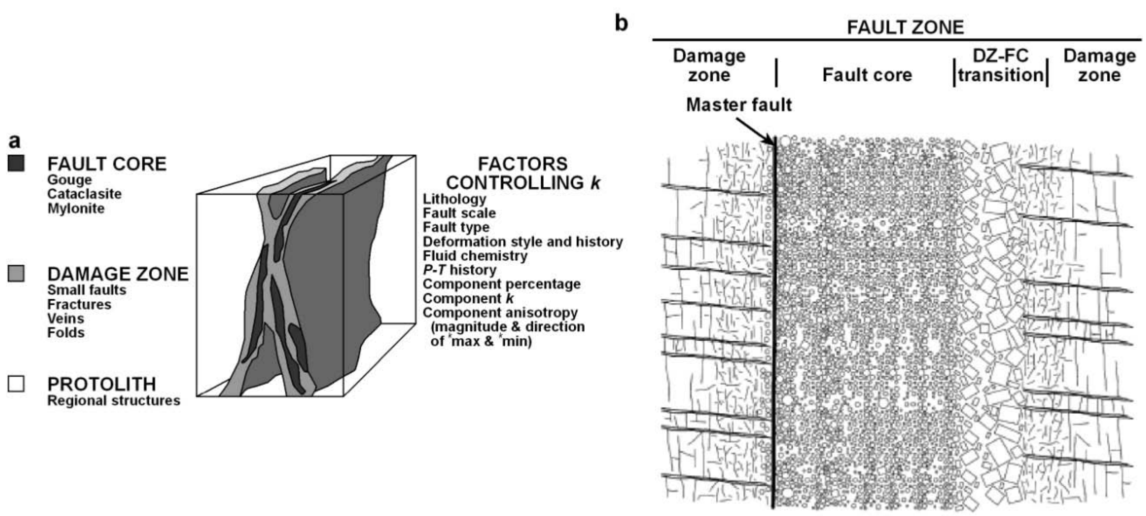

Fig. 1.7. Fault related damage: (**a**) Conceptual model of a fault zone: k, bulk 2-D permeability (from Caine et al., 1996); (**b**) Detailed conceptual sketch of a fault zone in carbonate rocks, viewed perpendicular to the shear direction (from Billi et al., 2003).

By definition, a fault core can range from a single slip surface, or collection of slip surfaces, to a broader zone of cataclasis. Damage zones are typically made up of networks of small faults, fractures and veins that can cause anisotropy, particularly in terms of the permeability and elastic properties of the material.

1.4.2 Fault reactivation

We define fault reactivation as '*the accommodation of geologically separable displacement events (at intervals >1Ma) along pre-existing structures*' (after Holdsworth et al., 1997). Reactivation can be split into two geometric types, where: (1) reactivated faults display different senses of relative displacement during successive events, and (2) faults display similar senses of relative displacement during successive events.

In the text we also refer to 'recurrent reactivation.' We define this simply as repeated kinematic episodes accommodated by the same fault zone during successive events that may occur at intervals <1Ma.

1.4.3 Transfer and accommodation zones

Transfer and accommodation zones (e.g. **Fig. 1.8**) occur in all tectonic settings, from thrust belts to rifts. In the simplest of geometric expressions, for every dip-slip fault, contractional or extensional, there are four end-member terminations; two parallel, and two perpendicular to strike (Faulds and Varga, 1998), beyond which there must be transfer or accommodation. In reality, brittle failure does not involve the formation of a single fault, rather the linking together of segments (Peacock, 2002; Walsh et al., 2003). Nevertheless, the complexity of transfer-zone geometry has potentially been far underestimated.

Transfer and accommodation zone studies have been applied to regions undergoing shortening (e.g. Dahlstrom, 1970; O'Keefe and Stearns, 1982), regions of extension (e.g. Gibbs, 1984; Rosendahl, 1987; Morley et al., 1990), and in analogue modelling of the two (e.g. Calassou et al., 1993; Acocella et al., 1999). The nomenclature has also been applied to oblique- or strike-slip settings (e.g. McClay and White, 1995), with transfer and accommodation geometries varying considerably from their dip-slip equivalents. The distinction between transfer- and accommodation- zones commonly appears to be arbitrary, and frequently the two terms are used interchangeably. This has resulted in their usage becoming quite confused and cumbersome (e.g. Peacock et al., 2000). 'Transfer zone' in particular appears to have become a vernacular phrase, used to link any overlapping fault set. Most often, 'transfer zone' is just used to describe any lineament trending normal to a set of basin-bounding faults, and the kinematics are assumed to be strike-slip or oblique in order to fit with the observed basin geometry. For the purposes of this thesis, we define transfer and

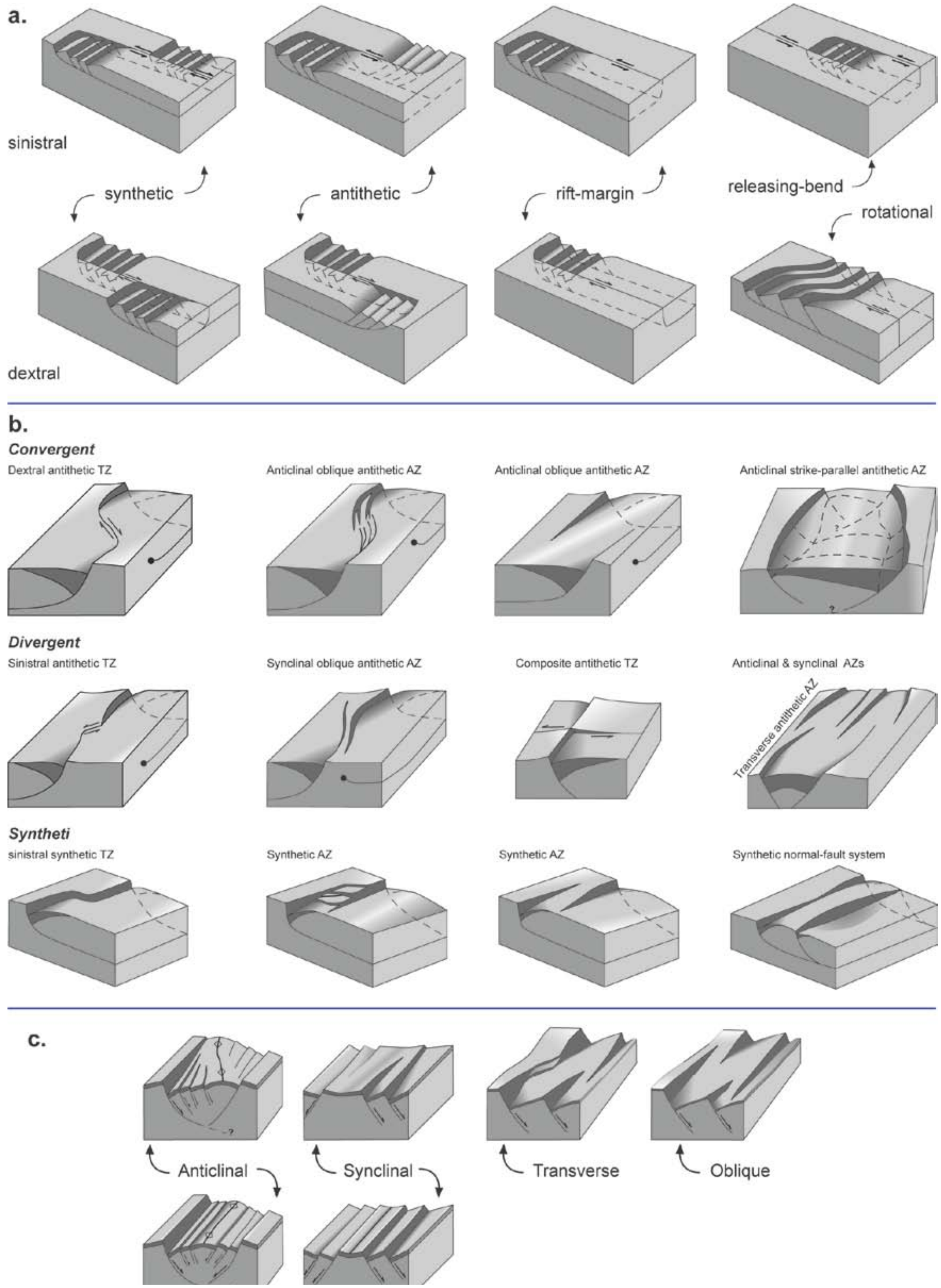

Fig. 1.8. Idealised sketch representations of (**a**) sinistral and dextral transfer zones and (**b-c**) accommodation zones. (From Faulds and Varga, 1998).

accommodation zones following the Faulds and Varga (1998) definitions, i.e. a transfer zone is defined as a discrete zone of strike-slip and oblique-slip faulting that generally trends parallel to the extension direction and typically facilitate a transfer of strain between extended domains arranged in an en echelon pattern (e.g. **Fig. 1.8a**). An accommodation zone is an area of soft-linked rift segmentation, typically characterised by a zone of overlapping normal faults where strain is transferred as a set of relay structures (e.g. **Fig. 1.8b, c**).

1.5 Thesis outline

Chapters 2-6 are described individually below. The main data sections, *Chapters 2-5*, have been written as standalone manuscripts to be submitted for publication; these are recast for the thesis if/when appropriate. As such, each chapter contains a specific introduction, background, discussion and conclusions. The background sections for each chapter represent a content-specific synopsis of *Chapter 2*, and may therefore be skipped at the reader's discretion. This also applies to deformation-history recap sections in *Chapters 4* and *5*, which provide a synopsis of *Chapter 3*. Co-authors for each manuscript provided scientific advice and discussion, and appropriate editorial guidance. For the sake of consistency, pronouns referring to the author (myself) will appear in the plural form (i.e. *we* replaces *I*) throughout as an acknowledgement of co-author contributions. The thesis only contains manuscripts for which I am the 1st

author, and I have been responsible for more than 90% of the primary data collection, interpretation and paper writing.

Chapter 2 – *The geological context of the study.*

This chapter represents a summary of the geology of the Faroe Islands and the formation of the Faroe-Shetland basin and the NE Atlantic, based primarily on published references, but also incorporating regional-scale remote-sensed analyses of the islands carried out as part of the present study.

Chapter 3 – *Island- to outcrop-scale fault kinematic study.*

This chapter is a structural study of the Faroe Islands detailing fault/fracture kinematics related to tectonics, based on detailed remote-sensed analyses and field-mapping. Detailed mapping and structural analyses are used to determine distinct deformation events, which are fitted into a regional to super-regional context.

Chapter 4 – *Outcrop-scale study of 'regionally late' faults on the Faroe Islands.*

This chapter provides an in-depth characterisation of the regionally post-magmatic structures detailed in *Chapter 3*, primarily based on field analysis, but incorporating evidence from micro-structural analysis.

Chapter 5 – *Meso- to micro-scale analysis of Faroese fault-zones and fault-rocks.*

This chapter focuses on fault zone architecture in order to understand the deformation mechanisms associated with the large-scale kinematic events (as detailed in *Chapter 3*).

Chapter 6 – Discussion, c*onclusions, and future work*.

This chapter elaborates on the discussion section of the preceding chapters, and conclusions drawn throughout the body of the thesis are summarised. This study also reveals areas of interest for possible future research, with suggestions as to studies that may be of importance to both the scientific and industrial communities.

2

The Faroe Islands Basalt Group: North Atlantic Igneous Province, NE Atlantic margin

2.1 Introduction

The NE Atlantic margin is a passive continental margin extending from Lofoten, Norway, in the northeast to offshore western Ireland in the southwest (**Fig. 2.1a**). It is characterised by a continuous chain of NE-SW oriented Devono-Carboniferous and later basins that appear to be segmented along their axis by NW-SE trending lineaments commonly referred to as “transfer zones” (Rumph et al., 1993; Doré et al., 1997; Kimbell et al., 2005). Much of the outer, oceanward region of the margin is covered by a thick pile of flood-volcanics, forming part of the Palaeogene North Atlantic Igneous Province (NAIP; **Fig. 2.1b, c**). As far as the petroleum industry is concerned, the basins are somewhat underexplored, in part due to this volcanic masking, but also to the previously prohibitively deep waters. In the past decade, the Faroes sector of the margin has been opened for licensing rounds, and based on the presence of several large fields in the nearby UK sector (e.g. Clair, Foinaven and Schiehallion) a rapid exploration upsurge has been sparked.

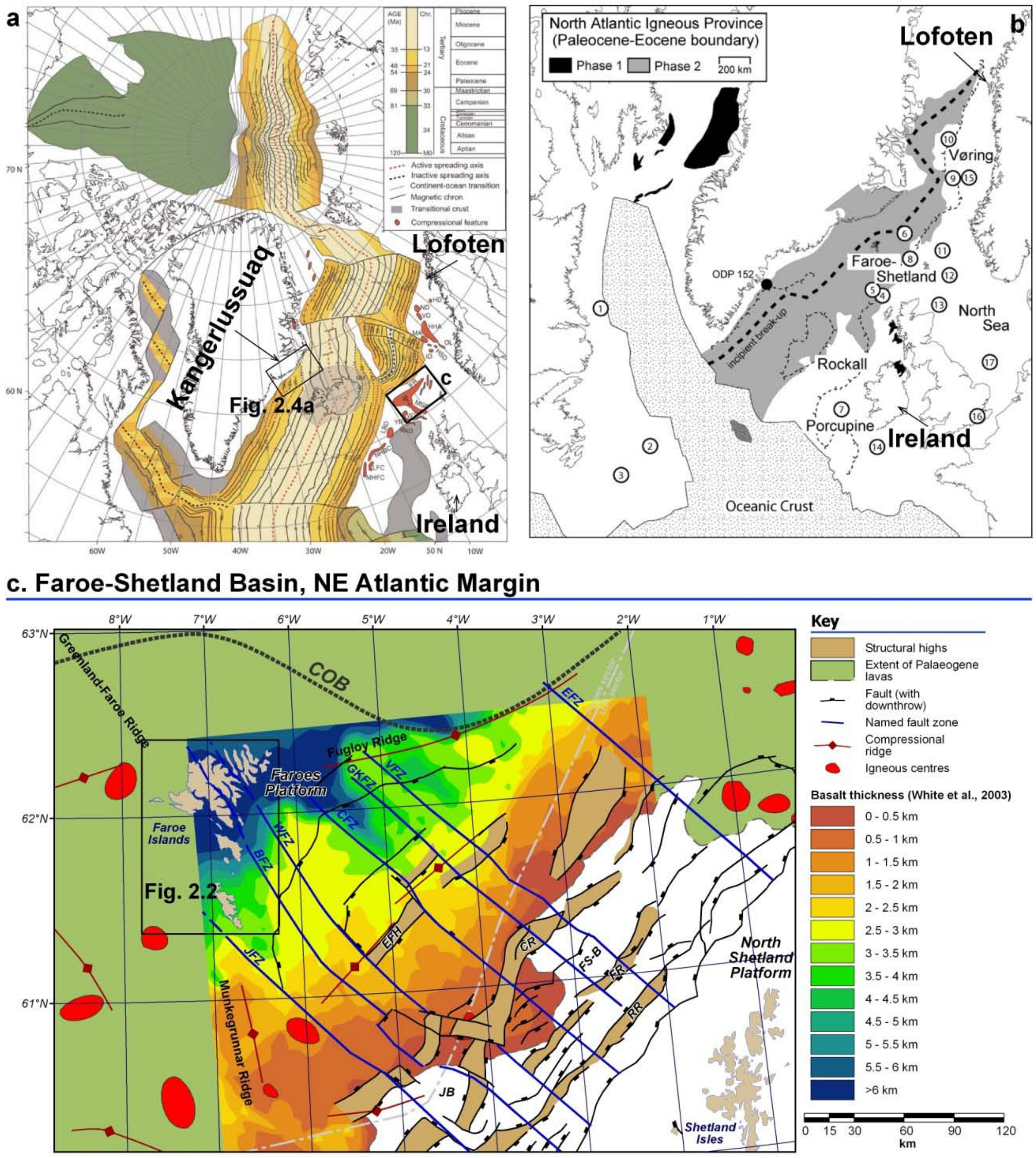

Fig. 2.1. (**a**) Super-regional plate tectonic map of the NE Atlantic, Labrador Sea / Baffin Bay and Arctic Ocean. (Figure 1 of Doré et al., 2008; abbreviations: **AD**, Alpin Dome; **FR**, Fugløy Ridge; **HD**, Hedda Dome; **HHA**, Helland Hansen Arch; **HSD**, Havsule Dome; **ID**, Isak Dome; **IIM**, Iceland Insular Margin; **LBD**, Lousy Bank Dome; **LFC**, Lyonesse Fold Complex; **MA**, Modgunn Arch; **MGR**, Munkagunnar Ridge; **MHFC**, Mid-Hatton Bank Fold Complex; **ND**, Naglfar Dome; **NHBA**, North Hatton Basin Anticline; **NHBC**, North Hatton Bank Fold Complex; **OL**, Ormen Lange Dome; **VD**, Vema Dome; **WTR**, Wyville Thomson Ridge; **YR**, Ymir Ridge). (**b**) North Atlantic tectonic reconstruction for the Palaeocene/Eocene boundary, immediately prior to plate separation between Europe and Greenland (Figure 7 in Saunders et al., 2008); (**c**) Structural

(Fig. 2.1 continued) elements map of the Faroe-Shetland Basin, NE Atlantic Margin. **EFH**, East Faroe High; **FS-B**, Flett Sub-Basin; **JB**, Judd Basin; **CR**, Corona Ridge; **FR**, Flett Ridge; **RR**, Rona Ridge; **BFZ**, Brynhild Fault-Zone; **CFZ**, Clair Fault-Zone; **EFZ**, Erlend Fault-Zone; **GKFZ**, Grimur Kamban Fault-Zone; **JFZ**, Judd Fault-Zone; **VFZ**, Victory Fault-Zone; **WFZ**, Westray Fault-Zone**.** (After Stoker et al., 1993; Rumph et al., 1993; Lundin and Doré, 1997; Sørensen, 2003; White et al., 2003; Jolley and Morten, 2007; Ellis et al., 2009).

The purpose of this chapter is to introduce the margin- to island-scale geological history of the Faroes and the NE Atlantic Margin, including formation of the NE Atlantic, and its marginal basins, and emplacement of the NAIP. The second half of the chapter details remote-sensing analyses undertaken as part of this study, upon which field-based analyses were then directed (as detailed in *Chapters 3-5*).

2.2 Geological setting: a review

2.2.1 The North Atlantic Igneous Province

The NAIP was emplaced during the Palaeocene and Eocene, across an area of 1.3 x 10^6 km^2, and is believed to represent a volume of mainly mafic igneous extrusive rocks (basalts) in excess of 1.8 x 10^6 km^3 (Eldholm and Grue, 1994). Magneto-stratigraphy and radiometric dating (U-Pb and Ar-Ar) indicate that the NAIP was emplaced in two main phases (**Fig. 2.1b**; Saunders et al., 1997, 2007). The first phase occurred within magnetochron 26r (Selandian, 62-59Ma), with intra-plate magmatism in the British Isles, SE and W. Greenland, and Baffin, and possibly, central E. Greenland (Saunders et al., 2007). Phase 2 occurred within Chron 24r (Palaeocene - Eocene, ~56.5-54Ma), and was focussed on the passive margins between NW Europe, and E. Greenland.

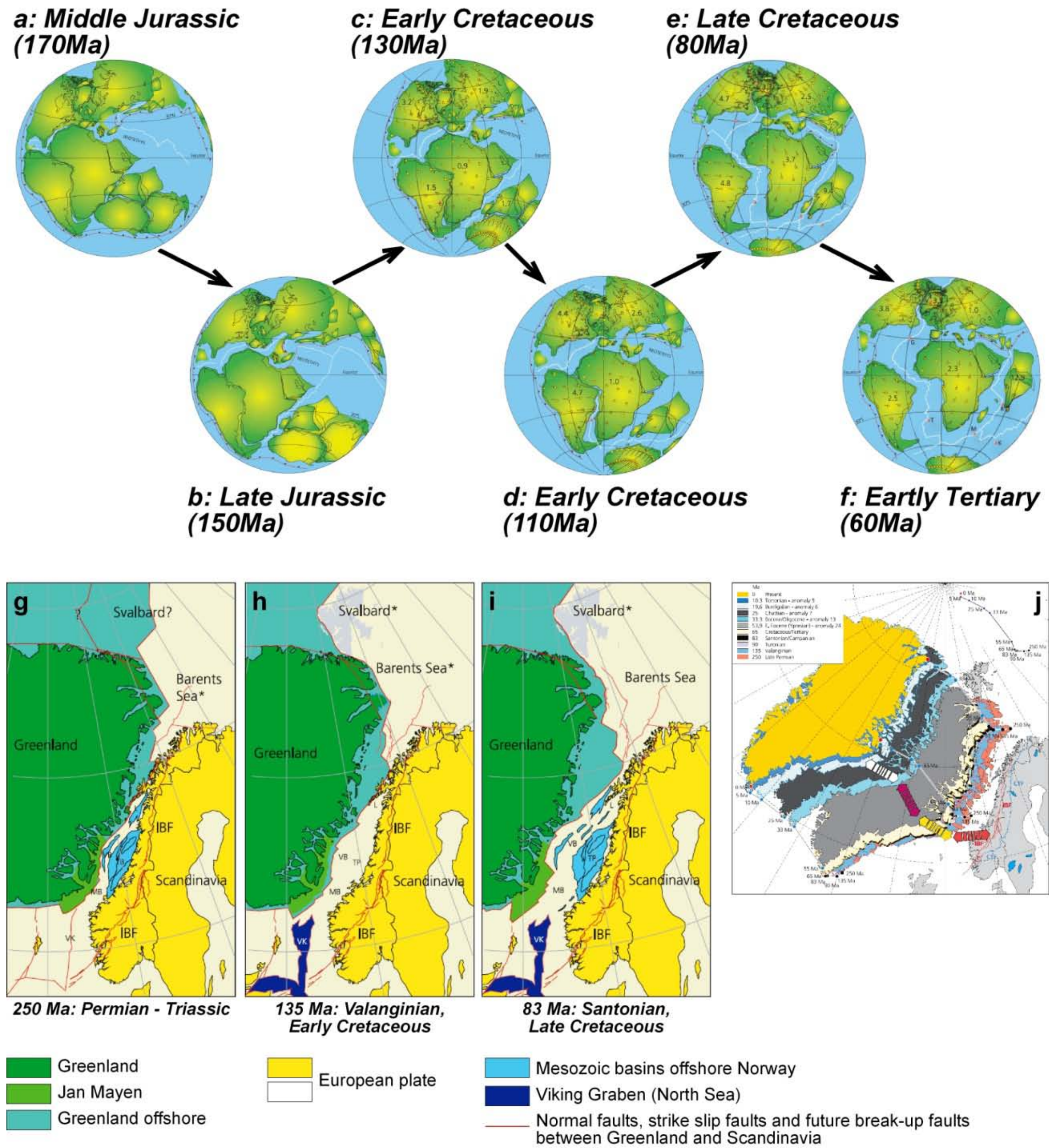

Fig. 2.2. (**a-f**) Stepwise plate reconstructions from the Middle Jurassic (a) to the Early Tertiary (f). (Mosar et al., 2002; Torsvik et al., 2002). (g-i) Pre-break-up plate tectonic reconstructions during the Late Permian (**g**: 250 Ma), Early Cretaceous (**h**: 135 Ma – Valanginian) and Late Cretaceous (**i**: 83 Ma - Santonian/Campanian). (Adapted from Figure 9 of Mosar et al., 2002). (**j**) Sequential reconstruction of separation between Greenland and Scandinavia (Figure 10 in Mosar et al., 2002).

The emplacement of the NAIP is believed to be contemporaneous with rifting of the continental lithosphere that occurred during the build up to the opening of the NE Atlantic. The genesis of the igneous province can be, and has been related to the development of regional elevated asthenosphere temperatures driven by a mantle hot-spot (i.e. the putative Iceland Plume; e.g. White, 1988; Hansen et al., 2009, and references therein). At present this hot-spot lies beneath Iceland and is responsible for the generation of igneous crust in excess of 15km thickness, and has, during the development of the N. Atlantic, led to the formation of the 25-30km thick igneous Greenland-Faroe ridge (**Fig. 2.1c**; Vink 1984).

2.2.2 The development of the NE Atlantic continental margins

From the early Permian until the Early Palaeocene, North America, Greenland and Europe were conjoined, forming parts of the evolving Pangaean and Laurasian continents (**Fig. 2.2a-f**). From as early as the Carboniferous, the present-day NE Atlantic region, like its neighbouring areas and much of Pangaea, was subjected to a series of rift events during a prolonged period of continental reorganisation. By the mid-Jurassic (**Fig. 2.2a**), continental break-up was achieved in the central Atlantic. During the late Jurassic (**Fig. 2.2b**), sea-floor spreading in the Central Atlantic connected north-eastwards to Neotethys, via the Gibraltar-Azores transform, resulting in the break-up of Pangaea, and the birth of Laurasia and Gondwana. Throughout the Cretaceous (**Fig. 2.2c-e**) and into the Palaeogene (**Fig. 2.2f**), Central Atlantic spreading continued as a northward unzipping of Laurasia, between North America and Greenland through the Labrador Sea, and out into Baffin Bay. During the Palaeocene, and into the early Eocene, continental rifting between Eurasia and Greenland culminated in formation of the NE Atlantic, eventually causing a shut-down of spreading in the Labrador Sea. Numerous studies have addressed the continental break-up between Greenland and Eurasia (Lundin and Doré, 1997; Doré et al., 1999; Lundin and Doré, 2002). Only a brief synopsis is given here.

The build-up to the formation of the NE Atlantic arguably extends back to the Devonian, with collapse of the Caledonian Orogeny leading to the development of several basins in the proto North Atlantic region (Roberts et al., 1999), followed by subsequent rifts in the Devono-Carboniferous, Permo-Triassic, Cretaceous and Palaeocene (Coward, 1990). In the Carboniferous to the Permo-Triassic, N-S trending half-grabens (**Fig. 2.2g**) accommodated continental conglomerate and sandstone deposits in East Greenland, with shelf to deep-shelf carbonate deposition recorded in the Barents Sea region (Torsvik et al., 2002). Rift basins of that age were reactivated during Jurassic-Cretaceous rift events (**Fig. 2.2h, i**), before outboard migration of the rift axis. The reactivation of pre-existing faults and fabrics in the continental lithosphere as it experiences rift-related deformation is recognised worldwide (e.g. Sibson, 1995; Holdsworth et al., 1997; Wilson et al., 2009), and such a phenomenon is commonly invoked to explain Cretaceous and later rift segmentation on the Atlantic margins.

During the Late Jurassic, and possibly as early as the Permo-Triassic, E-W extension in the northern North Sea resulted in the development of N-S trending rift basins such as the Viking and Central grabens (Badley et al., 1988; Bartholomew et al., 1993; Færseth et al., 1995; Doré et al., 1999; **Fig. 2.2j**). Rifting continued into the Early Cretaceous, with the regional extension vector rotated into a more NW-SE orientation (**Fig. 2.2j**). Rifting became refocused onto the Atlantic margin, at this time initiating a NE-SW trending chain of basins extending from the SW Barents Sea, through the Faroe-Shetland basin and down to the Rockall trough (Doré et al., 1999). As mentioned previously, basins formed at that time and trend are thought to be segmented by a series of NW-SE trending lineaments, termed 'transfer-zones,' that appear to run sub-parallel to the oceanic transform faults. Onshore studies of the geology exposed adjacent to transfer zones in the Faroe Islands (Ellis et al., 2009) have interpreted them as major strike-slip fault zones. Recent offshore studies in the Faroe-Shetland Basin (Moy and Imber, 2009) however, indicate that some of these features may be related to igneous intrusions, transfer of extensional stress between en-echelon rift segments, and low seismic data-resolution, with little or no evidence for the regional development of strike-slip fault zones. Extension continued along a NW-SE vector through the Cretaceous and into the Palaeogene, as a precursor to continental break-up and ocean-floor spreading during Chron 24r (ca. 56 – 54 Ma; Berggren et al., 1995; Saunders et al., 1997). Evidence for this continental extensional faulting is best preserved in sections west of Lofoten, such as in the Vøring Basin, and down to the Møre Basin (**Figs. 2.2h, i**). The Palaeocene stratigraphy thickens rapidly westwards from the Møre Basin, before becoming obscured by a cover of thick trap-style basalts of the NAIP.

Three post-North Atlantic opening compressional phases have been reported within the Faroe-Rockall region, based on the development of folds and basin inversion structures (Anderson and Boldreel, 1995; Boldreel and Anderson, 1998; **Fig. 2.1a, c**), the timings of which are constrained to be as follows: 1) *Late Palaeocene to Early Eocene*, affecting the Wyville-Thompson, Munkegrunnar and Ymir Ridges, possibly related to the interplay between ridge-push from the newly formed NE Atlantic, and Tethyan closure events and associated Alpine stresses; 2) *Oligocene*, forming NE-SW to ENE-WSW-trending fold axes developed between the Hatton Bank and to the east of the Faroe Islands, related to initiation of the Kolbeinsey ridge; and 3) *Miocene*, forming NW-trending anticlines to the N, W, and SW of the Faroe Islands, which have been related to changes in the magnitude of forces driving the Eurasian plate.

2.2.3 The development and significance of NW-SE-trending lineaments

Many of the regional basins developed along the NE Atlantic margin appear to be segmented by NW-SE-trending lineaments that are commonly referred to as transfer zones (e.g. Rumph et al., 1993; Doré et al., 1997; Naylor et al., 1999; Ellis et al., 2002; Ellis et al., 2009). Such zones are believed to facilitate differential extension within the basins, and may be rooted in the pre-existing Precambrian and younger structures developed in the continental basement along the margin (e.g. Wilson et al., 2006 and references therein). Structures of this kind should have a dominantly strike-slip motion sense associated with them. In terms of the Faroe-Shetland Basin (FSB), left-lateral oblique-slip displacements are commonly invoked along transfer-zones prior to and during continental break-up (e.g. Ellis et al., 2009). Plate reconstructions indicate that prior to continental break-up, the Faroe Islands were located no more than 120km from the Kangerlussuaq region of East Greenland (Saunders et al., 1997; Larsen et al., 1999; **Figs. 2.1b, 2.2g-j**). Studies of the sedimentary succession of Kangerlussuaq indicate that sedimentation in the area was controlled by major NW-SE-trending faults (Larsen and Whitham, 2005). Similarly, heavy mineral and phytogeographic analyses suggest a strong NW-SE-oriented control on infilling within the FSB from the East Greenland and Shetland areas (Jolley and Morten, 2007). Notably, distinct heavy mineral segregations within the FSB require NW-SE sediment channelling from point sources along the margin. When considering the nature of these NW-SE lineaments, it is therefore important to include evidence from East Greenland.

Primarily on the basis of sedimentary thickness variations, the Kangerlussuaq basin (**Fig. 2.3a**) is believed to have developed over 3 broad stages, involving: (1) initiation, (2) infill, and (3) re-inititiation to extinction phases, lasting from the late Cretaceous through to the Palaeogene (Larsen and Whitham, 2005). Thickening appears to have occurred within the Cretaceous, pre-volcanic and post-volcanic Palaeogene, most notably from NE to SW across Nansen Fjord, a large NW-SE trending fjord located east of Kangerlussuaq (**Fig. 2.3b**). Problematically, this therefore puts the critical controlling

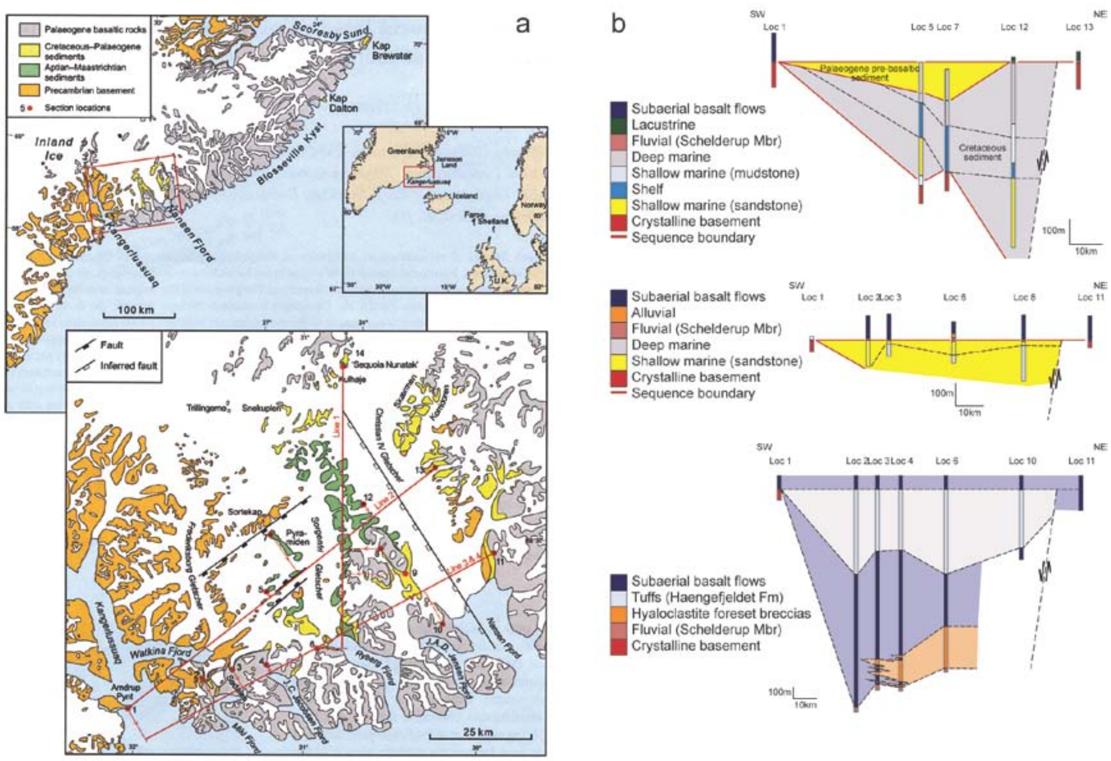

Fig. 2.3. (**a**) Geological map of the Kangerlussuaq area in southern East Greenland showing distribution of Cretaceous-Palaeogene sediments and Palaeogene basaltic rocks. Red lines indicate positions of cross-sections in *b*. (Figure 2 of Larsen and Whitham, 2005). (**b**) Geological cross sections corresponding to lines in *a*. (Redrawn from Figure 7 of Larsen and Whitham, 2005).

structure in the sub-sea and sub-ice regions of the fjord, i.e. it is not exposed at the surface (**Fig. 2.3a**).

Neither the FSB nor East Greenland have yet yielded true kinematic data to constrain the development of the NW-SE trending lineaments that span the continental margins. Due to a lack of sub-areal exposure, inferences as to the actual kinematics have been built largely on the resultant stratigraphic thickness variations, rather than on observed structures. Offshore studies specifically targeting the so-called 'transfer' lineaments have found no obvious evidence for large lateral displacements (e.g. Moy and Imber, 2009; see also Wilson et al. 2006 for an equivalent onshore study of such features in the Lofoten margin in Norway). Instead, they appear to be complex zones with varying characteristics from one lineament to the next, as well as along the trend of a single lineament. Furthermore, and rather curiously, the lineament spacings in the FSB are markedly shorter than they are between lineaments elsewhere along the margin. We therefore argue that this presents grounds for viewing the NW-SE trending lineaments on a case-by-case basis, rather than collectively.

Projections of three of the Faroe-Shetland transfer zone lineaments intersect the Faroe Islands: from SW to NE, the Judd, Brynhild, and Westray lineaments (**Fig. 2.1c**). (The Clair lineament trend is also aligned with a fjord in the Faroes, between Svinoy and Fugloy (**Figs. 2.1c** and **2.4**), however intriguingly, no structural maps of the region show a continuation of the lineament into the islands). The Faroe Islands present a unique opportunity in the region to study the sub-seismic-scale nature, kinematics, and possible effects on sedimentation/magmatic emplacement, of these basin-scale transfer zones.

2.2.4 The Faroe Islands Basalt Group

The Faroe Island Basalt Group (FIBG) represents a small part of the NAIP (**Figs. 2.1** and **2.4**), and was emplaced between Chrons 26 and 24 (59 – 56 Ma), at which time the Faroe Islands and East Greenland were less than 120km apart, based on plate reconstructions and geochemical correlations between sequences (Larsen et al., 1999; Lundin and Doré, 2002). Remnants of the FIBG are exposed on the Faroe Islands, with a true thickness of ~3km, and an overall stratigraphic thickness in excess of 6.6km (**Fig. 2.4**; Passey and Bell, 2007), of which about 3km is exposed above sea level (Ellis et al., 2002). The FIBG is dominated by tholeiitic basalt lavas indicating that their eruption was during a period experiencing a high degree of partial melting of the mantle (Waagstein, 1988). The FIBG is divided into some 7 Formations based on lithology and the development of mappable disconformity surfaces (Rasmussen and Noe-Nygaard, 1969 & 1970; Passey et al. 2006) and geochemistry (Waagstein, 1988). The lower-most of these, the *Lopra Formation*, is not exposed sub-aerially, and has only been encountered in the onshore borehole Lopra-1/1A (Rasmussen and Noe-Nygaard, 1970; Hald and Waagstein, 1984; Passey and Bell, 2007). The Lopra Formation comprises a

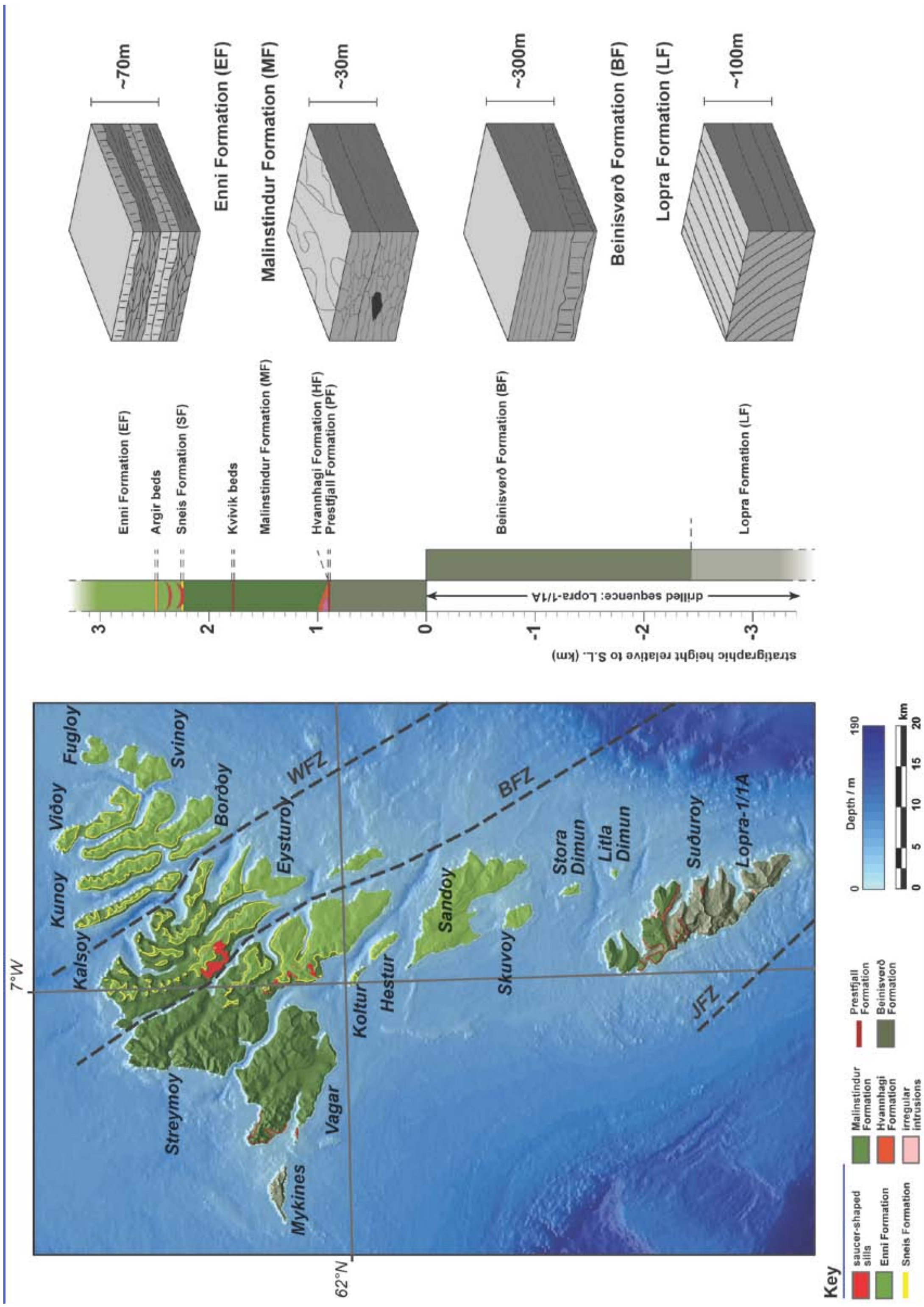

Fig. 2.4. Simplified geological map of the Faroe Islands, with gross stratigraphic column for the Faroe Islands Basalt Group, and typical facies architectures of the 4 major formations in the group (Lopra, Beinisvørð, Malinstindur and Enni Formations). (After Passey and Bell, 2007; Passey, 2008).

>1km thick sequence of volcaniclastic rocks and hyaloclastites (Ellis et al., 2002), and was emplaced into marine waters believed to be, initially, about 200m deep. Prograding clinoform sets imaged in seismic-sections (Smallwood and Gill, 2002; Jerram et al., 2009) indicate that regional subsidence was continuous at this time, and faster than emplacement of the Lopra Formation.

Above the Lopra Formation is the ca. 3.3km thick *Beinisvørð Formation* (**Fig. 2.4**), of which only 900m is exposed on the islands. The Beinisvørð Formation generally comprises aphyric, laterally extensive sheet lobes, with minor intercalated volcaniclastic horizons, and was emplaced at or around sea level, requiring that subsidence and emplacement rates were comparable throughout. Exposure of the Beinisvørð Formation is limited to the southern island, Suðuroy, and in the west of the northern islands, Vagar and Mykines (**Fig. 2.4**). Lavas of the Beinisvørð Formation typically display very well developed columnar (cooling) jointing, which ranges from simple colonnades in lower parts of the flows, to complex upper entablature zones in some instances. Above this lies the 3-15m thick *Prestfjall Formation*, comprising coals, mudstones and sandstones deposited in swamps, lacustrine and fluvial environments, during a hiatus in volcanic activity (Rasmussen and Noe-Nygaard, 1969 & 1970; Lund, 1983 &1989; Passey and Bell, 2007). Volcanic activity resumed, resulting in the deposition of about 50m of basaltic tuffs interbedded with volcaniclastic floodplain facies and flow deposits forming the *Hvannhagi Formation*. Exposure of the Prestfjall and Hvannhagi Formations is limited to Suðuroy and west Vagar (**Fig. 2.4**).

Trap-style volcanism continued with the eruption of the <1.4km thick *Malinstindur Formation* (**Fig. 2.4**), subaerial compound basalt lavas that are initially olivine-phyric evolving upwards within the sequence to aphyric, and then plagioclase-phyric. The Malinstindur Formation is particularly well exposed on the northern islands of Vagar, Streymoy and Eysturoy, at low-altitudes on the north-eastern islands, and in the north of Suðuroy. Jointing within the Malinstindur Formation is more poorly developed than that in the Beinisvørð Formation, however it remains a notable and easily identifiable feature. Above the Malinstindur Formation lie the c.25m thick, laterally extensive volcaniclastic sandstones and conglomerates of the *Sneis Formation*, which is divided into two parts: the basal, ~50cm thick Sund bed, and the thick conglomerates above. The Sund bed is a reddened unit, predominantly composed of medium grained volcaniclastic sands. The conglomerates above are generally greyish red, matrix-supported, with sub-angular to sub-rounded clasts. Lateral variations of the conglomerate dominated facies, from N-S, indicate that it was sourced from the North, and transported southwards, with the internal architecture and lithofacies indicating mass flow events of varying concentrations.

The Sneis Formation is overlain by about 900m of the *Enni Formation* (**Fig. 2.4**), which comprises low-TiO_2 and high-TiO_2 (MORB-like) interbedded simple (sheet lobes) and compound tholeiitic lavas. The 900m is a minimum thickness, with a significant amount (in the order of hundreds of metres) eroded from the top of the volcanic pile (Waagstein et al., 2002). The Enni Formation is exposed in a north to north-east arcing trend from Sandoy across the northern islands (**Fig. 2.4**).

There are a number of notable sheet-like intrusions on the islands, including the large 'saucer-shaped' *Streymoy* and *Eysturoy sills*, and the *Fugloy-Svinoy sill*. The Streymoy and Eysturoy sills are transgressive, lying stratigraphically close to the Sneis Formation (**Fig. 2.4**). The Eysturoy sill occupies an area of about 16km^2, and ranges in thickness from 10-55m (Rasmussen and Noe-Nygaard, 1970). Generally the Eysturoy sill dips SW, displaying a pronounced flat section at the level of the Sneis Formation. The Streymoy sill also ranges from ~10-55m thickness, but only covers an area of about 13km^2, and displays a much more saucer-like geometry, again with numerous ramp- and flat-sections, cutting upwards from within the top part of the Malinstindur Formation, becoming flat at the level of the Sneis Formation, and then ramping upwards again into the Enni Formation.The Fugloy-Svinoy sill is slightly higher in the succession and is found entirely within the Enni Formation. Again it is transgressive, ramping upwards on Svinoy to the SE, and to the NE on Fugloy (Rasmussen and Noe-Nygaard, 1970). In total, the sill has an area of about 2.5km^2, and ranges in thickness from 15-36m.

2.3 Remote-sensed data: acquisition and implications

2.3.1 Stratigraphic horizon modeling

Individual lava units commonly display considerable relief at their upper and lower contacts, due to the effects of erosion (during periods of volcanic quiescence) or fluidization of wet sediments as a result of fuel-coolant interaction (FCI) processes (e.g. Kokelaar, 1982) during emplacement (**Fig. 2.5**). In such cases it is difficult to accurately measure a representative true-dip of the horizons at a local or outcrop scale using a compass-clinometer. The method employed here uses a combination of field observations and remote-sensing analyses to create a regional structural map of the horizons developed across the islands.

Field observations (**Fig. 2.6a**) were used to identify flow-unit tops that form crag-lines, or topographic benches, which were mapped and digitized using high-resolution aerial

Fig. 2.5. (**a**) Centimetre and (**b**) decimetre scale topographic undulations on sedimentary horizons within the FIBG (both examples from the Malinstindur Formation, Eysturoy). Such undulations are common and, combined with the surface topography of the lava units, reduce the accuracy of field-based unit inclination measurements.

photographs and topography from digital elevation data (**Fig. 2.6b**). The locations of the crag-lines were then verified using derivatives of the topography (such as slope and break-in-slope) in ArcGIS™. These georeferenced lines can then be directly imported into 3D modeling software packages such as GOCAD® (of Paradigm™). The lines can then be used to model geometrically accurate surfaces, provided that there are more than two points (two points only representing a plunging line) and that the points are more than 10m apart, as dictated by the resolution of the topographic data (**Fig. 2.6c**).

The layering orientation data that result from this method (**Fig. 2.7a**) closely parallel the results of more typical, detailed field studies (notably Rasmussen, 1990) and are therefore deemed to accurately represent horizon geometry (e.g. **Fig. 2.6a**). The layering data record the development of an apparent broad monoclinal fold-like feature (**Fig. 2.7b**), with an arcing hinge located offshore to the west and around to the north. Based on available seismic data (e.g. Sørensen, 2003), it is however more likely that beyond the fold hinge lies an antithetic fold-limb, completing an asymmetrical fold architecture, with the Faroes sitting near the apex on the steep limb. Generally, horizon inclination decreases up-stratigraphy through the FIBG, with the largest, ~8° (SE) dips, observed on Mykines within the Beinisvørð Formation (**Fig. 2.7a**). This decreases to ~3° (SE) in the Malinstindur Formation on Vagar, and Streymoy, and again to ~1-2° (SE) in the Enni Formation in the NE (e.g. Borðoy, Viðoy, etc.). High eastward dips, ~6° (E), are recorded on Sandoy within the youngest exposed units of the FIBG. In

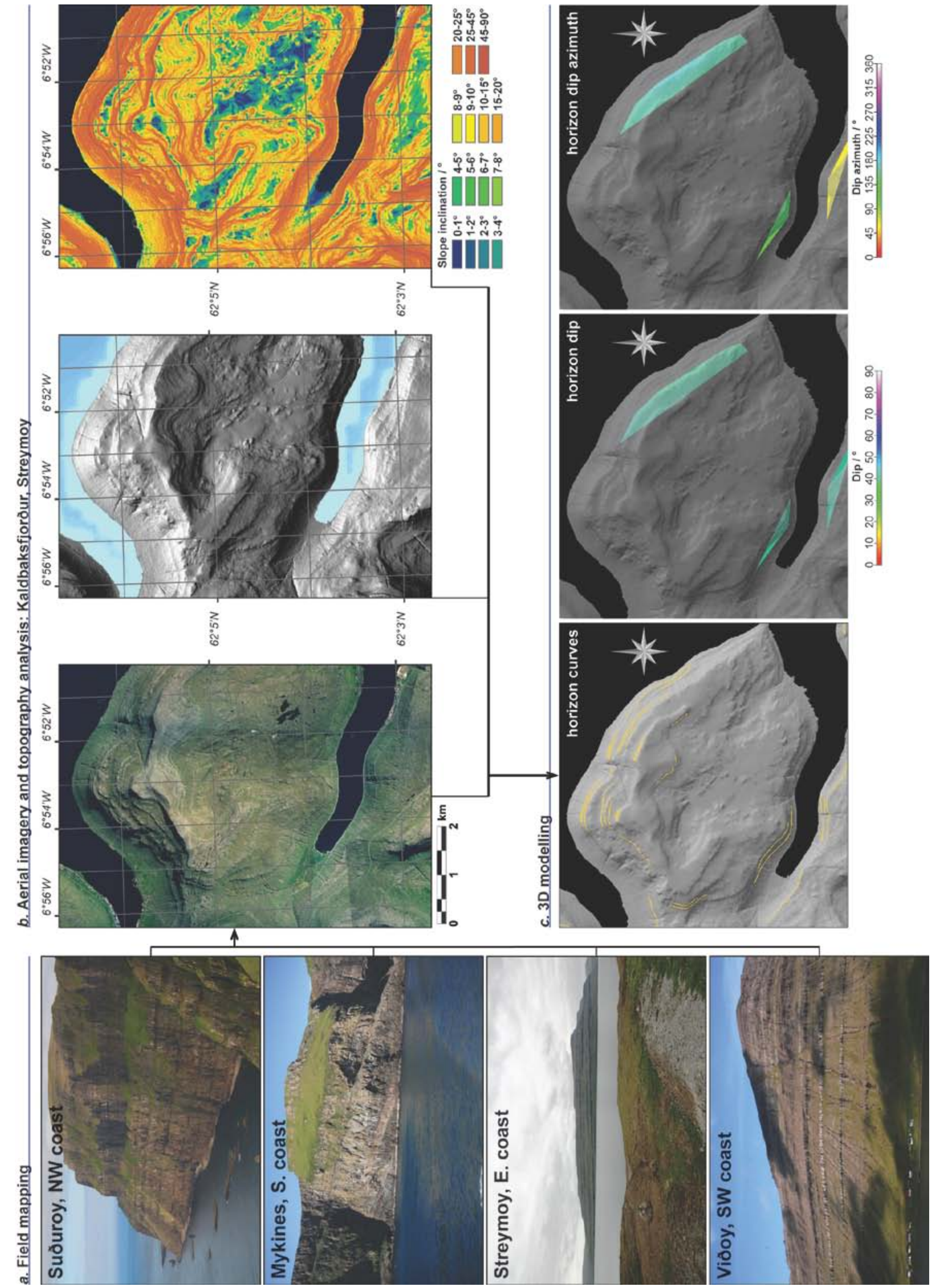
a. Field mapping
Suðuroy, NW coast
Mykines, S. coast
Streymoy, E. coast
Viðoy, SW coast
b. Aerial imagery and topography analysis: Kaldbaksfjorður, Streymoy
6°56'W
6°54'W
6°52'W
62°5'N
62°3'N
km
Slope inclination / °
c. 3D modelling
horizon curves
horizon dip
horizon dip azimuth
Dip / °
Dip azimuth / °

Fig. 2.6. (*Previous page*) Methodology for creating geological horizons: (**a**) Crag-lines representative of flow unit tops, bottoms and sedimentary strata are mapped in the field. (**b**) Field maps are digitised in ArcGIS, and crag line positions verified using high-res aerial/satellite imagery and topographic derivatives such as hillshades, slope and aspect (not shown). (**c**) Geo-referenced crag line shapefiles are imported into Gocad, and draped onto topography. 3D curves with a sufficient extent (>30m) are used to create planes, representative of the geological horizon.

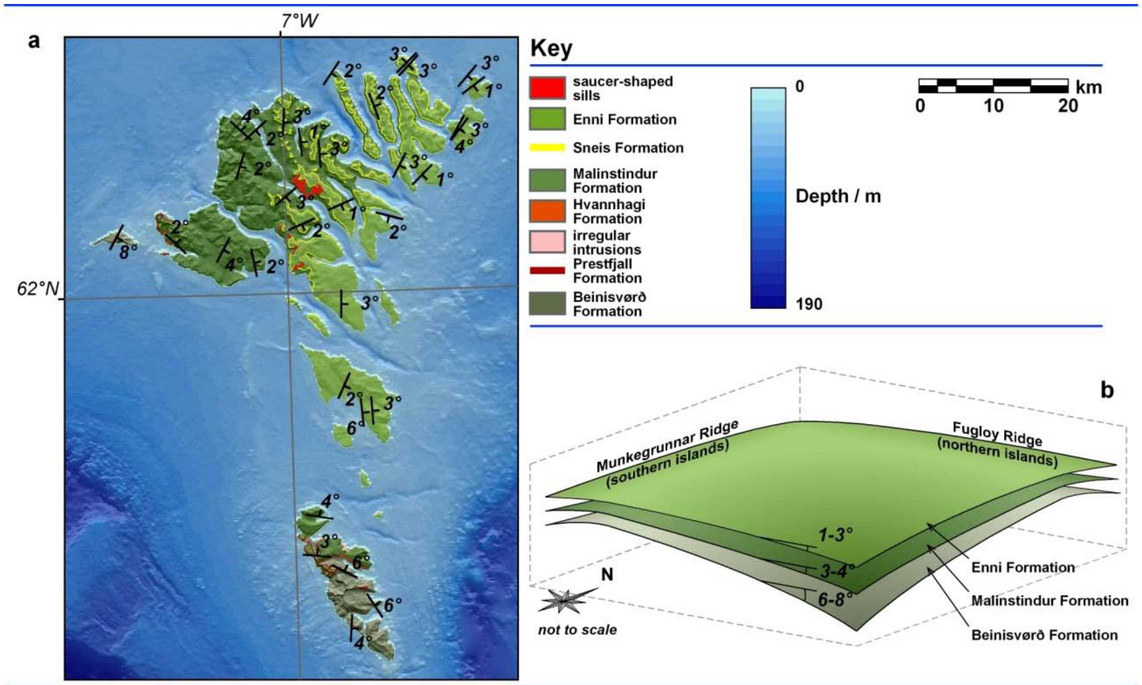

Fig. 2.7. (**a**) Simplified horizon orientation map for the Faroe Islands, based on the analysis described in Figure 6. (**b**) Simplified conceptual model for the fold architecture of the Faroe Platform. Folds have developed through time, resulting in a decreasing horizon inclination up stratigraphy. Evidence from offshore seismic surveys indicates that the Munkegrunnar and Fugloy ridges are marginally asymmetric folds, with the Faroes located off-axis on the steeper fold limb.

the south, on Suðuroy, units are more E to NE dipping, with values of 8° (E) in the east, decreasing westwards to ~1° (NE) at the coast (**Fig. 2.7a**).

Fold architecture across the islands is indicative of progressive fold growth through time. Areas that do not obey this relationship are closely associated with large offset faults (e.g. Skopunarfjorður, between Streymoy and Sandoy; Passey, 2009), and may indicate localised fault-block-rotations (see *Chapter 3*). The westward decrease in dip on Suðuroy may relate to the effect of down-warping during subsidence-related movement on the Judd Fault Zone nearby offshore, or to the proximity of a fold-axis (i.e. the Munkegrunnar Ridge; **Figs. 2.1 and 2.7b**).

2.3.2 'Saucer-shaped' sill geometry

The Faroe Islands are host to numerous large 'saucer-shaped' sills. Here we focus on two such intrusions: the main Streymoy and Eysturoy sills. Both are located on their respective island's western coasts and form a prominent crag that is lower in the SW and generally ramps upwards towards the island interior in both cases. Some previous workers (e.g. Geoffroy et al., 1994) have suggested that the sills relate to an island-wide, synmagmatic, compression event, based on their apparent geometric similarities with thrust-faulting on the Islands.

The model created in this study uses a similar methodology to that used for the stratigraphic horizon modelling. As these sills form a prominent crag-line, the top exposure can easily be mapped using topography and aerial photographs (**Fig. 2.8a-c**). Again, remote-sensed picks have been verified during field study to assess the validity of the methodology. An obvious limitation to the technique is that the top surface of the sills may not represent the actual top, more an erosional surface. However, field-based observations indicate that the picked surfaces are likely within (+/-) 5m of the actual height of the sill top and therefore within the limiting resolution of the topography used during modelling. However, other sills on the islands (e.g. the Fugloy-Svinoy sill) are not such prominent features, and are therefore not included here.

From these models, it is clear that the sill geometries are rather more complex than previously detailed. In particular, the Streymoy sill displays numerous ramp and flat sections, and both sills display a broad flat section running NW-SE, roughly through the midline of their extent (**Fig. 2.9**). In the field it is clear that this flat section in some areas relates to the presence of the sedimentary Sneis Formation and it may be that other flat sections are related to the presence of other minor volcaniclastic horizons within the stratigraphy. The sills are also cut by numerous mineralised thrust and strike-slip faults (though not dykes; see *Chapter 3*), associated with N-S extension and E-W compression (event 2b; this study). It is therefore inferred that non-tectonic processes such as intrusion rate, and thickness of the overburden, likely control sill geometry in these two cases (e.g. Menand, 2008).

Fig. 2.8. (Next *page*) Methodology for creating 3D models of the Streymoy and Eysturoy sills. (Method described in Figure 6).

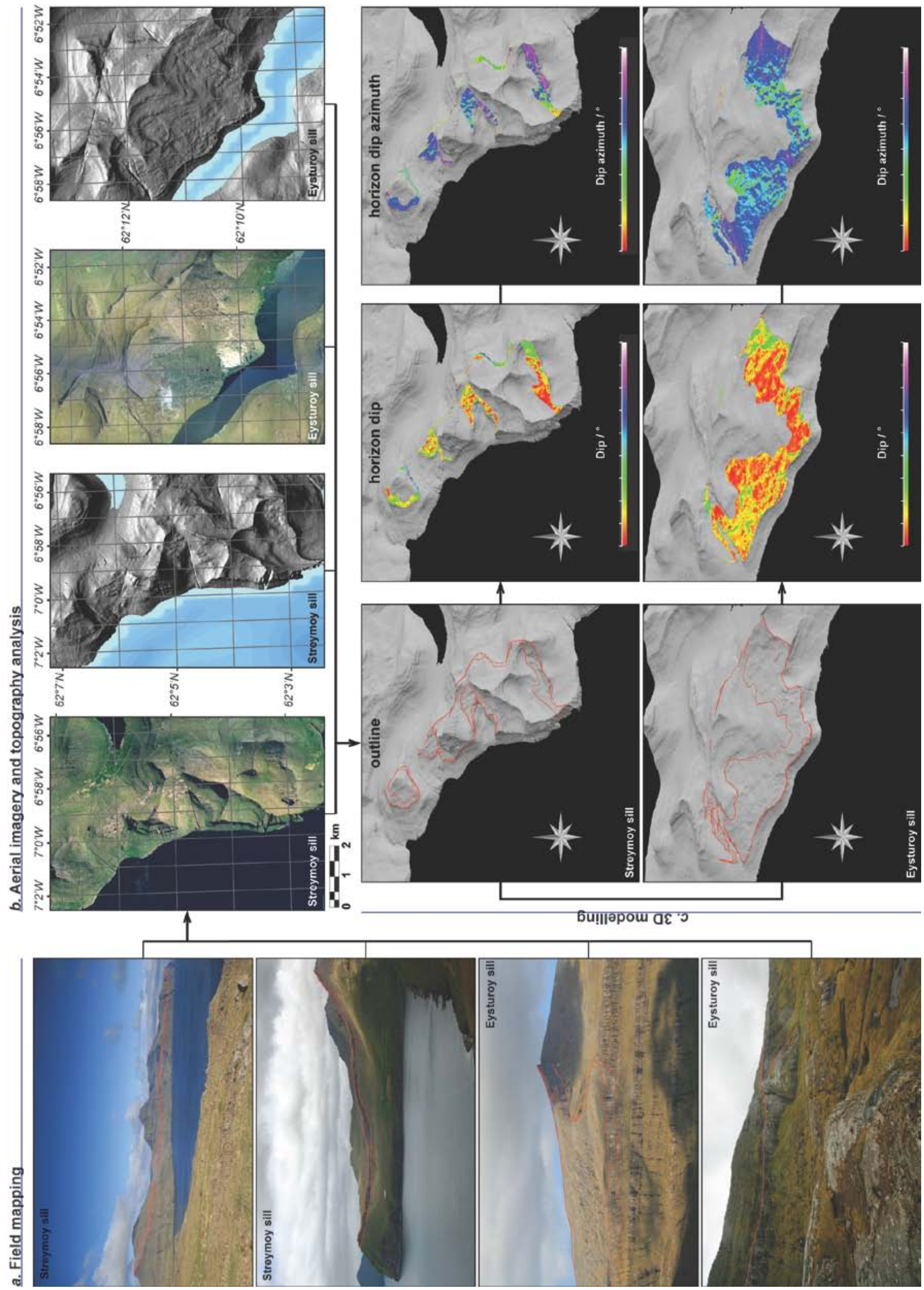
a. Field mapping
Streymoy sill
Streymoy sill
Eysturoy sill
Eysturoy sill
b. Aerial imagery and topography analysis
Streymoy sill
Streymoy sill
Eysturoy sill
Eysturoy sill
km
c. 3D modelling
outline
horizon dip
horizon dip azimuth
Streymoy sill
Eysturoy sill
Dip / °
Dip azimuth / °

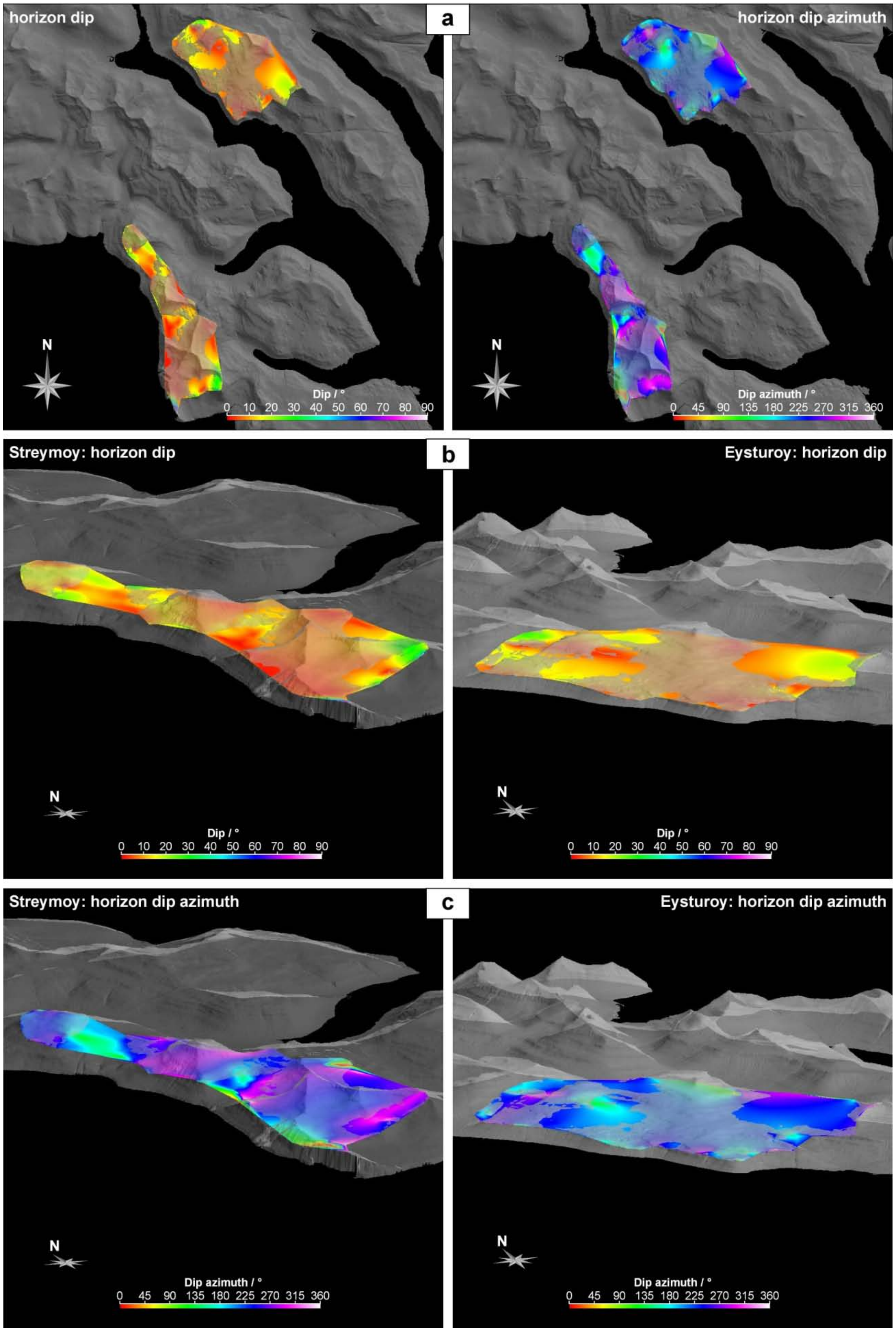
horizon dip
a
horizon dip azimuth
N
Dip / °
0 10 20 30 40 50 60 70 80 90
Dip azimuth / °
0 45 90 135 180 225 270 315 360
Streymoy: horizon dip
b
Eysturoy: horizon dip
Streymoy: horizon dip azimuth
c
Eysturoy: horizon dip azimuth

Fig. 2.9. (*Previous page*) Surfaces representative of the sill exposures (shown in Figure 8) are simplified and projected in order to fill gaps in the model (i.e. where the sills continue below the surface, or where they have been eroded). (Topography is displayed with a 50% transparency). See text for details.

2.3.3 Lineament analysis

2.3.3.1 Lineament analyses

Three lineament analyses targeting the orientations, lengths and spacing of dykes and faults, were conducted at different scales, using topographic (10m resolution) and bathymetric data (30m resolution), and 2D aerial and satellite images (0.5m resolution). The scales (1:250k, 1:50k and 1:5k) were strictly adhered to during analyses in order to appreciate any scaling bias and length vs. orientation relationships. Cross-referencing with published maps combined with close examination of the aerial photographs and field observations (**Fig. 2.10a-c**), ensures that the lineaments picked correspond to faults and dykes, and avoids the picking of any man-made or purely erosional features (e.g. road-cuttings and cliff or crag lines respectively). The spatial analyses of the lineaments were performed in ArcGIS™, with orientations recalculated and verified in Global Mapper™. Lineaments have been grouped into rose diagrams using arbitrarily referenced 5km grids (**Fig. 2.11**), by island, and by the youngest Formation they cut. Lineaments from the 1:50,000 analysis have been projected onto the topography to create planes within GOCAD®, in order to assess their 3D orientations.

Problems arise when trying to assess the nature of individual lineaments, as well as in attempting statistical analysis of lengths and spacing. In terms of their nature, it is not possible to remotely identify dykes as opposed to faults due in part to the resolution of the aerial images. In the field it is apparent that most dykes are reactivated by later faults (see *Chapter 3*). Nor can any means of discrimination be derived from the lineament orientation; fault and dyke sets (relating to specific events: *Chapter 3*) are closely grouped in terms of trend and large scale inclination (i.e. inclined individual faults appear to stack more or less vertically as fault zones, to the same collective inclination as similarly oriented dykes). The results of lineament spacing, and orientation vs. length analyses have not been included within this study for the following reasons: (1) Exposure, and the resolution of aerial images and digital elevation models is insufficient to resolve a representative proportion of faults and dykes; (2) There is evidence for numerous events and therefore, without detailed structural reconstructions, it is not possible to determine original spacings within an individual event; (3) The shape and size of the islands results in data truncation and censoring.

Lineament orientation analysis appears to be relatively unbiased by scaling, in that orientation dominance does not appear to change markedly across the different picking scales. Any differences between the 1:5,000 and 1:50,000 analyses are attributed to the resolution of the aerial images at those scales (i.e. minor lineaments,

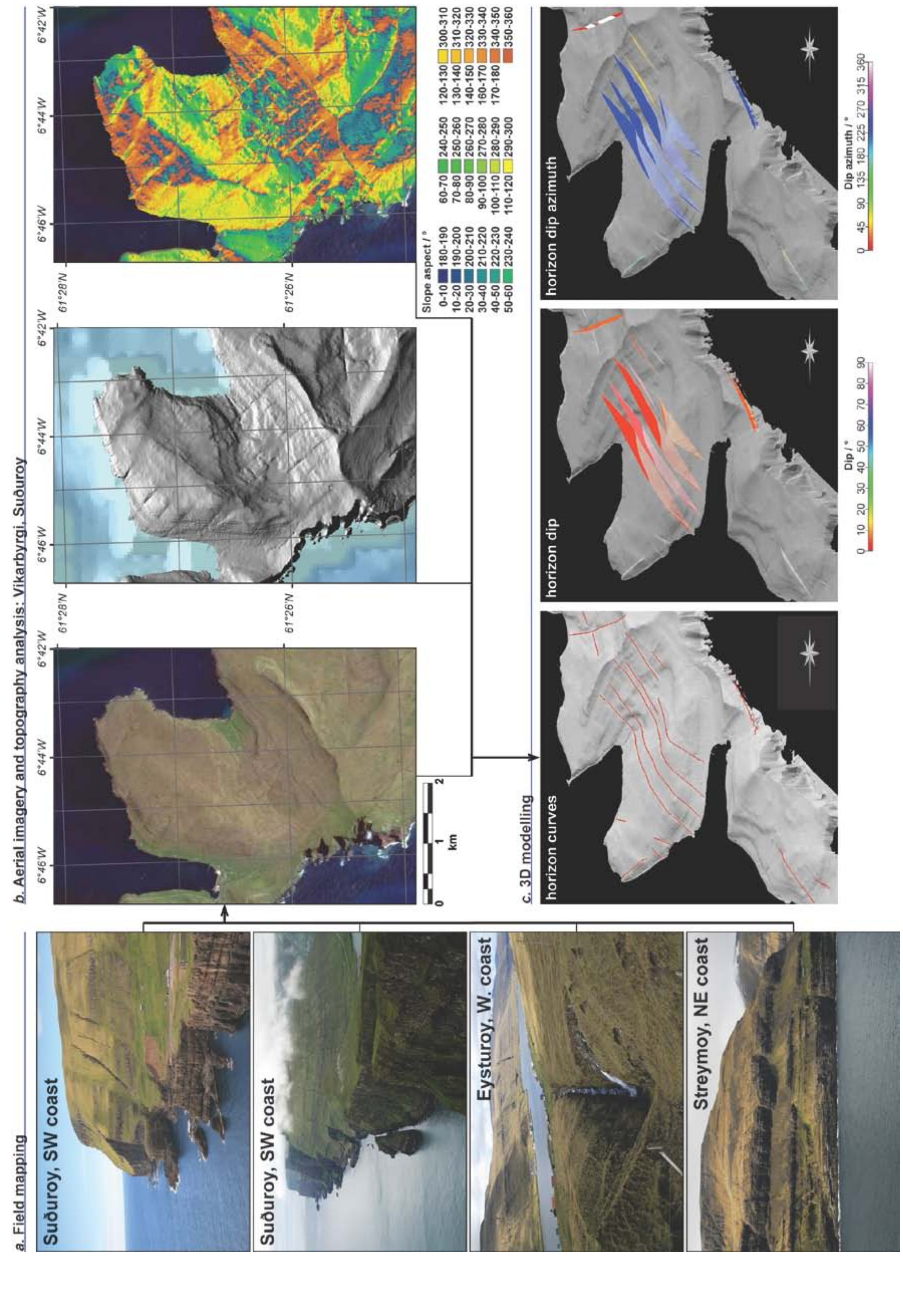
a. Field mapping
Suðuroy, SW coast
Suðuroy, SW coast
Eysturoy, W. coast
Streymoy, NE coast
b. Aerial imagery and topography analysis: Vikarbyrgi, Suðuroy
6°46'W
6°44'W
6°42'W
61°28'N
61°26'N
0
1
2
km
Slope aspect / °
c. 3D modelling
horizon curves
horizon dip
horizon dip azimuth
Dip / °
Dip azimuth / °

Fig. 2.10. (*Previous page*) (**a-c**) Methodology for creating 3D representations of lineaments across the Faroe Islands. (Method described in Figure 6).

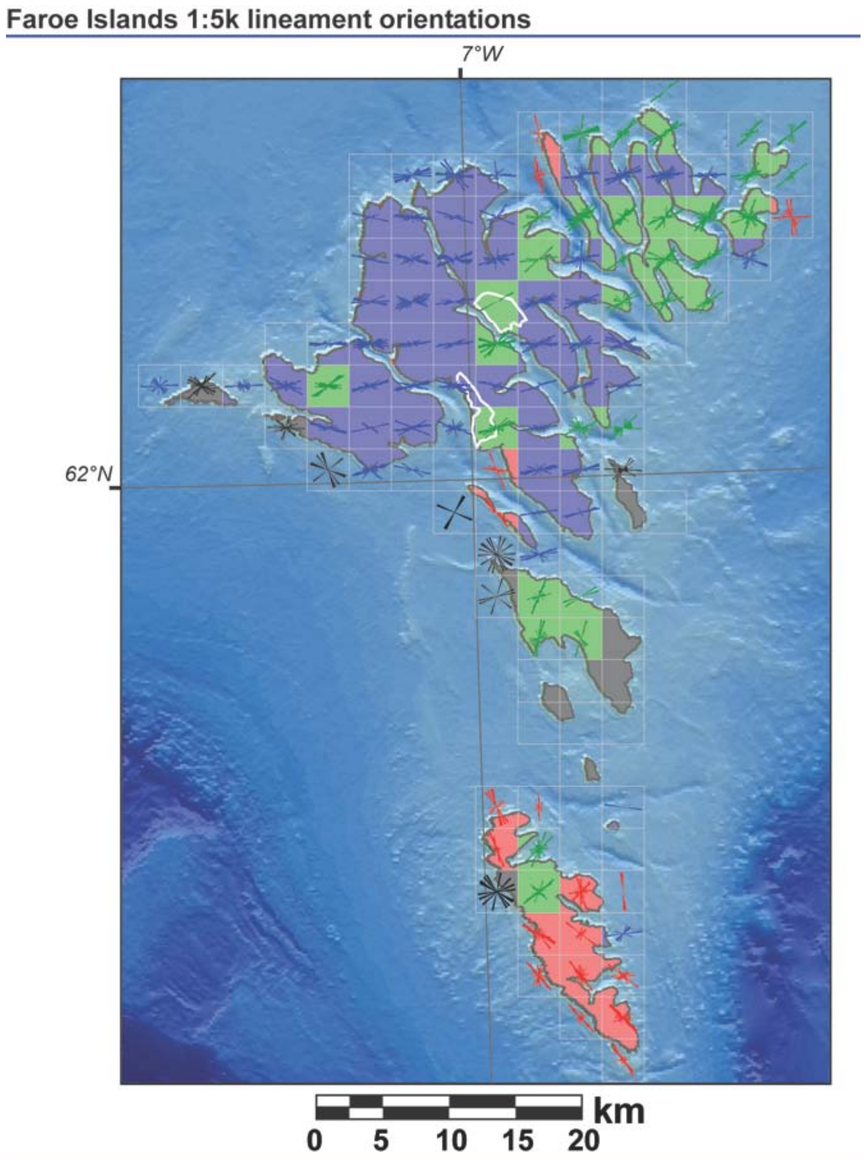

Fig. 2.11. 1:5k lineament analysis rose diagrams separated into 5km^2 bins. (Streymoy and Eysturoy sills outlined in white).

which commonly occur as subsidiary features to larger structures, are not so apparent in the larger scale analysis). At both scales, the dominant lineament trend and style varies markedly across the islands, correlating well with the age of the host lithology (**Figs. 2.11, 2.12**). In the southern island, Suðuroy, the dominant trend is generally NW-SE to NNW-SSE, corresponding to surfacing of the Beinisvørð Formation. In the west of the Northern Islands, there is a trend dominance of ESE-WNW through to ENE-WSW, which generally corresponds to the Malinstindur Formation. In the east of the Northern Islands, the dominant trend is ENE-WSW to NE-SW, and corresponds to the areal extent of the Enni Formation. This trend also appears dominant further to the west, most notably over significant outcrops of the Streymoy and Eysturoy saucer-shaped sills (white outlines in **Figure 2.11**). This relationship is indicative of a change in structural orientation through time, here suggesting a progressive anticlockwise rotation in strike/trend. In 3D, poles-to-planes created for the lineaments of the 1:50,000 analysis (**Fig. 2.12**) appear to show an apparent bimodal distribution in the majority of cases. However, it is likely that this bimodal grouping is an artifact of the

Fig. 2.12. (*Next page*) Lineaments picked at (**a**) 1:250,000, (**b**) 1:50,000 and (**c**) 1:5,000 scales, with rose diagrams for the major formations (Beinisvørð, Malinstindur and Enni Formations) exposed on the islands where possible. The dominant trend appears to change through time with NW-SE dominance in the Beinisvørð Formation, E-W dominance in the Malinstindur and ENE-WSW dominance in the Enni Formation. The clearest changes are observed in the 1:50,000 analysis, perhaps reflecting a fault damage:length and dyke width:length relationship. (**d**) Planes representative of the 1:50,000 lineaments, generated in Gocad, split by island and age, displayed as poles to planes in equal area, lower hemisphere stereographic projections. Again, a strong correlation is observed between plane orientation and host-rock age.

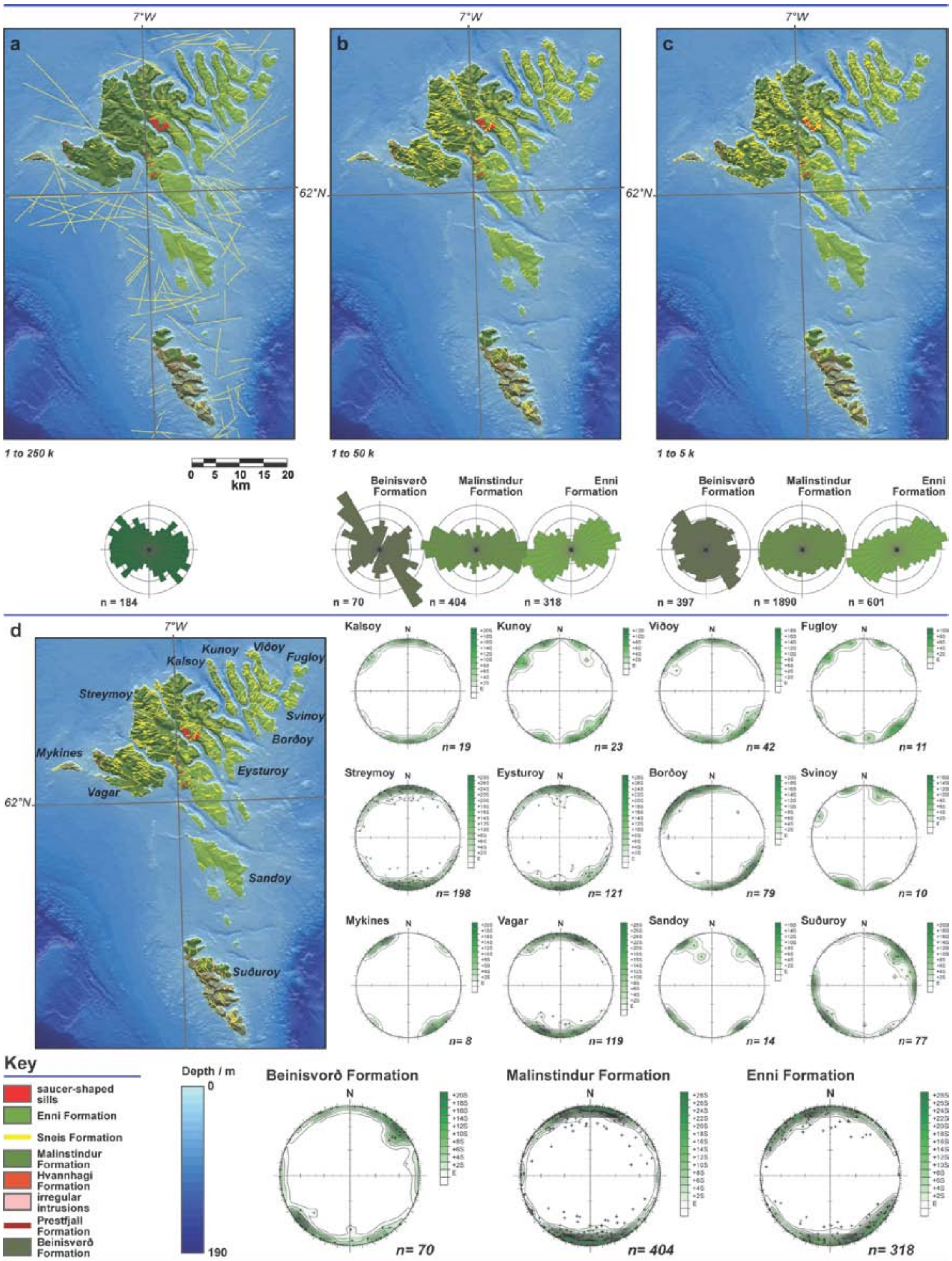

7°W
a
b
c
62°N
1 to 250 k
0 5 10 15 20
km
1 to 50 k
1 to 5 k
Beinisvørð Formation
Malinstindur Formation
Enni Formation
n = 184
n = 70
n = 404
n = 318
n = 397
n = 1890
n = 601
d
Kunoy
Viðoy
Fugloy
Kalsoy
Streymoy
Svinoy
Borðoy
Mykines
Eysturoy
Vagar
Sandoy
Suðuroy
Kalsoy n= 19
Kunoy n= 23
Viðoy n= 42
Fugloy n= 11
Streymoy n= 198
Eysturoy n= 121
Borðoy n= 79
Svinoy n= 10
Mykines n= 8
Vagar n= 119
Sandoy n= 14
Suðuroy n= 77
Key
saucer-shaped sills
Enni Formation
Sneis Formation
Malinstindur Formation
Hvannhagi Formation
irregular intrusions
Prestfjall Formation
Beinisvørð Formation
Depth / m
0
190
Beinisvorð Formation n= 70
Malinstindur Formation n= 404
Enni Formation n= 318

methodology and the scale of the analysis (i.e. the lineaments do not represent individual fault surfaces, rather fault zones), with fault data sets collected in the field displaying a more quadrimodal distribution. Notably, the majority of the stereonets display near symmetrical pole groupings, the exceptions being those with very few data points, and Suðuroy and the Beinisvørð Formation. These two examples show that the SW dipping planes are shallower than the NE dipping counterparts. This could be a reflection of their age relative to the timing of the regional tilting. Strata on Suðuroy are generally inclined at about 4-6° E to NE (**Fig. 2.7**); conjugate structures formed prior to this eastward tilting may therefore have a relatively steeper eastward dipping set and shallower westward dipping set.

A progressive rotation of the structural trend is also supported by cross-cutting evidence preserved across the islands, with NW-SE- and N-S-oriented lineaments consistently cut by ENE-WSW- to ESE-WNW-oriented lineaments, which are in turn cut by NE-SW- to NNE-SSW-oriented lineaments, where observed (detailed in the following chapter). These cross-cutting relationships are apparent on all scales used during the analysis, most commonly at the metre-scale, but potentially up to hectometre-scale, as indicated by lateral shifts in deep bathymetric troughs (e.g. **Fig. 2.13**). This may explain the trend irregularities of the 'transfer zone' lineaments as they pass through the islands, with lateral shifts of the order of hundreds of metres occurring across ENE and ESE trending lineaments (e.g. the Brynhild 'transfer zone': **Fig. 2.13a-d**). Some correlation is also possible between these lineament trends and the shape of the islands. For instance, the SW coast of Suðuroy is markedly linear, oriented NW-SE (e.g. **Fig. 2.4**); embayments and promontories are aligned with ENE-WSW- and ESE-WNW-oriented troughs in the bathymetry, which continue on the eastern side of the island (e.g. **Fig. 2.12a**). The island of Kalsoy, a thin NW-SE oriented slither, becomes abruptly wider at its southern end, where it is apparently abutted against an ESE-WNW oriented bathymetric trough; across that trough, the coast of Eysturoy is, again, highly linear in the same orientation (e.g. **Fig. 2.4**). Furthermore, an ESE-WNW trending straight line can be drawn through Skopunarfjorður (**Fig. 2.13e**), along the north coast of Sandoy, and the SW coast of Vagar into a lineament on Mykines, as well as an ENE-WSW line drawn along the north of the northern islands; again, perhaps an indication of regional-scale structural trends (**Fig. 2.12a**).

2.3.3.2 Dyke trends vs. compositions

Lava compositions in the FIBG vary most notably in TiO_2 content, with a clear division between the relatively high-TiO_2 (2.09-3.90%) and low-TiO_2 (0.73-1.93%: MORB-type) groups (Hald and Waagstein, 1991). These variations occur both through time and spatially: the older Beinisvorð and Hvannhagi Formations and the lowermost 500m of the Malinstindur Formation have high-TiO_2 compositions, whereas the rest of the younger Malinstidur Formation and the northern Enni Formation have low-TiO_2 compositions, inter-fingering with high-TiO_2 compositions from the southern Enni

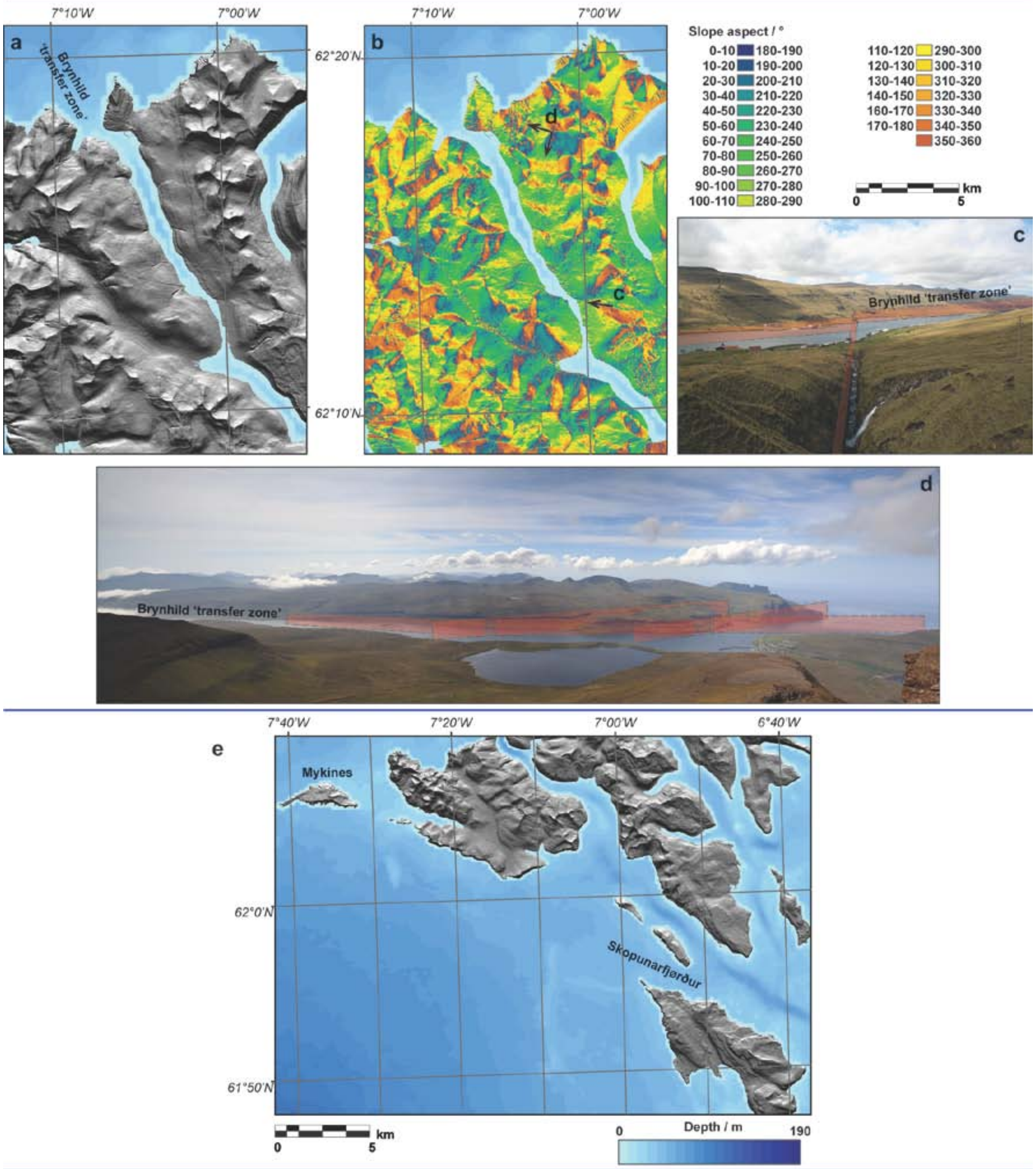

Fig. 2.13. (**a-d**) The NW-SE trend of the Brynhild 'transfer zone' appears to shift laterally in close association with ESE-WNW trending lineaments, perhaps indicating relatively large offsets (i.e. hectometre-scale). (**e**) The Skopunarfjørður strait is marked by a continuous ESE-WNW bathymetric low that appears to line up with an ESE trending lineament on Mykines.

Formation (Hald and Waagstein, 1991). On the basis that the dominant lineament trends appear to relate to the age of the host lithology, the lineament analysis has also been compared to published data on dyke orientations (**Fig. 2.14**; Rasmussen and Noe-Nygaard, 1969) and chemistry (Hald and Waagstein, 1991) in order to assess the possibility of orientation-controlled composition. Like the lavas, intrusives on the Islands can be grouped by relative enrichment of TiO_2. In general however, there appears to be no statistical correlation between dyke chemistry and orientation (**Fig. 2.14**). Nor is there a notable correlation between dyke orientation and the age of the country rock. These points most likely indicate that both high- and low-TiO_2 magmas

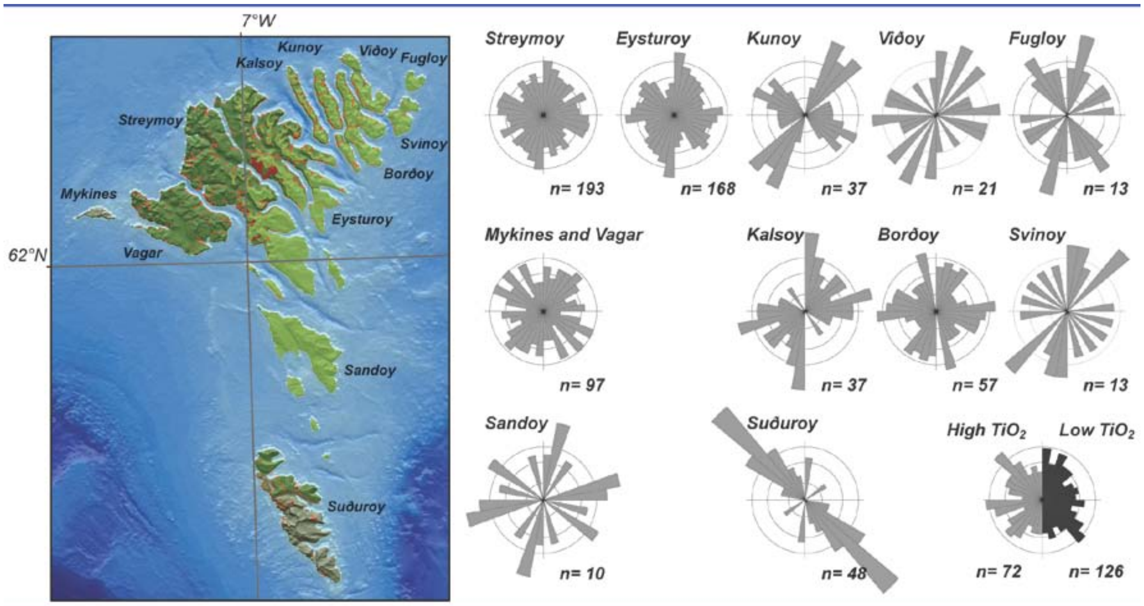

Fig. 2.14. Dyke orientations split by island (based on data from Rasmussen and Noe-Nygaard, 1969). No statistical correlation between orientation and host age is observed, with the exception of the Beinisvørð Formation on Suðuroy, which again has a dominant NW-SE trend, and nor is there any correlation between age and chemistry (based on data from Hald and Waagstein, 1990).

were emplaced until the end of magmatism associated with the FIBG. Low- TiO_2 magmas appear to be concentrated in the north, and could be an indication of their relative proximity to a MORB-type source (i.e. that related to the incipient NE Atlantic).

2.4 Summary

As part of the NAIP, the FIBG was emplaced during a period of continental rifting immediately prior to break up and the onset of sea-floor spreading in the NE Atlantic. The tectonic history captured on the Faroe Islands is therefore short compared with the proposed deformation history of the NW-SE lineaments in the region (i.e. the transfer zones). However, lineament analyses suggest that brittle deformation has occurred as a set of distinct events resulting in rotation of the dominant structural trend through time, rather than as a continuous deformation controlled by transfer zones. Stratigraphic layering analyses (*section 2.3.1*; **Figs. 6, 7**) indicate a progressive folding throughout emplacement of the FIBG, and most likely into post-magmatic times. In the following chapters, we aim to build upon, test and discuss these hypotheses with the addition of detailed kinematic and fault rock studies on the Faroe Islands.

3

Onshore evidence for progressive changes in rifting directions during continental break-up in the NE Atlantic and the role of NW-SE trending structures in the Faroe-Shetland Basin

Abstract

The NE Atlantic margin plays host to numerous Cretaceous and later basins, developed during the build up to plate separation and formation of the N. Atlantic Ocean. Current models for this invoke NW-SE extension within the basins, which are segmented by regional-scale NW-SE trending strike-slip faults, termed 'transfer zones'. Currently there is a paucity of information concerning the true kinematics of the so-called transfer zones; the present paper aims to fill this gap using abundant field data collected on the Faroe Islands.

Structures in the Faroe Islands provide evidence for a 6-stage tectonic evolution, here split into 3 broad phases: (1a) E-W to NE-SW extension, accommodated by dip-slip N-S and NW-SE trending faults. Continued NE-SW extension (1b) was accommodated by the emplacement of a regionally significant NW-SE- and NNE-SSW-oriented dyke swarm. Event 1 affects the majority of the FIBG stratigraphy, resulting in thickness variations, most notably across the Judd, Brynhild and Westray ('transfer') fault-zones. Continued magmatism and anticlockwise rotation of the extension vector led to (2a) the emplacement of ENE-WSW and ESE-WNW conjugate dykes. Their intrusion heralds the onset of N-S crustal extension and was followed by (2b) crustal extrusion involving both E-W shortening and further N-S extension facilitated primarily by slip on ENE-WSW (dextral) and ESE-WNW (sinistral) conjugate strike-slip faults. During the final stages of this event (2c), the regional extension vector rotated into a NW-SE orientation that was accommodated predominantly by slip along NE-SW oriented dextral-oblique-slip faults. Event 2 began towards the end of magmatism associated with the FIBG, and most likely continued through to the onset of oceanic-spreading on the Aegir ridge (ca. 55 Ma). Both Events 1 and 2 display multiple generations of calcite and zeolite hydrothermal

mineralisation as tensile and shear hydraulic veins, implying some degree of burial. Finally, (3) Event 1 and 2 structures were reactivated as extension and extensional-hybrid features, characterised best by the entrainment of clastic material along fault planes. Relative timings of Event 3 structures suggest they formed during a period of compression and uplift following the formation of a through-going mid-ocean ridge system (i.e. on the Reykjanes, Kolbeinsey and Mohns ridges).

The progressive anticlockwise rotation of the extension vector identified here is broadly consistent with the latest NE Atlantic continental break-up reconstructions. Importantly, the evidence preserved onshore for the Palaeogene and onwards, suggests that basin-scale NW-SE structures acted as normal faults during a precursor margin-parallel extension event prior to oceanic opening in the Faroe-Iceland sector. This model does not preclude the possibility that the NW-SE structures reactivate pre-Cenozoic transfer faults in the underlying margin.

This study emphasises the importance of carrying out detailed field studies in addition to the more usual seismic-scale modelling studies, in order to validate basin kinematics.

3.1 Introduction

Basins located along the NE Atlantic margin are long believed to share similarities in terms of their tectono-magmatic styles and timings (Lundin and Doré, 1997). As a result, structural models formulated in basins with relatively minor igneous content (e.g. the Møre and Vøring basins) are commonly applied to the less well understood regions masked by volcanics, such as the Faroe-Shetland basin (FSB). Basins along the margin appear to be segmented by NW-SE trending lineaments that are commonly referred to as transfer zones (e.g. Rumph et al., 1993; Doré et al., 1997; Naylor et al., 1999; Ellis et al., 2002; Ellis et al., 2009). Such zones are believed to facilitate differential extension within the basins, and may be rooted in the pre-existing structure of the basement along the margin (e.g. Wilson et al., 2006 and references therein). Structures of this kind should have a dominantly strike-slip motion sense associated with them. In terms of the FSB, left-lateral oblique-slip displacements are commonly invoked along transfer zones prior to and during continental break-up (Ellis et al., 2009).

The thick sequence of volcanic rocks preserved in the Faroes region form part of the extensive Palaeogene flood basalts of the North Atlantic Igneous Province (NAIP) that cover much of the continental margin (**Fig. 3.1**). The NAIP is estimated to have a volume of 1.8 x 10^6 km^3, covering an area of 1.3 x 10^6 km^2 (Eldholm and Grue, 1994). Thicknesses on the NE Atlantic margin range from >6km, towards the continent-ocean

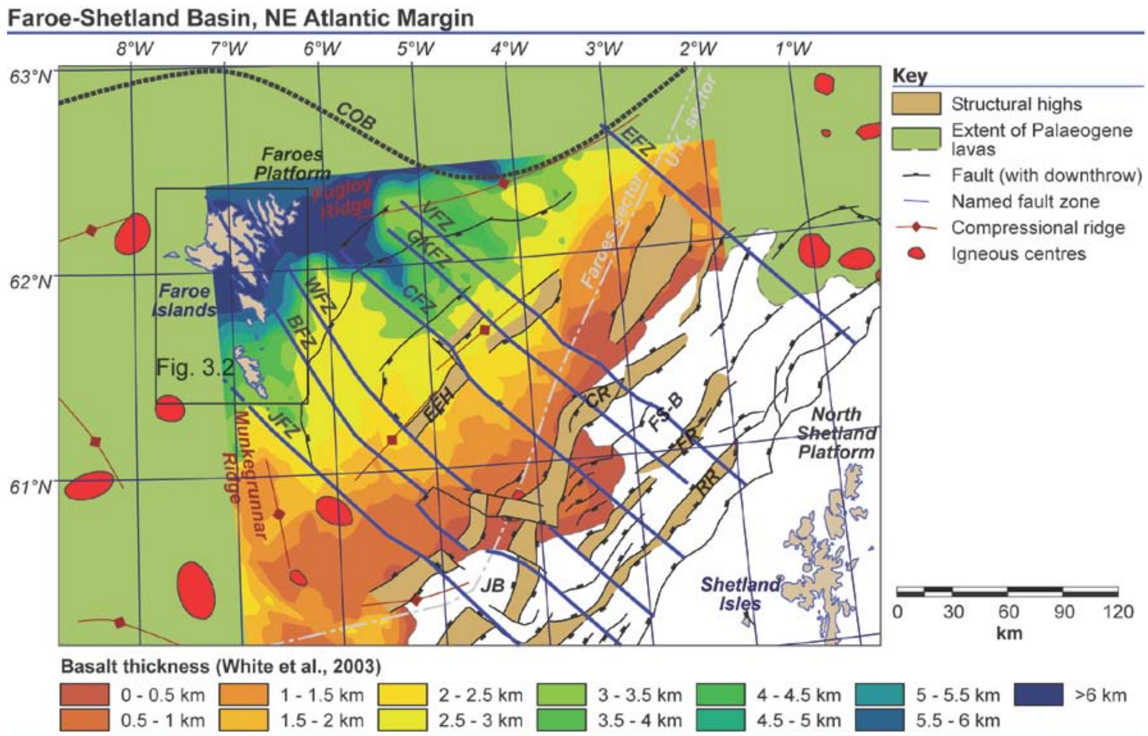

Fig. 3.1. Structural elements map of the Faroe-Shetland Basin, NE Atlantic Margin. **EFH** East Faroe High; **FS-B** Flett Sub-Basin; **JB** Judd Basin; **CR** Corona Ridge; **FR** Flett Ridge; **RR** Rona Ridge; **BFZ** Brynhild Fault-Zone; **CFZ** Clair Fault-Zone; **EFZ** Erlend Fault-Zone; **GKFZ** Grimur Kamban Fault-Zone; **JFZ** Judd Fault-Zone; **VFZ** Victory Fault-Zone; **WFZ** Westray Fault-Zone**.** (After Stoker et al., 1993; Rumph et al., 1993; Lundin and Doré, 1997; Sørensen, 2003; White et al., 2003; Jolley and Morten, 2007; Ellis et al., 2009).

boundary, to 0km in the south-eastern FSB (**Fig. 3.1**; White et al., 2003). Remnants of the Faroe Islands Basalt Group (FIBG; after Passey and Bell, 2007) on the Faroe Islands (**Fig. 3.2**) represent the only onshore exposures of the NAIP in the region, and are therefore collectively the only location where sub-seismic scale structures can be studied. The purpose of this study is to use structures exposed on the Faroe Islands to make inferences about the regional tectonics during late-continental break-up and sea-floor spreading; features that are otherwise ambiguous using current geophysical techniques.

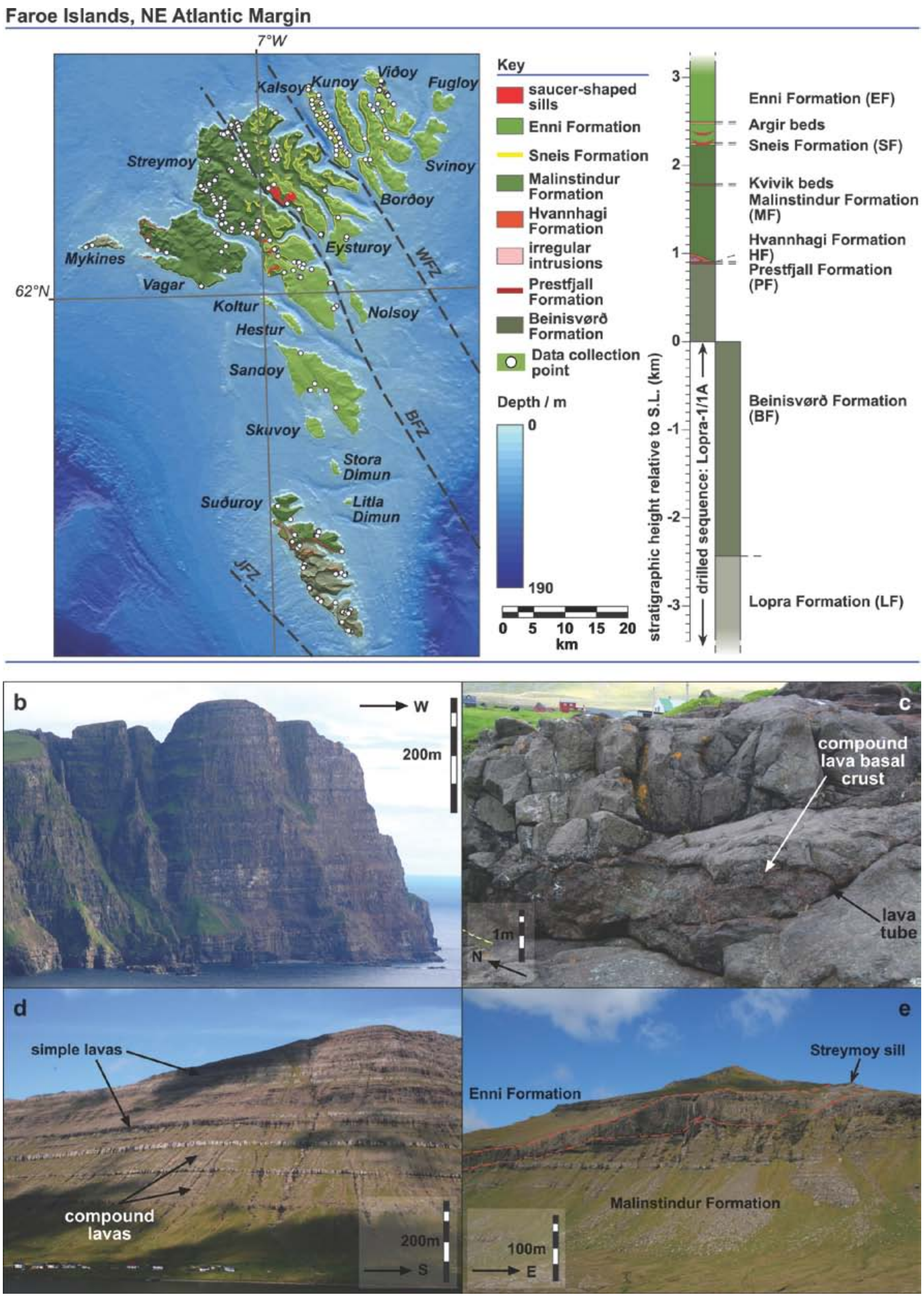
Faroe Islands, NE Atlantic Margin
7°W
62°N
Mykines
Vagar
Streymoy
Kalsoy
Kunoy
Viðoy
Fugloy
Svinoy
Borðoy
Eysturoy
Koltur
Hestur
Nolsoy
Sandoy
Skuvoy
Stora Dimun
Litla Dimun
Suðuroy
WFZ
BFZ
JFZ
Key
saucer-shaped sills
Enni Formation
Sneis Formation
Malinstindur Formation
Hvannhagi Formation
irregular intrusions
Prestfjall Formation
Beinisvørð Formation
Data collection point
Depth / m
0
190
0 5 10 15 20
km
stratigraphic height relative to S.L. (km)
drilled sequence: Lopra-1/1A
Enni Formation (EF)
Argir beds
Sneis Formation (SF)
Kvivik beds
Malinstindur Formation (MF)
Hvannhagi Formation HF)
Prestfjall Formation (PF)
Beinisvørð Formation (BF)
Lopra Formation (LF)
b
W
200m
c
compound lava basal crust
lava tube
1m
N
d
simple lavas
compound lavas
200m
S
e
Streymoy sill
Enni Formation
Malinstindur Formation
100m
E

Fig. 3.2. (*Previous page*) **(a)** Simplified hillshaded geological and bathymetric map of the Faroe Islands and insular shelf, with gross stratigraphic column for the Fare Islands Basalt Group (after Passey and Bell 2007; Passey, 2009). **(b)** Laterally extensive simple (sheet) lava units of the Beinisvørð Formation, at Beinisvørð, on the SW coast of Suðuroy. Units range in thickness, from <5m to >20m. **(c)** Overlapping compound lava units and lava tubes of the Malinstindur formation at Viðareiði, NW Viðoy. Individual units are less extensive laterally, than simple lavas, and range in thickness from <1m to slightly over 2m. **(d)** The Enni Formation above Hvannasund, SW Viðoy. Simple lava units generally form prominent benches, with the thinner compound units forming the steep slopes in between. **(e)** The large Steymoy 'saucer-shaped' sill at Sátán, West Streymoy. The sill broadly displays a ramp-flat-ramp architecture, with the flats corresponding to volcaniclastic horizons (such as the Sneis Formation).

'Transfer zone' trends in the FSB are thought to project through the Faroe Islands (**Fig. 3.1**; Rumph et al., 1993) and should therefore be apparent onshore (**Fig. 3.2**). In particular, structures and offsets relating to (from southwest to northeast) the Judd, Brynhild and Westray lineaments should be evident on the Islands. Recent work has suggested that movements along those faults are responsible for all structures seen on the Faroe Islands, as part of a complex and continuous deformation regime (Ellis et al., 2009). Such 3-D (non-plane strain) non-coaxial strains may occur when continental separation is oblique to the plate boundary and/or when the basin bounding or intrabasinal faults reactivate pre-existing structures that lie at an oblique angle to the regional extension direction (Dewey, 2002; De Paola et al., 2005). In this case, the transfer zone trends (NW-SE) are parallel to the inferred plate separation direction (also NW-SE).

An alternative model has proposed that structures are related to a rotation of Cenozoic rifting directions immediately prior to and during continental break-up (Doré et al., 1999). In this model, variations in rift orientation would result in successive fault and fracture sets, though these could ultimately be influenced by pre-existing material anisotropies within the basin (e.g. basin-wide dykes or dyke swarms and basement structure). It is generally agreed by most authors that, following continental break-up, Cenozoic compression has resulted in the development of mild growth folds on various scales and orientations along the margin (e.g. Anderson and Boldreel, 1995; Boldreel and Anderson, 1998; Ritchie et al., 2008). Such features should also be evident in the Faroes.

In the present paper, we summarise the onshore structural geometries and kinematics preserved in the Faroe Islands and reconstruct the tectonic evolution using abundant cross-cutting relationships preserved at multiple scales, and supported by deformation history systematics (e.g. Potts and Reddy, 1999). These findings are then compared to the predictions made by existing regional tectonic models in order to better constrain the regional evolution of the NE Atlantic margin during continental breakup.

3.2 Regional geological setting

3.2.1 Faroe Islands stratigraphy

Much of the NE Atlantic volcanic passive margin is covered by Palaeocene trap-style volcanics (**Fig. 3.1**); the NAIP, of which the Faroe Island Basalt Group (FIBG) is a part, which is believed to have been emplaced immediately prior to continental break-up. Remnants of the FIBG are exposed on the Faroe Islands, with an overall stratigraphic thickness in excess of 6.6 km (**Fig. 3.2a**; Passey and Bell, 2007). The FIBG is dominated by tholeiitic basalt lavas, divided into 7 formations based on lithology and disconformity surfaces (Rasmussen and Noe-Nygaard, 1969 & 1970; Passey et al. 2006) and geochemistry (Waagstein, 1988). The lower-most of these, the Lopra Formation, is not exposed sub-aerially, and has only been encountered in the (onshore) borehole Lopra-1/1A (Rasmussen and Noe-Nygaard, 1970; Hald and Waagstein, 1984; Passey and Bell, 2007).

The Lopra Formation is a >1km thick sequence of hyaloclastites, volcaniclastic rocks and invasive lavas/sills (**Fig. 3.2a**; Ellis et al., 2002). Above the Lopra Formation lies the ca.3.3km thick Beinisvørð Formation, of which only the upper 900m is exposed on the islands. The Beinisvørð Formation generally comprises aphyric, laterally extensive sheet lobes, with minor intercalated volcaniclastic horizons (**Fig. 3.2b**). Exposure of the Beinisvørð Formation is limited to the southern island, Suðuroy, and to the west of the northern islands, Vagar and Mykines. Above this lies the 3-15m thick Prestfjall

Formation, comprising coals, mudstones and sandstones deposited in swamps, lacustrine and fluvial environments, during a hiatus in volcanic activity (Rasmussen and Noe-Nygaard, 1969 & 1970; Lund, 1983 &1989; Passey and Bell, 2007). Volcanic activity resumed, resulting in the deposition of about 50m of basaltic tuffs interbedded with volcaniclastic floodplain facies and flow deposits forming the Hvannhagi Formation. Exposure of the Prestfjall and Hvannhagi Formations is limited to Suduroy and west Vagar.

Trap-style volcanism continued with eruption of the <1.4km thick Malinstindur Formation, subaerial compound basalt lavas (**Fig. 3.2c**) that are initially olivine-phyric evolving to aphyric, and then plagioclase-phyric. The Malinstindur Formation is particularly well exposed on the northern islands of Vagar, Streymoy and Eysturoy, at low-altitudes on the north-eastern islands, and in the north of Suduroy. Above these lie the laterally extensive volcaniclastic sandstones and conglomerates of the Sneis Formation. These are overlain by about 900m of the Enni Formation, which comprises low-TiO_2 and high-TiO_2 interbedded simple (sheet lobes) and compound tholeiitic lavas (**Fig. 3.2d**), which is exposed in a north to north-east arcing trend from Sandoy across the northern islands. The 900m is a minimum thickness, with a significant amount (in the order of hundreds of metres) eroded from the top of the volcanic pile (Waagstein et al., 2002).

Notable intrusions on the islands include the large 'saucer-shaped' Streymoy and Eysturoy sills, and the Fugloy-Svinoy sill. The Streymoy and Eysturoy sills are transgressive, lying stratigraphically around the level of the Sneis Formation (**Fig. 3.2a**). The Eysturoy sill occupies an area of about 16km^2, and ranges in thickness from 10-55m (Rasmussen and Noe-Nygaard, 1970). Generally the Eysturoy sill dips SW, displaying a pronounced flat section at the level of the Sneis Formation. The Streymoy sill (**Fig. 3.2e**) covers an area of about 13km^2, and displays a much more saucer-like geometry, again with numerous ramp- and flat-sections, from within the top part of the Malinstindur Formation, becoming flat at the level of the Sneis Formation, and then ramping upwards again into the Enni Formation. The Fugloy-Svinoy sill is slightly higher in the succession, found entirely within the Enni Formation (**Fig. 3.2a**). Again it is transgressive, ramping upwards on Svinoy to the SE, and to the NE on Fugloy (Rasmussen and Noe-Nygaard, 1970). In total, the sill has an area of about 2.5km^2, and ranges in thickness from 15-36m.

3.2.2 Existing structural models

Few structural studies have focused on the Faroe Islands; the two of note (Geoffroy et al., 1994; Ellis et al., 2009) address the problem using very different approaches, and the resulting structural models also contrast markedly. The two models will be referred to here simply as the Geoffroy and Ellis models, respectively.

3.2.2.1 The Geoffroy model

The Geoffroy model derives from an extensive kinematic analysis of structures in a selection of locations in the Faroe Islands, East Greenland and the British Tertiary Igneous Province, forming part of the principal author's largely unpublished Ph.D. thesis. On the Faroes, some 2700 kinematic measurements were taken at 90 sites across the Islands. Kinematic data were grouped using cross-cutting relationships observed on published maps (Rasmussen and Noe-Nygaard, 1969) and in the field, and principal stresses calculated using the stress inversion method described by Angelier (1990). The results suggest a polyphase brittle deformation sequence, which were split into four events: three synmagmatic, and one post-magmatic. The first event, supposedly occurring during emplacement of the Malinstindur Formation, records a NE-SW to ENE-WSW extension, facilitated on strike-slip faults trending between 150° - 170°, and similarly oriented dykes. The second event (supposedly contemporaneous with the Enni Formation) is characterised by widespread ENE-WSW (dextral) and ESE-WSW (sinistral) conjugate strike-slip faults, later intruded by similarly oriented dykes, which collectively result in a N-S extension, and E-W compression. The third event, occurring purportedly towards the end of emplacement of the Enni Formation, represents a period of pure compression, termed the "*Faeroe Compressional Crisis*", immediately preceeding and continued through the emplacement of the saucer shaped sills on the islands. The final event (believed to be post-magmatic, based on the lack of associated intrusives) represents a WNW-ESE transtension facilitated by strike-slip tectonism.

Key relationships underlying this model centre around those that exist between intrusions and faults/fractures. Hence, it is suggested that: a) the dykes are intruded along existing strike-slip faults and (b) that the sills are intruded coeval with thrust faulting during a regional compression. The model predicts the following in terms of cross-cutting relationships: (1) a series of cross-cutting relationships where: NW-SE faults and dykes are cut by E-W trending conjugate faults and dykes, that are in turn cut by NE/SW dipping thrust faults and the major sills, all of which are cut by NE-SW trending conjugate faults; (2) Dyke margins should exhibit slip-indicators, inherited from the existing (reactivated) faults. Dykes are predicted to have been subjected to shear reactivation and should therefore display internal features indicative of this. These predictions and relative timings are appraised in *section 3.3.4*.

3.2.2.2 The Ellis model

The Ellis model is based on tectonostratigraphic evidence resulting from a recent intensive stratigraphic mapping and characterization of the FIBG by the Faroese Earth and Energy Directorate, Jarðfeingi. In some respects, the Ellis model is simpler than the Geoffroy model, requiring only one continuous deformation regime, resulting from boundary fault conditions (i.e. the development of transfer zones). In the model, faults, fractures and intrusives result from a complex 3-D strain, with continued recurrent deformation producing the observed structural orientations. On the Islands it is noted that a repeated thickening of the FIBG occurs, from NE to SW, into the narrow seaways where the Westray, Brynhild and Judd transfer zones are thought to be located as they run through/near to the islands. Key marker horizons on the Islands throughout the stratigraphy are shown to thicken in the inferred hangingwalls of these features. For example: (1) the coal measures of the Prestfjall Formation thicken from 0.5m to 2m, from east to west across Suðuroy, into the Judd transfer zone; (2) the Sneis Formation (and other notable marker units such as the Kvivik and Argir Beds (within the Malinstindur and Enni Formations respectively; **Fig. 3.2**) thicken and/or are lower on the NE side of the Brynhild and Westray transfer zones. This is also the case between Streymoy and Sandoy, and a branch or splay of the Brynhild Transfer zone has been invoked (following evidence in Passey, 2009) with a down-to-the south motion-sense.

As the deformation is supposed to be continuous, this model predicts that all structures should mutually cross-cut and/or interact with each other. Somewhat problematically, the largest features (i.e. the transfer zones) are projected along the fjords, and as such, field studies have to rely on adjacent proxies in order to determine their presence, nature and kinematics.

In the following section, we present a new set of detailed field observations concerning the geometry and kinematics of deformation structures preserved in the Faroe Islands and their evolution through time.

3.3 Main structural events

3.3.1 Regional scale structure

3.3.1.1 Lineament analysis

Three, scaled lineament analyses were conducted using topographic (10m resolution) and bathymetric data (30m resolution), and 2D aerial and satellite images (0.5m resolution). During the lineament analysis, scales (1:250k, 1:50k and 1:5k) were strictly adhered to in order to appreciate any scaling bias and length vs. orientation relationships. Cross-referencing with published maps combined with close examination of the aerial photographs and field observations, ensures that the lineaments picked correspond to faults and dykes, and avoids any man-made or purely erosional features (e.g. road-cuttings and cliff or crag lines respectively). Spatial and statistical analysis of the lineaments was performed in ArcGIS™, using arbitrarily referenced 5km grids, by island, and by the youngest formation they cut.

The dominant lineament trend and style varies markedly across the islands, correlating well with the age of the host lithology (**Fig. 3.3**). In the southern island, Suðuroy, the dominant trend is generally NW-SE to NNW-SSE, corresponding to surfacing of the Beinisvørð Formation. In the west of the Northern Islands, there is a trend dominance of ESE-WNW through to ENE-WSW, which generally corresponds to the Malinstindur Formation. In the east of the Northern Islands, the dominant trend is ENE-WSW to NE-SW, and corresponds to the areal extent of the Enni Formation. This trend also appears

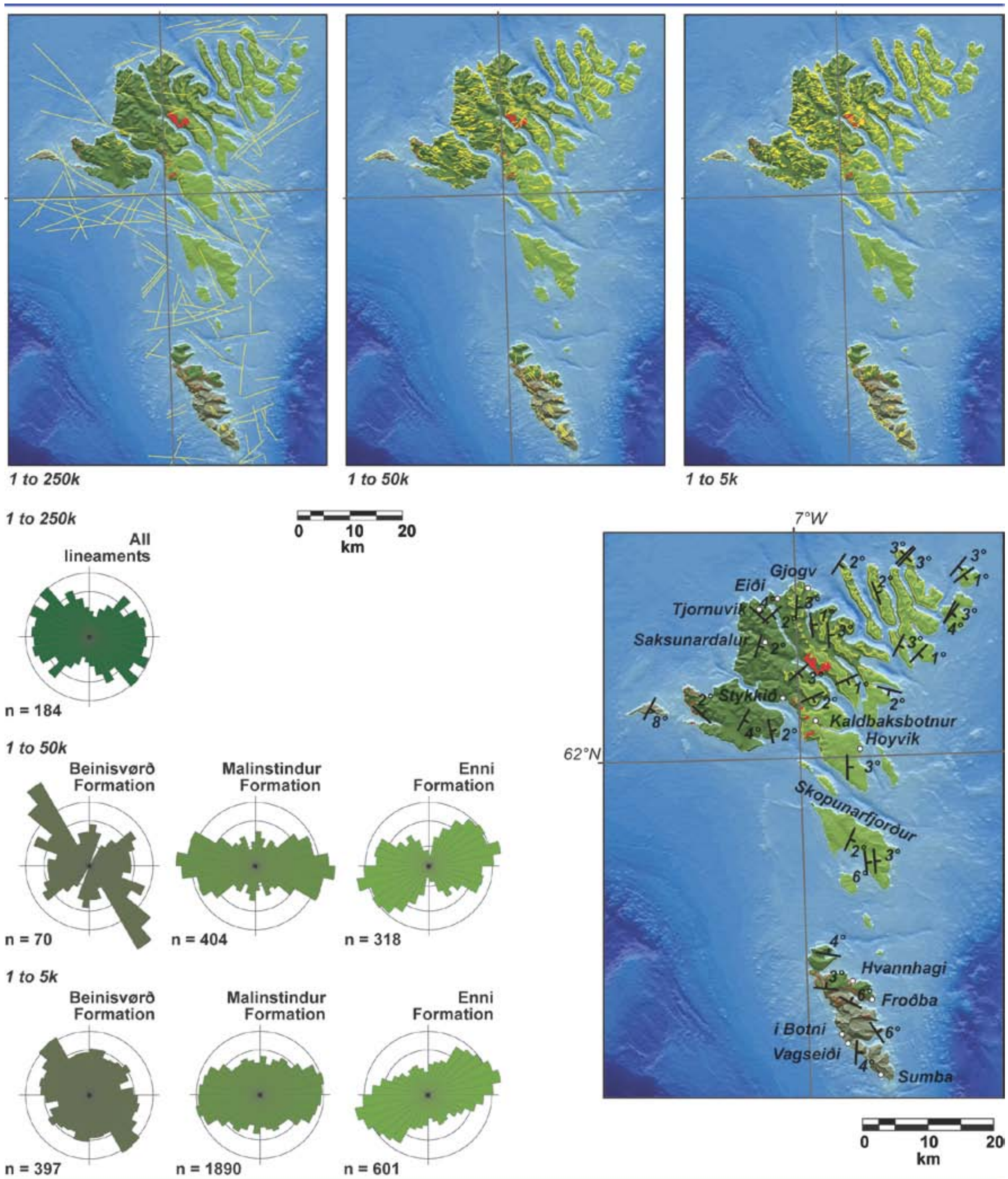

Fig. 3.3. 1:250,000, 1:50,000 and 1:5,000 scaled lineament analyses (top left to top right), with corresponding rose diagrams (left) detailing lineament trends with respect to formation age, and fold architecture across the islands (bottom right - see text for explanation). (Offshore extent of formations is unknown, hence no discrimination is made for the 1:250,000 study). A clear rotation through time in orientation dominance is noted.

dominant further to the west, most notably over significant outcrops of the Streymoy and Eysturoy saucer-shaped sills. This relationship is indicative of a change in structure orientation through time, here suggesting a progressive anticlockwise rotation. This is supported by cross-cutting evidence across the islands, with NW-SE and N-S oriented lineaments cut by ENE-WSW to ESE-WNW oriented lineaments, which are in turn cut by NE-SW to NNE-SSW oriented lineaments, where observed (detailed later in this chapter). Those cross-cutting relationships are apparent on all scales used during the analysis, most commonly at the metre-scale, but potentially up to hectometre-scale, as indicated by lateral shifts in deep bathymetric troughs (**Fig. 3.3**). This may explain the trend irregularities of the 'transfer zone' lineaments as they pass through the islands; lateral shifts in the order of hundreds of metres occurring across ENE and ESE trending lineaments. Some correlation is also made between these lineament trends and the shape of the islands. For instance, the SW coast of Suðuroy is markedly linear, oriented NW-SE; embayments and promontories are aligned with ENE-WSW and ESE-WNW oriented troughs in the bathymetry, which continue on the eastern side of the island. The island of Kalsoy, a thin NW-SE oriented slither, becomes abruptly wider at its southern end, where it is apparently abutted against an ESE-WNW oriented bathymetric trough; across that trough, the coast of Eysturoy is, again, highly linear in the same orientation. Furthermore, an ESE-WNW trending straight line can be drawn through Skopunarfjorður (**Fig. 3.3**), along the north coast of Sandoy, and the SW coast of Vagur, as well as an ENE-WSW line drawn along the north of the northern islands; again, perhaps an indication of the regional-scale structure.

3.3.1.2 Stratigraphic horizon modeling

Individual lava units commonly display considerable relief at their upper and lower contacts, due to erosion (during periods of volcanic quiescence) or fuel-coolant style reactions with wet sediments during emplacement, making it difficult to accurately measure true-dip of the horizons at a local or outcrop scale using conventional field equipment (i.e. compass-clinometer). A combination of field observations and remote-sensing analyses were used here to create a structural map of the horizons across the islands.

Generally, horizon inclination decreases up-stratigraphy through the FIBG, with the largest, ~8° (SE), observed on Mykines within the Beinisvørð Formation (**Fig. 3.3**). This decreases to ~3° (SE) in the Malinstindur Formation on Vagar, and Streymoy, and again to ~1-2° (SE) in the Enni Formation in the NE (e.g. Borðoy, Viðoy, etc.). High eastward dips, ~6° (E), are recorded on Sandoy within the youngest exposed units of the FIBG. In the south, on Suðuroy, units are more E to NE dipping, 8° (E) in the east, decreasing westwards to ~1° (NE) at the coast.

Fold architecture across the islands is indicative of a growth through time. Areas that do not obey this relationship are closely associated with large offset faults (e.g. Skopunarfjorður, between Streymoy and Sandoy; Passey, 2009), and may indicate fault-block-rotations. The westward decrease in dip on Suðuroy may relate to the effect of down-warping during subsidence-related movement on the Judd Fault nearby offshore, or to the proximity of a fold-axis (i.e. the Munkegrunnar Ridge; **Fig. 3.1**).

3.3.2 Outcrop-scale structures

The outcrop-scale deformation structures preserved in the Faroe Islands are exclusively brittle and are associated both with the intrusion of igneous sheets (dykes or sills) and in many (though not all) cases by the associated development of mineral veins (mainly carbonate). Later structures are also associated with the development and deformation of clastic infills and generally lack associated mineralization. All features likely formed during deformation at shallow, upper crustal depths (up to 5km), with the final events likely occurring in near-surface environments (<1km depth).

During this study, structural measurements and field observations were recorded from over 400 localities across the islands. These observations provide clear evidence for a polyphase history of faulting and igneous intrusion events, followed by regionally-late fault reactivation, possibly during uplift. For convenience, these events are split into 6 groups based on orientations, kinematics and cross-cutting relationships: these are then interpreted to be the constituent manifestations of 3 broad regional tectonic events. In total, about 1800 slip surfaces were measured, and when possible, kinematic data have been inverted to infer the palaeostress orientations using MyFault™ software of Pangaea Scientific Limited. The program offers five inversion methods, from a simple shear tensor average (Sperner et al., 1993), to the Fry's Hyperplane average (Fry, 1999, 2001). This function is beneficial, as different methods invoke different assumptions, and so comparisons can be made quickly and easily. In this study, we have chosen methods that reflect the fault/fracture characteristics best, and produce the least spread in uncertainties during recalculations (using the bootstrap resampling method). Importantly the inversions are only used here as a guide, and based on the typical 10°-15° variation in principal stress orientations between different methodologies, we refer only to compass-quadrants to describe inferred horizontal stress directions.

3.3.3 Event 1: ENE-WSW to NE-SW extension

Event 1 is split into 2 parts: (1a) ENE-WSW extension typically facilitated on NW-SE and N-S trending dip-slip faults; and (1b) NE-SW extension accommodated by the intrusion of a regionally significant dyke swarm typically oriented NW-SE and NNE-SSW. Event 1 features are best exposed in the Beinisvørð Formation on Suðuroy, particularly on the west coast at I Botni, Vagseiði and Sumba, but are also observed throughout the Malinstindur Formation on the northern islands.

3.3.3.1 Event 1a

Event 1a faults are generally subvertical within the basaltic units, commonly becoming shallower within sediment interlayers, palaeosol sequences and volcaniclastic breccias (**Fig. 3.4a**). They are associated with numerous phases of calcite and zeolite

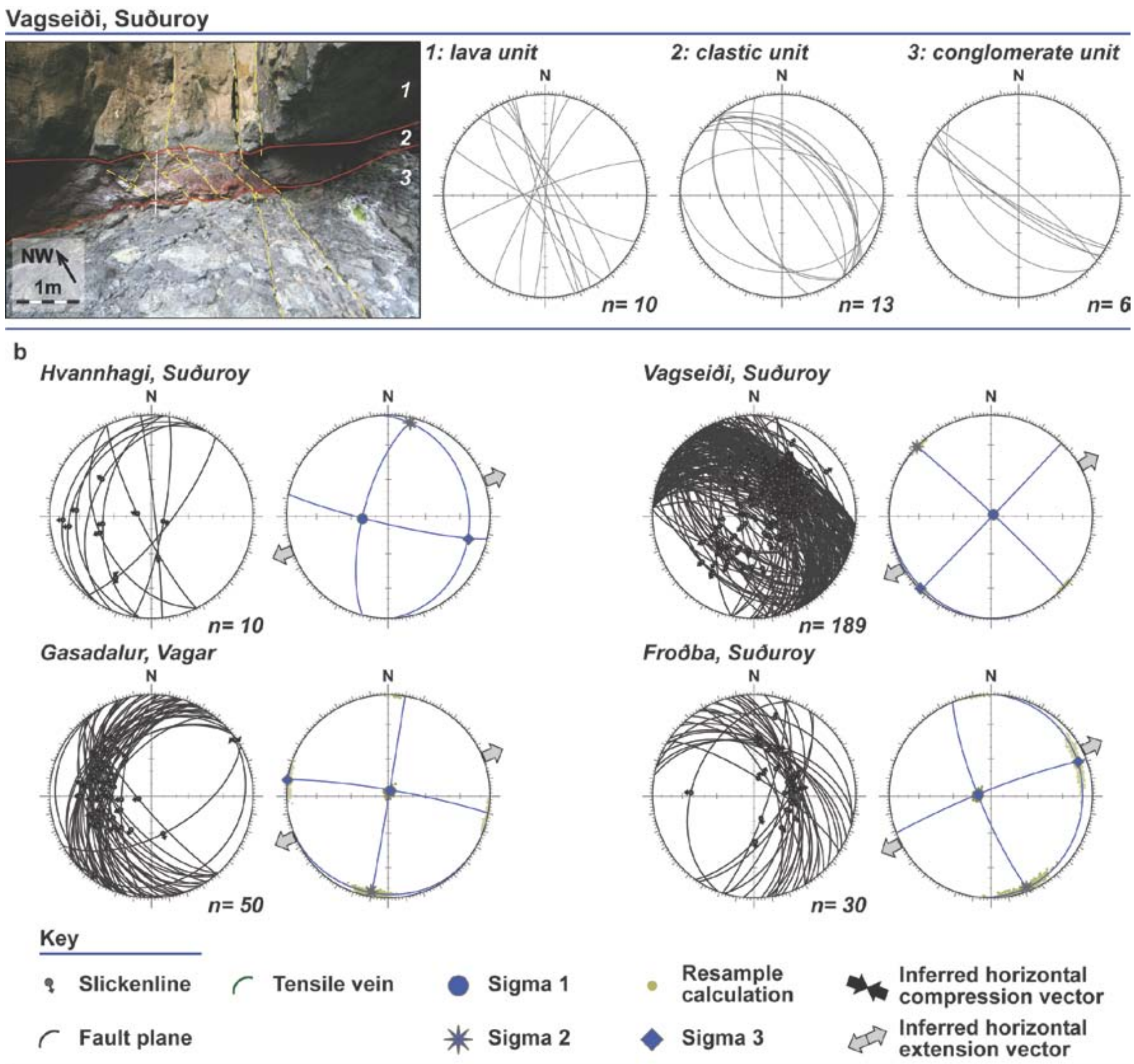

Fig. 3.4. (a) Event 1 fracture plane reorientation at Vagseiði, Suðuroy. Within the lava unit, faults and fractures typically exploit the existing cooling joints, and as such, where possible, structural measurements have been taken within the interbasaltic volcaniclastic horizons. **(b)** Stereographic projections showing examples of Event 1a fault planes, and inversion calculations. (Locations indicated on **Figure 3.3**).

mineralisation, in the form of tensile (mode-I) and shear/hydraulic (mixed-mode) fractures, which consistently record dip-slip fault movements, resulting in a NE-SW extension vector (**Fig. 3.4b**). The numerous mineralisation overprints, coupled with the presence of well-developed fault-damage- and core-zones likely indicates a prolonged and recurring deformation on individual faults. Offsets range from a few centimetres (e.g. Vagseiði; **Fig. 3.5a-e**) to a few metres (e.g. Sumba; **Fig. 3.5f, g**), and in some cases, decametres (e.g. I Botni; **Fig. 3.5h**). The largest determined offsets occur on faults in (and obscured by) the present day fjords, and result in a repeated stratigraphic thickening across the islands from NE to SW (Ellis et al., 2009). The oldest stratigraphic marker horizon affected by this thickening is the coal-bearing Prestfjall formation which displays about 2m thickening from east to west on Suðuroy (Rasmussen and Noe-Nygaard, 1969, 1970; Ellis et al., 2009), over a lateral distance of some 7-8km, into the projected trend of the Judd Fault Zone (**Fig. 3.2**). In the Northern Islands, the Malinstindur and Enni Formations display notable offsets and thickening from NE to SW into the Westray Fault Zone (between Kalsoy and Eysturoy) and again into the Brynhild Fault Zone (between Eysturoy and Streymoy; **Fig. 3.2**). The youngest marker unit affected by these movements are the Argir beds, which occur roughly a third of the way up the Enni Formation. The depth of palaeo-accommodation on the NE side of the Brynhild and Westray Fault Zones is estimated to be a maximum of 50-80m, and again indicates a prolonged deformation with minor vertical offsets at any one time (Ellis et al., 2009).

3.3.3.2 Event 1b

Event 1b dykes are typically 2-15m thick, vertical to subvertical, and commonly display irregular cm-m-scale offshoots and m-scale bifurcations (**Fig. 3.6a, b**). Commonly

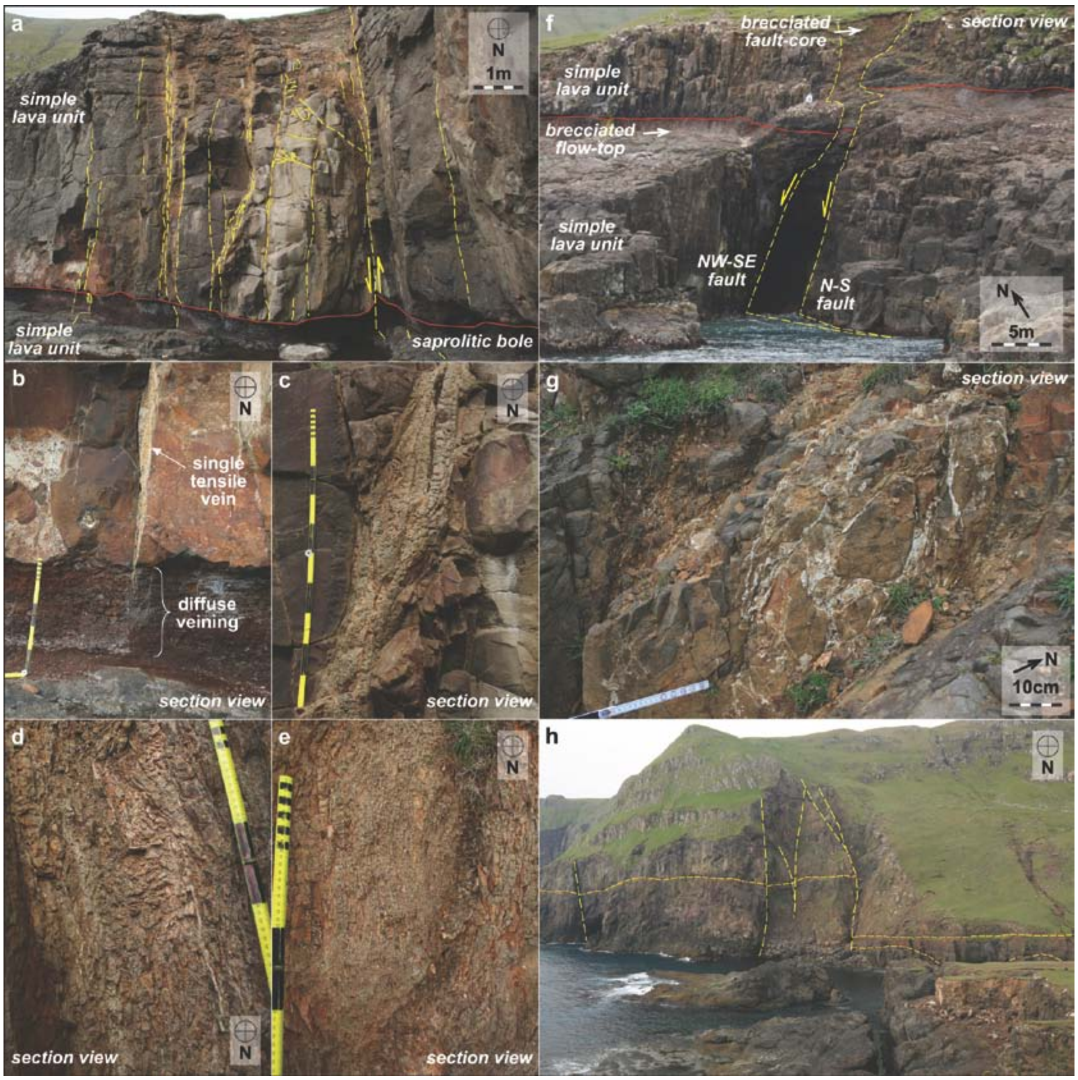

Fig. 3.5. Event 1a faults **(a-e)** N-S trending normal fault at Vagseiði, Suðuroy, displays ~15cm apparent offset down to the west. The fault displays a well developed fault core and damage zone, asymmetrically focused in the hanging-wall of the fault. The damage zone **(a-c)** is about 6m wide and exhibits mode-I and mixed-mode fractures characterised by vuggy/euhedral crystal growths and shear-veins respectively. The core **(d-e)** is 5-40cm wide, and exhibits brecciation of the wall-rocks and mineral veins. **(f-g)** N-S and NW-SE trending dip-slip faults at Sumba, SW Suðuroy, displaying ~2.5m down to the west displacements across a well developed fault core. **(h)** Large offset (~30m) N-S trending fault at I Botni, Suðuroy, again displays a well developed fault core.

margins have a semi-polygonal shape in plan view, as dictated by the existing joint pattern within the host lava units (**Fig. 3.6a-c**) rather than exploiting existing faults (i.e. those of Event 1a) and a consistent absence of mineralisation in the NW-SE dykes of this event further suggests that they are later than the NW-SE and N-S faults. Where matched on opposite sides of a dyke, margin irregularities indicate a NE-SW extension vector. On some minor dykes, the trend changes locally, from NW-SE to ENE-WSW and back again; the ENE-WSW sections are consistently thinner compared to adjacent NW-SE segments, in keeping with a NE-SW extension vector (**Fig. 3.6d**). Only minor vertical offsets are observed across Event 1b dykes, and it is inferred that NE-SW extension at this time was accommodated purely by the volume increase resulting from widespread intrusions.

The height within stratigraphy to which Event 1 structures are observed, combined with the stratigraphic thickening evidence detailed in Ellis et al. (2009), indicates that Event 1 occurred during emplacement of the majority of the FIBG. Palaeostress inversions performed on related structures (e.g. **Fig. 3.3b**) combined with direct evidence from dyke-margin irregularities (e.g. **Fig. 3.6**) detail an island-wide deformation, characterised by a distinct NE-SW extension (**Fig. 3.7**). This extension vector is supported by inversions in Geoffroy et al. (1994), although this study finds that the faults are predominantly dip-slip as opposed to strike-slip, as suggested in their study.

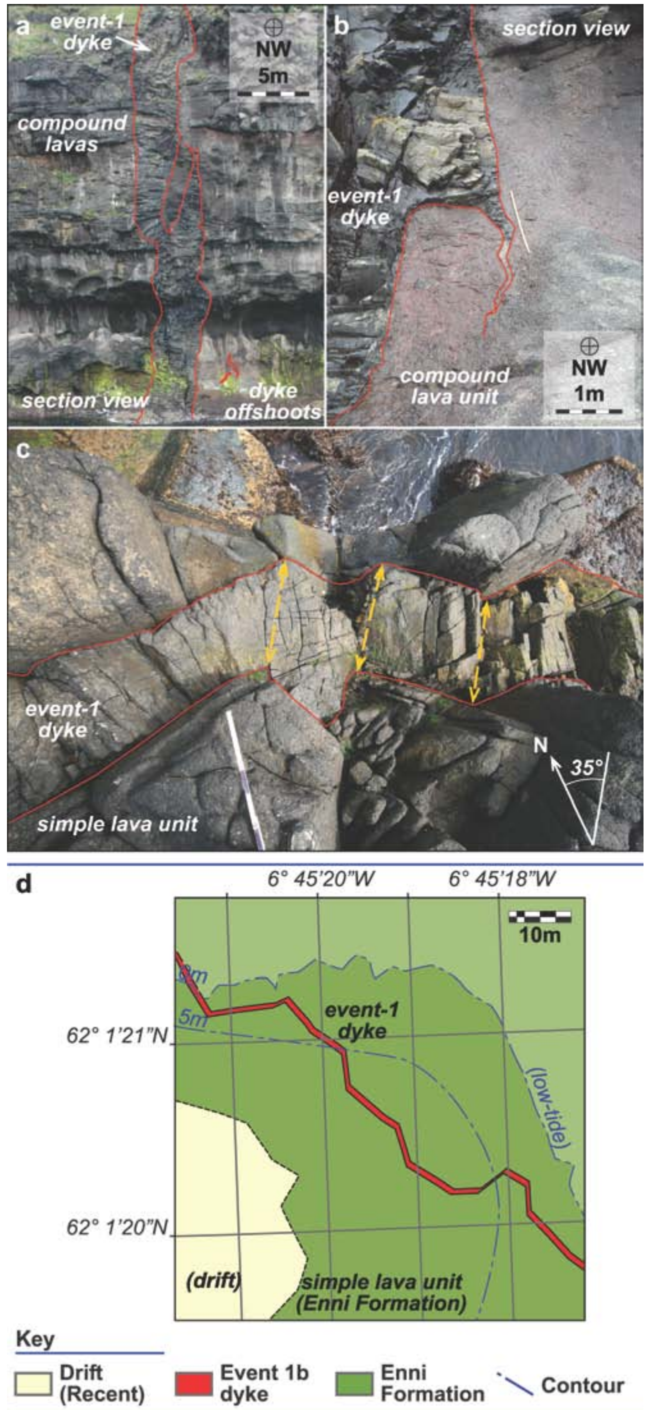

Fig. 3.6. (a-b) Anastamosing N-S trending Event 2b dyke at Gjogv, NE Eysturoy, displays irregular margins and minor bifurcations and offshoots, ranging from mm-dm widths that are continuous for many metres, often along the cooling joint structure of the country rock. **(c)** NW-SE trending dyke at Hoyvik, S. Streymoy, exhibits an irregular margin and local thinning **(d)**, indicating a NE-SW extension. (Locations indicated on **Figure 3.3**).

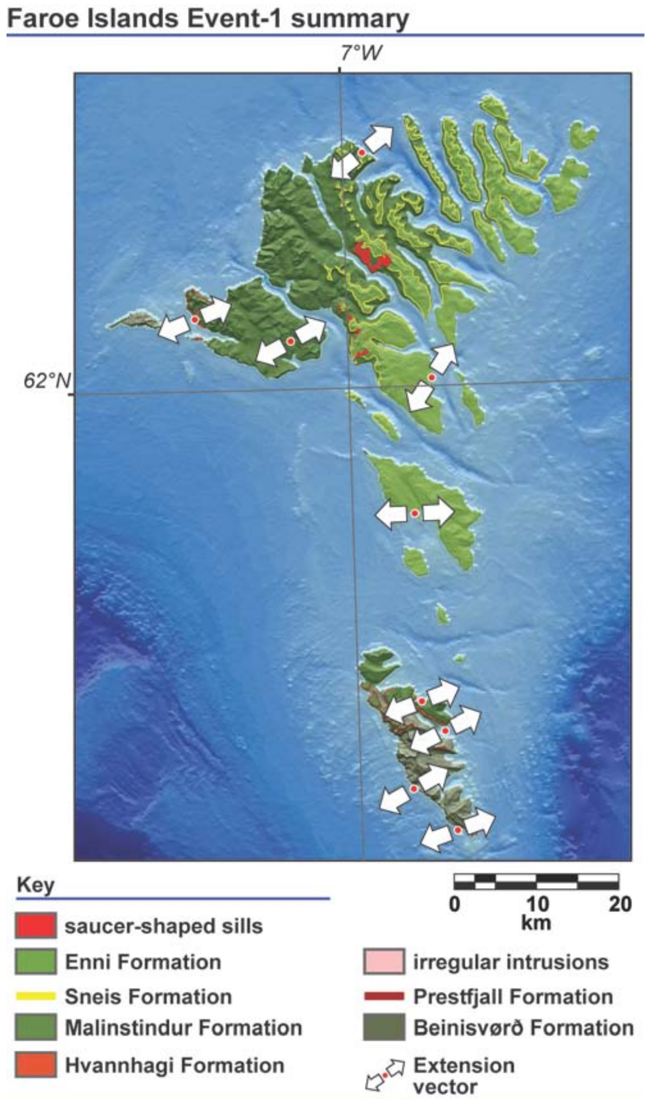

Fig. 3.7. Event 1 inferred horizontal stress summary map, indicating an island wide, ENE-WSW to NE-SW extension.

3.3.4 Event 2: N-S to NW-SE extension

Across the Islands and at multiple scales, Event 1 faults and dykes are consistently offset by ENE-WSW and ESE-WNW trending dykes and faults (**Fig. 3.8**). This relationship is abundantly clear at both map- and outcrop-scales at all observed intersections; selected examples are provided here. Event 2 is split into 3 subdivisions:

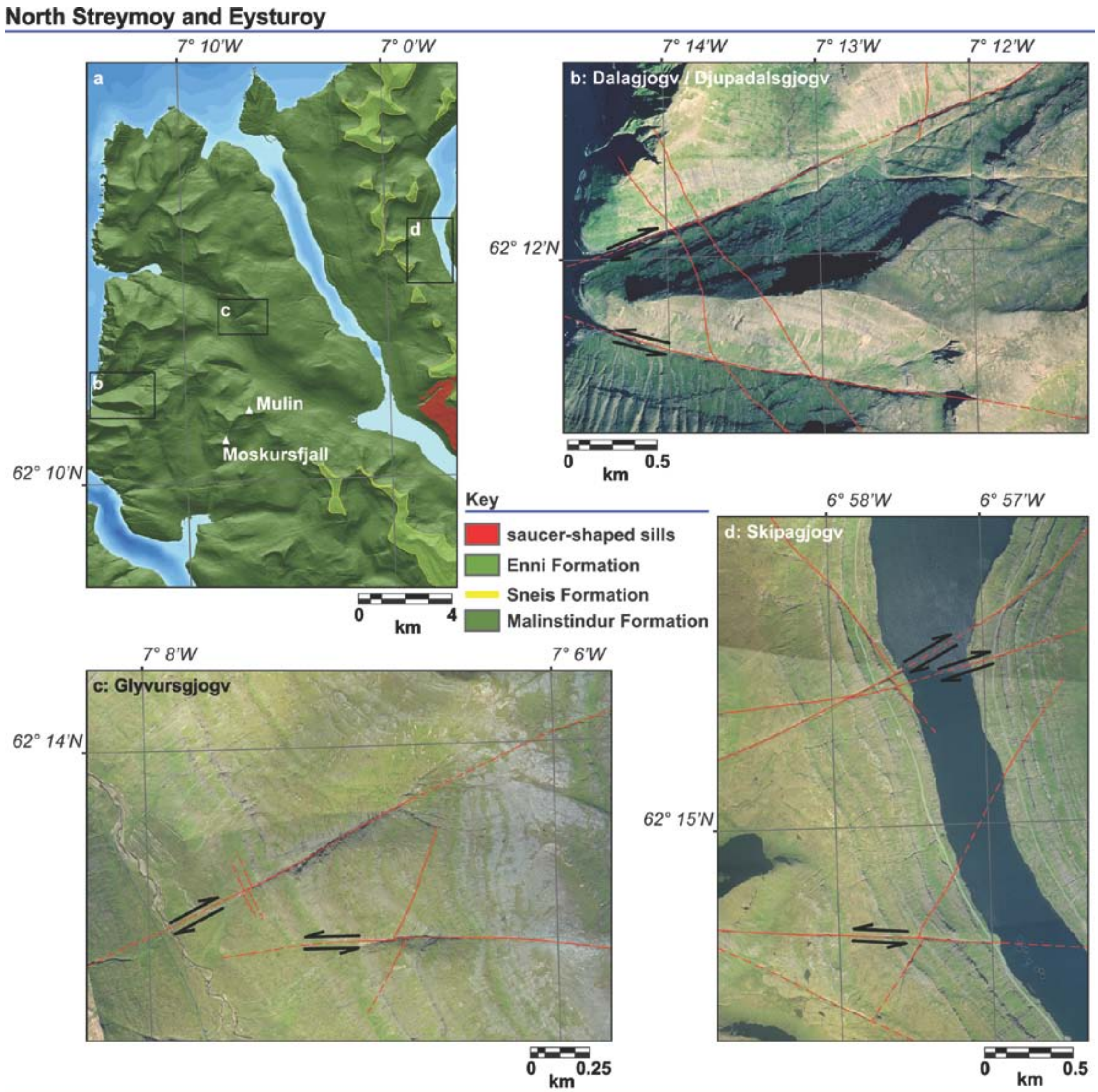

Fig. 3.8. (a) Location map for cross-cutting relationships at: **(b)** Dalagjógv and Djúpadalsgjógv, Streymoy; **(c)** Glyvursgjogv, Streymoy; **(d)** Skipagjogv, Eysturoy. Typically, offsets across the ENE-WSW set are minor (<10m) with larger offsets across the ESE-WNW set (10-30m).

(2a) the emplacement of ENE-WSW and ESE-WNW conjugate dykes, facilitating N-S extension; (2b) crustal extrusion involving both E-W shortening and further N-S extension facilitated primarily by slip on ENE-WSW (dextral) and ESE-WNW (sinistral) conjugate strike-slip faults; During the final stages of this event (2c), the regional extension vector rotated into a more NW-SE orientation that was taken up predominantly by slip along NE-SW oriented dextral-oblique-slip faults.

3.3.4.1 Event 2a

Event 2a dykes are typically vertical, 2-8m thick and oriented ENE-WSW and ESE-WNW forming a conjugate set, as exemplified by those that form the gullies of Dalagjógv and Djúpadalsgjógv on the west coast of Streymoy, to the north of Vestmanna (**Fig. 3.8b**). The dykes are poorly exposed, but are inferred to occur over a few kilometres based on the development of well-defined gully features. The dyke at Djúpadalsgjógv is continuous for about 2.3km and most likely continues eastwards between the mountains of Múlin (663m) and Moskursfjall (624m) (**Fig. 3.8a**). The dyke at Dalagjógv is continuous for about 2.9km, but is easily linked to numerous other dyke outcrops within gjogvs (meaning steeply sided canyons, gullies, or sea-inlets) towards the east-northeast, across Saksunardalur, and into Glyvursgjogv (**Fig. 3.8c**). Gjogvs (and dyke outcrops) along that particular trend can be linked all the way to the east coast of Streymoy, totalling just over 10km (**Fig. 3.8a**). Where observed, NW-SE- and N-S-oriented dykes are always offset across these dykes (e.g. at Dalagjógv/Glyvursgjogv and Djúpadalsgjógv, Streymoy; Skipagjogv, Eysturoy; **Fig. 3.8b-d**), with the larger offsets generally observed across the ESE-WNW set.

As with the Event 1 dykes, those of Event 2 display irregular margins that appear to exploit the polygonal jointing of the host lava units. Contrary to assessments in previous studies (e.g. Geoffroy et al., 1994), no evidence has been found to indicate that the dykes intrude existing faults of a similar orientation. However, commonly, ENE-WSW and ESE-WNW mineralised faults and fractures are observed within Event 2a dykes (**Fig. 3.8a**), with damage zones formed in both the dykes and adjacent country rocks. On that basis, we believe that the dykes were intruded first, and later exploited by faulting episodes (Events 2b and c). Further to this, in instances where the large saucer-shaped sills and Event 2 structures intersect, the dykes are clearly cut by the sills, which are in turn cut by the faults (i.e. the dykes are older than the sills, which are older than the faults).

3.3.4.2 Event 2b

Event 2a dykes are consistently host to similarly oriented (Event 2b) mineralised faults and tensile veins, again forming a conjugate set, which combined result in an E-W compression, and N-S extrusion (**Fig. 3.9a**). Such faults are not limited to the dykes, and in the northern islands are by far the most prevalent set of structures seen in exposures. Sub-vertical faults of this set almost always display strike-slip motion sense, as indicated by well developed slickenfibres in fault zones (two notable exceptions are addressed later in this section). As with Event 1 faults, mineralisation predominantly takes the form of calcite and various types of zeolite, with numerous mineral

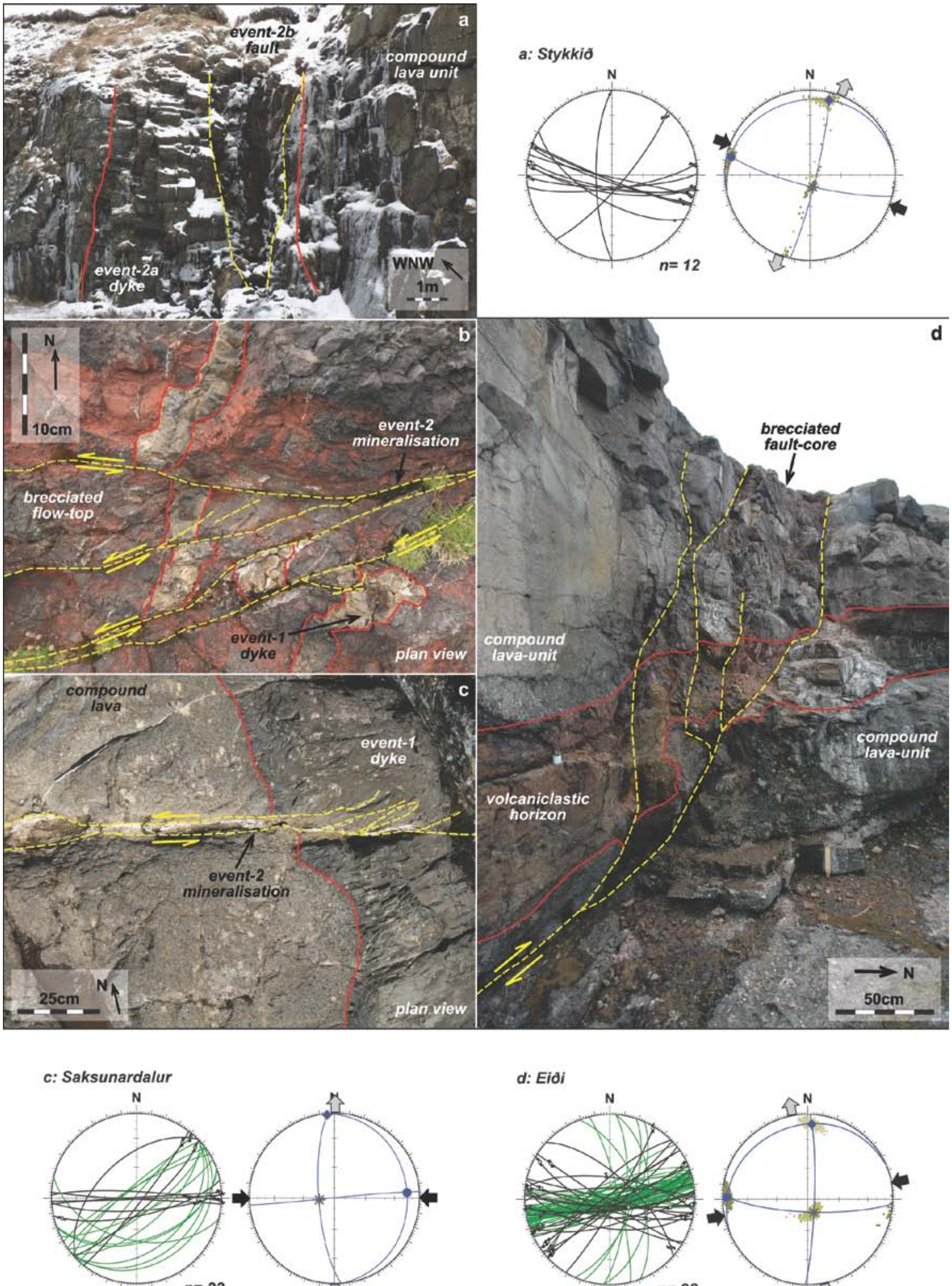
a
event-2b fault
compound lava unit
event-2a dyke
WNW
1m
a: Stykkið
N
n= 12
b
N
10cm
event-2 mineralisation
brecciated flow-top
event-1 dyke
plan view
c
compound lava
event-1 dyke
event-2 mineralisation
25cm
plan view
d
brecciated fault-core
compound lava-unit
volcaniclastic horizon
compound lava-unit
N
50cm
c: Saksunardalur
n= 22
d: Eiði
n= 98

Fig. 3.9. (*Previous Page*) Event 2b faults **(a)** ESE-WNW trending Sinistral strike-slip fault at Stikkið, Streymoy, exploits a similarly oriented Event 2a dyke which displays irregular polygonal margins. **(b-c)** Sinistral offsets of NW-SE trending Event 1b dykes at Sumba, Suðuroy, and Glyvursgjogv, Streymoy. **(d)** ENE-WSW trending dextral strike-slip fault at Eiði, N. Eysturoy, displays ~3.5m total displacement across a well developed fault core and damage zone. (Locations indicated on **Figure 3.3**).

overprints and well developed fault-core/damage zones (**Fig. 3.9**) indicating a recurrent fault activity through time. In all observed strike-slip instances, the conjugate pair consists of an ENE-WSW (dextral) set and an ESE-WNW (sinistral) set. Offsets range from millimetres-centimetres (**Fig. 3.9**), to many metres (e.g. **Fig. 3.8**), and possibly to a few hundreds of metres (as suggested in *section 3.3.1*).

As part of an extensive mapping campaign, Passey (2009) identified a large offset fault between Streymoy and Sandoy; the ESE-WNW trending Skopunarfjørður fault, with a purported dextral offset of 4.2-6.2 km and a vertical offset between 200-300 m (**Fig. 3.10**). Though there is likely to be a fault within the fjord at that location based on the presence of an elongate steep bathymetric low, it is rather unlikely that a fault in that trend would display a dextral offset, on the basis that in all other instances, ESE-WNW faults are sinistral. However, localities most proximal to Skopunarfjørður display Event 2b faults with a predominantly *dip-slip* motion sense (**Fig. 3.10**). We therefore suggest that the Skopunarfjørður fault is dip-slip with about 200-300 m vertical displacement. Notably, the other instance of predominantly dip-slip displacements associated with Event 2b occur in the northern-most part of the study area, in North Viðoy. It is

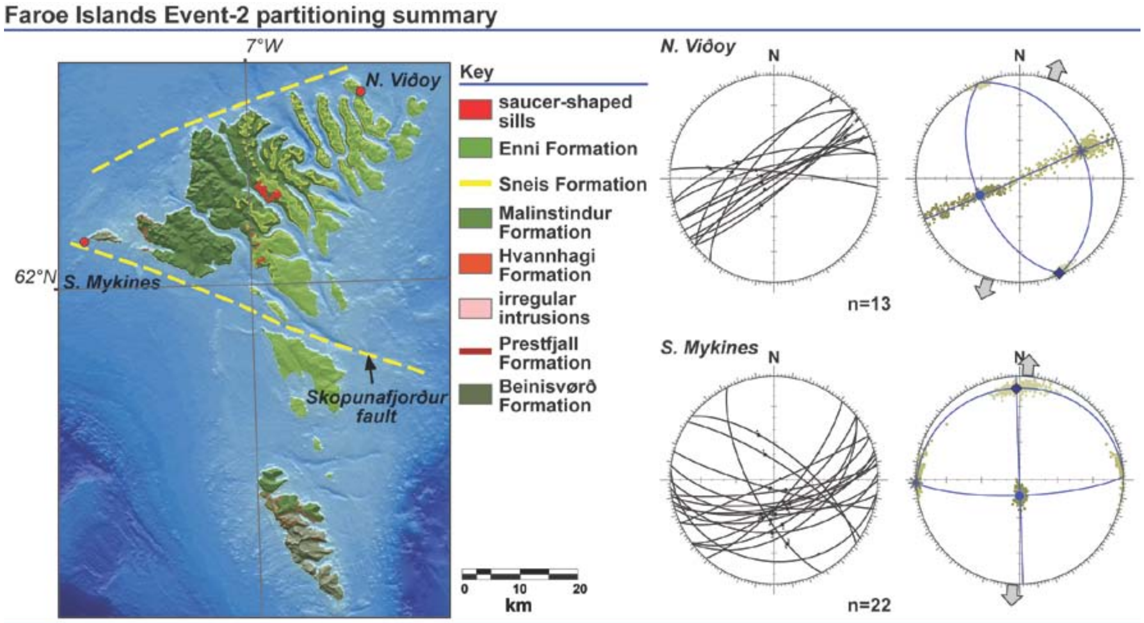

Fig. 3.10. Event 2 faults in S. Mykines and N. Viðoy are predominantly dip-slip, and may indicate the presence of large displacement (200-300m; Passey, 2009) faults in the nearby offshore.

therefore proposed that there may be a large offset ENE-WSW oriented dip-slip fault in the nearby offshore region. This pattern of major dip-slip normal faults bounding a domain dominated by smaller-scale conjugate strike-slip faults may suggest a regional scale strain partitioning – it may also contribute to the current physiographic expression of the Faroe Islands. (**Fig. 3.10**).

A component of the E-W shortening associated with Event 2b is accommodated by reverse faults (**Fig. 3.11**). Where observed, thrusts (and, occasionally, associated low-angle normal faults reflecting a locally spoon-shaped geometry of some faults) clearly interlink with the E-W conjugate faults, commonly operating as detachments to their strike-slip counterparts (**Fig. 3.11b**). In some instances, the two fault styles display a

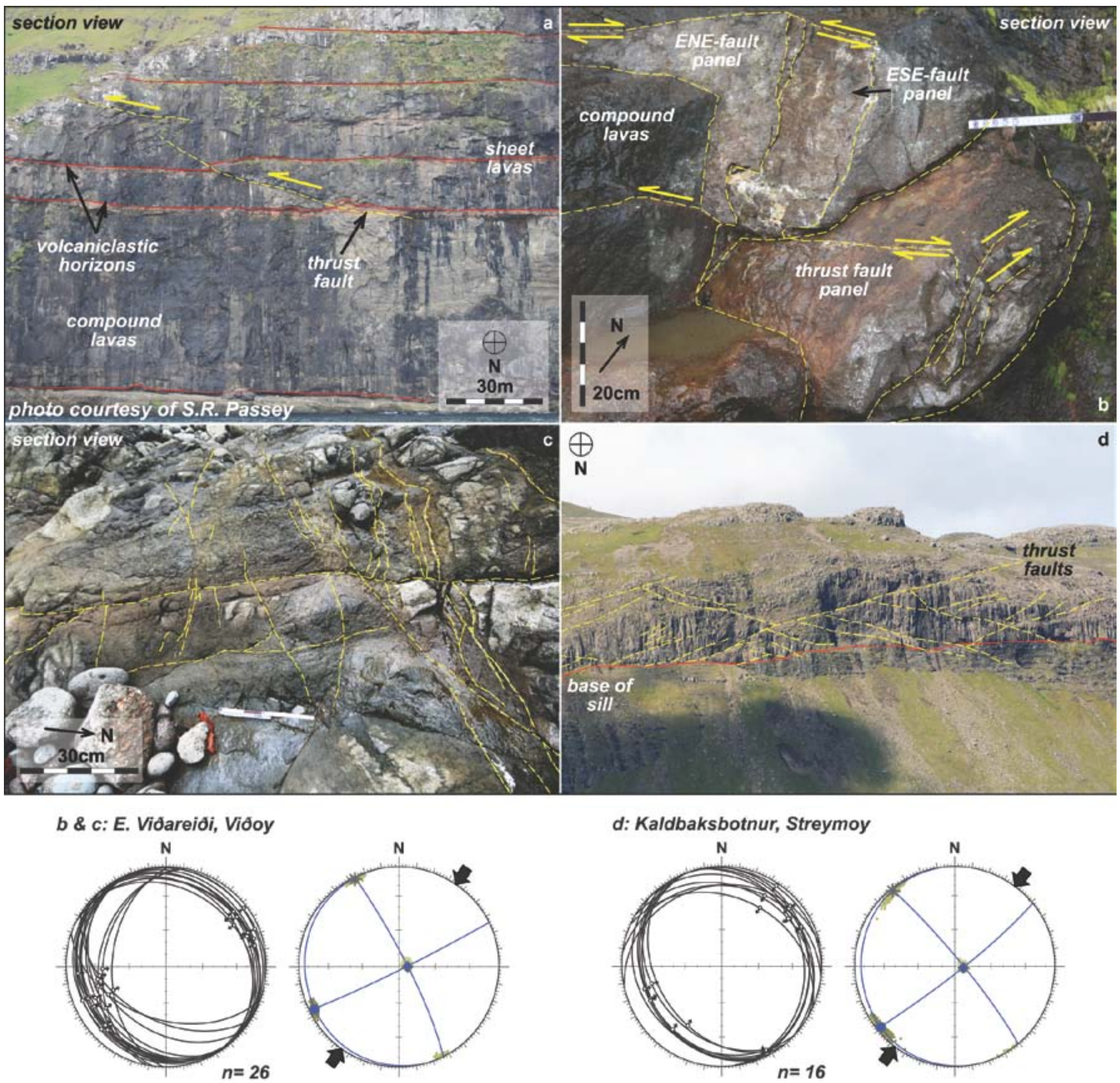

Fig. 3.11. Part of the E-W compression associated with Event 2 is taken up on minor displacement thrust faults, distributed across the islands. These range from metre-scale offsets **(a)**, to cm- and mm-scale offsets **(b)**. In some instances it is clear that the thrusts and E-W conjugate faults are genetically related **(b)** and in others that there is a mutual cross-cutting relationship **(c)**. Thrusts are also clearly evident cross-cutting the large saucer-shaped sills (e.g. Streymoy sill; **d**) and must therefore post-date their intrusion. (Locations indicated on **Figure 3.3**).

clear mutual cross-cutting relationships (**Fig. 3.11c**), and they are therefore deemed to be concurrent. Offsets are minor, ranging from millimetre to metre scales (**Fig. 3.11a**), but they appear to be widely distributed across the islands.

3.3.4.3 Event 2c

The final stage of Event 2 is characterised by limited strike-slip tectonism along NNE-SSW and NE-SW oriented dextral faults, which are most common in the far north of the Islands, such as is observed at Tjornuvik, northern Streymoy. At Tjornuvik, Event 2a dykes and 2b faults/fractures are clearly offset by a pair of dextral faults (**Fig. 3.12a-e**). The most notable of these offsets occurs across the bay (**Fig. 3.12b**), where a large ESE-WNW trending dyke displays a total apparent offset of 80-100m. At the western end of the bay, north of the beach, a single NE-SW trending Event 1 dyke appears to bifurcate just landward of the low-tide mark, springing an auxiliary NNE-SSW oriented dyke marked by a line of gullies parallel to the coast (**Fig. 3.12b, c**). At that locality, a set of E-W oriented Event 2b zeolite and calcite veins invade the Event 1b dykes. Those veins appear to be cut by similar mineral veins oriented parallel to the dyke, apparently exploiting the cooling-joint structure (**Fig. 3.12f, g**); this set display a more oblique (dextral) motion sense to the E-W oriented slickenlines. It is therefore inferred that this represents a continuation of the anticlockwise rotation of structures, and by corollary, the extension vector, to NW-SE. A possible alternative, however, is that this may be a local reorientation caused by the existing material anisotropy, e.g. the Event 1 dykes, and/or the existing cooling joints. The latter suggestion seems less likely as similar kinematics and cross-cutting relationships are observed in other localities, where no dykes are present, such as in eastern Viðareiði, Viðoy (**Fig. 3.11b & c**).

Structures associated with Event 2 demonstrably post-date those of Event 1, and must therefore have occurred towards the end of emplacement of the FIBG or later. They are the most abundant features across the islands, and record a distinct, island-wide N-S to NW-SE extension, coupled with an E-W compression (**Fig. 3.13**). Dykes of Event 1 are cut by the large saucer-shaped sills on Streymoy and Eysturoy, which are all cut by the strike-slip and thrust faults of Event 2b and c. Structures associated with Events 2b and c are observed through to the top of the remaining stratigraphy, and may therefore entirely post-date the FIBG.

Fig. 3.12. (*Next page*) **(a-b)** Aerial photograph of Tjornuvik, NE Streymoy, detailing major faults (yellow) and dykes (red). **(c)** Photograph of the west side of Tjornuvik bay, showing the Event 2a dyke offset across the Event 2c faults. **(d-e)** Well developed Event 2b slickenfibres on exposed fault panels at the pier section (indicated in **a-c**). **(f-g)** Reactivated Event 1 dykes displaying Event 2c mineralisation. In (**g**), zeolite and calcite veins are clearly reoriented along the cooling joint system within the dyke.

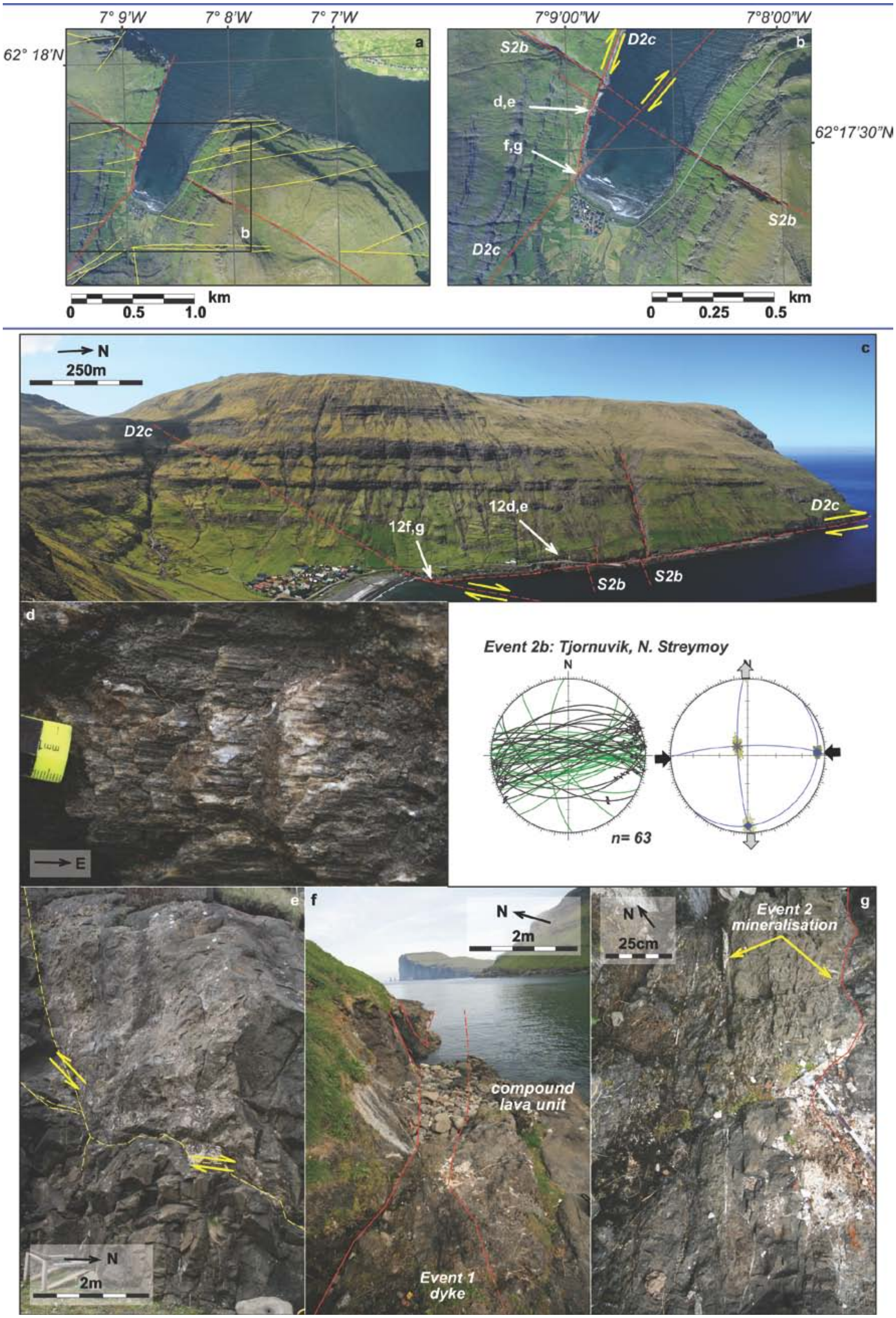
7° 9'W
7° 8'W
7° 7'W
62° 18'N
a
b
km
0
0.5
1.0
7°9'00"W
7°8'00"W
S2b
D2c
d,e
f,g
62°17'30"N
S2b
D2c
km
0
0.25
0.5
N
250m
c
D2c
12d,e
12f,g
D2c
S2b
S2b
d
E
Event 2b: Tjornuvik, N. Streymoy
N
n= 63
e
N
2m
f
N
2m
compound lava unit
Event 1 dyke
g
N
25cm
Event 2 mineralisation

3.3.5 Event 3: Regionally late reactivation

The Faroe Islands Basalt Group was emplaced at or around sea-level to a stratigraphic thickness in excess of 6.6km (Passey and Bell, 2007), and therefore a comparable magnitude of subsidence is required. Volcaniclastic sediments deposited into marine waters are now elevated above sea-level in the order of hundreds of metres. To date, the mechanism leading to this uplift has remained uncertain and no onshore studies have identified the structures likely responsible for it.

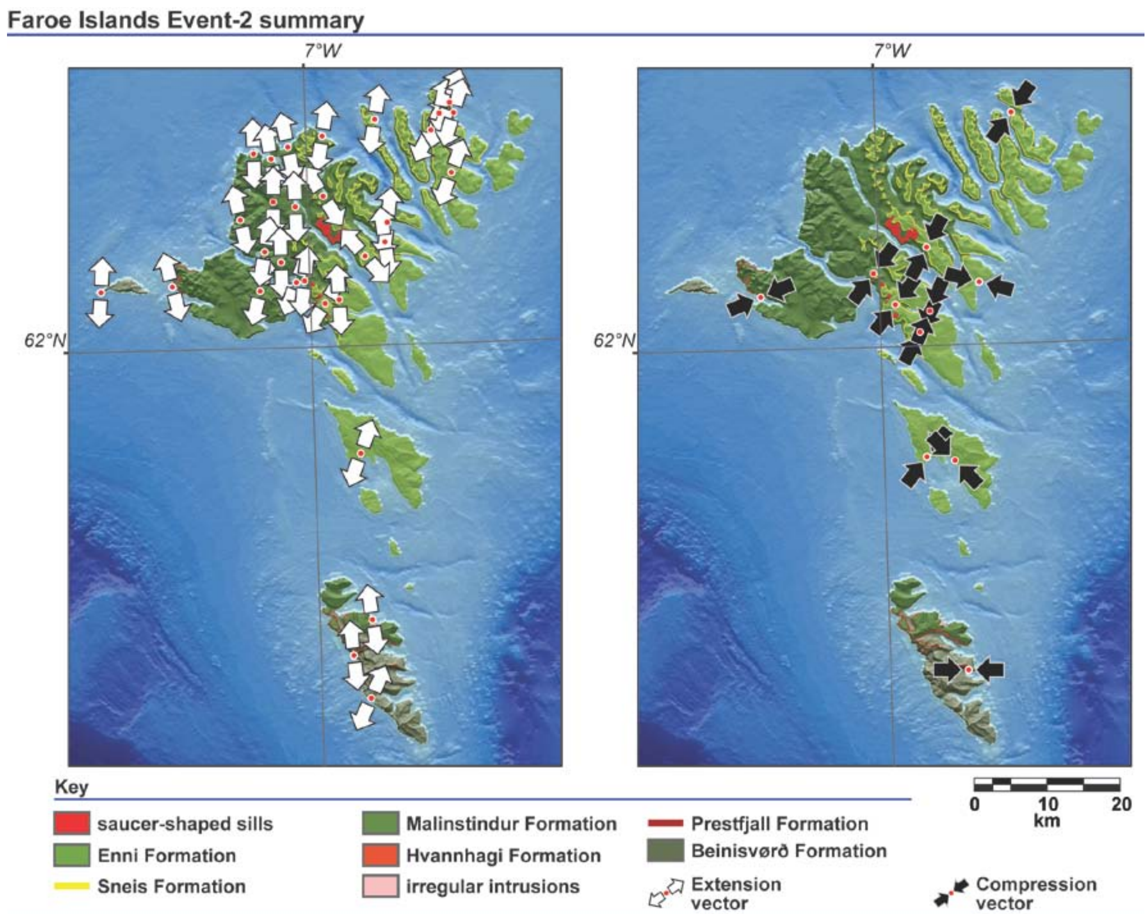

Fig. 3.13. (a) Event 2 inferred horizontal stress summary map from the E-W conjugate strike-slip faults, indicating an island wide N-S to NW-SE extension. (b) Inferred horizontal stress summary map from the Event 2 thrust faults, generally indicating E-W to NE-SW compression.

On the Islands, there is significant evidence for a late-stage reactivation of the existing structures, particularly on the SW coast of Suðuroy (**Fig. 3.14a, b, f**). Reactivation of both Event 1 and 2 structures is exemplified by the entrainment and local deformation of clastic infils that display only very minor mineralisation (Walker et al., 2009). Event 3 structures include:

1) Thin (0.1-0.3m wide) clay smears associated with pre-existing faults, that have been reactivated, cross-cutting early fault rocks and mineralisation features (**Fig. 3.14a**).

2) Wider (0.3-1m wide) clastic infills developed along pre-existing mineralised faults that display internal faults and/or asymmetric drag-fabrics defined by clast alignments, often suggesting the opposite sense of motion to the original kinematics of the host fault (**Fig. 3.14b, c**).

3) Saucer-shaped, 0.1-0.6m thick, clastic horizons that display fluvial to debris-flow lithofacies, preserving sedimentary structures, such as cross-bedding, channel bar and scour-structures (**Fig. 3.14d**).

4) Anastomosing mm-scale and planar dm-scale injection features are also developed that exploit pre-existing fractures within the surrounding basaltic units (**Fig. 3.14e**).

Walker et al. (2009; *Chapter 4* of the current thesis) provide a more detailed description of these features. The virtual absence of a cement, and the sedimentary

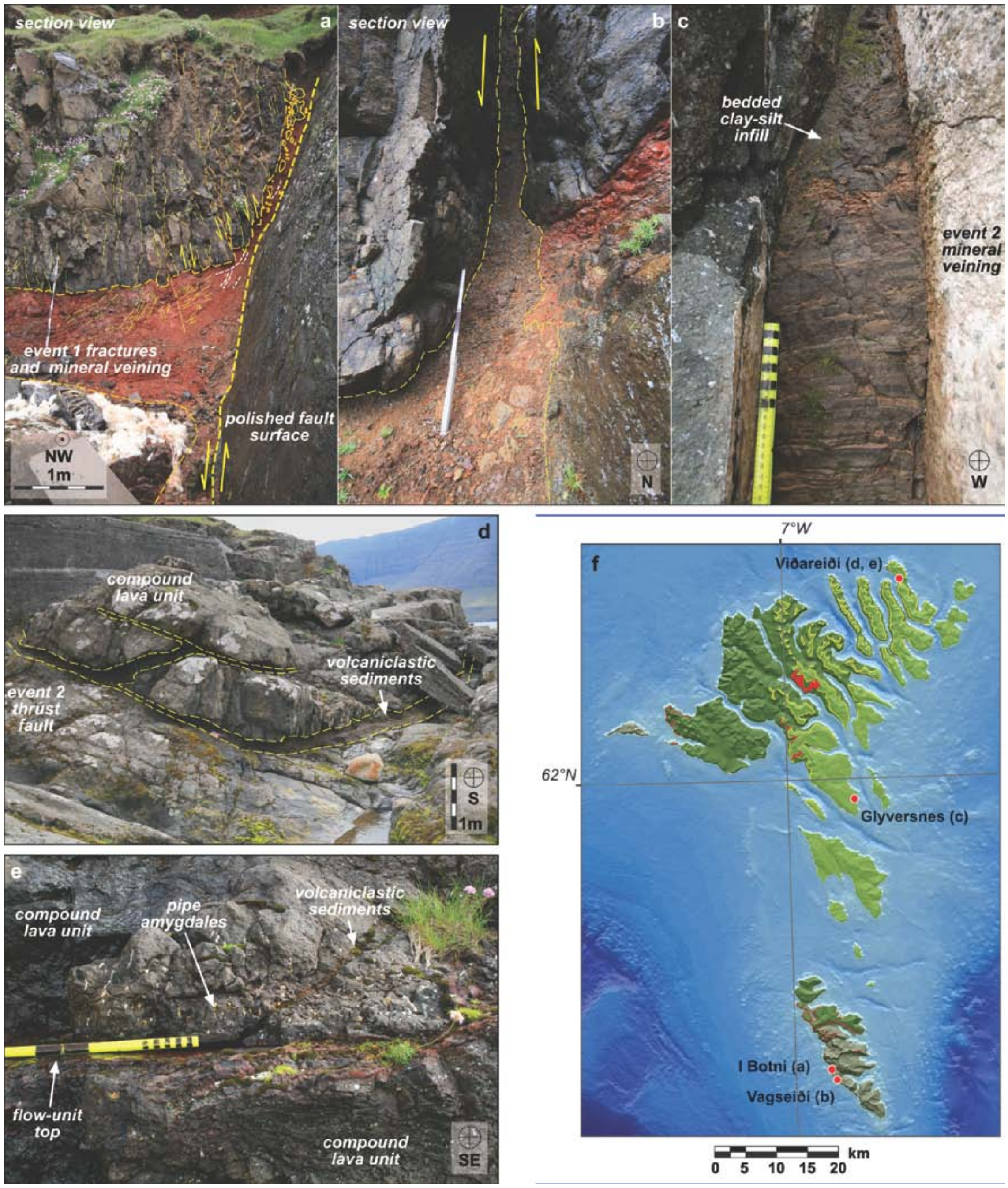

Fig. 3.14. Examples of Event 3 structures: **(a)** Reactivated Event 1 fault at I Botni. Calcite slickensides on the right are polished over, and Event 1 mineralisation (thick-long dashed lines) are cut and truncated by a later sub-vertical fabric (thin white dashed lines) within the clay horizon. The smear clearly contains mineralised, rotated clasts of Event 1 fault-wall rocks. (**b**) N-S trending Event 1 fault with later, matrix-supported chaotic breccia fill (ruler is 80cm tall). The clay horizon on the right has been dragged down to the west as well as being mixed with materials sourced from horizons above (not in photo). (**c**) Fine silts and clays deposited into an open Event 2 fault. The sedimentary material is well bedded, deposited during gravitational

(Fig.3.14 continued) settling, indicating the fault was open for a period of time. Faulting within the sediments is extensional, most likely relating to further dilation of the void through time. (**d**) At the Viðareiði pier section, otherwise subhorizontal clastic horizons commonly display ramp sections of about 45°, which cross-cut solid state features within the surrounding basalt units. Internally the clastic horizons display fragile sedimentary lithofacies such as planar and cross laminations, bar structures and imbrication, most likely indicating that the cavity was progressively filled by gravitational settling processes. (**e**) Clastic intrusions that commonly cut through lava solid state features such as pipe amygdales. (**f**) Location map for a-e.

nature of the infills suggests that these features may have formed in the near surface, perhaps at depths less than 1km.

3.3.6 Event summary and relevance to transfer fault models

Structures on the islands provide evidence for a 3-phase tectonic evolution (**Fig. 3.15**): (1a) an initial anticlockwise rotation from earlier E-W, to NE-SW extension (**Fig. 3.15a**), accommodated by dip-slip N-S, then NW-SE trending faults. Continued NE-SW extension (1b) was accommodated by emplacement of a regionally significant NW-SE- and NNE-SSW-oriented dyke swarm (**Fig. 3.15b**). Event 1 affects the majority of the FIBG stratigraphy. It is suggested that movement along faults corresponding to the inferred locations of the Judd, Brynhild and Westray fault-zones where they pass through the islands resulted in the thickness variations recorded by Ellis et al., (2009). Continued magmatism and anticlockwise rotation of the extension vector led to (2a) the emplacement of ENE-WSW and ESE-WNW conjugate dykes. Their intrusion heralds the onset of N-S crustal extension and was followed by (2b) crustal extrusion involving both E-W shortening and further N-S extension (**Fig. 3.15c**) facilitated primarily by slip on ENE-WSW (dextral) and ESE-WNW (sinistral) conjugate strike-slip faults. During the final stages of this event (2c), the regional extension vector rotates still further anticlockwise into a NW-SE orientation (**Fig. 3.15d**) that was taken up predominantly on NE-SW oriented dextral-oblique-slip faults. Event 2 began towards the end of magmatism associated with the FIBG, and most likely continued through to the onset of oceanic-spreading on the Aegir ridge (ca. 54 Ma, see below). Both events 1 and 2 display multiple generations of calcite and zeolite mineralisation in both tensile and shear hydraulic vein arrays, which suggests that hydrothermal mineralisation occurred both as a precursor to the development of a through-going surface, and during fault-slip (Blenkinsop, 2008). Zeolite and calcite mineral growth implies some degree of burial, most likely to depths in excess of a kilometre. Finally, (3) the reactivation of some faults may have helped to facilitate uplift (**Fig. 3.15e**), an event characterised by the entrainment of clastic material along fault planes, with only minor mineralisation, suggesting a near surface deformation environment (<1 km depth).

The Ellis model is based around large displacement strike-oblique-slip faults located within the fjords through the Faroe Islands, which project towards the FSB (**Figs. 3.1, 3.2**). However, no direct kinematics are observed on these faults (or fault-zones), with the only dependable constraints coming from the stratigraphic thickening experienced across them. Importantly, in all observed instances, faults (and dykes) of this orientation (NW-SE) display little to no lateral displacement. It therefore seems

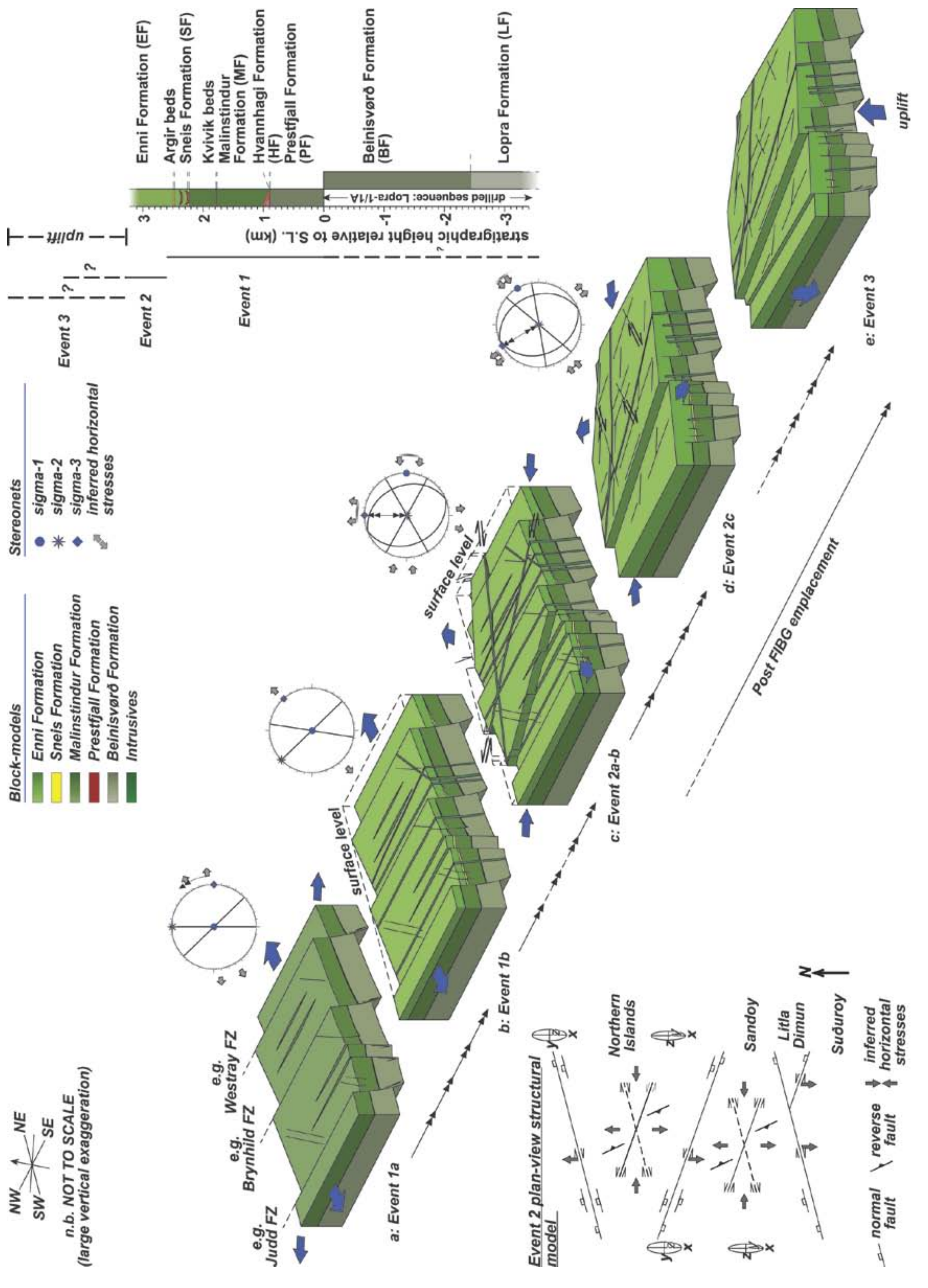

Fig. 3.15. Simplified summary block models for structures observed on the Faroe Islands (see text for details), and their timings relative to the FIBG, as constrained by stratigraphic thickening and offsets (Ellis et al., 2009; Passey, 2009; *this study*).

unlikely that the faults within the fjords are any different, and we propose that they should therefore be viewed simply as normal faults within the Faroes region. Our model is consistent with basalt thickness variations nearby offshore (**Fig. 3.1**; e.g. White et al., 2003), and supports heavy mineral trace studies that indicate NW-SE-oriented palaeo-lows existed during the Palaeogene (e.g. Jolley and Morton, 2007). Evidence from the Faroes may therefore still find application within the Faroe-Shetland Basin, despite the clear differences in terms of stretching magnitude.

3.4 Discussion

3.4.1 Deformation history systematics

If used throughout a study, the application of deformation history systematics can help to determine the most probable series of events with a given set of structures. An initial aim of this study was to test the two existing models concerning the development and timing of structures on the Faroe Islands, i.e. A single cyclic, left-lateral transtension event on basin-scale transfer zones resulting in a complex 3D strain (Ellis et al., 2009) *vs.* a polyphase deformation history during the progressive reorientation of rifting vectors through time resulting in cross-cutting structural sets (Geoffroy et al., 1994). The findings of the present study support the latter model, but also reveal significant evidence that contradicts the sequence, timings and grouping of structures proposed by Geoffroy et al. (1994).

In this section we assess the deformation history deduced during the present study using the methodology described in Potts and Reddy (1999). In order to do this most effectively, Events 1, 2 and 3 are split into their constituent sub-groups to give six structure-sets (e.g. Event 1a and b, Event 2a, b and c, and Event 3). Note that we have not separated structures that are observed in the field to link together and to be kinematically compatible, e.g. the Event 2b conjugate strike slip faults, thrusts and LANF sets. For a non-cyclic deformation history, these sets will ideally have a total of 15 relationships, as calculated using Equation 1 of Potts and Reddy (1999):

$$\mathrm{P}n = \frac{n(n-1)}{2}$$

where, *n* = the number of different structures and P*n* = the number of relationships for a non-cyclic, polyphase deformation history. If more than 15 relationships are observed, then a progressive cyclic history should be invoked. However, only 12 relationships are observed (**Fig. 3.16**), and so a non-cyclic history is the more likely. Thus key relationships that might lend support to the Ellis model are missing.

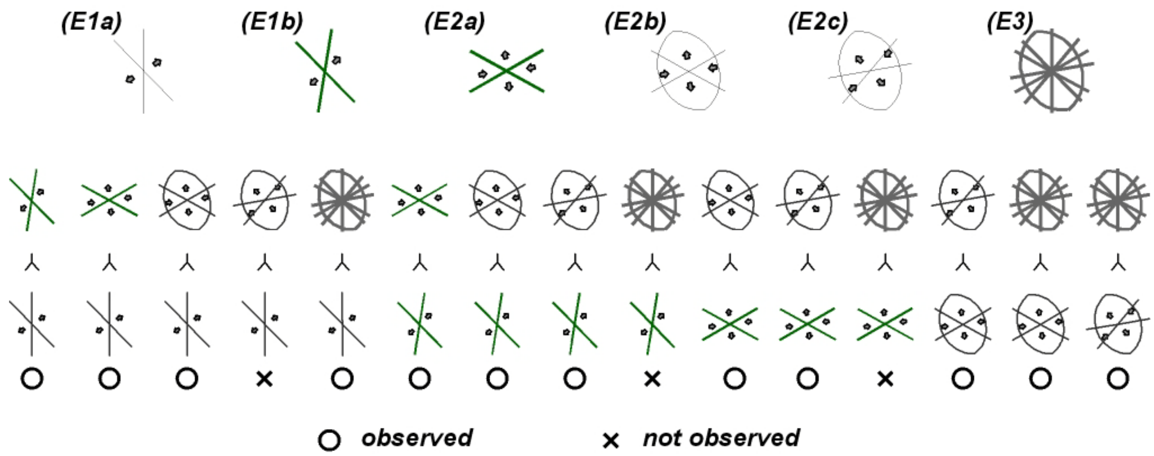

Fig. 3.16. Summary of cross-cutting relationships observed in the Faroe Islands. Instances where relationships are not observed can be fit in by tracking their position relative to the other relationships.

3.4.2 Regional subsidence mechanisms

The majority of the FIBG was emplaced at or around sea-level to a gross stratigraphic thickness in excess of 6.6km, requiring therefore a comparable magnitude of subsidence over the duration of the Palaeocene. Offsets across individual faults on the Faroe Islands rarely exceed 100m, and collectively, can only realistically account for a minor fraction of the overall regional subsidence. Clearly faulting within the Faroe Islands is not responsible for the regional subsidence, more the result of it. It would therefore be beyond the scope of the present study to infer the actual subsidence mechanisms. However, we would like to draw attention to the apparent coincidence between subsidence and lava emplacement rates. This could be indication that the load presented by the dense (~2.8kg/cm^3; Nelson et al., 2009) basalts of the FIBG, could cause isostatic disequilibrium and subsidence. The Faroes Block is an isolated micro-continent (Bott, 1983), and would therefore potentially be prone to rapid responses to loading or unloading. In this model, emplacement of the first extrusives (i.e. the Lopra Formation hyaloclastites) would induce minor subsidence, being only marginally denser than the underlying continental crust. This would cause infilling of the basin, by prograding hyaloclastites, until extrusion became subaerial (i.e. emplacement of the Beinisvord Formation). This could continue indefinitely, depending on the magmatic supply rate, as a positive feedback mechanism.

3.4.3 The NE Atlantic Margin and continental break-up: constraints from the Faroe Islands

Basins along the NE Atlantic margin preserve a record of processes that occurred during the build-up to continental separation and formation of the NE Atlantic. Inferences are often made concerning the kinematics responsible for the development of the present day structural architecture of those basins, based on the results of regional-scale numerical models and interpretation of seismic reflection datasets. The paucity of suitable field analogues means that subtleties within this process may be overlooked, which could have significant implications for basin-sediment distributions that are important in hydrocarbon exploration. Here the events described in *section 3.3* are addressed in terms of their regional and super-regional contexts.

During emplacement of the FIBG (59-56Ma: Palaeocene), central North Atlantic spreading propagated northwards solely through the Labrador Sea and Baffin Bay, separating the North American plate from Greenland, with no oceanic crust developed in the (present day) NE Atlantic (Pitman and Talwani, 1972; Srivastava and Tapscott, 1986; Torsvik et al., 2001; Gaina et al., 2009; **Fig. 3.17a**). The FSB lies roughly along strike from the Møre Margin to the NE, from which Cretaceous rifting events likely propagated southwards into the FSB, before a northwesterly jump and eventual separation on the Aegir Ridge occurred (Carr and Scotchman, 2003). NW-SE and N-S oriented Event 1 structures record an ENE-WSW to NE-SW extension throughout this time; an angle of almost 90° to the eventual plate motion (NW-SE). NW-SE oriented structures are present across the region, and display varied degrees of throw. The largest offsets observed are in East Greenland (km-scale; Larsen and Whitham, 2005), decreasing through the Faroe Islands (hm-scale) into almost sub-seismic resolution scale in the FSB. This is apparently coincident with crustal thickness and elevation across the region, with the largest offsets in the topographic highs, decreasing into the lows (the FSB), and may therefore relate to gravitational potential stresses. We hypothesize that excess GPE is generated by regional-scale differences in surface heat flow, topography, and crustal thickness and density (related in part to magmatism) and could perhaps be related to the spreading direction of the central and northwestern North Atlantic at the time (i.e. through the Labrador Sea towards Baffin Bay). Despite the Faroes being well over a thousand kilometres from the Atlantic at the time, it is possible that with the East Greenland-Faroes region being higher than the spreading

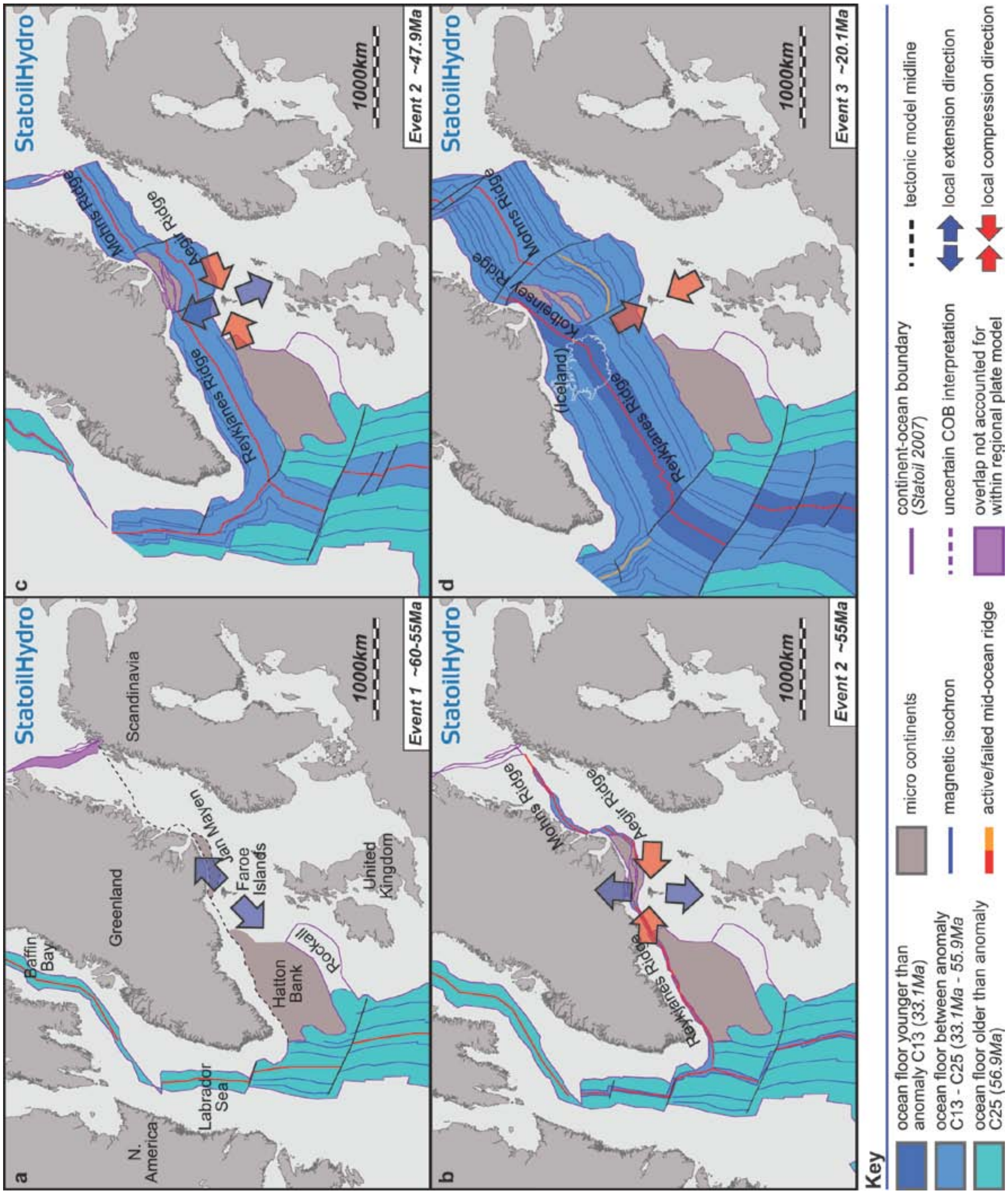

Fig. 3.17. North Atlantic plate reconstructions from the Palaeocene to Miocene, focused on the Faroe Islands. **(a)** 60-55Ma: N. Atlantic spreading initially propagates northwards through the Labrador Sea and Baffin Bay, splitting the (now) North American plate from Greenland. Rifting in the Faroes region is NE-SW oriented. **(b)** 55Ma: Spreading begins to the east of Greenland, with a progressive ‘unzipping’ from north to south, from the Barents Sea down towards the southern N. Atlantic. Initial break-up occurs with formation of the Mohns, Aegir and Reykjanes ridges. Combined, the extension vector related to spreading on the Aegir and Reyjanes ridges is N-S at this time; ridge and transform faults form a conjugate set to facilitate this extension

vector. **(c)** 47.9Ma: Greenland begins to move relatively westwards away from the European continent with an associated anticlockwise rotation in the extension vector. **(d)** 20.1Ma: Spreading on the Aegir ridge shuts, jumping to the Kolbeinsey ridge. A combination of mechanisms (e.g. body force) led to compression and uplift of the surrounding continental margins. Present day continental outlines are shown for reference only. (Original images courtesy of StatoilHydro).

ridge and its surroundings (i.e. the Møre and Kilda basins), excess GPE would be generated in the continental interior, resulting in extension (e.g. Pascal and Cloetingh, 2008). Topographic reconstructions for the Palaeocene to Eocene (e.g. Jones and White, 2003; Maclennan and Jones, 2006; Nisbet et al., 2009; **Fig. 3.18**) suggest that the Faroes region was relatively high compared to the Atlantic ridge and the basins developed to the NE and SW. Such conditions could have resulted in NE-SW oriented extension in the Faroes region, and mild compression in the surrounding lows.

By the early Eocene (55Ma), minor sea-floor spreading had initiated on the Mohns and Aegir Ridges in the Norwegian-Greenland Sea, propagating southwards, and the Reykjanes Ridge in the NE Atlantic, as the Greenland and Eurasian continents began to separate (Ziegler, 1988; Lundin, 2002; **Fig. 3.17b**). The Aegir Ridge represents a large embayment on the margin, and is linked to the Mohns and Reykjanes ridges by large transform faults. The ENE-WSW and ESE-WNW oriented continental margin to the north of the Faroes forms an open, northward-pointing ‘v’ (**Fig. 3.17b**). Faults with the same orientations are observed en-mass on the Faroe Islands as a conjugate pair that facilitates N-S extension. Evidence on the Islands therefore suggests that the initial

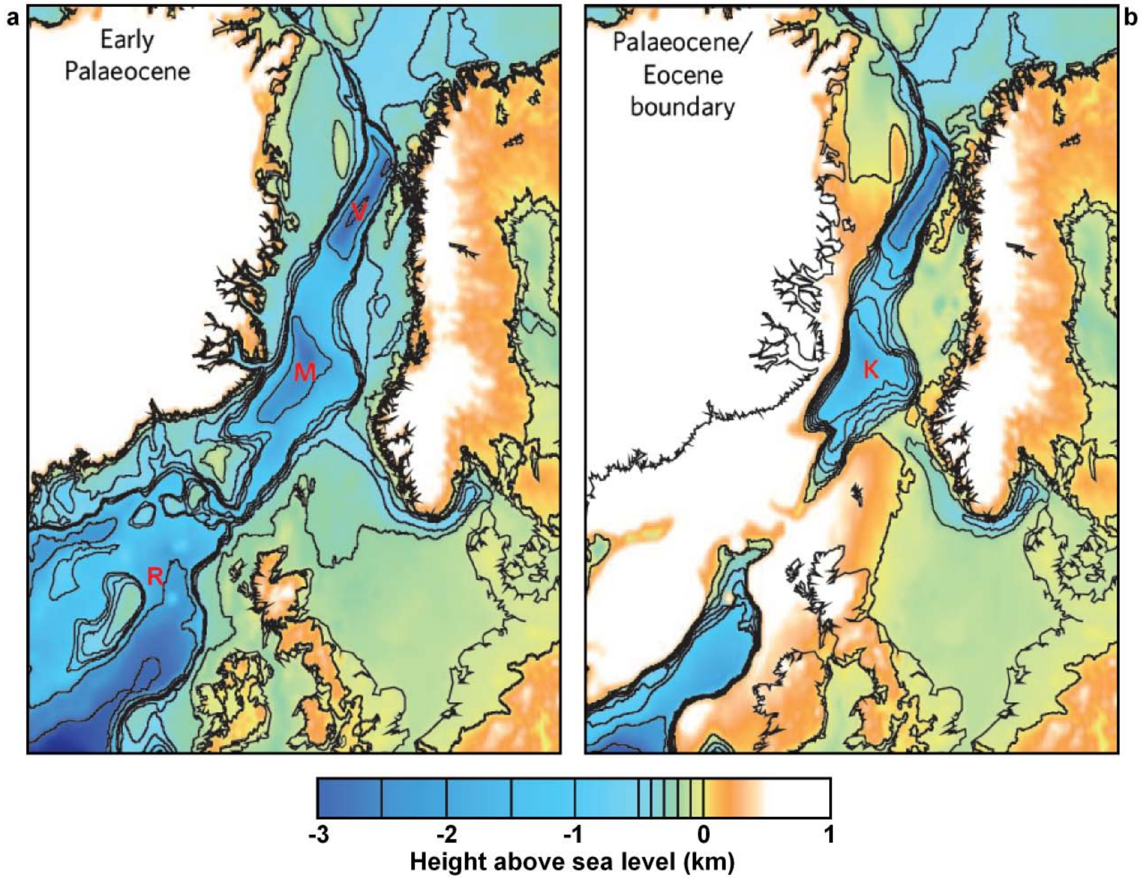

Fig. 3.18. (**a**) Palaeocene and (**b**) Palaeocene-Eocene topographic reconstructions for the N. Atlantic region (Figure 1 of Nisbet et al., 2009). Throughout the Palaeocene, and into the Eocene, the Faroe Islands are relatively high compared with their surroundings (i.e. the Møre (M) and Vøring (V) regions, and the Kilda basin (K) to the NE, and Rockall region (R) to the SW). The resultant gravitational potential energy caused by this relative elevation may be sufficient to drive extension preferentially in the Greenland, Faroe and Shetland areas.

stages of plate separation involved N-S extension with, perhaps, oblique spreading on the Aegir and Reykjanes Ridges, and transtension on the linking transform faults. With time, Greenland began to drift relatively westwards from Europe resulting in an anticlockwise rotation of the extension vector into a more NW-SE orientation (**Fig. 3.17c**).

Spreading on the Aegir ridge ceased as part of a ridge-jump to the Kolbeinsey Ridge (Talwani and Eldholm, 1977), with continued spreading to the present day (**Fig. 3.17d**). With sea floor spreading established, the dominant forces on the NE Atlantic continental margin became compressional, which throughout the Cenozoic is typically attributed to the action of a combination of body-forces. These include ridge-push and gravitational potential stresses related to lithospheric thickness and elevation variations in the continental interior (e.g. the Scotland Massif and the Scandes Orogenic belt), coupled to additional horizontal compressive stresses relating to Iceland and its insular margin (Cloetingh et al., 2008; Doré et al., 2008; Pascal and Cloetingh, 2008). Such lateral forces would undoubtedly be varied across the region due to the asymmetric structure and timings of the marginal basins. Further to this, the location of pre-existing structures of varied age (Caledonian to Recent) and significance (local to regional scales), could explain the multiple compressional-structure orientations developed along the margin. Significantly, the regionally-late structures developed on the Faroe Islands (Event 3) are typically tensile features with associated clastic infills. If developed during compression, it is possible the structures are local tensile features developed on the outer-edges of regional-scale compressional folds (e.g. Ramsay and Huber, 1987), or as a result of gravitational instabilities developed on topographic-highs.

3.5 Conclusions

- Spatially and temporally-related suites of brittle faults, hydrothermal mineralization and intrusive igneous sheets (dyke swarms and sills) are recognized throughout the Faroe Islands and formed during and after extrusion of the FIBG.
- Structural relationships observed in the field indicate a progressive reorientation in the regional stretching directions through time, from NE-SW to N-S to NW-SE extension, leading to polyphase deformation rather than a continuous, cyclic deformation regime.
- NW-SE oriented faults are dip-slip in all observed cases. In the absence of any evidence to the contrary, it is inferred that these structures are indicative of movements on the basin-scale faults within the fjords (i.e. the Judd, Brynhild and Westray faults). The kinematics of these faults and the similarly oriented dykes indicates a distinct period of NE-SW extension, possibly relates to an excess gravitational potential energy within the continental interior relative to the mid-ocean ridge in the western North Atlantic. Progressive displacements on these faults throughout the Palaeocene are responsible for thickness variations within the FIBG, and similarly aged strata within the FSB.
- The progressive anticlockwise rotation of the extension vector identified seems consistent with the most recently published NE Atlantic continental break-up reconstructions, and illustrates the importance of carrying out detailed field

studies, in addition to the more usual margin-scale modeling studies, in order to validate plate reconstructions.

4

The nature and significance of post-magmatic faults and associated clastic infills on the NE Atlantic margin: evidence from the Faroe Islands

Abstract

Detailed geological observations have revealed the hitherto unrecognised development of regionally-late, fault-related deformation structures on the Faroe Islands that are typically associated with different styles of clastic sedimentary infilling. These include: 1) Thin (0.1-0.3m wide) clay smears associated with pre-existing faults that have been reactivated, cross-cutting early fault rocks and mineralisation features. 2) Wider (0.3-1m wide) clastic infills developed along pre-existing mineralised faults, that display internal faults and/or asymmetric drag-fabrics defined by clast alignments, often suggesting the opposite sense of movement to the original host fault. 3) Saucer-shaped, 0.1-0.6m thick clastic horizons that display fluvial to debris-flow lithofacies, preserving sedimentary structures, such as cross-bedding, channel bar and scour-structures. 4) Anastomosing mm-scale and planar dm-scale injection features that exploit pre-existing fractures within the surrounding basaltic units. In general, the clastic infills (2) occur as discontinuous lenses developed along reactivated faults, sourced partly from the local volcanic wall rocks, but predominantly from the clastic strata preserved locally between individual basaltic flow units. These structures post-date all other episodes of faulting recognised in the Faroe Islands and, unlike earlier episodes, lack significant amounts of associated mineralisation. It is proposed that this reflects their development at shallow depths (near to the surface) and very late in the geological history, possibly during regional uplift. The saucer-shaped clastic horizons are associated with decametre-scale displacements and the development of tilted hanging-wall blocks adjacent to certain large faults. They are interpreted as sediment infills of subterranean cave networks formed due to the partial dismemberment of pre-existing lava flow units, related to adjacent, near-surface fault movements. Clastic injections in the area likely

result from the localised development of fluid overpressures in trapped, water-saturated sediment infills caused by the jostling of fault-blocks during subsequent faulting.

Structures equivalent to the late, clastic-filled faults of the Faroes may occur in other parts of the NE Atlantic margin, particularly along the axes of gentle regional-scale folds that are widely developed in the region. Displacements observed are all well below seismic resolution, and such structures may be more widespread across the region than previously anticipated. Importantly, the probable unsealed nature of the clastic infills makes them potential fluid-migration pathways, both up- and across-faults within the Cenozoic volcanic sequences of the NE Atlantic region.

4.1 Introduction

Much of the NE Atlantic Margin is covered in a thick pile of trap-style volcanics, part of the North Atlantic Igneous Province (NAIP; emplaced ~62-54 Ma; Saunders et al., 1997), of which the Faroe Islands Basalt Group (FIBG; Passey et al., 2006; Passey and Bell 2007) is a constituent. The FIBG was emplaced at or around sea-level during the Palaeocene, to a true thickness of about 3km, requiring a comparable magnitude of subsidence during the eruption period. To date, most of the structures preserved on the Faroe Islands have been attributed to subsidence-related deformation (Geoffroy et al., 1994; Ellis et al., 2009; Passey, 2009). These record a progressive anticlockwise rotation in the regional extension vector, from NE-SW to NW-SE, which can be related to changes in the location and kinematics of ocean spreading in the North Atlantic region (Walker et al., 2008; *Chapter 3*). To date, no onshore studies have accounted for the subsequent events related to uplift that must have occurred to bring the Faroe Islands to their current elevation (the highest peak, Slættaratindur, at 882m a.s.l.). The principal aim of this study is to highlight the role of regionally late fault reactivation in forming open, subterranean voids, fissures and caves which subsequently have become infilled by clastic sediments. Unlike other earlier faulting episodes, these infills are not associated with widespread mineralisation and may represent unsealed faults. We also detail other styles of fault reactivation that are believed to be coeval with these late reactivations, possibly during regional uplift following plate separation and sea-floor spreading.

4.2 Geological setting

4.2.1 Faroe Islands stratigraphy

The FIBG is dominated by tholeiitic basalt lavas, divided into seven formations based on lithology and the presence of regionally recognised disconformity surfaces (Rasmussen and Noe-Nygaard, 1969 & 1970; Passey et al. 2006) and geochemistry (Waagstein, 1988). The formations relevant to the present study are (from oldest to youngest) the Beinisvørð, Malinstindur and Enni Formations (**Fig. 4.1**).

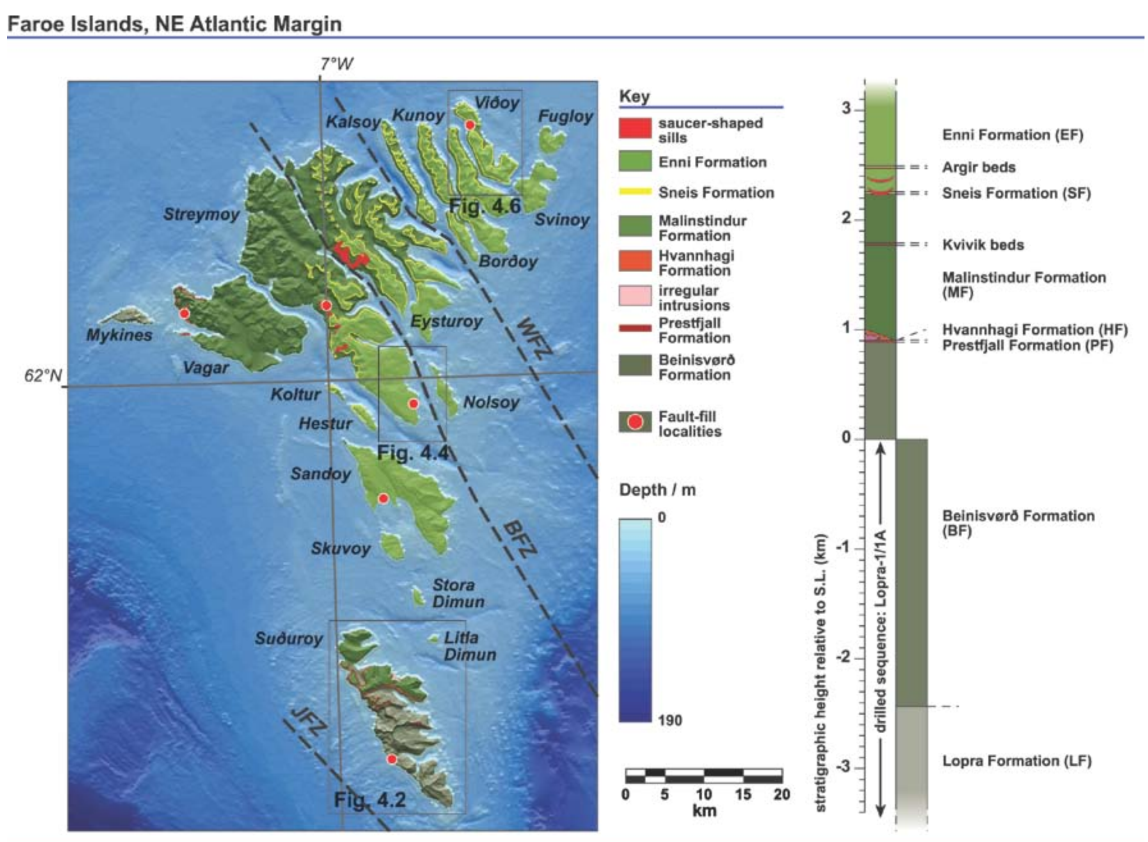

Fig. 4.1. Hill-shaded simplified geological, and bathymetric map of the Faroe Islands and insular shelf with gross stratigraphic column for the Faroe Islands Basalt Group (after Passey, 2009).

The Beinisvørð Formation (BF) is ca.3.3km thick, of which only 900m is exposed above sea level on the Islands. The BF generally comprises aphyric, laterally extensive sheet lobes, often separated by minor volcaniclastic horizons (Passey and Bell, 2007). The sheet lobes display well-developed columnar joints that are commonly exploited during faulting, and can result in a considerable local steepening in fault plane dips compared to faults cutting adjacent clastic horizons located between lava flows (*Chapters 3 and 5*). Exposure of the BF is limited to the southern island, Suðuroy, and in the far west on Vagar and Mykines (**Fig. 4.1**).

The overlying Malinstindur Formation (MF) is <1.4km thick and comprises subaerially emplaced, compound basalt lavas that are initially olivine-phyric evolving to aphyric, and then plagioclase-phyric types. Again, lavas are commonly separated by minor clastic horizons, typically volcaniclastic sandstones and siltstones, which were deposited during periods of volcanic quiescence (Ellis et al., 2002). The MF is particularly well exposed on the northern islands of Vagar, Streymoy and Eysturoy, at low altitudes on the north-eastern islands (Kalsoy, Borðoy, Kunoy and Viðoy), and in the north of Suðuroy (**Fig. 4.1**).

The lowermost 900m of the youngest unit, the Enni Formation (EF), is exposed on the Islands, and comprises low-TiO_2 and high-TiO_2 interbedded simple (sheet lobes) and compound tholeiitic lavas. The 900m is a minimum thickness, with a significant amount (in the order of hundreds of metres) eroded from the top of the volcanic pile (Waagstein et al., 2002). The EF is exposed in a north to northeast arcing trend from Lítla Dímun across Sandoy and the northern islands, reflecting the general (southeasterly) dip direction (**Fig. 4.1**).

Units on the Faroe Islands generally display a southeasterly dip, the largest of which are observed in the Beinisvørð Formation in Mykines, ~8°, and decreasing up-stratigraphy to become sub-horizontal (i.e. ~1°) in the Enni Formation on Fugloy, Svinoy and Viðoy (**Fig. 4.1**). This architecture suggests regional-scale fold-growth throughout the Palaeocene during emplacement of the FIBG, as discussed in *section 4.4.2*. Notably, the complex interplay between Palaeogene uplift and regional differential subsidence, and the effects of fault-block rotation, have likely resulted in numerous over-steepened units on outcrop (e.g. units in the Malinstindur Formation, Viðareiði, Viðoy: ~15-20° increase in inclination) and island-scales (e.g. the Enni Formation on Sandoy: ~3-4° increase in inclination).

4.2.2 Faroe Islands structural evolution

Structures developed in the FIBG provide clear evidence for a multi-phase rift-reorientation through time (Geoffroy et al., 1994) before and during continental break-up, followed by a significant phase of uplift (Walker et al., 2008; *Chapter 3*). Distinct phases of faulting and dyke intrusion are recognised. This began with (Event 1a) ENE-

WSW to NE-SW extension, accommodated by N-S- and NW-SE-trending dip-slip faults. Continued NE-SW extension was accommodated by the emplacement of a regionally significant swarm of NW-SE- and NNE-SSW-oriented dykes (Event 1b). Collectively, Events 1a and b affect the majority of the FIBG stratigraphy, resulting in thickness variations, most notably across the Judd, Brynhild and Westray Fault Zones (**Fig. 4.1**). Continued magmatism and an anticlockwise rotation of the extension vector led to (Event 2a) the emplacement of ENE-WSW and ESE-WNW conjugate dykes. Their intrusion marks the onset of N-S crustal extension and was followed by (Event 2b) fault-accommodated crustal extrusion involving both E-W shortening and further N-S extension facilitated primarily by slip on ENE-WSW (dextral) and ESE-WNW (sinistral) conjugate strike-slip faults, many of which are developed in the same locations as the immediately preceding conjugate dykes. A component of this E-W shortening was facilitated additionally by the development of minor-offset thrust faults which dip mainly to the SW or NE. During the final stages of this event (Event 2c), the regional extension vector rotated into a more NW-SE orientation that was preferentially accommodated by slip along NE-SW trending (dextral) oblique-slip faults. Based on the timing relative to Event 1, and an apparent thickening of the Enni Formation across hectometre-scale offset, E-W-trending faults (Passey, 2009; Ellis et al., 2009), Event 2 most likely began towards the end of magmatism associated with the FIBG, coeval with the onset of oceanic-spreading on the Aegir ridge (ca.54-51 Ma; Lenoir et al., 2003); it may have continued through to the linkage of the Reykjanes, Kolbeinsey and Mohns Ridges. Events 1 and 2 are associated with multiple generations of calcite and zeolite mineralisation in linked arrays of tensile and shear hydraulic veins. Field and thin section observations suggest that mineral growth occurred both as a precursor to the development of through-going slip surfaces, and during fault-slip with precipitation of minerals along irregular fault surfaces (Blenkinsop, 2008). The final deformation (Event 3), and the subject of the present paper, involves the reactivation of some faults, the entrainment of clastic material along fault planes, and a general absence of mineralisation.

4.3 Event 3 features: detailed geological characteristics

Event 3 fault-related deformation structures on the Faroe Islands are quite distinctive from, and consistently cross-cut structures formed during Events 1 and 2. Characteristically, these faults are usually associated with entrained clastic sediments and can be subdivided into four related categories based on their geological and textural characteristics and the processes believed to be responsible for their formation. The development of two of these categories is controlled directly by faulting processes, whilst the other two represent more complex interactions between near-surface deformation, fracturing, sedimentation and fluid flow processes. All are thought to have formed at very shallow crustal depths (<2km) and may have developed during regional uplift of the Faroe Islands.

4.3.1 Clastic smears

A small proportion of faults in the Faroe Islands (<15%) preserve clastic materials smeared along or dragged into the exposed fault plane. In all cases, the clastic material appears to be derived from adjacent sedimentary horizons developed between lava flows that are offset along the faults. The two best preserved type examples detailed here result from the late reactivation of Event 1 faults located on the western coast of Suðuroy, at the I Botni power station (**Fig. 4.2**).

The larger of the two faults at I Botni is a NNE-SSW (025°) trending dip-slip fault formed during Event 1 that displays ~30m displacement down to the east, across a well developed 3-5m wide damage zone (**Fig. 4.2c**). Fault rocks within the Event 1 damage zone display widespread calcite and zeolite mineralisation in tensile (mode I) veins and shear hydraulic veins/fractures, and also in vuggy infillings between brecciated blocks. Within the fault core, however, these features are cross-cut and therefore post-dated by the development of polished fault surfaces that lack mineralisation. The clastic marker horizon is also smeared and polished, with a minimum 1-1.5m down to the west displacement (**Fig. 4.2d, e**), as measured from the base of the marker horizon, to the lower limits of the exposed smear. This is the opposite offset sense compared to the Event 1 host fault, and again, the clastic smear cuts mineral veins within the fault.

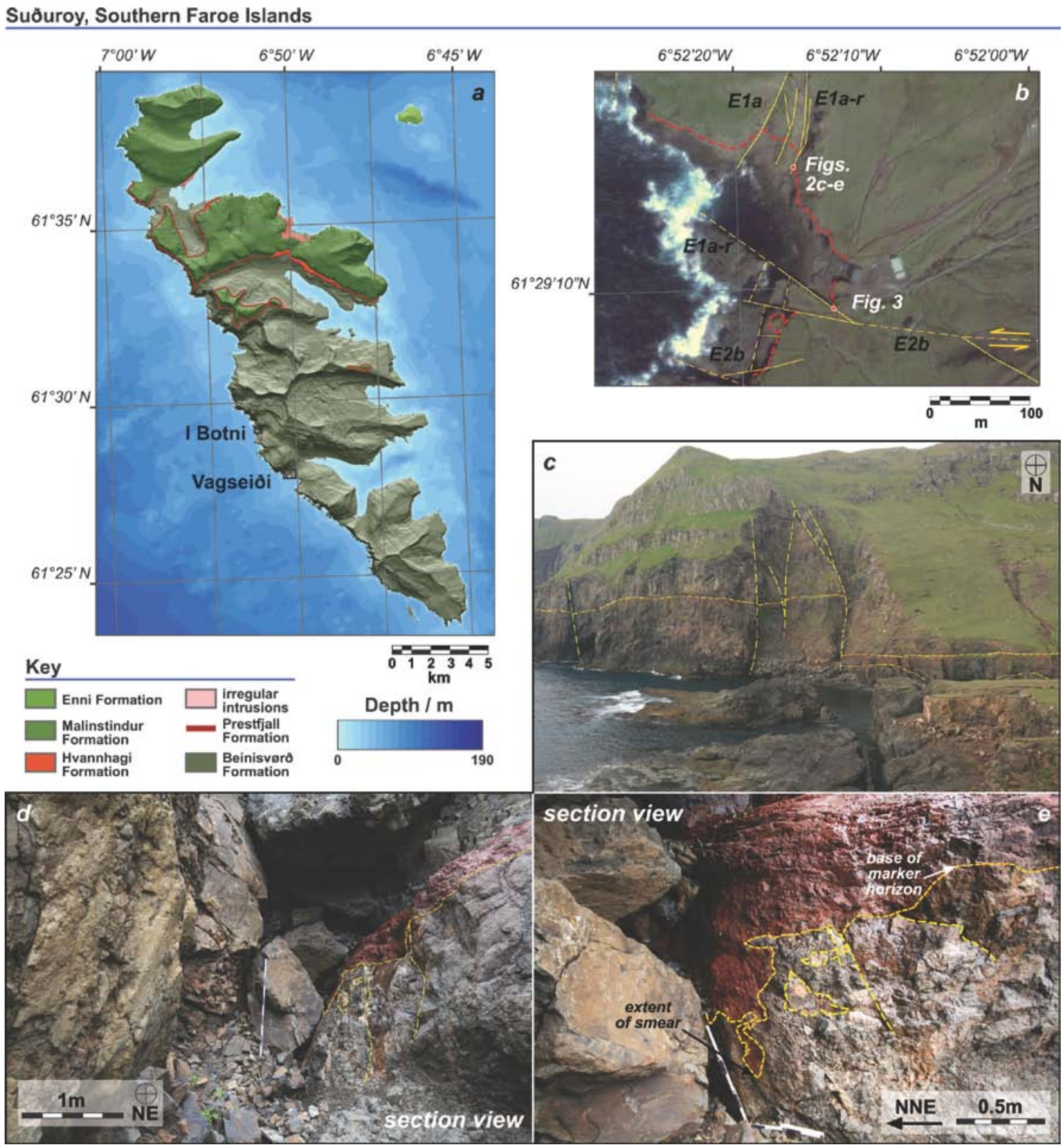

Fig. 4.2. (**a**) Simplified hillshaded geological map of Suðuroy with surrounding bathymetry. Location of I Botni (**Figures 4.2** and **4.3**) and Vagseiði (**Figure 4.5**) indicated by the labelled boxes. (**b**) Satellite photograph centred on the reactivated faults at I Botni. Marker volcaniclastic horizons outlined in dark red. (Base image from *GoogleEarth*). (**c**) Overview of the NNE-SSW trending fault at I Botni. Note the large down-to-the-east sense of offset as indicated by the marker horizons. (Height of the peak, left of centre, is ~180m a.s.l.); (**d**) clay horizon on the right is dragged down ~1.5m to the west, cutting Event 1 mineralisation, opposite to the kinematics of the host fault; (**e**) Zoomed view of the extent of the clay smear, with corrugations on the surface.

The smaller of the faults, located about 150m to the south of the previous exposure, is a NW-SE- (149°) trending dip-slip fault (**Fig. 4.2b, 4.3**). Here a ~1m thick volcaniclastic clay unit is offset in the hangingwall down to the northeast. The exact amount of displacement is unknown due to a lack of exposure in the adjacent footwall, but is presumed to be $\leq$4m based on the surrounding stratigraphy. Clastic material is demonstrably dragged into the fault plane forming a layer 10-30cm wide (**Fig. 4.3a, b**). Again, the fault displays fracturing, brecciation and calcite and zeolite mineralisation associated with Event 1 movements, here focused mainly in the hangingwall, and along the master fault (**Fig. 4.3c, d**). Calcite slickenfibres are clearly overprinted on the master fault by a more oblique-slip set of slickensides associated with the later movement along a polished slip surface. Sub-horizontal to sub-vertical Event 1 calcite veins within the clastic horizon are truncated by a weakly developed vertical to sub-vertical fabric within the clastic material that is smeared along the fault plane. Furthermore, mineralised Event 1 fault wall-rocks are entrained within the clastic smear whose matrix lacks mineralisation (**Fig. 4.3b**).

Both examples are interpreted to represent typical shear-smears (Weber et al., 1978), with a minor addendum, resulting from the contrast in mechanical properties between the (weak) tuff horizon, and the (strong) basalt flow units. In the case of the second example (**Fig. 4.3**), the smear does not appear to obey typical shear-smear geometries (i.e. becoming thinner with distance from the source horizon). A likely reason for this is

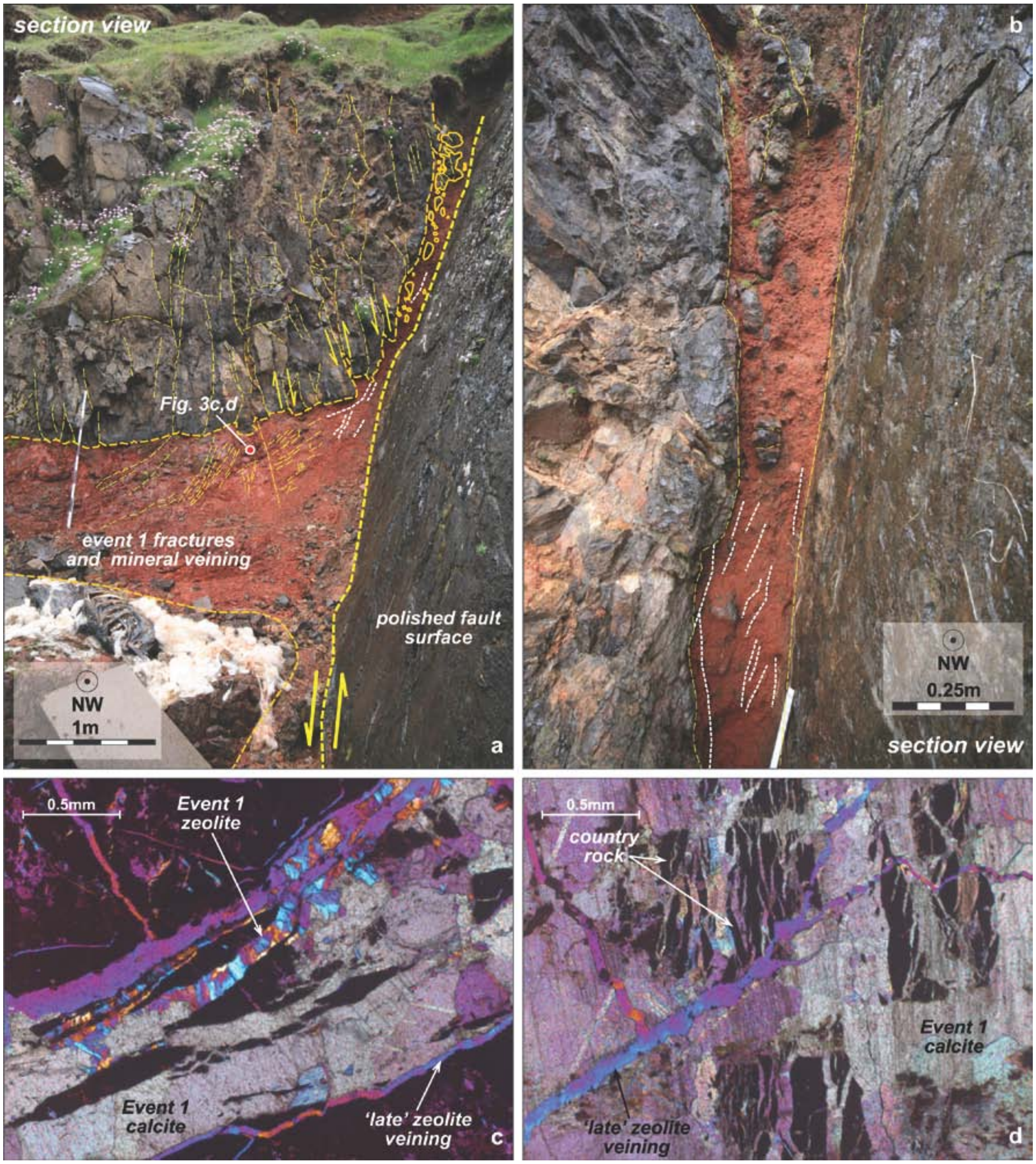

Fig. 4.3. (**a**) NW-SE trending fault at I Botni. Calcite slickensides on the right are polished over, and Event 1 mineralisation (thick-long dashed lines) are cut and truncated by a later sub-vertical fabric (thin white dashed lines) within the clay horizon. (**b**) Zoomed view of fault shear-smear. The smear clearly contains mineralised, rotated clasts of Event 1 fault-wall rocks. (**c & d**) Red-tinted crossed-poles photographs of the basaltic tuff horizon (location indicated in **3a**). Event 1 zeolite and calcite mineralization is a pervasive feature throughout the basaltic tuff horizon. A 'late' zeolite veining cross-cuts Event 1 mineralisation, and could be related to reactivation of the adjacent fault during Event 3.

the differential reactivation of minor faults and fractures in the hangingwall of the main fault, which could cause localised thickening and thinning of the smear. As with typical shear-smears, all materials within the fault plane are derived from the immediate wall rock horizons (i.e. basaltic rocks and a single volcaniclastic horizon).

4.3.2 Clastic infills and drags

Displacements along irregular fault planes can lead to the development of features such as dilation jogs and pure tensile (mode I) fractures in the subsurface. At shallow crustal depth (<1-2km), this can result in the formation of persistent voids or even cave systems (Loucks 1999; Woodcock et al., 2006; Wright et al., 2009). Such voids may become infilled more-or-less immediately (i.e. by implosion brecciation; Sibson, 1987), or remain open for a longer period of time, depending on the relative strength of the surrounding wall rocks and the amount of rock overburden (i.e. depth). In the latter situation, faults can become filled through time, for instance, by gravitational collapse or fault-related brecciation of the roof/wall rocks, sedimentary deposition during intrastratal fluid-flow, mineral-veining, or a combination of these processes. In several locations within the FIBG (six identified localities during the present study; **Fig. 4.1**), the development of such voids has been followed by infilling with clastic sediment which has then, in some cases, undergone deformation during subsequent fault movements. Here we present two examples of such clastic fault infills; one of predominantly fine sediments at Glyvursnes, Streymoy (**Figs. 4.1, 4.4**), and one of matrix-supported breccia at Vagseiði, Suðuroy (**Figs. 4.2a & 4.5**).

Glyvursnes quarry is located about 3.5km south of the capital, Torshavn, in the SE of Streymoy (**Fig. 4.4a, b**). The subvertical Event 2 fault of interest here trends ESE-WNW and displays a negligible offset (cm scale) down to the north (**Fig. 4.4c**). Faults, fault-rocks and fractures in the area are typically calcite and zeolite mineralised, which often form vuggy growths on the wall rocks as a result of predominantly tensile mode of opening. Event 2 mineralisation is truncated against a sediment fill that forms lenses developed along the irregular fault plane (**Fig. 4.4c**); the sediments lack mineralisation and must therefore post-date Event 2. The sediment infill comprises a matrix-supported conglomerate, overlain by sub-horizontal laminated silts and muds (**Fig. 4.4d**) indicating a progressive infilling from bottom to top by means of gravitational settling. The laminae are themselves offset by a linked network of minor normal faults suggesting further fault activity following and possibly during deposition. In some places, the laminations are rotated into subvertical dips adjacent to faults and are partially dismembered (**Fig. 4.4e**). In such instances it is suggested that contiguous blocks of laminated sediments were dragged and rotated during repeated displacements and minor dilation along the main fault.

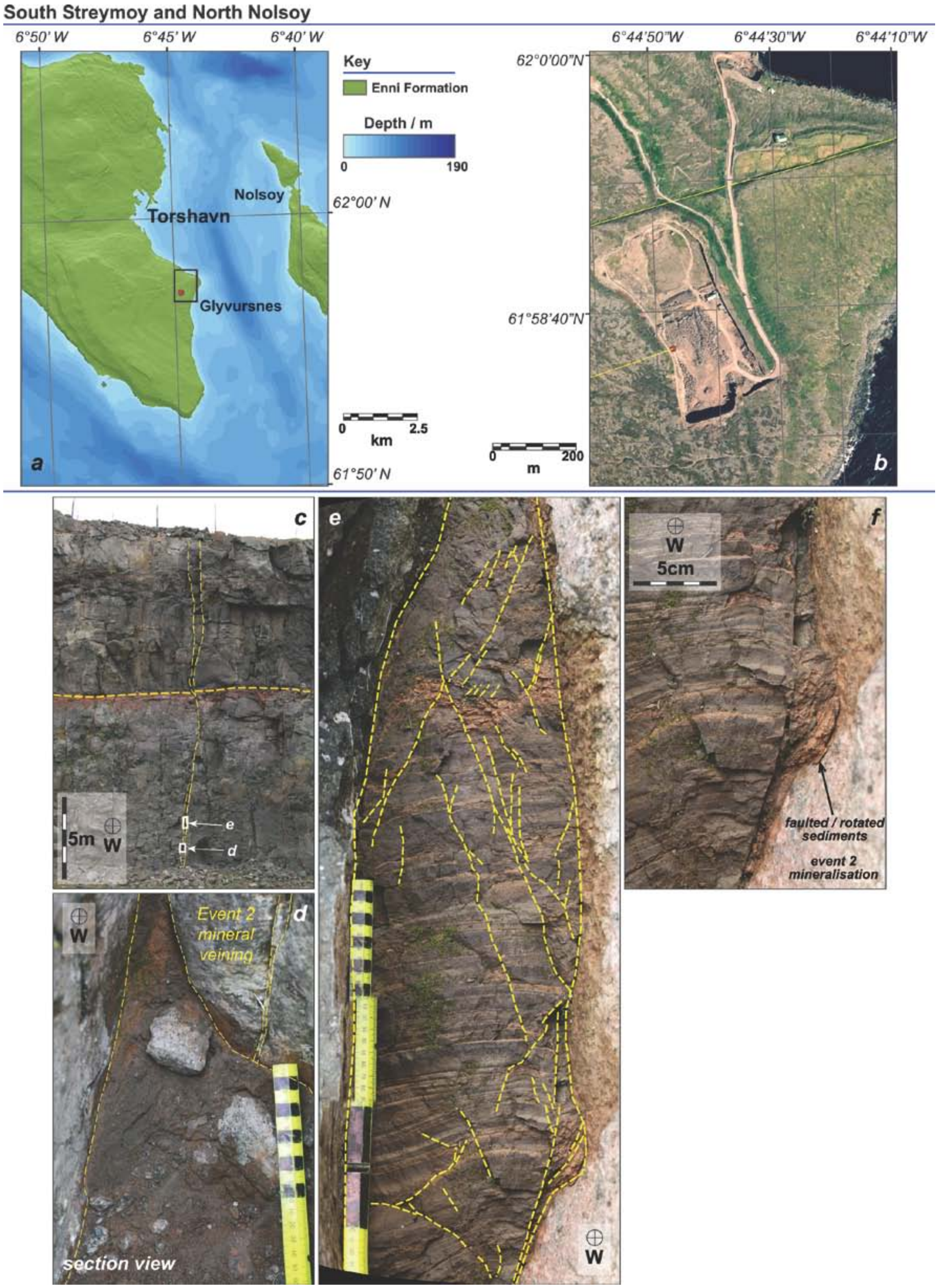
South Streymoy and North Nolsoy
6°50' W
6°45' W
6°40' W
Key
Enni Formation
Depth / m
0
190
Nolsoy
Torshavn
62°00' N
Glyvursnes
0
2.5
km
61°50' N
a
6°44'50"W
6°44'30"W
6°44'10"W
62°0'00"N
61°58'40"N
0
200
m
b
c
5m
W
e
d
e
W
f
W
5cm
faulted / rotated sediments
event 2 mineralisation
W
Event 2 mineral veining
d
section view

Fig. 4.4. (*Previous page*) (**a**) Simplified geological and topographic map centred on south Streymoy with surrounding bathymetry. Location of the study fault at Glyvursnes is indicated by the circle. (**b**) Aerial photograph of Glyvursnes quarry; locations of c-e indicated by red circle. (**c**) Overview of the fault at Glyvursnes quarry, one of many Event 2 faults observed in the quarry walls. (**d**) Zoomed view of the lowermost section of the fault exposure, with late, matrix supported clastic material abutted against Event 2 mineralisation. (**e**) Fine clastics (≤1mm, clays and silts) deposited by gravitational settling, from the bottom upwards. Extension faults offset the laminae, most likely reflecting the continued dilation of the host fault. Note that some laminations have been faulted, rotated and dragged during this dilation (bottom right; **f**). (**f**) Rotated and faulted laminations probably resultant of continued reactivation and dilation of the host fault.

The second example is found at Vagseiði (**Fig. 4.5a**), located on the west coast of Suðuroy, about 1.25km west of Vagur (**Fig. 4.2a**). The fault trends NW-SE (152°) and originally formed during NE-SW extension associated with Event 1a, displaying ~10-15m down-to-the-northeast displacement (**Fig. 4.5b**). The Event 1a fault rocks are mineralised with numerous phases of calcite and zeolite. Clastic infills up to 1.5m wide are periodically exposed along the fault at various localities, the lowermost of which is close to the shore, several tens of metres up the hill slope (**Fig. 4.5a**). Lenses of volcaniclastic materials derived from intrastratal sedimentary horizons are observed being entrained along the main fault, although compared to the sediments at Glyvursnes, they are generally much coarser, forming a matrix-supported chaotic breccia (**Fig. 4.5c, d, e**) (Woodcock et al., 2006). The provenance of the clasts is not always entirely apparent, although it is presumed that the majority are genetically related to the succession exposed immediately above, based on mineralogical and petrological similarities. About 70m from the coast along the fault (at 40m a.s.l.), the infill bifurcates to the east up a subsidiary fault (**Fig. 4.5d**). Here the stratigraphy is

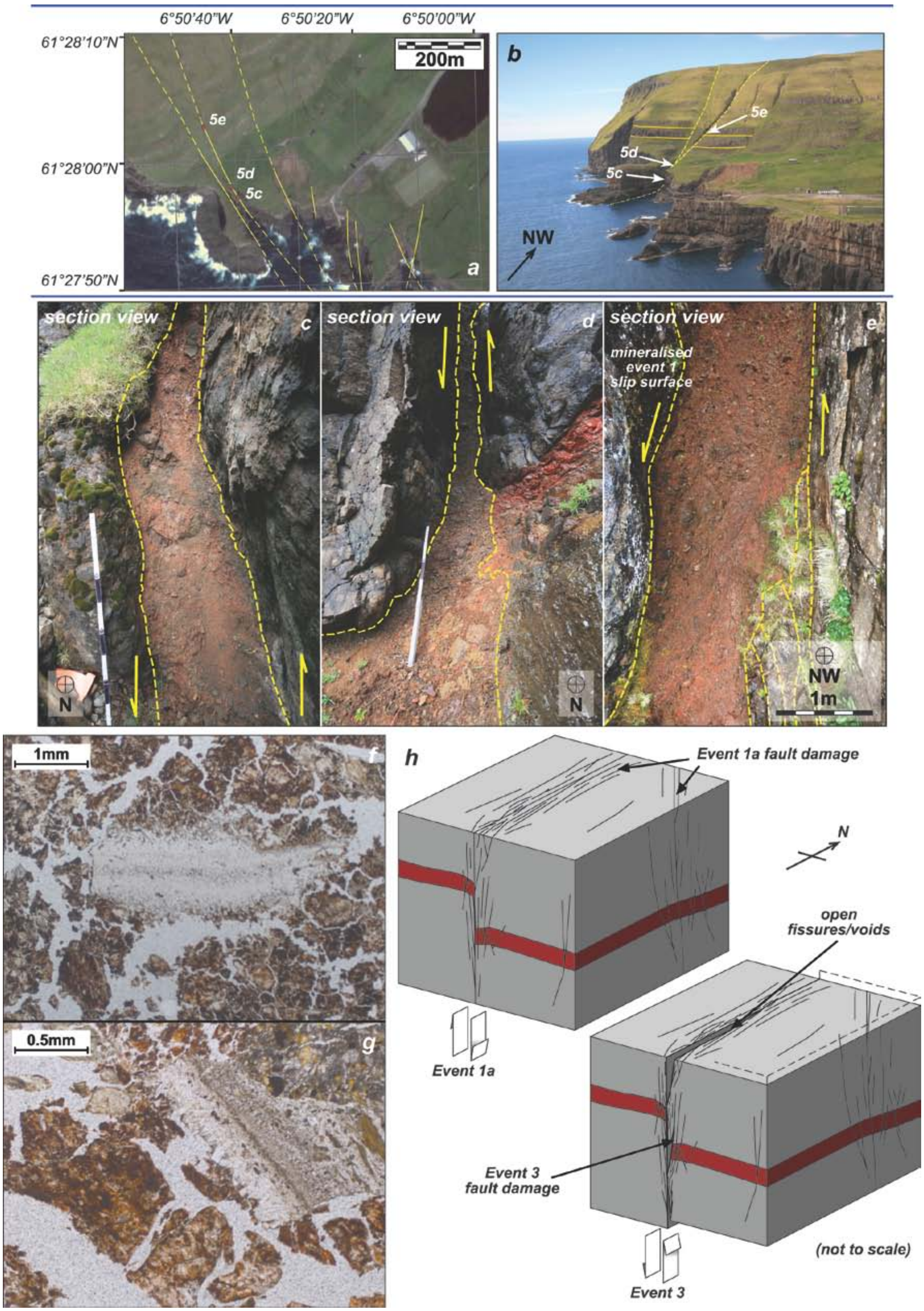
6°50'40"W
6°50'20"W
6°50'00"W
61°28'10"N
61°28'00"N
61°27'50"N
200m
5e
5d
5c
a
b
NW
section view
c
d
e
N
NW
1m
mineralised event 1 slip surface
1mm
f
0.5mm
g
h
Event 1a fault damage
N
open fissures/voids
Event 1a
Event 3 fault damage
Event 3
(not to scale)

Fig. 4.5. (*Previous page*) (**a**) Satellite photograph of the coast at Vagseiði. (**b**) Overview of the fault at Vagseiði (location indicated in **Figure 4.2**). The fault is NW-SE trending and displays ~10-15m displacement, down to the east (height to 'd' is ~95m a.s.l.). (**c**) Lowermost exposed lens of matrix-supported chaotic breccia, bound by Event 1 mineralised fault-rocks (large divisions on ruler are 10cm). (**d**) N-S trending offshoot fault with matrix-supported chaotic breccia fill (ruler is 80cm tall). Clay horizon on the right (E) has been dragged down to the west, opposite to the sense of motion of the host fault. (**e**) Chaotic breccia with asymmetric fabric again indicating a down to the west sense of motion. No mineralisation is observed within the clastic material along this fault. (**f** & **g**) Plane-polarised photographs of the clastic infills, sampled from just below **e**. Individual clasts contain basaltic Event 1 fault rocks and associated zeolite mineralisation (e.g. centre of **f**; right of centre of **g**). Generally, clasts are held together by clay minerals and (in these instances, zeolite mineralisation. (**h**)Summary model for the formation of persistent subsurface fissures and voids, based on the outcrops at Vagseiði. Reactivation of the Event 1a faults results in voids along the irregular fault plane. These voids are later filled by inward collapse of the wall rocks, and by more exotic materials from further afield in the stratigraphy.

relatively offset 75cm down to the west, resulting in drag and mixing of the clastic (tuff) horizon with the more distally-sourced breccia material. Further up the fault, about 170m to the NW (at 95m a.s.l.), the chaotic breccia displays a clear drag-fabric, picked out by clast alignments, indicating a down to the west sense of movement which is cut by a dip-slip, unmineralised fault (**Fig. 4.5e**). Again, claystone material is interleaved with coarse breccia, but here the clastic infill appears to display a highly inclined grading. As with the Glyversenes fault, this is interpreted as representing a sedimentary grading, resulting from gravitational depositional processes; the grading was most likely sub-horizontal, and has subsequently been dragged by later fault movements into its present inclination.

It appears that materials (particularly the fines forming the matrix) within both of these examples are not solely sourced from the surrounding wall rocks, and the development of graded bedding in the uppermost clastic fills may indicate the development of persistent open cavities along the pre-existing fault (**Fig. 4.5h)**. These subsurface fissures would have been open for a period of time and infilled, followed by repeated subsequent faulting episodes. The lack of mineralisation coupled with the deposition of sediment, suggests that these features formed at very shallow crustal depths, close to the surface.

4.3.3 Saucer-shaped clastic infills

These features are only found clearly preserved in one location on the west coast of Viðoy, at the village of Viðareiði (**Fig. 4.6a, b, c**). The topographic low in which the village of Viðareiði sits, appears to be bound by large offset (≥20m) faults, creating an E-W trending graben. Immediately to the north of the Viðareiði pier section, a fault-bound block appears to be rotated; units are inclined to around 15-20° rather than the typical 1-3° regional dip (**Fig. 4.6b, c**). This rotation may have resulted from reactivation of Event 2 faults, in the near surface during Event 3.

The pier section at Viðareiði is host to an overlapping succession of compound lavas, and lava tubes of the Malinstindur Formation, separated by numerous irregular saucer-shaped clastic horizons 0.3-0.6m thick (**Fig. 4.6b-e**). The lava units typically preserve a

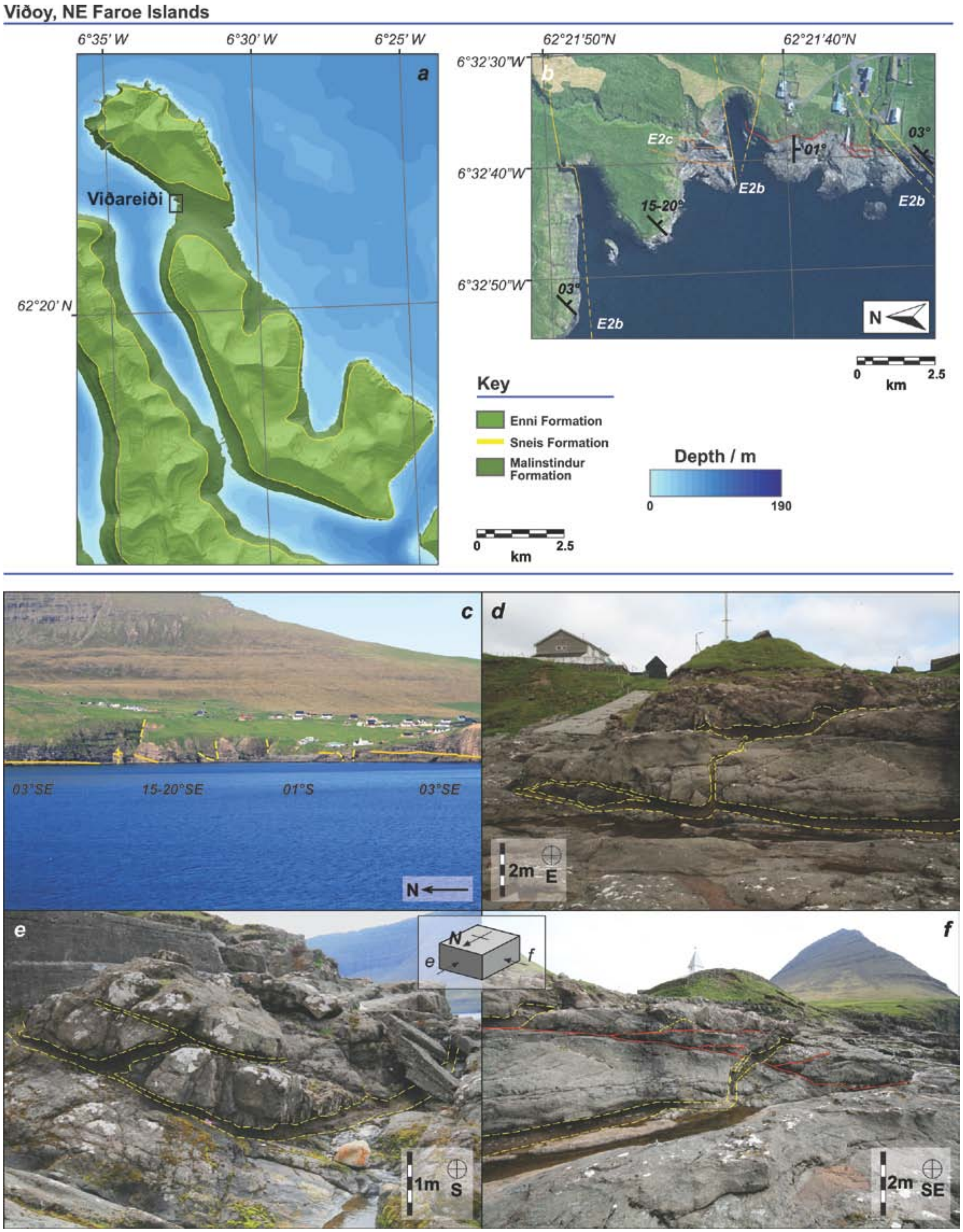

Fig. 4.6. (**a**) Simplified geological and topographic map of Viðoy with surrounding bathymetry. (**b**) Aerial photograph of the Viðareiði pier section detailing major faults and the location of the Viðareiði clastic horizons (outlined in dark red). (**a**) Overview of the west coast of Viðoy at Viðareiði. To the north of the village on the coast, a fault-bound section exhibits a much steeper inclination than that of the surrounding units, most likely indicating a rotation resulting

(Fig. 4.6 continued) from faulting. (**d**) The Viðareiði pier section comprising overlapping, subhorizontal compound lava units, separated by 0.3-0.6m thick clastic horizons (delimited by dashed lines). In some instances the clastic horizons are linked by vertical injections, exploiting mineralised faults (detailed in **Figure 4.8**); (**e** and **f**) Clastic horizons commonly display ramps sections of about 45°, which cross-cut solid state features within the surrounding basalt units.

well developed lower crust, core, and upper crust. The lower crust is characterised by pipe amygdales that start a few centimetres from the base of the unit and are often curved in the palaeoflow direction. The core is generally a massive zone with more globular-shaped amygdales, and irregular joints ranging in orientation, from sub-horizontal to sub-vertical. In the upper crust, amygdales are spherical to globular, and the groundmass often exhibits a progressive reddening towards the top. Both the lower and upper crusts commonly exhibit classic rope-structures on the bounding surfaces that are characteristic of pahoehoe-type lavas. These lava flow features are important when considering the nature of the contact relationships between the clastic horizons and the lava units.

The clastic horizons are typically sub-horizontal, but in some instances more steeply inclined (45-75°) ramp sections are observed. Mineralised Event 2 strike-slip faults are developed within the basalt units and are either cross-cut by, or sometimes filled with clastic material. The ramp sections are also discordant, cross-cutting solid-state lava unit features (**Fig. 4.6d-f**). Ramps of this nature occur in three-dimensions, and overall give the clastic horizons a saucer-shaped geometry, akin to that of saucer-shaped intrusions. However, the sedimentary units preserve clear sedimentary structures on mm- to cm-scales, including planar and cross-laminations, bar structures and scour structures (**Fig. 4.7**). These features are completely undeformed and show that the clastics were not emplaced by forceful injection, but rather were laid down as fluvial- to debris-flow-type deposits. Planar laminations at the top of the horizons appear to 'drape' the topography of the lava unit above, and are equivalent to gravitational settling laminae, implying that there was free space between the lava flows that became filled through time, followed by settling of the units above 'indenting' the sediment fills. In order to gravitationally deposit those materials, we infer that the free space must therefore have been larger than the thickness of the exposed remnants. Further evidence for a filling through time is provided by the clast-provenance. In some instances, fragments of the lava unit above have clearly fallen down into and become buried by the clastics below (**Fig. 4.7a**); the fragile lithofacies above such fragments are undisturbed and must therefore have been deposited afterwards. Internally, the sediments display only very minor mineralisation. Where discrete veins are observed, they are markedly more passive than those observed in in-situ volcaniclastic sediments (e.g. **Fig. 4.7c**), anastamosing around and between grains, rather than through them; in no observed instances do they appear to cause grain-scale deformation (**Fig. 4.7d**).

Collectively, the cross-cutting relationships with the lava flows and features observed within the clastic horizons indicate that there was an open cave network in the subsurface, which post-dates faulting associated with Event 2. It is well known from

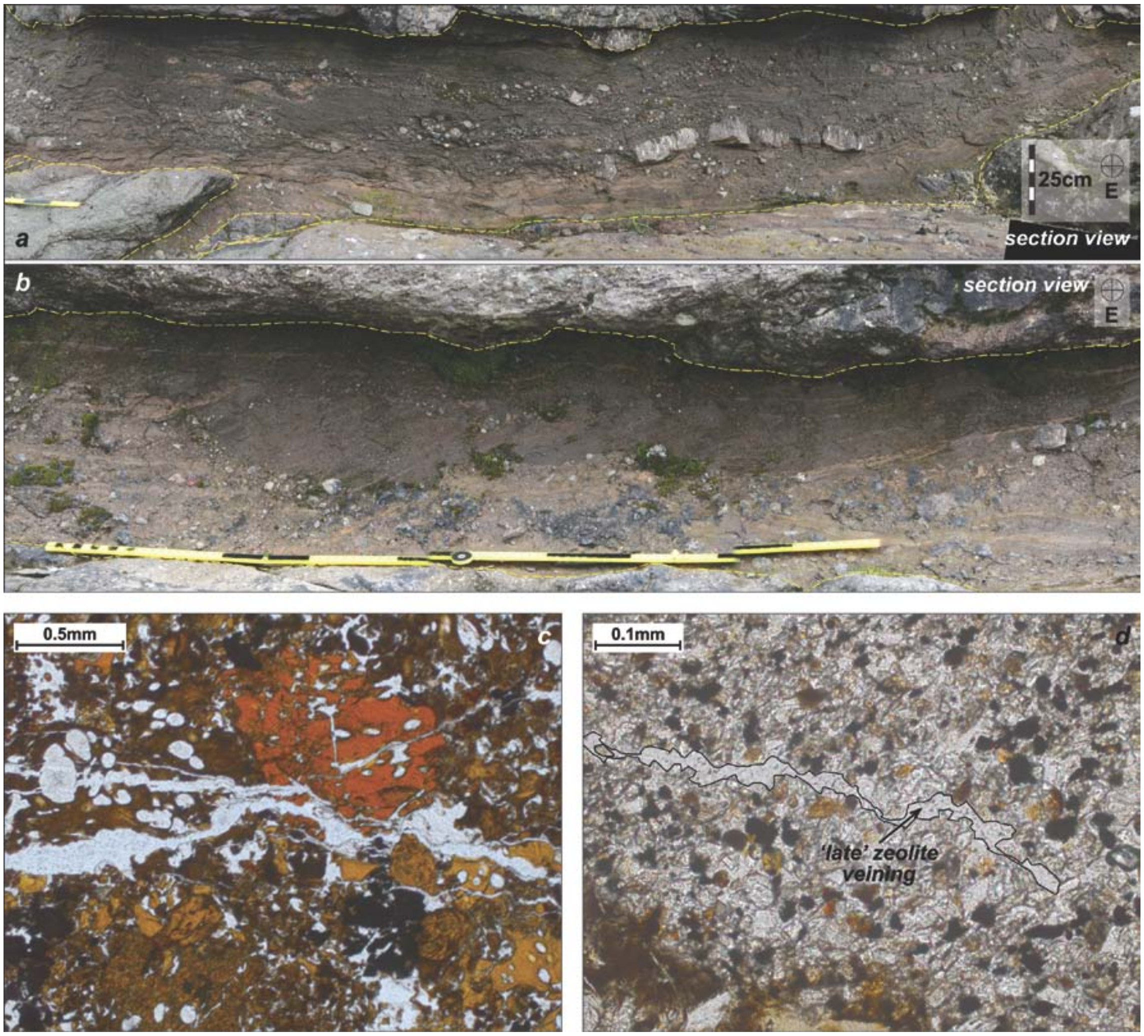

Fig. 4.7. Internally the clastic horizons display fragile sedimentary lithofacies such as: (**a**) planar and cross laminations, bar structures and imbrication, as well as (**b**) erosional features (scour structures) infilled with cross laminated sedimentary fill. In **a** there is a raft of the lower crust of the basalt unit above, surrounded by undisturbed sedimentary structures, indicating a progressive filling through time. Also, the planar laminations at the top of both **a** and **b** drape the bottom surface topography of the unit above, most likely indicating that the cavity was larger during deposition and has subsequently closed. (**c**) Plane-polarized photograph of 'in-situ' volcaniclastic sediments from an Event 2 fault on Eysturoy. Zeolite mineralisation is dominant in this section, and has resulted in brecciation at the grain-scale. (**d**) Zeolite veins within the Viðareiði sediments (outlined in centre) anastamoses around grains, with no evidence for grain-scale deformation.

direct field evidence and analogue modeling that rocks such as basalt commonly exhibit pre-existing weaknesses and anisotropies that may be reactivated at some distance from active faults (e.g. Gudmundsson, 1992, 1995; Acocella et al., 2003; Holland et al., 2006). Partial fragmentation of the stratigraphy along such weaknesses could therefore result in the formation of interlinked voids, fissures, or cave networks, particularly at the near surface where fault movements are likely to have had a significant tensile component (Holland et al., 2006). It has also been shown that the style of faulting differs between thick and thin layered sequences, with preferential disintegration of thin layers, and the development of through-going master-faults in thick layers. Furthermore, fault-bound blocks are likely to become rotated during faulting. It is proposed, therefore, that the faults bounding the E-W trending graben were reactivated during Event 3 (**Fig. 4.8**), in the near surface (<1km depth), leading to the tilting, fracturing and partial dismemberment of the lava flows due to tensile/mixed-mode faulting. The resulting cave-systems are only observed within the graben, and coincide with the thinner overlapping terminations of the compound-lava units; to the north and south, the individual units display a regular thickness in the order of 2m or more. We therefore suggest that the cave-system relates to preferential disintegration of the thinner units, during reactivation of the large bounding faults.

4.3.4 Clastic intrusions

Clastic intrusions have been reported from several geological settings worldwide, with various associated causative mechanisms being proposed (e.g. Richter, 1966; Jolly et al., 1998; Rijsdijk et al., 1999; Phillips and Alsop, 2000; Jonk et al., 2004; Le Heron and

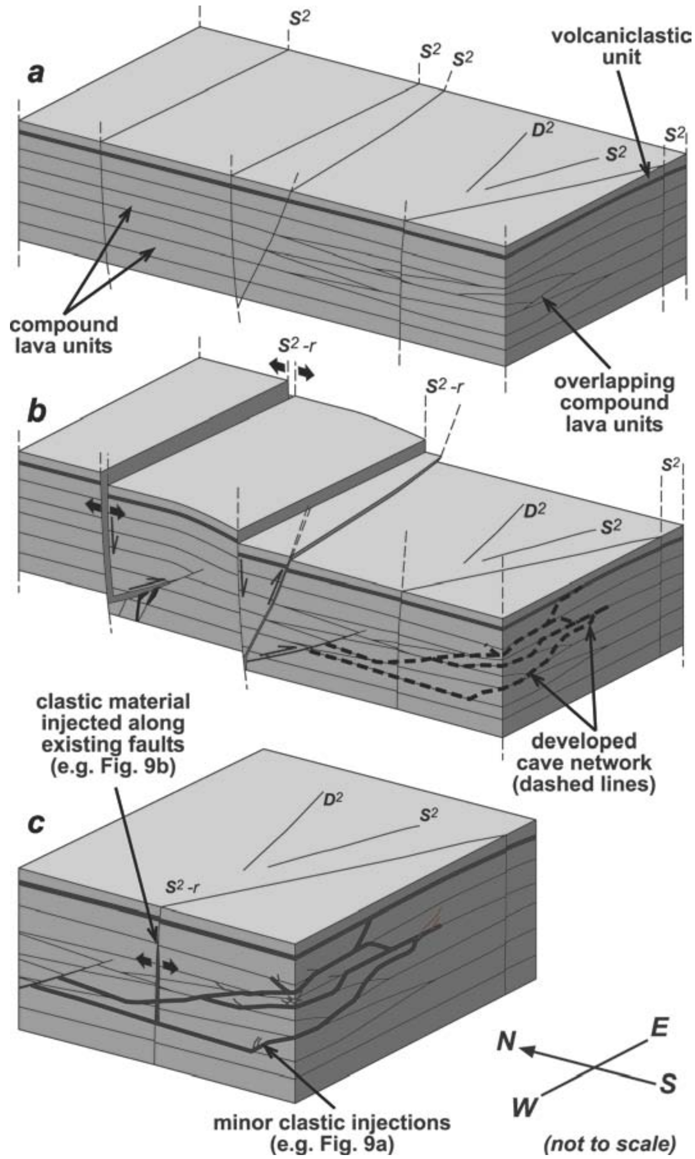

Fig. 4.8. Summary model for the clastic horizons and intrusions observed at Viðareiði. (**a**) The existing stratigraphy is dominated by compound lava units that are individually thinner at the pier section. (**b**) Reactivation of existing Event 2 faults during uplift results in fault-block rotations and a preferential disintegration in the thinner cover units. This disintegration creates a subterranean cave network. Permeating waters carry and deposit clastic debris throughout the cave network. (**c**) Further movements on nearby faults results in localised overpressure and fluidisation of the clastic materials, and intrusion along existing material anisotropies (i.e. faults etc.).

Etienne, 2005; Goździk and van Loon, 2007). At Viðareiði, two styles of clastic veins are observed: 1) 0.1-0.3m wide planar veins exploiting pre-existing mineralised faults; and 2) thin anastamosing veins which cross-cut lava unit solid-state features (**Fig. 4.9a,b**) and sedimentary features within the subhorizontal clastic horizons. The wider veins appear to be sourced from the coarse clastic materials (0.5-10cm) within the subhorizontal horizons, cutting the planar marginal laminations and dragging them upwards (**Fig. 4.9c**). They display a chaotic matrix-supported texture, and where observed, are clearly injected from below, up pre-existing faults and joints. The thinner vein style generally ranges from 0.1-1cm wide, and are continuous up to many metres. They range in attitude and inclination along a single vein, and are not linked or associated with any particular existing structures or anisotropies (i.e. they will exploit existing weaknesses and form their own fracture along a single vein). Internally, these veins are composed of fine materials (≤1mm), such as clays and silts, and in some cases (though very rarely) display a poorly developed margin parallel lamination. Within the subhorizontal clastic horizons, clays appear to have been remobilised and injected through the coarser materials (**Fig. 4.9d-e**).

It is proposed that the clastic injections in the area likely result from the localised development of fluid overpressures in water-saturated, cave sediments. This was probably triggered by the jostling of fault blocks and fragmented lava flow lobes during nearby fault movements (**Fig. 4.8c**).

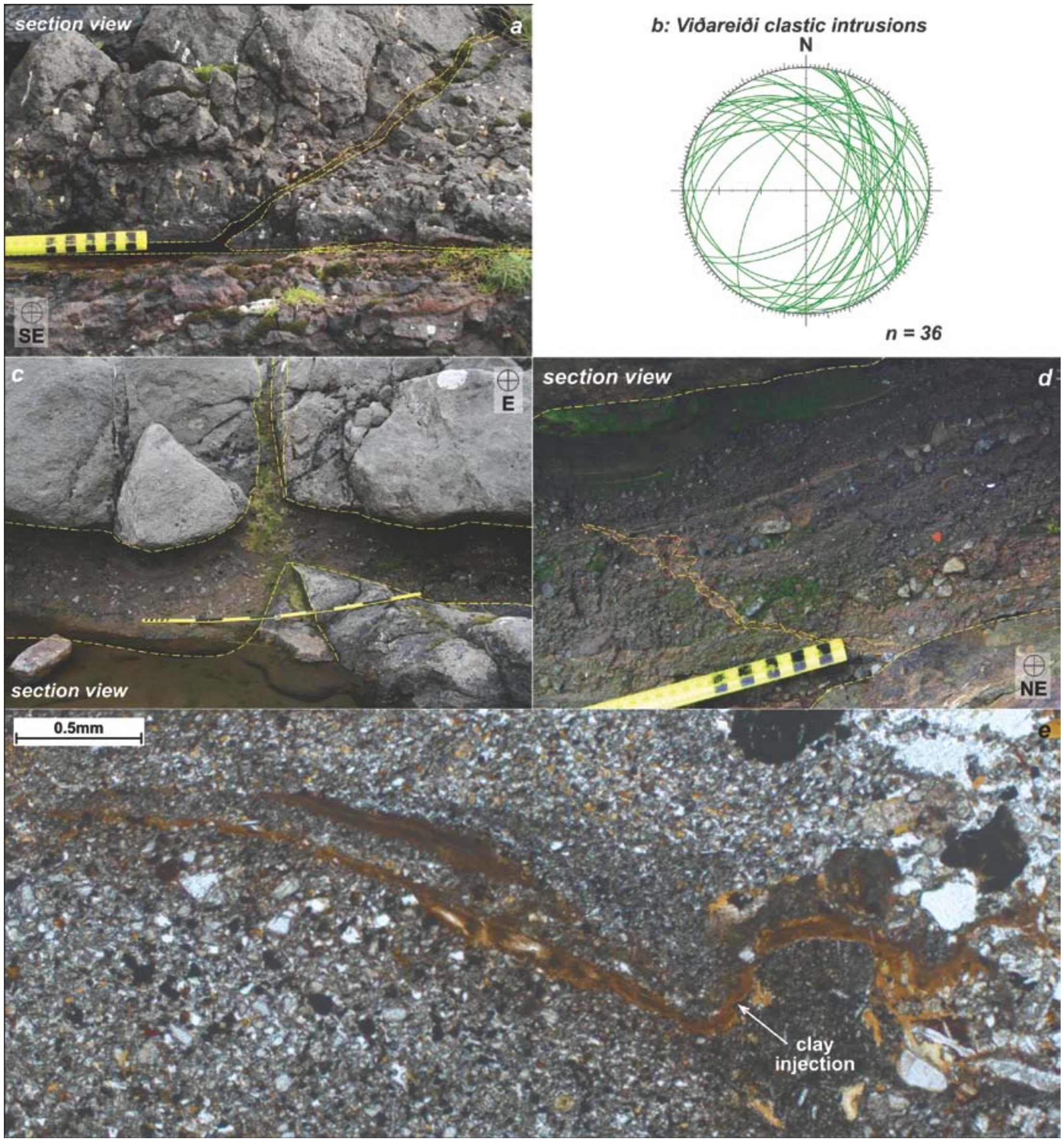

Fig. 4.9. Clastic intrusions that: (**a-b**) display various orientations and cut through lava solid state features such as pipe amygdales; (**c**) exploit Event 2 mineralised faults; and (**c**) cut through the original clastic horizons. (**d-e**) Micro-scale clay injections with the Viðareiði sediments.

4.3.5 Summary

The features detailed in the previous section demonstrably post-date and locally reactivate the mineralised subsidence-related structures (i.e. Events 1 and 2) detailed by Walker et al., (2008) (see *Chapter 3*). These (Event 3) structures consistently lack intrinsic mineralisation, and consistently develop a significant tensile component in their formation. The absence of a cement, and clear preservation of delicate sedimentary features in the infills suggests that these features may have formed in the near surface, perhaps at depths less than 1-2km.

4.4 Discussion

4.4.1 The nature and significance of the fissures and caves

It would be useful to know whether the features described here formed as persistent sub-surface fissures, voids or caves and at what time they were infilled with sediment. The fissure fills at Vagseiði (*section 4.3.2*) are well exposed as lenses over a vertical distance in excess of 100m, rather than a continuous conduit along the extent of the fault. This suggests that the fissures are the result of irregularities on the fault surfaces; geometric incompatibilities, that result in the localised formation of voids. The exotic polymict nature of the infills may indicate that the lenses are connected laterally by thinner fissures, or that the void and cave systems were extensive enough to source numerous stratigraphic source lithologies. There is no clear evidence of linkage by thin fissures (though out-of-plane connectivity cannot be discounted at this time). However, the parent Event 1 fault displays a 10-15m offset, so the resulting juxtaposition provided a greater number of possible source lithologies for individual voids.

Palynological studies could be used to decipher whether the fissures and caves were open at surface. If not connected to the surface, the only palynomorphs present in cored samples would be of Palaeocene age, i.e. material derived wholly from reworking of the interlava sedimentary horizons. Unpublished works on Viðareiði have shown that the fine-grained sediments contain abundant aseptate fungal mycellae, which are not age diagnostic. However, spore colour indicates a thermal alteration index (TAI) of 1.5 (D. W. Jolley, 2009, pers. comm.), which could suggest that either mildly hydrothermal springs were feeding the cave-system water, or that the spores are of Palaeocene age. In the latter case, the TAI would result from heating of the source material during lava emplacement, or during burial.

It is not possible at the present time, with the evidence at hand, to suggest whether the features detailed in this study occur within the phreatic or vadose zones, nor is there any reasonable constraint on the actual depth of their formation, besides the assumption that deep (>1km) fault rocks are likely to display increasing proportions of cement. In all cases, there are numerous reasonable hypotheses for the source of sediment, and for the styles of their deposition. For instance, the nature of the infills in the Glyvursnes case (fine fills) may indicate that the void lay within the vadose zone, above the water table, allowing a progressive infilling with fine sediments. However, this would also be possible were they deposited in a hydrodynamic system within the phreatic zone.

On the basis of the available evidence, the extent of the exposures and the available palynology, we believe the clastic infills do represent pervasive features, and would therefore suggest that they are further examples of subsurface fissure infills to be added to the growing literature on the subject (e.g. Loucks 1999; Woodcock et al., 2006; Wright et al., 2009).

4.4.2 Regional significance of Event 3

The Event 3 structures demonstrably post-date those associated with Events 1 and 2 and therefore must have formed at some time following the Palaeocene. In general, mid-Palaeogene to Neogene structures developed along the NE Atlantic Margin are related to compression and regional uplift. There is a rich literature on the nature and timings of compression and uplift in the Faroe-Shetland Basin (FSB) and adjacent regions (e.g. Boldereel and Anderson, 1993, 1998; Anderson and Boldreel, 1995; Doré and Lundin, 1996; Ritchie et al., 2003; Sørensen 2003; Smallwood, 2004; Johnson et al., 2005). Within the FSB, Cenozoic compression has generally resulted in the mild development of growth folds of varying scale and orientation (Ritchie et al., 2008). Whilst these have developed at low strain levels (NE-SW-directed, post-basalt crustal shortening of <1% across the Faroes Platform; Anderson et al., 2002), the substantial amplitudes and areal extent of the resultant folds and domes makes them interesting hydrocarbon exploration targets (Doré et al., 2008). The Faroe Islands sit at the junction of three such anticlinal structures: the ENE-WSW trending Fugloy Ridge (to the east); the NNW-SSE trending Munkagrunnur Ridge (to the south); and the NW-SE trending Iceland-Faroe Ridge (to the NW) (Smallwood, 2008) (**Fig. 4.10**). The first two are anticlinal structures that relate, at least in part, to compression, with their location and orientation most likely controlled by basement structure (Doré et al., 1997). The Fugloy Ridge grew during several tectonic episodes in the Palaeocene, through to, perhaps, the mid-Miocene. Growth of the Munkagrunnur Ridge is more difficult to date as there are no preserved post-lava sediments on the ridge. The Iceland-Faroe Ridge relates to interaction between the proto-Iceland plume and the Mid-Atlantic ridge, throughout continental break-up and sea floor spreading (Bott and Gunnarsson, 1980).

Compression in this setting is typically attributed to a combination of body-forces, such as ridge-push and gravitational potential stresses related to lithospheric thickness and elevation variations in the continental interiors, coupled to additional horizontal compressive stresses relating to Iceland and its insular margin (Cloetingh et al., 2008; Doré et al., 2008; Pascal and Cloetingh, 2008). Kilometre-scale uplift also affected a large area during emplacement of the North Atlantic Igneous Province, including the continental margins of NW Europe, Greenland and Canada (Maclennan and Jones, 2006; Saunders et al., 2007). This consisted of transient uplift, related to the regional, rapid emplacement of hot asthenosphere, and a permanent uplift caused by addition of igneous material into and onto the crust, before and during continental break-up (Larsen and Saunders, 1998).

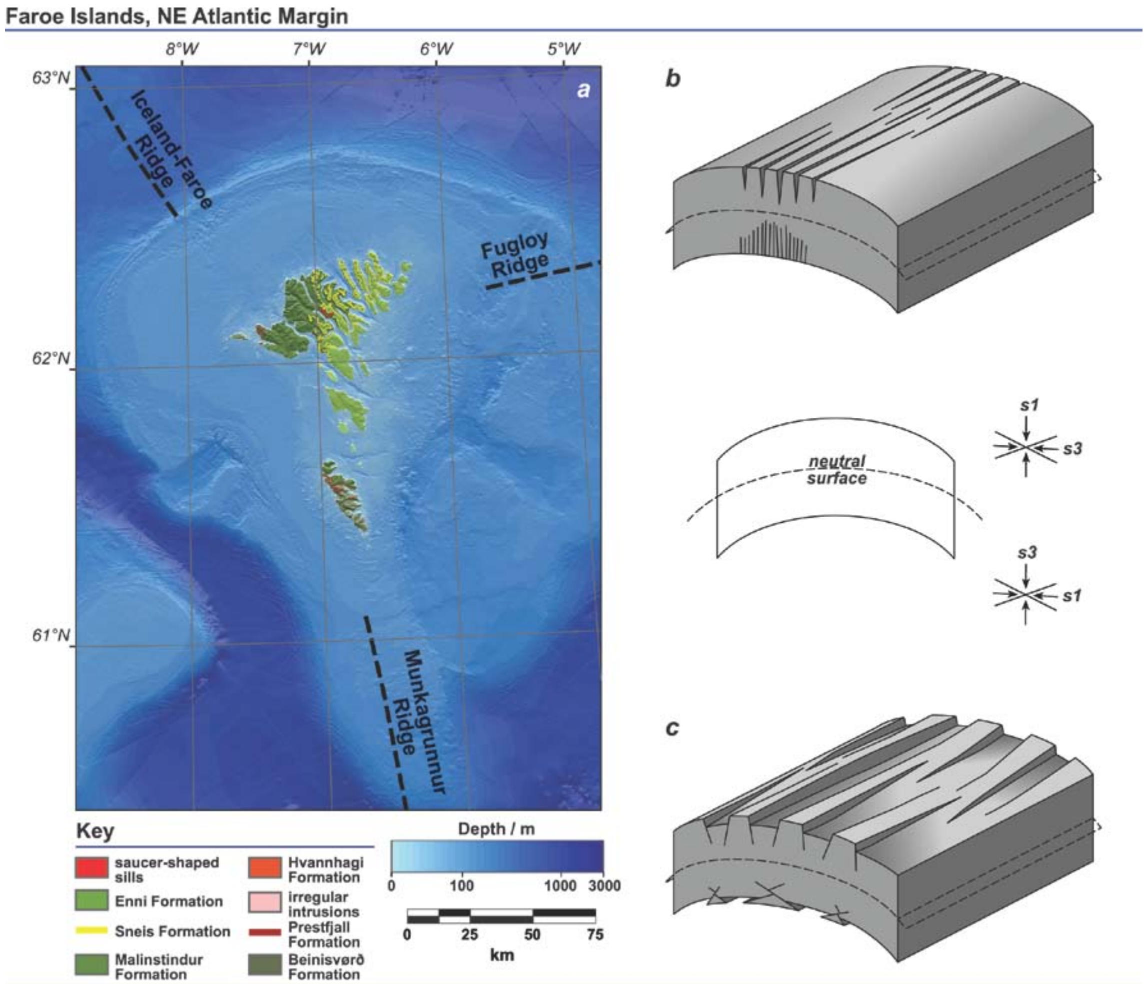

Fig. 4.10. (**a**) Hill-shaded simplified geological map of the Faroe Islands, with hill-shaded bathymetric map of the Faroes shelf detailing axial-lines of the Munkagrunnur, Fugloy, and Iceland-Faroes ridges (after Boldreel and Anderson, 1998; Passey and Bell, 2007; Bathymetry courtesy of Knud Simonsen, Univ. Faroe Islands). (**b**) Secondary features associated with tangential longitudinal folding and (**c**) typical orientations of normal faults and thrusts developed in a thick, flexured unit (after Price and Cosgrove, 1990).

Most Event 3 features on the Faroe Islands are not shortening structures; on the contrary, they are typically extensional or tensile features. In the absence of age dating for these features, it is not yet possible to determine whether they formed concurrent with, or subsequent to compression and uplift features found along the NE Atlantic margin. It is worth pointing out, however, that there are numerous mechanisms that would allow localised extension during regional shortening (e.g. dilational fractures on folds: Ramsay and Huber 1987 Price and Cosgrove, 1990; Cosgrove and Ameen, 2000; **Fig. 4.10b, c**), particularly in a regional topographic high (i.e. outer arc of an anticlinal hinge zone), such as that represented by the Faroe Islands and insular margin. Event 3 structures are found throughout the available onshore exposures of the lavas, though rarely does this exceed a few hundred metres thickness. It is unknown whether these features formed at greater depths. If they are present, they are potentially of major importance to hydrocarbon trapping and migration, since they represent significant potential fluid-flow pathways. If these structures relate to the development of regional-scale Cenozoic folds (i.e. the Munkagrunnar and Fugloy ridges), then it is likely that they would not be limited to the Faroes, and would be expected to be developed along the hinge zones of similar antiformal folds along the margin, including in offshore regions. Further work, in equivalent onshore settings could aim to test this hypothesis. As the Faroes archipelago represents the only land mass in the region, such studies would need to find suitable analogues elsewhere, such as East or West Greenland, or within the British Tertiary Igneous Province, or further afield on another volcanic passive margin (e.g. the South Atlantic).

4.5 Conclusions

- The features detailed in the present paper post-date, and commonly reactivate the faults, fault-rocks and fractures developed during Events 1 and 2 (*see Chapter 3*). The minor input, and passive nature of late mineralisation within the clastic materials most likely indicates post-burial, near-surface fault movements (<1km depth?). Based on the relative timing, it is proposed that these movements relate to uplift during continental break-up and sea-floor spreading on the NE Atlantic.

- The kinematics indicated by offset markers and the localized development of clastic drag fabrics are the opposite sense to those of the host fault. In most cases, the inland area lies in the fault footwalls; if the footwalls are uplifted, this may partially explain the location of the Faroe Islands.

- The fault smears and infills may be widespread offshore. The likely unsealed nature of the clastic infills may mean that these faults present fluid-flow pathways, particularly at higher levels, but also potentially deeper, within the Faroe-Shetland Basin. The open cavities that originally form would introduce very significant localised permeability, facilitating both cross-fault and cross-stratal rapid migration of fluids, including hydrocarbons.

5

Faults, fault-rocks and fractures in basalts: Faroe Islands, NE Atlantic Margin

Abstract

To date, few field studies have focused on the characterization of faults, fractures and the associated fault rocks within continental flood basalt provinces. The Faroe Islands are largely made up of basaltic lava units of the Faroe Islands Basalt Group (FIBG) and are situated above the Palaeogene rift axis of the Faroe-Shetland Basin (FSB) on the NE Atlantic margin, forming part of the extensive Palaeogene flood basalts of the North Atlantic Igneous Province (NAIP) that blanket the area. Exhumed brittle deformation structures developed on the islands are kinematically and temporally related to the period leading up to continental separation and the onset of sea-floor spreading on the NE Atlantic, and can be split into syn- and post-regional magmatic fault events. This study documents the development of these regionally syn-magmatic fault arrays, and contrasts them with later post-magmatic fault-reactivation at shallow burial depths, and the development of potentially high-permeability pathways through the FIBG during the latter event, and assesses the mechanics of dyke and sill intrusion on the islands. Mineralised syn- to post-magmatic fault sets display a recurring zeolite-calcite-zeolite trend in mineralisation products, which precipitate during successive phases of fault development. Fault style and damage zone width appear to relate to the stage of fault development, with early fault/vein meshes linking to form through-going structures with associated damage zones. Dykes and sills are found to form their own fractures, rather than exploiting existing sets. Dyke propagation appears to be buoyancy-driven, with magmatic pressure overcoming the minimum compressive stress, whereas sills more likely relate to exploitation of weak layers in the stratigraphy, with propagation controlled by the effects of viscous dissipation. We find that, in particular, faults in basalts are in many ways comparable to faults

formed at shallow crustal depths in carbonate rocks and crystalline basement, most likely reflecting the similarities in their mechanical properties under near-surface pressures and temperatures. The nature and style of the post-magmatic fault infills provides compelling evidence to suggest that subterranean cavities associated with faults were persistent features within the FIBG, and if they are structurally linked to faults cutting the underlying basin fill sediments, could facilitate significant hydrocarbon migration from deep reservoirs.

5.1 Introduction

Important advances have been made in the characterisation of fault-rock assemblages in layered clastic sequences focusing on 2-D and 3-D geometries (e.g. Brock and Engelder; 1977; Billi et al., 2003), as well as damage-growth through time (e.g. Aydin and Johnson, 1978; Cox and Sholz, 1988; Antonellini and Aydin, 1994; Shipton and Cowie, 2001), but to date this has not been attempted in layered volcanics. In clastic rocks, variations in lithology and layer thickness controls, result in different styles of fault-rock formation, and greatly influence the distribution of fault-related damage (e.g. Kim et al., 2004). Basalt morphology (and by corollary, physical properties; Planke, 1994; Bücker et al., 1998) can vary markedly vertically between thick, jointed simple flows (sheet-lobes) and thinly layered compound flows (e.g. Jerram, 2002), and individually with internal morphologies including highly vesicular flow-tops, massive flow-cores and amygdaloidal bases. Lateral variations are also important, with varying vesicularity and textures dependant on eruptive style, flow supply-rate and emplacement mechanisms. Flow units are also commonly interlayered with volcaniclastic horizons, again with contrasting physical properties, particularly between well-lithified and poorly-lithified units.

Many upper crustal fault zones contain significant volumes of brecciated wall rock, which can potentially form permeability pathways for the migration of mineralising hydrothermal fluids or hydrocarbons (Sibson, 1986, 1989; Roberts, 1994; Cowan, 1999;

Woodcock et al., 2006, 2007). Commonly fault-breccia formation is assumed to be a geologically instantaneous process, resulting from a sudden difference in fluid pressures between a dilational fault jog and its surrounding country rocks following fault slip, which leads to inward implosion (e.g. Sibson, 1986). However, at shallow crustal depths (0-2km), mechanically strong rocks (e.g. crystalline/carbonate rocks) may be able to support dilational fault jog features as persistent, high permeability, open subterranean cavities, that become more gradually filled by fragments of the surrounding wall rocks through time (Woodcock et al., 2006; Wright et al., 2009). Understanding the development of fault breccias is therefore scientifically and economically important, as the two breccia types have markedly contrasting sealing and fluid flow histories.

The Faroe Islands - the location of the present study - sit above the Palaeogene axis of the Faroe-Shetland basin on the NE Atlantic margin. The islands are largely made up of Palaeocene-age basaltic lava units (the Faroe Islands Basalt Group: FIBG; part of the North Atlantic Igneous Province: NAIP) that were emplaced during precursor igneous events to continental break up, and sea-floor spreading in the NE Atlantic. Deformation structures developed on the islands include variously oriented fault-sets (relating to anticlockwise rotation of the extension direction through time) and broad regional anticlines that form a trilete pattern centred on the islands (e.g. the Munkegrunnar and

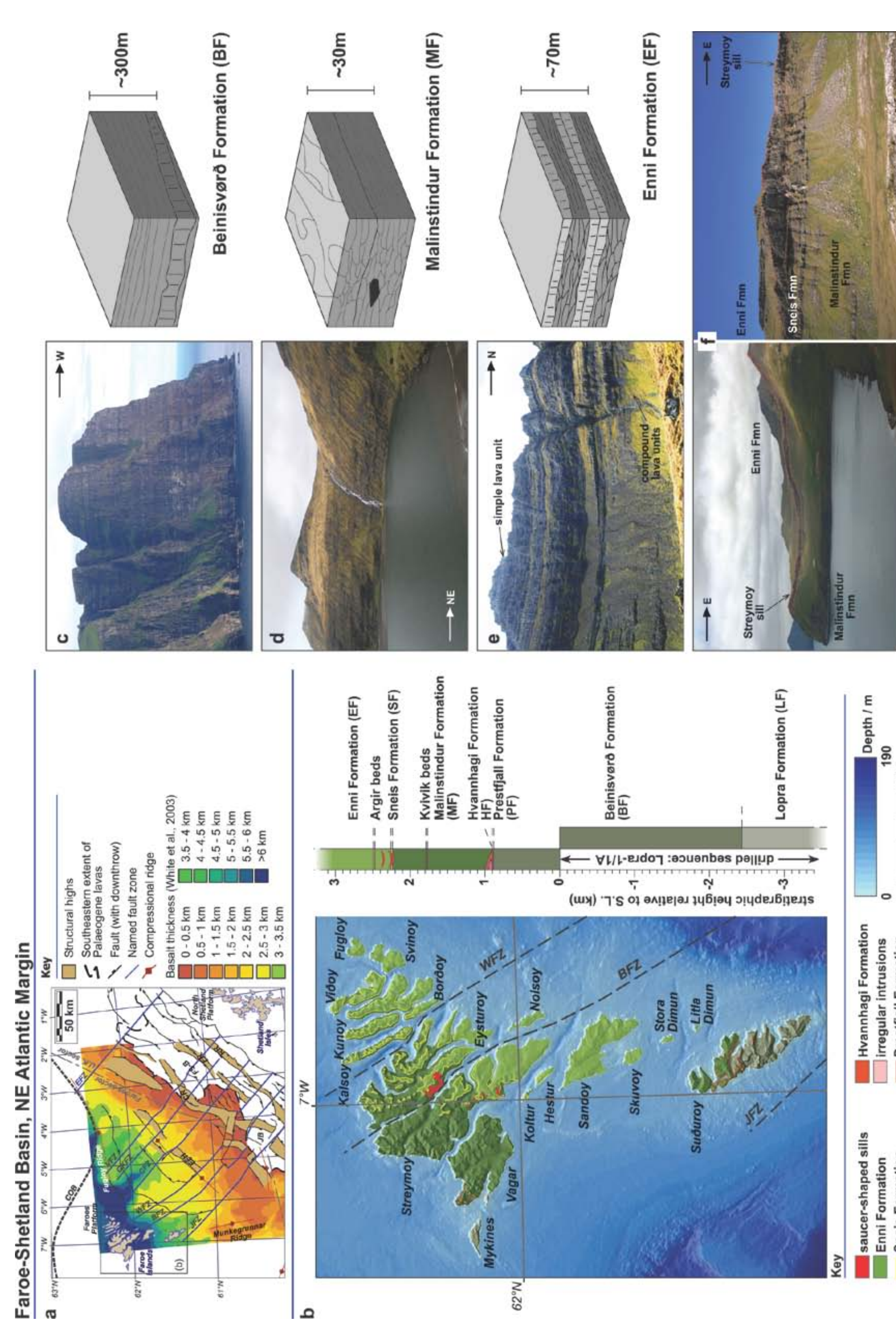
Faroe-Shetland Basin, NE Atlantic Margin
a
Key
Structural highs
Southeastern extent of Palaeogene lavas
Fault (with downthrow)
Named fault zone
Compressional ridge
Basalt thickness (White et al. 2003)
0 - 0.5 km
0.5 - 1 km
1 - 1.5 km
1.5 - 2 km
2 - 2.5 km
2.5 - 3 km
3 - 3.5 km
3.5 - 4 km
4 - 4.5 km
4.5 - 5 km
5 - 5.5 km
5.5 - 6 km
>6 km
50 km
Faroe Islands
Faroes Platform
Munkegrunnur Ridge
North Shetland Platform
Shetland Isles
b
7°W
62°N
Mykines
Streymoy
Vagar
Koltur
Hestur
Sandoy
Skuvoy
Suduroy
Kalsoy
Kunoy
Viđoy
Fugloy
Svinoy
Borđoy
Eysturoy
Nolsoy
Stora Dimun
Litla Dimun
WFZ
BFZ
JFZ
Key
saucer-shaped sills
Enni Formation
Sneis Formation
Malinstindur Formation
Hvannhagi Formation
irregular intrusions
Prestfjall Formation
Beinisvørð Formation
stratigraphic height relative to S.L. (km)
drilled sequence: Lopra-1/1A
Enni Formation (EF)
Argir beds
Sneis Formation (SF)
Kvívík beds
Malinstindur Formation (MF)
Hvannhagi Formation HF)
Prestfjall Formation (PF)
Beinisvørð Formation (BF)
Lopra Formation (LF)
Depth / m
190
0
km
0 5 10 15 20
c
W
d
NE
e
N
simple lava unit
compound lava units
f
E
Streymoy sill
Malinstindur Fmn
Enni Fmn
Sneis Fmn
~300m
Beinisvørð Formation (BF)
~30m
Malinstindur Formation (MF)
~70m
Enni Formation (EF)

Fig. 5.1. (*Previous page*) (**a**) Simplified structural elements map of the Faroe-Shetland Basin, NE Atlantic margin with location of the Faroe Islands: **EFH**, East Faroe High; **FS-B**, Flett Sub-Basin; **JB**, Judd Basin; **CR**, Corona Ridge; **FR**, Flett Ridge; **RR**, Rona Ridge; **BFZ**, Brynhild Fault-Zone; **CFZ**, Clair Fault-Zone; **EFZ**, Erlend Fault-Zone; **GKFZ**, Grimur Kamban Fault-Zone; **JFZ**, Judd Fault-Zone; **VFZ**, Victory Fault-Zone; **WFZ**, Westray Fault-Zone**.** (After Stoker et al., 1993; Rumph et al., 1993; Lundin and Doré, 1997; Sørensen, 2003; White et al., 2003; Jolley and Morten, 2007; Ellis et al., 2009). (**b**) Simplified geological map of the Faroe Islands and gross stratigraphic column for the Faroe Island Basalt Group (after Passey, 2009). (**c-e**) Photographs of the Beinisvord (c), Malinstindur (d) and Enni (e) Formations with block diagrams displaying their typical characteristics (after Passey and Bell, 2007). (**f**) Photographs of the Streymoy sill which cuts through stratigraphy from the Malinstinur Formation, into the Enni Formation.

Fugloy ridges; **Fig. 5.1a**). These deformation structures were formed and evolved immediately before, during and following continental break-up (*see Chapters 2 and 3*). Folds on the islands, and similar structures offshore, are active targets for hydrocarbon exploration in the Faroes sector of the NE Atlantic margin. Recent work in the Faroe Islands has highlighted the role of syn-magmatic, and post-magmatic (regionally-late) fault-reactivation in the development of, potentially, very high-permeability pathways (fault voids and infills) through the FIBG (*see Chapter 4*). This is supported by evidence from layered clastic sequences which indicate that open fissures, similar to those observed on the Faroes, are common along upper crustal fault-zones (e.g. Woodcock et al., 2006; Woodcock and Mort, 2008; Wright et al., 2009) and in crystalline basement rocks below unconformities with sedimentary sequences (e.g. Beacom et al. 1999). The principal aim of the present paper is to characterise faults, fault rocks and fractures within the FIBG, with respect to timings, kinematics, confining pressure, fluid pressures and temperature. We also critically test the applicability of fault-characterisation models developed in layered clastic-sequences to fault architectures in layered basaltic sequences.

5.2 Geological context

5.2.1 Stratigraphy of the Faroe Islands

The Faroe Island Basalt Group (FIBG) represents a small part of the North Atlantic Igneous Province (NAIP; **Fig. 5.1**), and was emplaced between Chrons 26 and 24 (59 – 56 Ma), at which time the Faroe Islands and East Greenland were less than 120km apart, based on plate reconstructions and geochemical correlations between sequences (Larsen et al., 1999; Lundin and Doré, 2002). Parts of the FIBG are exposed on the Faroe Islands, with an overall stratigraphic thickness in excess of 6.6km (**Fig. 5.1b**; Passey and Bell, 2007), of which about 3km is exposed above sea level (Ellis et al., 2002). The FIBG is dominated by tholeiitic basalt lavas indicating that their eruption occurred a period experiencing a high degree of partial melting of the mantle (Waagstein, 1988). This study focuses on fault outcrops and fault rocks within four of the seven formations of the FIBG (the Beinisvørð, Prestfjall, Malinstindur and Enni Formations) and also the Streymoy sill, and therefore we will forego a full description of the stratigraphy (a more complete description can be found in Passey and Bell, 2007; Passey, 2009; and *Chapter 2*).

The lowermost and oldest formation exposed on the islands is the ca.3.3km thick *Beinisvørð Formation* (**Fig. 5.1b, c**), of which only the upper 900m is exposed. The Beinisvørð Formation generally comprises aphyric, laterally extensive sheet lobes, with minor intercalated volcaniclastic horizons, emplaced at or around sea level, requiring that subsidence and emplacement rates be comparable throughout. Exposure of the Beinisvørð Formation is limited to the southern island, Suðuroy, and in the west of the northern islands, Vagar and Mykines (**Fig. 5.1b**). Above this lies the 3-15m thick *Prestfjall Formation* (**Fig. 5.1b**), comprising coals, mudstones and sandstones deposited in swamps, lacustrine and fluvial environments, during a hiatus in volcanic activity (Rasmussen and Noe-Nygaard, 1969 & 1970; Lund, 1983 &1989; Passey and Bell, 2007).

Trap-style volcanism continued with the eruption of the <1.4km thick *Malinstindur Formation* (**Fig. 5.1b, d**), subaerial compound basalt lavas that are initially olivine-phyric evolving upwards within the sequence to aphyric, and then plagioclase-phyric. The Malinstindur Formation is particularly well exposed on the northern islands of Vagar, Streymoy and Eysturoy, at low-altitudes on the north-eastern islands, and in the north of Suduroy. Above the Malinstindur Formation are the ~25m thick volcaniclastics of the *Sneis Formation*.

Above the Sneis Formation are 900m of the uppermost *Enni Formation* (**Fig. 5.1b, e**), which comprises low-TiO_2 and high-Ti O_2 (MORB-like) interbedded simple (sheet lobes) and compound tholeiitic lavas. The 900m is a minimum thickness, with a significant amount (in the order of hundreds of metres) likely eroded from the top of the volcanic pile (Waagstein et al., 2002). The Enni Formation is exposed in a north- to north-east-arcing trend from Sandoy across the northern islands (**Fig. 5.1b**).

There are a number of notable sheet-like intrusions on the islands, including the large 'saucer-shaped' *Streymoy* and *Eysturoy* sills, and the *Fugloy-Svinoy* sill. The Streymoy sill is transgressive, lying stratigraphically close to the Sneis Formation (**Fig. 5.1b, f**). The sill ranges from ~10-55m thickness, and covers an area of about 13km^2, displaying a saucer-like geometry with numerous ramp- and flat-sections, cutting upwards from within the top part of the Malinstindur Formation, becoming flat at the level of the Sneis Formation (**Fig. 5.1b**), and then ramping upwards again into the Enni Formation.

5.2.2 Deformation history

Structures developed in the FIBG provide clear evidence for a multi-phase rift-reorientation through time (Geoffroy et al., 1994; *Chapter 3*) before and during continental break-up, followed by a significant phase of uplift (*see Chapters 3 and 4*). Distinct phases of faulting and dyke intrusion are recognised which, based on kinematics, geometry and cross-cutting relationships, can be split into 3 broad events.

This began with (*Event 1a*) ENE-WSW to NE-SW extension, accommodated by N-S- and NW-SE-trending dip-slip faults. Continued NE-SW extension was accommodated by the emplacement of a regionally significant swarm of NW-SE- and NNE-SSW-oriented dykes (*Event 1b*). Collectively, Events 1a and b affect the majority of the FIBG stratigraphy, likely resulting in thickness variations, most notably across the Judd, Brynhild and Westray Fault Zones (**Fig. 5.1a, b**). Continued magmatism and an anticlockwise rotation of the extension vector led to (*Event 2a*) the emplacement of ENE-WSW and ESE-WNW conjugate dykes. Their intrusion marks the onset of N-S crustal extension and was followed by (*Event 2b*) fault-accommodated crustal extrusion involving both E-W shortening and further N-S extension facilitated primarily by slip on ENE-WSW (dextral) and ESE-WNW (sinistral) conjugate strike-slip faults, many of which are developed in the same locations as the immediately preceding conjugate dykes. A component of this E-W shortening was facilitated additionally by the development of minor-offset thrust faults which dip mainly to the SW or NE. During the final stages of this event (*Event 2c*), the regional extension vector rotated into a more NW-SE orientation that was preferentially accommodated by slip along NE-SW trending (dextral) oblique-slip faults. Based on the timing relative to Event 1, and an apparent thickening of the Enni Formation across hectometre-scale offset, E-W-trending faults (Passey, 2009; Ellis et al., 2009), Event 2 most likely began towards the end of magmatism associated with the FIBG, coeval with the onset of oceanic-spreading on the Aegir ridge (ca.54-51 Ma; Lenoir et al., 2003); it may have continued through to the linkage of the Reykjanes, Kolbeinsey and Mohns Ridges. Events 1 and 2 are associated with multiple generations of calcite and zeolite mineralisation in linked arrays of tensile and shear hydraulic veins. The final deformation (*Event 3*), involves the post-magmatic reactivation of some faults, and is most clearly observed in instances where clastic material has been entrained along fault planes (*see Chapter 4*).

5.2.3 Faults in Basalts

The general characteristics and mechanics of near-surface faults in basalts are well documented (e.g. Gudmundsson 1992, 2000; Acocella et al., 2003; Grant and Kattenhorn, 2003; Martel and Langley, 2006), but few studies have addressed the internal architecture and structure of basalt-hosted fault zones (e.g. Holland et al., 2006). Most existing studies are focused around the use of scaled models in order to address fault character at larger scales (dam-km), with little to no account of smaller scale features such as fracture/fault linkage, fault rock assemblages and mineralisation phases.

Using analogue modeling studies (cohesive hemihydrate powders) and field observations, Holland et al. (2006) have shown that near-surface faults in basalts display a dominant tensile component, due to the solid, brittle nature of the material. This tensile opening produces a near-surface cavity, within which brecciated fault rocks, surface waters and sediments can accumulate. At deeper levels, faults close and will display typical characteristics reflecting fault slip and/or hydrofracture processes.

This depth-controlled relationship is rarely observed along the same fault in the field, due to limitations in the surface topographic separation, but has clear implications for fluid flow and transmission models, particularly in relation to depth, and the presence of poorly lithified/cemented sediments and/or open cavities along faults.

5.3 Fault characteristics

5.3.1 Event 1 faults

Event 1 faults and fractures are typically oriented NW-SE to N-S, displaying dip-slip motion senses and locally tensile openings, accommodating an ENE-WSW extension. These faults typically display centimetre- to metre-scale offsets, and rarely exceed decametre-scale total displacements. The best exposures of these faults are found in the Beinisvørð Formation (**Figs. 5.1b, 5.2a**), particularly in the SW of Suðuroy at Vagseiði (**Figs. 5.2b, 5.3**), Sumba (**Figs. 5.2c, 5.4**) and I Botni (**Figs. 5.2d, 5.5**). Figures 3-5 are ordered in sequence from small displacement (**Fig. 5.3**) through to large displacement faults (**Fig. 5.5**).

Faults associated with Event 1 commonly display prominent damage zones which are particularly well developed in the fault hanging walls (e.g. **Figs. 5.3b, 5.4a,b** and **5.5a,b**). These zones vary in nature and damage intensity depending on the distance from the master fault, and magnitude of displacement. However, damage width does

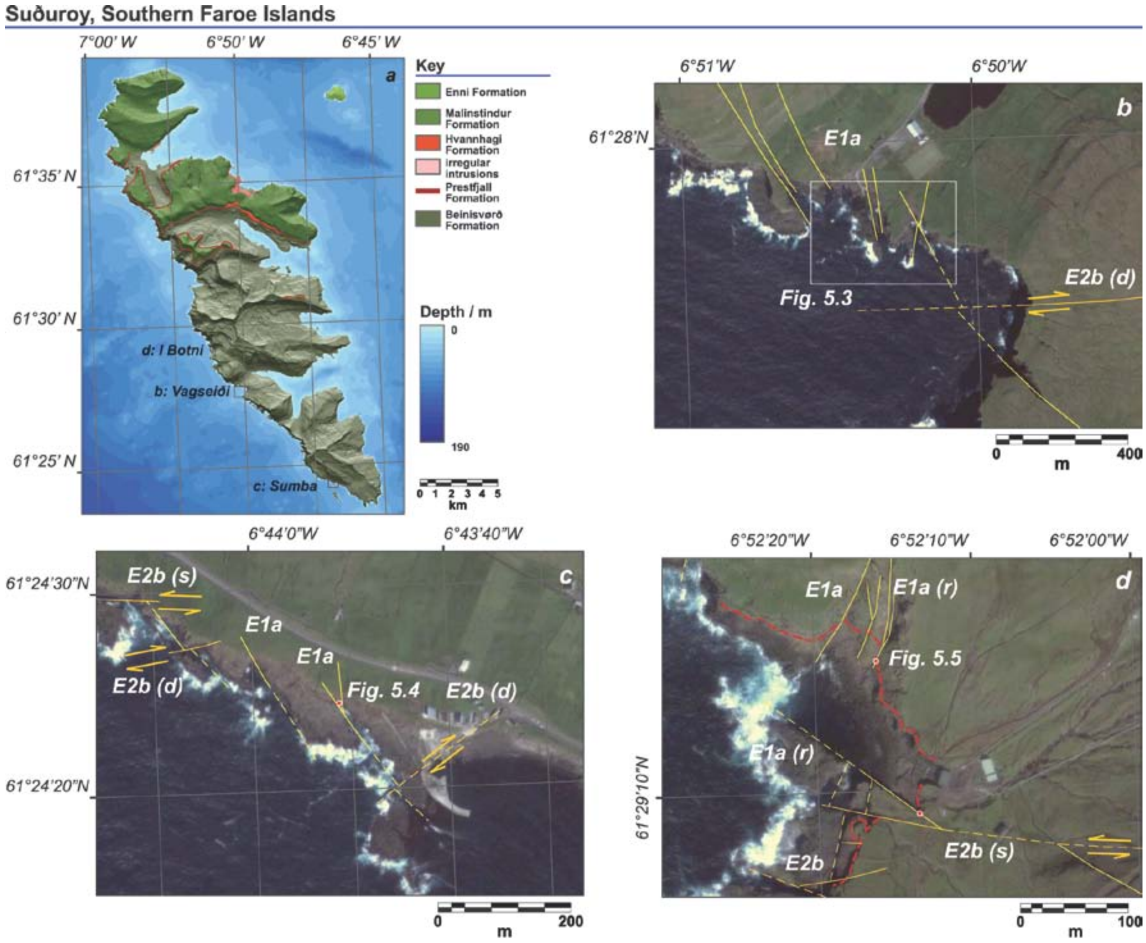

Fig. 5.2. (**a**) Simplified geological map of Suðuroy, with locations of b-d, and **Figures 5.3, 5.4, 5.5**. (**b-d**) Satellite images and structural (field) interpretations for Vagseiði, Sumba and I Botni respectively.

not appear to be markedly affected by increased displacement (e.g. **Figs. 5.3b, 5.4b, 5.5b**). On larger displacement faults (e.g. I Botni: **Fig. 5.5**) damage intensity clearly increases rapidly into the master fault, from gouge and breccias in the core, to cataclasite and foliated cataclasite (**Fig. 5.5c-e**). Smaller offset faults also display increased damage towards the master fault, with either a reduction in grain size (**Fig. 5.4f-g**), or increased brecciation (**Fig. 5.3c-h**), depending on the magnitude of offset. In some cases (e.g. Vagseiði: **Fig. 5.3**), faults also switch from being tensile (**Fig. 5.3c, d**),

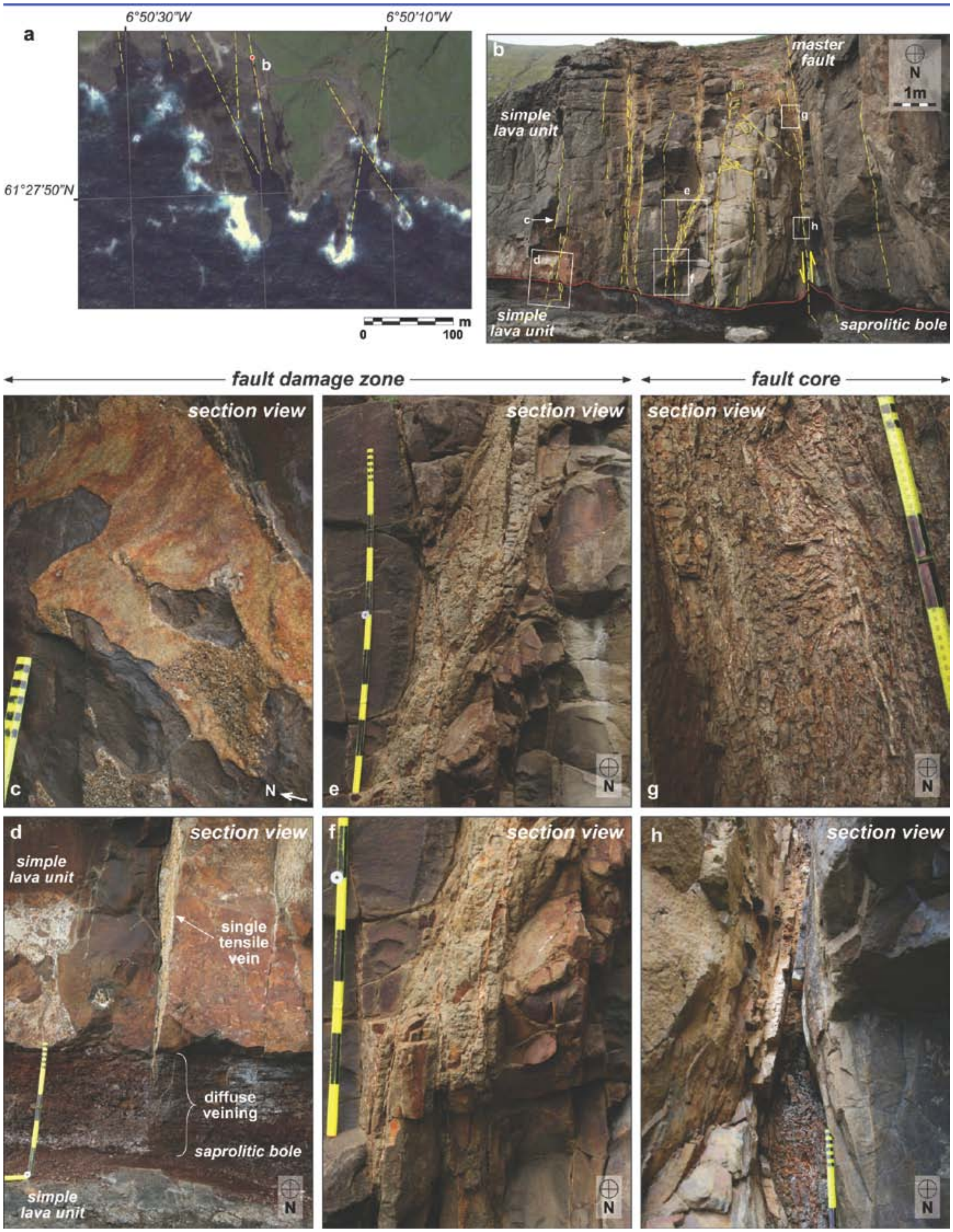

Fig. 5.3. (**a**) Event 1 faults at Vagseiði (location in **Figure 5.2**). (**b**) N-S trending dip slip fault displaying ~15cm displacement down to the west, and a large (~6m) damage zone focused in the fault hanging wall. The nature and intensity of deformation changes markedly towards the master fault, with (**c-d**) pure tensile veining at distances of 4-6m from the master fault; (**e-f**) minor offset shear tensile faults 1-4m from the master fault; and (**g-h**) intense brecciation within a 1m wide zone from the master fault (i.e. the fault core).

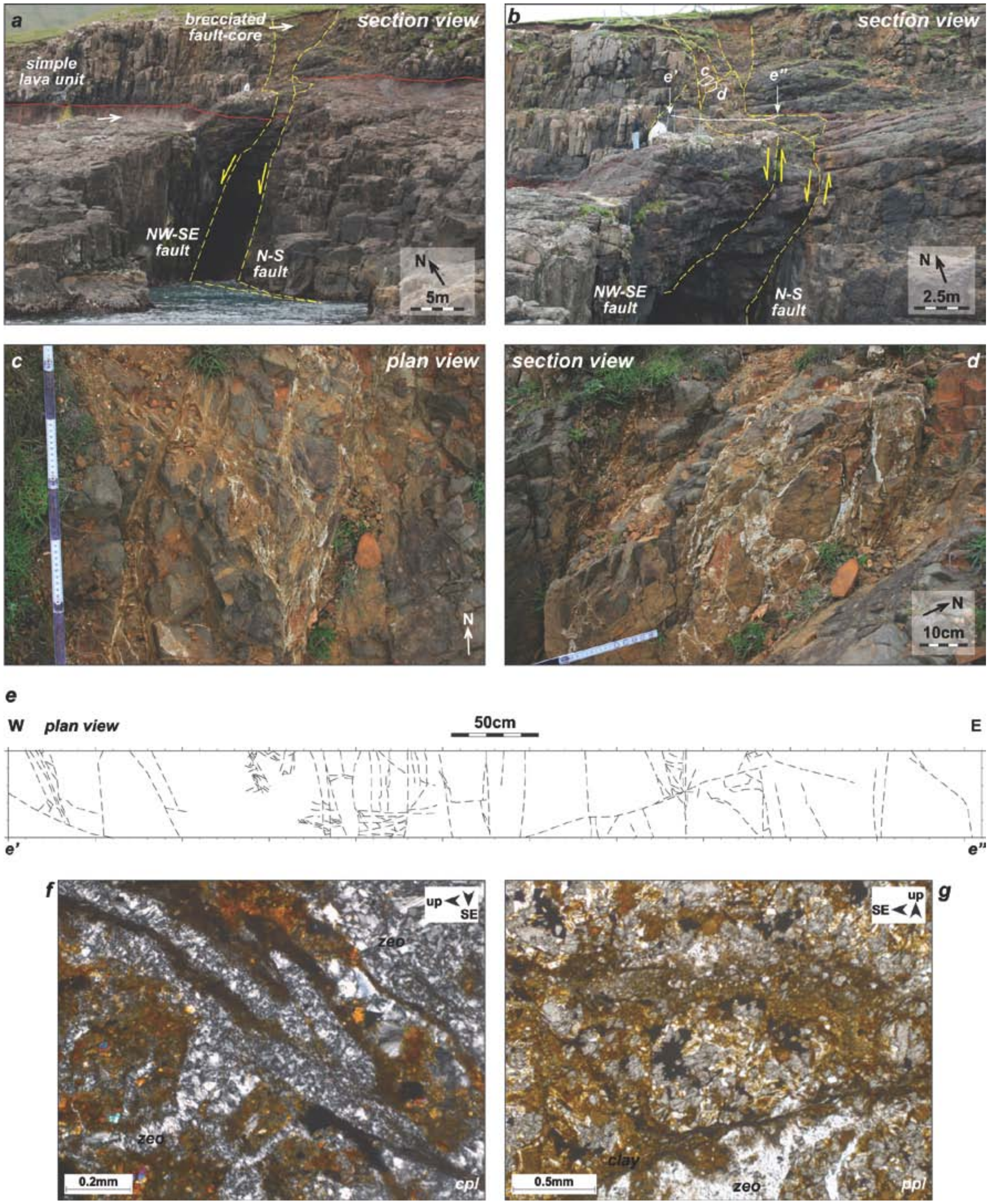

Fig. 5.4. (**a**) N-S and NW-SE trending dip-slip faults displaying a cumulative 4.5m, down to the west displacement (location in **Figure 5.2**). (**b**) The fault displays a well developed fault core and damage zone focused in the hanging wall of the N-S trending fault. (**c-e**) The fault core is characterised by variously oriented tensile (mode I) and shear-tensile (mixed-mode) veins. (**f**) Fault-related mineralisation is dominated by zeolites (*zeo*), which in places, (**g**) are brecciated and entrained along later slip planes.

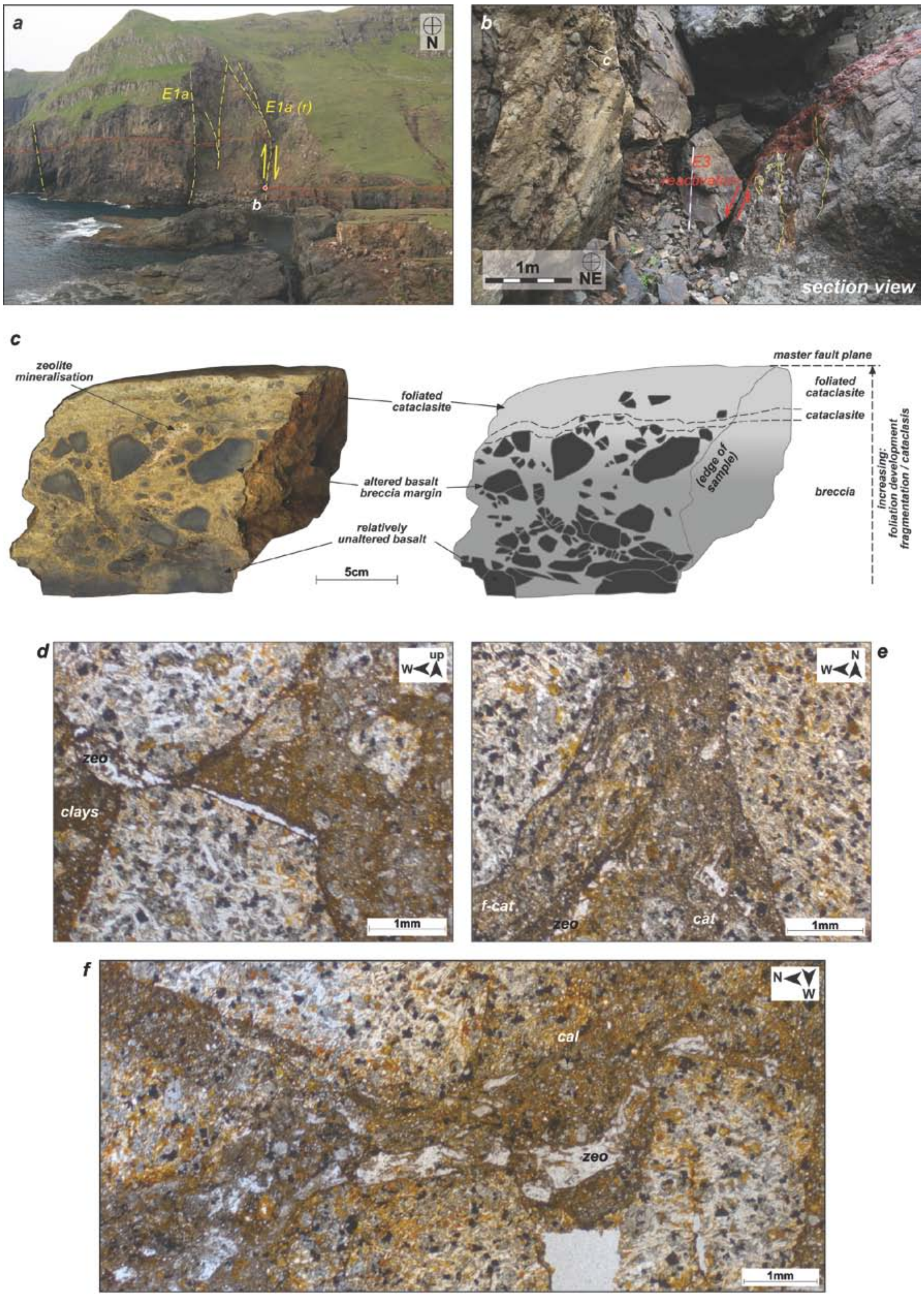
a
N
E1a
E1a (r)
b
b
c
E3 reactivation
1m
NE
section view
c
zeolite mineralisation
foliated cataclasite
altered basalt breccia margin
relatively unaltered basalt
5cm
(edge of sample)
master fault plane
foliated cataclasite
cataclasite
breccia
increasing: foliation development fragmentation / cataclasis
d
up
W
zeo
clays
1mm
e
N
W
f-cat
zeo
cat
1mm
f
N
W
cal
zeo
1mm

Fig. 5.5. (*Previous page*) (**a**) N-S trending dip-slip, Event 1a fault (reactivated during Event 3), displaying ~30m displacement, down to the east at I Botni (location in **Figure 5.2**). (**b**) The 3-5m wide fault zone displays extensive zeolite mineralisation (*zeo*) as discrete veining, and well developed dip-slip corrugations on fault surfaces. (**c**) Fault rock sample (located in *b*), shows increasing deformation intensity towards the master fault, from brecciation, to foliated cataclasite (*f-cat*), and only minor mesoscopic mineralisation. (**d**) Plane polarized light photograph of breccia and (**e**) cataclasite (*cat*) from the respective zones in *c*. Cross-cutting fabrics in *e* indicate recurrent reactivation: a NNW-SSE fabric is cut by a NNE-SSW fabric. (**f**) Zeolite and calcite mineralisation (*cal*) is fragmented and entrained within cataclasites, again, most likely indicating reactivation, with phases of faulting, mineral precipitation and further faulting episodes.

to shear-tensile (**Fig. 5.3e, f**), to shear with localised compression (developing crumpled vein sets within the fault core: **Fig. 5.3g, h**) towards the master fault. This change is most likely caused by the elastic response of the material, as the unit is dragged into the master fault.

In all observed cases, it is clear that Event 1 faults have acted as conduits for hydrous fluids through the basalt pile. Calcite and zeolite mineralisation are a ubiquitous feature in Event 1 fault zones, with brecciation and reworking relationships indicating that they precipitate in three stages (earliest to latest): (1) minor elongate and blocky zeolite mineralisation; (2) blocky calcite mineralisation forming equant crystals; (3) zeolite mineralisation forming predominantly elongate crystals. Commonly, fragments of the host rock and/or bubble trails are observed within the early zeolite and calcite mineralisation (**Fig. 5.6**), most likely representing a previous position of the vein wall, and indicating a crack seal mechanism for vein formation (Ramsay, 1980; Petit et al., 1999). These mineralising fluids are also likely responsible for the preferential chemical decomposition of feldspars (producing various clay minerals) observed within the fault zones. On the basis of cross-cutting relationships, the formation of these clays appears to be a precursor to the precipitation of the early zeolite (e.g. **Fig. 5.4f, g**), and most likely results from the formation of a mesh of micro-fractures and faults in the build-up to the formation of through-going faults. Material degradation in this manner along early faults may sufficiently weaken the incipient fault zone and further focus

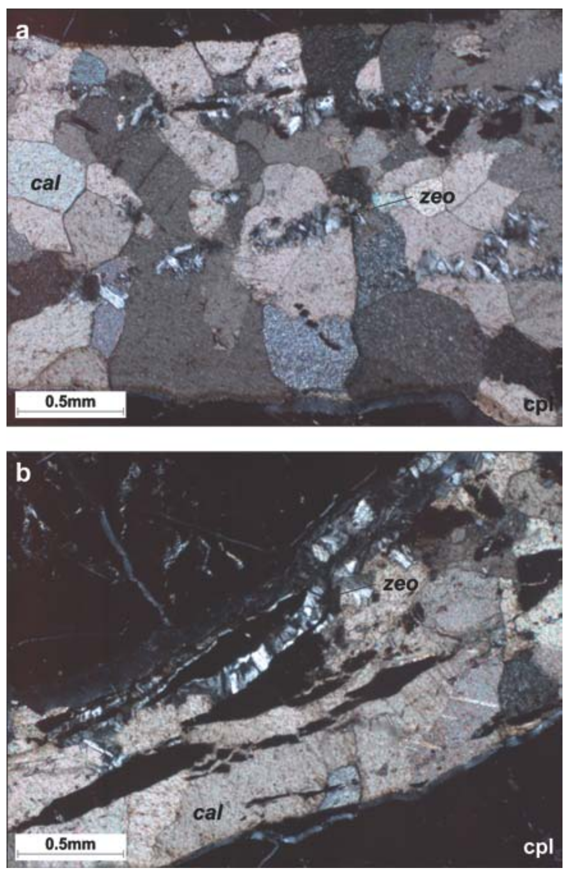

Fig. 5.6. Crossed poles micrograph of calcite (*cal*) and zeolite (*zeo*) mineralisation of Event 1 within a volcanic tuff at I Botni. (**a**) Zeolite vein material and host rock fragments indicate the location of the vein walls before further dilation and calcite mineralisation. (**b**) Fragments of the country rock are arranged in an en echelon pattern, and indicate the previous location of the vein walls. Unlike in *a*, zeolite mineralisation remains fixed to the vein wall.

deformation through them, rather than forming new faults. Clear evidence of the recurrent reactivation of the existing fault zones is seen from the development of foliated clay-rich cataclasites containing variously deformed clasts and fragments of calcite and zeolite (e.g. **Fig. 5.5c, f**), together with numerous examples of brecciated and cross-cutting zeolite and calcite mineralisation (e.g. **Figs. 5.3g** and **5.4g**).

5.3.2 Event 1 and 2 dykes

Event 1 and 2 faulting episodes are separated by a period of dyke and sill emplacement. These intrusions require the formation of fractures, which rather than being filled by hydrous fluids, become filled by magma instead. Event 1 dykes are typically oriented NW-SE to NNE-SSW, and Event 2 dykes are typically oriented ENE-WSW to ESE-WNW. Widths are similar between the sets, with most being 2-5m wide, occasionally (<10%) reaching 20m. In plan view, the dykes appear to exploit existing cooling joints within the lavas, forming localised corners which are offset normal to the main dyke trend. No instances of faults reactivated by intrusions have been observed during this study (which will be discussed in *section 5.4.3*), and in all observed cases, there are minor to no lateral offsets. In section view, in certain cases, dykes appear to have an en-echelon style segmentation (e.g. **Fig. 5.7a,b**), and in both orientations, numerous, variously oriented offshoots and bifurcations are observed splaying from the main dyke (e.g. **Fig. 5.7c**). This indicates that dykes were not emplaced as a single buoyant sheet, but rather as a set of inter-fingering sheets or lobes that link through

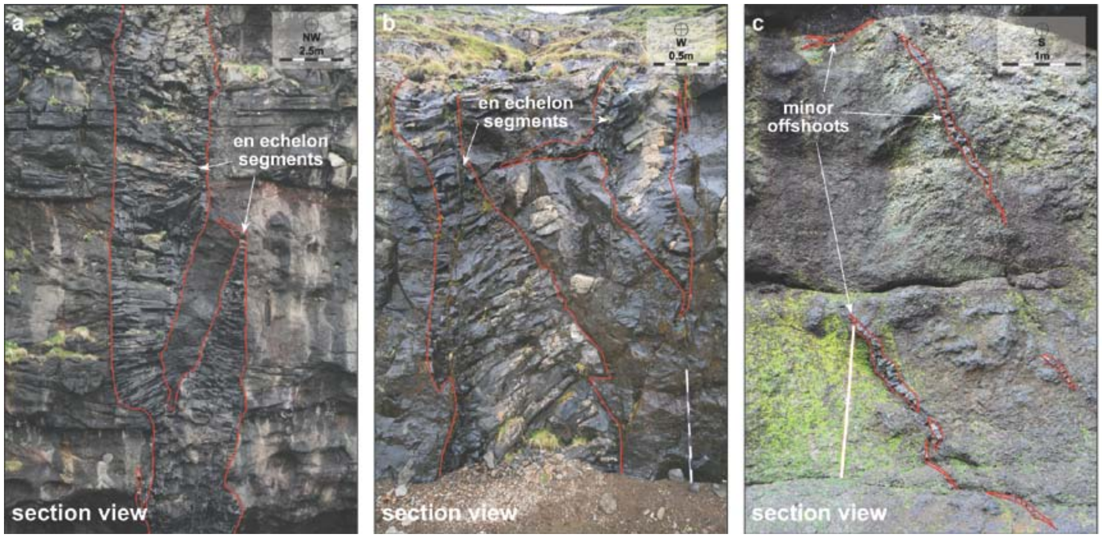

Fig. 5.7. (**a-b**) En echelon segmentation of dykes, with very minor (cm-dm-scale) vertical offsets indicates mixed mode (I/III) opening during dyke propagation. (**c**) Minor dyke offshoots peripheral to the main dyke (not pictured – 2m to right of photo) are most likely indication that dykes propagated as a set of linking lobes or sheets.

time during propagation (e.g. Pollard et al., 1975). It is also suggestive that, although ultimately minor, based on the total offsets, there was a component of out-of-plane slip during dilation (i.e. a mixed mode I/mode III opening).

In the case of dykes and sills, magmatic pressure drives fracture propagation. This can result from: (1) excess magma at the source body; (2) magma buoyancy (relative to the country rock); and (3) gradients of tectonic stress normal to the dyke plane (Speight et al., 1982; Walker, 1987; Rubin, 1995; Gudmundsson and Brenner, 2004). With respect to point 3, dyke orientations are similar to faults of their associated events, and demonstrably opened at ~90° to the main trend of the dyke. This suggests that they likely relate to the same tectonic episodes as their respective fault-sets (i.e. Event 1 is a NE-SW oriented extension event, and early-mid Event 2 is a N-S oriented extension event), with extension accommodated by an increase in volume, rather than vertical thinning. This in itself is a possible indication that regional stresses outweighed those imposed by overpressure at the magmatic source, since the inferred orientation of *σ3* is consistent in the presence and absence of magmatism.

5.3.3 Event 2 sills

In all observed instances, Event 1 and 2 dykes are cut by the large saucer-shaped sills on Eysturoy and Streymoy, which are in turn cut by Event 2 faults (**Fig. 5.8a-c**). The Eysturoy and Streymoy sills are reasonably large, covering an area of 16km^2 and 13km^2 respectively (Rasmussen and Noe-Nygaard, 1969, 1970), and both range from 10-55m thickness. Sill geometry is reasonably complex, with numerous flat and ramp sections giving them a general transgressive saucer-shape, with the lowest points in the west to west-southwest, nearest their respective fjords (please see *Chapter 2* for full details on sill geometry). The sills are reasonably high within the stratigraphy (**Fig. 5.1b**) occurring only within the uppermost kilometre, which could relate to a controlling influence of the zone of neutral buoyancy, though there are clearly further controls to consider based on the transgressive nature of the sills.

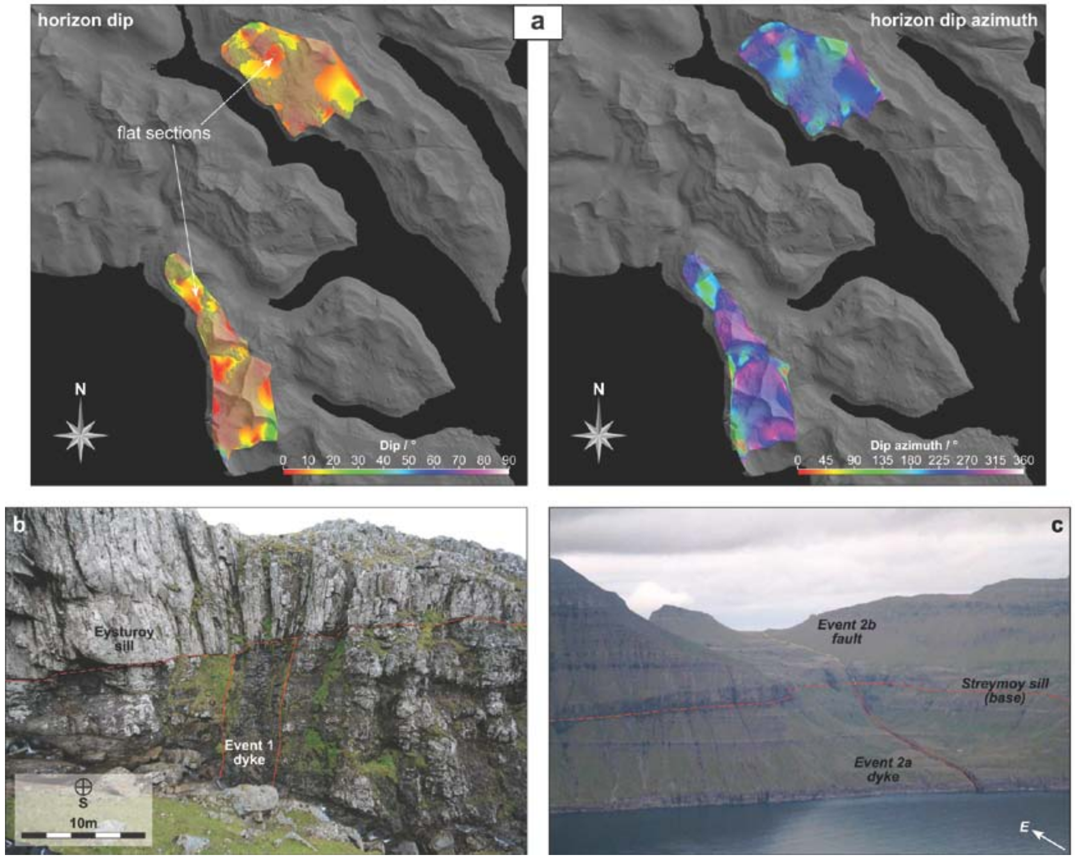

Fig. 5.8. (**a**) Models for the Streymoy and Eysturoy sills based on outcrop data, and projected through the subsurface. The sills display a complex 'saucer-shaped' geometry with numerous flat and ramp sections. A notable flat section occurs within the centre of each of the sills, corresponding to the stratigraphic level of the sedimentary Sneis Formation. (**b**) An Event 1 dyke is cut by the Eysturoy sill and (**c**) and Event 2 dyke is cut by the Streymoy sill. Both sills are cut by Event 2 faults (e.g. *c*).

Flat sections of the sills are apparently coincident with sedimentary horizons in the stratigraphy. In particular, a large flat section in both the Eysturoy and Streymoy sills occurs roughly in the middle of their elevation range, corresponding loosely to the position of the Sneis Formation (**Fig. 5.1b, f**). Horizontal weaknesses such as bedding are a commonly invoked reason for the attitude and placement of sills within a particular stratigraphic column (e.g. Pollard, 1973; Pollard and Johnson, 1973;

Kavanagh et al., 2006), and this feature is most likely a reflection of the relative weakness of the Sneis Formation compared with the basalt lavas above and below. Internally, the sills appear to comprise a set of lobes, which, as with dyke emplacement, would have inflated and linked through time, rather than forming as a single sheet. The ramp geometry may therefore be related to this inflation process. As the sill propagates, extending its length, it becomes thicker due to the elastic deformation of the adjacent country rocks (Menand, 2008). As a result, the viscous dissipation induced by magma flow decreases, and unless the source pressure decreases at a comparable rate, propagation must accelerate in order to balance the pressures. If sill propagation accelerates, it will continue to thicken, and strain rate within the surrounding country rock will have to follow suit. Hence, faster propagation will lead to the transgressive emplacement of the sill through brittle deformation (i.e. fault propagation) of the country rock into the relatively stronger, rigid Enni Formation basalts above the relatively weaker, elastic Sneis Formation sands (though this upwards propagation may only be as far as the next weak layer). This method of propagation is clearly different to the dynamics of dyke propagation, which instead appear to be controlled by time-dependant failure of the country rock (whereby failure at the dyke tip results from pressure build up within the dyke), rather than the effects of viscous dissipation. These differences are likely reflected in the widths/thicknesses of the dykes (2-20m) relative to the sills (10-55m). During a time-dependant failure mechanism, a dyke would propagate at an approximately constant velocity, even if the source pressure remained constant (Menand and Tait, 2002). Hence, for identical source pressure conditions, sills would in general propagate faster and be thicker than dykes.

The emplacement of the saucer-shaped sills implies a switch of the minimum compressive stress to a vertical orientation, similar to that of the later thrust faults associated with Event 2. This is could be considered to be a problem in terms of the regional stress field, since generally at the time $\sigma 3$ is thought to be horizontal in a N-S orientation. However, like the thrust faults, sill emplacement is most likely a testament to the 3-dimensional complexity of the event (as will be detailed in the following section).

5.3.4 Event 2 faults

Event 2 faults and fractures are typically oriented between ENE-WSW and ESE-WNW as conjugate strike-slip sets with a dextral (mean ENE) and sinistral (mean ESE) pair that accommodate a N-S oriented extension, and simultaneous E-W compression. Kinematically, Event 2 is seemingly more complex than Event 1, and perhaps as a consequence, fault-rock styles are also more complex. Here we separate the varied styles into groups based on interpretations as to their development and their possible relationship to displacement magnitude.

5.3.4.1Shear hydraulic fracture/vein sets

Minor offset faults, fractures and veins are the most common feature of brittle deformation in the Faroe Islands, with few (if any) outcrops being completely barren of fractures (e.g. **Fig. 5.9c-f**). Generally, these structures are small (mm-cm widths and 1-3m in length) and isolated (**Fig. 5.9c**), and terminate within a single basalt flow unit. In more developed instances, individual structures link to form broader and more continuous sets or meshes, though again, offsets are negligible (e.g. **Fig. 5.9d-f**).

These faults, fractures and veins are most likely representative of the regionally distributed, relatively low strain within the FIBG. Had deformation been more sustained, these features could have continued to grow and link to form through-going faults with related damage zones (e.g. **Fig. 5.10**).

5.3.4.2Fault zone-forming clusters

Larger displacement faults in the FIBG have typically been preferentially eroded by surface processes, forming deeply incised gullies and inlets that can be mapped at the macro-scale (e.g. **Fig. 5.10a**). At the meso-scale, it is clear that these gullies comprise well developed and linked clusters of faults, fractures and veins arranged in broad zones of damage, across which statigraphic horizons are offset (e.g. **Fig. 5.10b**). The damage zones of Event 2 are comparable to those of Event 1 (see *section 5.3.1.1*), displaying characteristics such as brecciation (**Fig. 5.10c**) and the development of

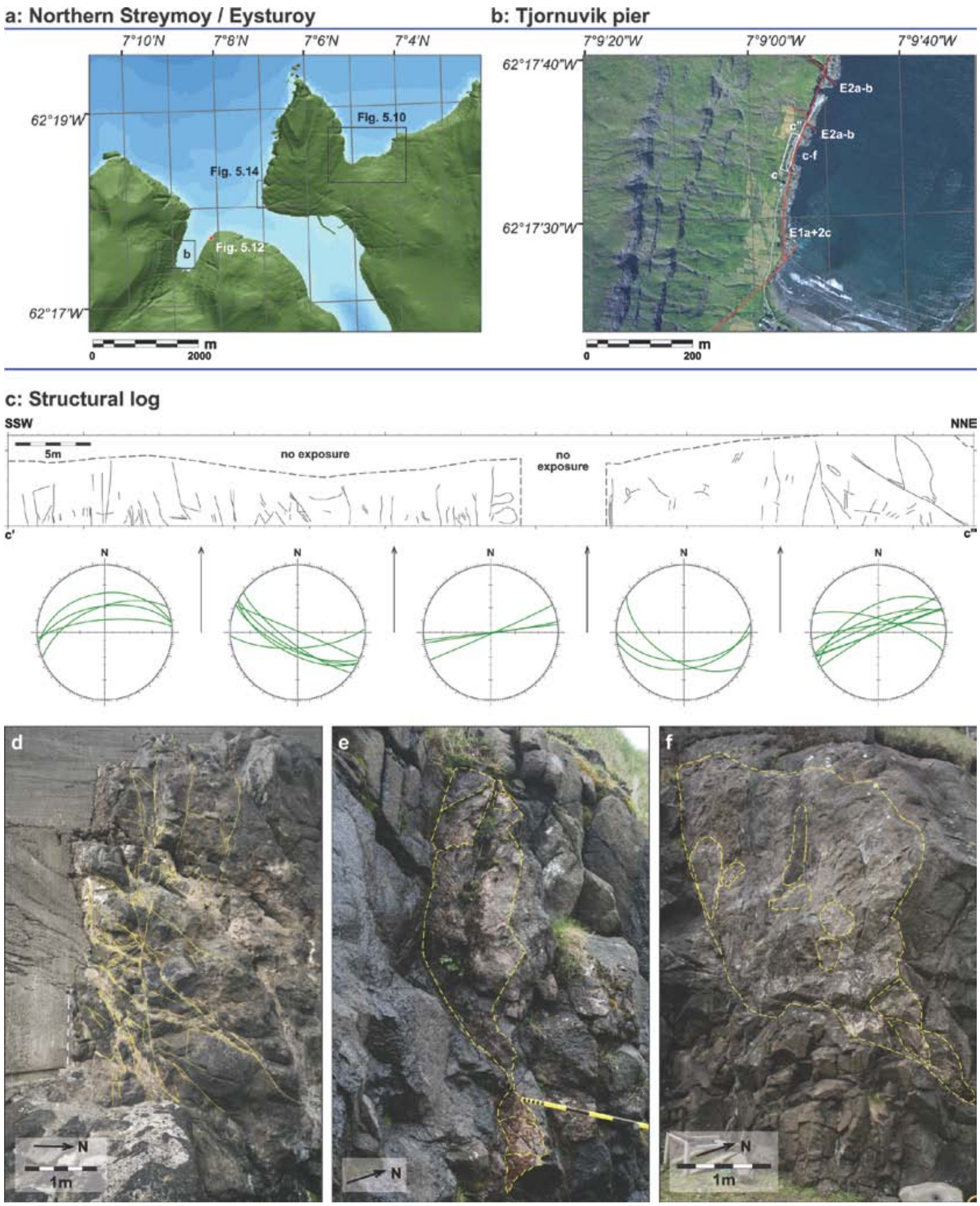

Fig. 5.9. (**a**) Simplified geological map of NE Streymoy and NW Eysturoy indicating locations of Tjornuvik (b), and East and West Eiði (**Figures 5.8, 5.9, 5.11, 5.12**). (**b**) Aerial photograph of Tjornuvik bay showing the locations of *c-f*, and major structures responsible for significant displacements. (**c**) Structural log (section view; location in *b*) showing hydraulic fracture/vein distributions across the section. Veins tend to be isolated from each other, causing very little damage to the surrounding host unit. (**d-f**) Better developed veins form linkages with those nearby resulting in minor clusters (e.g. *d*). There is still little damage associated with these veins, and negligible offsets are observed. Resulting exposed fault surfaces comprise a collection of mis-oriented vein surfaces rather than a single plane (e.g. *e,f*).

tensile and extensional hybrid veins (**Fig. 5.10d**), which can generally be split into a damage zone and fault core based on the intensity of the damage and identification of master slip surfaces (e.g. **Fig. 5.10e**). As with Event 1 faults, those of Event 2 developed with successive phases of early zeolite, calcite and further, later, zeolite mineralisation (**Fig. 5.11a, b**), with cross-cutting and reworking relationships indicating they were precipitated in that order. Changes in zeolite texture are observed in most veins, with numerous small crystals closer to the margin, increasing in size and decreasing in number towards the interior. This coincides with a notable preferred crystallographic orientation in the elongate crystals, which appear to have grown inward from the margin, forming a medial line in the centre. This is most likely indication that competitive growth favoured well oriented crystals (Dickson, 1993; Oliver and Bons, 2001; e.g. **Fig. 5.11c**). Vein-wall parallel host rock fragments are also observed within the smaller crystals (e.g. **Fig. 5.11c**) presumably marking the former position of the vein wall, indicating episodic opening and the operation of a crack-seal style mechanism. The larger crystals in the vein centre do not display such features, most likely indicating that they grew into an open, fluid-filled cavity (detailed further in *section 5.3.4.3*).

5.3.4.3Fault cavity infills

As noted in the previous section, some vein fills indicate precipitation into a fluid-filled cavity, rather than by an incremental crack-seal mechanism. Veins of this style are a common feature of fault zones in the FIBG, occurring up-/down-dip and along-strike of

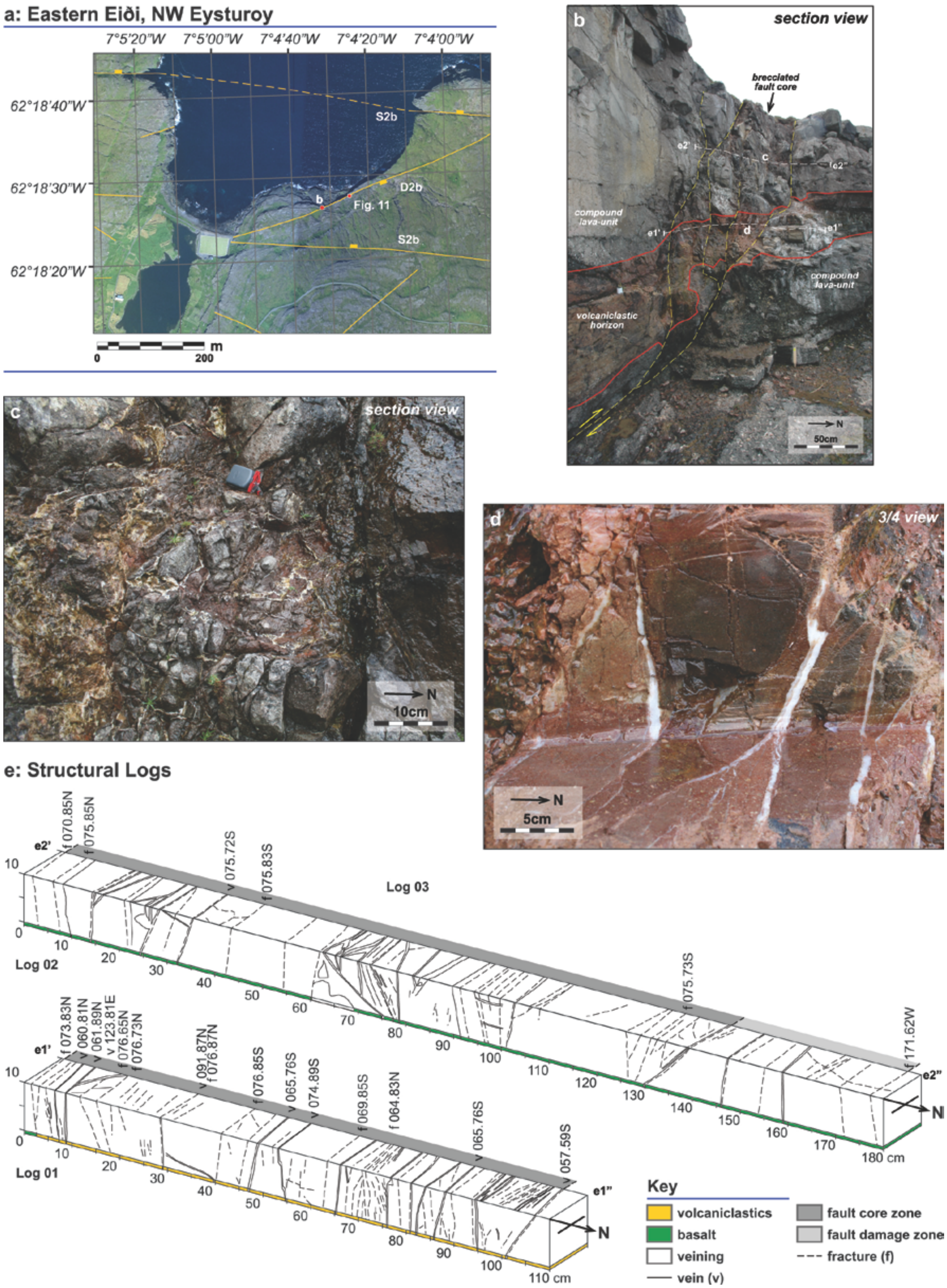
a: Eastern Eiði, NW Eysturoy
7°5'20"W
7°5'00"W
7°4'40"W
7°4'20"W
7°4'00"W
62°18'40"W
62°18'30"W
62°18'20"W
S2b
D2b
b
Fig. 11
S2b
0
200
m
b
section view
brecciated fault core
e2'
c
e2"
compound lava-unit
e1'
d
e1"
compound lava-unit
volcaniclastic horizon
N
50cm
c
section view
N
10cm
d
3/4 view
N
5cm
e: Structural Logs
e2'
f 070.85N
f 075.85N
v 075.72S
f 075.83S
Log 03
v 075.73S
f 171.62W
e2"
N
Log 02
10 20 30 40 50 60 70 80 90 100 110 120 130 140 150 160 170 180 cm
e1'
f 073.83N
v 060.81N
v 061.89N
v 123.81E
f 076.65N
f 076.73N
v 091.87N
f 076.87N
f 076.85S
v 065.76S
v 074.89S
f 069.85S
f 064.83N
v 065.76S
v 057.59S
e1"
N
Log 01
10 20 30 40 50 60 70 80 90 100 110 cm
Key
volcaniclastics
basalt
veining
vein (v)
fault core zone
fault damage zone
fracture (f)

Fig. 5.10. (*Previos page*) (**a**) Aerial photograph of eastern Eiði, NW Eysturoy (location in **Figure 5.7**) showing structures with notable displacements, and locations of *b* and **Figure 5.10**. (**b**) Photograph of an ENE-WSW trending Event 2b fault zone displaying an overall dextral offset with downthrow to the south (total ~4.5m displacement), which varies depending on the lithology with (**c**) basaltic units disaggregating to form breccias, and (**d**) volcaniclastic units being dragged into the master fault plane, and forming discrete tensile and shear tensile veins. (**e**) Fault damage varies both along strike and up/down dip of the master fault, becoming much thinner through the volcaniclastic horizon. Below *c*, the fault zone decreases to a single plane, with a minimal (cm-scale) peripheral damage zone.

the fault-zone forming clusters described previously. They are also commonly superimposed on existing shear hydraulic fractures and veins (e.g. **Fig. 5.11c**). Though these features also occur along Event 1 faults, there are far fewer compared to Event 2.

Cavity infills appear to take two forms which are differentiated based on their internal characteristics and mode of formation. They include: (1) individual or linked sets of tensile veins comprising >90% cement/crystalline infill and (2) cemented breccias that are emplaced rapidly into a cavity containing <<90% mineral cement. Individual or linked sets of tensile veins occur across the islands in most outcrops (e.g. **Fig. 5.9**), usually in conjunction with shear hydraulic fracture/vein sets, presumably accommodating a part of the extension of Event 2. Typically these veins are no more than 1-2cm wide, but in some cases they can be over 0.5m (**Fig. 5.12a,b**) and occasionally exceed 1 metre in thickness. Vuggy mineral precipitates in these larger examples indicate that there was an open cavity, allowing unencumbered growth from

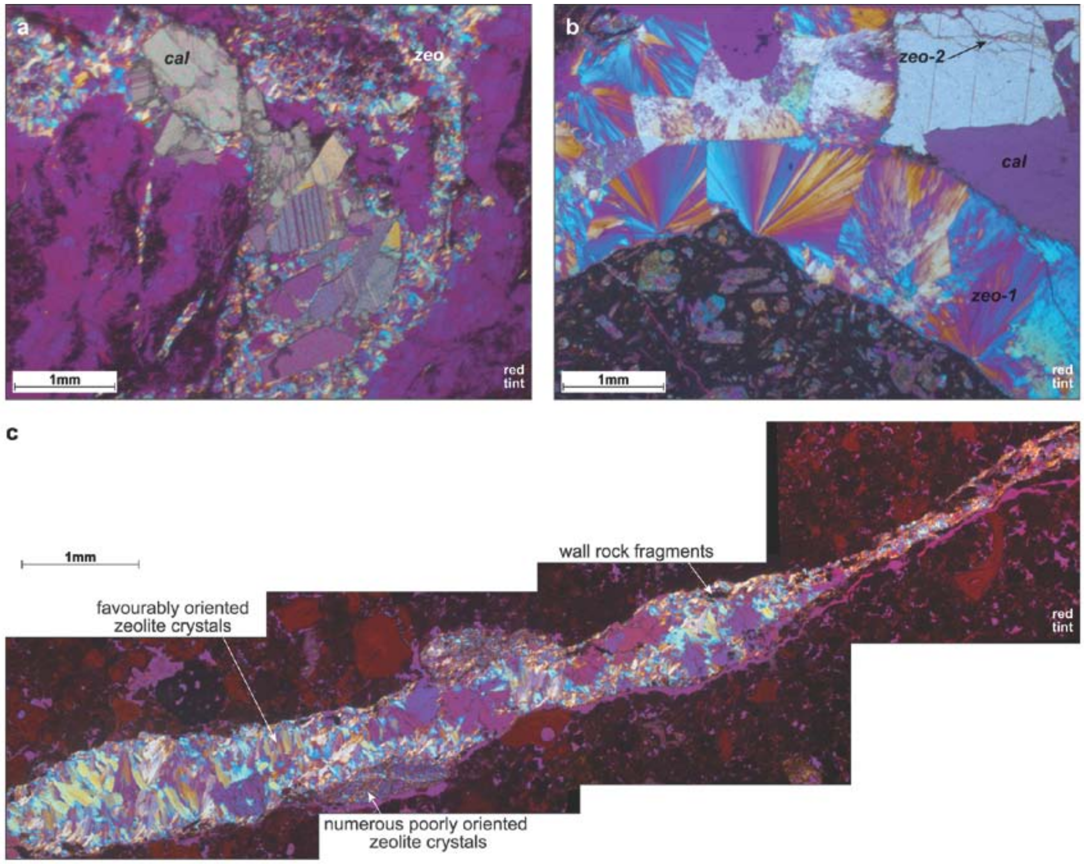

Fig. 5.11. Event 2 mineralisation phases. (**a**) Early calcite is dragged into a later fault, followed by zeolite precipitation. (**b**) Early zeolite is followed by calcite mineralisation. The fractures are developed in the calcite, into which further zeolite has precipitated. (**c**) Multi-phase zeolite mineralisation, with early, small zeolite crystals lining the margins of the vein, followed by later, large zeolite crystals in the vein core. The size of the crystals most likely reflects the available space within a fluid filled cavity, indicating an increase in strain rate through time.

the margins inwards (**Fig. 5.12c,d**). In all observed cases, an initial zeolite mineralisation is superseded by calcite (**Fig. 5.12c**), which is followed by a final zeolite phase (**Fig. 5.12d**).

Cemented breccias are only associated with larger displacement faults (e.g. **Figs. 5.10, 5.13, 5.14**), and appear to occur along zones of dilation resulting from irregularities on the fault surface, and/or oblique motion during faulting. The intensity of brecciation varies from fault to fault, with examples of mosaic breccias (e.g. **Fig. 5.13**) to chaotic breccias being preserved (e.g. **Fig. 5.13**; Woodcock and Mort, 2008). The style does not

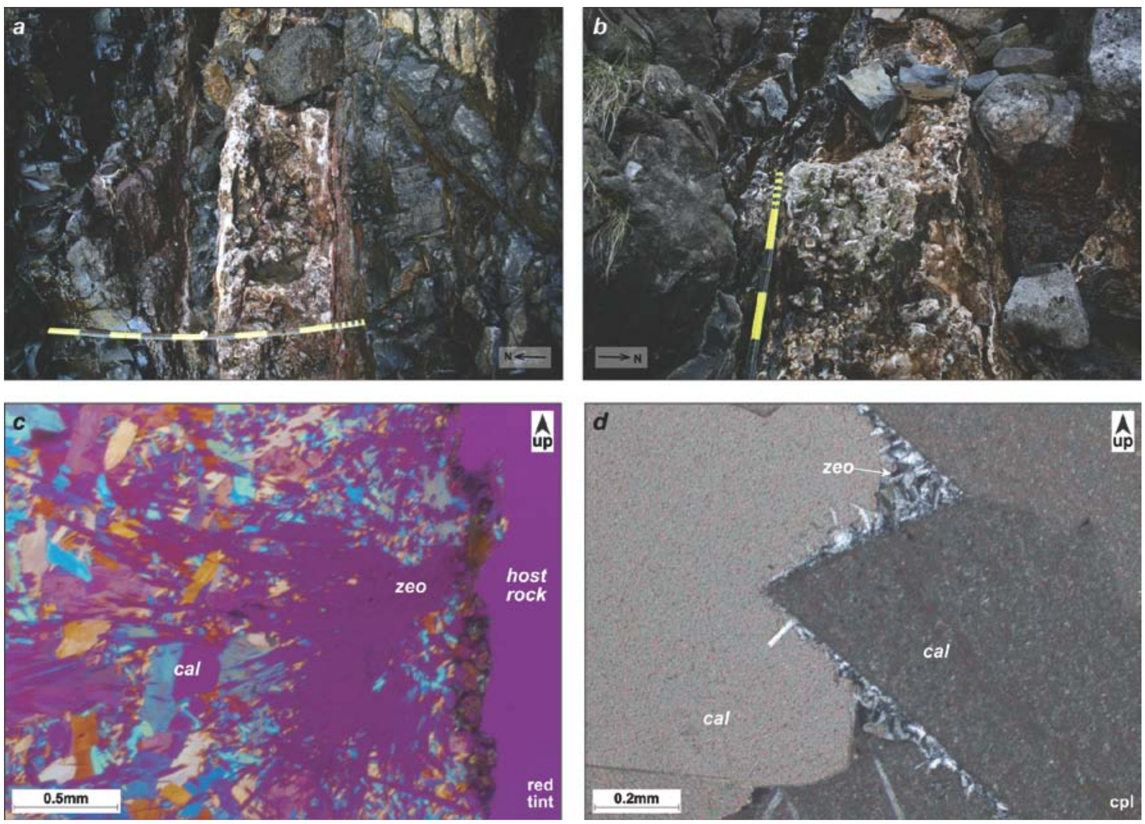

Fig. 5.12. Vein fills from Tjornuvik (a, c, d: fault location indicated in Figure 7) and Langasandur (b: eastern Streymoy). (**a-b**) Thick (0.5-0.75m) tensile vein fills comprising >90% mineralisation. In both cases, the majority of the infill is zeolite, with small (<1cm) crystals lining the vein walls, and enclosing a larger (up to 1.5cm) crystal core. (**c**) Acicular zeolite minerals nucleating on the vein wall in a hemi-radial configuration, requiring an open space in the vein during growth. (**d**) Blocky calcite mineralisation with later, vuggy zeolite growth, again, indicating an open space and free transmission of fluids through the vein.

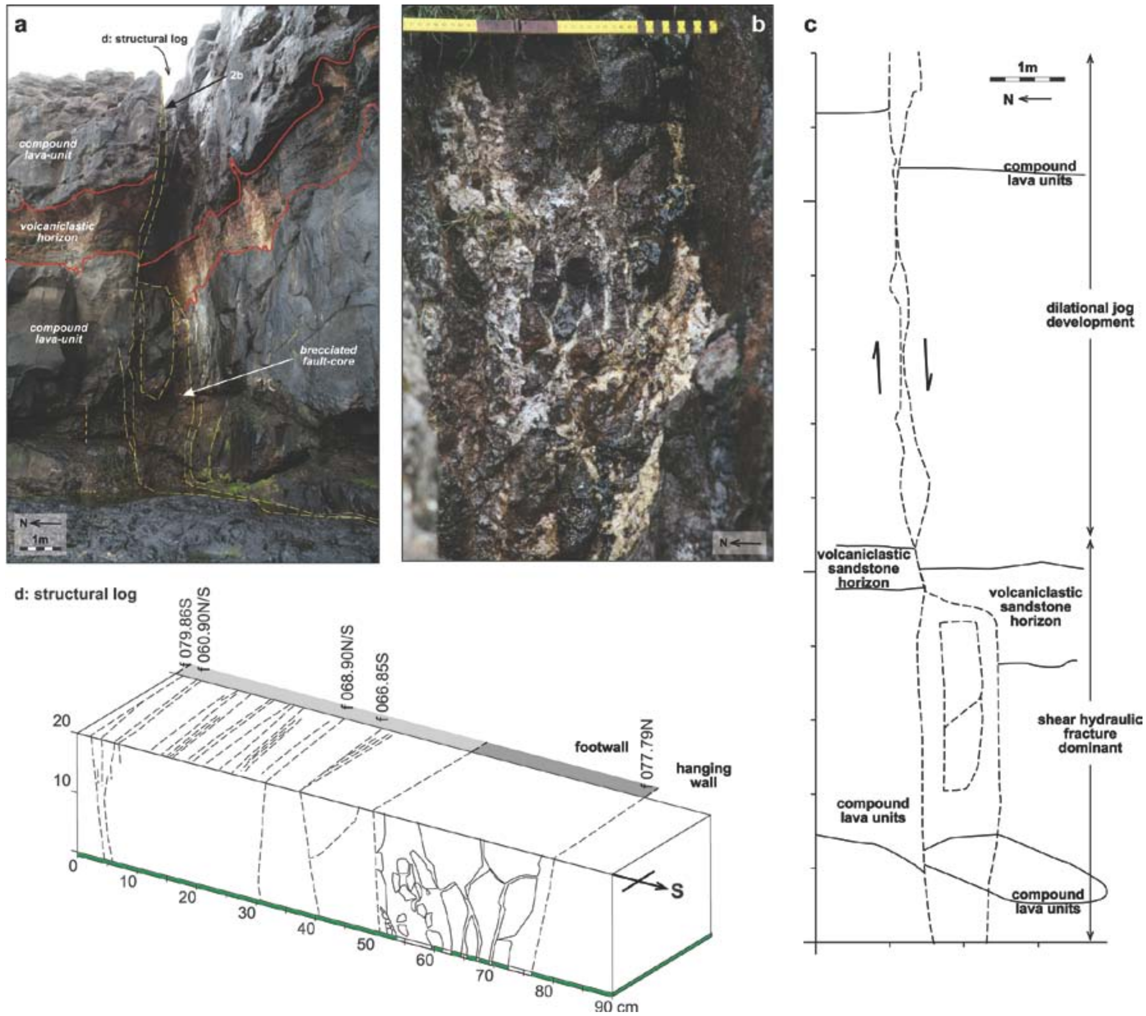

Fig. 5.13. Dextral, Event 2b fault at Eastern Eiði, NW Eysturoy (location in **Figures 7 and 8**). (**a**) The fault displays a well developed fault core bound by master faults, and minor peripheral damage. (**b**) The fault core changes in nature across the volcaniclastic horizon, from shear hydraulic fractures/veins below, to intensely mineralised breccias above. These styles can be split into two zones (**c**) with these breccias limited to a zone of dilational jogs between the master faults. (**d**) Structural log of the fault shows that damage is focused in the fault footwall, as opposed to the hanging wall, as in Event 1 faults (e.g. **Fig. 5**).

appear to be related to displacement magnitudes, with the faults in **Figures 5.13** and **5.14** both displaying ~4.5m displacement, yet very different infills. In both cases, a proportion of the clasts are cement supported (**Figs. 5.13b, 5.14b, c, d**), indicating that cementation was synkinematic. However, vuggy overgrowths on those clasts (e.g. **Fig.**

5.14c) require a persistent open space, and it is therefore unlikely that cementation was fully sealing in the case of chaotic breccias. It is also likely therefore, that fluid flow through these cavities was relatively long-lived, continuing into post-kinematic times.

Generally, the rapidly filled cavity breccias (e.g. **Fig. 5.14**) are equivalent to the implosion breccias of Sibson (1986), and most likely form as a result of implosion caused by a sudden difference in fluid pressures between a dilational fault jog and its surrounding country rock following fault slip. Fluid transmission would generally be limited to the period of fault movement, and the fault cavity itself would therefore be a transient feature. However, the following exceptions to this are noted based on the following observations: (1) the occurrence of cm-thick tensile zeolite veins within the chaotic breccias as well as brecciated calcite mineralisation (e.g. **Fig. 5.14b, c, e**). This is consistent with faults which were subjected to repeated opening and filling, and as a result, fluids would be able to flow through the fault zone at numerous times; and (2) vuggy overgrowths on chaotic breccias suggests that the cavities were not fully cemented following implosion – it is therefore possible that the infilling of these faults was not entirely associated with fault movements, but could instead be the result of a gradual filling through time.

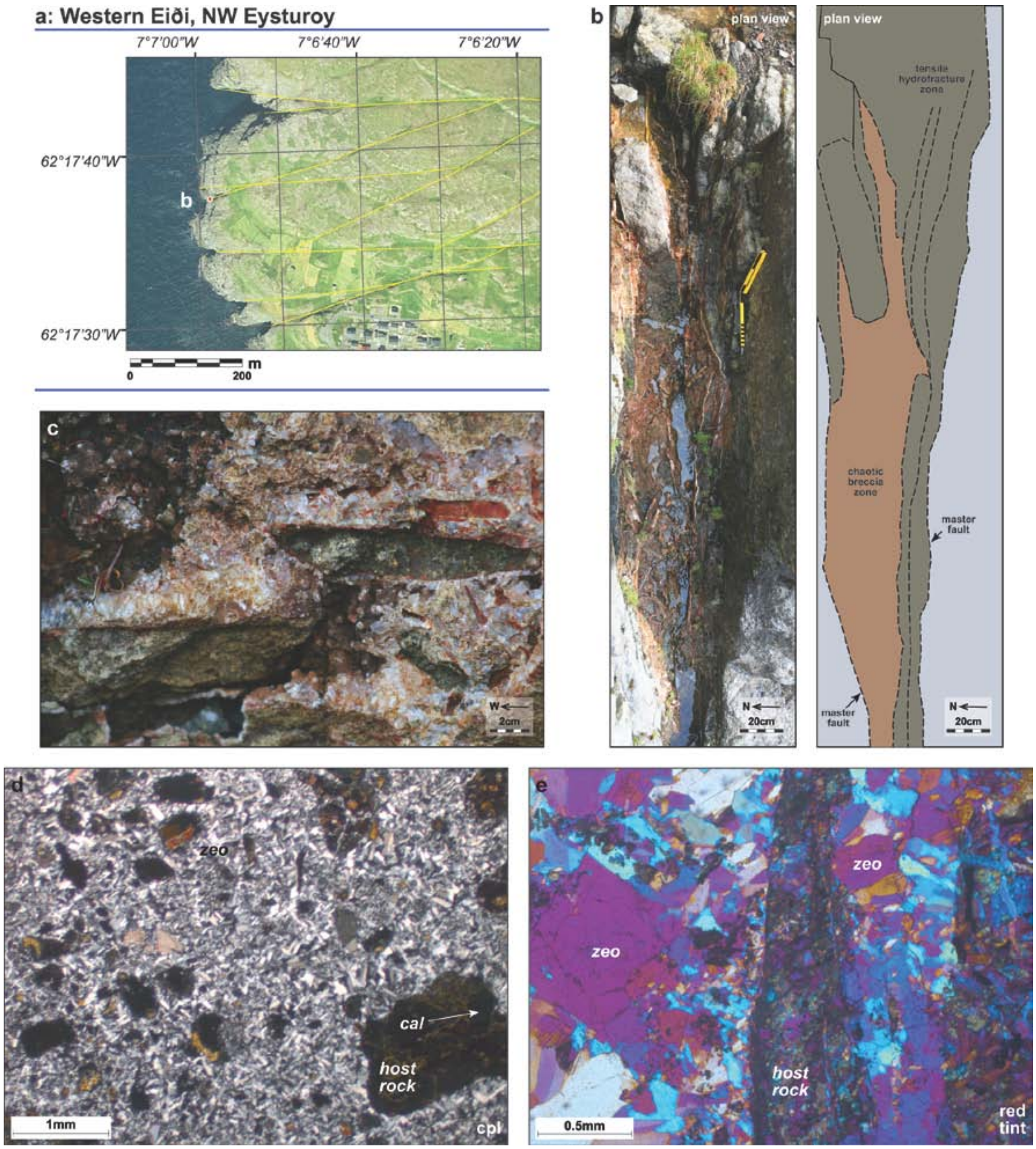

Fig. 5.14. (**a**) Overview of Event 2 faults in western Eiði, indicating the location of the fault of interest. (**b**) The fault varies in width from about 5-75cm. The thicker parts correspond to the development of chaotic breccias, with thinner sections, and the periphery of the thicker section, displaying tensile veining as standard. (**c-d**) The chaotic breccia zone is composed of large volumes of zeolite mineralisation (up to ~75% volume), with polymictic clasts that appear to have been sourced from the surrounding basaltic wall rocks, and a nearby volcaniclastic horizon. Twinned calcite mineralisation is brecciated and supported within the zeolites, suggesting repeat opening events. (**e**) Tensile veins in the core zone are typically composed of zeolite, with occasional, minor calcite.

5.3.5 Event 3

Fault styles and fault rock assemblages of Event 3 are described in *Chapter 4*: only a synopsis is given here.

Event 3 structures are best exposed where faulted clastic materials are developed along pre-existing weaknesses (i.e. reactivated Event 1 and 2 faults), and can be split into 2 groups based on their textural characteristics: (1) shear and (2) tensile reactivation. Event 3 shear faults effectively entrain the contiguous host rocks into the fault plane as a shear-smear (e.g. **Fig. 5.15a-b**; see Weber et al., 1978), whereas the tensile faults become filled with new sedimentary materials from the surface, or from the stratigraphic succession above (i.e. gravitational filling: e.g. **Fig. 5.15c-d**) or below (i.e. fluidization filling: e.g. **Fig. 5.15e-f**). Event 3 is associated with little to no additional mineralisation. In some cases, a very minor amount of silicate (most likely zeolite) veining (<<1% volume) is observed, but this appears to have been emplaced very passively (intergranular fracturing around intact grains as opposed to intragranular or transgranular fracturing). Typically, the infills are loosely held together by the lithostatic pressure (overburden) and/or by the presence of a weak clay cement (which is easily displaced by hydrous fluids). As a result of this relative absence of cement, the volcaniclastic materials entrained along the fault are likely to be effectively unsealed, and therefore represent a potentially high permeability pathway, even to the present day.

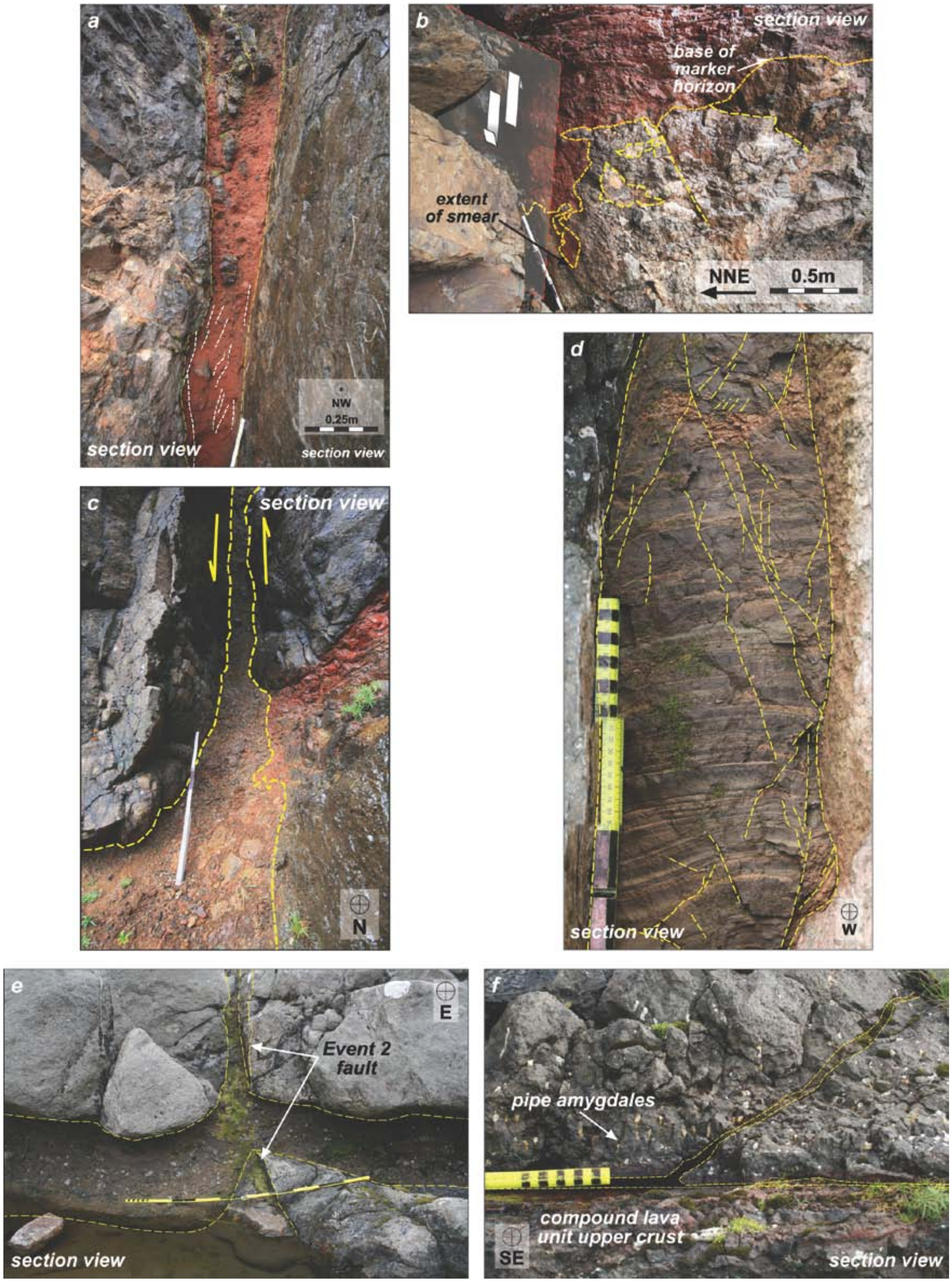

Fig. 5.15. Event 3 fault rock styles can broadly be split into: (**a-b**) Shear smears, (**c-d**) tensile infills, and (**e-f**) injection fills. See text for explanation.

5.3.6 Summary: Structural style and development

Based on observations made in the field during the present study, faults in the Faroe Islands appear to develop through a series of stages of fault linkage and damage zone formation (**Fig. 5.16**), broadly similar to those developed in layered clastic sequences (Childs et al., 1996; Walsh et al., 2002, 2003; Childs et al., 2003). **Figure 14** details an example of fault growth for an Event 2 fault system – Event 1 faults develop similarly, but with σ1 and σ2 switched, resulting in a typical normal fault configuration; Event 3 faults may develop similarly to **Figure 5.16c-d**, along the existing Event 1 or 2 faults. During the initial stages of deformation, in cases where jointing is poorly developed, a mesh of extension fractures and micro faults will form and link (**Fig. 5.16a-b**; e.g. Sibson, 1996). Once established, this mesh focuses deformation, forming a through-going fault zone and bypassing other early-developed fractures and faults immediately adjacent to it. In cases where columnar jointing is well developed, faults are focused along the existing anisotropy, forming through-going faults that are typically initially tensile-dominant due to their steep pre-existing dips in a stress field where sigma 3 is horizontal. Further movement across the fault zone may then result in the formation of a preferential master fault (**Fig. 5.16c-*i***), or continue within the fault zone, resulting in the local development of dilational jogs (**Fig. 5.16c-*ii***). Recurrent reactivation of the master fault will result in preferential damage within the hangingwall, leading to the formation of an asymmetric damage zone and fault core (**Fig. 5.16d**).

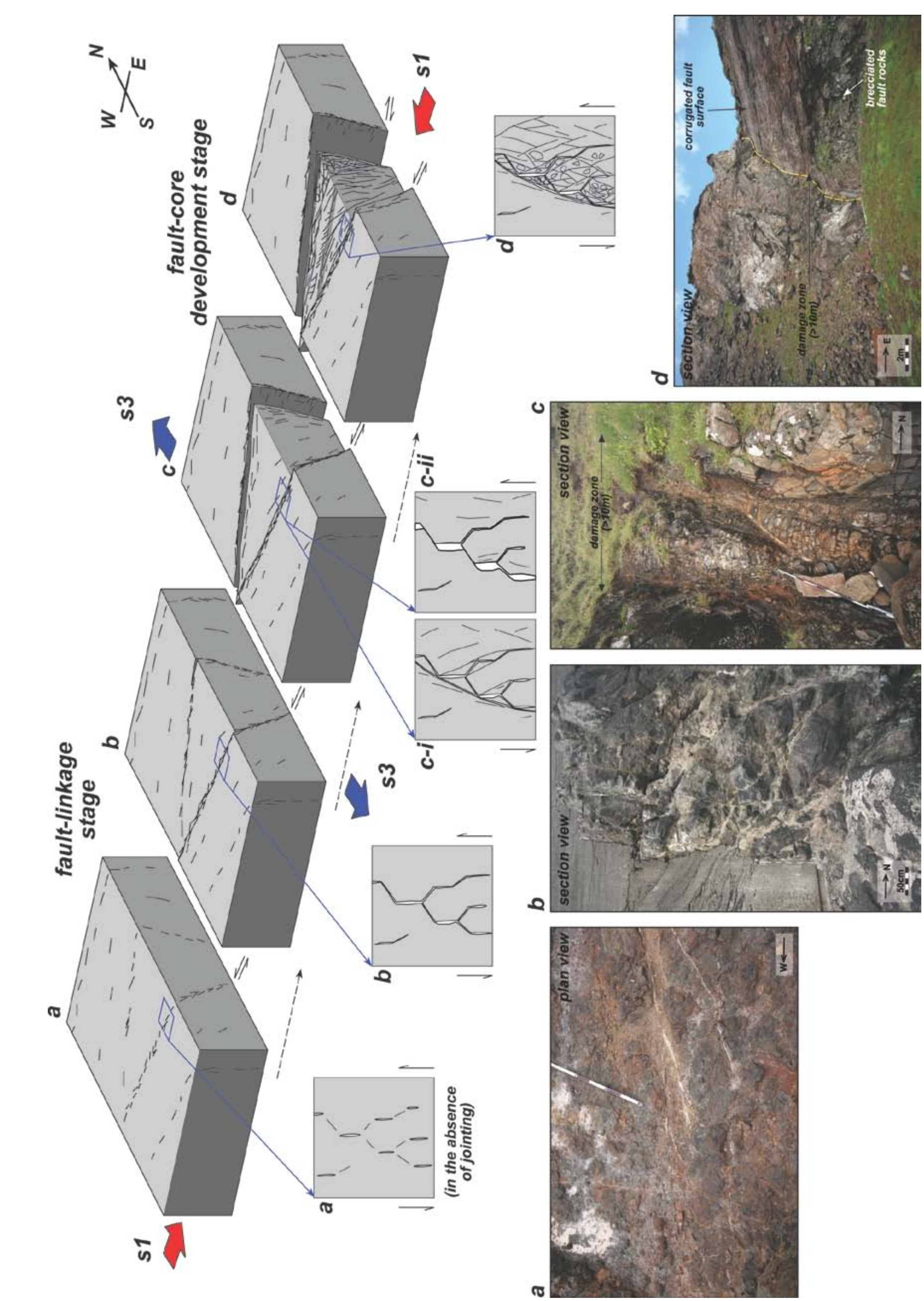

fault-linkage stage
fault-core development stage
W
N
E
S
s1
s3
a
b
c
d
c-i
c-ii
(in the absence of jointing)
plan view
section view
damage zone (>10m)
corrugated fault surface
brecciated fault rocks
50cm
2m

Fig. 5.16. (*Previous page*) Generic fault evolution model based on a conjugate E-W trending Event 2 fault-pair: (**a**) Initial fault development occurs as a mesh of faults and extension fractures which through time (**b**) link to form a set. (**c**) Repeat movements on this fault set result in either the development of (*c-i*) a through-going shear-tensile (mixed-mode) fault or (*c-ii*) zones of tensile (mode-I) on fault planes perpendicular to the extension direction, and shear-tensile (mixed-mode) on fault planes oblique to the extension direction. (**d**) Recurrent reactivation of the fault will result in damage development preferentially focused into the hangingwall, with decreasing intensity away from the master fault.

Mineralisation associated with Events 1 and 2 most commonly occurs as synkinematic growth of zeolites, followed by calcite, and finally synkinematic to postkinematic zeolite overgrowths. Early zeolite growth most likely relates to the inital stages of fault development (**Fig. 5.16a-b**), with calcite following shortly after (**Fig. 5.16b-c**). Later zeolites generally form in more mature fault zones (**Fig. 5.16c-d**), and are particularly well developed where fault plane asperities produce dilational jogs during movement. Event 3 faults are relatively barren of mineralisation, and as such, the fault rocks are likely notably permeable even to the present day. The repeat occurrence of zeolite-calcite-zeolite mineralisation in both Events 1 and 2, probably implies a change in fluid chemistry during fault development. Our suggestion is that initial zeolite mineralisation could be due to the influx of surrounding alkaline pore fluids, which precipitate in the newly formed fracture. Once this zeolite precipitation has removed the various oversaturated metals in the fluid, the relatively increased saturation of Calcium may then allow the precipitation of calcite. Final zeolite mineralisation may then simply indicate recharge and a return to the normative ‘dirty’ waters percolating through the FIBG. Clearly this tentative hypothesis remains to be tested by future studies.

5.4 Discussion

5.4.1 Damage vs. displacement

Faults in the Faroe Islands do not generally appear to obey a ‘damage vs. displacement’ relationship (i.e. where damage increases proportionally to increasing displacement), since the largest offsets directly observed across a fault zone (~30m, such as those at I Botni: **Fig. 5.5**), display damage zone widths similar to minor (centimetre-scale) displacements, such as those at Vagseiði (**Fig. 5.3**). This is true of individual events, as well as for cross-comparisons between Events 1 and 2. Event 3 is not considered here as the related damage and displacements are not necessarily quantifiable.

A possible reason for damage zone width limitation may be related, at least in part, to the pre-fault structure of the basalts. Commonly, the lava flow units display a well developed jointing. In particular, thicker units, such as those of the Beinisvørð Formation (**Fig. 5.1b, c**) exhibit zones of vertical columnar (polygonal) jointing. Such joints likely have very little (perhaps no) tensile strength, and often display vuggy or euhedral crystal growths indicating that they have been dilated, allowing infilling by, and flow of mineral-bearing fluids. During faulting it is possible that the joints acted as decoupling surfaces, resulting in sustained movement within a certain distance of any one fault, and no further (i.e. the joints help to partition and localise strain). This is supported by the observation that sedimentary interbeds often host faults and fractures that are more widely distributed and display a more typical Andersonian geometry compared to adjacent basalt lava flows (**Fig. 5.17**).

The effect of jointing within the basalt flow units could be considered a limitation in terms of palaeostress calculations, and as such we suggest where possible, that such analyses should in the first instance, be verified using faults in the sedimentary interbeds within the succession (as has been standard practice during the present study).

5.4.2 Depth and temperature during deformation: mineralogical constraints

5.4.2.1 Zeolites

Deformation-related mineralisation within the FIBG is principally spread between calcite and numerous members of the zeolite family. Zeolites are a common result of the reaction between volcanic rocks and alkaline waters, and are therefore very

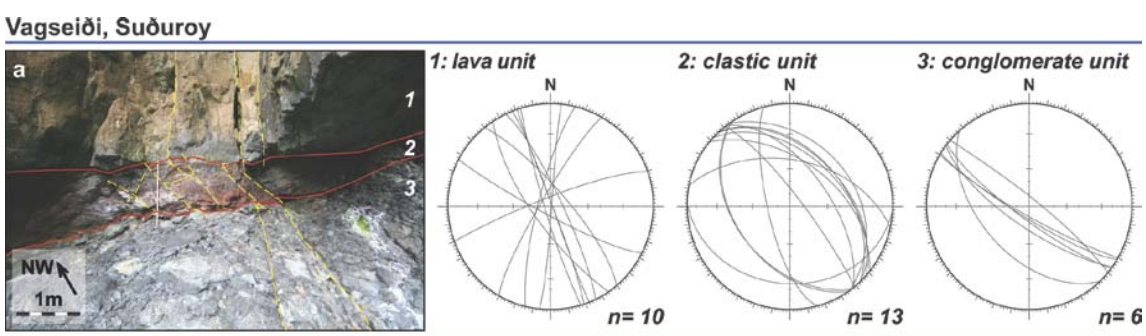

Fig. 5.17. Event 1 fracture reorientation through a lava-sediment-conglomerate sequence at Vagseiði, Suðuroy. Exploitation of vertical to sub-vertical joints in the lava results in oversteepened fractures, whereas sedimentary units, lacking joints, display more typical normal fault inclinations (i.e. between 58°-68°: Anderson, 1942).

widespread in the FIBG. In principle, index zeolite minerals can be used to constrain the regional geothermal gradient, and this zonation property has previously been used to constrain thicknesses and relative timing of regional deformation of volcanic piles (Walker, 1960; Jorgensen, 1984; Neuhoff et al., 1997). However, since the Faroese faults demonstrably act as fluid flow pathways, it is possible to rapidly distribute relatively hot fluids throughout the FIBG, and fault-bound zeolites could therefore be affected by fluid temperatures in addition to the geothermal gradient. Future, geochemically-oriented studies could test this assumption by sampling mineralised fault rocks and the adjacent country rock zeolites. This could provide information on the temperature differential between faults and their surroundings, and if sampled as sets moving away from the fault, could potentially be used to look at heating effects and heat dissipation in the country rock.

5.4.2.2 Calcite

Various, definable styles of calcite twinning (such as tabular thin or thick twins) will form at different temperatures, hence they can be used as a rough guide to micro-scale differential stress, as well as temperatures during deformation (Jamison and Spang, 1976; Laurent et al., 1990). Twinning will occur if the critical resolved shear stress (between 5-15MPa; Jamison and Spang, 1976; Lacombe and Laurent, 1996; Laurent et al., 2000) on potential twin planes is exceeded (Passchier and Trouw, 2005). It should be noted that the reliability of this technique is dependent on a homogenous stress distribution within the sample, which is perhaps unlikely, so, calcite twinning will only be used as a qualitative guide here.

Calcite is common in Event 1 and 2 fault zones in the Faroe Islands (**Fig. 5.18**). The calcite twinning style varies from fault-to-fault, and between the Events, with common thick tabular twins developed in Event 1 faults (**Fig. 5.18a-c**), and a mix of tabular thick and thin twins developed in Event 2 faults (**Fig. 5.18d-e**). Narrow twinning (<1µm thick; Burkhard, 1993) is generally considered to indicate temperatures below 200°C. Thicker twinning (<1µm) may be an indication of an elevated temperature during deformation (i.e. ~200°C; Groshong et al., 1984; Rowe and Rutter, 1990; Ferrill et al., 2004), since at higher temperatures, existing twins will widen rather than create new ones. The paucity of thick twins in small offset fault samples (e.g. **Fig. 5.18f**) compared with higher magnitude offset faults (e.g. **Fig. 5.18b**) may therefore be an indication of the strain rate, or simply be a reflection of the total strain. Thus, low strain-rates at temperatures in excess of 200°C may result in low numbers of thick twins, with increased strain-rates resulting in increased twin numbers. Alternatively, large offset faults may be (and likely are) the result of prolonged and incremental deformation within a fault zone, which could result in creation of new twins, despite higher temperatures.

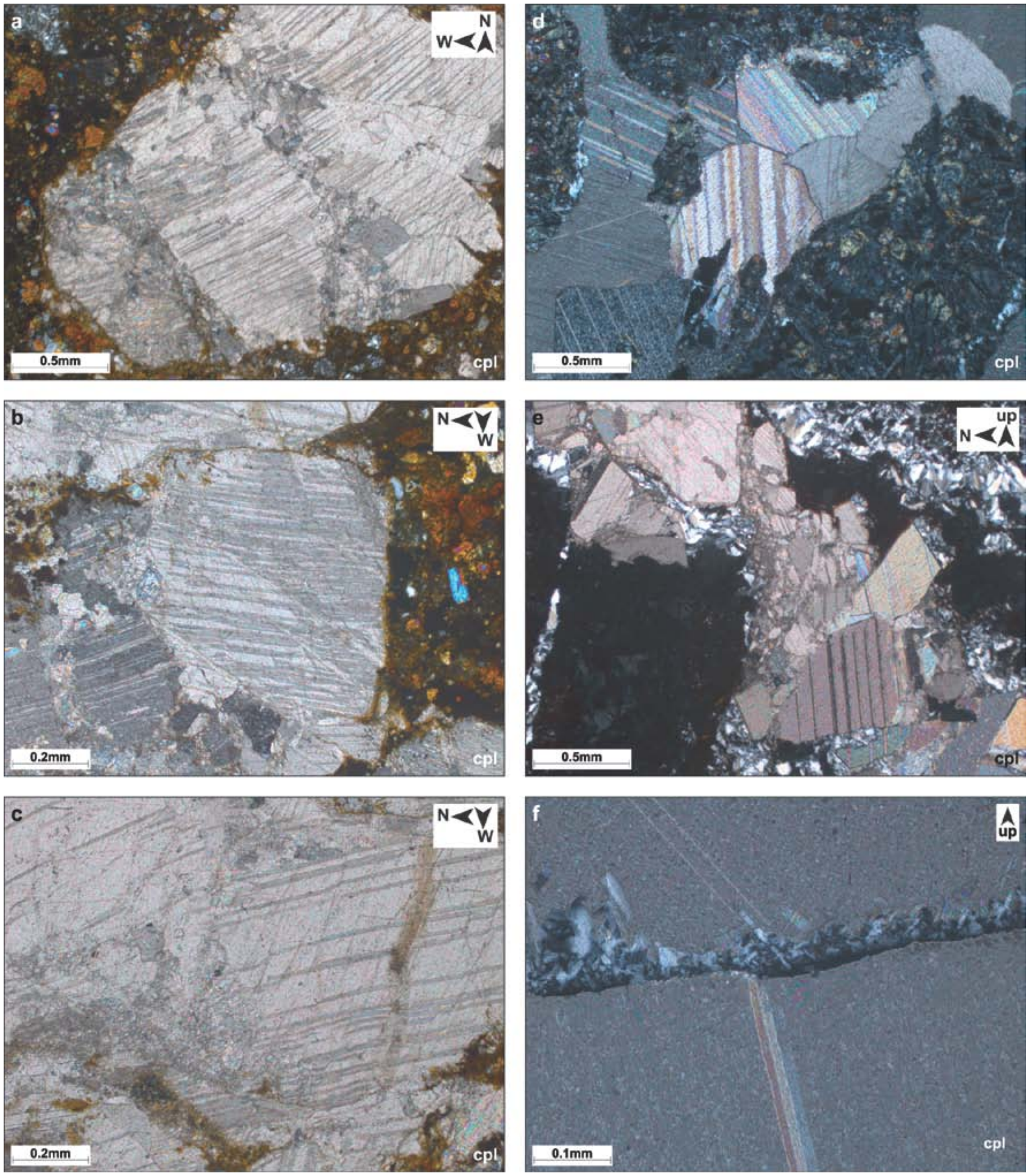

Fig. 5.18. Calcite twinning in Event 1 (a-c) and 2 (d-f) fault rocks. (**a-c**) Calcite in Event 1 faults typically displays intense tabular thick twins, and in most cases is also well fractured and brecciated, relating to its early precipitation, and later reworking during fault evolution. (**d-f**) Calcite twinning in Event 2 faults is split between tabular thin and tabular thick sets. Again, crystals are fractured by later fault movements.

5.4.2.3 Feldspars and quartz

Plagioclase feldspars occur in abundance in the basaltic units throughout the FIBG, as both a constituent of the groundmass, and as phenocrysts (e.g. **Fig. 5.19a-c**). Quartz is very rare due to the low total silica of the basalts, but occasionally phenocrysts are observed (e.g. **Fig. 5.19d**). In very low-grade metamorphic conditions (<300°C), quartz and feldspar will deform by brittle fracturing, with quartz, lacking a cleavage, demonstrably the stronger of the two (Chester and Logan, 1987; Evans, 1988). At low

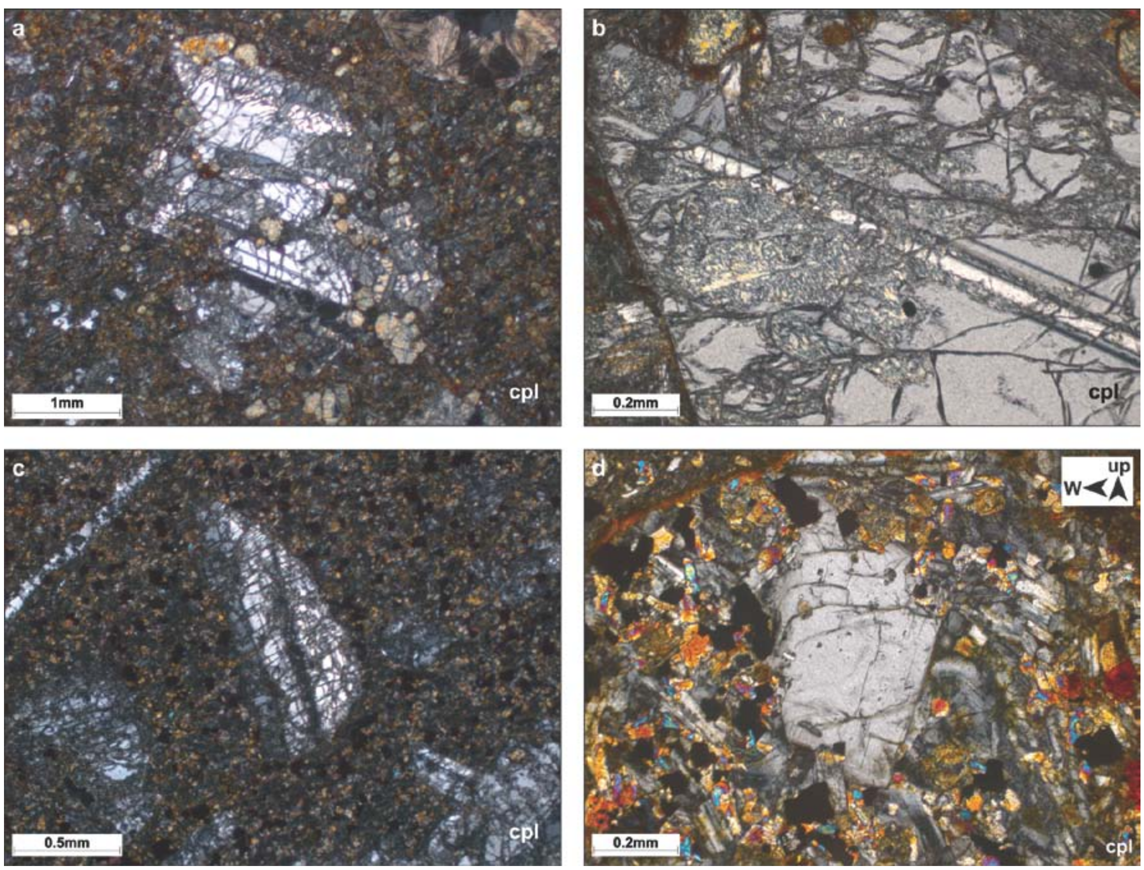

Fig. 5.19. Feldspar (**a-c**) and quartz (**d**) phenocrysts display markedly different magnitudes of fracturing, here most likely indicating very-low grade metamorphic conditions (<300°C) during deformation.

to medium grades however, this is reversed, with quartz deforming first by dislocation creep, and feldspar becoming stronger (e.g. Tullis and Yund, 1977; Simpson, 1985).

Feldspar phenocrysts (e.g. **Fig. 5.19a-c**) in the FIBG are markedly more deformed than their quartz counterparts (e.g. **Fig. 5.19d**), indicating that quartz acts as the stronger of the two minerals. This could be a reflection of the temperatures during deformation, and by proxy, may indicate reasonably shallow depths. This is supported by the calcite twinning observations referred to above, and when combined, indicates that temperatures likely did not exceed 300°C, and were most likely to have been around 150-200°C. With a geothermal gradient of less than 50°C (Glassley, 2006), the ultimate maximum depth at which these fault rocks formed was ~6km, and most likely substantially shallower (2-4km) if only a few hundred metres of the FIBG has been removed (Waagstein, 2002), and the total thickness of the remnant FIBG exposed on the islands is less than 3.5km (i.e. the maximum burial depth at any point on the Faroe Islands is unlikely to exceed 4km). Again, it should be noted that faults cutting through the FIBG formed conduits to hydrous fluids, and if these were hydrothermal in origin, temperatures experienced within faults may have been elevated compared to those of the surroundings. In such a case, depths indicated by calcite deformation may therefore only be considered a maximum - it is suggested that fluid inclusion studies could be used to test these results.

This may cause problems, however, when considering the tensile nature of the evolving faults, and the formation of open cavities. For example, assuming a lithostatic pressure gradient of 25-29MPa/km for the basalt pile, under dry conditions, a fault will form at 2km depth (~50MPa) when the rock strength is overcome. After a stress drop during fault formation, a pre-faulting stress condition is restored, at which point a compressive $\sigma 3$ (typically 0.6 of $\sigma 1$ in extensional systems) will return to ~30MPa, directed against the fault-cavity walls. The occurrence of numerous mineralisation products within the faults is a likely indication that faulting did not occur under dry conditions. It is therefore likely that the rock strength was overcome primarily due to increased pore-fluid pressures, which could then pressurize a resulting fault cavity. It is then dependant on the pressures in the cavity, and the mechanical strength of the basalt wall rocks whether cavity will remain open as a fluid-filled feature. In the case of Event 3, faulting is most likely to have occurred in the absence of pressurised fluids, and with these constraints in mind, it must therefore have formed in the upper 2km or so in order to maintain a persistent subterranean cavity without wall rock failure. This is however very poorly constrained at the present time, and future studies using fluid inclusion techniques could be used to further elucidate the P-T conditions during formation. Furthermore, there is a notable difference in the relative mechanical strengths between basalts and the presumably weaker interleaved volcaniclastic horizons, which may or may not be important in the development, persistence and extent of these cavities. Indeed this difference may help to explain the entrainment/smearing of clastic interbeds observed in many fault zones.

5.4.3 Why don't magmatic intrusives exploit existing faults?

Understanding the controls on dyke propagation direction is important in inferring both ancient and modern stress fields from dyke trends. Clearly, there is a significant difference in conditions between dykes that propagate their own fractures, and those that exploit existing faults and fractures. In the former case, a set of dykes should form normal to the minimum compressive stress (*σ3*) of the host rock (Anderson, 1936; **Fig. 5.20a**). In the latter case, dykes may reactivate existing, optimally oriented fractures (forming magma-filled, extensional hybrids), provided the magmatic pressure exceeds the ambient compressive stress perpendicular to the fracture (i.e. the normal stress; **Fig. 5.20b**), however, this condition will not last if the fracture is mis-oriented to the principal stress directions since the ambient resolved shear stress on that fracture is reduced to zero by the intrusion itself (Rubin, 1995). This condition would be most

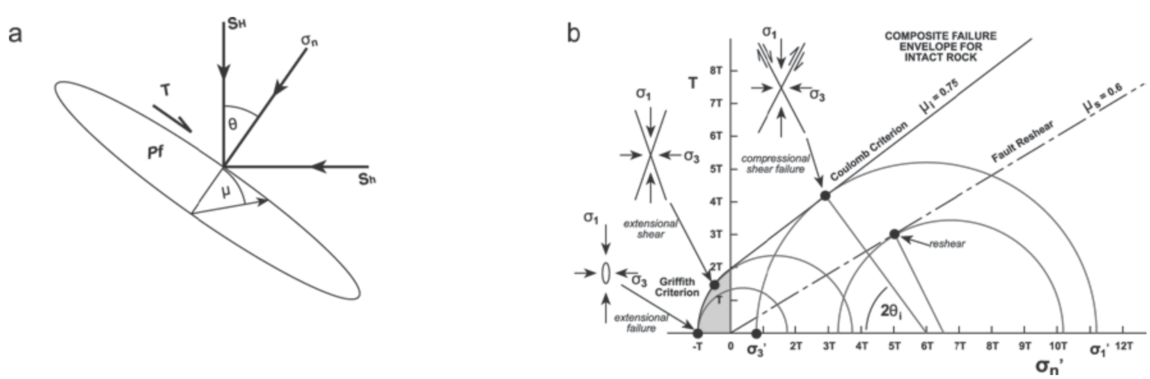

Fig. 5.20. (**a**) Stresses controlling the mode of opening of a magma-filled crack. Fluid pressure (Pf) must exceed the normal stress (σ_n) acting on the walls of the crack. The normal stress can be expressed in terms of fracture orientation (θ), and the maximum (SH) and minimum (Sh) principal stresses (Delaney et al., 1986). (**b**) Mohr diagram with failure envelope for intact rock (solid, bold line) and reshear condition for a cohesionless fault (or joint), and critical stress circles for 3 modes of brittle failure, and for reshear on an optimally oriented cohesionless fault (Sibson, 2004).

likely to occur in a system with high differential stress. Since no examples of dykes exploiting pre-existing faults are observed, it can be inferred that the magmatic pressure only exceeded the minimum compressive stress, and perhaps, that differential stress was low (which is further supported by the tensile, to hybrid opening observed across dykes; **Fig. 5.20b**). However, preferentially oriented faults (i.e. those that are normal to $\sigma 3$) would be expected to reactivate during hydraulic tensile fracturing, particularly considering the majority of faults are comprised of predominantly incohesive fault rocks such as gouge and breccia.

The answer may lie in the well developed joint networks inherent to the basalts, and the relative amounts of sealing mineralisation that has occurred along joints and faults during earlier events. Fault zones and joint networks in the Faroes are typically well mineralised, but there are notable characteristic differences between the styles. The faults tend to have developed through time, with phases of mineralisation, shear/hydraulic fracturing and cementation which may lead to some degree of re-strengthening of the fault zone. Joints on the other hand, though mineralised, are activated as tensile features during deformation. Mineralisation is not sealing in these cases, and joints have the potential to remain relatively weak leading to their exploitation during magmatic events, thus bypassing the faults. The role of jointing in fault development on the otherhand is particularly clear in instances where faults exploit dykes, which is a very common feature on the islands.

5.4.4 Fracture/vein set evolution

In section 5.3, fault styles and damage have been demonstrably related to fault evolution, whereby, maturing fractures will develop into linked sets, which will then develop into clusters, forming wider zones of damage (**Fig. 5.16**). So far this has been described in terms of parallel to sub-parallel sets of hydrofractures related to a single, continuous deformation event. However, commonly mutual cross-cutting relationships are observed between sets of sub-vertical, and sub-horizontal veins (**Fig. 5.21**). The reciprocal cross-cutting indicates that they are part of the same continuous event, even though such changes in vein orientation require significant permutations in the local principal stresses. The tensile nature of the veins suggests that the minimum compressive stress ($\sigma 3$, where $\sigma 1 > \sigma 2 > \sigma 3$) is oriented at ~90° to the vein walls for each set (Secor, 1965; Sibson, 1981), which therefore seemingly requires that the principal stress orientations are rotated cyclically. This seems unlikely. As these veins are related to the same tectonic phase, it is more likely that these permutations of the principal

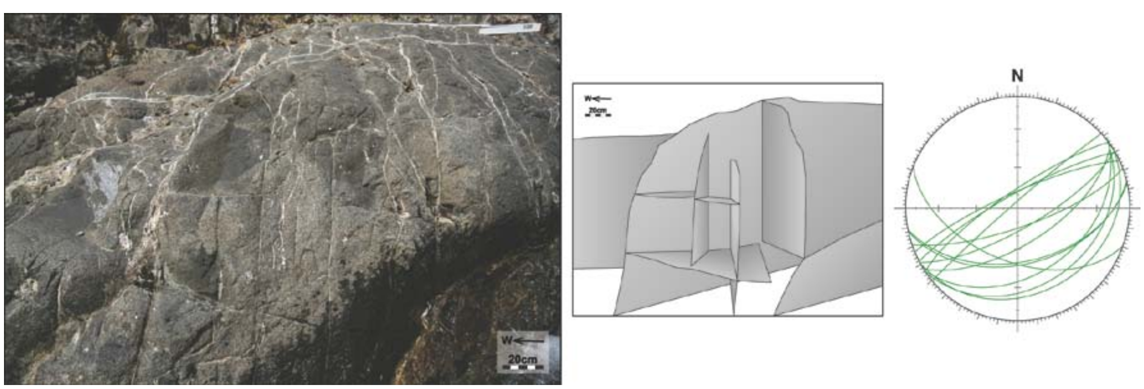

Fig. 5.21. Commonly, fault zones comprise numerous, variously oriented hydrofracture sets, requiring local principal stress permutations, and perhaps indicating phases of pressure release and recharge, brought about by the sealing potential of individual vein sets, and low permeability barriers in the FIBG.

stresses are due to local, possibly pore-elastic effects (e.g. Ramsay and Huber, 1983; Bai et al., 2002) and that there is a low value for the differential stress (e.g. see Colletini et al., 2006).

Under low values for differential stress (i.e. $\sigma 1\text{-}\sigma 3 < 4T$, where T is the tensile strength of the rock) hydraulic fractures will form when the condition $\sigma'3 = -T$ (Sibson, 1981, 2000; where $\sigma'3 = \sigma 3 - P$; P being the pore pressure: Hubbert and Rubey, 1959) is achieved. It is possible that, if mineral precipitation along joints, fractures and faults is sealing, and the influx of (hydrothermal) fluids is continuous, pore fluid pressure will build up, resulting in failure if supra-lithostatic values are reached (Colletini et al., 2006). Failure results in the formation of a fluid-filled crack, and a drop in the normal effective stress to zero. Since the fluid filled crack has a tensile strength of zero, it cannot decrease further with increasing fluid pressure, provided that this increase exceeds the cementation (healing) rate (otherwise the fracture would regain tensile strength and future deformation would occur along it). Recharge of the system, and further reductions in normal effective stresses will result in a switch in the minimum compressive stress orientation forming orthogonal tensile vein arrays (first between $\sigma 2$ and $\sigma 3$, then between $\sigma 1$ and $\sigma 3$ in successive fracturing episodes). This model fits with faults and fault zones across the islands, which require numerous fault and recharge events, and the hypothesis that material failure is driven by elevated pore-fluid pressures. This may also be an indication not only that early faults are sealing in sub-parallel sets (i.e. stages indicated in **Fig. 5.16a-b**), but that there are existing barriers to fluid flow within the volcanic pile in order to allow the initial fluid build-up (such as the presence of relatively impermeable lavas or tuffs acting as pressure seals).

5.5 Conclusions

Deformation processes and phases of mineralisation are similar between Event 1 and 2 faults (i.e. zeolite – calcite – zeolite), but contrast markedly with the hydrofracture-free conditions of Event 3, potentially relating to syn-magmatic (1-2) vs. post-magmatic (3) timings and palaeodepths at which the events occurred. This may also indicate that fluids circulating within the FIBG were hydrothermally dominated, with only a minor meteoric input.

Event 1 and 2 faults through basaltic units of the FIBG appear to develop through stages of fault linkage and damage zone formation, similar to models for the development of faults in layered clastic sequences. During the fault rock evolution, early fault meshes and linked fault sets displaying little damage appear to be sealing. By contrast those that are more evolved, comprising zones of fault-related damage, and that cut the stratigraphy, act as conduits for hydrous fluids.

Event 1 and 2 dykes appear to have formed their own fractures, rather than exploiting existing faults. This implies that the stresses induced by buoyancy only exceeded the minimum compressive stress, rather than the ambient compressive state of the host rock. Dyke propagation was most likely magmatic buoyancy-driven, resulting in a time-dependant failure of the host rock. This is in contrast to the emplacement of the sills, which most likely seeded at an interface in the stratigraphy between a weak, more ductile material (i.e. a sedimentary horizon), and a rigid material (i.e. basalt lavas) above. Following this initial development, sill growth and propagation would likely be controlled by viscous dissipation, leading to the complex ramp and flat architecture, with rapid intrusion resulting in upward ramping of the sill.

The deformation characteristics of calcite, feldspars and quartz indicate deformation depth of the exhumed Event 1 and 2 fault rocks is quite shallow, at about 2-4km. Constraints imposed by the lithostatic pressure gradient and mechanical strength of basalts and their ability to sustain open fractures in the absence of fluid overpressures suggest that Event 3 faults most likely occurred at shallower depths; perhaps in the order of 0-2km.

Infilled cavities at dilational jogs along irregular fault planes were filled during, and commonly for a period after movement on the fault, rather than geologically instantaneously as a result of a simple implosion. Fluid transmission along and across the faults may therefore have been reasonably long-lived in the case of mineralising fluids. If structurally linked to faults cutting the underlying basin fill sediments, this could facilitate significant hydrocarbon migration from deep reservoirs.

6

Discussion, conclusions and future research

6.1 Discussion

6.1.1 Structural evolution: the fault-dyke-fault cycle

As shown in the preceding chapters, the Cenozoic structural evolution of the Faroes region involves an anticlockwise reorientation through time in the regional extension direction, from NE-SW to NW-SE (e.g. **Fig. 6.1a**). However, the mode of extension during rifting changed markedly throughout this rotation (e.g. **Fig. 6.1b, c**), most notably in terms of an apparent switch from hydrous fluid-driven (faulting) events, to magma-driven (dyke) events and back again (e.g. **Fig. 6.1**). Since the timing and kinematics of rift rotation can be temporally linked with the build-up to, and onset of sea-floor spreading, the change in structural style may too be linked to these processes. We must, however, first consider all coincident conditions during the structural evolution of the NE Atlantic region. For instance, structures associated with Events 1 and 2 are syn-magmatic, and late Event 2 and Event 3 structures are post-magmatic. Exhumed faults therefore record deformation at increasing distances from the main rift axis (**Fig. 6.1d**), and at variable depths (**Fig. 6.1e**) with respect to the thickness of the FIBG through the time.

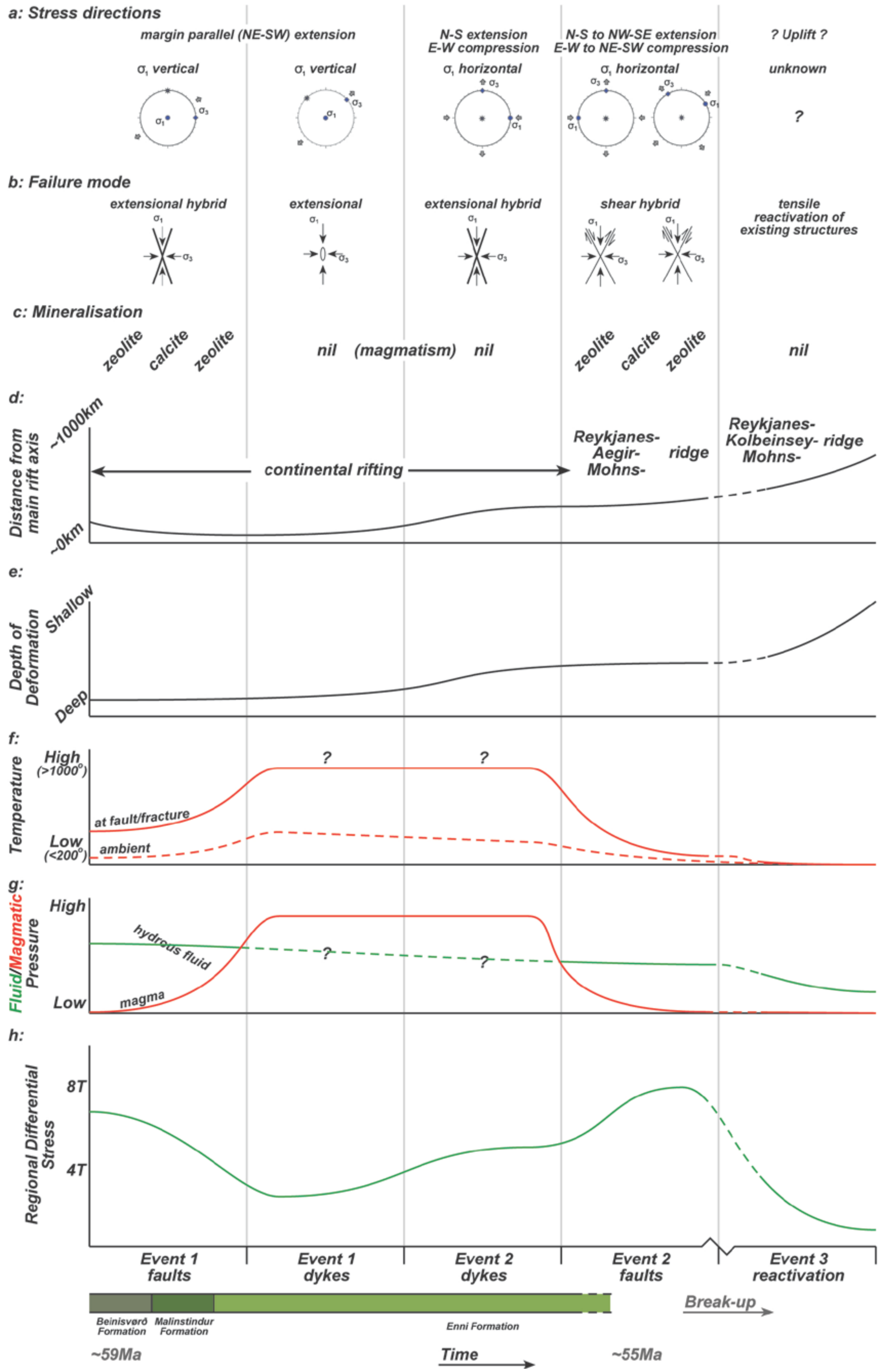

a: Stress directions
margin parallel (NE-SW) extension
N-S extension
E-W compression
N-S to NW-SE extension
E-W to NE-SW compression
? Uplift ?
σ1 vertical
σ1 vertical
σ1 horizontal
σ1 horizontal
unknown
b: Failure mode
extensional hybrid
extensional
extensional hybrid
shear hybrid
tensile reactivation of existing structures
c: Mineralisation
zeolite
calcite
zeolite
nil
(magmatism)
nil
zeolite
calcite
zeolite
nil
d:
Distance from main rift axis
~1000km
~0km
continental rifting
Reykjanes- Aegir- Mohns- ridge
Reykjanes- Kolbeinsey- Mohns- ridge
e:
Depth of Deformation
Shallow
Deep
f:
Temperature
High (>1000°)
Low (<200°)
at fault/fracture
ambient
g:
Fluid/Magmatic Pressure
High
Low
hydrous fluid
magma
h:
Regional Differential Stress
8T
4T
Event 1 faults
Event 1 dykes
Event 2 dykes
Event 2 faults
Event 3 reactivation
Break-up
Beinisvørð Formation
Malinstindur Formation
Enni Formation
~59Ma
Time
~55Ma

Fig. 6.1. (*Previous page*) Summary diagram detailing the mode of failure, stress directions mineralisation phases, as well as hypothesized relative relationships to and between deformation temperature, fluid/magmatic pressure, and regional differential stresses, for structural Events 1, 2 and 3.

A switch from faults to dykes could lead to an increase in deformation temperatures within faults/fractures, with Event 1 fault rocks suggesting temperatures in the order of 170-200°C, and basaltic dykes likely intruded with a local magma temperature in excess 1000°C; **Fig. 6.1f**). Magmatism at this time could relate to a thinned lithosphere or the introduction of hot asthenosphere, or both. In any case, the ambient temperature would also likely be elevated (**Fig. 6.1f**) as a reflection of the steeper geothermal gradient imposed due to thinning.

Dykes in the Faroe Islands do not obviously reactivate existing faults, perhaps indicating that hydrous-fluid pressures had decreased following Event 1a and that fractures were sealed by mineralization. It appears that magmatic-fluid pressure then increased to a point where magma-driven fractures were generated widely during dyking (**Fig. 6.1g**). The switch from faults to dykes is also consistent with a drop in the (regional) differential stress (**Fig. 6.1h**), from just under 8*T* (where *T* is the tensile strength of the rock) during the shear to hybrid hydrofracturing seen during Event 1a faulting, to less than 4*T* during tensile fracturing accompanying dyke intrusion (**Fig. 6.1b**) (Hancock, 1985; Sibson, 1998). The change in dyke geometry, from tensile (Event 1b) to hybrid (Event 2a), and the later switch back to shear fracturing and faulting

(Events 2b,c), is a likely indication that regional differential stress progressively increased during Event 2. The tensile nature of Event 3 faults is again, likely indication of a drop in differential stress, though, as speculated in this thesis, this would also be expected as a reflection of the relatively near-surface faulting conditions during the event.

Rifting in the area was reasonably prolonged, occurring in phases from the Devono-Carboniferous, through to break-up in the Eocene (Moy and Imber, 2009). The location of the rift axis changed through time, apparently shifting NW from the Faroe Shetland Basin (FSB) towards the eventual continent-ocean boundary (COB) (**Fig. 6.1d**), which coincides with an increase in strain rate: relatively slow during the Mesozoic in the FSB, and fast in the Cenozoic to the NW (Geoffroy, 2005). A slow strain rate could result in an outboard rift migration if the upwelled asthenosphere has time to thermally equilibrate (since this material will essentially be an unfaulted peridotite, and therefore be stronger than the surrounding faulted crust; e.g. Allen and Allen, 2005)[1]. Given the observed large time gaps between rift events along the insipient margin (e.g. between Permo-Triassic rifting and Cretaceous rifting; Coward, 1990), it would be highly likely that the lithosphere would heal in this way, and result in a shift in the focus of rifting. The increase in strain rate in the Cenozoic may, therefore, simply be a function of the

[1] Thermal equilibration in this manner can lead to subsidence following rifting, as the new, cooled material will be denser than the asthenosphere below. Hence, though no longer actively rifting, the FSB could continue to thermally subside, with the amount of subsidence varying depending on the degree of rift segmentation, and the presence of intrusives within the crust.

growth of the Iceland plume, resulting in an increase in the areal extent of lithospheric thinning by hotter-than-normal mantle, taking over from a ‘healed’ rift system. Due to the effects of strain softening, a fast strain rate, could result in localized extension (Kusznir and Park, 1987). In theory then, the Faroe Islands could be situated between an old diffuse rift system (the FSB) and a relatively young localized rift system (i.e. the developing rift to the NW, prior to sea-floor spreading), and were never on the active axis of rifting. The resulting strain recorded between the two rifts would be reasonably distributed, and, at any single location, strain would be relatively minor, as it is on the Faroes. This could also mean that from the Palaeocene onwards, the axis of rifting was not focused on the FSB rift axis, but to the NW, thereby explaining the rather subdued Cenozoic fault histories in the southeastern FSB (e.g. Moy and Imber, 2009); subsidence in the FSB could therefore be simply related to thermal subsidence.

With this as a working hypothesis, we can perhaps relate the switch from faults to dykes to faults, to changes in the locus of active deformation relative to the Faroe Islands. In this model, the axis of rifting during the Late Cretaceous to Early Palaeocene would be focused on the margins of the FSB (**Fig. 6.2a**), bypassing its older, strain hardened sub-basins. Deformation at the Faroes for this time would therefore be accommodated by faulting (i.e. resulting in Event 1a faults) Following this, Palaeocene deformation would jump towards the growing Iceland plume in the NW (**Fig. 6.2b**), where the upwelling mantle would result in a quickly developing, localized rift. This period corresponds to the Event 1b and 2a dykes on the Faroes. As the area of active deformation associated with this rift increased, and as the effective distance between the heat source and the Faroes increased (through crustal stretching), deformation in

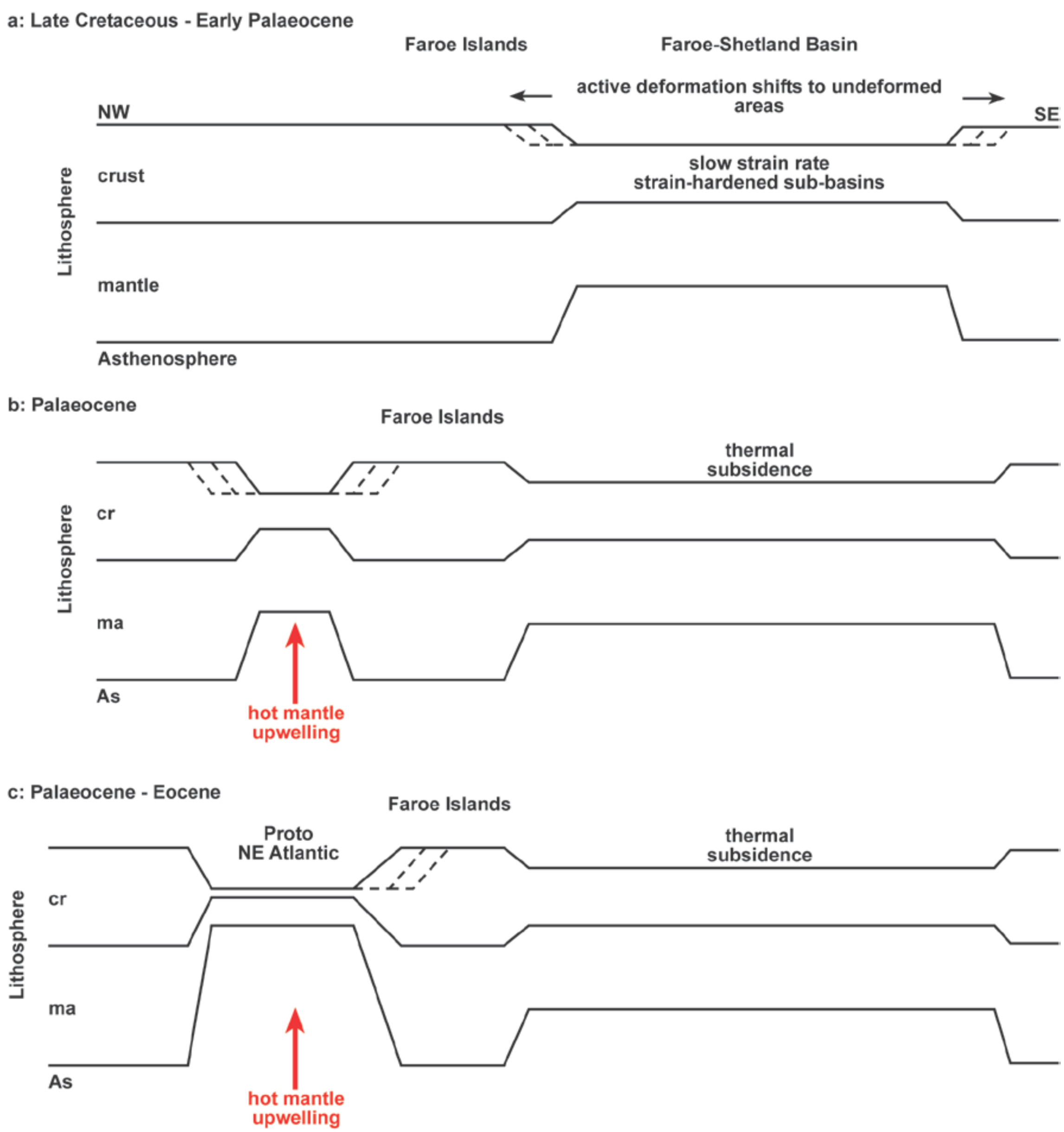

Fig. 6.2. Summary model for the switch in rifting in the NE Atlantic area, from SE of the Faroes towards the NW, from (**a**) the Late Cretaceous to the (**b**) Palaeocene, through to the (**c**) Palaeocene-Eocene. See text for explanation. (Based on Figure 15 of Kusznir and Park, 1987).

the Faroes area switched back to faulting (**Fig. 6.2c**). This would then continue to be the dominant style of deformation through break-up, until a time when all extension was accommodated by sea floor spreading.

6.2 Conclusions

1. Spatially and temporally-related suites of brittle faults, hydrothermal veins and intrusive igneous sheets (dyke swarms and sills) that formed during and after extrusion of the FIBG are recognised throughout the Faroe Islands. These are split into three groups based on geological characteristics and cross-cutting relationships termed Events 1, 2 and 3. Stress inversion techniques and structural relationships observed in the field indicate a progressive reorientation in the regional stretching directions, from NE-SW, to N-S, to NW-SE, through time, leading to the observed polyphase deformation.

2. Event 1 and 2 faults cutting basaltic units of the FIBG appear to develop through stages of fault linkage and damage zone formation, broadly similar to those seen in layered clastic sequences. During fault rock evolution, early fault meshes and linked fault sets displaying little damage are likely to be sealing; by contrast, those that are more evolved, comprising zones of fault-related damage, and that cut the stratigraphy, appear to act as conduits for hydrous fluids. Sequential phases of mineralisation are similar between Event 1 and 2 faults (i.e. zeolite – calcite – zeolite), and contrast markedly with the generally hydrostatic fluid pressure conditions of Event 3, potentially reflecting the syn-magmatic (1-2) vs. post-magmatic (3) timings of the events, together with their different palaeodepths (2-4 km vs. 0-2km). This may also indicate that fluids circulating within the FIBG during events 1 and 2 were hydrothermally dominated which is perhaps unsurprising given their close association with magmatic intrusions (Event 1 and 2 dykes and the Event 2 sills).

3. Event 1 and 2 dykes appear to have formed their own fractures, rather than exploiting existing faults. This implies that the stresses induced by buoyancy only exceeded the minimum compressive stress, rather than the shearing resistance of the host rock. Dyke propagation was most likely magma buoyancy-driven, resulting in failure of the host rock. This is in contrast to the emplacement of the sills, which most likely seeded at an interface in the stratigraphy between weak, more ductile material (i.e. a sedimentary horizon), and rigid material (i.e. basalt lavas) above. Following this initial development, sill growth and propagation would likely be controlled by viscous dissipation, leading to the complex ramp and flat architecture, with rapid intrusion resulting in upward ramping of the sill.

4. The deformation characteristics of calcite, feldspars and quartz indicate deformation depths for the exhumed Event 1 and 2 fault rocks to be quite shallow, at a maximum of about 2-4km. Constraints imposed by the lithostatic pressure gradient (~25MPa/km) suggest that Event 3 faults most likely occurred at still shallower depths; perhaps in the order of 0-2km. This is consistent with recognition of sediment fills during event 3 and, more generally with the range of likely burial depths possible given the likely thickness of the FIBG.

5. Infilled cavities at dilational jogs along irregular fault planes were filled during and for a period after movement on the fault, rather than geologically instantaneously as a result of implosion. Fluid transmission during Events 1 and 2, along and across the faults may therefore have been reasonably long-lived in the case of mineralising fluids. If structurally linked to faults cutting the underlying basin fill sediments, this could facilitate significant hydrocarbon migration from deep reservoirs during these periods following fault movements.

6. NW-SE oriented Event 1 faults are dip-slip in all observed cases. In the absence of any evidence to the contrary, it is inferred that these structures are indicative of movements on the basin-scale faults located within the fjords (i.e. the Judd, Brynhild and Westray faults). The kinematics of these faults and the similarly oriented dykes indicates a distinct period of early NE-SW extension, which could theoretically relate to an excess gravitational potential energy within the continental interior relative to the mid-ocean ridge in the western North Atlantic at this time. Progressive displacements on these faults throughout the Palaeocene are responsible for thickness variations within the FIBG, and probably similarly aged strata within the FSB offshore.

7. The progressive anticlockwise rotation of the extension vector identified seems to be consistent with the most recently published NE Atlantic continental break-up reconstructions, particularly in terms of an initial N-S extension during early sea floor spreading on the Reykjanes, Aegir, and Mohns ridges, and a rotation to NW-SE extension, following a ridge jump, from the Aegir ridge to the Kolbeinsey ridge. This illustrates the importance of carrying out detailed field studies, in addition to the more usual margin-scale modeling studies, in order to validate plate reconstructions.

8. Post-FIBG deformation typically involves the entrainment of clastic materials along faults during reactivation of deformation structures developed during Events 1 and 2. The general lack of mineralisation within the clastic materials most likely indicates post-burial, near-surface fault movements (<2km depth?). Based on the relative timing, it is proposed that these movements relate to or follow uplift during continental break-up and sea-floor spreading on the NE Atlantic.

9. The kinematics indicated by offset markers and the localised development of clastic drag fabrics are typically the opposite sense to those of the host fault. In most cases, the inland area lies in the fault footwalls; if the footwalls are uplifted, this may partially explain the location of the Faroe Islands above sea level at the present day.

10. Event 3 fractures may be related to fold growth on the margin. If so, they may be widespread offshore, particularly where such large, open folds are developed. The likely unsealed nature of the clastic infills may mean that these faults present fluid-flow pathways, particularly at higher levels, but also potentially deeper, within the Faroe-Shetland Basin. The open cavities that originally form would introduce very significant localised permeability, facilitating both cross-fault and cross-stratal rapid migration of fluids, including hydrocarbons.

6.3 Future research

6.3.1 High-resolution geophysics

This study has predominantly been limited to the areal extent of the Faroe Islands. All but the largest deformation structures observed on the islands would not be apparent in seismic reflection data sets, presenting a clear problem in terms of the scalability from onshore to offshore. Few studies of the deep structure of the Faroe Islands have been attempted, with most geophysical acquisition being terminated on the flanks of the Faroes Platform to the southeast.

Recent, high-resolution magnetic surveys over the Norway Basin have highlighted the existence of margin-normal lineaments that trend NW-SE and pass out into the oceanic crust (Gernigon et al., 2009). These lineaments have only become apparent with the acquisition of the high-resolution magnetic data – features within the more regional data remain ambiguous. A similar high-resolution magnetic study over the Faroes Platform could potentially be used to detail the extent of known fracture zones and dykes, and indicate the location and extent of previously unidentified deformation structures. This would be particularly useful in assessing the continuity of the NW-SE faults through the Faroese fjords. Structural element maps of the FSB (e.g. Ellis et al., 2009) often show a set of continuous NW-SE lineaments that extend from the West of Shetland area, to the Faroe Islands (a distance in excess of 250km in places). However, displacement estimates and kinematic analyses suggest that, at least in the Faroes, these are dip-slip faults with offsets of no more than ~80m. The trend of these lineaments is also disrupted by local promontories in the Faroes, which appear coincident with later faults and dykes, and most likely represent hectometre scale offsets of the NW-SE features. It is therefore highly unlikely that each lineament is a single line along its entire length as is typically shown. High-resolution geophysical surveys over the Faroes Platform would therefore be of benefit, not only in terms of better defining the position of the lineaments, but may also help in understanding their evolution through time with respect to later rift events.

6.3.2 Experimental rock deformation and permeability and fracture distribution studies

To date few studies have addressed the mechanical properties of basalts, and none have focused on the FIBG. The physical properties of basalt change markedly from the bottom to the top of a single flow unit, as well as laterally (due to differing vesicularity from proximal to distal flows formed relative the original source) and from unit to unit. These lithological variations may well be reflected in the mechanical strength of the rocks. Of particular importance could be the differences deformation style between hyaloclastites (e.g. the Lopra Formation), simple flow units (e.g. the Beinisvørð Formation) and compound lava units (e.g. the Malinstindur Formation). Results from recently drilled wells in the Faroes sector of the margin indicate significant fluid losses throughout the basalt flow units, but not in the hyaloclastites beneath. This may suggest that differences between continuous flow units are not as important as the differences between flow units and hyaloclastites. Alternatively, it may be an indication that deformation style changes with depth, from shallow open fractures, to sealed deeper fractures. Certainly this would mirror the changes in fracture styles seen onshore through time.

Simple triaxial friction experiments (at room temperature, effective normal stress of ~25-30MPa, and loading rates of 0.1µm/s and 1µm/s) could be used on cored well and hand samples collected from the islands to provide some insights into the mechanical behavior of FIBG rocks. It would be preferable, however, to perform the deformation experiments at more realistic temperatures and strain rates. Mineralogical constraints from Faroese fault rocks suggest deformation more likely occurred at ~200°C.The results could be used to test the frictional properties and permeability of the fault rocks, which would therefore have direct applicability to drilling prospects in the Faroes sector, and potentially to future drilling campaigns in the Icelandic and Norwegian Jan Mayen licenses.

This study has shown that faults in the FIBG grow and link through time. The different stages of this growth are characterised by an increasing degree of damage during development. The permeability characteristics of those faults are therefore dependant on the stage of their development. Ideally, changes in fault rock permeability could be tested using experimental deformation techniques, as well as using available samples from fault rocks on the islands. The purpose of this would be to test damage zone development and permeability at different stages of fault development experimentally (using triaxial deformation apparatus: see *section 6.3.4*) as well as measuring differing permeabilities across developed fault zones (i.e. from a fault core, into the damage zone, and through into undeformed wall rock).

Future studies could also specifically target fault rocks and fault/fracture/vein spacings and orientations in order to quantify their local connectivity, as well as, more broadly, their regional significance as fluid flow conduits or barriers. Previous studies in layered sedimentary rocks have shown that there is a strong correlation between host lithology and vein spacing (e.g. Simpson, 2000; Gillespie et al., 2001), and therefore, it is unlikely that existing fracture/vein distribution models can be applied to the FIBG.

6.3.3 Radiogenic and stable isotope analyses and fluid inclusion studies in mineralised fault-rocks

During the present study, we have indicated a relative time-scale for the development of deformation structures in the FIBG (determined from cross-cutting relationships and stratigraphic extent), as well as identifying a general fluid flow history for sampled fault rocks. Future studies could use radiogenic and stable isotope analyses to: (1) Provide absolute dates for the development of faults in the FIBG using Ar/Ar dating techniques on fault-bourne alkali feldspars, or potentially U/Pb dating techniques on minor galena mineralisation observed; (2) Oxygen isotope analysis on fluid inclusions in order to assess the likely sources of mineralising fluids.

Fluid inclusions, hosted primarily in quartz and calcite can provide an opportunity to determine fluid compositions, densities, temperatures and pressures at the time of fluid entrapment (Touret, 2001). Fluid inclusion analysis therefore has the potential to provide a vast range of important data pertaining to the development of Faroese fault rocks, such as constraining the depth of fault formation and mineralisation, as well as evolution of vein materials through time within a single fault.

Collectively, these analyses on mineralised fault rocks could substantially improve our knowledge of fluid transmission during fault rock development in the FIBG, and could be applied more broadly to the related offshore stratigraphy. Changes in the style, rate of formation and physical properties of faults at different levels within the FIBG are of critical importance to the hydrocarbon industry in terms of being able to establish fluid flow histories and the sealing potential of basalt fault rocks for both sub- and intra-basalt plays.

6.3.4 Numerical Modeling and passive margin studies

Models for the formation of the NE Atlantic margin rely heavily on basin-scale structural studies, from which the kinematics are inferred through changes in sedimentary thicknesses and fault architectures, rather than being directly observed. The NE-SW trending continental basins along the NE Atlantic margin (e.g. Faroe-Shetland, Møre, and Vøring basins) attest to the overall relative NW-SE extension that must have occurred to produce the present day regional plate configuration. Structures that lie at a high angle to the basin trend (i.e. NW-SE trending structures) are typically given a strike- to oblique-slip motion sense for the sake of compatibility with the model: these are the so-called "transfer zones". However, this study indicates that structures oblique to the NE-SW basin-bounding faults differ in relative timing, and are formed due to an early phase of margin-parallel extension. Thus the earliest structures observed on the islands are NW-SE to N-S trending *dip-slip* faults and dykes, which record a prolonged NE-SW extension during the mid- to late-Palaeocene (59-55Ma) with little or no strike-slip displacement. Similarly oriented structures in the Faroe-Shetland Basin, and for that matter, in East Greenland, are temporally linked and are potentially kinematically related. If so, immediately prior to the onset of plate separation and sea-floor spreading, the NE Atlantic was subjected to regional NE-SW extension: almost 90° to the present day kinematics.

One possibility is that the Faroes and East Greenland, being elevated relative to the basins to the NE and SW, may have been in a state of extension, due to excess gravitational potential energy (GPE). Numerical models could be used to test this as a possible driving mechanism, taking into account palaeo-topography, -crustal thicknesses, and -heat flow, in order to gauge the resulting gravitational potential stresses (e.g. Pascal, 2006). However, margin-perpendicular lineaments are seen along the entire NE Atlantic margin, and many other passive margins for that matter. Typically, these lineaments are also termed transfer zones, and designated a strike-slip sense in order to accommodate margin-normal extension. This assumption needs to be reconsidered in the light of the findings of the present study. In some cases (e.g. the East African Rift and Madagascar; e.g. Rabinowitz et al., 1983; Coffin and Rabinowitz, 1987, 1988), phases of margin parallel extension have been identified, suggesting that such margin-parallel early rifting phases may represent a previously overlooked feature of rift dynamics. Future research projects could target this subject area. Identification of a region with a combination of accessibility (for kinematic data acquisition) and detailed geophysical coverage (in order to assess the deeper structure) would, however, be crucial in advancing the topic beyond current understanding.

Rasmussen & Noe-Nygaard (1969) dyke orientation data vs. Hald & Waagstein (1991) chemical analysis

A Aphyric (tight-blue) basalt

P Porphyritic basalt

F Feldspathic basalt

O Olivine basalt

Rasmussen & Noe-Nygaard, 1969			Hald & Waagstein, 1991																											
No.	Or	Type	ID-1	ID-2	Grouping	SiO2	TiO2	Al2O3	Fe2O3	FeO	MnO	MgO	CaO	Na2O	K2O	P2O5	LOI	Sum	Cr	Co	Ni	Zn	Rb	Sr	Y	Zr	Ba	V	Mg
11	135	A	Str-11b	h	High-Ti N. Streymoy	48.55	2.86	13.82	4.52	8.16	0.19	7.17	10.47	2.36	0.14	0.25	1.23	99.73	297	60	133	111	1	261	38	170	56	372	53.90
36	120	A	Str-36	h	High-Ti N. Streymoy	48.65	2.90	13.72	3.45	9.45	0.20	7.13	10.61	2.46	0.20	0.26	1.29	100.32	298	62	126	110	5	255	36	183	62	339	53.50
73	35	A	Str-73	h	High-Ti N. Streymoy	48.40	2.85	13.58	3.63	9.13	0.19	7.16	10.48	2.46	0.33	0.26	0.96	99.44	311	67	121	117	5	248	33	172	75	348	53.90
74	25	A	Str-74	h	High-Ti N. Streymoy	47.53	2.89	13.78	3.39	9.50	0.20	7.66	10.76	2.20	0.37	0.26	1.08	99.62	303	64	125	117	5	243	35	174	83	349	55.20
75	115	A	Str-75	h	High-Ti N. Streymoy	48.87	2.88	13.68	2.91	9.84	0.19	6.75	10.70	2.40	0.22	0.25	1.03	99.72	297	68	123	115	3	257	35	169	75	350	52.30
87	45	F	Str-87	h	High-Ti N. Streymoy	48.99	2.86	13.78	2.73	10.01	0.20	7.06	10.57	2.47	0.21	0.25	0.96	100.10	293	62	127	112	4	254	35	172	66	345	53.40
130	100		Str-130	h	High-Ti N. Streymoy	48.61	2.79	13.67	2.81	9.82	0.20	7.11	10.59	2.32	0.17	0.24	1.04	99.38	311	70	123	113	4	253	34	171	64	345	53.80
153	145		Str-153	h	High-Ti N. Streymoy	49.20	2.83	13.75	2.76	9.94	0.20	7.20	10.53	2.24	0.36	0.25	0.73	99.97	291	63	121	111	7	256	35	171	76	347	54.00
218	40	A	Str-218	h	High-Ti N. Streymoy	48.38	2.90	13.89	4.39	8.38	0.19	7.16	10.54	2.32	0.27	0.26	0.97	99.65	299	60	133	109	4	261	36	179	76	349	54.00
20	35	A	Va-20	j	High-Ti North Vágar	46.75	3.81	13.26	4.54	8.87	0.23	6.81	10.66	2.32	0.58	0.40	1.04	99.26	323	68	123	123	12	321	40	239	122	341	51.50
24	75	A	Va-24	j	High-Ti North Vágar	46.40	3.90	13.73	5.19	7.97	0.22	6.25	10.78	2.30	0.51	0.41	1.45	99.11	326	58	126	123	11	319	43	249	126	351	50.00
28	90	A	Va-28	j	High-Ti North Vágar	46.52	3.44	14.59	5.44	7.16	0.18	6.44	10.74	2.25	0.45	0.36	1.84	99.41	392	61	167	116	7	324	40	214	94	306	51.90
47	60	A	Va-47	j	High-Ti North Vágar	47.15	3.75	13.33	4.59	8.68	0.23	7.15	10.38	2.46	0.57	0.41	0.97	99.67	303	57	131	113	15	326	42	240	112	323	53.00
2	75	A	Sa-2	k	High-Ti Sandoy	47.31	3.54	14.11	6.77	7.15	0.18	5.56	10.53	2.30	0.59	0.35	1.56	99.46	194	63	109	129	15	297	39	221	124	389	46.80
4	85	A	Sa-4	k	High-Ti Sandoy	48.58	3.50	14.03	5.27	7.78	0.21	4.85	10.59	2.38	0.53	0.36	1.26	99.34	192	60	108	119	15	298	38	218	114	385	43.90
5	85	A	Sa-5	k	High-Ti Sandoy	46.65	3.64	14.42	5.20	8.10	0.20	5.43	10.53	2.49	0.54	0.35	1.61	99.17	191	61	106	131	12	289	38	226	119	401	46.20
2	45	F	My-2	i	High-Ti South Vágar	48.61	2.61	14.04	3.11	9.86	0.21	6.42	10.82	2.46	0.22	0.23	1.47	100.05	173	70	100	110	3	250	33	151	93	389	50.60
73	45	P	Va-73	i	High-Ti South Vágar	48.54	2.62	13.68	2.82	10.61	0.22	6.94	10.54	2.40	0.20	0.24	1.16	99.96	166	62	96	111	3	236	35	152	67	372	51.60
79	35	P	Va-79	i	High-Ti South Vágar	48.25	2.53	13.90	3.93	9.13	0.21	6.90	10.76	2.85	0.19	0.22	1.47	100.35	175	70	100	109	3	236	33	143	54	377	52.40
80	90	A	Va-80	i	High-Ti South Vágar	47.42	2.73	15.09	5.68	8.25	0.22	6.59	10.27	2.33	0.52	0.24	1.26	100.60	162	67	94	124	15	229	34	156	71	394	49.90
88	55	A	Va-88	i	High-Ti South Vágar	48.68	2.62	13.72	3.19	10.29	0.22	6.97	10.58	2.36	0.21	0.23	0.97	100.03	153	59	89	107	4	237	34	153	64	372	51.70
134	175	A	Ey-134	i	High-Ti South Vágar	48.67	2.69	13.54	3.00	10.60	0.23	6.67	10.69	2.36	0.20	0.24	1.09	99.99	177	74	95	119	4	232	35	154	66	398	50.30
209	120	A	Str-209	i	High-Ti South Vágar	48.61	2.61	13.70	3.02	10.29	0.21	6.64	10.72	2.30	0.27	0.23	1.06	99.66	168	78	95	108	9	236	32	152	72	377	50.80
217	140	A	Str-217	i	High-Ti South Vágar	48.63	2.58	13.91	3.11	10.11	0.22	6.76	10.77	2.46	0.21	0.23	1.14	100.13	170	68	97	110	4	239	31	147	61	376	51.40
11	135	F	Str-11a	f	high-Ti big feldspar	48.64	3.21	13.90	3.57	9.82	0.20	5.59	10.25	2.45	0.42	0.29	1.05	99.39	118	61	79	117	11	252	41	199	83	430	46.50
37	40	F	Va-37	f	high-Ti big feldspar	48.56	3.11	14.19	2.90	10.25	0.21	5.96	10.48	2.47	0.22	0.27	1.15	99.78	108	55	81	110	4	262	38	193	75	397	48.40
51	85	F	Va-51	f	high-Ti big feldspar	48.67	3.39	12.98	4.45	9.62	0.25	6.14	10.09	2.52	0.58	0.30	0.93	99.92	123	63	81	126	12	239	42	213	93	457	47.70
56	120	F	Ey-56	f	high-Ti big feldspar	48.90	3.13	14.06	3.19	10.11	0.21	5.83	10.45	2.45	0.26	0.28	0.87	99.86	107	67	74	107	5	228	35	172	78	406	47.60
67	90	F	Str-67	f	high-Ti big feldspar	48.47	3.29	13.45	2.83	10.86	0.22	6.11	10.42	2.52	0.28	0.29	1.19	99.93	112	65	81	117	4	251	40	203	83	420	48.00

No.	Or	Type	ID-1	ID-2	Grouping	SiO2	TiO2	Al2O3	Fe2O3	FeO	MnO	MgO	CaO	Na2O	K2O	P2O5	LOI	Sum	Cr	Co	Ni	Zn	Rb	Sr	Y	Zr	Ba	V	Mg
105	70	F	Str-105	f	high-Ti big feldspar	47.49	3.25	14.22	4.00	9.67	0.22	6.07	10.67	2.50	0.15	0.30	1.34	99.87	121	61	85	125	-1	265	41	204	60	441	48.00
179	135	F	Ey-179	f	high-Ti big feldspar	48.03	3.02	14.70	3.35	9.61	0.20	5.65	10.60	2.54	0.22	0.28	1.23	99.43	111	60	93	114	4	269	37	186	66	408	47.50
216	130	F	Str-216	f	high-Ti big feldspar	48.70	3.05	14.84	3.48	9.36	0.20	5.50	10.73	2.62	0.22	0.28	0.98	99.96	111	63	88	115	4	272	39	190	75	393	47.10
13	105	P	Va-13	g	high-Ti feldspar g'phyric	49.29	2.82	14.29	2.63	10.22	0.20	6.13	10.37	2.54	0.23	0.25	1.19	100.34	95	65	82	109	4	267	34	169	81	340	50.30
18	170	P	Va-18	g	high-Ti feldspar g'phyric	48.23	3.11	13.42	3.20	10.56	0.22	6.31	10.50	2.27	0.17	0.28	1.26	99.54	101	61	68	120	3	266	38	190	67	388	48.70
21	45	P	Ku-21	g	high-Ti feldspar g'phyric	47.67	2.98	13.90	5.56	8.40	0.20	6.05	10.05	2.33	0.24	0.26	1.48	99.13	119	71	78	118	4	264	33	179	77	377	47.70
25	50	P	Ku-25a	g	high-Ti feldspar g'phyric	49.07	2.86	14.27	3.76	9.13	0.21	6.18	10.28	2.33	0.29	0.26	0.99	99.64	108	77	83	117	3	269	41	172	96	386	50.00
29	155	P	Va-29	g	high-Ti feldspar g'phyric	49.06	2.79	14.37	2.24	10.58	0.20	6.12	10.31	2.52	0.24	0.24	1.12	99.80	94	60	81	111	5	272	33	170	76	345	49.60
30	75	P	Ka-30	g	high-Ti feldspar g'phyric	48.99	2.84	14.33	4.23	8.68	0.21	6.11	10.17	2.62	0.41	0.25	1.07	99.92	103	54	78	109	7	263	34	171	86	357	49.70
35	20	P	Va-35	g	high-Ti feldspar g'phyric	49.02	3.03	13.44	2.74	10.71	0.21	6.00	10.22	2.42	0.26	0.27	1.05	99.38	113	87	71	117	5	255	37	185	78	385	47.90
40	90	P	Ey-40	g	high-Ti feldspar g'phyric	48.58	2.83	14.42	3.61	9.23	0.21	6.03	10.42	2.57	0.20	0.25	1.18	99.53	107	55	79	112	1	273	34	167	74	363	49.40
45	175	P	Ey-45	g	high-Ti feldspar g'phyric	49.04	2.79	14.47	4.21	8.53	0.20	5.81	10.63	2.48	0.36	0.26	0.93	99.71	123	54	86	104	5	268	36	171	91	338	48.80
48	125	P	Va-48	g	high-Ti feldspar g'phyric	49.08	2.88	13.94	2.73	10.31	0.20	6.03	10.27	2.46	0.22	0.25	1.15	99.53	105	57	75	113	5	265	35	177	84	357	48.80
55	80	P	Va-55	g	high-Ti feldspar g'phyric	48.78	2.84	14.06	3.42	9.37	0.20	6.22	10.27	2.48	0.24	0.24	1.34	99.46	97	62	80	113	3	268	38	168	75	357	50.30
57	155	P	Va-57	g	high-Ti feldspar g'phyric	48.93	2.85	14.35	3.34	9.58	0.20	5.91	10.33	2.48	0.24	0.29	1.35	99.85	102	54	77	115	3	267	35	171	74	361	48.70
64	15	P	Str-64	g	high-Ti feldspar g'phyric	49.03	2.87	14.33	2.60	10.30	0.20	5.68	10.53	2.53	0.21	0.26	1.41	99.95	104	61	80	110	3	265	35	172	66	360	47.60
68	15	P	Str-68	g	high-Ti feldspar g'phyric	49.02	2.87	14.24	2.72	10.22	0.20	5.98	10.45	2.40	0.22	0.25	1.32	99.90	104	70	82	118	4	262	35	170	76	366	48.80
108	150	P	Str-108	g	high-Ti feldspar g'phyric	48.72	2.89	14.27	3.17	9.84	0.20	5.80	10.42	2.48	0.21	0.25	1.15	99.41	99	55	77	111	5	277	36	174	68	355	48.00
115	150	P	Str-115	g	high-Ti feldspar g'phyric	48.64	2.89	14.14	2.90	10.07	0.20	6.13	10.44	2.39	0.21	0.25	1.19	99.45	104	65	82	111	4	266	34	172	66	371	49.40
1	5	A	Ko-1	a	Low-Ti	48.16	1.26	14.79	3.30	7.69	0.19	8.71	12.39	2.22	0.10	0.10	0.88	99.80	455	61	176	78	1	118	27	62	40	297	62.30
1	135	A	Su-1	a	Low-Ti	48.92	1.30	15.12	3.45	7.52	0.19	8.15	12.13	2.13	0.10	0.09	1.09	100.19	364	60	143	80	1	125	26	63	28	326	60.80
2	85	A	Str-2	a	Low-Ti	46.84	0.88	14.48	3.08	7.25	0.19	12.03	11.82	1.65	0.03	0.06	1.34	99.65	787	76	356	74	-1	79	23	39	11	262	70.80
2	140	A	F-2	a	Low-Ti	48.54	1.44	13.83	3.79	8.36	0.21	7.34	12.46	2.30	0.08	0.11	1.17	99.62	322	63	106	90	0	102	34	69	26	376	55.80
3	15	A	Sv-3	a	Low-Ti	47.43	1.07	14.90	3.27	7.50	0.19	8.82	11.69	1.90	0.86	0.08	1.78	99.50	413	65	144	77	24	101	25	49	33	294	63.10
4	145		Vid-4	a	Low-Ti	47.63	1.00	15.05	2.65	7.74	0.20	10.34	12.51	1.72	0.04	0.07	0.76	99.72	555	82	256	79	0	86	25	44	10	288	67.40
4	170	A	Str-4-5	a	Low-Ti	48.62	1.71	13.35	3.18	10.96	0.24	6.25	11.33	2.28	0.09	0.14	1.33	99.48	82	66	62	109	1	100	40	90	38	421	47.80
5	0	A	Ka-5	a	Low-Ti	48.59	1.20	14.23	2.57	8.94	0.21	8.05	12.61	1.74	0.03	0.10	1.17	99.44	372	61	110	91	1	81	31	54	18	343	59.10
5	145	A	Sv-5	a	Low-Ti	48.23	1.01	15.03	2.85	7.55	0.19	9.19	12.90	1.87	0.07	0.07	0.94	99.91	532	60	169	69	0	96	25	42	18	297	64.80
6	30	A	Sv-6	a	Low-Ti	49.11	1.42	14.39	3.92	7.38	0.20	8.01	12.24	2.03	0.16	0.13	1.08	100.07	370	54	120	75	3	143	27	68	45	286	59.80
7	40	A	Ku-7	a	Low-Ti	48.38	1.44	14.41	2.74	8.91	0.21	7.65	12.39	2.21	0.06	0.10	0.86	99.36	361	70	129	94	0	108	34	69	11	380	57.60
7	45	A	Sv-7	a	Low-Ti	47.01	1.05	14.80	4.71	5.76	0.19	8.58	11.52	1.96	0.41	0.08	3.10	99.18	431	74	152	77	8	99	23	45	27	297	63.40
7	130	A	Sa-7	a	Low-Ti	47.80	1.19	14.62	3.54	7.40	0.19	9.67	12.32	1.84	0.06	0.09	1.29	100.00	519	65	205	75	0	101	27	53	17	308	64.90
8	15	A	B-8	a	Low-Ti	48.34	0.99	15.40	3.89	6.55	0.18	7.46	13.29	2.16	0.03	0.07	1.38	99.75	404	66	135	75	1	88	24	43	17	317	60.00
8	30	P	Ku-8	a	Low-Ti	48.84	1.46	14.52	2.68	9.11	0.21	7.43	12.48	2.30	0.08	0.11	0.96	100.19	373	71	131	87	0	105	32	72	23	379	56.60
9	10	A	Ka-9	a	Low-Ti	46.64	1.05	13.88	2.60	7.65	0.18	12.70	12.04	1.60	0.03	0.08	1.07	99.53	1098	66	431	69	1	106	22	46	21	281	72.00
9	30	A	Ku-9	a	Low-Ti	49.09	1.58	13.34	2.45	10.92	0.24	7.00	11.73	2.16	0.08	0.12	1.03	99.73	231	71	87	106	1	92	39	77	20	402	51.90

No.	Or	Type	ID-1	ID-2	Grouping	SiO2	TiO2	Al2O3	Fe2O3	FeO	MnO	MgO	CaO	Na2O	K2O	P2O5	LOI	Sum	Cr	Co	Ni	Zn	Rb	Sr	Y	Zr	Ba	V	Mg
9	140	A	Su-9	a	Low-Ti	48.37	1.31	15.34	3.70	7.35	0.19	7.83	12.22	2.01	0.07	0.11	1.30	99.79	364	59	153	80	1	123	27	63	32	323	59.70
11	10	A	Sv-11	a	Low-Ti	47.43	0.91	14.98	2.76	7.69	0.18	10.29	12.68	1.75	0.03	0.06	0.93	99.70	513	61	224	70	1	78	22	39	11	274	67.20
11	135	A	Su-11	a	Low-Ti	48.55	1.28	14.95	2.96	8.02	0.20	8.36	12.12	1.98	0.09	0.10	1.55	100.18	349	61	147	75	2	122	28	62	33	336	61.30
12	10	O	Sv-12	a	Low-Ti	43.95	0.77	9.49	2.25	8.55	0.18	22.62	8.01	1.12	0.15	0.06	2.05	99.20	2289	98	1141	73	0	70	15	34	24	194	81.20
12	45	A	Vid-12	a	Low-Ti	46.69	1.01	13.57	2.68	8.55	0.20	8.42	12.77	1.83	0.17	0.08	3.32	99.28	361	57	105	77	1	64	26	46	26	319	60.80
12	150	A	F-12	a	Low-Ti	48.51	1.43	13.56	2.40	9.61	0.21	7.82	12.54	2.16	0.07	0.10	1.02	99.43	344	77	103	89	1	98	32	67	23	379	57.30
12	175	A	Va-12	a	Low-Ti	45.79	0.85	12.13	2.27	8.23	0.19	17.16	10.01	1.35	0.03	0.06	1.16	99.22	1598	78	711	69	0	73	23	35	19	219	77.20
13	170	A	Sv-13	a	Low-Ti	47.75	0.95	14.80	2.19	8.16	0.19	9.75	12.67	1.70	0.04	0.06	0.94	99.19	601	60	237	72	0	74	26	41	5	290	66.10
14	55	A	Ka-14	a	Low-Ti	48.14	1.03	16.10	4.14	6.26	0.19	7.06	13.23	1.96	0.06	0.06	1.29	99.53	515	55	205	80	0	84	26	45	20	355	58.80
15	40	A	Va-15	a	Low-Ti	45.41	0.84	12.30	3.11	7.55	0.18	16.88	10.06	1.38	0.05	0.06	1.34	99.16	1575	82	699	71	2	75	22	34	13	220	76.70
15	135	A	B-15	a	Low-Ti	48.38	1.39	14.60	3.85	7.83	0.22	8.31	12.09	1.98	0.15	0.12	1.03	99.94	371	63	121	89	1	110	32	73	37	314	59.80
16	30		Vid-16	a	Low-Ti	48.69	1.27	14.74	2.78	8.06	0.19	8.38	12.30	1.79	0.07	0.11	1.00	99.39	414	74	145	81	1	129	26	64	23	314	61.60
16	165	A	B-16	a	Low-Ti	46.73	1.08	14.76	3.06	7.68	0.19	9.99	12.64	1.78	0.06	0.07	1.14	99.21	516	65	209	74	1	102	26	48	13	291	65.90
17	5	A	Va-17	a	Low-Ti	45.28	0.73	11.99	2.36	7.90	0.18	17.55	10.00	1.22	0.14	0.05	2.05	99.45	1513	86	723	68	2	83	18	28	11	192	78.00
17	45	A	Str-17	a	Low-Ti	46.64	1.02	13.52	3.19	7.26	0.19	13.77	11.54	1.49	0.08	0.08	1.02	99.81	1127	70	494	68	1	97	22	43	19	258	73.30
18	0	A	B-18	a	Low-Ti	47.39	1.10	15.04	1.60	8.92	0.20	9.96	12.80	1.65	0.03	0.08	0.92	99.70	521	85	217	73	1	102	25	47	10	290	66.00
18	115	A	Ku-18	a	Low-Ti	47.70	0.97	15.22	2.93	7.62	0.19	9.37	12.56	1.78	0.03	0.06	1.11	99.55	483	70	204	72	-1	84	25	41	14	281	64.90
19	5	A	Va-19	a	Low-Ti	48.32	1.34	14.75	3.92	6.95	0.20	8.25	12.02	1.97	0.12	0.11	1.13	99.08	373	54	142	86	2	131	27	68	40	309	61.40
20	75	A	Ey-20	a	Low-Ti	48.99	1.45	13.98	4.02	7.31	0.19	7.61	12.03	1.99	0.18	0.12	1.61	99.48	385	55	115	85	3	145	30	74	57	319	58.50
21	130		Su-21	a	Low-Ti	48.53	1.30	14.81	3.40	8.13	0.21	7.44	12.44	2.23	0.09	0.11	1.04	99.72	325	64	121	87	0	92	29	60	20	352	57.30
22	120	A	Va-22	a	Low-Ti	48.42	1.30	14.80	3.37	7.57	0.19	7.91	12.35	1.78	0.05	0.11	1.43	99.27	370	55	150	81	1	132	26	68	35	311	60.10
23	125	A	Su-23	a	Low-Ti	48.50	1.30	15.02	2.74	8.22	0.20	8.12	11.94	2.10	0.12	0.10	1.09	99.45	364	58	145	81	0	121	26	64	27	320	60.60
23	150	A	Ka-23	a	Low-Ti	49.08	1.57	13.62	3.44	9.48	0.24	7.11	11.89	2.16	0.09	0.13	1.08	99.89	228	76	92	109	3	89	39	76	25	396	53.30
24	130	A	Su-24	a	Low-Ti	49.06	1.44	13.91	3.02	9.39	0.23	7.27	12.13	2.20	0.09	0.12	1.05	99.90	262	63	97	93	0	87	35	69	22	392	54.80
25	50	A	Ku-25B	a	Low-Ti	48.18	1.00	15.32	2.76	7.29	0.19	9.13	12.82	1.76	0.04	0.08	1.15	99.72	507	60	185	69	0	93	27	48	16	297	65.40
26	70	A	Ku-26	a	Low-Ti	47.90	1.32	14.81	2.22	8.52	0.20	8.46	12.95	2.10	0.05	0.10	0.89	99.51	411	59	166	74	-3	123	26	63	23	331	61.90
27	30	A	Ku-27	a	Low-Ti	46.32	0.79	13.38	2.55	7.92	0.18	14.93	10.77	1.41	0.02	0.05	1.10	99.42	1167	88	575	69	0	64	19	33	7	261	74.70
27	135	A	Su-27	a	Low-Ti	48.20	1.42	14.67	3.90	8.25	0.20	6.88	12.58	2.17	0.08	0.11	1.31	99.78	309	63	111	91	1	90	32	69	14	377	54.20
28	65	A / P	Ka-28	a	Low-Ti	48.10	1.08	15.22	1.36	8.60	0.19	8.69	12.93	2.02	0.05	0.09	1.40	99.71	476	58	173	65	1	92	27	52	23	302	64.10
29	115	A	B-29	a	Low-Ti	47.11	1.03	15.08	3.38	7.13	0.19	10.23	12.49	1.76	0.06	0.07	0.92	99.92	521	62	223	70	1	98	23	41	10	267	67.00
29	135	A	Su-29	a	Low-Ti	48.68	1.29	15.03	2.82	8.18	0.20	8.04	12.16	1.96	0.09	0.10	1.03	99.57	360	56	148	85	1	124	25	62	33	325	60.30
30	25	A	B-30	a	Low-Ti	46.99	1.03	15.11	2.48	7.84	0.18	10.17	12.62	1.66	0.02	0.07	1.11	99.29	516	61	215	70	0	100	25	43	15	272	67.10
30	120	O	Ku-30	a	Low-Ti	47.93	1.15	15.00	4.17	6.95	0.19	8.70	12.60	1.85	0.11	0.08	1.32	100.07	381	62	135	74	3	98	27	51	20	284	62.20
30	135	A	Su-30	a	Low-Ti	48.63	1.27	15.20	2.79	8.24	0.19	7.74	12.33	2.04	0.13	0.10	1.27	99.94	387	60	158	82	1	124	26	64	42	333	59.30
31	15	A	Va-31	a	Low-Ti	45.98	0.84	12.34	11.41	0.00	0.19	17.09	10.05	1.67	0.05	0.06	0.33	100.00	1528	73	670	67	0	75	21	32	7	214	77.10
31	75	A	Ka-31	a	Low-Ti	48.20	1.31	14.80	3.31	7.40	0.19	8.68	12.34	1.84	0.25	0.10	1.61	100.02	426	58	165	78	2	122	27	62	16	327	62.90

No.	Or	Type	ID-1	ID-2	Grouping	SiO2	TiO2	Al2O3	Fe2O3	FeO	MnO	MgO	CaO	Na2O	K2O	P2O5	LOI	Sum	Cr	Co	Ni	Zn	Rb	Sr	Y	Zr	Ba	V	Mg
32	40	O	Ku-32	a	Low-Ti	47.51	0.99	15.00	3.04	7.14	0.18	10.57	12.48	1.68	0.08	0.07	0.93	99.68	656	72	279	72	2	99	23	45	17	279	68.40
32	80	A	Ey-32	a	Low-Ti	47.51	1.28	14.72	2.40	8.25	0.19	8.67	12.61	1.93	0.50	0.10	1.51	99.67	430	53	158	76	9	124	28	61	21	330	62.70
32	110	A	Ka-32	a	Low-Ti	45.70	0.75	12.91	2.80	7.56	0.18	16.40	10.33	1.41	0.02	0.05	1.36	99.49	1222	81	623	74	1	62	19	32	12	232	76.70
32	135	A	Su-32	a	Low-Ti	48.63	1.39	14.68	3.10	8.45	0.21	7.27	12.10	2.11	0.15	0.11	1.09	99.29	289	58	120	88	1	129	28	72	43	341	56.70
33	50	O	Ku-33	a	Low-Ti	47.60	1.43	12.13	2.33	8.39	0.18	12.39	7.60	3.14	1.71	0.13	2.85	99.89	1043	71	404	85	23	191	18	92	196	228	70.50
33	125	A	B-33	a	Low-Ti	48.34	1.30	14.25	3.37	7.76	0.20	8.21	12.57	2.13	0.07	0.10	1.04	99.34	388	60	151	79	1	99	31	62	27	356	60.60
34	35	A	B-34	a	Low-Ti	46.70	0.86	14.97	4.74	6.04	0.17	9.48	11.58	1.88	0.42	0.07	3.09	100.00	788	77	372	79	4	141	24	30	27	268	65.00
35	105	A	Ku-35	a	Low-Ti	48.80	1.40	15.29	4.45	6.68	0.20	7.61	11.96	2.35	0.20	0.13	1.18	100.26	383	64	139	89	2	142	27	70	55	294	59.00
36	105	A	Ku-36	a	Low-Ti	49.07	1.39	14.04	2.86	9.64	0.23	7.32	12.19	2.15	0.10	0.11	0.99	100.09	265	73	100	98	0	93	34	71	28	393	54.80
36	140	A	Su-36	a	Low-Ti	49.03	1.40	14.43	2.66	8.82	0.21	7.60	11.93	2.02	0.15	0.11	1.11	99.48	302	62	119	84	3	130	29	70	39	353	57.80
36	145	A	Ey-36	a	Low-Ti	47.52	0.98	14.93	2.42	8.01	0.20	9.64	12.80	1.84	0.03	0.07	0.91	99.36	445	64	199	75	0	83	27	42	11	311	65.70
38	0	A	Ey-38	a	Low-Ti	48.48	1.18	14.36	4.09	7.45	0.20	7.91	12.69	1.91	0.03	0.09	1.35	99.75	361	54	117	84	0	83	27	52	15	347	59.00
38	50	A	Va-38	a	Low-Ti	48.34	1.77	14.11	3.46	7.76	0.19	8.24	12.55	1.98	0.15	0.14	1.20	99.91	404	52	121	88	3	183	29	87	46	301	60.50
39	90	A	Ey-39	a	Low-Ti	46.32	0.82	13.28	2.72	7.72	0.19	14.51	10.86	1.69	0.04	0.06	1.04	99.24	1238	74	532	69	1	72	23	36	13	253	74.30
41	115	A	Va-41	a	Low-Ti	48.66	1.44	14.32	4.77	6.97	0.20	7.99	12.40	1.99	0.07	0.13	1.19	100.14	384	64	120	87	1	130	29	74	22	338	58.90
42	50	A	Ey-42	a	Low-Ti	46.68	1.05	14.13	3.14	7.10	0.18	12.44	11.96	1.62	0.07	0.08	1.01	99.47	1053	67	408	73	0	102	23	48	7	274	71.70
42	60	A	B-42	a	Low-Ti	46.96	0.92	14.75	2.84	7.52	0.18	11.23	11.92	1.85	0.06	0.06	1.44	99.74	669	68	320	76	2	80	24	38	14	271	69.30
46	10	O	Str-46	a	Low-Ti	45.06	0.77	11.00	1.86	8.59	0.18	20.50	8.90	1.15	0.03	0.06	0.96	99.01	1817	133	960	66	0	70	18	33	18	194	80.20
47	140	A	Su-47	a	Low-Ti	47.60	1.58	14.71	5.21	6.61	0.21	7.24	12.26	1.85	0.12	0.15	1.54	99.08	130	62	84	93	0	203	28	73	59	336	56.40
47	165	A	B-47	a	Low-Ti	48.72	1.41	14.20	3.89	7.44	0.20	7.27	12.85	2.05	0.04	0.10	1.24	99.41	392	69	144	84	0	100	32	68	17	374	57.30
48	100	A	Ey-48	a	Low-Ti	47.89	1.30	15.03	2.96	7.65	0.19	8.60	12.91	1.98	0.06	0.10	1.05	99.72	421	57	169	80	1	120	27	62	22	327	62.80
48	165	A	B-48	a	Low-Ti	48.84	1.32	14.32	3.78	7.49	0.19	7.74	12.87	2.32	0.06	0.10	1.23	100.26	396	62	151	82	1	101	31	62	13	364	59.20
50	80	A	Ka-50	a	Low-Ti	48.09	1.58	14.16	2.93	8.28	0.19	8.52	12.22	2.06	0.16	0.12	1.11	99.43	457	55	197	83	3	141	27	78	25	336	61.20
53	165	A	B-53	a	Low-Ti	48.53	1.32	14.25	3.28	7.90	0.20	8.05	12.61	2.14	0.06	0.09	0.90	99.33	384	65	151	85	1	100	29	63	16	351	60.00
57	90	A	B-57	a	Low-Ti	47.74	1.03	15.27	2.41	8.23	0.19	8.53	12.66	1.77	0.07	0.08	1.13	100.13	396	63	132	72	1	92	25	46	25	287	62.40
58	20	A	Ey-58	a	Low-Ti	48.64	1.54	13.76	2.59	9.51	0.22	7.51	12.38	2.12	0.06	0.11	1.06	99.50	325	60	119	87	0	106	35	75	18	372	56.20
58	175	A	Va-58	a	Low-Ti	47.96	1.23	15.00	2.82	8.12	0.20	9.03	12.60	1.76	0.06	0.13	1.13	100.04	438	56	174	82	1	118	27	60	24	309	63.20
59	175	A	Va-59	a	Low-Ti	47.88	1.51	14.10	3.61	6.99	0.19	10.08	11.84	2.19	0.18	0.12	1.49	100.18	583	56	214	74	0	172	23	70	37	250	66.60
59	175		Va-59	a	Low-Ti	47.71	1.47	14.19	3.84	6.70	0.18	9.97	11.83	1.87	0.19	0.11	1.62	99.71	611	57	224	81	2	173	23	67	39	248	66.50
61	35	O	B-61	a	Low-Ti	47.69	0.98	15.35	6.06	5.47	0.22	7.26	12.04	1.94	0.06	0.07	2.28	99.94	1029	74	629	84	1	84	24	42	13	280	57.30
61	65	A	Str-61	a	Low-Ti	48.43	1.06	15.33	3.56	7.30	0.20	7.72	12.74	1.89	0.06	0.08	1.66	100.04	359	57	130	80	0	101	27	54	28	304	59.80
62	155	O	Str-62	a	Low-Ti	45.29	0.81	11.77	2.23	8.34	0.18	17.94	9.56	1.40	0.23	0.06	1.53	99.35	1586	107	787	71	6	77	20	36	15	203	77.80
63	95	A	B-63	a	Low-Ti	47.71	1.29	14.65	2.57	8.03	0.19	8.76	12.29	2.35	0.10	0.10	1.75	99.74	433	68	163	79	2	111	27	61	21	324	63.20
69	35	A	Va-69	a	Low-Ti	45.18	0.81	11.60	1.80	8.71	0.19	19.11	9.52	1.30	0.15	0.06	1.53	99.94	1628	80	797	70	4	90	18	32	4	210	78.90
70	130	A	Va-70	a	Low-Ti	49.21	1.46	14.19	3.87	7.53	0.20	7.86	12.13	2.29	0.16	0.13	1.56	100.60	389	68	116	86	1	143	29	77	67	318	59.10
82	125	A	Ey-82	a	Low-Ti	48.80	1.42	14.59	3.04	8.59	0.20	7.46	12.40	2.09	0.06	0.10	0.96	99.72	361	60	143	89	1	104	32	69	28	361	57.10

No.	Or	Type	ID-1	ID-2	Grouping	SiO2	TiO2	Al2O3	Fe2O3	FeO	MnO	MgO	CaO	Na2O	K2O	P2O5	LOI	Sum	Cr	Co	Ni	Zn	Rb	Sr	Y	Zr	Ba	V	Mg
84	120	A	Va-84	a	Low-Ti	48.88	1.33	14.66	11.99	0.00	0.20	8.56	12.17	1.97	0.08	0.12	-0.09	99.87	410	72	151	83	0	129	29	67	39	319	61.60
91	25	A	Va-91	a	Low-Ti	47.77	1.25	14.71	3.14	7.91	0.19	8.97	12.37	1.73	0.12	0.10	0.88	99.13	443	64	170	81	4	116	30	61	35	301	62.80
93	25	O	Ey-93	a	Low-Ti	45.73	0.91	11.82	2.26	8.37	0.19	17.58	10.27	1.40	0.03	0.07	0.84	99.49	1624	85	842	80	1	96	21	43	12	243	77.40
102	15	A	Ey-102	a	Low-Ti	48.74	1.22	14.32	2.99	8.61	0.21	8.26	12.61	1.98	0.06	0.09	1.08	100.18	394	60	122	94	1	83	29	56	11	353	59.60
105	135	A	Ey-105	a	Low-Ti	47.09	0.94	14.49	3.68	6.82	0.18	11.26	12.15	1.51	0.02	0.07	1.42	99.65	635	65	302	74	0	74	24	41	15	271	69.20
106	160	O	Str-106	a	Low-Ti	44.92	0.77	10.98	1.66	8.70	0.18	20.82	8.82	1.50	0.03	0.06	1.21	99.65	1789	83	911	68	0	72	20	32	9	198	80.50
107	125	A	Ey-107	a	Low-Ti	48.78	1.23	14.31	3.29	8.27	0.21	8.14	12.71	2.05	0.03	0.09	0.99	100.10	389	60	100	83	1	81	29	52	21	343	59.40
108	100	A	Ey-108	a	Low-Ti	48.21	1.40	14.69	3.31	7.65	0.21	7.44	12.44	2.09	0.07	0.10	1.05	99.44	378	70	133	88	3	102	33	67	18	383	57.50
111	55	P	Ey-111	a	Low-Ti	48.43	1.42	14.55	2.93	8.67	0.21	7.40	12.53	2.26	0.05	0.10	1.30	99.87	364	63	137	85	-1	105	32	67	19	368	57.00
112	105	A	Str-112	a	Low-Ti	48.15	1.38	14.67	3.01	8.46	0.21	7.91	12.52	2.00	0.06	0.10	0.99	99.47	357	60	128	79	1	110	33	69	21	352	58.90
112	130	A	Ey-112	a	Low-Ti	48.55	1.53	13.88	3.67	8.67	0.22	7.40	12.37	2.26	0.10	0.12	1.21	99.99	354	73	128	95	1	105	35	78	32	396	55.50
124	35	A	Ey-124	a	Low-Ti	49.12	1.49	14.58	3.01	8.51	0.21	7.46	12.46	2.21	0.12	0.11	0.78	100.07	379	66	139	89	4	103	33	69	31	377	57.30
129	25	O	Ey-129	a	Low-Ti	45.89	0.96	12.94	3.38	7.44	0.20	15.11	10.90	1.53	0.05	0.07	0.99	99.47	1326	77	623	74	1	94	20	43	3	260	74.50
130	65	A	Ey-130	a	Low-Ti	47.51	0.94	15.18	3.43	6.99	0.20	10.54	12.35	2.08	0.06	0.07	0.99	100.34	595	64	259	75	1	78	23	40	6	276	67.90
130	100	A	Str-130	a	Low-Ti	44.56	0.85	10.98	2.14	8.21	0.18	20.59	8.64	1.13	0.15	0.06	2.00	99.51	1840	90	950	67	3	139	19	33	24	183	80.40
132	5	A	Str-132	a	Low-Ti	46.42	0.89	13.67	3.32	6.74	0.18	13.35	11.08	1.62	0.17	0.06	1.74	99.25	1085	69	448	67	6	90	21	32	9	238	73.50
135	85	A	Ey-135	a	Low-Ti	47.36	1.25	14.55	3.79	7.54	0.19	9.23	12.53	1.77	0.03	0.09	1.49	99.83	522	60	194	80	1	104	28	59	13	321	63.00
149	140	A	Ey-149	a	Low-Ti	48.59	1.40	14.62	3.52	7.80	0.20	7.77	12.55	2.19	0.07	0.10	1.19	99.99	389	61	141	86	0	105	34	67	29	355	58.90
151	80	A	Str-151	a	Low-Ti	48.53	1.55	14.52	4.58	7.49	0.23	7.03	12.57	2.34	0.14	0.11	1.40	100.48	403	69	141	95	4	106	35	75	35	403	55.00
153	145	A	Str-153	a	Low-Ti	48.45	1.65	14.54	5.05	7.28	0.30	6.83	12.16	2.06	0.16	0.15	1.18	99.82	130	61	79	104	3	161	31	80	49	414	53.90
154	155	A	Str-154	a	Low-Ti	48.81	1.47	14.31	3.83	7.88	0.21	7.72	12.17	2.44	0.06	0.31	1.19	100.22	395	62	118	91	1	143	28	78	36	327	57.90
156	175	A	Ey-156	a	Low-Ti	47.11	1.17	14.53	2.36	8.58	0.19	10.33	12.38	1.67	0.05	0.09	1.20	99.68	550	68	243	86	1	118	24	54	17	297	66.10
158	170	A	Str-158	a	Low-Ti	48.27	1.66	13.56	4.37	9.68	0.24	6.19	11.41	2.26	0.14	0.13	1.26	99.16	78	61	65	103	3	100	39	87	37	411	47.90
159	140	A	Str-159	a	Low-Ti	48.23	1.40	14.86	4.33	6.48	0.21	7.55	12.43	1.96	0.08	0.12	1.53	99.17	396	55	140	85	1	150	27	73	38	313	59.50
160	25	A	Str-160	a	Low-Ti	48.66	1.66	14.56	4.75	6.74	0.26	6.74	12.71	2.38	0.31	0.13	1.22	100.13	443	67	166	91	12	140	31	83	48	366	55.30
174	95	A	Str-174	a	Low-Ti	46.73	0.94	15.17	4.97	5.76	0.17	9.70	12.29	1.79	0.07	0.06	1.83	99.47	679	72	306	73	2	78	28	42	11	291	65.70
177	65	A	Ey-177	a	Low-Ti	46.51	0.79	13.62	2.25	8.10	0.18	14.29	11.17	1.47	0.06	0.06	0.96	99.48	1066	75	501	74	1	69	23	34	17	257	74.10
178	85	A	Ey-178	a	Low-Ti	48.87	1.54	13.71	3.03	8.67	0.21	7.58	11.94	2.13	0.13	0.14	1.48	99.43	305	62	101	85	0	145	31	81	55	311	57.30
187	10	A	Ey-187	a	Low-Ti	48.07	1.60	14.07	2.34	8.99	0.20	8.41	12.39	2.03	0.15	0.12	0.88	99.25	458	64	189	82	3	141	29	79	35	343	60.50
188	160	A	Str-188	a	Low-Ti	47.82	1.46	14.09	3.36	7.01	0.18	10.12	11.93	1.75	0.14	0.12	1.67	99.66	601	56	225	73	1	174	22	68	38	250	67.10
190	15	A	Str-190	a	Low-Ti	48.59	1.47	14.37	4.48	7.02	0.19	7.16	12.42	2.27	0.16	0.11	1.07	99.30	368	55	130	84	5	106	32	75	32	385	56.70
190	30	A	Ey-190	a	Low-Ti	48.75	1.75	13.38	4.37	10.05	0.26	6.19	11.01	2.41	0.15	0.13	1.06	99.51	80	63	62	107	3	101	41	90	50	419	47.20
191	95	A	Ey-191	a	Low-Ti	47.85	1.31	14.97	2.10	8.70	0.19	8.72	13.08	1.81	0.04	0.10	0.83	99.71	389	61	163	72	1	121	26	62	16	317	62.50
197	100	A	Ey-197	a	Low-Ti	48.44	1.51	13.91	4.44	8.40	0.22	6.47	11.70	2.38	0.22	0.14	1.49	99.31	176	62	74	102	3	145	36	76	82	389	51.30
203	125	A	Ey-203	a	Low-Ti	48.83	1.62	13.72	3.58	10.13	0.24	6.51	11.45	2.15	0.14	0.13	1.25	99.77	95	67	67	105	1	100	39	81	35	389	49.60
223	95	A	Str-223	a	Low-Ti	48.90	1.49	14.23	4.20	7.26	0.20	7.55	12.06	2.26	0.20	0.13	1.19	99.69	372	66	119	89	5	143	28	80	56	332	58.00

No.	Or	Type	ID-1	ID-2	Grouping	SiO2	TiO2	Al2O3	Fe2O3	FeO	MnO	MgO	CaO	Na2O	K2O	P2O5	LOI	Sum	Cr	Co	Ni	Zn	Rb	Sr	Y	Zr	Ba	V	Mg
224	75	A	Str-224	a	Low-Ti	47.85	1.18	14.66	2.90	8.17	0.19	9.30	12.48	1.81	0.04	0.09	0.88	99.55	455	61	186	78	0	107	25	56	18	317	63.60
1	145	A	My-1	b	Other high-Ti	47.22	3.62	12.99	4.71	9.60	0.25	5.58	10.10	2.67	0.97	0.43	1.43	99.57	95	62	62	120	24	342	40	239	248	361	44.90
2	130	A	Su-2	b	Other high-Ti	48.24	2.40	13.47	12.36	0.00	0.19	8.67	11.52	2.26	0.26	0.20	0.34	99.90	456	51	182	83	3	277	29	132	63	265	61.20
2	135		Ey-1	b	Other high-Ti	48.31	2.17	13.84	2.19	10.42	0.21	7.03	11.49	2.35	0.18	0.20	0.93	99.33	153	63	97	100	1	201	30	119	53	373	53.40
3	0	A	Ka-3	b	Other high-Ti	48.58	3.05	13.60	3.23	10.22	0.21	6.45	10.37	2.37	0.27	0.28	1.14	99.77	212	62	106	114	5	257	36	182	86	410	49.80
3	0	A	Su-3	b	Other high-Ti	50.13	2.67	13.46	3.13	8.60	0.19	6.81	10.46	2.34	0.24	0.23	1.31	99.57	339	63	119	113	5	245	36	165	81	339	54.70
4	140	A	Su-4	b	Other high-Ti	49.40	2.68	14.07	3.18	9.10	0.22	6.20	10.48	2.37	0.39	0.24	1.01	99.35	134	59	79	109	7	266	34	171	91	376	51.20
8	60	A	Su-8	b	Other high-Ti	48.20	2.27	13.79	3.74	8.86	0.21	6.92	11.64	2.14	0.08	0.20	1.39	99.46	201	62	90	102	0	200	32	129	41	392	53.40
11	135	A	Va-11	b	Other high-Ti	48.35	2.10	13.88	3.52	7.66	0.22	8.24	12.03	2.19	0.12	0.18	1.39	99.88	508	57	140	88	1	256	25	116	41	286	60.60
12	5	A	Ey-12	b	Other high-Ti	48.56	2.17	13.85	3.44	9.06	0.20	7.16	11.56	2.34	0.37	0.19	0.97	99.86	160	61	98	99	11	197	30	117	49	366	54.40
13	75	A	Ka-13	b	Other high-Ti	48.02	2.86	13.79	4.36	8.52	0.21	7.38	10.54	2.24	0.12	0.25	1.19	99.47	302	58	127	112	0	268	36	173	51	351	54.50
14	170	A	Su-14	b	Other high-Ti	47.77	2.09	14.56	3.24	8.03	0.19	7.73	11.97	2.14	0.07	0.16	1.23	99.18	390	61	168	87	1	306	25	106	34	298	58.80
33	110	A	Su-33	b	Other high-Ti	48.45	2.90	13.67	4.50	9.19	0.22	6.36	10.29	2.80	0.44	0.30	1.02	100.12	165	58	69	105	5	283	38	181	138	391	49.30
34	30	A	Va-34	b	Other high-Ti	48.46	2.13	14.15	3.35	7.57	0.18	7.97	12.16	2.37	0.25	0.18	1.03	99.81	508	55	138	87	4	270	26	121	58	269	60.40
34	135	A	Su-34	b	Other high-Ti	48.46	2.46	13.29	1.86	9.44	0.20	8.42	11.58	2.06	0.14	0.22	1.05	99.17	550	67	170	99	1	274	31	138	54	313	60.50
39	140	A	Su-39	b	Other high-Ti	48.26	2.35	12.74	2.53	9.27	0.20	9.89	11.34	1.82	0.12	0.20	1.03	99.74	685	65	274	91	3	261	29	129	51	270	63.40
43	80	A	Va-43	b	Other high-Ti	48.57	2.77	13.71	2.59	9.96	0.20	7.20	10.35	2.37	0.19	0.24	1.11	99.27	314	60	129	112	3	250	34	164	66	325	54.20
47	110	A	Str-47	b	Other high-Ti	49.07	2.13	13.44	4.04	9.37	0.23	6.61	11.07	2.58	0.19	0.20	1.29	100.23	71	60	63	113	4	169	35	127	67	435	50.70
52	165	A	B-52	b	Other high-Ti	48.51	2.91	13.55	2.93	10.22	0.21	6.74	10.40	2.34	0.24	0.27	1.26	99.58	212	61	108	116	5	252	34	172	74	405	51.50
71	135	A	Va-71	b	Other high-Ti	48.92	2.79	14.66	3.68	8.62	0.20	6.56	10.55	2.34	0.34	0.24	1.07	99.99	251	55	110	105	5	266	34	166	68	319	52.60
101	130	A	Va-101	b	Other high-Ti	48.63	3.00	13.67	5.36	7.75	0.19	6.46	10.52	2.11	0.36	0.25	1.25	99.55	305	67	103	113	7	243	37	175	82	344	51.00
166	55	P	Ey-166	b	Other high-Ti	48.22	2.50	15.36	2.67	8.89	0.18	6.42	11.17	2.30	0.14	0.21	1.18	99.25	167	58	103	102	1	288	29	138	65	307	53.50
175	145	A	Ey-175	b	Other high-Ti	46.80	3.01	14.48	5.72	7.69	0.25	6.37	10.48	2.55	0.59	0.26	1.73	99.95	327	57	139	120	16	242	36	181	80	374	50.10
200	85	P	Ey-200	b	Other high-Ti	49.21	2.23	13.28	3.15	10.43	0.23	6.34	10.88	2.34	0.32	0.23	1.23	99.86	72	57	61	109	7	168	39	136	85	431	49.20
201	45	P	Ey-201	b	Other high-Ti	49.08	2.21	13.16	2.96	10.66	0.23	6.49	10.80	2.27	0.28	0.22	1.01	99.38	69	73	60	115	3	164	39	133	90	442	49.60

Rasmussen and Noe-Nygaard (1969)
Repeated dyke numbers counted as a single dyke during this study

Fugloy

8	9			

Viðoy

24	25			
20	21			
15	16			

Borðoy

3	4	70		
5	6			
8	14			
65	63			
60	59	58	57	
12	13			
28	29			
32	33	35		
34	36			
52	51	50		
47	46	45	44	43

Kunoy

3	6	7		
15	16	36	37	39
31	32	33		
28	29	30		
17	27			
22	23			

Kalsoy

3	4			
4	5			
47	48	49		
8	45			
9	10	40		
11	44			
14	39			
15	38	37		
18	19	35	34	
21	22			
24	33			
25	26	32		
27	31			
28	30			

Eysturoy

2	4			
3	5			
7	8			
17	18			
31	32	33	34	
48	49			
23	24			

65	66	67	92			
71	72	73				
145	144					
112	113	114				
130	131	132				
107	109					
94	95	96				
98	88	87	59	196	197	
81	82	83				
53	57	58				
52	54	55	56			
174	192	191	186	51		
182	183					
17	18					
19	20	22				
187	188					
189	190					
168	169	170	180			
171	175					
177	195					
203	204					
157	158	159	160			

Streymoy

27	36	38				
39	40					
78	79					
80	81					
50	51					
52	53					
83	84					
85	86					
62	63					
64	65					
108	109	111	116	115		
106	107	114	113			
105	81	60				
59	81	60				
59	75	77				
88	89					
90	91					
92	93	112	118			
120	134					
150	151	152				
156	160	161				
139	140	141				
129	130					
132	133					
143	144	146				
182	183					
145	179					
147	148					
187	190	191	192			
188	189	193				
215	197	198	199	200	221	216
204	205					

209	217		
222	223		
218	219		
226	227	228	229
1	7	8	
4	5		

Vagar

76	105	
84	85	86
87	88	
100	101	99
78	81	
37	39	
38	45	
43	44	
61	62	63
52	55	
66	67	
32	29	
26	27	
30	31	

Hestur

1	3

Nolsoy

2	3

Sandoy

3	4
7	8

Suðuroy

10	11	
17	18	
20	22	23
27	28	
29	30	
42	43	

MyFault calculation outputs

Event1

1. W. Sandur

#	Dip Azim	Dip	Trend	Plunge	Type	QF	Wt	Slip Sense
1	71	73	94	72	Straia	[4]	1.	Normal
2	75	53	83	53	Straia	[4]	1.	Normal
3	79	81	113	79	Straia	[4]	1.	Normal
4	118	70				[4]	1.	Tension Fracture
5	125	79				[4]	1.	Tension Fracture
6	103	82				[4]	1.	Tension Fracture
7	112	86				[4]	1.	Tension Fracture
8	102	81				[4]	1.	Tension Fracture
9	99	82				[4]	1.	Tension Fracture
10	100	89				[4]	1.	Tension Fracture
11	116	85				[4]	1.	Tension Fracture

2. Hvannhagi

#	Dip Azim	Dip	Trend	Plunge	Type	QF	Wt	Slip Sense	Norm. Stress	Shear Stress	Max. Shear	Misfit Angle	Fault Angle
1	100	80	111	80	Straia	[4]	1.	Normal	.254	.433	.435	5.	30.2
2	277	51	261	50	Straia	[4]	1.	Left Normal	.109	.289	.303	17.9	18.4
3	277	27	275	27	Straia	[4]	1.	Normal	.462	.493	.494	4.	42.4
4	293	40	307	39	Straia	[4]	1.	Right-Normal	.261	.402	.439	23.5	30.7
5	302	17	268	14	Straia	[4]	1.	Left Normal	.654	.464	.476	12.8	54.
6	303	25	263	20	Straia	[4]	1.	Left Normal	.528	.478	.499	16.6	46.5
7	129	76	210	31	Straia	[4]	1.	Normal-Right SS	.322	.162	.41	66.7	28.8
8	244	46	253	46	Straia	[4]	1.	Normal	.289	.314	.373	32.8	24.4
9	244	81	282	79	Straia	[4]	1.	Normal	.206	-.147	.256	125.1	10.2
10	84	88	171	57	Straia	[4]	1.	Right-Normal	.194	.354	.363	13.2	22.8

3. Froðba

#	Dip Azim	Dip	Trend	Plunge	Type	QF	Wt	Slip Sense	Norm. Stress	Shear Stress	Max. Shear	Misfit Angle	Fault Angle
1	96	61	96	61	Straia	[4]	1.	Normal	.503	.481	.491	11.5	44.2
2	106	67	84	65	Straia	[4]	1.	Normal	.375	.463	.483	16.6	37.7
3	107	53	119	52	Straia	[4]	1.	Normal	.614	.487	.487	.2	51.6
4	108	79	163	71	Straia	[4]	1.	Right-Normal	.188	.387	.39	7.3	25.6
5	291	39	273	38	Straia	[4]	1.	Left Normal	.355	.466	.477	12.4	36.4
6	123	62	112	62	Straia	[4]	1.	Normal	.447	.484	.486	3.8	40.7
7	125	66	179	53	Straia	[4]	1.	Right-Normal	.381	.397	.47	32.3	36.4
8	96	61	96	61	Straia	[4]	1.	Normal	.433	.462	.47	10.	39.2
9	106	67	84	65	Straia	[4]	1.	Normal	.368	.423	.424	3.4	33.
10	107	53	119	52	Straia	[4]	1.	Normal	.585	.436	.452	15.2	46.9
11	108	79	163	71	Straia	[4]	1.	Right-Normal	.223	.264	.321	34.7	20.9
12	291	39	273	38	Straia	[4]	1.	Left Normal	.494	.452	.453	2.	41.1
13	123	62	112	62	Straia	[4]	1.	Normal	.48	.401	.402	2.7	36.9
14	125	66	179	53	Straia	[4]	1.	Right-Normal	.429	.3	.379	37.7	32.7
15	12	45	2	45	Straia	[4]	1.	Normal	.614	.395	.395	2.3	45.3
16	17	48	5	47	Straia	[4]	1.	Normal	.575	.406	.408	5.7	43.3
17	18	21	15	21	Straia	[4]	1.	Normal	.903	.237	.253	21.	68.9
18	25	51	17	51	Straia	[4]	1.	Normal	.533	.426	.427	4.9	41.8
19	31	48	6	45	Straia	[4]	1.	Left Normal	.58	.424	.44	15.8	45.7
20	33	76	13	75	Straia	[4]	1.	Normal	.191	.28	.297	19.4	18.5
21	35	49	26	49	Straia	[4]	1.	Normal	.565	.449	.451	5.1	45.4
22	44	48	31	47	Straia	[4]	1.	Normal	.584	.463	.466	7.	47.8
23	47	62	39	62	Straia	[4]	1.	Normal	.355	.449	.451	5.7	34.5
24	52	58	63	58	Straia	[4]	1.	Normal	.419	.474	.477	6.6	39.1
25	57	51	37	49	Straia	[4]	1.	Left Normal	.54	.483	.49	9.9	46.7
26	59	61	73	60	Straia	[4]	1.	Normal	.371	.471	.476	8.8	37.
27	60	74	22	70	Straia	[4]	1.	Left Normal	.176	.365	.373	12.2	24.2
28	60	56	51	56	Straia	[4]	1.	Normal	.457	.492	.492	2.2	42.1
29	66	52	61	52	Straia	[4]	1.	Normal	.531	.497	.498	1.6	46.7
30	68	60	78	60	Straia	[4]	1.	Normal	.395	.482	.488	9.4	38.9
31	74	55	65	55	Straia	[4]	1.	Normal	.49	.5	.5	1.	44.4

32	77	56	81	56	Straia	[4]	1.	Normal	.477	.493	.498	8.6	43.6
33	78	72	139	56	Straia	[4]	1.	Right-Normal	.22	.328	.411	37.	27.7
34	80	60	84	60	Straia	[4]	1.	Normal	.414	.483	.489	9.3	39.8
35	82	51	80	51	Straia	[4]	1.	Normal	.571	.489	.492	6.3	48.9
36	83	60	101	59	Straia	[4]	1.	Normal	.42	.466	.488	17.	39.9
37	86	62	67	61	Straia	[4]	1.	Normal	.393	.478	.478	.2	38.

4. Vagseiði

#	Dip Azim	Dip	Trend	Plunge	Type	QF	Wt	Slip Sense	Norm. Stress	Shear Stress	Max. Shear	Misfit Angle	Fault Angle
1	90	63	90	63	Straia	[4]	1.	Normal	.444	.478	.489	12.3	40.9
2	90	25	99	25	Straia	[4]	1.	Normal	.962	.19	.191	4.6	78.8
3	92	65	85	65	Straia	[4]	1.	Normal	.404	.469	.485	14.6	38.8
4	102	67	128	65	Straia	[4]	1.	Right-Normal	.347	.474	.476	5.1	36.1
5	102	61	143	54	Straia	[4]	1.	Right-Normal	.449	.475	.497	17.2	42.1
6	103	79	149	74	Straia	[4]	1.	Right-Normal	.166	.371	.372	5.2	24.1
7	283	63	331	53	Straia	[4]	1.	Right-Normal	.059	.212	.233	24.6	13.8
8	89	71	80	71	Straia	[4]	1.	Normal	.318	.431	.453	17.9	32.9
9	90	63	90	63	Straia	[4]	1.	Normal	.352	.309	.359	30.6	25.8
10	90	25	99	25	Straia	[4]	1.	Normal	.841	.301	.333	25.5	63.7
11	92	65	85	65	Straia	[4]	1.	Normal	.343	.295	.34	29.8	23.8
12	102	67	128	65	Straia	[4]	1.	Right-Normal	.381	.209	.299	45.6	22.
13	102	61	143	54	Straia	[4]	1.	Right-Normal	.438	.207	.337	52.1	28.
14	103	79	149	74	Straia	[4]	1.	Right-Normal	.309	.083	.209	66.6	10.
15	283	63	331	53	Straia	[4]	1.	Right-Normal	.449	.2	.329	52.6	27.9
16	89	71	80	71	Straia	[4]	1.	Normal	.27	.24	.299	36.7	17.7
17	184	61	188	61	Straia	[4]	1.	Normal	.375	.372	.4	21.3	30.2
18	5	79	360	79	Straia	[4]	1.	Normal	.176	.135	.236	55.	9.8
19	5	51	22	50	Straia	[4]	1.	Right-Normal	.467	.432	.439	10.4	37.8
20	5	58	25	56	Straia	[4]	1.	Right-Normal	.372	.397	.408	13.8	30.8
21	6	51	353	50	Straia	[4]	1.	Normal	.463	.386	.442	29.	37.8
22	6	61	43	55	Straia	[4]	1.	Right-Normal	.329	.388	.391	6.5	27.8
23	7	57	9	57	Straia	[4]	1.	Normal	.375	.386	.418	22.5	31.8
24	7	47	10	47	Straia	[4]	1.	Normal	.518	.432	.452	17.3	41.8

25	8	49	14	49	Straia	[4]	1.	Normal	.484	.435	.452	15.6	39.7
26	8	68	24	67	Straia	[4]	1.	Normal	.24	.302	.336	26.1	20.7
27	188	63	220	59	Straia	[4]	1.	Right-Normal	.33	.392	.396	7.3	28.3
28	9	49	9	49	Straia	[4]	1.	Normal	.48	.429	.454	19.2	39.7
29	9	49	38	45	Straia	[4]	1.	Right-Normal	.48	.454	.454	.8	39.7
30	10	72	324	65	Straia	[4]	1.	Left Normal	.191	.173	.298	54.4	16.7
31	10	49	346	47	Straia	[4]	1.	Left Normal	.476	.374	.456	34.8	39.7
32	11	65	13	65	Straia	[4]	1.	Normal	.255	.327	.365	26.4	23.7
33	11	54	13	54	Straia	[4]	1.	Normal	.398	.416	.441	19.4	34.7
34	11	48	15	48	Straia	[4]	1.	Normal	.487	.444	.46	15.1	40.7
35	12	44	2	44	Straia	[4]	1.	Normal	.546	.426	.465	23.6	44.7
36	13	43	358	42	Straia	[4]	1.	Left Normal	.558	.416	.467	27.	45.6
37	14	46	338	40	Straia	[4]	1.	Left Normal	.508	.341	.469	43.3	42.6
38	14	55	34	53	Straia	[4]	1.	Right-Normal	.371	.437	.441	7.4	33.6
39	195	89	279	81	Straia	[4]	1.	Normal	.092	.065	.169	67.2	2.4
40	16	55	23	55	Straia	[4]	1.	Normal	.363	.43	.444	14.4	33.6
41	17	76	17	76	Straia	[4]	1.	Normal	.122	.194	.248	38.7	12.6
42	197	43	209	42	Straia	[4]	1.	Normal	.596	.466	.467	2.9	48.4
43	17	59	63	49	Straia	[4]	1.	Right-Normal	.301	.415	.419	8.3	29.6
44	18	65	347	62	Straia	[4]	1.	Left Normal	.22	.293	.367	37.1	23.6
45	19	82	347	81	Straia	[4]	1.	Normal	.08	.09	.181	60.1	6.6
46	19	66	21	66	Straia	[4]	1.	Normal	.204	.331	.357	22.2	22.6
47	19	47	25	47	Straia	[4]	1.	Normal	.476	.469	.477	10.2	41.6
48	20	70	346	66	Straia	[4]	1.	Left Normal	.157	.242	.314	39.4	18.5
49	20	47	26	47	Straia	[4]	1.	Normal	.473	.472	.478	9.8	41.5
50	20	43	31	42	Straia	[4]	1.	Normal	.539	.479	.48	4.9	45.5
51	21	52	21	52	Straia	[4]	1.	Normal	.39	.45	.465	14.6	36.5
52	21	60	21	60	Straia	[4]	1.	Normal	.272	.394	.414	17.8	28.5
53	21	69	37	68	Straia	[4]	1.	Normal	.162	.308	.324	18.4	19.5
54	22	81	344	79	Straia	[4]	1.	Normal	.069	.104	.181	54.9	7.5
55	22	33	28	33	Straia	[4]	1.	Normal	.695	.448	.45	5.6	55.5
56	22	72	70	64	Straia	[4]	1.	Right-Normal	.129	.285	.288	8.1	16.5
57	23	79	13	79	Straia	[4]	1.	Normal	.074	.149	.2	42.	9.5

58	23	74	19	74	Straia	[4]	1.	Normal	.108	.227	.262	30.	14.5
59	23	51	25	51	Straia	[4]	1.	Normal	.4	.461	.471	12.2	37.5
60	24	41	355	37	Straia	[4]	1.	Left Normal	.562	.403	.484	33.6	47.5
61	204	51	182	49	Straia	[4]	1.	Left Normal	.449	.436	.48	24.7	40.5
62	24	45	11	44	Straia	[4]	1.	Normal	.496	.456	.486	20.3	43.5
63	24	53	14	53	Straia	[4]	1.	Normal	.365	.438	.463	19.2	35.5
64	204	90	159	90	Straia	[4]	1.	Normal	.045	.026	.127	77.9	1.5
65	24	33	30	33	Straia	[4]	1.	Normal	.692	.452	.453	4.7	55.5
66	24	47	44	45	Straia	[4]	1.	Right-Normal	.462	.484	.484	2.3	41.5
67	24	67	58	63	Straia	[4]	1.	Right-Normal	.172	.344	.346	5.	21.5
68	205	89	284	85	Straia	[4]	1.	Normal	.042	.054	.126	64.9	2.5
69	28	54	31	54	Straia	[4]	1.	Normal	.339	.456	.461	8.9	34.5
70	28	39	37	39	Straia	[4]	1.	Normal	.588	.485	.485	1.4	49.5
71	28	35	51	33	Straia	[4]	1.	Right-Normal	.655	.461	.47	11.	53.5
72	29	50	43	49	Straia	[4]	1.	Normal	.401	.481	.481	.4	38.4
73	29	45	48	43	Straia	[4]	1.	Right-Normal	.485	.49	.492	5.4	43.4
74	30	44	22	44	Straia	[4]	1.	Normal	.5	.479	.494	13.9	44.4
75	31	74	332	61	Straia	[4]	1.	Left Normal	.079	.179	.25	44.3	14.4
76	31	60	33	60	Straia	[4]	1.	Normal	.241	.412	.417	9.5	28.4
77	31	64	38	64	Straia	[4]	1.	Normal	.186	.373	.377	9.	24.4
78	32	61	20	60	Straia	[4]	1.	Normal	.224	.392	.408	16.	27.4
79	32	50	43	49	Straia	[4]	1.	Normal	.395	.483	.483	.6	38.4
80	33	60	17	59	Straia	[4]	1.	Normal	.236	.399	.418	16.9	28.4
81	33	71	45	71	Straia	[4]	1.	Normal	.101	.285	.29	9.9	17.4
82	34	46	25	46	Straia	[4]	1.	Normal	.46	.484	.495	11.9	42.4
83	214	61	206	61	Straia	[4]	1.	Normal	.268	.429	.437	11.1	30.6
84	34	39	30	39	Straia	[4]	1.	Normal	.581	.486	.491	8.3	49.4
85	34	88	114	79	Straia	[4]	1.	Right-Normal	.011	.019	.065	73.3	.4
86	34	74	74	69	Straia	[4]	1.	Right-Normal	.072	.246	.246	2.	14.4
87	35	19	58	18	Straia	[4]	1.	Right-Normal	.877	.312	.328	17.7	69.4
88	36	42	27	42	Straia	[4]	1.	Normal	.527	.488	.497	11.4	46.4
89	216	63	205	63	Straia	[4]	1.	Normal	.235	.412	.42	11.	28.6
90	37	33	31	33	Straia	[4]	1.	Normal	.679	.461	.466	8.5	55.4

91	217	47	244	44	Straia	[4]	1.	Right-Normal	.496	.48	.498	15.6	44.6
92	38	44	7	40	Straia	[4]	1.	Left Normal	.491	.447	.499	26.4	44.4
93	38	47	37	47	Straia	[4]	1.	Normal	.439	.493	.495	4.6	41.4
94	39	78	353	73	Straia	[4]	1.	Left Normal	.035	.166	.179	22.2	10.4
95	40	63	23	62	Straia	[4]	1.	Normal	.185	.379	.387	11.5	25.4
96	220	68	225	68	Straia	[4]	1.	Normal	.162	.367	.367	1.4	23.6
97	220	81	233	81	Straia	[4]	1.	Normal	.036	.182	.183	5.6	10.6
98	40	67	45	67	Straia	[4]	1.	Normal	.134	.339	.34	2.1	21.4
99	221	53	193	49	Straia	[4]	1.	Left Normal	.39	.459	.487	19.5	38.6
100	221	52	211	52	Straia	[4]	1.	Normal	.407	.487	.491	7.5	39.6
101	41	49	36	49	Straia	[4]	1.	Normal	.403	.488	.49	4.8	39.4
102	41	39	41	39	Straia	[4]	1.	Normal	.576	.494	.494	1.6	49.4
103	42	49	24	48	Straia	[4]	1.	Left Normal	.402	.477	.49	13.2	39.4
104	42	85	122	63	Straia	[4]	1.	Right-Normal	.004	.057	.06	15.8	3.4
105	223	90	133	65	Straia	[4]	1.	Left Normal	.001	.024	.029	34.3	1.6
106	223	67	189	63	Straia	[4]	1.	Left Normal	.174	.365	.379	15.5	24.6
107	223	33	217	33	Straia	[4]	1.	Normal	.729	.443	.444	5.1	58.6
108	224	32	216	32	Straia	[4]	1.	Normal	.745	.433	.436	6.7	59.6
109	224	55	226	55	Straia	[4]	1.	Normal	.356	.479	.479	1.3	36.6
110	224	55	229	55	Straia	[4]	1.	Normal	.356	.478	.479	3.3	36.6
111	225	48	210	47	Straia	[4]	1.	Left Normal	.476	.493	.499	9.2	43.6
112	45	60	29	59	Straia	[4]	1.	Normal	.226	.415	.418	7.	28.4
113	45	78	76	76	Straia	[4]	1.	Normal	.033	.174	.177	9.8	10.4
114	46	42	37	42	Straia	[4]	1.	Normal	.524	.497	.499	5.8	46.4
115	46	59	44	59	Straia	[4]	1.	Normal	.241	.427	.427	.8	29.4
116	47	38	33	37	Straia	[4]	1.	Left Normal	.593	.484	.491	9.4	50.4
117	48	67	24	65	Straia	[4]	1.	Left Normal	.134	.338	.339	5.4	21.4
118	48	47	34	46	Straia	[4]	1.	Left Normal	.438	.491	.495	7.5	41.4
119	48	41	47	41	Straia	[4]	1.	Normal	.542	.497	.498	1.3	47.4
120	48	49	50	49	Straia	[4]	1.	Normal	.403	.489	.49	3.6	39.4
121	229	89	142	71	Straia	[4]	1.	Left Normal	.005	.055	.058	19.	2.6
122	49	44	35	43	Straia	[4]	1.	Left Normal	.49	.495	.499	7.	44.4
123	49	45	48	45	Straia	[4]	1.	Normal	.473	.498	.498	2.	43.4

124	49	67	54	67	Straia	[4]	1.	Normal	.135	.337	.34	7.7	21.4
125	50	48	31	46	Straia	[4]	1.	Left Normal	.422	.486	.492	9.2	40.4
126	50	59	31	58	Straia	[4]	1.	Left Normal	.244	.425	.427	5.	29.4
127	50	74	57	74	Straia	[4]	1.	Normal	.066	.237	.243	11.8	14.4
128	50	56	55	56	Straia	[4]	1.	Normal	.29	.447	.451	7.6	32.4
129	50	45	58	45	Straia	[4]	1.	Normal	.474	.491	.498	9.6	43.4
130	51	47	55	47	Straia	[4]	1.	Normal	.44	.49	.494	7.4	41.4
131	51	53	56	53	Straia	[4]	1.	Normal	.339	.466	.471	8.	35.4
132	51	64	81	61	Straia	[4]	1.	Right-Normal	.175	.351	.376	20.9	24.4
133	232	50	224	50	Straia	[4]	1.	Normal	.446	.494	.494	.2	41.6
134	52	54	52	54	Straia	[4]	1.	Normal	.324	.462	.464	5.8	34.4
135	52	61	54	61	Straia	[4]	1.	Normal	.218	.404	.408	8.1	27.4
136	52	54	78	51	Straia	[4]	1.	Right-Normal	.324	.431	.464	21.8	34.4
137	53	80	104	74	Straia	[4]	1.	Right-Normal	.031	.126	.155	35.5	8.4
138	234	56	225	56	Straia	[4]	1.	Normal	.348	.471	.471	1.7	35.6
139	54	75	46	75	Straia	[4]	1.	Normal	.065	.224	.232	14.9	13.4
140	54	62	62	62	Straia	[4]	1.	Normal	.207	.387	.398	13.	26.4
141	54	48	76	46	Straia	[4]	1.	Right-Normal	.426	.457	.49	21.3	40.4
142	55	58	42	57	Straia	[4]	1.	Normal	.266	.434	.435	1.7	30.4
143	55	65	48	65	Straia	[4]	1.	Normal	.17	.362	.365	8.	23.4
144	55	46	68	45	Straia	[4]	1.	Normal	.462	.475	.494	15.6	42.4
145	236	33	229	33	Straia	[4]	1.	Normal	.734	.438	.438	.7	58.6
146	56	57	61	57	Straia	[4]	1.	Normal	.284	.432	.442	12.2	31.4
147	57	37	58	37	Straia	[4]	1.	Normal	.618	.477	.481	7.8	51.4
148	57	54	99	46	Straia	[4]	1.	Right-Normal	.332	.368	.462	37.2	34.4
149	58	47	44	46	Straia	[4]	1.	Left Normal	.45	.489	.489	1.5	41.4
150	58	59	54	59	Straia	[4]	1.	Normal	.258	.42	.425	9.3	29.4
151	58	74	82	73	Straia	[4]	1.	Normal	.084	.221	.252	28.3	14.4
152	59	75	17	70	Straia	[4]	1.	Left Normal	.079	.235	.239	11.1	13.4
153	59	61	35	59	Straia	[4]	1.	Left Normal	.233	.407	.407	.8	27.4
154	59	55	61	55	Straia	[4]	1.	Normal	.321	.445	.455	11.8	33.4
155	59	65	68	65	Straia	[4]	1.	Normal	.18	.347	.366	18.7	23.4
156	60	61	40	59	Straia	[4]	1.	Left Normal	.235	.406	.407	3.5	27.4

157	60	59	58	59	Straia	[4]	1.	Normal	.264	.416	.425	11.7	29.4
158	60	71	57	71	Straia	[4]	1.	Normal	.117	.278	.294	19.2	17.4
159	60	84	124	77	Straia	[4]	1.	Right-Normal	.036	.05	.128	67.2	4.4
160	60	44	82	42	Straia	[4]	1.	Right-Normal	.504	.444	.491	25.1	44.4
161	241	42	220	40	Straia	[4]	1.	Left Normal	.595	.477	.481	7.8	49.6
162	61	54	54	54	Straia	[4]	1.	Normal	.342	.455	.459	7.8	34.4
163	61	61	63	61	Straia	[4]	1.	Normal	.238	.392	.407	15.3	27.4
164	62	43	41	41	Straia	[4]	1.	Left Normal	.525	.485	.488	6.	45.4
165	62	51	65	51	Straia	[4]	1.	Normal	.392	.46	.473	13.6	37.4
166	62	62	90	59	Straia	[4]	1.	Right-Normal	.228	.345	.397	29.5	26.4
167	62	54	87	51	Straia	[4]	1.	Right-Normal	.345	.407	.459	27.4	34.4
168	63	25	27	21	Straia	[4]	1.	Left Normal	.807	.354	.388	24.3	63.4
169	243	84	307	77	Straia	[4]	1.	Right-Normal	.06	.098	.174	55.6	7.6
170	64	49	42	47	Straia	[4]	1.	Left Normal	.43	.478	.478	2.7	39.4
171	64	45	47	44	Straia	[4]	1.	Left Normal	.496	.485	.485	.6	43.4
172	64	54	52	53	Straia	[4]	1.	Normal	.351	.454	.457	6.7	34.4
173	65	54	73	54	Straia	[4]	1.	Normal	.354	.43	.456	19.3	34.4
174	65	69	115	59	Straia	[4]	1.	Right-Normal	.156	.223	.322	46.1	19.4
175	246	57	233	56	Straia	[4]	1.	Normal	.361	.451	.455	7.	34.6
176	66	53	71	53	Straia	[4]	1.	Normal	.372	.439	.46	17.5	35.4
177	67	56	86	54	Straia	[4]	1.	Right-Normal	.33	.393	.442	27.2	32.4
178	69	68	121	56	Straia	[4]	1.	Right-Normal	.184	.209	.335	51.4	20.5
179	70	51	62	51	Straia	[4]	1.	Normal	.417	.455	.463	11.	37.5
180	250	61	254	61	Straia	[4]	1.	Normal	.316	.4	.425	19.8	30.5
181	251	81	171	47	Straia	[4]	1.	Left-Normal Diag.	.113	.228	.228	1.	10.5
182	71	51	49	49	Straia	[4]	1.	Left Normal	.42	.461	.462	2.5	37.5
183	72	62	91	61	Straia	[4]	1.	Normal	.268	.335	.393	31.4	26.5
184	74	65	51	63	Straia	[4]	1.	Left Normal	.241	.351	.365	16.	23.5
185	74	65	88	64	Straia	[4]	1.	Normal	.241	.309	.365	32.	23.5
186	76	60	74	60	Straia	[4]	1.	Normal	.312	.374	.404	22.3	28.5
187	256	65	265	65	Straia	[4]	1.	Normal	.29	.344	.388	27.4	26.5
188	76	69	107	66	Straia	[4]	1.	Right-Normal	.21	.237	.326	43.4	19.5
189	79	65	50	62	Straia	[4]	1.	Left Normal	.268	.348	.361	15.7	23.6

190	79	40	88	40	Straia	[4]	1.	Normal	.617	.412	.451	23.8	48.6
191	80	41	75	41	Straia	[4]	1.	Normal	.605	.438	.45	13.3	47.6
192	80	81	151	64	Straia	[4]	1.	Right-Normal	.151	.025	.217	83.4	7.6
193	80	58	140	38	Straia	[4]	1.	Right-Normal Diag.	.358	.162	.412	66.8	30.6
194	262	56	246	55	Straia	[4]	1.	Normal	.438	.42	.428	11.2	35.4
195	262	79	229	77	Straia	[4]	1.	Normal	.19	.202	.257	38.4	12.4
196	84	61	84	61	Straia	[4]	1.	Normal	.341	.342	.385	27.3	27.7
197	84	68	87	68	Straia	[4]	1.	Normal	.266	.27	.33	35.1	20.7

5. Sumba

#	Dip Azim	Dip	Trend	Plunge	Type	QF	Wt	Slip Sense
1	59	83	121	75	Straia	[4]	1.	Right-Normal
2	244	55	219	52	Straia	[4]	1.	Left Normal
3	283	78	235	72	Straia	[4]	1.	Left Normal

6. Gasadalur

#	Dip Azim	Dip	Trend	Plunge	Type	QF	Wt	Slip Sense	Norm. Stress	Shear Stress	Max. Shear	Misfit Angle	Fault Angle
1	284	59	284	59	Straia	[4]	1.	Normal	.268	.416	.432	15.9	30.
2	284	35	307	33	Straia	[4]	1.	Right-Normal	.659	.468	.471	7.2	53.9
3	286	44	300	43	Straia	[4]	1.	Normal	.504	.496	.497	1.2	44.9
4	287	59	268	58	Straia	[4]	1.	Left Normal	.258	.396	.431	23.3	29.8
5	288	51	269	49	Straia	[4]	1.	Left Normal	.381	.445	.482	22.6	37.8
6	288	52	278	52	Straia	[4]	1.	Normal	.365	.457	.478	16.8	36.8
7	288	31	281	31	Straia	[4]	1.	Normal	.716	.434	.45	15.4	57.7
8	288	40	289	40	Straia	[4]	1.	Normal	.568	.488	.494	8.6	48.7
9	293	58	326	53	Straia	[4]	1.	Right-Normal	.259	.428	.437	11.5	30.5
10	294	56	299	56	Straia	[4]	1.	Normal	.289	.452	.453	3.4	32.4
11	295	58	271	56	Straia	[4]	1.	Left Normal	.256	.414	.436	18.6	30.4
12	295	43	285	43	Straia	[4]	1.	Normal	.506	.489	.5	12.	45.4
13	295	36	305	36	Straia	[4]	1.	Normal	.627	.483	.484	2.9	52.3
14	297	45	305	45	Straia	[4]	1.	Normal	.47	.499	.499	2.4	43.3
15	300	32	307	32	Straia	[4]	1.	Normal	.69	.461	.462	3.7	56.1
16	301	50	304	50	Straia	[4]	1.	Normal	.382	.485	.485	1.6	38.1

17	304	38	305	38	Straia	[4]	1.	Normal	.589	.489	.49	1.7	49.9
18	307	37	270	31	Straia	[4]	1.	Left Normal	.607	.426	.484	28.5	50.7
19	308	57	292	56	Straia	[4]	1.	Normal	.273	.438	.438	2.4	30.7
20	312	39	313	39	Straia	[4]	1.	Normal	.577	.482	.485	7.	48.5
21	313	37	317	37	Straia	[4]	1.	Normal	.612	.472	.478	9.3	50.5
22	314	29	322	29	Straia	[4]	1.	Normal	.74	.42	.43	12.5	58.4
23	319	33	326	33	Straia	[4]	1.	Normal	.683	.435	.451	15.	54.2
24	320	45	324	45	Straia	[4]	1.	Normal	.491	.461	.478	15.4	42.2
25	142	15	56	1	Straia	[4]	1.	Left SS	.955	.072	.205	69.6	77.7
26	322	44	279	35	Straia	[4]	1.	Left Normal	.513	.445	.475	20.7	43.1
27	151	59	163	58	Straia	[4]	1.	Normal	.401	.378	.442	31.1	34.1
28	284	59	284	59	Straia	[4]	1.	Normal	.269	.441	.441	.4	31.1
29	284	35	307	33	Straia	[4]	1.	Right-Normal	.674	.446	.467	17.	55.
30	286	44	300	43	Straia	[4]	1.	Normal	.521	.489	.496	9.9	45.9
31	287	59	268	58	Straia	[4]	1.	Left Normal	.27	.435	.439	7.6	30.9
32	288	51	269	49	Straia	[4]	1.	Left Normal	.401	.477	.485	10.2	38.8
33	288	52	278	52	Straia	[4]	1.	Normal	.384	.48	.481	4.1	37.8
34	288	31	281	31	Straia	[4]	1.	Normal	.736	.434	.437	6.9	58.7
35	288	40	289	40	Straia	[4]	1.	Normal	.59	.487	.487	1.4	49.8
36	293	58	326	53	Straia	[4]	1.	Right-Normal	.292	.4	.441	25.	31.5
37	294	56	299	56	Straia	[4]	1.	Normal	.324	.448	.454	9.1	33.5
38	295	58	271	56	Straia	[4]	1.	Left Normal	.295	.437	.439	5.7	31.4
39	295	43	285	43	Straia	[4]	1.	Normal	.542	.486	.487	3.1	46.4
40	295	36	305	36	Straia	[4]	1.	Normal	.658	.456	.464	10.7	53.4
41	297	45	305	45	Straia	[4]	1.	Normal	.51	.476	.485	11.1	44.3
42	300	32	307	32	Straia	[4]	1.	Normal	.723	.427	.433	9.8	57.1
43	301	50	304	50	Straia	[4]	1.	Normal	.432	.465	.472	10.1	39.1
44	304	38	305	38	Straia	[4]	1.	Normal	.633	.457	.46	7.4	50.9
45	307	37	270	31	Straia	[4]	1.	Left Normal	.652	.413	.451	23.8	51.7
46	308	57	292	56	Straia	[4]	1.	Normal	.34	.426	.427	4.9	31.7
47	312	39	313	39	Straia	[4]	1.	Normal	.628	.441	.448	10.2	49.5
48	313	37	317	37	Straia	[4]	1.	Normal	.66	.429	.438	12.	51.4
49	314	29	322	29	Straia	[4]	1.	Normal	.776	.375	.387	14.2	59.3

50	319	33	326	33	Straia	[4]	1.	Normal	.726	.39	.405	15.3	55.1
51	320	45	324	45	Straia	[4]	1.	Normal	.553	.42	.437	16.	43.1
52	142	15	56	1	Straia	[4]	1.	Left SS	.952	.089	.207	64.4	76.7
53	322	44	279	35	Straia	[4]	1.	Left Normal	.572	.403	.431	20.9	44.
54	151	59	163	58	Straia	[4]	1.	Normal	.444	.339	.393	30.2	33.3
55	273	50	285	49	Straia	[4]	1.	Normal	.426	.494	.494	1.7	40.7
56	274	66	264	66	Straia	[4]	1.	Normal	.176	.372	.379	11.	24.7
57	275	42	296	40	Straia	[4]	1.	Right-Normal	.562	.488	.496	10.6	48.5
58	278	49	297	47	Straia	[4]	1.	Right-Normal	.437	.489	.496	9.3	41.4
59	229	64	247	63	Straia	[4]	1.	Normal	.387	.351	.369	18.1	28.8
60	229	45	243	44	Straia	[4]	1.	Normal	.637	.412	.417	8.8	47.8
61	230	81	259	80	Straia	[4]	1.	Normal	.233	.169	.232	43.4	11.8
62	231	55	224	55	Straia	[4]	1.	Normal	.491	.376	.417	25.6	37.7
63	232	51	254	49	Straia	[4]	1.	Right-Normal	.542	.425	.428	6.3	41.7
64	236	37	245	37	Straia	[4]	1.	Normal	.726	.403	.41	10.5	55.5
65	237	61	212	58	Straia	[4]	1.	Left Normal	.383	.325	.406	36.8	31.5
66	240	51	231	51	Straia	[4]	1.	Normal	.51	.407	.45	25.3	41.4
67	242	43	279	37	Straia	[4]	1.	Right-Normal	.623	.442	.451	11.7	49.3
68	246	7	216	6	Straia	[4]	1.	Left Normal	.991	.048	.095	59.8	84.5
69	251	55	241	55	Straia	[4]	1.	Normal	.405	.422	.46	23.4	36.9
70	251	48	255	48	Straia	[4]	1.	Normal	.515	.465	.477	12.7	43.9
71	254	41	250	41	Straia	[4]	1.	Normal	.619	.452	.472	16.8	50.7
72	254	49	266	48	Straia	[4]	1.	Normal	.489	.477	.481	6.9	42.7
73	257	41	241	40	Straia	[4]	1.	Left Normal	.611	.433	.477	24.8	50.5
74	258	42	221	36	Straia	[4]	1.	Left Normal	.592	.361	.482	41.5	49.5
75	264	56	286	54	Straia	[4]	1.	Right-Normal	.345	.466	.467	1.3	35.2
76	266	41	267	41	Straia	[4]	1.	Normal	.592	.484	.489	8.3	50.
77	269	40	253	39	Straia	[4]	1.	Left Normal	.604	.458	.488	20.	50.9

7. Sanavagur

#	Dip Azim	Dip	Trend	Plunge	Type	QF	Wt	Slip Sense
1	32	77	103	55	Straia	[4]	1.	Right-Normal
2	238	72	262	70	Straia	[4]	1.	Normal
3	46	67	54	67	Straia	[4]	1.	Normal

Event 2

1. Muli

#	Dip Azim	Dip	Trend	Plunge	Type	QF	Wt	Slip Sense	Norm. Stress	Shear Stress	Max. Shear	Misfit Angle	Fault Angle
1	145	80	233	12	Straia	[4]	1.	Normal-Right SS	.372	.478	.483	8.4	37.5
2	156	65	245	3	Straia	[4]	1.	Right SS	.326	.379	.437	29.7	30.8
3	160	90	250	-12	Straia	[4]	1.	Reverse-Right SS	.119	.279	.323	30.2	20.1
4	178	69	260	20	Straia	[4]	1.	Normal-Right SS	.122	.169	.257	49.1	10.2
5	354	84	90	-45	Straia	[4]	1.	Right-Reverse Diag.	.008	.067	.088	40.2	4.9
6	354	19	241	-8	Straia	[4]	1.	Reverse-Left SS	.493	-.005	.254	91.	16.7
7	26	67	317	40	Straia	[4]	1.	Left-Normal Diag.	.256	.398	.43	22.1	29.6
8	199	87	132	82	Straia	[4]	1.	Normal	.103	.063	.278	76.9	15.3

2. Norðdepil

#	Dip Azim	Dip	Trend	Plunge	Type	QF	Wt	Slip Sense	Norm. Stress	Shear Stress	Max. Shear	Misfit Angle	Fault Angle
1	312	81	45	-20	Straia	[4]	1.	Reverse-Right SS	.278	.444	.447	6.8	31.7
2	344	60	83	-16	Straia	[4]	1.	Reverse-Right SS	.034	-.048	.137	110.5	.7
3	340	72	76	-18	Straia	[4]	1.	Reverse-Right SS	.005	.055	.066	33.1	3.6
4	324	70	55	-2	Straia	[4]	1.	Right SS	.105	.303	.303	3.	18.4
5		71	281	29	Straia	[4]	1.	Normal-Left SS	.071	.227	.256	27.5	15.3
6	357	85	266	-11	Straia	[4]	1.	Reverse-Left SS	.07	.227	.237	16.6	12.6
7	310	86	41	-11	Straia	[0]	1.	Reverse-Right SS	.329	.463	.465	4.8	34.3
8	330	64	56	9	Straia	[0]	1.	Normal-Right SS	.064	.223	.227	9.9	12.

9	358	70	4	70	Straia	[0]	1.	Normal	.056	.02	.228	84.9	13.4
10	318	78	48		Straia	[0]	1.	Right SS	.184	.38	.387	11.	25.4
11	357	76	267	1	Straia	[0]	1.	Left SS	.049	.212	.214	8.2	12.6
12	346	54	77	-2	Straia	[0]	1.	Right SS	.069	-.044	.193	103.3	2.6

3. Klaksvik

#	Dip Azim	Dip	Trend	Plunge	Type	QF	Wt	Slip Sense	Norm. Stress	Shear Stress	Max. Shear	Misfit Angle	Fault Angle
1	272	83	182	4	Straia	[0]	1.	Left SS	.07	.094	.228	65.7	11.7
2	251	85	161	5	Straia	[0]	1.	Left SS	.066	-.091	.24	112.2	13.8
3	277	78	191	18	Straia	[0]	1.	Normal-Left SS	.129	.189	.294	50.1	15.5
4	42	62	352	51	Straia	[0]	1.	Left Normal	.282	.071	.328	77.4	15.5
5	55	89	145	18	Straia	[0]	1.	Normal-Right SS	.125	.172	.259	48.4	10.2
6	302	78	8	62	Straia	[0]	1.	Right-Normal	.288	.065	.298	77.3	9.9
7	296	71	20	17	Straia	[0]	1.	Normal-Right SS	.301	-.099	.344	106.8	18.
8	288	70	19	-4	Straia	[4]	1.	Right SS	.265	-.181	.364	119.9	20.8
9	323	73	51	6	Straia	[4]	1.	Right SS	.472	-.166	.227	137.3	10.3

4. Gjogv

#	Dip Azim	Dip	Trend	Plunge	Type	QF	Wt	Slip Sense	Norm. Stress	Shear Stress	Max. Shear	Misfit Angle	Fault Angle
1	321	69	48	8	Straia	[4]	1.	Right SS	.305	.411	.434	19.	31.1
2	321	69	27	47	Straia	[4]	1.	Right-Normal	.305	.4	.434	23.	31.1
3	321	69	57	-16	Straia	[4]	1.	Reverse-Right SS	.305	.307	.434	45.	31.1
4	132	58	238	-24	Straia	[4]	1.	Reverse-Right SS	.19	.248	.284	29.3	15.4
5	106	45	216	-19	Straia	[4]	1.	Reverse-Right SS	.364	.268	.268	1.5	18.8
6	127	70	228	-27	Straia	[4]	1.	Reverse-Right SS	.265	.381	.391	13.	26.3
7	128	56	239	-28	Straia	[4]	1.	Reverse-Right SS	.223	.254	.295	30.8	16.7
8	121	54	230	-24	Straia	[4]	1.	Reverse-Right SS	.281	.296	.313	18.8	19.4
9	120	67	222	-27	Straia	[4]	1.	Reverse-Right SS	.338	.4	.404	8.6	29.3
10	347	67	69	17	Straia	[4]	1.	Normal-Right SS	.12	.129	.213	52.6	8.5
11	324	58	34	28	Straia	[4]	1.	Normal-Right SS	.349	.411	.413	4.2	30.4
12	341	67	63	18	Straia	[4]	1.	Normal-Right SS	.141	.216	.263	34.8	13.7
13	331	78	53	33	Straia	[4]	1.	Normal-Right SS	.133	.319	.319	1.	19.4
14	332	78	58	18	Straia	[4]	1.	Normal-Right SS	.124	.292	.307	18.2	18.5

15	168	84	262	-36	Straia	[4]	1.	Reverse-Right SS	.004	-.04	.054	137.6	2.8
16	151	90	241	-39	Straia	[4]	1.	Reverse-Right SS	.07	.248	.254	12.5	15.2
17	189	81	100	8	Straia	[4]	1.	Left SS	.164	.364	.364	3.4	23.3
18	202	89	113	32	Straia	[4]	1.	Normal-Left SS	.326	.41	.443	22.2	32.4

5. Eiði

#	Dip Azim	Dip	Trend	Plunge	Type	QF	Wt	Slip Sense	Norm. Stress	Shear Stress	Max. Shear	Misfit Angle	Fault Angle
1	316	74	48	-9	Straia	[4]	1.	Right SS	.529	.424	.44	15.5	39.2
2	121	84	211	-3	Straia	[4]	1.	Right SS	.742	.435	.435	1.1	59.2
3	169	85	257	20	Straia	[4]	1.	Normal-Right SS	.048	.169	.205	34.3	11.5
4	157	88	247	4	Straia	[4]	1.	Right SS	.173	.356	.367	14.2	23.1
5	175	79	264	4	Straia	[4]	1.	Right SS	.011	.106	.106	1.8	6.1
6	325	87	55	-8	Straia	[4]	1.	Right SS	.359	.441	.461	16.6	34.3
7	325	88	55	-13	Straia	[4]	1.	Reverse-Right SS	.357	.431	.462	21.1	34.4
8	154	83	245	-6	Straia	[4]	1.	Right SS	.205	.4	.4	1.6	26.5
9	162	66	249	7	Straia	[4]	1.	Right SS	.129	.315	.321	11.	19.
10	42	68	128	9	Straia	[4]	1.	Normal-Right SS	.539	-.407	.451	154.6	41.2
11	174	80	294	-70	Straia	[4]	1.	Right-Reverse	.015	.041	.122	70.5	7.
12	184	84	277	-29	Straia	[4]	1.	Reverse-Right SS	.007	-.019	.073	105.4	3.3
13	137	89	227	9	Straia	[4]	1.	Right SS	.484	.476	.49	14.	42.8
14	160	80	248	14	Straia	[4]	1.	Normal-Right SS	.127	.32	.332	15.2	20.7
15	142	82	231	10	Straia	[4]	1.	Normal-Right SS	.39	.473	.486	13.5	38.4
16	183	83	273	-4	Straia	[4]	1.	Right SS	.004	-.03	.053	124.8	2.2
17	188	62	281	-6	Straia	[4]	1.	Right SS	.058	-.11	.178	128.	4.
18	188	73	297	-47	Straia	[4]	1.	Right-Reverse Diag.	.018	-.109	.119	155.9	5.7
19	176	72	270	-13	Straia	[4]	1.	Reverse-Right SS	.017	.073	.118	51.7	5.8
20	212	88	121	-20	Straia	[4]	1.	Reverse-Left SS	.276	.443	.446	6.1	31.5
21	193	79	99	-20	Straia	[4]	1.	Reverse-Left SS	.04	.187	.195	15.6	11.4
22	8	69	352	68	Straia	[4]	1.	Normal	.179	.27	.287	20.3	9.8
23	189	86	99	-5	Straia	[4]	1.	Left SS	.028	.143	.156	24.2	8.5
24	210	76	118	-8	Straia	[4]	1.	Left SS	.216	.406	.407	3.4	27.1
25	14	89	284	-12	Straia	[4]	1.	Reverse-Left SS	.076	.188	.251	41.6	14.
26	359	79	268	-4	Straia	[0]	1.	Left SS	.081	-.032	.199	99.3	.3

27	174	78	263	6	[4]	1.	Tension Fracture	.016	.124	7.2
28	108	69	205	-18	[4]	1.	Tension Fracture	.873	.318	70.6
29	174	82	266	-12	[4]	1.	Tension Fracture	.016	.123	7.7
30	94	52	232	-44	[4]	1.	Tension Fracture	.868	.23	81.1
31	176	81	268	-10	[4]	1.	Tension Fracture	.008	.089	5.5
32	175	83	267	-19	[4]	1.	Tension Fracture	.014	.109	7.3
33	114	66	211	-14	[4]	1.	Tension Fracture	.797	.385	64.9
34	171	89	262	-29	[4]	1.	Tension Fracture	.045	.185	14.2
35	94	74	198	-41	[4]	1.	Tension Fracture	.981	.115	84.4
36	171	81	262	-5	[4]	1.	Tension Fracture	.031	.171	10.3
37	170	82	261	-7	[4]	1.	Tension Fracture	.038	.187	11.5
38	172	83	264	-12	[4]	1.	Tension Fracture	.027	.156	10.
39	176	85	269	-33	[4]	1.	Tension Fracture	.013	.101	7.9
40	161	86	252	-10	[4]	1.	Tension Fracture	.122	.319	21.2
41	171	90	261	-31	[4]	1.	Tension Fracture	.048	.189	15.
42	429	61	330	-16	[4]	1.	Tension Fracture	.862	.267	76.5
43	165	87	256	-14	[4]	1.	Tension Fracture	.084	.265	18.
44	165	89	255	-18	[4]	1.	Tension Fracture	.089	.268	19.
45	436	81	347	3	[4]	1.	Tension Fracture	.946	.222	77.
46	169	86	260	-17	[4]	1.	Tension Fracture	.05	.207	14.
47	168	85	259	-13	[4]	1.	Tension Fracture	.055	.22	14.4
48	167	86	258	-14	[4]	1.	Tension Fracture	.065	.236	15.7
49	165	89	255	-18	[4]	1.	Tension Fracture	.089	.268	19.
50	165	89	255	-18	[4]	1.	Tension Fracture	.089	.268	19.
51	349	89	78	28	[4]	1.	Tension Fracture	.064	.218	17.1
52	165	90	255	-20	[4]	1.	Tension Fracture	.092	.269	19.5
53	165	86	256	-12	[4]	1.	Tension Fracture	.082	.265	17.5
54	165	88	256	-16	[4]	1.	Tension Fracture	.086	.267	18.4
55	343	87	72	22	[4]	1.	Tension Fracture	.121	.299	22.9
56	344	88	73	21	[4]	1.	Tension Fracture	.108	.285	21.5
57	161	86	252	-10	[4]	1.	Tension Fracture	.122	.319	21.2
58	165	87	256	-14	[4]	1.	Tension Fracture	.084	.265	18.
59	165	89	255	-18	[4]	1.	Tension Fracture	.089	.268	19.

60	170	90	260	-28	[4]	1.	Tension Fracture	.054	.202	15.7
61	351	89	80	33	[4]	1.	Tension Fracture	.052	.193	15.7
62	166	88	257	-17	[4]	1.	Tension Fracture	.078	.253	17.6
63	165	89	255	-18	[4]	1.	Tension Fracture	.089	.268	19.
64	164	90	254	-18	[4]	1.	Tension Fracture	.101	.282	20.3
65	170	90	260	-28	[4]	1.	Tension Fracture	.054	.202	15.7
66	345	86	73	26	[4]	1.	Tension Fracture	.107	.276	22.
67	350	81	71	45	[4]	1.	Tension Fracture	.096	.236	22.9
68	342	81	67	28	[4]	1.	Tension Fracture	.158	.317	27.7
69	176	89	267	-49	[4]	1.	Tension Fracture	.024	.123	11.2
70	166	86	257	-13	[4]	1.	Tension Fracture	.073	.25	16.6
71	167	90	257	-22	[4]	1.	Tension Fracture	.075	.242	17.9
72	164	90	254	-18	[4]	1.	Tension Fracture	.101	.282	20.3
73	170	88	261	-24	[4]	1.	Tension Fracture	.048	.196	14.3
74	156	78	246	1	[4]	1.	Tension Fracture	.175	.38	24.8
75	320	80	49	8	[4]	1.	Tension Fracture	.455	.46	46.1
76	161	90	251	-15	[4]	1.	Tension Fracture	.131	.32	22.9
77	166	90	256	-21	[4]	1.	Tension Fracture	.083	.256	18.7
78	352	85	77	45	[4]	1.	Tension Fracture	.064	.199	18.4
79	366	86	282	58	[4]	1.	Tension Fracture	.047	.173	15.7
80	170	84	261	-13	[4]	1.	Tension Fracture	.04	.189	12.2
81	165	77	254	4	[4]	1.	Tension Fracture	.076	.265	16.
82	169	89	259	-24	[4]	1.	Tension Fracture	.058	.213	15.7
83	351	85	77	42	[4]	1.	Tension Fracture	.069	.209	18.9
84	159	77	248	2	[4]	1.	Tension Fracture	.139	.345	21.9
85	345	78	66	36	[4]	1.	Tension Fracture	.149	.292	28.1
86	340	80	65	26	[4]	1.	Tension Fracture	.183	.337	29.8
87	185	86	91	-46	[4]	1.	Tension Fracture	.013	.101	7.9
88	338	75	60	27	[4]	1.	Tension Fracture	.232	.354	34.7
89	365	89	277	58	[4]	1.	Tension Fracture	.03	.141	12.5
90	353	81	70	55	[4]	1.	Tension Fracture	.082	.211	21.6
91	167	84	258	-10	[4]	1.	Tension Fracture	.061	.234	14.9
92	345	88	74	23	[4]	1.	Tension Fracture	.099	.272	20.7

93	170	81	261	-4		[4]	1.	Tension Fracture	.037		.187	11.3	
94	168	85	259	-13		[4]	1.	Tension Fracture	.055		.22	14.4	
95	162	88	252	-13		[4]	1.	Tension Fracture	.115		.307	21.1	
96	156	78	246	1		[4]	1.	Tension Fracture	.175		.38	24.8	
97	320	80	49	8		[4]	1.	Tension Fracture	.455		.46	46.1	
98	161	90	251	-15		[4]	1.	Tension Fracture	.131		.32	22.9	

6. Funnigfjorður

#	Dip Azim	Dip	Trend	Plunge	Type	QF	Wt	Slip Sense	Norm. Stress	Shear Stress	Max. Shear	Misfit Angle	Fault Angle
1	324	70	50	11	Straia	[4]	1.	Normal-Right SS	.33	.275	.442	51.5	26.8
2	137	65	233	-14	Straia	[4]	1.	Reverse-Right SS	.097	.221	.27	34.9	8.9
3	253	89	343	-2	Straia	[4]	1.	Right SS	.943	.086	.142	52.9	61.7
4	289	76	19	1	Straia	[4]	1.	Right SS	.662	.41	.473	29.8	54.5
5	311	68	32	22	Straia	[4]	1.	Normal-Right SS	.468	.44	.483	24.4	38.8
6	300	66	25	12	Straia	[4]	1.	Normal-Right SS	.615	.427	.477	26.4	49.
7	6	79	70	66	Straia	[4]	1.	Right-Normal	.34	.094	.407	76.7	13.
8	11	89	96	79	Straia	[4]	1.	Right-Normal	.342	.053	.431	83.	22.6
9	206	62	193	61	Straia	[4]	1.	Normal	.557	.105	.496	77.8	48.
10	352	87	76	63	Straia	[4]	1.	Right-Normal	.139	.095	.305	71.9	5.3
11	325	71	299	69	Straia	[4]	1.	Normal	.31	.359	.434	34.3	25.5
12	162	65	32	-54	Straia	[4]	1.	Left-Reverse	.038	-.077	.188	114.4	10.1
13	184	67	106	27	Straia	[4]	1.	Normal-Left SS	.219	.397	.412	15.8	27.6
14	182	59	109	26	Straia	[4]	1.	Normal-Left SS	.233	.42	.422	5.7	28.7
15	350	75	262	7	Straia	[4]	1.	Left SS	.243	.193	.367	58.3	2.4
16	191	59	97	-7	Straia	[4]	1.	Left SS	.347	.43	.476	25.3	36.
17	21	78	295	19	Straia	[4]	1.	Normal-Left SS	.538	.416	.416	1.1	24.2
18	173	40	90	6	Straia	[4]	1.	Left SS	.339	.317	.445	44.6	27.4

7. Strendur

#	Dip Azim	Dip	Trend	Plunge	Type	QF	Wt	Slip Sense	Norm. Stress	Shear Stress	Max. Shear	Misfit Angle	Fault Angle
1	329	81	57	14	Straia	[4]	1.	Normal-Right SS	.072	.256	.256	2.8	15.3
2	324	85	54	2	Straia	[4]	1.	Right SS	.117	.321	.321	.5	20.
3	315	79	45	-1	Straia	[4]	1.	Right SS	.241	.422	.426	7.5	29.1

4	315	79	45	-2	Straia	[4]	1.	Right SS	.241	.421	.426	8.5	29.1
5	163	86	256	-35	Straia	[4]	1.	Reverse-Right SS	.012	-.037	.084	116.4	.3
6	343	85	71	19	Straia	[4]	1.	Normal-Right SS	.	.021	.021	5.7	1.1
7	131	82	223	-16	Straia	[4]	1.	Reverse-Right SS	.306	.408	.444	23.	31.2
8	302	90	32	9	Straia	[4]	1.	Right SS	.446	.487	.494	9.7	41.4
9	342	87	249	-44	Straia	[4]	1.	Left-Reverse Diag.	.001	-.017	.037	118.1	1.9
10	1	69	267	-11	Straia	[4]	1.	Reverse-Left SS	.118	.22	.282	38.8	14.1
11	13	65	289	13	Straia	[4]	1.	Normal-Left SS	.257	.389	.389	.4	23.7
12	349	82	259	1	Straia	[4]	1.	Left SS	.009	.083	.089	21.7	4.5
13	16	81	286	-2	Straia	[4]	1.	Left SS	.273	.44	.44	.9	30.7
14	224	77	138	17	Straia	[4]	1.	Normal-Left SS	.766	.4	.414	15.	59.8
15	177	83	95	49	Straia	[4]	1.	Left-Normal Diag.	.075	.229	.249	22.8	13.9
16	130	85	216	36	Straia	[0]	1.	Normal-Right SS	.316	.388	.454	31.3	32.8
17	149	88	239	10	Straia	[0]	1.	Normal-Right SS	.072	.25	.25	1.4	14.4
18	128	88	217	29	Straia	[0]	1.	Normal-Right SS	.346	.42	.47	26.5	35.2
19	49	68	136	7	Straia	[0]	1.	Right SS	.75	-.373	.379	169.5	53.4

8. Gotogjogv

#	Dip Azim	Dip	Trend	Plunge	Type	QF	Wt	Slip Sense	Norm. Stress	Shear Stress	Max. Shear	Misfit Angle	Fault Angle
1	329	81	64	-31	Straia	[4]	1.	Reverse-Right SS	.363	.128	.464	74.	34.
2	153	39	334	-39	Straia	[4]	1.	Reverse	.207	-.262	.314	146.5	.6
3	156	80	251	-25	Straia	[4]	1.	Reverse-Right SS	.114	.313	.318	9.2	19.6
4	171	62	293	-45	Straia	[4]	1.	Right-Reverse	.01	-.055	.082	132.2	1.1
5	354	81	140	-79	Straia	[4]	1.	Reverse	.186	-.313	.322	166.1	10.9
6	132	75	239	-47	Straia	[4]	1.	Right-Reverse Diag.	.383	.429	.474	25.	36.
7	136	69	222	11	Straia	[4]	1.	Normal-Right SS	.293	.378	.435	29.8	29.2
8	137	67	206	40	Straia	[4]	1.	Right-Normal Diag.	.271	.215	.421	59.3	27.1
9	137	65	223	8	Straia	[4]	1.	Right SS	.264	.383	.413	21.9	25.8
10	140	63	299	-61	Straia	[4]	1.	Right-Reverse	.222	.123	.385	71.4	22.4
11	146	72	232	13	Straia	[4]	1.	Normal-Right SS	.178	.315	.376	33.1	23.7
12	146	72	275	-63	Straia	[4]	1.	Right-Reverse	.178	.242	.376	49.9	23.7
13	150	69	288	-63	Straia	[4]	1.	Right-Reverse	.124	.168	.32	58.3	18.9
14	150	69	252	-29	Straia	[4]	1.	Reverse-Right SS	.124	.306	.32	17.3	18.9

15	150	61	234	11	Straia	[4]	1.	Normal-Right SS	.115	.287	.291	9.8	14.3
16	150	61	298	-57	Straia	[4]	1.	Right-Reverse	.115	.069	.291	76.2	14.3
17	325	82	46	48	Straia	[4]	1.	Right-Normal Diag.	.401	.473	.479	9.4	37.3
18	152	80	281	-74	Straia	[4]	1.	Right-Reverse	.154	.247	.361	46.7	23.1
19	155	53	250	-6	Straia	[4]	1.	Right SS	.1	.189	.249	40.5	6.3
20	156	83	246	-4	Straia	[4]	1.	Right SS	.135	.28	.339	34.1	21.
21	156	84	245	9	Straia	[4]	1.	Right SS	.142	.23	.346	48.3	21.5
22	332	73	61	3	Straia	[4]	1.	Right SS	.422	.323	.456	44.9	33.7
23	160	66	222	46	Straia	[4]	1.	Right-Normal	.039	.112	.184	52.5	9.5
24	168	42	333	-41	Straia	[4]	1.	Right-Reverse	.145	-.281	.289	166.7	7.5
25	171	60	263	-3	Straia	[4]	1.	Right SS	.016	.006	.106	87.	2.
26	172	52	269	-9	Straia	[4]	1.	Reverse-Right SS	.059	-.058	.201	106.9	6.
27	173	42	273	-9	Straia	[4]	1.	Reverse-Right SS	.147	-.119	.299	113.4	10.5
28	173	86	266	-38	Straia	[4]	1.	Reverse-Right SS	.066	.156	.212	42.8	6.9
29	174	77	304	-70	Straia	[4]	1.	Right-Reverse	.015	.101	.104	14.7	2.4
30	174	90	264	-59	Straia	[4]	1.	Right-Reverse	.097	.226	.249	24.8	7.5
31	349	77	105	-62	Straia	[4]	1.	Right-Reverse	.247	-.264	.366	136.1	16.9
32	177	45	273	-6	Straia	[4]	1.	Right SS	.125	-.139	.289	118.8	12.1
33	177	89	269	-57	Straia	[4]	1.	Right-Reverse	.088	.183	.233	37.9	4.4
34	177	86	267	-6	Straia	[4]	1.	Right SS	.065	-.005	.203	91.5	3.2
35	177	86	121	83	Straia	[4]	1.	Normal	.065	-.197	.203	166.5	3.2
36	177	51	253	16	Straia	[4]	1.	Normal-Right SS	.074	-.011	.234	92.6	10.
37	179	77	269	1	Straia	[4]	1.	Right SS	.022	-.078	.122	130.1	2.1
38	182	78	101	36	Straia	[4]	1.	Normal-Left SS	.035	.035	.157	77.1	4.4
39	182	66	96	8	Straia	[4]	1.	Left SS	.023	.149	.15	8.	8.7
40	184	65	119	42	Straia	[4]	1.	Left-Normal Diag.	.035	.159	.184	30.	10.8
41	186	65	134	53	Straia	[4]	1.	Left Normal	.047	.146	.212	46.4	12.5
42	189	65	104	11	Straia	[4]	1.	Normal-Left SS	.068	.252	.252	.8	15.1
43	189	56	102	5	Straia	[4]	1.	Left SS	.101	.269	.297	24.8	17.7
44	207	54	184	52	Straia	[4]	1.	Left Normal	.294	.207	.454	62.8	32.5
45	158	85	72	36	Straia	[4]	1.	Normal-Left SS	.132	-.33	.332	173.3	20.1
46	180	55	128	42	Straia	[4]	1.	Left Normal	.057	.216	.216	1.3	10.9
47	181	51	97	7	Straia	[4]	1.	Left SS	.088	.182	.261	45.8	12.9

48	181	39	95	3	Straia	[4]	1.	Left SS	.199	.187	.349	57.6	16.4
49	182	71	108	39	Straia	[4]	1.	Left-Normal Diag.	.021	.089	.136	49.2	7.
50	182	71	119	52	Straia	[4]	1.	Left Normal	.021	.059	.136	64.2	7.
51	183	58	97	6	Straia	[4]	1.	Left SS	.054	.186	.219	32.	12.3
52	187	45	108	11	Straia	[4]	1.	Normal-Left SS	.167	.291	.345	32.5	18.8
53	188	51	104	7	Straia	[4]	1.	Left SS	.125	.273	.317	30.5	18.2
54	191	86	102	11	Straia	[4]	1.	Normal-Left SS	.128	.192	.283	47.3	9.7
55	195	46	106	1	Straia	[4]	1.	Left SS	.215	.334	.393	31.7	24.3
56	201	45	124	13	Straia	[4]	1.	Normal-Left SS	.275	.425	.43	8.7	28.6
57	210	58	163	47	Straia	[4]	1.	Left Normal	.322	.287	.467	52.2	34.6

9. Lambi

#	Dip Azim	Dip	Trend	Plunge	Type	QF	Wt	Slip Sense	Norm. Stress	Shear Stress	Max. Shear	Misfit Angle	Fault Angle
1	262	24	59	-22	Straia	[4]	1.	Right-Reverse	.686	.449	.449	1.7	54.
2	272	25	30	-12	Straia	[4]	1.	Reverse-Right SS	.673	.398	.462	30.5	54.2
3	94	8	197	-2	Straia	[4]	1.	Reverse-Right SS	.246	-.331	.377	151.4	22.2
4	73	23	285	-20	Straia	[4]	1.	Left-Reverse	.098	-.021	.231	95.2	7.1
5	54	53	209	-50	Straia	[4]	1.	Right-Reverse	.105	.214	.306	45.7	18.8
6	20	70	291	3	Straia	[4]	1.	Left SS	.207	-.027	.317	94.8	13.8
7	4	85	274	4	Straia	[4]	1.	Left SS	.39	-.074	.292	104.8	9.7
8	359	89	269	8	Straia	[4]	1.	Left SS	.438	-.098	.261	112.1	7.4
9	128	87	217	12	Straia	[4]	1.	Normal-Right SS	.705	.109	.195	56.1	33.4
10	125	84	213	17	Straia	[4]	1.	Normal-Right SS	.702	.051	.207	75.7	33.7
11	349	79	80	-3	Straia	[4]	1.	Right SS	.402	.198	.275	44.	6.2
12	38	83	129	-5	Straia	[4]	1.	Right SS	.428	-.109	.454	103.9	35.4
13	46	18	29	17	Straia	[0]	1.	Left Normal	.099	.263	.273	15.6	14.7
14	316	17	343	15	Straia	[0]	1.	Right-Normal	.389	.075	.485	81.1	38.3
15	53	90	323	70	Straia	[0]	1.	Left Normal	.625	-.343	.472	136.6	50.6
16	54	32	81	29	Straia	[0]	1.	Right-Normal	.024	.009	.115	85.5	.6
17	56	18	44	18	Straia	[0]	1.	Left Normal	.104	.266	.268	5.3	13.3
18	59	18	73	18	Straia	[0]	1.	Right-Normal	.106	.222	.268	34.	13.
19	34	59	93	40	Straia	[0]	1.	Right-Normal Diag.	.101	-.239	.277	149.8	15.1
20	37	63	117	19	Straia	[0]	1.	Normal-Right SS	.149	-.196	.335	125.8	19.8

21	29	25	80	16	Straia	[0]	1.	Right-Normal Diag.	.054	.211	.222	18.2	12.8
22	136	42	68	18	Straia	[0]	1.	Normal-Left SS	.425	.097	.257	67.8	2.8
23	52	26	62	26	Straia	[0]	1.	Normal	.042	.139	.168	34.2	6.5
24	9	60	70	40	Straia	[0]	1.	Right-Normal Diag.	.143	-.053	.249	102.2	.2
25	16	41	43	38	Straia	[0]	1.	Right-Normal	.038	.049	.166	72.7	7.3
26	33	71	108	37	Straia	[0]	1.	Normal-Right SS	.237	-.302	.384	142.	23.4
27	31	39	68	33	Straia	[0]	1.	Right-Normal	.003	.023	.044	58.6	1.7
28	92	22	96	22	Straia	[0]	1.	Normal	.159	.058	.275	77.8	8.4
29	19	45	33	44	Straia	[0]	1.	Normal	.033	-.04	.139	106.6	3.2
30	239	79	326	17	Straia	[0]	1.	Normal-Right SS	.813	-.066	.378	100.	62.9
31	80	74	167	11	Straia	[0]	1.	Normal-Right SS	.537	-.241	.475	120.5	44.
32	27	81	117	2	Straia	[0]	1.	Right SS	.354	-.097	.401	104.	26.

10. Kalsoy

#	Dip Azim	Dip	Trend	Plunge	Type	QF	Wt	Slip Sense	Norm. Stress	Shear Stress	Max. Shear	Misfit Angle	Fault Angle
1	116	89	206	23	Straia	[4]	1.	Normal-Right SS	.686	.442	.464	17.6	55.9
2	128	67	210	17	Straia	[4]	1.	Normal-Right SS	.531	.454	.462	10.	41.7
3	135	89	225	-13	Straia	[4]	1.	Reverse-Right SS	.362	.454	.481	19.2	37.
4	320	63	58	-15	Straia	[4]	1.	Reverse-Right SS	.305	.35	.407	30.8	26.
5	146	80	233	19	Straia	[4]	1.	Normal-Right SS	.22	.402	.402	2.9	26.3
6	326	82	55	5	Straia	[4]	1.	Right SS	.187	.385	.386	3.5	25.
7	327	82	55	15	Straia	[4]	1.	Normal-Right SS	.174	.365	.375	13.2	24.1
8	328	59	45	20	Straia	[4]	1.	Normal-Right SS	.237	.35	.351	4.1	18.1
9	329	80	61	-9	Straia	[4]	1.	Right SS	.15	.34	.35	14.1	21.8
10	156	67	242	10	Straia	[4]	1.	Normal-Right SS	.187	.284	.328	29.9	16.3
11	336	84	67	-11	Straia	[4]	1.	Reverse-Right SS	.073	.252	.259	13.2	15.4
12	158	61	252	-8	Straia	[4]	1.	Right SS	.221	.171	.326	58.4	14.2
13	340	79	71	-4	Straia	[4]	1.	Right SS	.048	.188	.202	21.9	11.
14	166	75	254	6	Straia	[4]	1.	Right SS	.072	.122	.207	53.8	6.9
15	349	90	79	1	Straia	[4]	1.	Right SS	.005	.049	.063	39.2	3.
16	173	83	263	-2	Straia	[4]	1.	Right SS	.02	-.02	.108	100.5	.5
17	182	85	272	-5	Straia	[4]	1.	Right SS	.043	-.175	.187	159.7	9.6
18	14	75	318	64	Straia	[4]	1.	Left Normal	.162	.209	.358	54.3	22.3

19	16	65	337	59	Straia	[4]	1.	Left Normal	.227	.254	.384	48.5	23.4
20	23	70	349	66	Straia	[4]	1.	Left Normal	.295	.184	.439	65.2	30.5
21	163	89	73	-8	Straia	[4]	1.	Left SS	.028	-.158	.16	169.3	9.1
22	357	76	265	-8	Straia	[4]	1.	Left SS	.028	.078	.141	56.2	5.8
23	11	83	282	7	Straia	[4]	1.	Left SS	.11	.313	.313	1.	19.3
24	21	73	284	-21	Straia	[4]	1.	Reverse-Left SS	.258	.356	.426	33.2	28.9
25	29	77	296	-11	Straia	[4]	1.	Reverse-Left SS	.371	.461	.479	15.5	36.9
26	32	72	300	-7	Straia	[4]	1.	Left SS	.427	.472	.483	12.1	39.2

11. Mykinesholmur

#	Dip Azim	Dip	Trend	Plunge	Type	QF	Wt	Slip Sense	Norm. Stress	Shear Stress	Max. Shear	Misfit Angle	Fault Angle
1	164	60	185	58	Straia	[4]	1.	Right-Normal	.184	.38	.387	10.9	25.3
2	196	83	204	83	Straia	[4]	1.	Normal	.101	.051	.179	73.6	4.2
3	171	72	155	71	Straia	[4]	1.	Normal	.058	.229	.23	5.2	13.6
4	180	63	178	63	Straia	[4]	1.	Normal	.17	.35	.362	14.9	23.1
5	168	66	182	65	Straia	[4]	1.	Normal	.111	.31	.315	10.2	19.5
6	176	48	182	48	Straia	[4]	1.	Normal	.381	.471	.483	12.8	37.8
7	156	69	201	61	Straia	[4]	1.	Right-Normal	.088	.268	.271	7.8	16.1
8	143	57	169	54	Straia	[4]	1.	Right-Normal	.264	.407	.408	2.	27.8
9	142	71	197	59	Straia	[4]	1.	Right-Normal	.117	.256	.258	7.2	13.8
10	243	71	168	37	Straia	[4]	1.	Normal-Left SS	.439	.209	.225	21.6	20.2
11	166	69	147	68	Straia	[4]	1.	Normal	.08	.27	.271	5.2	16.4
12	172	81	130	78	Straia	[4]	1.	Normal	.011	.084	.09	20.9	4.7
13	38	67	341	52	Straia	[4]	1.	Left Normal	.378	.32	.322	5.2	23.8
14	34	77	340	69	Straia	[4]	1.	Left Normal	.271	.241	.262	22.9	14.2
15	142	49	103	42	Straia	[0]	1.	Left Normal	.385	.34	.459	42.3	35.8
16	155	89	67	64	Straia	[0]	1.	Left Normal	.018	-.091	.098	158.5	4.
17	131	75	59	49	Straia	[0]	1.	Left Normal	.15	.	.231	90.	9.9
18	142	49	131	49	Straia	[0]	1.	Normal	.385	.428	.459	21.3	35.8
19	155	89	76	85	Straia	[0]	1.	Normal	.018	-.072	.098	137.5	4.
20	131	75	120	75	Straia	[0]	1.	Normal	.15	.136	.231	54.	9.9
21	186	22	149	18	Straia	[0]	1.	Left Normal	.815	.36	.386	21.	64.3
22	188	69	155	65	Straia	[4]	1.	Left Normal	.136	.29	.3	15.3	17.6

12. Skarvanes

#	Dip Azim	Dip	Trend	Plunge	Type	QF	Wt	Slip Sense	Norm. Stress	Shear Stress	Max. Shear	Misfit Angle	Fault Angle
1	336	65	74	-16	Straia	[4]	1.	Reverse-Right SS	.003	-.049	.05	168.4	2.7
2	325	72	52	10	Straia	[4]	1.	Normal-Right SS	.024	.129	.151	31.2	8.8
3	308	70	28	25	Straia	[4]	1.	Normal-Right SS	.161	.264	.366	43.7	23.5
4	331	86	61	2	Straia	[4]	1.	Right SS	.047	.072	.153	62.1	6.
5	215	28	240	26	Straia	[4]	1.	Right-Normal	.434	-.141	.143	170.3	13.3
6	225	24	246	23	Straia	[4]	1.	Right-Normal	.413	-.128	.152	147.8	11.8
7	328	55	64	-8	Straia	[4]	1.	Right SS	.024	.04	.099	66.	2.
8	323	61	58	-10	Straia	[4]	1.	Reverse-Right SS	.027	.136	.145	19.9	7.7
9	320	78	51	-5	Straia	[4]	1.	Right SS	.072	.236	.252	20.4	14.9

13. Tjornuvik

#	Dip Azim	Dip	Trend	Plunge	Type	QF	Wt	Slip Sense	Norm. Stress	Shear Stress	Max. Shear	Misfit Angle	Fault Angle
1	351	57	76	8	Straia	[4]	1.	Right SS	.085	.177	.216	35.2	10.4
2	355	75	79	21	Straia	[4]	1.	Normal-Right SS	.008	.083	.083	6.3	4.5
3	351	41	69	10	Straia	[4]	1.	Normal-Right SS	.186	.206	.253	35.8	11.3
4	338	39	65	3	Straia	[4]	1.	Right SS	.264	.297	.323	23.2	19.5
5	145	78	235		Straia	[4]	1.	Right SS	.307	.406	.408	4.2	28.5
6	155	88	246	-15	Straia	[4]	1.	Reverse-Right SS	.162	.321	.345	21.3	21.4
7	165	79	258	-15	Straia	[4]	1.	Reverse-Right SS	.093	.15	.216	46.1	9.9
8	351	57	74	11	Straia	[4]	1.	Normal-Right SS	.085	.185	.216	31.2	10.4
9	355	75	77	29	Straia	[4]	1.	Normal-Right SS	.008	.083	.083	1.7	4.5
10	351	41	69	10	Straia	[4]	1.	Normal-Right SS	.186	.206	.253	35.8	11.3
11	355	75	84	3	Straia	[4]	1.	Right SS	.008	.075	.083	25.3	4.5
12	338	59	65	5	Straia	[4]	1.	Right SS	.17	.336	.345	12.6	21.3
13	173	90	263	10	Straia	[4]	1.	Normal-Right SS	.02	.092	.105	28.5	4.1
14	171	89	261	9	Straia	[4]	1.	Right SS	.03	.122	.132	22.	5.9
15	156	88	246	10	Straia	[4]	1.	Normal-Right SS	.15	.333	.333	3.	20.4
16	5	73	90	16	Straia	[4]	1.	Normal-Right SS	.013	-.074	.095	140.6	4.6
17	4	73	91	10	Straia	[4]	1.	Normal-Right SS	.011	-.064	.082	141.7	3.6
18	179	54	294	-30	Straia	[4]	1.	Reverse-Right SS	.223	-.189	.225	147.	7.2

19	171	45	287	-24	Straia	[4]	1.	Reverse-Right SS	.281	-.106	.192	123.5	2.6
20	332	58	69	-11	Straia	[4]	1.	Reverse-Right SS	.238	.358	.397	25.5	26.4
21	341	72	70	3	Straia	[4]	1.	Right SS	.101	.295	.298	8.5	18.2
22	159	90	249	-6	Straia	[4]	1.	Right SS	.115	.291	.299	13.2	17.9
23	329	87	59	4	Straia	[4]	1.	Right SS	.238	.414	.416	5.	28.2
24	354	81	83	7	Straia	[4]	1.	Right SS	.007	.08	.081	8.9	4.6
25	340	80	69	6	Straia	[4]	1.	Right SS	.1	.299	.299	3.1	18.4
26	11	58	271	-15	Straia	[4]	1.	Reverse-Left SS	.077	.097	.181	57.6	6.4
27	193	90	103	12	Straia	[4]	1.	Normal-Left SS	.08	.259	.263	9.7	15.6
28	11	77	280	-4	Straia	[4]	1.	Left SS	.04	.191	.191	1.4	11.1
29	211	55	139	23	Straia	[4]	1.	Normal-Left SS	.448	.384	.399	15.8	33.1
30	16	74	275	-33	Straia	[4]	1.	Reverse-Left SS	.077	.215	.256	32.9	15.1
31	267	70	70	-69		[4]	1.	Tension Fracture	.981		.107	88.2	
32	354	86	86	-28		[4]	1.	Tension Fracture	.011		.082	8.	
33	368	82	276	-13		[4]	1.	Tension Fracture	.026		.159	9.3	
34	182	90	92	49		[4]	1.	Tension Fracture	.019		.107	10.8	
35	180	87	97	67		[4]	1.	Tension Fracture	.024		.106	13.4	
36	361	87	267	-50		[4]	1.	Tension Fracture	.009		.075	7.7	
37	356	76	78	28		[4]	1.	Tension Fracture	.005		.063	4.6	
38	360	77	286	51		[4]	1.	Tension Fracture	.001		.022	2.8	
39	376	70	288	4		[4]	1.	Tension Fracture	.078		.246	19.	
40	368	85	276	-19		[4]	1.	Tension Fracture	.031		.17	10.5	
41	352	69	69	30		[4]	1.	Tension Fracture	.031		.154	12.5	
42	345	79	74	5		[4]	1.	Tension Fracture	.056		.229	13.7	
43	206	64	125	18		[4]	1.	Tension Fracture	.353		.411	44.9	
44	160	75	243	24		[4]	1.	Tension Fracture	.145		.267	31.6	
45	175	85	252	68		[4]	1.	Tension Fracture	.031		.109	15.9	
46	153	83	242	8		[4]	1.	Tension Fracture	.194		.356	31.1	
47	377	75	286	-3		[4]	1.	Tension Fracture	.086		.272	18.2	
48	233	79	145	8		[4]	1.	Tension Fracture	.703		.451	57.9	
49	353	86	85	-23		[4]	1.	Tension Fracture	.013		.096	8.7	
50	130	71	223	-8		[4]	1.	Tension Fracture	.517		.421	56.5	
51	333	79	62	3		[4]	1.	Tension Fracture	.184		.387	25.5	

52	365	88	274	-32		[4]	1.	Tension Fracture	.023		.137	10.3	
53	366	89	275	-31		[4]	1.	Tension Fracture	.03		.157	11.7	
54	163	65	231	38		[4]	1.	Tension Fracture	.172		.231	38.6	
55	169	72	234	52		[4]	1.	Tension Fracture	.106		.19	30.	
56	160	74	242	25		[4]	1.	Tension Fracture	.149		.266	32.4	
57	141	81	231	1		[4]	1.	Tension Fracture	.363		.44	42.4	
58	169	73	237	51		[4]	1.	Tension Fracture	.101		.188	29.1	
59	175	69	182	69		[4]	1.	Tension Fracture	.113		.184	31.6	
60	170	75	239	53		[4]	1.	Tension Fracture	.087		.177	26.9	
61	163	61	225	40		[4]	1.	Tension Fracture	.195		.227	42.3	
62	181	83	104	62		[4]	1.	Tension Fracture	.041		.14	17.5	
63	363	65	319	57		[4]	1.	Tension Fracture	.028		.104	15.1	

14. Tjornuvik - Haldarsvik

#	Dip Azim	Dip	Trend	Plunge	Type	QF	Wt	Slip Sense	Norm. Stress	Shear Stress	Max. Shear	Misfit Angle	Fault Angle
1	315	28	15	15	Straia	[4]	1.	Normal-Right SS	.319	.205	.373	56.7	28.1
2	146	75	239	-11	Straia	[4]	1.	Reverse-Right SS	.288	.397	.398	3.2	28.6
3	178	69	273	-14	Straia	[4]	1.	Reverse-Right SS	.07	-.046	.101	117.2	2.3
4	328	67	51	16	Straia	[4]	1.	Normal-Right SS	.289	.43	.452	17.9	32.4
5	38	17	279	-8	Straia	[4]	1.	Reverse-Left SS	.154	.031	.085	68.4	1.2
6	26	27	194	-26	Straia	[4]	1.	Right-Reverse	.122	-.079	.107	137.3	3.
7	339	15	79	-3	Straia	[4]	1.	Right SS	.203	.214	.222	14.7	14.5
8	134	32	291	-30	Straia	[4]	1.	Right-Reverse	.237	.151	.181	33.3	13.2
9	359	85	269	5	Straia	[4]	1.	Left SS	.007	-.027	.039	132.7	1.1
10	201	82	113	11	Straia	[4]	1.	Normal-Left SS	.168	.351	.352	5.7	22.7
11	196	88	106	11	Straia	[4]	1.	Normal-Left SS	.095	.275	.278	7.9	16.9
12	204	85	116	21	Straia	[4]	1.	Normal-Left SS	.194	.381	.382	5.5	25.2
13	200	89	110	13	Straia	[4]	1.	Normal-Left SS	.132	.328	.329	3.8	20.6
14	26	83	294	-17	Straia	[4]	1.	Reverse-Left SS	.177	.381	.381	1.7	24.9
15	199	77	113	17	Straia	[4]	1.	Normal-Left SS	.163	.333	.333	.8	21.3

15. Langasandur

#	Dip Azim	Dip	Trend	Plunge	Type	QF	Wt	Slip Sense	Norm. Stress	Shear Stress	Max. Shear	Misfit Angle	Fault Angle

1	312	69	49	-19	Straia	[4]	1.	Reverse-Right SS	.635	.401	.448	26.5	46.8
2	329	45	69	-10	Straia	[4]	1.	Reverse-Right SS	.54	.258	.366	45.3	23.8
3	130	83	218	13	Straia	[4]	1.	Normal-Right SS	.633	.463	.48	15.3	52.3
4	134	89	223	29	Straia	[4]	1.	Normal-Right SS	.57	.419	.495	32.1	49.
5	344	84	78	-33	Straia	[4]	1.	Reverse-Right SS	.123	.201	.32	51.1	19.
6	344	70	68	17	Straia	[4]	1.	Normal-Right SS	.202	.339	.359	19.5	18.1
7	181	89	269	58	Straia	[4]	1.	Right-Normal	.002	-.006	.045	97.1	2.
8	336	90	66	11	Straia	[4]	1.	Normal-Right SS	.208	.403	.405	5.7	27.
9	316	76	33	41	Straia	[4]	1.	Right-Normal Diag.	.559	.392	.48	35.4	45.4
10	158	89	249	-51	Straia	[4]	1.	Right-Reverse	.179	.263	.383	46.7	25.
11	349	69	328	68	Straia	[4]	1.	Normal	.169	.209	.324	49.8	13.3
12	38	90	308	-3	Straia	[4]	1.	Left SS	.331	.466	.47	6.8	35.
13	53	88	335	81	Straia	[4]	1.	Normal	.59	.103	.491	77.8	49.9
14	40	79	357	75	Straia	[4]	1.	Left Normal	.387	.17	.474	69.	36.
15	16	78	2	78	Straia	[4]	1.	Normal	.096	.177	.269	48.9	12.6
16	208	89	118	13	Straia	[4]	1.	Normal-Left SS	.179	.367	.383	16.9	25.
17	213	69	126	7	Straia	[4]	1.	Left SS	.287	.424	.43	9.7	28.1
18	212	82	123	8	Straia	[4]	1.	Left SS	.236	.422	.423	3.8	28.8

16. Saksunardalur

#	Dip Azim	Dip	Trend	Plunge	Type	QF	Wt	Slip Sense	Norm. Stress	Shear Stress	Max. Shear	Misfit Angle	Fault Angle
1	316	52	42	6	Straia	[4]	1.	Right SS	.343	.345	.377	23.8	25.1
2	137	78	229	-10	Straia	[4]	1.	Right SS	.122	.298	.307	13.8	18.1
3	128	85	219	-16	Straia	[4]	1.	Reverse-Right SS	.24	.416	.421	9.	28.7
4	178	89	89	40	Straia	[4]	1.	Normal-Left SS	.112	.249	.311	36.8	19.1
5	168	73	75	-11	Straia	[4]	1.	Reverse-Left SS	.065	.157	.224	45.6	12.2
6	2	84	272	-1	Straia	[4]	1.	Left SS	.158	.345	.346	4.2	21.3
7	177	78	89	11	Straia	[4]	1.	Normal-Left SS	.122	.323	.324	5.2	20.1
8	4	90	94	29	Straia	[4]	1.	Normal-Right SS	.184	-.343	.381	154.2	24.7
9	356	89	266	-1	Straia	[4]	1.	Left SS	.091	.28	.28	1.2	16.7
10	329	80	52	35		[4]	1.	Tension Fracture	.056		.211	15.8	
11	312	88	42	12		[4]	1.	Tension Fracture	.2		.4	26.5	
12	139	63	215	25		[4]	1.	Tension Fracture	.144		.265	30.2	

#	Dip Azim	Dip	Trend	Plunge	Type	QF	Wt	Slip Sense	Norm. Stress	Shear Stress	Max. Shear	Misfit Angle	Fault Angle
13	153	75	222	54		[4]	1.	Tension Fracture	.026		.113	13.	
14	324	81	50	25		[4]	1.	Tension Fracture	.088		.273	18.5	
15	318	79	44	21		[4]	1.	Tension Fracture	.157		.354	24.4	
16	143	74	228	18		[4]	1.	Tension Fracture	.076		.226	19.7	
17	160	47	132	43		[4]	1.	Tension Fracture	.215		.267	40.	
18	161	49	129	44		[4]	1.	Tension Fracture	.2		.268	38.1	
19	137	39	180	31		[4]	1.	Tension Fracture	.299		.243	51.2	
20	135	29	166	25		[4]	1.	Tension Fracture	.371		.209	60.6	
21	141	22	148	22		[4]	1.	Tension Fracture	.411		.187	66.	
22	194	49	112	9		[4]	1.	Tension Fracture	.447		.424	49.9	

17. Dalasgjogv/Djup'gjogv

#	Dip Azim	Dip	Trend	Plunge	Type	QF	Wt	Slip Sense	Norm. Stress	Shear Stress	Max. Shear	Misfit Angle	Fault Angle
1	166	81	258	-14	Straia	[4]	1.	Reverse-Right SS	.083	.269	.273	9.2	16.3
2	342	84	74	-17	Straia	[4]	1.	Reverse-Right SS	.168	.249	.334	41.8	18.1
3	172	52	317	-46	Straia	[4]	1.	Right-Reverse	.15	-.14	.293	118.4	12.3
4	165	86	256	-11	Straia	[4]	1.	Reverse-Right SS	.1	.288	.288	2.5	16.7
5	150	77	244	-18	Straia	[4]	1.	Reverse-Right SS	.285	.428	.451	18.4	32.2
6	164	82	258	-24	Straia	[4]	1.	Reverse-Right SS	.104	.286	.3	17.9	18.1
7	354	85	343	85	Straia	[4]	1.	Normal	.071	.157	.207	40.6	6.5
8	328	78	62	-17	Straia	[4]	1.	Reverse-Right SS	.373	.364	.431	32.5	30.1
9	4	67	277	7	Straia	[4]	1.	Left SS	.203	.086	.292	72.8	5.7
10	221	53	140	12	Straia	[4]	1.	Normal-Left SS	.342	.396	.399	7.6	24.8
11	180	72	84	-19	Straia	[4]	1.	Reverse-Left SS	.01	-.076	.087	150.8	3.7
12	191	74	103	7	Straia	[4]	1.	Left SS	.02	.13	.131	6.8	7.
13	208	73	112	-18	Straia	[4]	1.	Reverse-Left SS	.163	.344	.361	17.8	22.6
14	243	76	116	-67	Straia	[4]	1.	Left-Reverse	.698	.261	.442	53.7	54.2
15	207	86	116	-10	Straia	[4]	1.	Reverse-Left SS	.177	.378	.381	6.5	24.7
16	21	68	300	20	Straia	[4]	1.	Normal-Left SS	.284	.353	.378	21.	21.3
17	14	73	290	19	Straia	[4]	1.	Normal-Left SS	.185	.268	.32	33.1	14.5
18	37	77	310	12	Straia	[4]	1.	Normal-Left SS	.41	.462	.469	9.9	36.5
19	12	84	354	84	Straia	[4]	1.	Normal	.087	.19	.246	39.4	11.4

18. Dakid

#	Dip Azim	Dip	Trend	Plunge	Type	QF	Wt	Slip Sense	Norm. Stress	Shear Stress	Max. Shear	Misfit Angle	Fault Angle
1	325	89	55	-4	Straia	[4]	1.	Right SS	.133	.339	.339	2.2	21.3
2	343	84	71	18	Straia	[4]	1.	Normal-Right SS	.003	.054	.055	9.5	3.1
3	342	89	72	20	Straia	[4]	1.	Normal-Right SS	.007	.059	.08	42.1	4.3
4	172	52	249	16	Straia	[4]	1.	Normal-Right SS	.205	.015	.221	86.2	3.
5	311	55	47	-8	Straia	[4]	1.	Right SS	.328	.375	.387	14.7	26.8
6	323	64	56	-5	Straia	[4]	1.	Right SS	.178	.312	.333	20.3	19.8
7		87	90	-2	Straia	[4]	1.	Right SS	.057	-.23	.231	175.6	13.7
8	183	88	93	8		[4]	1.	Tension Fracture	.088		.276	18.1	
9	198	66	112	9		[4]	1.	Tension Fracture	.318		.398	42.3	

19. Vestmanna

#	Dip Azim	Dip	Trend	Plunge	Type	QF	Wt	Slip Sense	Norm. Stress	Shear Stress	Max. Shear	Misfit Angle	Fault Angle
1	135	87	226	-18	Straia	[4]	1.	Reverse-Right SS	.485	.475	.5	18.	44.2
2	139	86	230	-18	Straia	[4]	1.	Reverse-Right SS	.416	.468	.493	18.3	40.2
3	134	90	224	-2	Straia	[4]	1.	Right SS	.503	.498	.499	2.1	45.
4	147	60	221	26	Straia	[4]	1.	Normal-Right SS	.327	.394	.416	18.6	29.
5	220	83	302	48	Straia	[4]	1.	Right-Normal Diag.	.42	-.349	.49	135.4	40.
6	223	88	311	39	Straia	[4]	1.	Normal-Right SS	.477	-.41	.499	145.2	43.7
7	171	86	262	-19	Straia	[4]	1.	Reverse-Right SS	.021	.131	.142	23.3	8.3
8	158	90	248	-13	Straia	[4]	1.	Reverse-Right SS	.131	.33	.336	10.6	21.1
9	191	70	80	-45	Straia	[4]	1.	Left-Reverse Diag.	.075	.03	.216	82.	10.1
10	220	64	126	-7	Straia	[4]	1.	Left SS	.409	.438	.442	7.8	34.4
11	155	84	246	-8	Straia	[4]	1.	Right SS	.169	.368	.375	11.1	24.2
12	21	76	292	6	Straia	[4]	1.	Left SS	.175	.348	.355	12.1	22.
13	44	44	274	-32	Straia	[4]	1.	Left-Reverse Diag.	.527	.234	.347	47.6	31.8
14	12	52	277	-6	Straia	[4]	1.	Left SS	.244	.151	.284	57.9	12.
15	55	84	326	6	Straia	[4]	1.	Left SS	.69	.459	.46	4.2	55.9
16	17	76	295	30	Straia	[4]	1.	Normal-Left SS	.133	.307	.31	8.3	18.1

20. Stykkið

#	Dip Azim	Dip	Trend	Plunge	Type	QF	Wt	Slip Sense	Norm. Stress	Shear Stress	Max. Shear	Misfit Angle	Fault Angle
1	270	75	358	6	Straia	[0]	1.	Right SS	.689	.457	.457	1.3	55.5
2	199	83	110	10	Straia	[0]	1.	Left SS	.667	.467	.469	5.5	54.5
3	211	65	126	10	Straia	[0]	1.	Normal-Left SS	.828	.333	.361	22.9	63.8
4	190	78	99	-7	Straia	[4]	1.	Left SS	.522	.49	.499	11.4	46.3
5	179	79	88	-5	Straia	[4]	1.	Left SS	.337	.463	.473	11.6	35.5
6	201	87	111	-3	Straia	[4]	1.	Left SS	.693	.448	.454	9.3	55.6
7	187	76	96	-5	Straia	[4]	1.	Left SS	.475	.491	.499	10.1	43.5
8	172	77	83	4	Straia	[4]	1.	Left SS	.235	.421	.423	5.7	28.9
9	188	73	99	3	Straia	[4]	1.	Left SS	.496	.498	.498	1.8	44.5
10	194	88	104	7	Straia	[4]	1.	Left SS	.577	.486	.486	1.7	48.5
11	131	79	43	8	Straia	[4]	1.	Left SS	.047	-.191	.198	164.7	10.9
12	200	87	111	13	Straia	[4]	1.	Normal-Left SS	.677	.457	.46	6.9	54.6

21. Leynar

#	Dip Azim	Dip	Trend	Plunge	Type	QF	Wt	Slip Sense	Norm. Stress	Shear Stress	Max. Shear	Misfit Angle	Fault Angle
1	29	57	311	18	Straia	[4]	1.	Normal-Left SS	.552	.489	.492	6.5	47.2
2	24	68	305	25	Straia	[4]	1.	Normal-Left SS	.393	.488	.488	2.3	38.8
3	28	64	305	13	Straia	[4]	1.	Normal-Left SS	.481	.486	.499	13.2	43.9
4	34	65	313	19	Straia	[4]	1.	Normal-Left SS	.558	.495	.497	3.8	48.3
5	116	90	206	32	Straia	[4]	1.	Normal-Right SS	.589	.426	.436	12.3	42.2
6	280	70	192	5	Straia	[4]	1.	Left SS	.67	-.244	.272	153.7	32.
7	320	44	35	14	Straia	[4]	1.	Normal-Right SS	.406	.242	.305	37.4	6.9
8	342	75	291	67	Straia	[4]	1.	Left Normal	.056	.121	.178	47.2	1.3
9	347	62	336	62		[4]	1.	Tension Fracture	.157		.301	28.2	
10	349	49	328	47		[4]	1.	Tension Fracture	.315		.38	41.	
11	339	59	2	57		[4]	1.	Tension Fracture	.193		.302	33.	
12	361	54	314	43		[4]	1.	Tension Fracture	.303		.417	37.1	
13	330	60	25	45		[4]	1.	Tension Fracture	.216		.297	36.	
14	380	83	293	21		[4]	1.	Tension Fracture	.232		.414	29.6	
15	390	64	313	24		[4]	1.	Tension Fracture	.509		.5	45.5	

22. Kaldbaksbotnur

#	Dip Azim	Dip	Trend	Plunge	Type	QF	Wt	Slip Sense	Norm. Stress	Shear Stress	Max. Shear	Misfit Angle	Fault Angle
1	98	51	217	-31	Straia	[4]	1.	Right-Reverse Diag.	.218	.284	.351	35.9	21.3
2	111	56	226	-32	Straia	[4]	1.	Reverse-Right SS	.248	.242	.309	38.5	16.8
3	111	68	204	-6	Straia	[4]	1.	Right SS	.379	.159	.337	61.8	23.6
4	66	62	178	-35	Straia	[4]	1.	Reverse-Right SS	.475	.372	.498	41.6	43.4
5	44	87	329	79	Straia	[4]	1.	Left Normal	.86	-.292	.324	154.2	65.8
6	61	65	354	40	Straia	[4]	1.	Left-Normal Diag.	.536	-.387	.499	140.8	47.1
7	95	21	279	-21	Straia	[4]	1.	Reverse	.008	.025	.06	65.6	.9
8	310	33	72	-19	Straia	[4]	1.	Reverse-Right SS	.317	.362	.362	.6	23.8
9	10	50	230	-43	Straia	[4]	1.	Left-Reverse	.268	.29	.315	23.1	17.8
10	24	45	239	-39	Straia	[4]	1.	Left-Reverse	.218	.315	.344	23.8	20.6
11	28	35	234	-32	Straia	[4]	1.	Left-Reverse	.111	.225	.258	29.3	13.3
12	223	49	346	-32	Straia	[4]	1.	Right-Reverse Diag.	.816	.15	.381	66.8	63.9
13	50	45	244	-44	Straia	[4]	1.	Reverse	.218	.394	.405	13.1	27.
14	55	43	246	-42	Straia	[4]	1.	Reverse	.187	.376	.386	13.1	25.3
15	59	40	243	-40	Straia	[4]	1.	Reverse	.145	.346	.351	9.8	22.3
16	62	45	212	-41	Straia	[4]	1.	Right-Reverse	.208	.391	.405	15.2	27.1
17	64	40	266	-38	Straia	[4]	1.	Left-Reverse	.14	.315	.347	24.9	22.
18	64	52	213	-48	Straia	[4]	1.	Right-Reverse	.311	.451	.463	12.8	33.9
19	65	57	231	-56	Straia	[4]	1.	Reverse	.391	.487	.487	.4	38.7
20	68	25	252	-25	Straia	[4]	1.	Reverse	.014	.113	.118	16.8	6.8
21	253	3	80	-3	Straia	[4]	1.	Reverse	.128	.318	.331	15.9	20.6
22	74	41	251	-41	Straia	[4]	1.	Reverse	.14	.339	.343	7.6	21.5
23	76	44	240	-43	Straia	[4]	1.	Right-Reverse	.174	.372	.372	1.8	23.9
24	78	62	204	-48	Straia	[4]	1.	Right-Reverse	.439	.454	.48	19.	39.8
25	159	53	72	4	Straia	[4]	1.	Left SS	.356	.246	.313	38.2	20.3
26	164	53	83	12	Straia	[4]	1.	Normal-Left SS	.394	.232	.337	46.4	24.2

23. Kaldbaksfjorður

#	Dip Azim	Dip	Trend	Plunge	Type	QF	Wt	Slip Sense	Norm. Stress	Shear Stress	Max. Shear	Misfit Angle	Fault Angle
1	77	41	174	-6	Straia	[4]	1.	Right SS	.6	.306	.326	20.1	36.1
2	132	42	225	-3	Straia	[4]	1.	Right SS	.242	.081	.246	70.9	5.6

3	147	65	255	-34	Straia	[4]	1.	Reverse-Right SS	.076	-.183	.191	163.3	6.2
4	356	78	74	44	Straia	[4]	1.	Right-Normal Diag.	.363	-.293	.464	129.1	35.2
5	339	70	64	14	Straia	[4]	1.	Normal-Right SS	.168	-.242	.318	139.4	18.
6	291	84	21	1	Straia	[4]	1.	Right SS	.243	.42	.422	5.4	28.7
7	299	81	30	-8	Straia	[4]	1.	Right SS	.146	.313	.336	21.2	20.6
8	303	70	38	-14	Straia	[4]	1.	Reverse-Right SS	.148	.212	.295	44.	15.8
9	304	81	34	1	Straia	[4]	1.	Right SS	.095	.26	.273	17.3	15.7
10	136	64	230	-9	Straia	[4]	1.	Right SS	.074	.034	.178	78.9	3.7
11	358	84	86	15	Straia	[4]	1.	Normal-Right SS	.387	-.455	.481	161.1	37.8
12	296	79	212	28	Straia	[4]	1.	Normal-Left SS	.186	-.277	.37	138.6	23.4
13	281	86	193	31	Straia	[4]	1.	Normal-Left SS	.399	-.403	.486	146.1	38.8
14	325	83	235	2	Straia	[4]	1.	Left SS	.023	.09	.12	41.8	5.1
15	321	78	230	-5	Straia	[4]	1.	Left SS	.034	.008	.122	86.4	1.1
16	330	69	244	11	Straia	[4]	1.	Normal-Left SS	.107	.191	.231	34.4	9.5
17	327	73	245	24	Straia	[4]	1.	Normal-Left SS	.071	.169	.19	27.3	6.8
18	325	88	235	-5	Straia	[4]	1.	Left SS	.012	.083	.098	31.9	5.1
19	4	70	275	3	Straia	[4]	1.	Left SS	.497	.463	.463	1.4	40.9

24. Hvannhagi

#	Dip Azim	Dip	Trend	Plunge	Type	QF	Wt	Slip Sense	Norm. Stress	Shear Stress	Max. Shear	Misfit Angle	Fault Angle
1	333	15	314	14	Straia	[4]	1.	Left Normal	.943	.216	.218	7.7	75.4
2	161	65	149	65	Straia	[4]	1.	Normal	.198	.336	.356	19.3	23.6
3	348	80	33	76	Straia	[4]	1.	Normal	.075	.202	.203	4.5	11.8
4	181	82	263	45	Straia	[4]	1.	Right-Normal Diag.	.018	.095	.101	19.9	5.5
5	187	64	209	62	Straia	[4]	1.	Normal	.157	.36	.361	4.3	23.2
6	187	74	253	55	Straia	[4]	1.	Right-Normal	.055	.203	.222	24.1	13.2
7	196	82	250	76	Straia	[4]	1.	Right-Normal	.007	.082	.084	10.	4.8
8	196	87	278	69	Straia	[4]	1.	Right-Normal	.	-.003	.003	178.6	.2
9	197	80	191	80	Straia	[4]	1.	Normal	.014	.117	.117	.9	6.8
10	200	84	200	84	Straia	[4]	1.	Normal	.003	.047	.048	12.6	2.7
11	206	81	172	79	Straia	[4]	1.	Normal	.014	.098	.099	8.6	5.5
12	31	84	324	75	Straia	[4]	1.	Left Normal	.038	.167	.167	.5	9.6
13	212	32	210	32	Straia	[4]	1.	Normal	.665	.467	.467	.8	54.3

14	36	73	337	59	Straia	[4]	1.	Left Normal	.141	.314	.328	16.9	20.7
15	45	78	334	57	Straia	[4]	1.	Left Normal	.108	.249	.26	16.7	15.8

25. Famjin

#	Dip Azim	Dip	Trend	Plunge	Type	QF	Wt	Slip Sense	Norm. Stress	Shear Stress	Max. Shear	Misfit Angle	Fault Angle
1	48	78	320	11	Straia	[4]	1.	Normal-Left SS	.566	.485	.487	5.4	47.8
2	199	70	110	2	Straia	[4]	1.	Left SS	.199	.216	.261	34.3	9.
3	30	53	305	7	Straia	[4]	1.	Left SS	.352	.455	.457	6.2	34.2
4	19	67	297	17	Straia	[4]	1.	Normal-Left SS	.158	.363	.363	1.1	23.2
5	8	67	288	23	Straia	[4]	1.	Normal-Left SS	.061	.23	.231	5.3	13.4
6	21	65	298	15	Straia	[4]	1.	Normal-Left SS	.189	.388	.388	.8	25.4
7	347	57	100	-31	Straia	[4]	1.	Reverse-Right SS	.073	-.029	.172	99.8	.8
8	322	90	52	-30	Straia	[4]	1.	Reverse-Right SS	.357	.475	.479	7.6	36.6
9	138	70	219	22	Straia	[4]	1.	Normal-Right SS	.551	.48	.481	2.8	46.1

26. Hov

#	Dip Azim	Dip	Trend	Plunge	Type	QF	Wt	Slip Sense	Norm. Stress	Shear Stress	Max. Shear	Misfit Angle	Fault Angle
1	107	51	155	40	Straia	[4]	1.	Right-Normal	.925	.248	.263	19.6	74.
2	124	85	202	67	Straia	[4]	1.	Right-Normal	.426	.418	.467	26.5	37.5
3	136	64	206	35	Straia	[4]	1.	Right-Normal Diag.	.54	.493	.497	7.3	47.1
4	136	68	191	55	Straia	[4]	1.	Right-Normal	.488	.484	.5	14.6	44.3
5	143	65	277	-56	Straia	[4]	1.	Right-Reverse	.455	-.223	.493	116.9	41.8
6	145	76	181	73	Straia	[4]	1.	Normal	.292	.397	.454	29.1	32.6
7	148	65	229	18	Straia	[4]	1.	Normal-Right SS	.408	.399	.481	34.1	38.5
8	160	58	160	58	Straia	[4]	1.	Normal	.414	.399	.449	27.2	35.
9	302	85	34	-24	Straia	[4]	1.	Reverse-Right SS	.352	.409	.418	12.2	29.5
10	431	64	4	39		[4]	1.	Tension Fracture	.896		.226	81.6	
11	394	89	304	12		[4]	1.	Tension Fracture	.384		.358	50.5	
12	370	89	280	-9		[4]	1.	Tension Fracture	.122		.241	27.9	
13	400	71	318	22		[4]	1.	Tension Fracture	.546		.441	53.7	
14	248	80	138	-63		[4]	1.	Tension Fracture	.627		.213	86.	
15	363	79	276	13		[4]	1.	Tension Fracture	.068		.22	18.3	

27. Vagseiði

#	Dip Azim	Dip	Trend	Plunge	Type	QF	Wt	Slip Sense	Norm. Stress	Shear Stress	Max. Shear	Misfit Angle	Fault Angle
1	295	43	291	43	Straia	[4]	1.	Normal	.52	.412	.438	19.9	40.5
2	115	41	155	34	Straia	[4]	1.	Right-Normal	.717	.413	.423	12.5	55.3
3	119	71	145	69	Straia	[4]	1.	Normal	.276	.355	.379	20.6	25.2
4	124	41	163	34	Straia	[4]	1.	Right-Normal	.688	.437	.449	13.5	54.7
5	132	71	117	70	Straia	[4]	1.	Normal	.204	.334	.376	27.5	24.3
6	312	64	323	64	Straia	[4]	1.	Normal	.176	.328	.338	13.8	20.6
7	138	54	150	53	Straia	[4]	1.	Normal	.432	.488	.491	6.1	40.7
8	140	64	135	64	Straia	[4]	1.	Normal	.267	.42	.436	15.7	30.5
9	322	67	309	66	Straia	[4]	1.	Normal	.117	.295	.305	15.	18.4
10	144	65	158	64	Straia	[4]	1.	Normal	.24	.423	.425	5.	29.1
11	146	62	140	62	Straia	[4]	1.	Normal	.281	.439	.449	12.1	31.9
12	152	48	182	44	Straia	[4]	1.	Right-Normal	.505	.481	.499	15.5	45.2
13	155	52	158	52	Straia	[4]	1.	Normal	.432	.493	.493	1.5	40.9
14	157	47	170	46	Straia	[4]	1.	Normal	.517	.493	.496	6.	45.6
15	343	43	348	43	Straia	[4]	1.	Normal	.49	.481	.499	15.5	44.4
16	344	19	337	19	Straia	[4]	1.	Normal	.859	.344	.348	8.5	67.9
17	168	57	182	56	Straia	[4]	1.	Normal	.352	.444	.457	13.5	34.4
18	169	45	176	45	Straia	[4]	1.	Normal	.551	.474	.479	7.7	46.1
19	357	51	351	51	Straia	[4]	1.	Normal	.407	.455	.475	16.8	38.1
20	180	44	220	37	Straia	[4]	1.	Right-Normal	.578	.357	.454	38.1	45.8
21	2	53	23	51	Straia	[4]	1.	Right-Normal	.401	.369	.463	37.	36.7

28. Gasadalur

#	Dip Azim	Dip	Trend	Plunge	Type	QF	Wt	Slip Sense	Norm. Stress	Shear Stress	Max. Shear	Misfit Angle	Fault Angle
1	358	46	347	45	Straia	[4]	1.	Normal	.586	.452	.461	11.5	46.9
2		57	4	57	Straia	[4]	1.	Normal	.406	.459	.46	4.4	36.5
3	182	47	215	42	Straia	[4]	1.	Right-Normal	.391	.481	.483	6.	38.2
4	188	37	207	36	Straia	[4]	1.	Right-Normal	.539	.498	.498	1.8	47.2
5	211	38	227	37	Straia	[4]	1.	Right-Normal	.5	.469	.488	16.1	43.8
6	217	37	221	37	Straia	[4]	1.	Normal	.523	.473	.48	10.	44.4

29. Sandavagur

#	Dip Azim	Dip	Trend	Plunge	Type	QF	Wt	Slip Sense	Norm. Stress	Shear Stress	Max. Shear	Misfit Angle	Fault Angle
1	159	63	245	8	Straia	[4]	1.	Right SS	.053	.065	.155	65.3	1.2
2	2	81	93	-4	Straia	[4]	1.	Right SS	.136	-.287	.301	162.9	16.6
3	173	84	262	12	Straia	[4]	1.	Normal-Right SS	.03	-.167	.169	172.5	9.7
4	133	71	233	-26	Straia	[4]	1.	Reverse-Right SS	.229	.354	.4	27.8	26.3
5	132	87	223	-23	Straia	[4]	1.	Reverse-Right SS	.268	.433	.443	12.3	31.2
6	141	70	237	-15	Straia	[4]	1.	Reverse-Right SS	.135	.292	.318	23.5	18.8
7	134	81	227	-18	Straia	[4]	1.	Reverse-Right SS	.225	.407	.415	11.	28.
8	157	82	245	12	Straia	[4]	1.	Normal-Right SS	.01	.096	.101	18.3	5.8
9	161	89	251	-7	Straia	[4]	1.	Right SS	.01	.048	.078	52.4	2.8

30. N. Vidareiði

#	Dip Azim	Dip	Trend	Plunge	Type	QF	Wt	Slip Sense	Norm. Stress	Shear Stress	Max. Shear	Misfit Angle	Fault Angle
1	308	71	36	7	Straia	[4]	1.	Right SS	.252	.349	.378	22.8	.
2	320	85	50	1	Straia	[4]	1.	Right SS	.074	.236	.239	9.1	5.8
3	144	81	235	-7	Straia	[4]	1.	Right SS	.074	.178	.26	46.6	15.1
4	330	90	60	22	Straia	[4]	1.	Normal-Right SS	.012	.088	.105	32.9	4.3
5	336	88	66	9	Straia	[4]	1.	Right SS	.001	.013	.024	58.1	.7
6	319	63	279	56	Straia	[4]	1.	Left Normal	.231	.236	.379	51.5	12.1
7	140	80	206	67	Straia	[4]	1.	Right-Normal	.111	.259	.311	33.5	18.2
8	145	87	220	79	Straia	[4]	1.	Right-Normal	.042	.107	.194	56.6	9.6
9	336	84	283	80	Straia	[4]	1.	Normal	.008	.086	.087	10.2	4.
10	336	89	252	80	Straia	[4]	1.	Left Normal	.	.003	.012	73.4	.1
11	346	80	295	74	Straia	[4]	1.	Left Normal	.052	.189	.221	31.3	13.
12	347	70	293	58	Straia	[4]	1.	Left Normal	.138	.343	.344	5.2	21.6
13	5	85	279	38	Straia	[4]	1.	Normal-Left SS	.208	.352	.384	23.6	19.5

31. E. Vidareiði

#	Dip Azim	Dip	Trend	Plunge	Type	QF	Wt	Slip Sense	Norm. Stress	Shear Stress	Max. Shear	Misfit Angle	Fault Angle
1	133	65	240	-32	Straia	[4]	1.	Reverse-Right SS	.273	.347	.426	35.5	29.4
2	140	79	233	-15	Straia	[4]	1.	Reverse-Right SS	.186	.384	.389	9.5	25.6
3	141	85	235	-37	Straia	[4]	1.	Reverse-Right SS	.184	.341	.384	27.3	25.1

4	141	83	235	-30	Straia	[4]	1.	Reverse-Right SS	.18	.355	.383	21.7	24.9
5	321	65	52	-2	Straia	[4]	1.	Right SS	.307	.323	.36	26.4	23.1
6	143	72	241	-23	Straia	[4]	1.	Reverse-Right SS	.145	.314	.347	25.3	21.8
7	143	81	237	-22	Straia	[4]	1.	Reverse-Right SS	.151	.345	.358	15.2	22.8
8	324	82	47	40	Straia	[4]	1.	Right-Normal Diag.	.189	.337	.358	19.8	22.1
9	144	65	236	-5	Straia	[4]	1.	Right SS	.142	.317	.327	13.9	19.7
10	333	78	66	-15	Straia	[4]	1.	Reverse-Right SS	.124	.162	.263	52.1	13.1
11	293	25	282	25	Straia	[4]	1.	Left Normal	.524	-.141	.18	141.3	20.5
12	287	12	153	-8	Straia	[4]	1.	Left-Reverse Diag.	.475	.067	.112	53.	11.
13	150	78	71	41	Straia	[4]	1.	Left-Normal Diag.	.074	-.202	.261	140.9	15.7
14	354	83	273	51	Straia	[4]	1.	Left Normal	.066	.187	.188	5.3	7.6
15	7	64	289	22	Straia	[4]	1.	Normal-Left SS	.267	.321	.323	6.5	18.2
16	13	69	292	21	Straia	[4]	1.	Normal-Left SS	.301	.375	.375	2.3	24.5
17	194	64	105	3	Straia	[4]	1.	Left SS	.211	.387	.387	1.9	25.1
18	14	79	287	14	Straia	[4]	1.	Normal-Left SS	.27	.403	.403	2.1	27.
19	182	45	343	-43	Straia	[4]	1.	Right-Reverse	.179	-.218	.268	144.3	11.6
20	226	29	66	-27	Straia	[4]	1.	Left-Reverse	.479	.192	.301	50.3	25.5

32. W. Vidareiði

#	Dip Azim	Dip	Trend	Plunge	Type	QF	Wt	Slip Sense	Norm. Stress	Shear Stress	Max. Shear	Misfit Angle	Fault Angle
1	140	88	229	29	Straia	[0]	1.	Normal-Right SS	.076	.261	.264	9.1	15.9
2	137	89	226	40	Straia	[0]	1.	Right-Normal Diag.	.101	.277	.301	23.	18.5
3	115	89	204	35	Straia	[0]	1.	Normal-Right SS	.409	.457	.489	20.7	39.4
4	312	85	48	-49	Straia	[0]	1.	Right-Reverse Diag.	.141	.264	.342	39.5	21.4
5	313	89	43	-2	Straia	[0]	1.	Right SS	.139	.337	.345	11.7	21.7
6	303	85	34	-9	Straia	[0]	1.	Right SS	.261	.431	.431	2.2	29.8
7	144	68	229	11	Straia	[0]	1.	Normal-Right SS	.154	.259	.308	32.6	16.9
8	314	87	45	-20	Straia	[0]	1.	Reverse-Right SS	.122	.321	.325	8.4	20.2
9	345	66	79	-8	Straia	[0]	1.	Right SS	.1	-.227	.267	148.2	14.5
10	345	58	81	-9	Straia	[0]	1.	Reverse-Right SS	.155	-.247	.301	145.	16.
11	133	64	209	27	Straia	[0]	1.	Normal-Right SS	.285	.408	.408	.4	27.4
12	319	80	51	-13	Straia	[0]	1.	Reverse-Right SS	.066	.227	.234	14.2	13.2
13	141	82	227	28	Straia	[0]	1.	Normal-Right SS	.091	.279	.279	.6	16.6

14	331	89	61	-19	Straia	[0]	1.	Reverse-Right SS	.007	.08	.081	10.9	4.5
15	308	84	41	-25	Straia	[0]	1.	Reverse-Right SS	.188	.369	.383	15.6	24.8
16	325	81	56	-5	Straia	[0]	1.	Right SS	.027	.145	.148	11.2	7.9
17	316	87	47	-11	Straia	[0]	1.	Reverse-Right SS	.101	.299	.299	.6	18.3
18	136	88	226	-3	Straia	[0]	1.	Right SS	.114	.298	.318	20.7	19.8
19	141	80	228	18	Straia	[0]	1.	Normal-Right SS	.101	.281	.288	12.7	17.1
20	304	83	37	-26	Straia	[0]	1.	Reverse-Right SS	.241	.399	.416	16.3	28.1
21	137	71	218	25	Straia	[0]	1.	Normal-Right SS	.193	.364	.366	5.3	22.8
22	149	75	259	-52	Straia	[0]	1.	Right-Reverse	.076	-.065	.222	107.1	10.7
23	329	89	61	-64	Straia	[0]	1.	Right-Reverse	.013	.086	.113	40.4	6.5
24	188	85	274	41	Straia	[0]	1.	Right-Normal Diag.	.276	-.33	.421	141.6	28.8
25	338	44	115	-35	Straia	[0]	1.	Right-Reverse	.242	-.29	.293	172.5	13.
26	344	60	76	-3	Straia	[0]	1.	Right SS	.135	-.205	.285	135.9	14.8
27	332	58	67	-8	Straia	[0]	1.	Right SS	.11	-.057	.215	105.4	5.2
28	150	77	228	42	Straia	[0]	1.	Right-Normal Diag.	.06	.194	.198	10.8	9.3
29	351	80	86	-29	Straia	[0]	1.	Reverse-Right SS	.086	-.273	.28	167.	17.
30	116	84	204	17	Straia	[0]	1.	Normal-Right SS	.414	.492	.492	1.8	40.
31	325	87	56	-13	Straia	[0]	1.	Reverse-Right SS	.029	.167	.167	.1	9.7
32	329	85	60	-16	Straia	[0]	1.	Reverse-Right SS	.009	.092	.094	10.6	5.3
33	134	79	214	41	Straia	[0]	1.	Right-Normal Diag.	.177	.356	.374	17.6	24.
34	133	80	216	34	Straia	[0]	1.	Normal-Right SS	.183	.373	.381	12.	24.7
35	311	38	245	18	Straia	[0]	1.	Normal-Left SS	.3	-.019	.239	94.4	1.7
36	128	89	218	-15	Straia	[4]	1.	Reverse-Right SS	.209	.352	.406	29.8	27.1
37	128	85	216	17	Straia	[4]	1.	Normal-Right SS	.225	.417	.417	.3	28.3
38	129	79	219	-1	Straia	[4]	1.	Right SS	.24	.391	.422	22.1	28.8
39	131	82	223	-11	Straia	[4]	1.	Reverse-Right SS	.198	.338	.396	31.5	26.2
40	122	75	214	-6	Straia	[4]	1.	Right SS	.362	.43	.474	24.8	36.2
41	137	86	47	3	Straia	[4]	1.	Left SS	.111	-.288	.313	156.6	19.4
42	1	65	273	5	Straia	[0]	1.	Left SS	.262	.409	.424	15.4	29.1
43	10	88	280	11	Straia	[0]	1.	Normal-Left SS	.316	.454	.455	4.3	33.1
44	358	84	274	44	Straia	[0]	1.	Left-Normal Diag.	.152	.293	.357	35.	22.7
45	179	79	84	-24	Straia	[0]	1.	Reverse-Left SS	.163	.27	.322	33.2	18.3
46	214	34	68	-29	Straia	[0]	1.	Left-Reverse	.491	.112	.157	44.6	12.9

47	208	26	65	-21	Straia	[0]	1.	Left-Reverse	.475	.038	.102	67.9	4.6

Event 2 Thrusts

1. Strendur

#	Dip Azim	Dip	Trend	Plunge	Type	QF	Wt	Slip Sense	Norm. Stress	Shear Stress	Max. Shear	Misfit Angle	Fault Angle
1	196	18	251	10	Straia	[4]	1.	Normal-Right SS	.002	.002	.032	86.2	.1
2	166	22	240	6	Straia	[4]	1.	Normal-Right SS	.035	.112	.15	41.7	6.7
3	248	31	239	31	Straia	[4]	1.	Normal	.119	-.291	.309	160.1	18.6
4	5	23	246	-12	Straia	[4]	1.	Reverse-Left SS	.261	.338	.373	24.9	23.5
5	126	26	244	-13	Straia	[4]	1.	Reverse-Right SS	.18	.36	.363	6.9	22.8
6	81	13	246	-13	Straia	[4]	1.	Right-Reverse	.177	.374	.38	9.8	24.7
7	212	29	46	-28	Straia	[4]	1.	Left-Reverse	.052	.216	.218	7.	12.6

2. Rituvik

#	Dip Azim	Dip	Trend	Plunge	Type	QF	Wt	Slip Sense	Norm. Stress	Shear Stress	Max. Shear	Misfit Angle	Fault Angle
1	258	19	77	-19	Straia	[4]	1.	Reverse	.06	.234	.235	4.6	13.9
2	308	24	91	-19	Straia	[4]	1.	Right-Reverse	.092	.195	.225	29.8	9.2
3	248	15	75	-15	Straia	[4]	1.	Reverse	.029	.169	.169	1.3	9.9
4	64	19	265	-18	Straia	[4]	1.	Left-Reverse	.166	.355	.369	16.1	23.7
5	114	24	257	-19	Straia	[4]	1.	Right-Reverse	.179	.363	.367	8.6	23.1
6	245	28	68	-28	Straia	[4]	1.	Reverse	.148	.354	.355	3.9	22.6
7	102	18	267	-17	Straia	[4]	1.	Right-Reverse	.133	.333	.335	6.5	20.9
8	114	25	258	-21	Straia	[4]	1.	Right-Reverse	.191	.373	.375	6.7	23.8
9	86	18	229	-14	Straia	[4]	1.	Right-Reverse	.149	.321	.356	25.5	22.7
10	104	11	271	-11	Straia	[4]	1.	Right-Reverse	.065	.24	.245	11.	14.6
11	58	13	244	-13	Straia	[4]	1.	Reverse	.096	.289	.29	1.1	17.5
12	291	27	78	-23	Straia	[4]	1.	Right-Reverse	.129	.277	.297	21.2	16.6
13	274	27	94	-27	Straia	[4]	1.	Reverse	.139	.332	.333	4.6	20.4

14	252	27	76	-27	Straia	[4]	1.	Reverse	.14	.347	.347	.1	21.9
15	101	21	265	-20	Straia	[4]	1.	Right-Reverse	.169	.368	.369	4.5	23.7
16	144	43	253	-17	Straia	[4]	1.	Reverse-Right SS	.278	.276	.328	32.7	17.5
17	258	35	90	-34	Straia	[4]	1.	Reverse	.251	.426	.432	9.4	29.9
18	131	7	251	-3	Straia	[4]	1.	Reverse-Right SS	.026	.15	.155	14.3	8.9
19	238	26	78	-25	Straia	[4]	1.	Left-Reverse	.119	.318	.321	8.3	19.9
20	152	33	249	-4	Straia	[4]	1.	Right SS	.161	.164	.27	52.7	11.
21	42	19	269	-13	Straia	[4]	1.	Left-Reverse Diag.	.15	.302	.341	27.8	20.9
22	230	30	77	-27	Straia	[4]	1.	Left-Reverse	.157	.347	.354	11.3	22.2
23	264	35	77	-35	Straia	[4]	1.	Reverse	.25	.427	.428	3.7	29.4
24	280	20	58	-15	Straia	[4]	1.	Right-Reverse Diag.	.068	.187	.234	37.	13.
25	246	17	59	-17	Straia	[4]	1.	Reverse	.042	.193	.2	15.1	11.8
26	36	11	243	-10	Straia	[4]	1.	Left-Reverse	.068	.237	.239	6.5	13.6
27	33	7	254	-5	Straia	[4]	1.	Left-Reverse Diag.	.039	.175	.184	17.9	10.3
28	108	2	270	-2	Straia	[4]	1.	Right-Reverse	.014	.109	.116	20.8	6.7
29	220	37	49	-37	Straia	[4]	1.	Reverse	.227	.384	.39	9.7	25.1
30	112	21	238	-13	Straia	[4]	1.	Reverse-Right SS	.15	.309	.345	26.3	21.4
31	12	15	266	-4	Straia	[4]	1.	Reverse-Left SS	.078	.171	.232	42.5	11.8
32	141	23	238	-3	Straia	[4]	1.	Right SS	.108	.18	.265	47.	13.6
33	70	8	257	-8	Straia	[4]	1.	Reverse	.052	.218	.221	9.	13.
34	253	9	65	-9	Straia	[4]	1.	Reverse	.005	.065	.071	24.3	4.
35	52	15	250	-14	Straia	[4]	1.	Left-Reverse	.114	.309	.31	6.	18.9
36	243	14	53	-14	Straia	[4]	1.	Right-Reverse	.023	.14	.149	20.	8.7
37	234	23	83	-20	Straia	[4]	1.	Left-Reverse	.085	.264	.275	16.	16.5
38	86	23	240	-21	Straia	[4]	1.	Right-Reverse	.215	.398	.41	14.	27.5
39	244	15	50	-15	Straia	[4]	1.	Right-Reverse	.028	.153	.166	23.3	9.7

3. W. Sandur

#	Dip Azim	Dip	Trend	Plunge	Type	QF	Wt	Slip Sense	Norm. Stress	Shear Stress	Max. Shear	Misfit Angle	Fault Angle
1	78	25	224	-21	Straia	[4]	1.	Right-Reverse	.143	.336	.347	14.2	21.8
2	89	20	253	-19	Straia	[4]	1.	Right-Reverse	.078	.26	.262	6.6	15.4
3	217	21	64	-19	Straia	[4]	1.	Left-Reverse	.129	.33	.334	9.7	21.
4	197	29	45	-26	Straia	[4]	1.	Left-Reverse	.189	.375	.376	2.8	23.7

5	272	15	70	-14	Straia	[4]	1.	Right-Reverse	.08	.237	.245	13.9	12.7
6	214	14	20	-14	Straia	[4]	1.	Right-Reverse	.059	.196	.236	34.	14.1

4. E.Sandur

#	Dip Azim	Dip	Trend	Plunge	Type	QF	Wt	Slip Sense	Norm. Stress	Shear Stress	Max. Shear	Misfit Angle	Fault Angle
1	92	20	89	20	Straia	[4]	1.	Normal	.961	.14	.152	23.3	75.1
2	252	39	249	39	Straia	[4]	1.	Normal	.415	.485	.492	9.2	40.
3	246	30	249	30	Straia	[4]	1.	Normal	.561	.49	.496	9.	48.5
4	237	41	230	41	Straia	[4]	1.	Normal	.368	.476	.48	7.3	37.1
5	224	35	251	32	Straia	[4]	1.	Right-Normal	.487	.479	.487	10.6	42.8
6	262	38	216	29	Straia	[4]	1.	Left Normal	.46	.463	.492	19.6	41.9
7	233	22	234	22	Straia	[4]	1.	Normal	.692	.457	.458	2.5	55.9
8	220	23	239	22	Straia	[4]	1.	Right-Normal	.688	.45	.452	4.7	54.8
9	252	29	253	29	Straia	[4]	1.	Normal	.585	.482	.492	11.8	49.9

5. Satan

#	Dip Azim	Dip	Trend	Plunge	Type	QF	Wt	Slip Sense	Norm. Stress	Shear Stress	Max. Shear	Misfit Angle	Fault Angle
1	57	40	53	40	Straia	[4]	1.	Normal	.294	-.445	.447	175.3	31.7
2	78	32	65	31	Straia	[4]	1.	Left Normal	.145	-.35	.352	173.4	22.4
3	202	26	68	-19	Straia	[4]	1.	Left-Reverse Diag.	.227	.409	.413	8.8	27.8
4	244	16	68	-16	Straia	[4]	1.	Reverse	.181	.375	.377	5.7	24.1
5	74	17	255	-17	Straia	[4]	1.	Reverse	.026	.127	.152	33.1	8.4
6	223	23	58	-22	Straia	[4]	1.	Left-Reverse	.249	.429	.432	7.8	29.9
7	211	35	46	-34	Straia	[4]	1.	Left-Reverse	.386	.462	.48	15.9	37.5
8	83	31	231	-27	Straia	[4]	1.	Right-Reverse	.124	.325	.329	8.9	20.5
9	80	32	210	-22	Straia	[4]	1.	Right-Reverse Diag.	.141	.31	.348	26.9	22.
10	92	23	269	-23	Straia	[4]	1.	Reverse	.041	.184	.197	21.	11.5

6. Skaelingsfjjall

#	Dip Azim	Dip	Trend	Plunge	Type	QF	Wt	Slip Sense	Norm. Stress	Shear Stress	Max. Shear	Misfit Angle	Fault Angle
1	334	49	59	5	Straia	[4]	1.	Right SS	.136	.064	.246	75.	5.7
2	331	51	57	5	Straia	[4]	1.	Right SS	.161	.091	.266	70.	8.
3	312	28	55	-7	Straia	[4]	1.	Reverse-Right SS	.081	.256	.268	17.1	15.9

4	22	38	33	37	Straia	[4]	1.	Normal	.142	-.299	.343	150.8	21.4
5	38	15	32	15	Straia	[4]	1.	Normal	.048	-.044	.182	103.9	8.3
6	26	20	29	20	Straia	[4]	1.	Normal	.039	-.093	.185	120.2	10.2
7	250	14	244	14	Straia	[4]	1.	Normal	.159	-.295	.329	153.4	18.7
8	49	35	62	34	Straia	[4]	1.	Right-Normal	.234	-.394	.418	160.4	28.3
9	10	18	61	11	Straia	[4]	1.	Right-Normal Diag.	.012	-.079	.099	142.8	5.
10	256	22	255	22	Straia	[4]	1.	Normal	.236	-.357	.404	152.	26.5
11	59	32	261	-30	Straia	[4]	1.	Left-Reverse	.235	.403	.407	8.2	26.9
12	38	44	267	-32	Straia	[4]	1.	Left-Reverse	.296	.451	.456	8.	32.9
13	42	19	241	-18	Straia	[4]	1.	Left-Reverse	.069	.187	.232	36.2	12.4
14	68	5	252	-5	Straia	[4]	1.	Reverse	.066	.018	.179	84.2	.2
15	14	27	243	-18	Straia	[4]	1.	Left-Reverse Diag.	.039	.191	.192	4.5	11.3
16	278	22	78	-21	Straia	[4]	1.	Right-Reverse	.169	.332	.368	25.8	23.5
17	223	22	229	22	Straia	[0]	1.	Normal	.288	-.382	.392	167.5	24.6
18	59	7	60	7	Straia	[0]	1.	Normal	.061	-.013	.174	94.3	2.2
19	238	25	245	25	Straia	[0]	1.	Normal	.314	-.4	.427	159.6	29.4
20	72	37	65	37	Straia	[0]	1.	Normal	.345	-.409	.445	156.9	32.1
21	306	29	258	20	Straia	[0]	1.	Left-Normal Diag.	.11	-.304	.31	169.3	19.
22	244	28	265	26	Straia	[0]	1.	Right-Normal	.348	-.363	.449	144.	32.7
23	267	8	268	8	Straia	[0]	1.	Normal	.093	-.13	.251	121.1	12.3
24	269	75	238	73	Straia	[0]	1.	Normal	.88	-.24	.296	144.1	66.5
25	254	62	233	60	Straia	[0]	1.	Left Normal	.835	-.365	.371	170.2	65.9
26	32	15	36	15	Straia	[0]	1.	Normal	.039	-.051	.165	108.	7.5
27	12	25	93	4	Straia	[0]	1.	Normal-Right SS	.027	-.146	.161	155.2	9.4
28	100	1	87	1	Straia	[0]	1.	Left Normal	.074	-.001	.192	90.2	3.9

7. Kaldbaksbotnur

#	Dip Azim	Dip	Trend	Plunge	Type	QF	Wt	Slip Sense	Norm. Stress	Shear Stress	Max. Shear	Misfit Angle	Fault Angle
1	31	21	234	-19	Straia	[4]	1.	Left-Reverse	.181	.382	.384	5.9	25.
2	8	20	211	-18	Straia	[4]	1.	Left-Reverse	.132	.325	.327	6.1	19.7
3	235	22	38	-21	Straia	[4]	1.	Right-Reverse	.082	.272	.274	7.7	16.6
4	236	35	30	-32	Straia	[4]	1.	Right-Reverse	.242	.412	.429	15.9	29.5
5	25	31	213	-31	Straia	[4]	1.	Reverse	.311	.446	.455	11.5	32.8

6	347	20	229	-10	Straia	[4]	1.	Reverse-Left SS	.093	.238	.263	25.3	13.8
7	242	22	64	-22	Straia	[4]	1.	Reverse	.078	.262	.268	12.	16.2
8	38	3	214	-3	Straia	[4]	1.	Reverse	.022	.128	.145	28.3	8.3
9	232	31	76	-29	Straia	[4]	1.	Left-Reverse	.188	.35	.39	26.2	25.6
10	74	14	229	-13	Straia	[4]	1.	Right-Reverse	.111	.292	.305	16.4	18.2
11	83	13	244	-12	Straia	[4]	1.	Right-Reverse	.097	.281	.283	6.6	16.3
12	246	21	73	-21	Straia	[4]	1.	Reverse	.067	.237	.249	18.1	14.9
13	44	14	245	-13	Straia	[4]	1.	Left-Reverse	.109	.307	.311	9.7	19.2
14	249	23	66	-23	Straia	[4]	1.	Reverse	.083	.271	.274	8.3	16.5
15	77	19	235	-18	Straia	[4]	1.	Right-Reverse	.167	.353	.359	11.	22.3
16	224	18	332	-6	Straia	[4]	1.	Reverse-Right SS	.053	.099	.218	63.	12.5

8. Kaldbaksfjorður

#	Dip Azim	Dip	Trend	Plunge	Type	QF	Wt	Slip Sense	Norm. Stress	Shear Stress	Max. Shear	Misfit Angle	Fault Angle
1	128	12	235	-3	Straia	[4]	1.	Reverse-Right SS	.031	.148	.168	28.	9.2
2	104	13	233	-8	Straia	[4]	1.	Reverse-Right SS	.06	.226	.236	16.7	13.9
3	231	24	55	-24	Straia	[4]	1.	Reverse	.109	.308	.312	8.9	19.3
4	253	21	70	-21	Straia	[4]	1.	Reverse	.094	.278	.283	11.	16.5
5	228	28	53	-28	Straia	[4]	1.	Reverse	.151	.354	.358	8.7	22.8
6	229	23	66	-22	Straia	[4]	1.	Left-Reverse	.097	.295	.296	2.2	18.1
7	259	2	83	-2	Straia	[4]	1.	Reverse	.008	-.016	.072	102.9	2.2
8	226	15	51	-15	Straia	[4]	1.	Reverse	.031	.168	.174	15.	10.2
9	257	52	58	-50	Straia	[4]	1.	Right-Reverse	.554	.476	.482	9.	46.
10	82	11	231	-9	Straia	[4]	1.	Right-Reverse	.064	.241	.244	7.9	14.6
11	256	46	121	-36	Straia	[4]	1.	Left-Reverse	.453	.392	.486	36.2	40.5
12	223	30	94	-20	Straia	[4]	1.	Left-Reverse Diag.	.169	.311	.372	33.3	23.9
13	301	9	84	-7	Straia	[4]	1.	Right-Reverse	.03	.057	.132	64.5	.7
14	249	15	97	-13	Straia	[4]	1.	Left-Reverse	.043	.191	.195	12.	10.8
15	231	60	97	-51	Straia	[4]	1.	Left-Reverse	.663	.451	.468	15.5	53.9
16	242	22	65	-22	Straia	[4]	1.	Reverse	.098	.292	.294	7.6	17.8
17	217	41	23	-40	Straia	[4]	1.	Right-Reverse	.312	.405	.451	26.	32.1
18	253	33	71	-33	Straia	[4]	1.	Reverse	.243	.419	.421	5.	28.3
19	221	19	68	-17	Straia	[4]	1.	Left-Reverse	.055	.224	.226	8.5	13.4

20	79	2	266	-2	Straia	[4]	1.	Reverse	.015	.078	.116	47.7	6.1
21	84	26	218	-19	Straia	[4]	1.	Right-Reverse Diag.	.228	.377	.418	25.7	28.3
22	76	25	213	-19	Straia	[4]	1.	Right-Reverse Diag.	.227	.375	.419	26.7	28.5
23	41	24	216	-24	Straia	[4]	1.	Reverse	.228	.397	.404	10.1	26.2
24	72	25	260	-25	Straia	[4]	1.	Reverse	.233	.401	.423	18.2	28.8
25	56	20	160	-5	Straia	[4]	1.	Reverse-Right SS	.175	.12	.375	71.3	24.
26	281	23	93	-23	Straia	[4]	1.	Reverse	.122	.284	.286	8.3	14.
27	38	12	206	-12	Straia	[4]	1.	Right-Reverse	.085	.257	.266	15.	15.
28	50	29	222	-29	Straia	[4]	1.	Reverse	.306	.447	.452	8.6	32.3
29	274	35	78	-34	Straia	[4]	1.	Right-Reverse	.27	.401	.406	8.9	25.6
30	208	18	44	-17	Straia	[4]	1.	Left-Reverse	.038	.186	.187	3.9	10.5
31	53	18	232	-18	Straia	[4]	1.	Reverse	.15	.351	.351	1.7	21.8
32	122	36	260	-28	Straia	[4]	1.	Right-Reverse	.244	.371	.375	7.9	21.3

9. Hov

#	Dip Azim	Dip	Trend	Plunge	Type	QF	Wt	Slip Sense	Norm. Stress	Shear Stress	Max. Shear	Misfit Angle	Fault Angle
1	273	26	132	-21	Straia	[4]	1.	Left-Reverse	.112	.281	.299	20.	17.4
2	41	9	257	-7	Straia	[4]	1.	Left-Reverse	.106	.259	.276	20.3	14.6
3	98	54	281	-54	Straia	[4]	1.	Reverse	.766	.4	.422	18.5	60.9
4	80	39	272	-38	Straia	[4]	1.	Reverse	.557	.479	.487	10.4	47.
5	44	12	254	-10	Straia	[4]	1.	Left-Reverse	.137	.299	.309	14.5	17.1
6	81	44	268	-44	Straia	[4]	1.	Reverse	.641	.468	.471	6.2	52.1

10. Bour

#	Dip Azim	Dip	Trend	Plunge	Type	QF	Wt	Slip Sense	Norm. Stress	Shear Stress	Max. Shear	Misfit Angle	Fault Angle
1	182	36	29	-33	Straia	[4]	1.	Left-Reverse	.117	.318	.319	5.6	19.8
2	174	41	29	-35	Straia	[4]	1.	Left-Reverse	.156	.345	.351	10.5	22.
3	83	32	191	-11	Straia	[4]	1.	Reverse-Right SS	.264	.388	.408	18.1	27.5
4	167	31	39	-20	Straia	[4]	1.	Left-Reverse Diag.	.05	.173	.204	32.2	11.4
5	209	35	25	-35	Straia	[4]	1.	Reverse	.147	.332	.339	12.2	21.
6	246	59	49	-58	Straia	[4]	1.	Reverse	.444	.363	.366	8.1	29.2
7	44	7	188	-6	Straia	[4]	1.	Right-Reverse	.126	.326	.328	6.5	20.4

11. W. Vidareiði

#	Dip Azim	Dip	Trend	Plunge	Type	QF	Wt	Slip Sense	Norm. Stress	Shear Stress	Max. Shear	Misfit Angle	Fault Angle
1	212	46	82	-33	Straia	[4]	1.	Left-Reverse	.367	.396	.439	25.7	32.4
2	220	38	79	-31	Straia	[4]	1.	Left-Reverse	.265	.384	.42	24.	28.5
3	199	46	64	-36	Straia	[4]	1.	Left-Reverse	.33	.371	.39	17.7	25.8
4	241	14	86	-13	Straia	[4]	1.	Left-Reverse	.02	.121	.138	29.3	8.
5	42	12	257	-10	Straia	[4]	1.	Left-Reverse	.088	.271	.283	16.6	17.2
6	54	9	252	-9	Straia	[4]	1.	Left-Reverse	.066	.246	.249	8.1	14.9
7	53	13	247	-13	Straia	[4]	1.	Left-Reverse	.104	.304	.305	4.3	18.8
8	281	33	74	-30	Straia	[4]	1.	Right-Reverse	.165	.334	.338	8.8	20.
9	272	45	66	-42	Straia	[4]	1.	Right-Reverse	.347	.448	.449	4.	33.
10	244	24	66	-24	Straia	[4]	1.	Reverse	.095	.293	.294	4.6	18.
11	250	11	68	-11	Straia	[4]	1.	Reverse	.007	.085	.085	6.3	4.9
12	28	15	231	-14	Straia	[4]	1.	Left-Reverse	.104	.299	.299	3.4	18.1
13	30	16	235	-15	Straia	[4]	1.	Left-Reverse	.117	.314	.314	.	19.2
14	44	3	233	-3	Straia	[4]	1.	Reverse	.024	.149	.152	12.5	8.9
15	230	11	46	-11	Straia	[4]	1.	Reverse	.009	.088	.088	6.6	4.7
16	245	17	61	-17	Straia	[4]	1.	Reverse	.036	.187	.187	.4	11.
17	228	17	46	-17	Straia	[4]	1.	Reverse	.038	.183	.183	1.	10.3
18	251	17	68	-17	Straia	[4]	1.	Reverse	.035	.184	.185	2.7	10.8
19	242	19	61	-19	Straia	[4]	1.	Reverse	.051	.219	.219	2.	13.
20	240	28	55	-28	Straia	[4]	1.	Reverse	.141	.346	.347	3.4	21.9
21	231	15	43	-15	Straia	[4]	1.	Reverse	.026	.153	.153	4.8	8.6
22	37	23	239	-22	Straia	[4]	1.	Left-Reverse	.209	.399	.399	1.	26.4
23	59	15	249	-15	Straia	[4]	1.	Reverse	.128	.333	.334	4.7	21.
24	50	20	232	-20	Straia	[4]	1.	Reverse	.186	.383	.388	8.9	25.4
25	64	4	247	-4	Straia	[4]	1.	Reverse	.031	.172	.172	1.2	10.
26	278	37	88	-37	Straia	[4]	1.	Reverse	.219	.38	.382	6.8	24.2

Palaeostress calculations

Event 1

2. Hvannhagi	*trend*	*plunge*
Stress Or.		
1	267	69
2	13	6
3	105	20
		std. dev.
Stress ratio	0.44	
Mean misfit angle	31.8	37.5
Mean fault angle	30.8	13.3
Mean friction angle	37	
Mean shear stress angle	0.324	0.038
Shortening/extension	264	40

6. Gasadalur	*trend*	*plunge*
Stress Or.		
1	11	87
2	198	3
3	288	0
		std. dev.
Stress ratio	0.38	0.02
Mean misfit angle	15.8	13.9
Mean fault angle	44.7	11.9
Mean friction angle	44	
Mean shear stress angle	0.418	0.0008
Shortening/extension	124	89

3. Froðba	*trend*	*plunge*
Stress Or.		
1	276	79
2	171	3
3	81	11
		std. dev.
Stress ratio	0.24	0.05
Mean misfit angle	9.9	10.8
Mean fault angle	39.8	9.2
Mean friction angle	40	
Mean shear stress angle	0.427	0.005
Shortening/extension	250	79

4. Vagseiði	*trend*	*plunge*
Stress Or.		
1	41	89
2	135	0
3	225	1
		std. dev.
Stress ratio	0.37	0.01
Mean misfit angle	19.3	17.6
Mean fault angle	31.3	14
Mean friction angle	32	
Mean shear stress angle	0.363	0.016
Shortening/extension	212	83

Event 2

1. Muli	*trend*	*plunge*
Stress Or.		
1	272	20
2	75	69
3	180	5
		std. dev.
Stress ratio	0.55	
Mean misfit angle	43.4	28
Mean fault angle	20.7	11.1
Mean friction angle	19	
Mean shear stress angle	0.229	0.033
Shortening/extension	207	4

2. Norðdepil	*trend*	*plunge*
Stress Or.		
1	255	3
2	353	74
3	164	16
		std. dev.
Stress ratio	0.59	0.07
Mean misfit angle	35.1	40.5
Mean fault angle	15.2	10.8
Mean friction angle	15	
Mean shear stress angle	0.205	0.032
Shortening/extension	174	19

4. Gjogv	*trend*	*plunge*
Stress Or.		
1	77	21
2	234	67
3	344	8
		std. dev.
Stress ratio	0.39	0.04
Mean misfit angle	26.6	31.4
Mean fault angle	21.3	8.6
Mean friction angle	22	
Mean shear stress angle	0.294	0.013
Shortening/extension	56	23

5. Eiði	*trend*	*plunge*
Stress Or.		
1	270	7
2	150	77
3	1	11
		std. dev.
Stress ratio	0.57	0.05
Mean misfit angle	44.7	50.2
Mean fault angle	20.3	15.9
Mean friction angle	22	
Mean shear stress angle	0.207	0.053
Shortening/extension	358	4

6. Funnigfjorður	*trend*	*plunge*
Stress Or.		
1	74	29
2	221	56
3	336	15
		std. dev.
Stress ratio	0.8	0.1
Mean misfit angle	46.1	30
Mean fault angle	28.3	17.1
Mean friction angle	32	
Mean shear stress angle	0.259	0.028
Shortening/extension	0	9

7. Strendur	*trend*	*plunge*
Stress Or.		
1	74	6
2	291	83
3	164	4
		std. dev.
Stress ratio	0.59	0.04
Mean misfit angle	32.7	47.8
Mean fault angle	23.8	16.9
Mean friction angle	24	
Mean shear stress angle	0.248	0.05
Shortening/extension	152	8

8. Gotogjogv	*trend*	*plunge*
Stress Or.		
1	79	14
2	341	29
3	193	57
		std. dev.
Stress ratio	0.38	0.1
Mean misfit angle	60.7	52.6
Mean fault angle	15.7	8.8
Mean friction angle	-	
Mean shear stress angle	0.09	0.018
Shortening/extension	346	21

9. Lambi	*trend*	*plunge*
Stress Or.		
1	80	30
2	337	21
3	217	52
		std. dev.
Stress ratio	0.58	0.14
Mean misfit angle	79.8	42.4
Mean fault angle	20.7	17.6
Mean friction angle	10	
Mean shear stress angle	0.019	0.04
Shortening/extension	232	11

10. Mik. - Husar	*trend*	*plunge*
Stress Or.		
1	262	4
2	39	85
3	172	4
		std. dev.
Stress ratio	0.59	0.06
Mean misfit angle	40.4	43.6
Mean fault angle	21.8	13.2
Mean friction angle	17	
Mean shear stress angle	0.253	0.033
Shortening/extension	198	5

11. Mykinesholmur	*trend*	*plunge*
Stress Or.		
1	167	79
2	267	2
3	358	11
		std. dev.
Stress ratio	0.14	0.09
Mean misfit angle	17.7	15.4
Mean fault angle	31.3	16.8
Mean friction angle		
Mean shear stress angle	0.342	0.016
Shortening/extension	349	66

12. Skarvanes	*trend*	*plunge*
Stress Or.		
1	248	11
2	2	65
3	154	22
		std. dev.
Stress ratio	0.41	
Mean misfit angle	80.8	63
Mean fault angle	10	6.7
Mean friction angle	10	
Mean shear stress angle	0.064	0.021
Shortening/extension	65	2

13. Tjornuvik	*trend*	*plunge*
Stress Or.		
1	87	10
2	315	76
3	179	10
		std. dev.
Stress ratio	0.41	0.03
Mean misfit angle	35.5	43.3
Mean fault angle	13.4	8.7
Mean friction angle	11	
Mean shear stress angle	0.185	0.024
Shortening/extension	87	13

14. Tjornuvik - Haldarsvik	*trend*	*plunge*
Stress Or.		
1	89	10
2	327	72
3	182	15
		std. dev.
Stress ratio	0.2	0.11
Mean misfit angle	40.4	50.1
Mean fault angle	17.1	10.8
Mean friction angle	14	
Mean shear stress angle	0.222	0.031
Shortening/extension	90	18

15. Langasandur	*trend*	*plunge*
Stress Or.		
1	93	0
2	191	87
3	3	3
		std. dev.
Stress ratio	0.7	0.1
Mean misfit angle	36.6	26.9
Mean fault angle	29.8	14.5
Mean friction angle	37	
Mean shear stress angle	0.303	0.019
Shortening/extension	187	5

16. Saksunardalur	*trend*	*plunge*
Stress Or.		
1	86	15
2	264	75
3	355	1
		std. dev.
Stress ratio	0.3	
Mean misfit angle	50.3	61.1
Mean fault angle	15.4	17.8
Mean friction angle	-	
Mean shear stress angle	0.152	0.57
Shortening/extension	26	9

17. Dalasgjogv/Djup'gjog	*trend*	*plunge*
Stress Or.		
1	271	8
2	148	75
3	3	12
		std. dev.
Stress ratio	0.6	0.08
Mean misfit angle	36.9	39.5
Mean fault angle	19.8	12.4
Mean friction angle	21	
Mean shear stress angle	0.247	0.026
Shortening/extension	348	7

18. Dakid	*trend*	*plunge*
Stress Or.		
1	256	2
2	11	85
3	166	5
		std. dev.
Stress ratio	0.44	
Mean misfit angle	49.9	62.2
Mean fault angle	13.2	9.8
Mean friction angle	10	
Mean shear stress angle	0.134	0.048
Shortening/extension	53	30

19. Vestmanna	*trend*	*plunge*
Stress Or.		
1	269	3
2	135	86
3	359	3
		std. dev.
Stress ratio	0.48	0.09
Mean misfit angle	37.6	45.4
Mean fault angle	30	14.2
Mean friction angle	33	
Mean shear stress angle	0.242	0.077
Shortening/extension	228	1

20. Stykkið	*trend*	*plunge*
Stress Or.		
1	279	7
2	169	80
3	8	6
		std. dev.
Stress ratio	0.3	0.29
Mean misfit angle	78.4	74.2
Mean fault angle	18.4	23.6
Mean friction angle	-	
Mean shear stress angle	0.005	0.052
Shortening/extension	18	10

21. Leynar	*trend*	*plunge*
Stress Or.		
1	261	35
2	81	55
3	171	0
		std. dev.
Stress ratio	0.62	
Mean misfit angle	34.7	50.9
Mean fault angle	32.6	18.4
Mean friction angle	43	
Mean shear stress angle	0.312	0.07
Shortening/extension	176	16

22. Kaldbaksbotnur	*trend*	*plunge*
Stress Or.		
1	57	18
2	148	5
3	252	72
		std. dev.
Stress ratio	0.44	0.06
Mean misfit angle	35.2	38.2
Mean fault angle	27.4	15
Mean friction angle	23	
Mean shear stress angle	0.253	0.042
Shortening/extension	59	9

23. Kaldbaksfjorður	*trend*	*plunge*
Stress Or.		
1	230	0
2	136	87
3	320	3
Stress ratio	0.47	0.06
Mean misfit angle	71.5	57.2
Mean fault angle	18.6	13.8
Mean friction angle	10	
Mean shear stress angle	0.041	0.076
Shortening/extension	232	3

24. Hvannhagi	*trend*	*plunge*
Stress Or.		
1	230	86
2	106	2
3	16	3
		std. dev.
Stress ratio	0.15	0.11
Mean misfit angle	21.7	44.1
Mean fault angle	18.2	20.7
Mean friction angle	-	
Mean shear stress angle	0.197	0.017
Shortening/extension	349	64

25. Famjin	*trend*	*plunge*
Stress Or.		
1	269	25
2	51	59
3	172	17
		std. dev.
Stress ratio	0.21	
Mean misfit angle	19.4	48.5
Mean fault angle	27.7	15.7
Mean friction angle	-	
Mean shear stress angle	0.343	0.036
Shortening/extension	308	11

26. Hov	*trend*	*plunge*
Stress Or.		
1	269	48
2	64	39
3	164	13
		std. dev.
Stress ratio	0.51	
Mean misfit angle	32	33.1
Mean fault angle	42.3	13.1
Mean friction angle	44	
Mean shear stress angle	0.336	0.049
Shortening/extension	321	9

27. Vagseiði	*trend*	*plunge*
Stress Or.		
1	272	83
2	62	6
3	153	3
		std. dev.
Stress ratio	0.41	0.03
Mean misfit angle	15.4	9.4
Mean fault angle	38.9	12.2
Mean friction angle	41	
Mean shear stress angle	0.416	0.004
Shortening/extension	281	84

28. Gasadalur	*trend*	*plunge*
Stress Or.		
1	247	81
2	110	7
3	19	6
		std. dev.
Stress ratio	0.44	
Mean misfit angle	8.3	5
Mean fault angle	42.9	4.5
Mean friction angle	44	
Mean shear stress angle	0.473	0
Shortening/extension	316	82

29. Sandavagur	*trend*	*plunge*
Stress Or.		
1	74	7
2	203	79
3	343	8
		std. dev.
Stress ratio	0.5	
Mean misfit angle	60.6	63.3
Mean fault angle	15.6	11.3
Mean friction angle	10	
Mean shear stress angle	0.139	0.065
Shortening/extension	298	8

30. N. Vidareiði	*trend*	*plunge*
Stress Or.		
1	248	55
2	66	35
3	157	1
		std. dev.
Stress ratio	0.82	0.09
Mean misfit angle	35.5	22.5
Mean fault angle	9.6	7.6
Mean friction angle	14	
Mean shear stress angle	0.187	0.015
Shortening/extension	153	1

31. E. Vidareiði	*trend*	*plunge*
Stress Or.		
1	76	1
2	171	78
3	346	12
		std. dev.
Stress ratio	0.46	0.08
Mean misfit angle	39.8	46.9
Mean fault angle	20.8	6
Mean friction angle	22	
Mean shear stress angle	0.23	0.04
Shortening/extension	320	8

32. W. Vidareiði	*trend*	*plunge*
Stress Or.		
1	246	16
2	50	73
3	155	4
		std. dev.
Stress ratio	0.49	0.04
Mean misfit angle	43.3	52.6
Mean fault angle	19.4	9.4
Mean friction angle	16	
Mean shear stress angle	0.192	0.056
Shortening/extension	275	15

Event 2 thrusts

1. Strendur	*trend*	*plunge*
Stress Or.		
1	243	12
2	151	9
3	25	75
		std. dev.
Stress ratio	0.47	
Mean misfit angle	49.7	57.9
Mean fault angle	15.5	9.3
Mean friction angle	10	
Mean shear stress angle	0.156	0.059
Shortening/extension	60	7

2. Rituvik	*trend*	*plunge*
Stress Or.		
1	254	5
2	164	2
3	50	84
		std. dev.
Stress ratio	0.5	0.01
Mean misfit angle	16.5	13.1
Mean fault angle	17.2	6.6
Mean friction angle	18	
Mean shear stress angle	0.268	0.009
Shortening/extension	261	69

3. W. Sandur	*trend*	*plunge*
Stress Or.		
1	54	1
2	144	5
3	314	85
		std. dev.
Stress ratio	0.57	
Mean misfit angle	13.7	10.8
Mean fault angle	18	4.6
Mean friction angle	19	
Mean shear stress angle	0.288	0.005
Shortening/extension	310	84

4. E.Sandur	*trend*	*plunge*
Stress Or.		
1	223	78
2	331	4
3	62	11
		std. dev.
Stress ratio	0.49	
Mean misfit angle	10.8	6.7
Mean fault angle	49.6	11.5
Mean friction angle	44	
Mean shear stress angle	0.437	0.012
Shortening/extension	65	65

5. Satan	*trend*	*plunge*
Stress Or.		
1	61	8
2	152	9
3	289	78
		std. dev.
Stress ratio	0.54	
Mean misfit angle	47.7	67.4
Mean fault angle	23.6	8.9
Mean friction angle	22	
Mean shear stress angle	0.182	0.105
Shortening/extension	261	68

6. Skaelingsfjjall	*trend*	*plunge*
Stress Or.		
1	67	5
2	336	20
3	170	69
		std. dev.
Stress ratio	0.55	0.05
Mean misfit angle	107	56.3
Mean fault angle	20	16.4
Mean friction angle	10	
Mean shear stress angle	0.085	0.068
Shortening/extension	157	81

7. Kaldbaksbotnur	*trend*	*plunge*
Stress Or.		
1	231	5
2	321	4
3	84	84
		std. dev.
Stress ratio	0.58	0.04
Mean misfit angle	17	14.3
Mean fault angle	19.2	6.4
Mean friction angle	20	
Mean shear stress angle	0.291	0.008
Shortening/extension	58	72

8. Kaldbaksfjorður	*trend*	*plunge*
Stress Or.		
1	243	4
2	153	5
3	12	83
		std. dev.
Stress ratio	0.61	0.03
Mean misfit angle	21	22.5
Mean fault angle	21.1	11.9
Mean friction angle	21	
Mean shear stress angle	0.289	0.016
Shortening/extension	305	84

9. Hov	*trend*	*plunge*
Stress Or.		
1	268	9
2	176	10
3	39	77
		std. dev.
Stress ratio	0.56	
Mean misfit angle	14.8	5.5
Mean fault angle	34.9	20.8
Mean friction angle	44	
Mean shear stress angle	0.365	0.009
Shortening/extension	94	67

10. Bour	*trend*	*plunge*
Stress Or.		
1	203	14
2	111	9
3	350	74
		std. dev.
Stress ratio	0.45	
Mean misfit angle	13.4	9.1
Mean fault angle	21.7	5.8
Mean friction angle	21	
Mean shear stress angle	0.321	0.005
Shortening/extension	223	56

11. W. Vidareiði	*trend*	*plunge*
Stress Or.		
1	244	6
2	334	1
3	78	84
		std. dev.
Stress ratio	0.51	0.01
Mean misfit angle	8	8
Mean fault angle	17.6	8.2
Mean friction angle	18	
Mean shear stress angle	0.272	0.011
Shortening/extension	242	72

Faroe Islands: Event 1Data localities

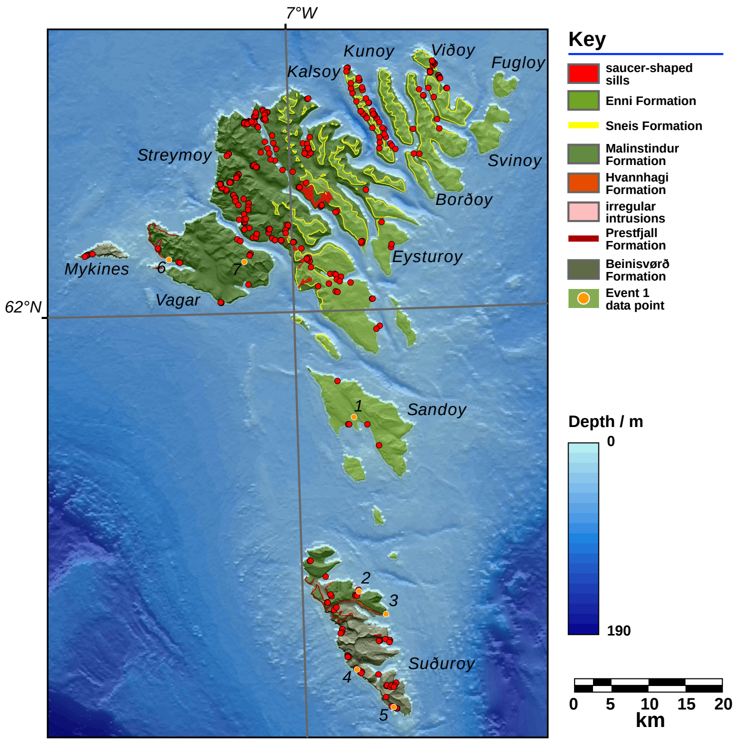

Max.	maximum principal stress	*S.R.*	Stress Ratio
Int.	intermediate principal stress	*MMA*	Mean Misfit Angle
Min.	minimum principal stress	*MFaA*	Mean Fault Angle
P S/E	Principal Shortening/Extension	*MFrA*	Mean Friction Angle
(values: trend . plunge)		*MSSA*	Mean Shear Stress Angle

Sandoy

1: W. Sandur - 6°49'34.438"W 61°50'46.809"N

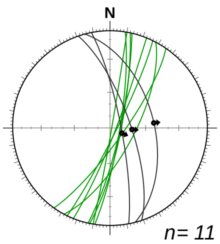

insufficient kinematic data for inversion

Suðuroy

2: Hvannhagi - 6°49'47.773"W 61°35'0.024"N

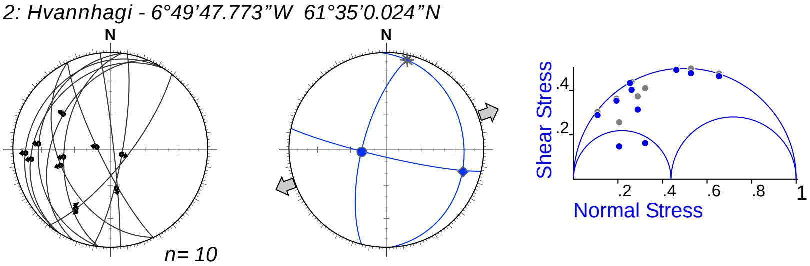

Max.	267.69
Int.	013.06
Min.	105.20
S.R.	0.44
MMA	31.8
MFaA	30.8
MFrA	37
MSSA	0.324
P S/E	264.40

Suðuroy

3: Froðba - 6°44’51.395”W 61°32’52.033”N

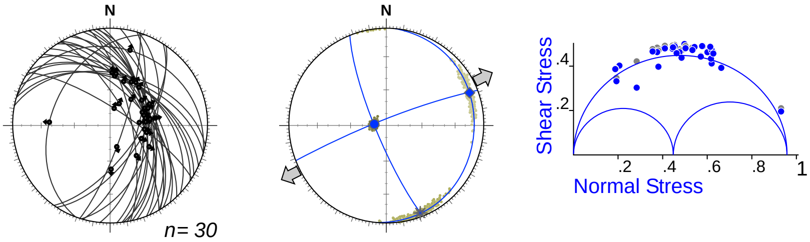

Max.	276.79
Int.	171.03
Min.	081.11
S.R.	0.24
MMA	9.9
MFaA	39.8
MFrA	40
MSSA	0.427
P S/E	250.79

4: Vagseiði - 6°50’15.869”W 61°27’51.419”N

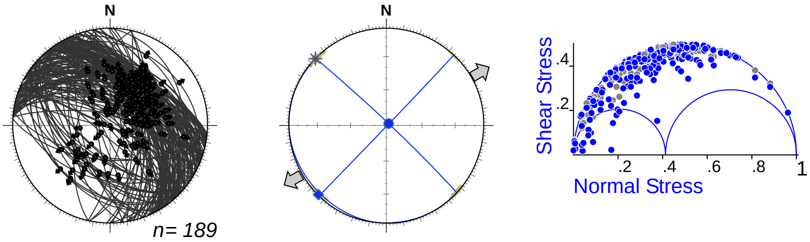

Max.	041.89
Int.	135.00
Min.	225.01
S.R.	0.37
MMA	19.3
MFaA	31.3
MFrA	32
MSSA	0.363
P S/E	212.83

5: Sumba - 6°43’38.802”W 61°24’23.195”N

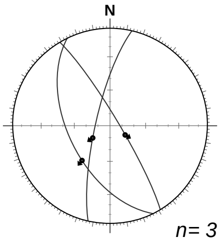

insufficient kinematic data for inversion

Vagar

6: Gasadalur - 7°26’12.974”W 62°6’25.501”N

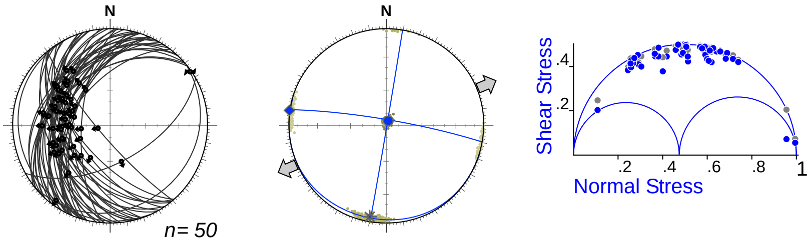

Max.	011.87
Int.	198.03
Min.	288.00
S.R.	0.38
MMA	15.8
MFaA	44.7
MFrA	44
MSSA	0.418
P S/E	124.89

7: Sandavagur - 7°9’44.689”W 62°5’5.258”N

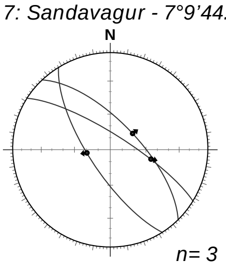

insufficient kinematic data for inversion

Faroe Islands: Event 2 Data localities

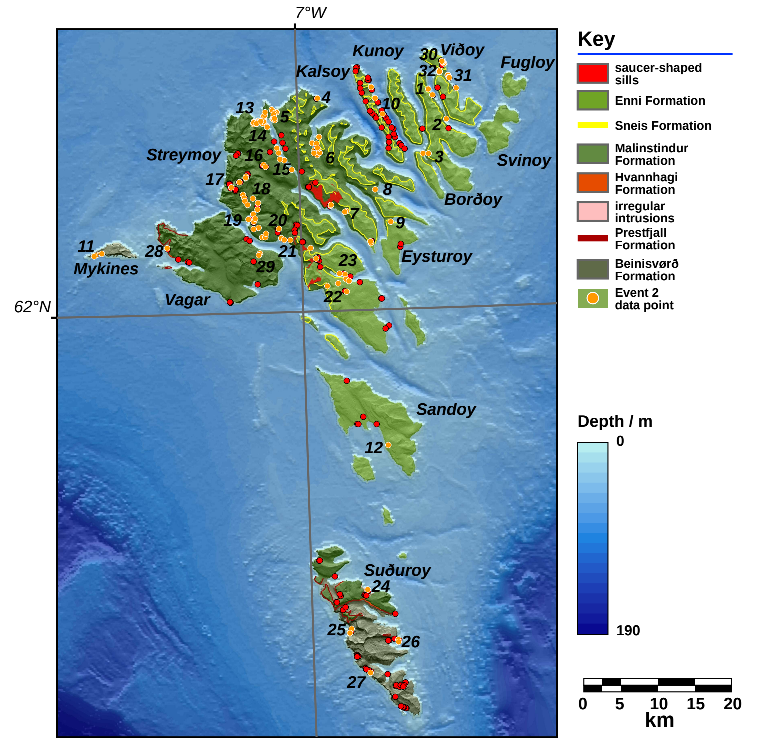

Max.	maximum principal stress	*S.R.*	Stress Ratio
Int.	intermediate principal stress	*MMA*	Mean Misfit Angle
Min.	minimum principal stress	*MFaA*	Mean Fault Angle
P S/E	Principal Shortening/Extension	*MFrA*	Mean Friction Angle
(values: trend . plunge)		*MSSA*	Mean Shear Stress Angle

Borðoy

1: Muli - 6°34’55.921”W 62°20’5.811”N to 6°34’6.392”W 62°19’29.661”N

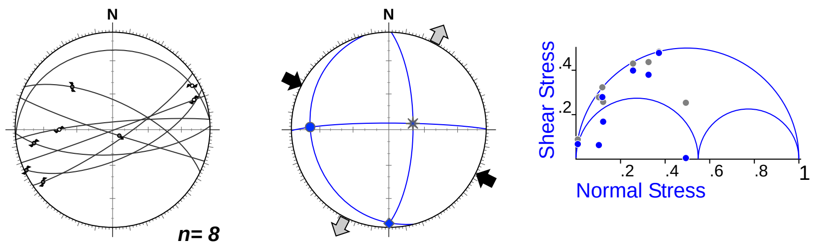

Max.	272.20
Int.	075.69
Min.	180.05
S.R.	0.55
MMA	43.4
MFaA	20.7
MFrA	19
MSSA	0.229
P S/E	207.04

2: Norðdepil - 6°31’40.019”W 62°17’20.214”N to 6°31’18.444”W 62°16’30.955”N

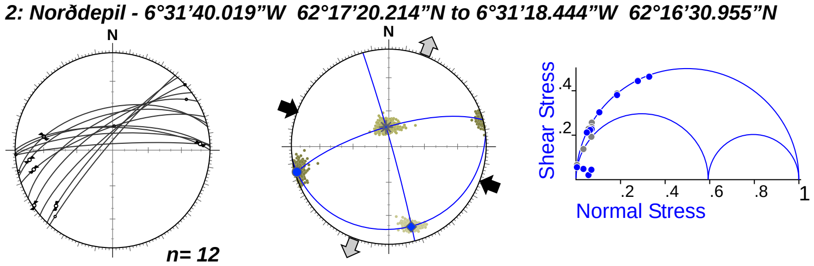

Max.	255.03
Int.	353.74
Min.	164.16
S.R.	0.59
MMA	35.1
MFaA	15.2
MFrA	15
MSSA	0.205
P S/E	174.19

3: Klaksvik - 6°36’24.089”W 62°14’19.245”N

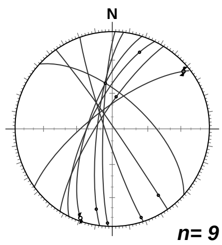

insufficient kinematic data for inversion

Eysturoy

4: Gjogv - 6°56'37.847"W 62°19'34.748"N

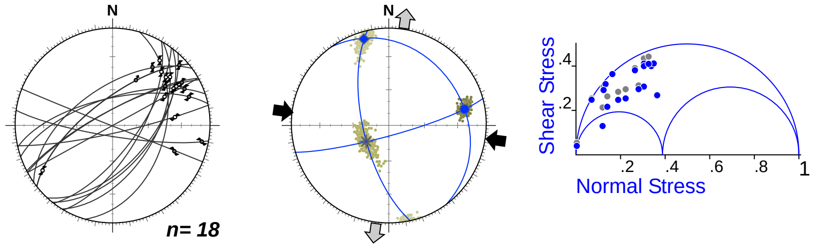

Max.	077.21
Int.	234.67
Min.	344.08
S.R.	0.39
MMA	26.6
MFaA	21.3
MFrA	22
MSSA	0.294
P S/E	056.23

5: Eiði - 7°4'29.959"W 62°18'28.778"N

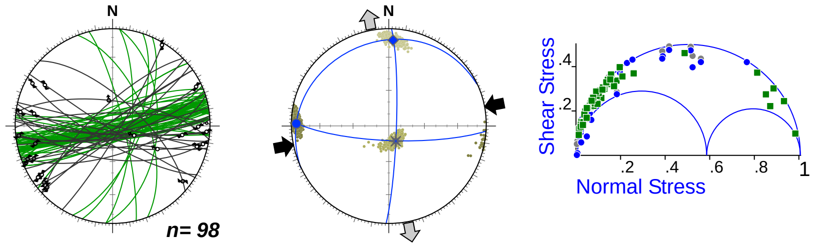

Max.	270.07
Int.	150.77
Min.	001.11
S.R.	0.57
MMA	44.7
MFaA	20.3
MFrA	22
MSSA	0.207
P S/E	358.04

6: Funningfjørður - 6°56'23.14"W 62°16'6.079"N to 6°56'49.279"W 62°14'28.847"N

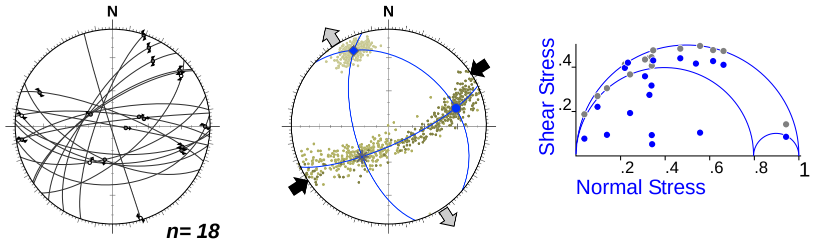

Max.	074.29
Int.	221.56
Min.	336.15
S.R.	0.8
MMA	46.1
MFaA	28.3
MFrA	32
MSSA	0.259
P S/E	000.09

7: Strendur - 6°51'32.206"W 62°9'20.541"N to 6°47'2.891"W 62°6'22.968"N

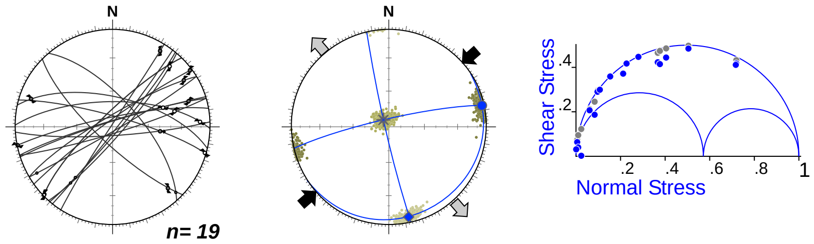

Max.	074.06
Int.	291.83
Min.	164.04
S.R.	0.59
MMA	32.7
MFaA	23.8
MFrA	24
MSSA	0.248
P S/E	152.08

8: Gotogjogv - 6°45'54.711"W 62°11'12.513"N

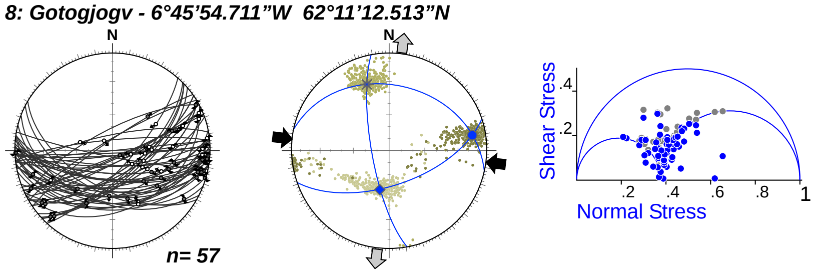

Max.	079.14
Int.	341.29
Min.	193.57
S.R.	0.38
MMA	60.7
MFaA	15.7
MFrA	- - -
MSSA	0.09
P S/E	346.21

9: Lambi - 6°43'6.514"W 62°8'14.466"N

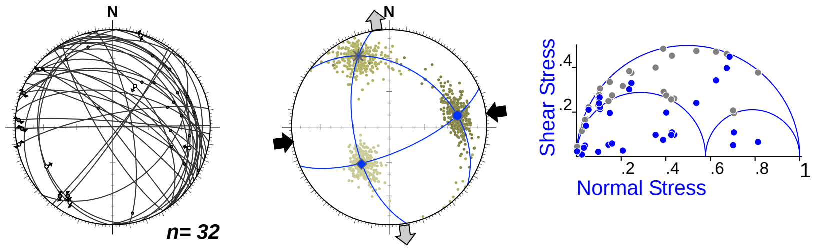

Max.	080.30
Int.	337.21
Min.	217.52
S.R.	0.58
MMA	79.8
MFaA	20.7
MFrA	10
MSSA	0.019
P S/E	232.11

Kalsoy

10: Mikladalur to Husar - 6°44’0.327”W 62°17’59.005”N to 6°41’58.574”W 62°16’9.236”N

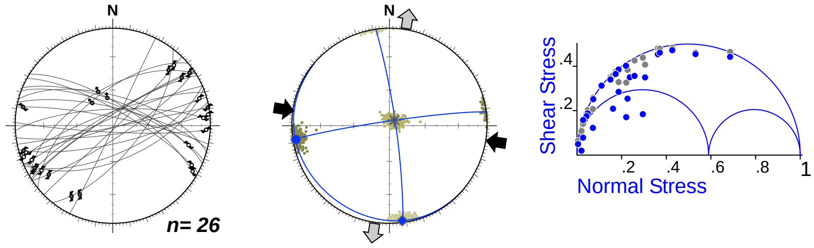

Max.	262.04
Int.	039.85
Min.	172.04
S.R.	0.59
MMA	40.4
MFaA	21.8
MFrA	17
MSSA	0.253
P S/E	198.05

Mykines

11: Mykinesholmur - 7°39’41.409”W 62°6’1.007”N to 7°40’17.859”W 62°5’51.23”N

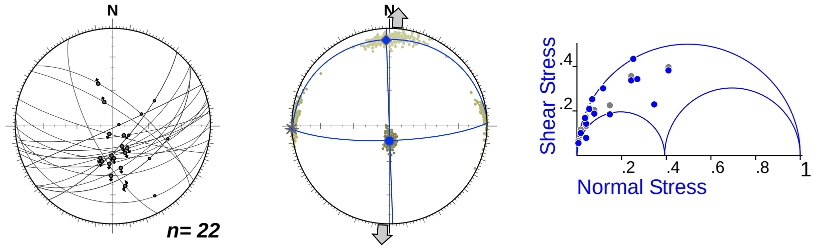

Max.	167.79
Int.	267.02
Min.	358.11
S.R.	0.14
MMA	17.7
MFaA	31.3
MFrA	- - -
MSSA	0.342
P S/E	349.66

Sandoy

12: Skarvanes - 6°45’2.946”W 62°48’8.177”N

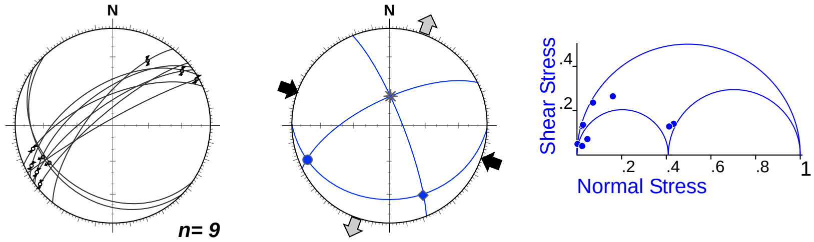

Max.	248.11
Int.	002.65
Min.	154.22
S.R.	0.41
MMA	80.8
MFaA	10.0
MFrA	10
MSSA	0.064
P S/E	065.02

Streymoy

13: Tjornuvik - 7°8’56.581”W 62°17’34.693”N

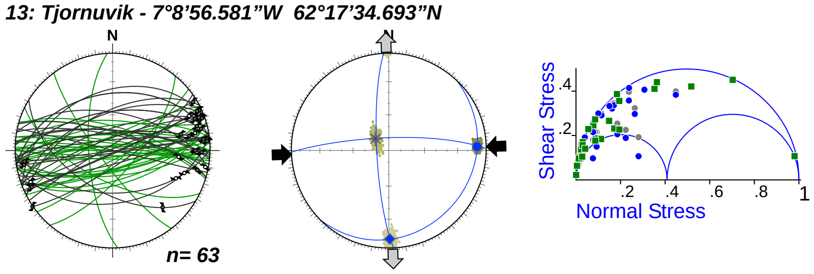

Max.	087.10
Int.	315.76
Min.	179.10
S.R.	0.41
MMA	35.5
MFaA	13.4
MFrA	11
MSSA	0.185
P S/E	087.13

14: Tjornuvik to Haldarsvik - 7°8’3.856”W 62°17’44.104”N

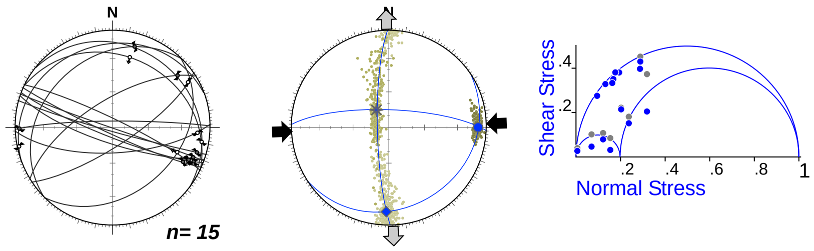

Max.	089.10
Int.	327.72
Min.	182.15
S.R.	0.2
MMA	40.4
MFaA	17.1
MFrA	14
MSSA	0.222
P S/E	090.18

Streymoy

15: Langasandur - 7°3'12.881"W 62°14'6.047"N

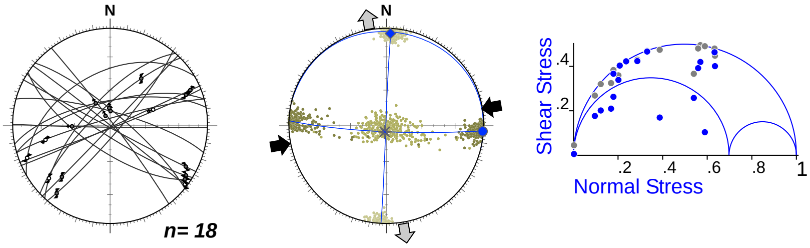

Max.	093.00
Int.	191.87
Min.	003.03
S.R.	0.7
MMA	36.6
MFaA	29.8
MFrA	37
MSSA	0.303
P S/E	187.05

16: Saksunardalur - 7°7'27.668"W 62°13'41.716"N to 7°6'45.692"W 62°13'33.459"N

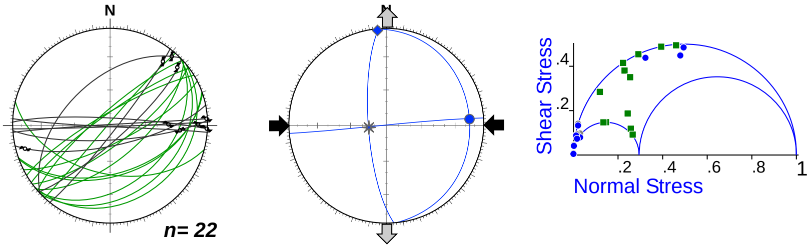

Max.	086.15
Int.	264.75
Min.	355.01
S.R.	0.3
MMA	50.3
MFaA	15.4
MFrA	- - -
MSSA	0.152
P S/E	026.09

17: Dalasgjogv & Djupadalasgjogv - 7°14'0"W 62°11'20"N to 7°10'50"W 62°12'32"N

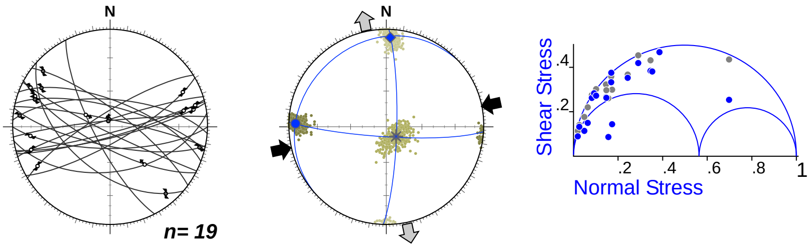

Max.	271.08
Int.	148.75
Min.	003.12
S.R.	0.6
MMA	36.9
MFaA	19.8
MFrA	21
MSSA	0.247
P S/E	348.07

18: Dakid - 7°11'28.125"W 62°11'4.102"N to 7°8'41.158"W 62°9'43.576"N

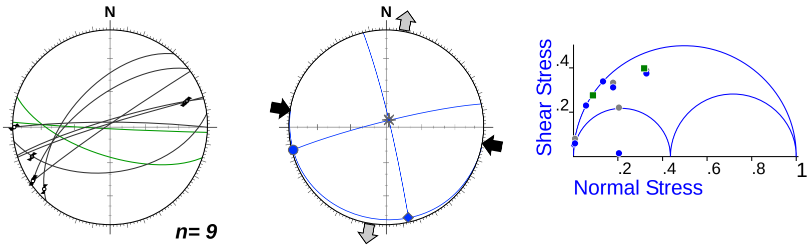

Max.	256.02
Int.	011.85
Min.	166.05
S.R.	0.44
MMA	49.9
MFaA	13.2
MFrA	10
MSSA	0.134
P S/E	053.30

19: Vestmanna - 7°10'26.216"W 62°8'51.47"N to 7°7'17.234"W 62°7'12.272"N

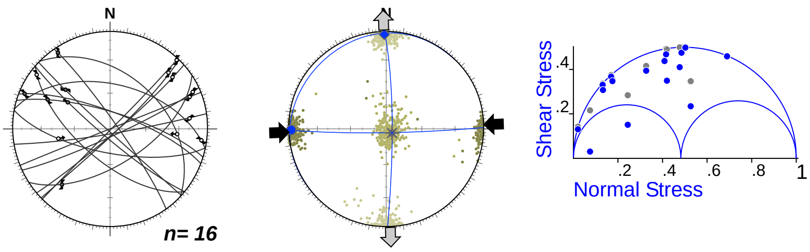

Max.	269.03
Int.	135.86
Min.	359.03
S.R.	0.48
MMA	37.6
MFaA	30
MFrA	33
MSSA	0.242
P S/E	228.01

20: Stykkið - 7°3'40.462"W 62°6'54.736"N

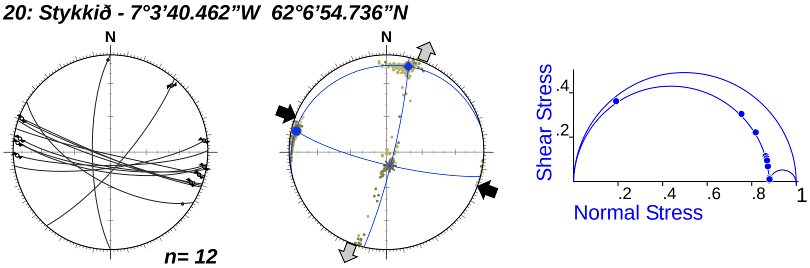

Max.	279.07
Int.	169.80
Min.	008.06
S.R.	0.3
MMA	78.4
MFaA	18.4
MFrA	- - -
MSSA	0.005
P S/E	018.10

Streymoy

21: Leynar - 7°2’31.278”W 62°6’53.314”N

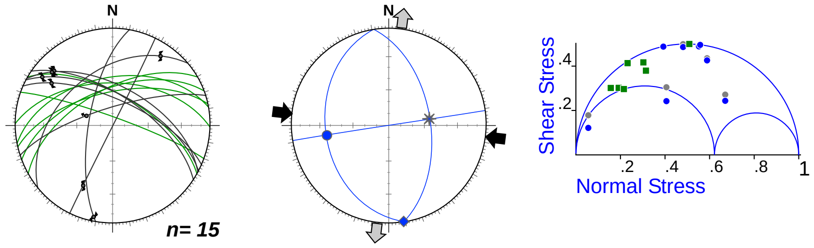

Max.	261.35
Int.	081.55
Min.	171.00
S.R.	0.62
MMA	34.7
MFaA	32.6
MFrA	43
MSSA	0.312
P S/E	176.16

22: Kaldbaksbotnur - 6°56’56.502”W 62°4’22.779”N

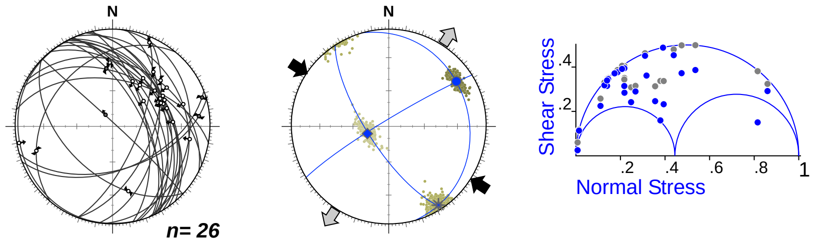

Max.	057.18
Int.	148.05
Min.	252.72
S.R.	0.44
MMA	35.2
MFaA	27.4
MFrA	23
MSSA	0.253
P S/E	059.09

23: Kaldbaksfjørður - 6°53’16.896”W 62°3’43.441”N to 6°51’13.173”W 62°3’25.869”N

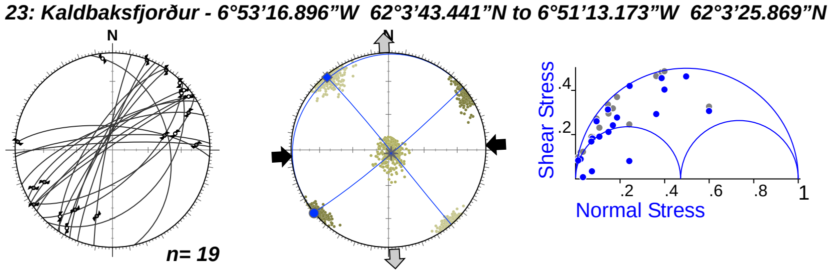

Max.	230.00
Int.	136.87
Min.	320.03
S.R.	0.47
MMA	71.5
MFaA	18.6
MFrA	10
MSSA	0.041
P S/E	232.03

Suðuroy

24: Hvannhagi - 6°49’48.017”W 61°35’0.312”N

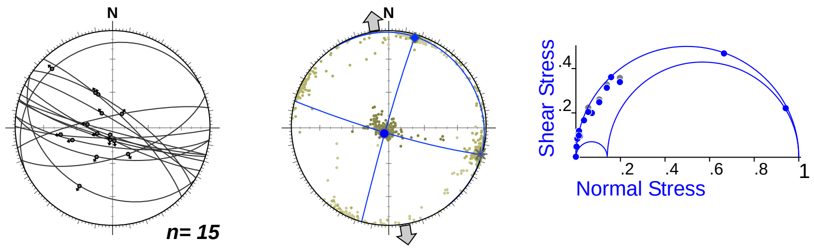

Max.	230.86
Int.	106.02
Min.	016.03
S.R.	0.15
MMA	21.7
MFaA	18.2
MFrA	- - -
MSSA	0.197
P S/E	349.64

25: Famjin - 6°53’13.528”W 61°31’36.976”N

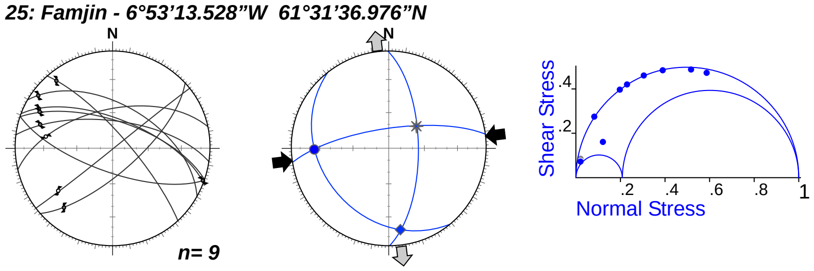

Max.	269.25
Int.	051.59
Min.	172.17
S.R.	0.21
MMA	19.4
MFaA	27.7
MFrA	- - -
MSSA	0.343
P S/E	308.11

26: Hov - 6°46’22.9”W 61°30’28.184”N

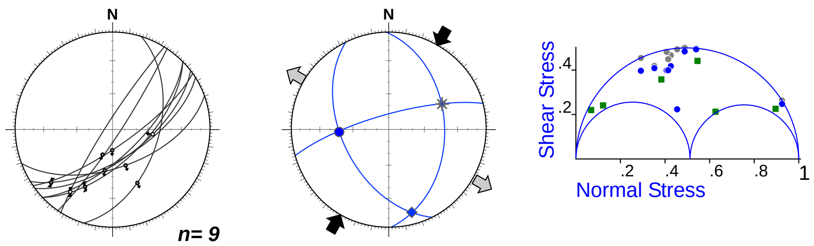

Max.	269.48
Int.	064.39
Min.	164.13
S.R.	0.51
MMA	32.0
MFaA	42.3
MFrA	44
MSSA	0.336
P S/E	321.09

Suðuroy

27: Vagseiði - 6°50'15.449"W 61°27'51.331"N

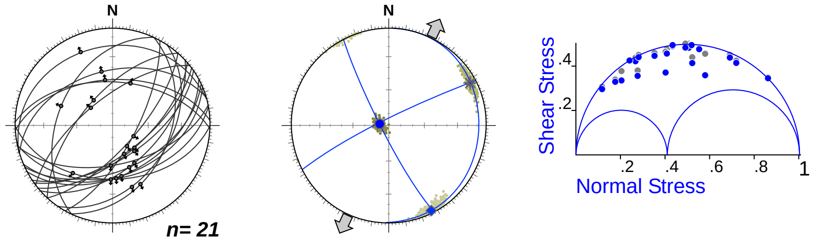

Max.	272.83
Int.	062.06
Min.	153.03
S.R.	0.41
MMA	15.4
MFaA	38.9
MFrA	41
MSSA	0.416
P S/E	281.84

Vagar

28: Gasadalur - 7°26'6.302"W 62°6'22.695"N

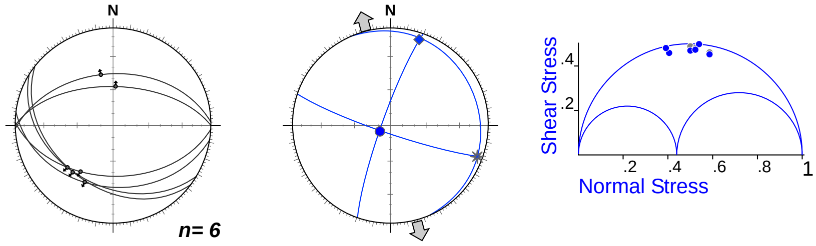

Max.	247.81
Int.	110.07
Min.	019.06
S.R.	0.44
MMA	8.3
MFaA	42.9
MFrA	44
MSSA	0.473
P S/E	316.82

29: Sandavagur - 7°8'28.385"W 62°5'46.699"N

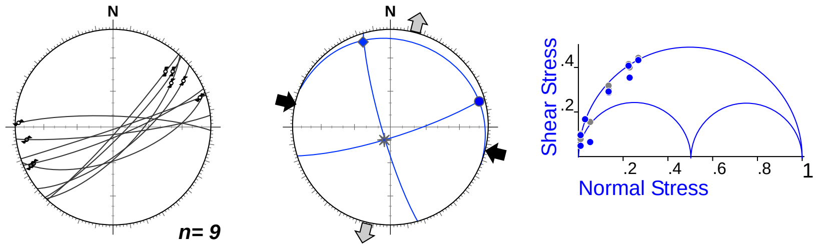

Max.	074.07
Int.	203.79
Min.	343.08
S.R.	0.5
MMA	60.6
MFaA	15.6
MFrA	10
MSSA	0.139
P S/E	298.08

Viðoy

30: N. Viðareiði - 6°32'11.929"W 62°22'36.941"N

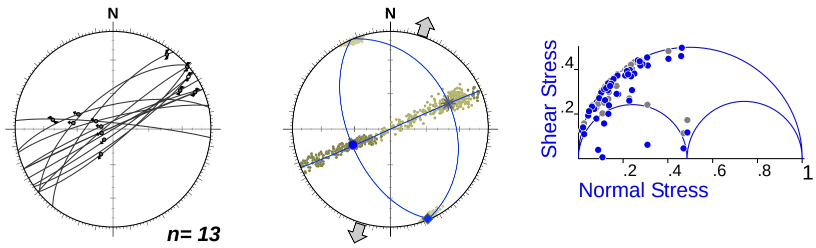

Max.	248.55
Int.	066.35
Min.	157.01
S.R.	0.82
MMA	35.5
MFaA	9.6
MFrA	14
MSSA	0.187
P S/E	153.01

31: E. Viðareiði - 6°31'3.296"W 62°21'16.332"N

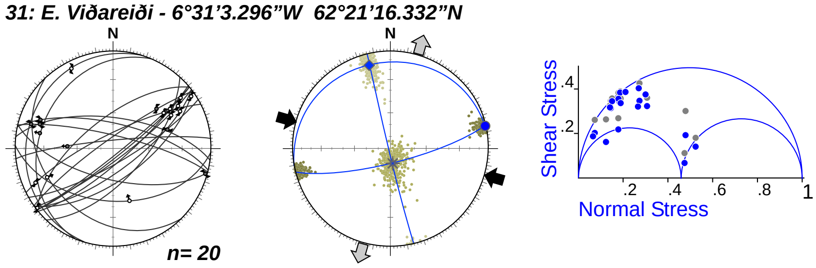

Max.	076.01
Int.	171.78
Min.	346.12
S.R.	0.46
MMA	39.8
MFaA	20.8
MFrA	22
MSSA	0.23
P S/E	320.08

Viðoy

32: W. Viðareiði - 6°32'40.754"W 62°21'36.984"N

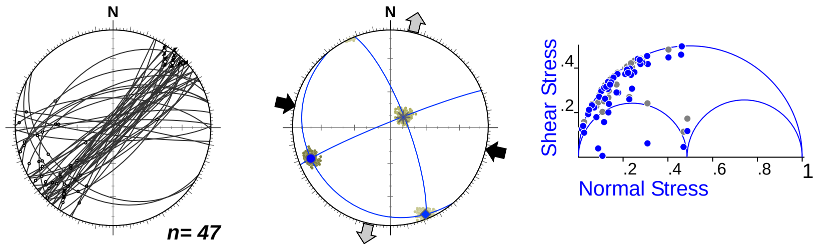

Max.	246.16
Int.	050.73
Min.	155.04
S.R.	0.49
MMA	43.3
MFaA	19.4
MFrA	16
MSSA	0.192
P S/E	275.15

Faroe Islands: Event 2 (thrust system) Data localities

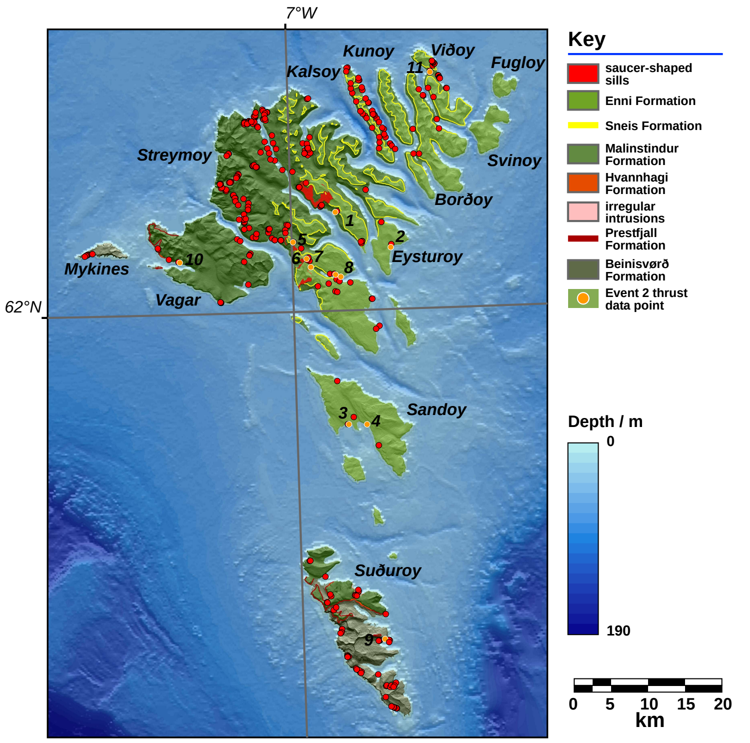

Max.	maximum principal stress	*S.R.*	Stress Ratio
Int.	intermediate principal stress	*MMA*	Mean Misfit Angle
Min.	minimum principal stress	*MFaA*	Mean Fault Angle
P S/E	Principal Shortening/Extension	*MFrA*	Mean Friction Angle
(values: trend . plunge)		*MSSA*	Mean Shear Stress Angle

Eysturoy

1: Strendur - 7°9’44.689”W 62°5’5.258”N

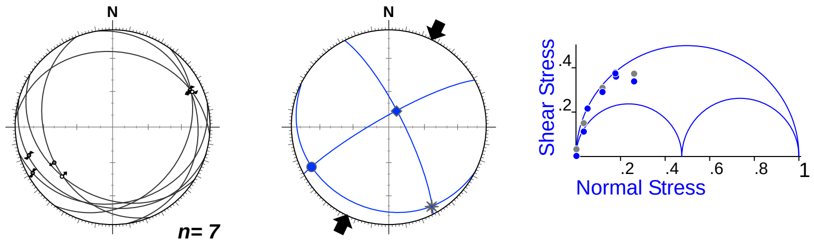

Max.	243.12
Int.	151.09
Min.	025.75
S.R.	0.47
MMA	49.7
MFaA	15.5
MFrA	10
MSSA	0.156
P S/E	060.07

2: Rituvik - 6°51’32.206”W 62°9’20.541”N to 6°47’2.891”W 62°6’22.968”N

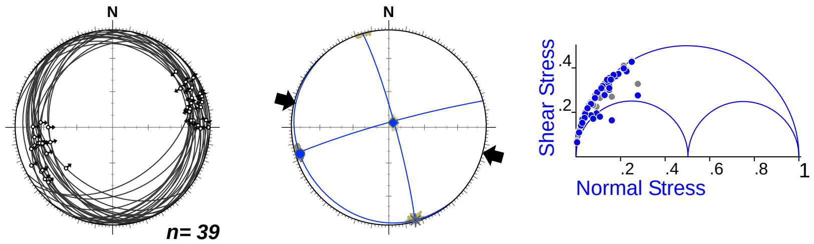

Max.	254.05
Int.	164.02
Min.	050.84
S.R.	0.5
MMA	16.5
MFaA	17.2
MFrA	18
MSSA	0.268
P S/E	261.69

Sandoy

3: W. Sandur - 6°50'37.284"W 61°50'6.378"N

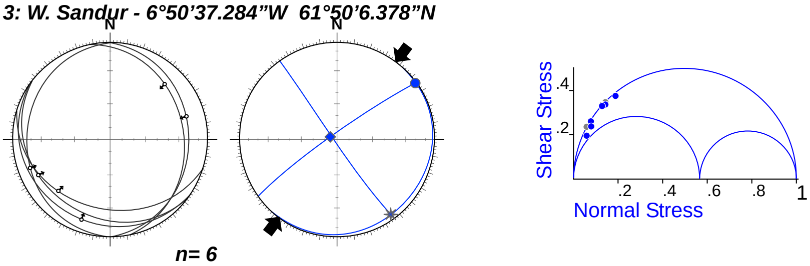

Max.	054.01
Int.	144.05
Min.	314.85
S.R.	0.57
MMA	13.7
MFaA	18
MFrA	19
MSSA	0.288
P S/E	310.84

4: E. Sandur - 6°47'9.594"W 61°50'2.664"N

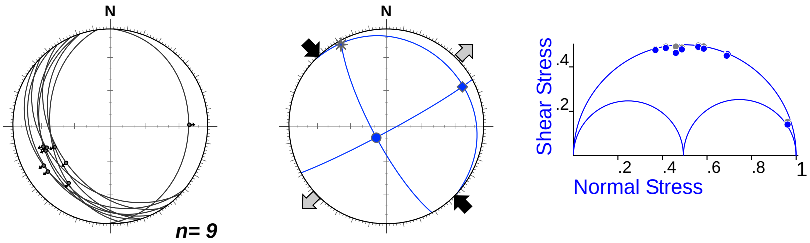

Max.	223.78
Int.	331.04
Min.	062.11
S.R.	0.49
MMA	10.8
MFaA	49.6
MFrA	44
MSSA	0.437
P S/E	065.65

Streymoy

5: Satan - 7°0'11.098"W 62°6'41.998"N

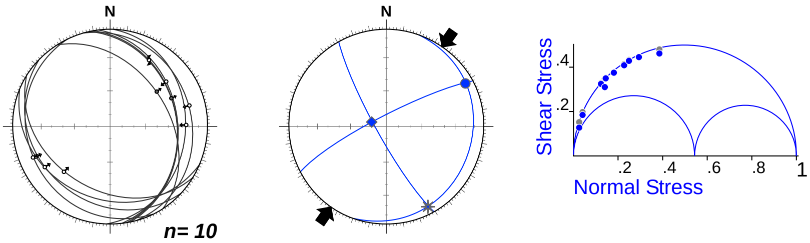

Max.	061.08
Int.	152.09
Min.	289.78
S.R.	0.54
MMA	47.7
MFaA	23.6
MFrA	22
MSSA	0.182
P S/E	261.68

6: Skaelingsfjall - 6°57'22.45"W 62°5'16.181"N

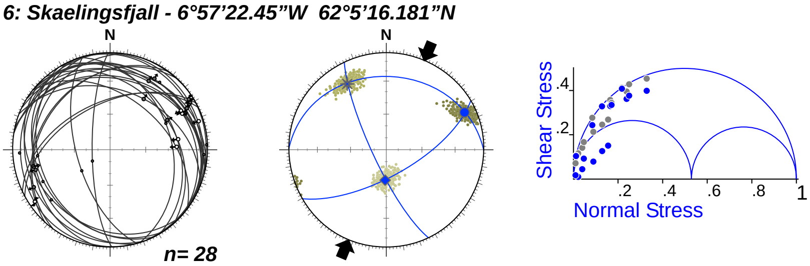

Max.	067.05
Int.	336.20
Min.	170.69
S.R.	0.55
MMA	107
MFaA	20
MFrA	10
MSSA	0.085
P S/E	157.81

7: Kaldbaksbotnur - 6°56'56.748"W 62°4'23.704"N

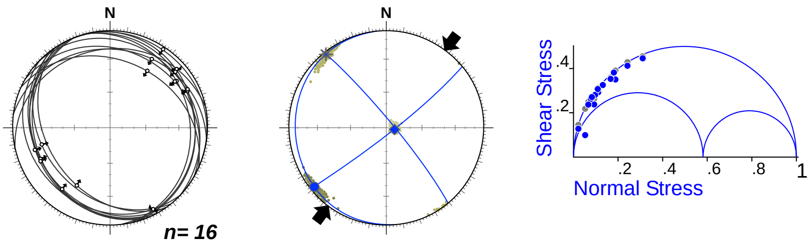

Max.	231.05
Int.	321.04
Min.	084.84
S.R.	0.58
MMA	17
MFaA	19.2
MFrA	20
MSSA	0.291
P S/E	058.72

8: Kaldbaksfjørður - 6°51'14.71"W 62°3'26.412"N

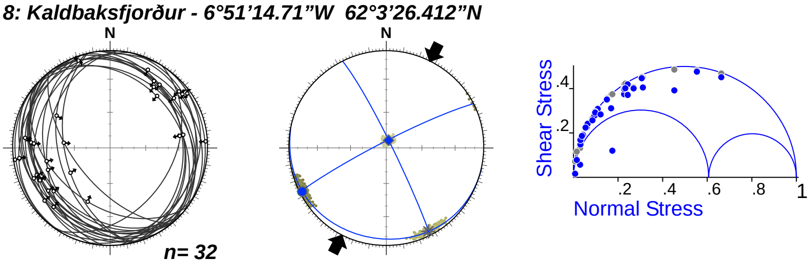

Max.	243.04
Int.	153.05
Min.	012.83
S.R.	0.61
MMA	21
MFaA	21.1
MFrA	21
MSSA	0.289
P S/E	305.84

Suðuroy

9: Hov - 6°44'27.288"W 61°30'31.818"N

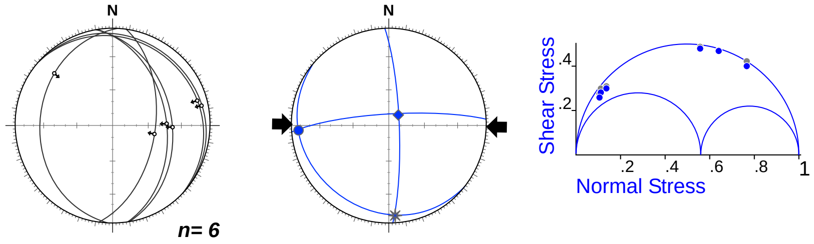

Max.	268.09
Int.	176.10
Min.	039.77
S.R.	0.56
MMA	14.8
MFaA	34.9
MFrA	44
MSSA	0.365
P S/E	094.67

Vagar

10: Bour - 7°24'8.26"W 62°5'24.539"N

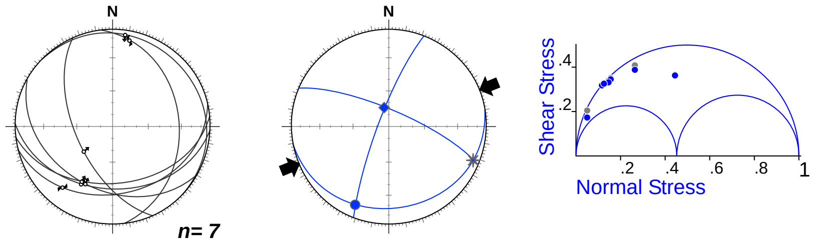

Max.	203.14
Int.	111.09
Min.	350.74
S.R.	0.45
MMA	13.4
MFaA	21.7
MFrA	21
MSSA	0.321
P S/E	223.56

Viðoy

11: W. Viðareiði - 6°32'39.031"W 62°21'39.528"N

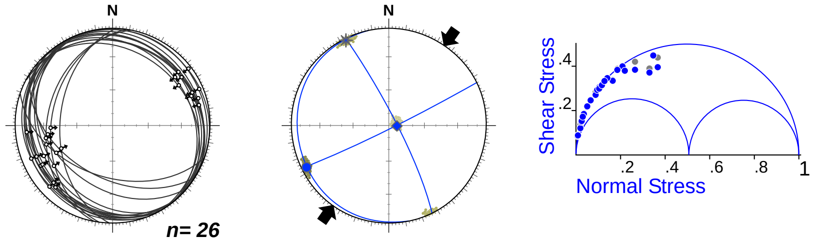

Max.	244.06
Int.	344.01
Min.	078.84
S.R.	0.51
MMA	8.0
MFaA	17.6
MFrA	18
MSSA	0.272
P S/E	242.72

Eiði, NW Eysturoy

Location

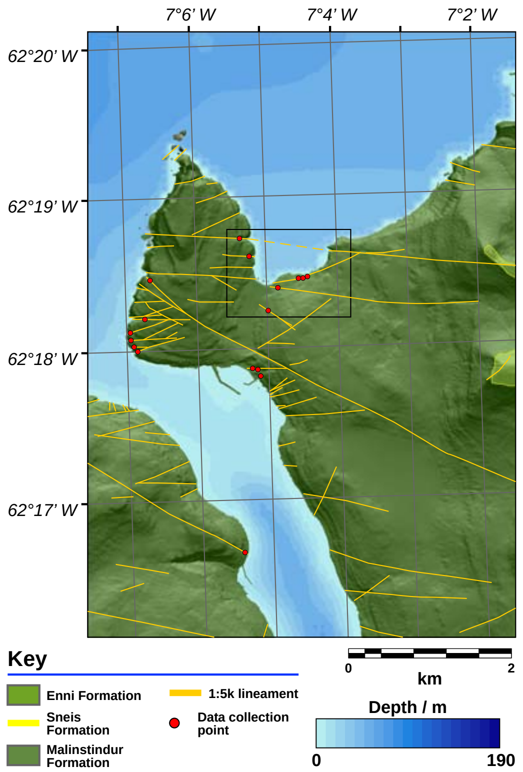

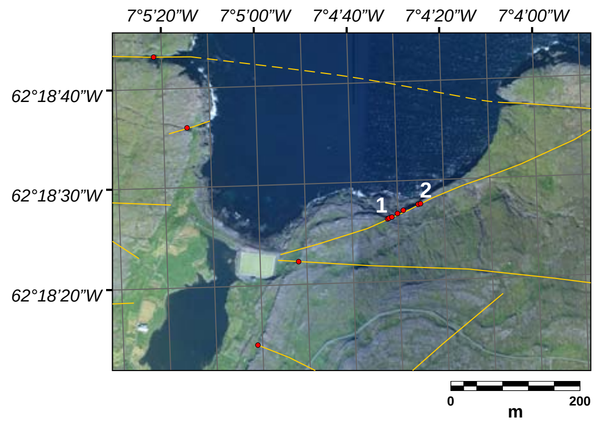

Structural data / Kinematic inversion *Eiði*

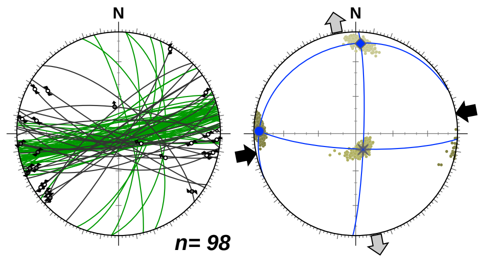

Fault / Fault zone characteristics

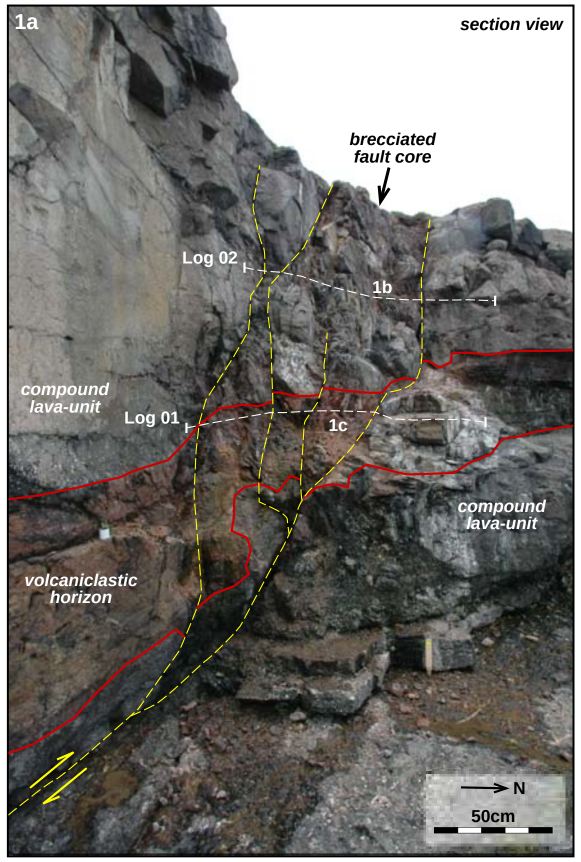

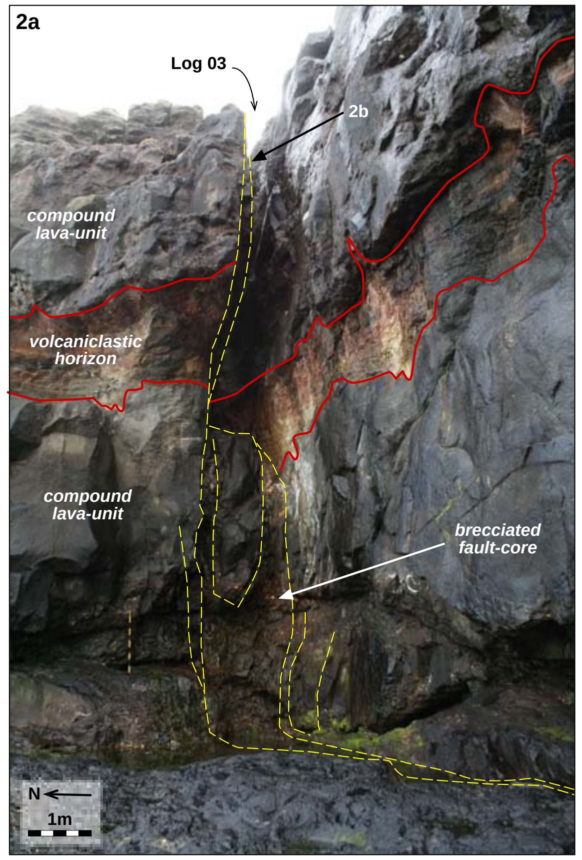

Structural Logs

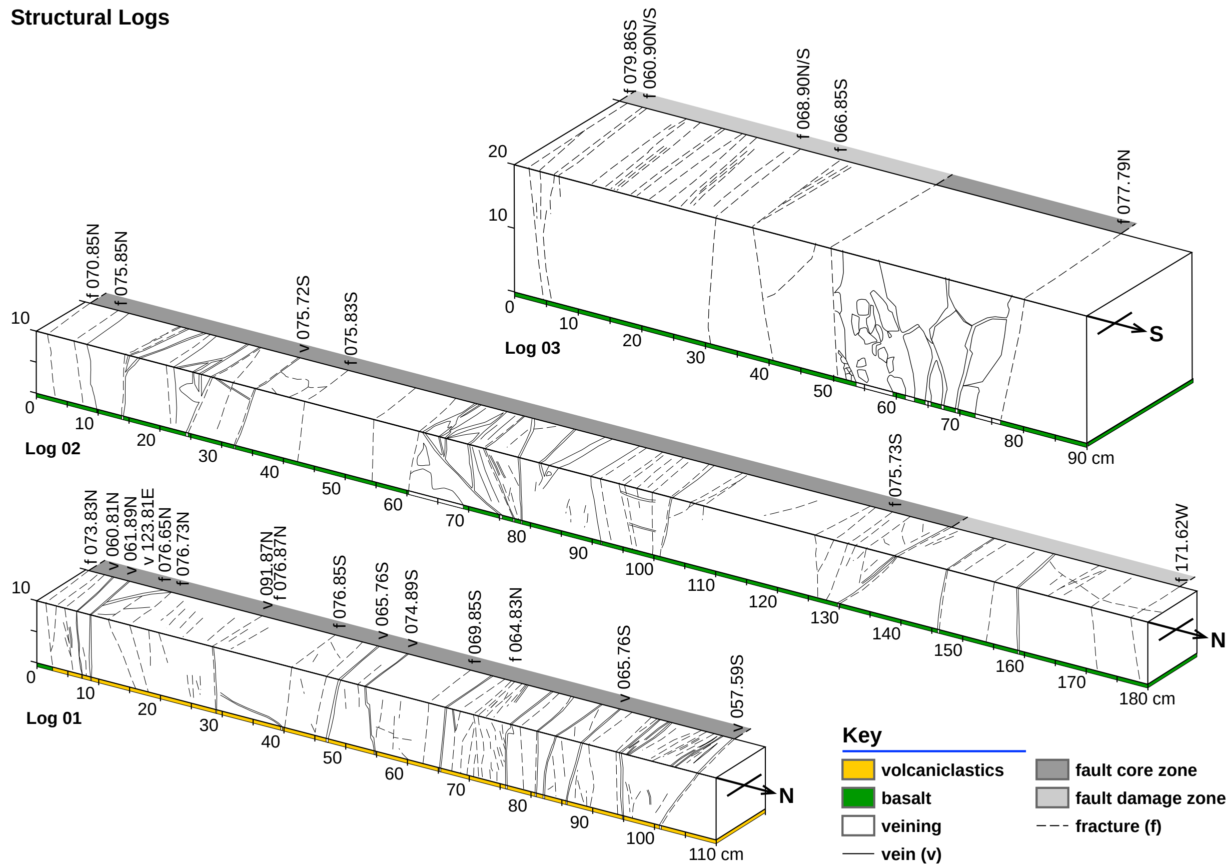

Faults in basalt

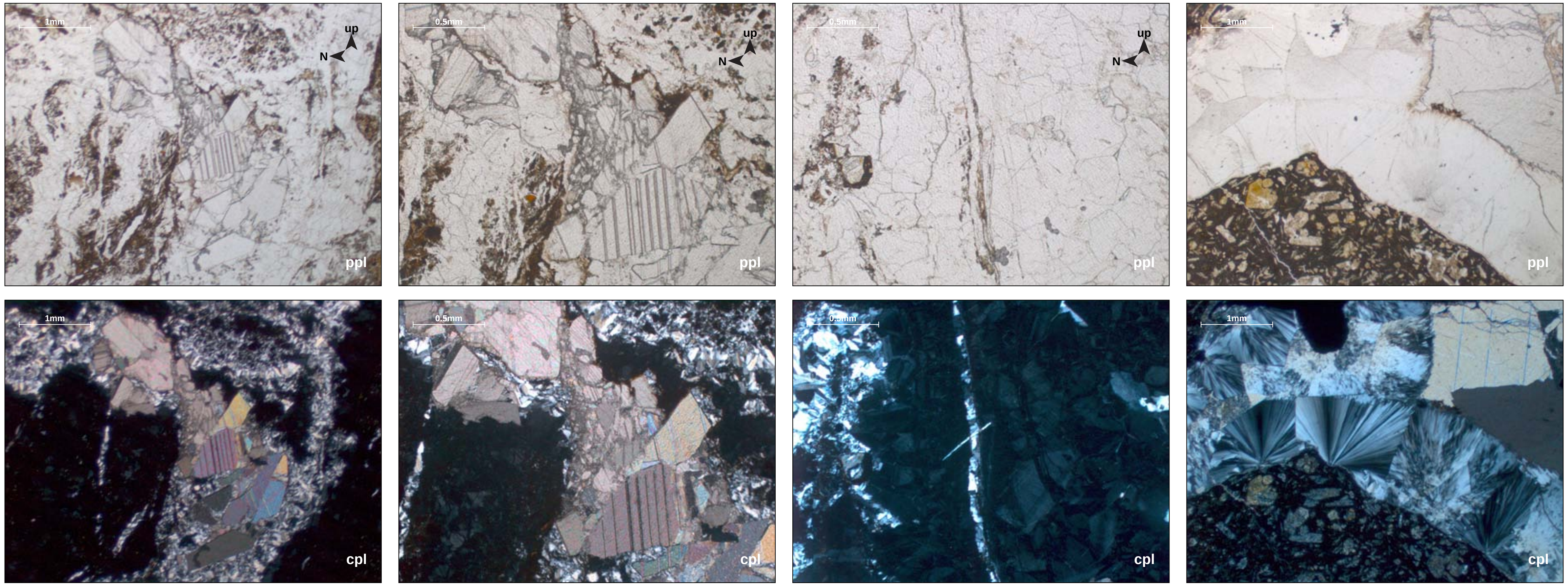

Faults in sediment

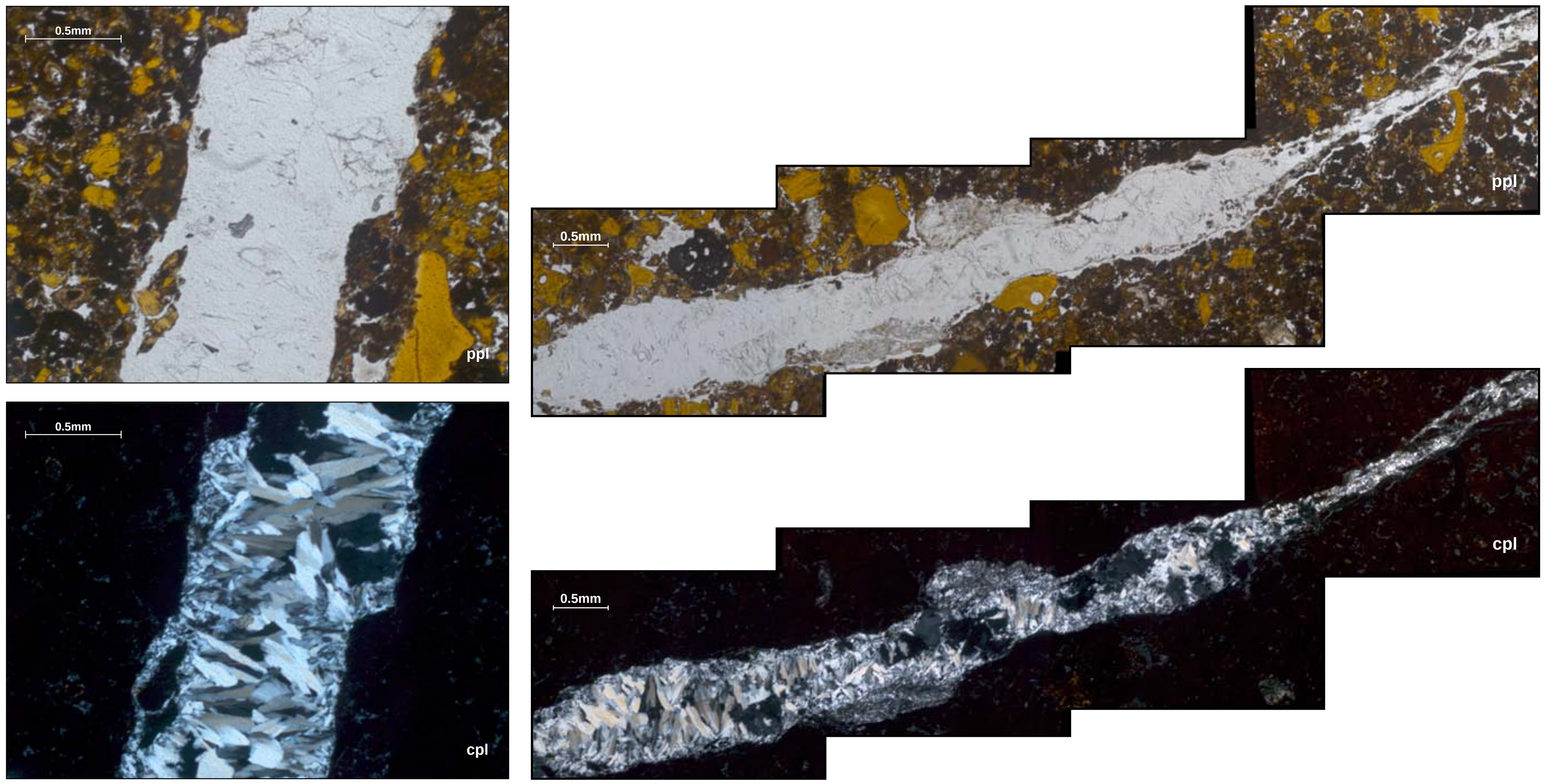

Eiði is located in the NW of Eysturoy, set within the upper third of the Malinstindur Formation. Most Faults and fractures are E-W oriented, displaying strike-slip lineations where apparent, which record a N-S extension, and E-W compression.

The fault of interest displays a dextral, down to the south, ~4.5m total offset, across a 0.1m to 2.0m damage zone, which varies depending on the host lithology: basaltic units disaggregate to form breccias, and volcaniclastic units being dragged into the master fault plane, and forming discrete tensile and shear tensile veins. Fault damage varies both along strike and up/down dip of the master fault, becoming much thinner through the volcaniclastic horizon. Below c, the fault zone decreases to a single plane, with a minimal (cm-scale) peripheral damage zone.

Eiði, NW Eysturoy

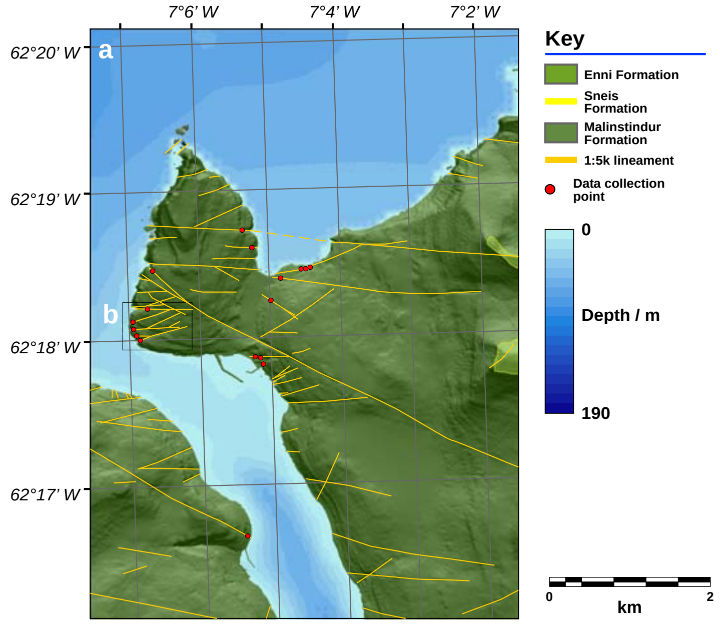

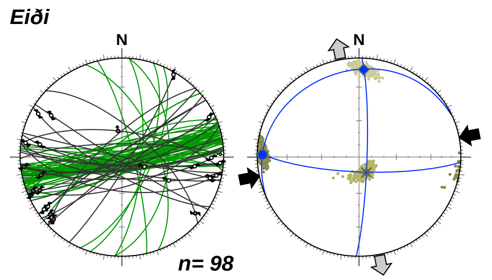

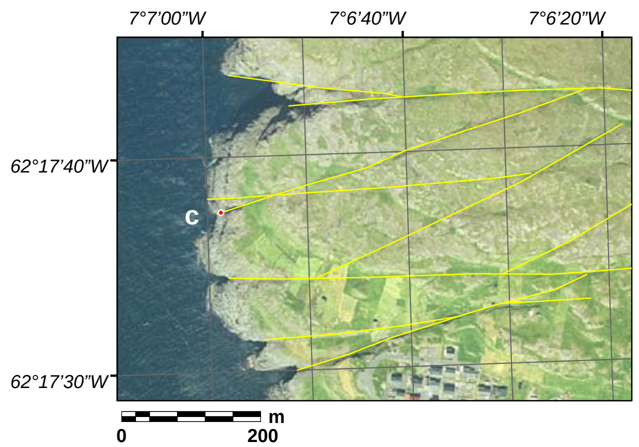

Eiði is located in the NW of Eysturoy, set within the upper third of the Malinstindur Formation. Most Faults and fractures are E-W oriented, displaying strike-slip lineations where apparent, recording a N-S extension, and E-W compression. Strain is accommodated across the area by small-offset extensional hybrid fractures, with sporadic larger (metre scale) offset faults developed every 50m or so. Of particular interest is a fault on the western coast of the headland, labelled *c* above.

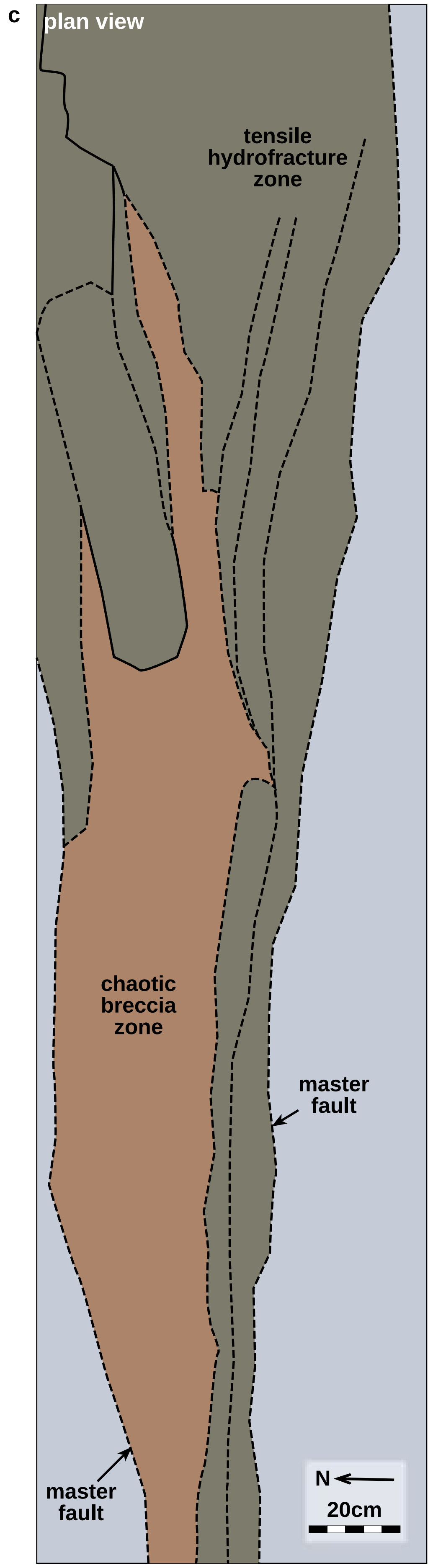

Tensile hydrofracture zone

Chaotic breccia zone

The fault in western Eiði, displays a 4m, down to the south offset, across a 0.5m to 6m damage zone. Internally the damage zone can be split into 2 zones (*left*), with a zone of tensile fractures enclosing a chaotic breccias core zone (*above and next page*).

Tensile fractures are filled with zeolite and/or calcite mineralisation that appear to have developed during successive faulting episodes of the same tectonic event.

The chaotic breccia comprises fragments of what are likely the wall rocks of the developing fault, including basalt clasts and vein fragments. The zone also harbours fragments of clastic sedimentary rock, presumably from the nearby sedimentary horizons. Zeolite overgrowth on these fragments most likely indicates that the system was not fully sealed following breccias, but instead, that fluid transmission was a prolonged process.

Tensile hydrofracture zone

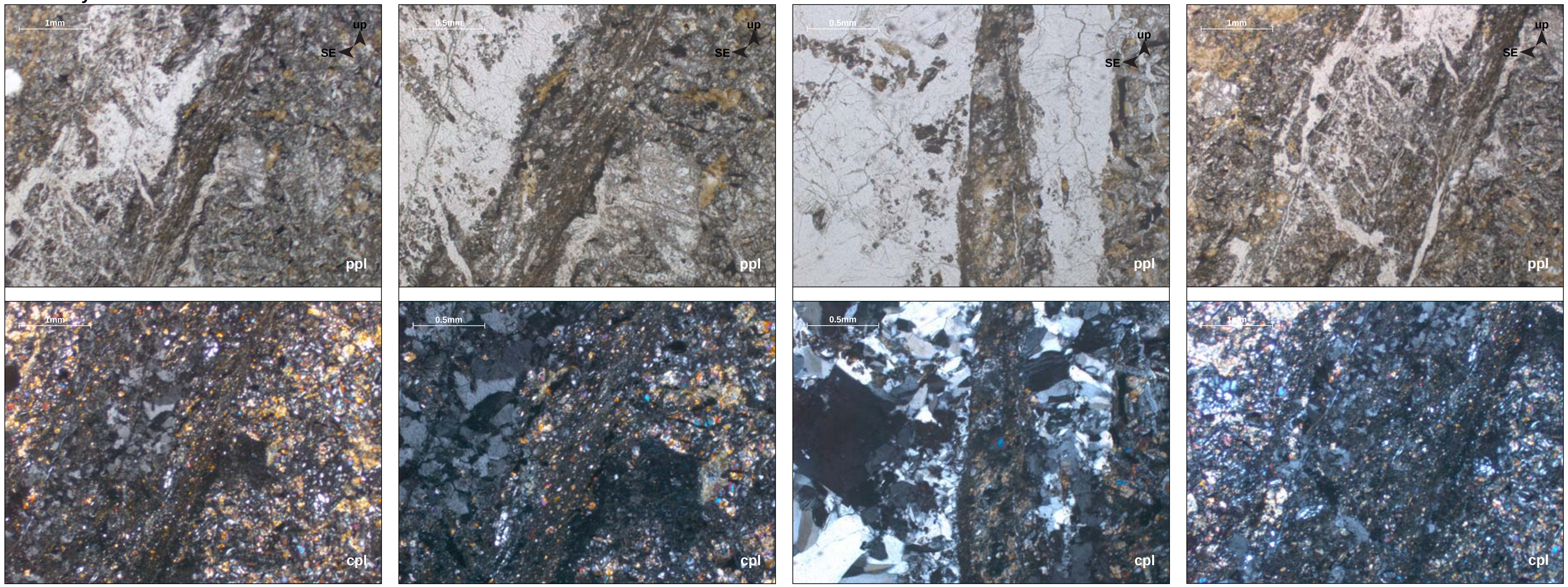

Chaotic breccia zone

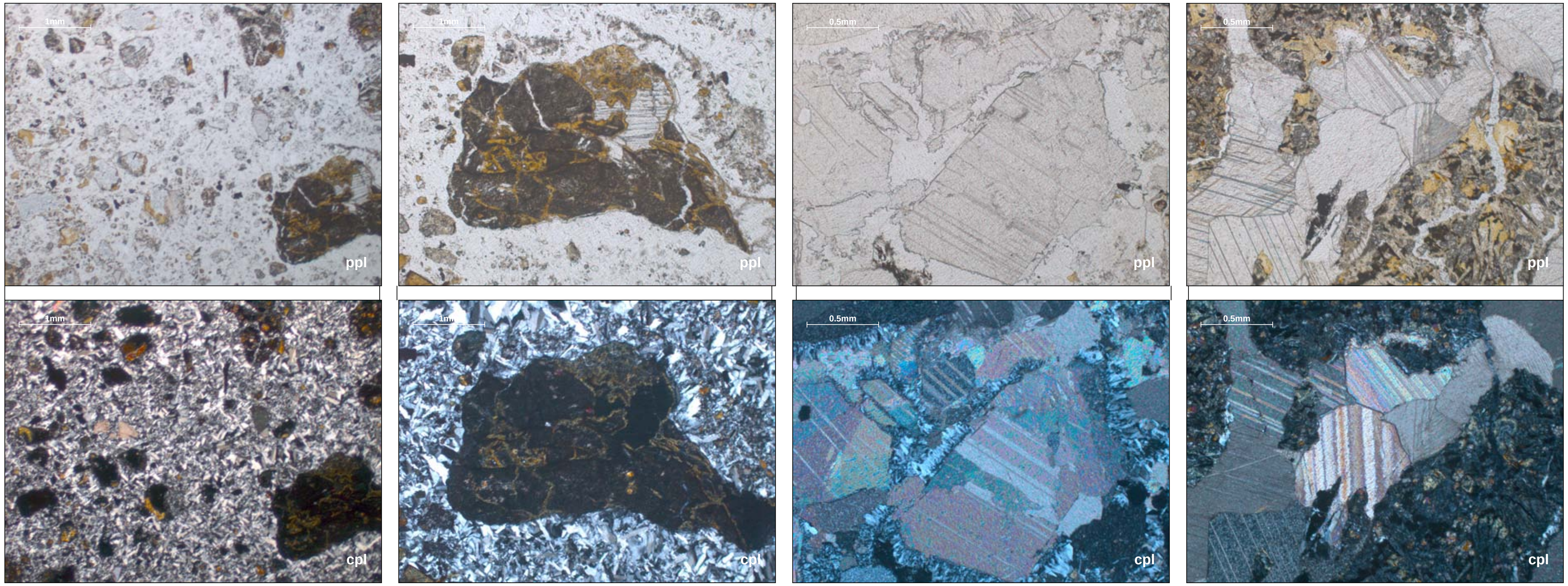

Gjogv, NE Eysturoy

Location

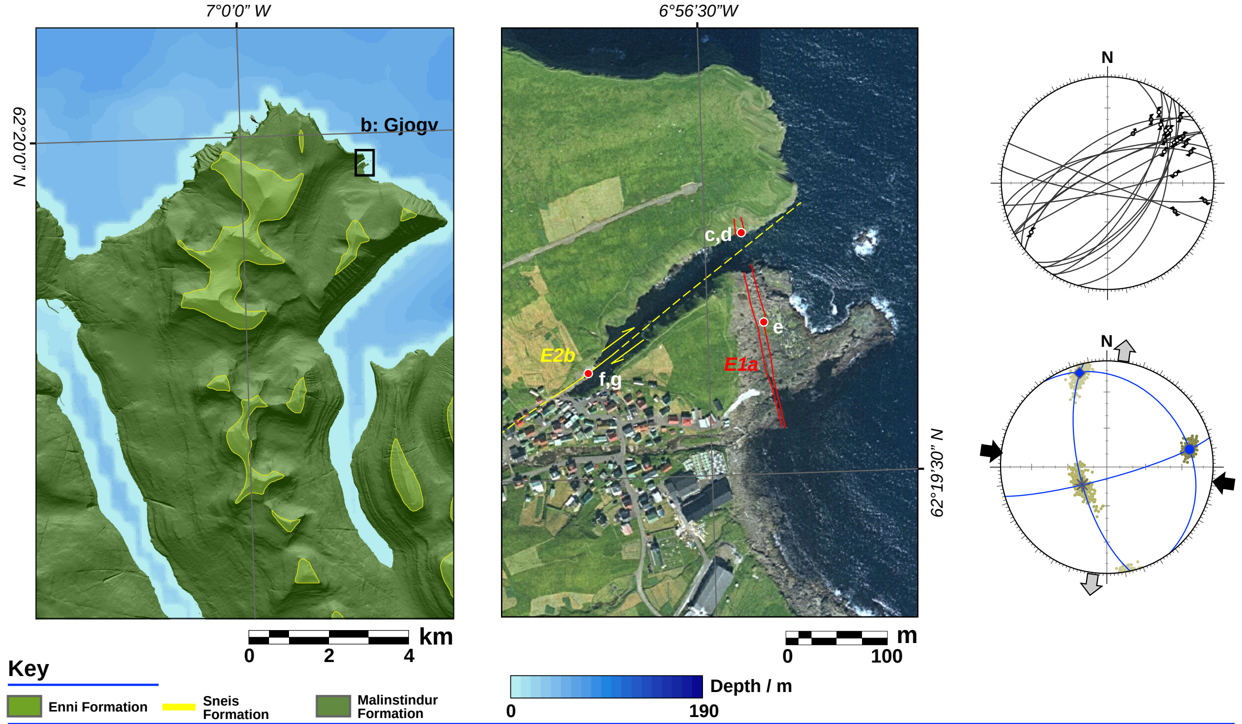

Event 1b: Dyke

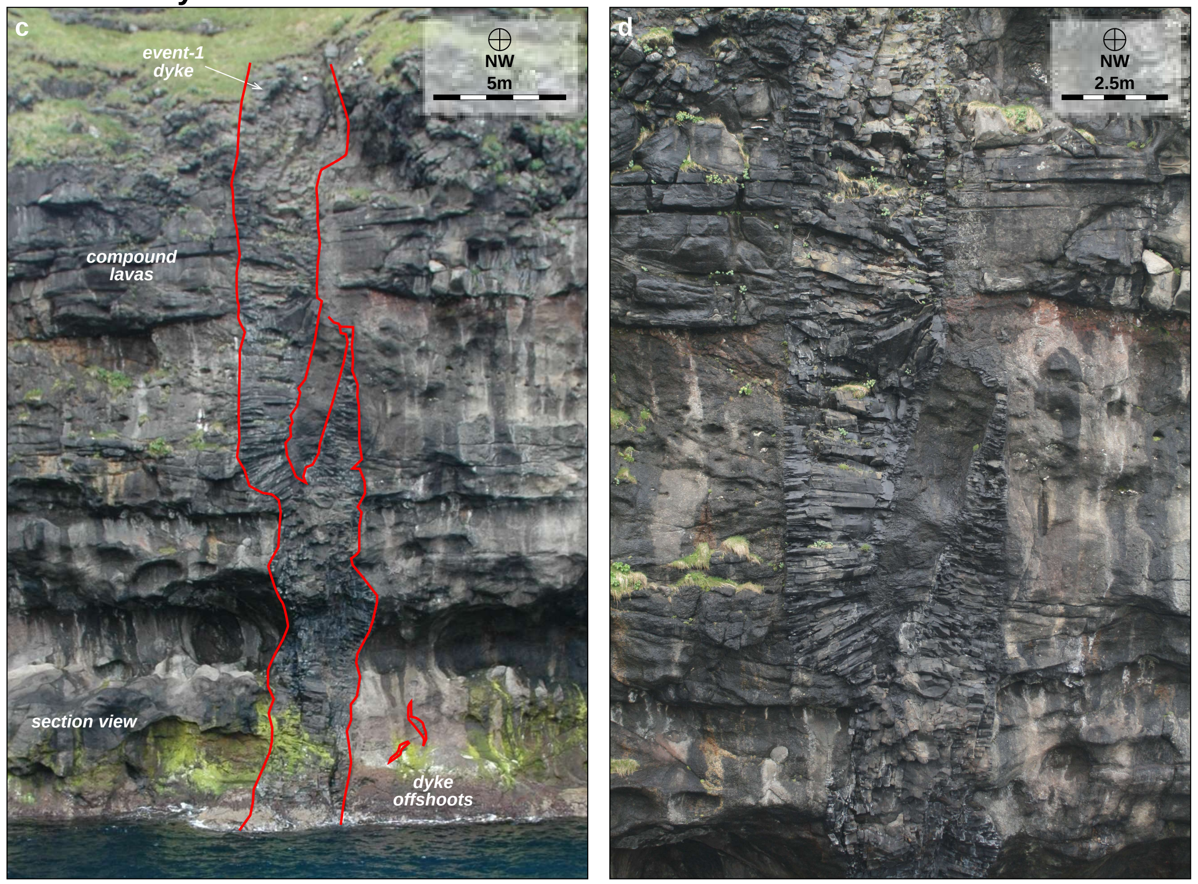

Event 2b: Fault

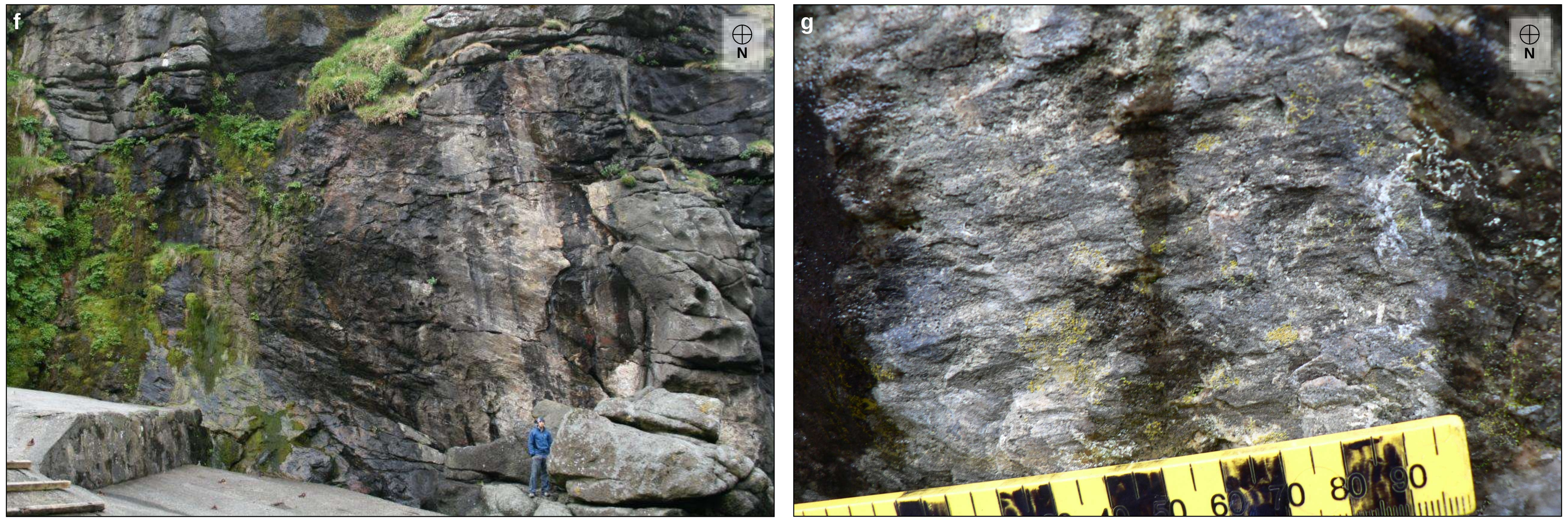

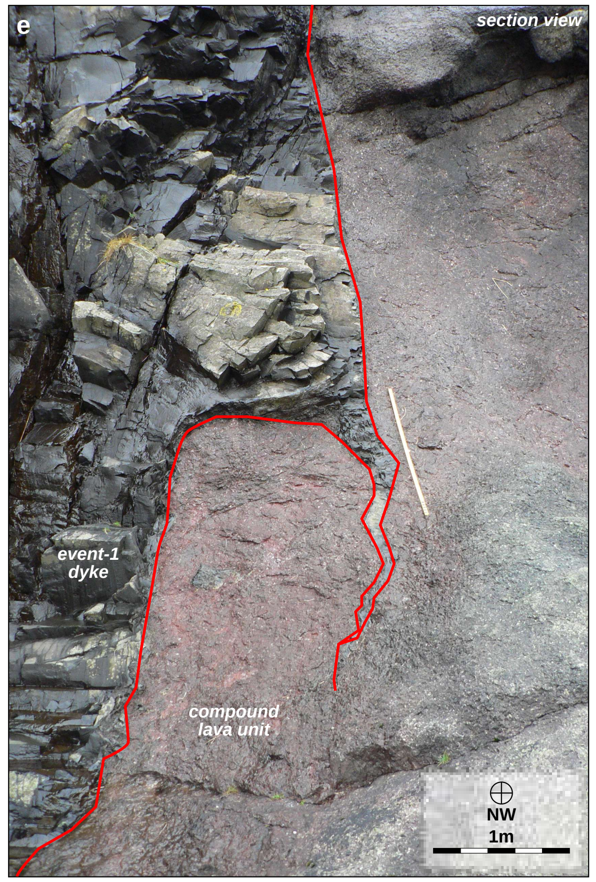

Gjogv is located in the NE of Eysturoy, and is set within the upper third of the Malinstindur Formation. The area is host to dykes of Event 1 and 2, and strike slip faults of Event 2. At the end of the coastal inlet (termed a gjogv, and hence the village name) is a well exposed Event 1 dyke, which can be traced for some 200m on the southern side of the gjogv, and seen in vertical section in the cliffs on the northern side. The margins of the dyke are exposed in plan and section view and provide a detailed insight into the 3-D geometry of the intrusion. In both planes, the dyke displays irregular margins, as well as numerous offshoots and bifurcations.

A set of strike-slip fault panels makes up the northern cliff face at the western end of the gjogv. The panels are linked to form one large fault plane, which also displays larger corrugations on the surface, parallel to the slip direction. Individual fault panels record slight variations in the slip direction, most likely indicating dilatation on either side of the fault.

Gotogjogv, Eysturoy

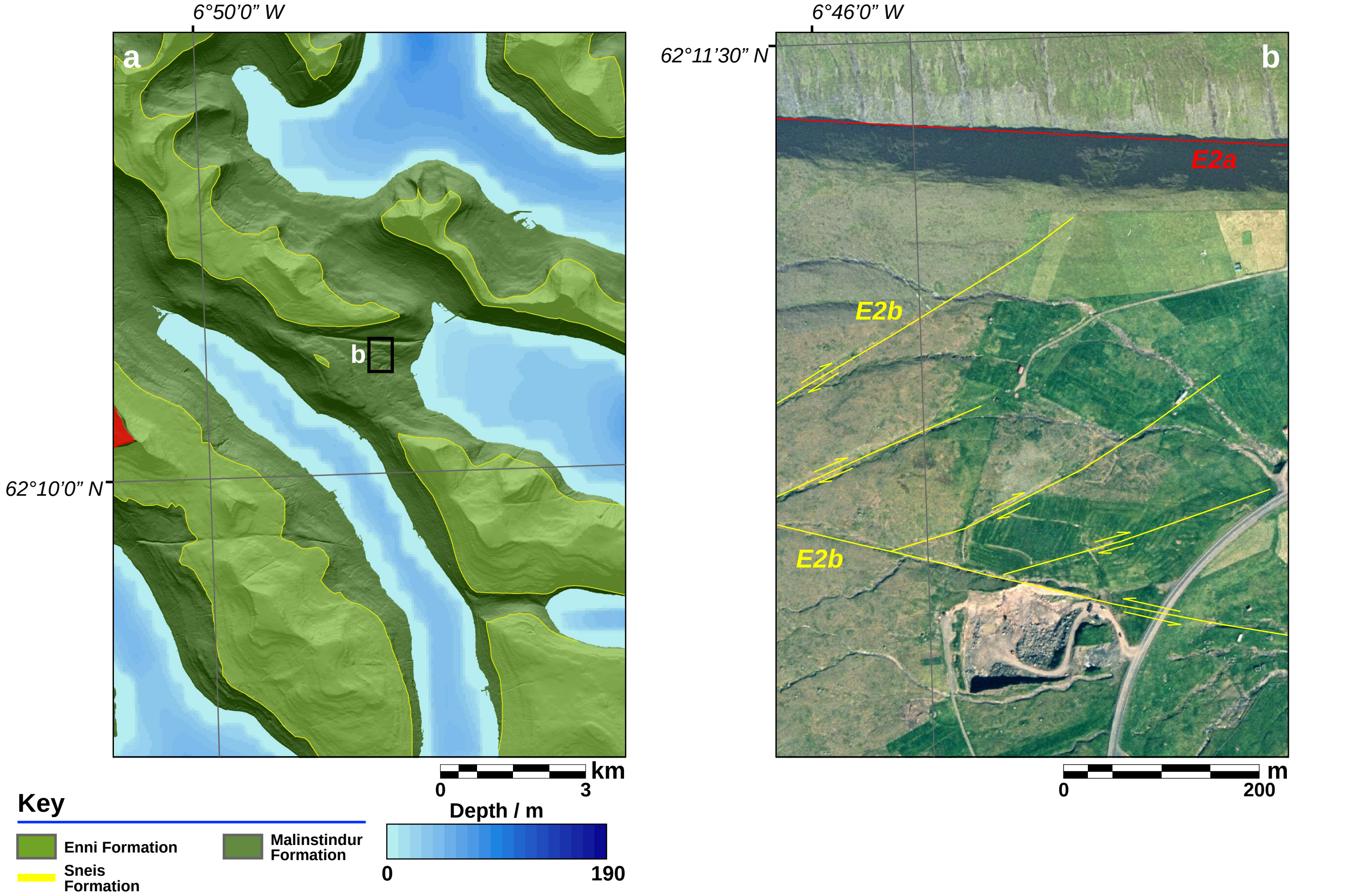

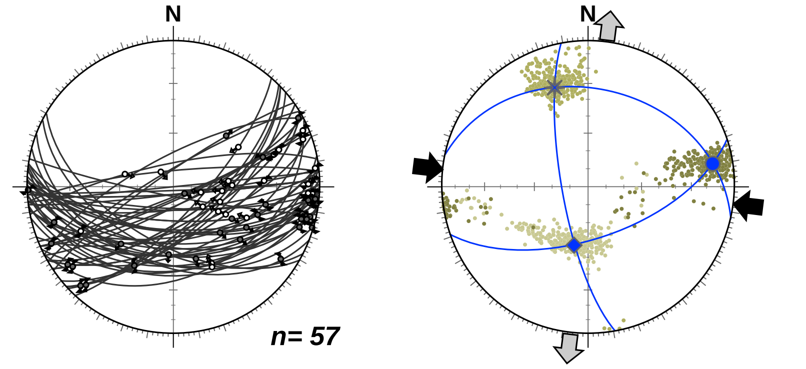

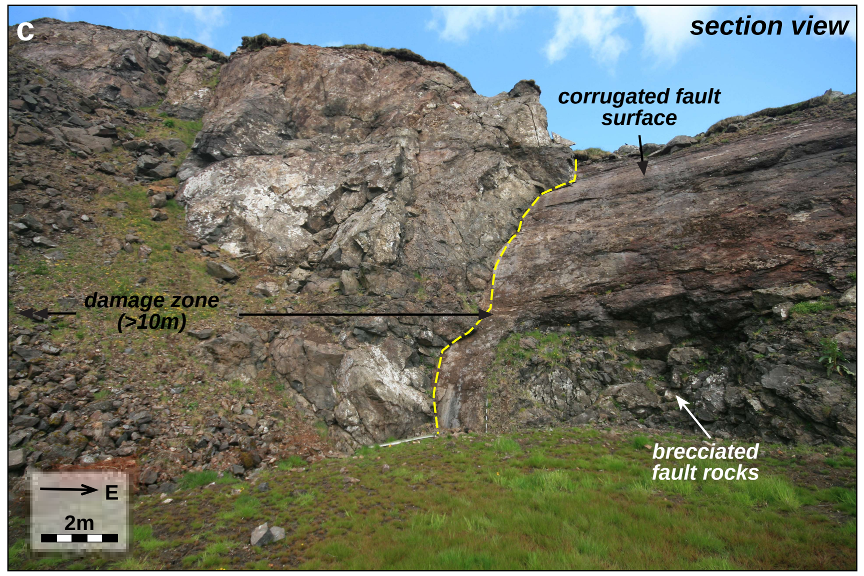

Gotogjogv is located in the eastern central part of Eysturoy, towards the top of the Malinstindur Formation. Structures in the area are predominantly E-W oriented. The fault of interest forms the northern face of a quarry, and displays obliquely oriented corrugations on the master fault surface, that lie roughly parallel to slickenfibres on the same surface. This part of the fault, and much of the peripheral damage (about 10m wide) are associated with Event 2. Within the fault damage zone, numerous zeolite and calcite mineralised fault panels display strike-slip slickenfibres, or tensile/vuggy mineral growth, indicating a N-S opening. However, these panels also display a polished surface in places, with dip-slip grooves and no clear contemporaneous mineralisation. Such features are therefore inferred as being later than Event 2, perhaps relating to Event 3 deformation.

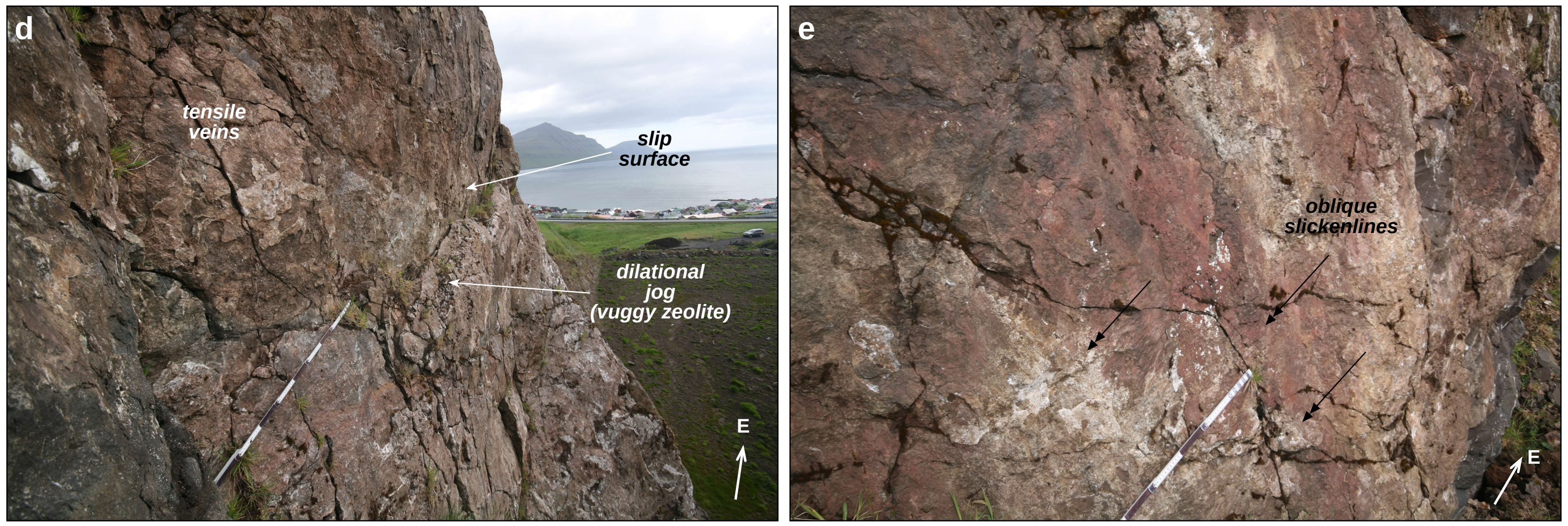

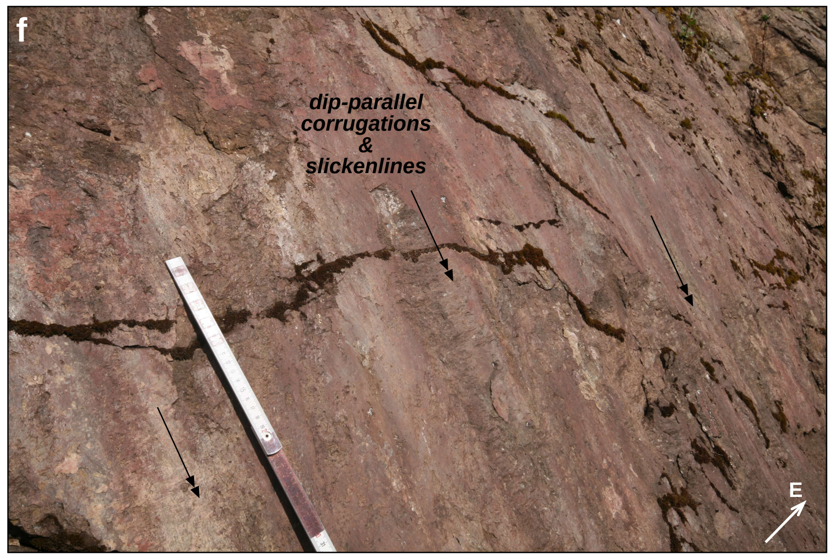

Eysturoy Sill

Location

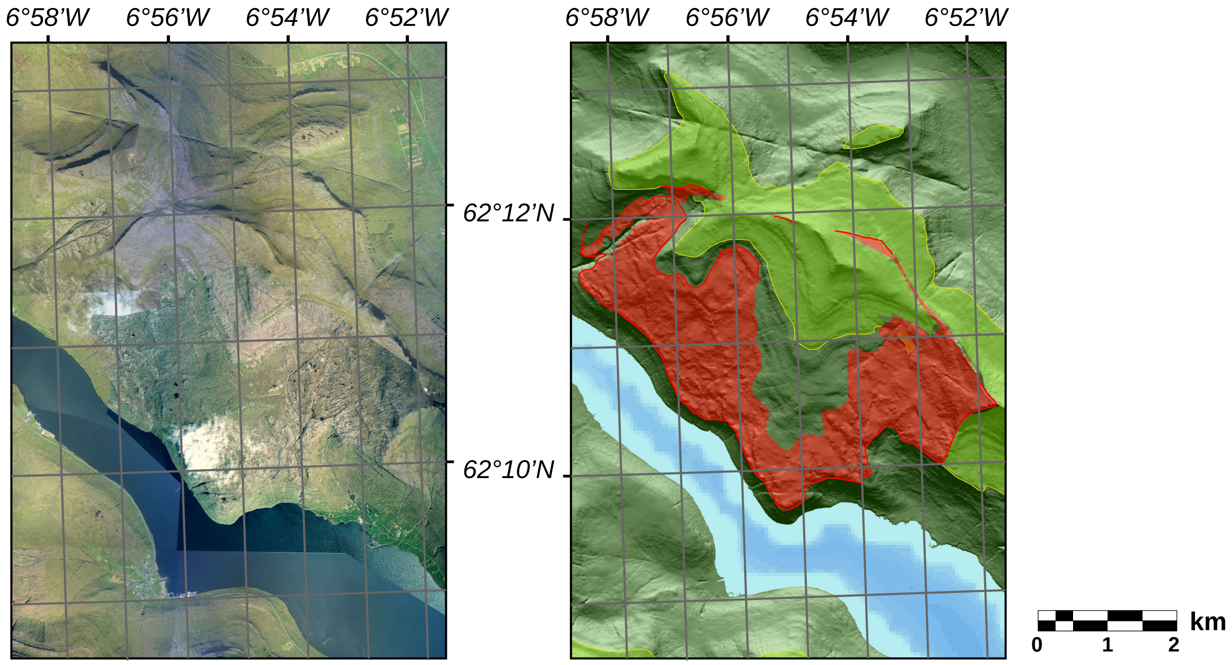

Sill Geometry

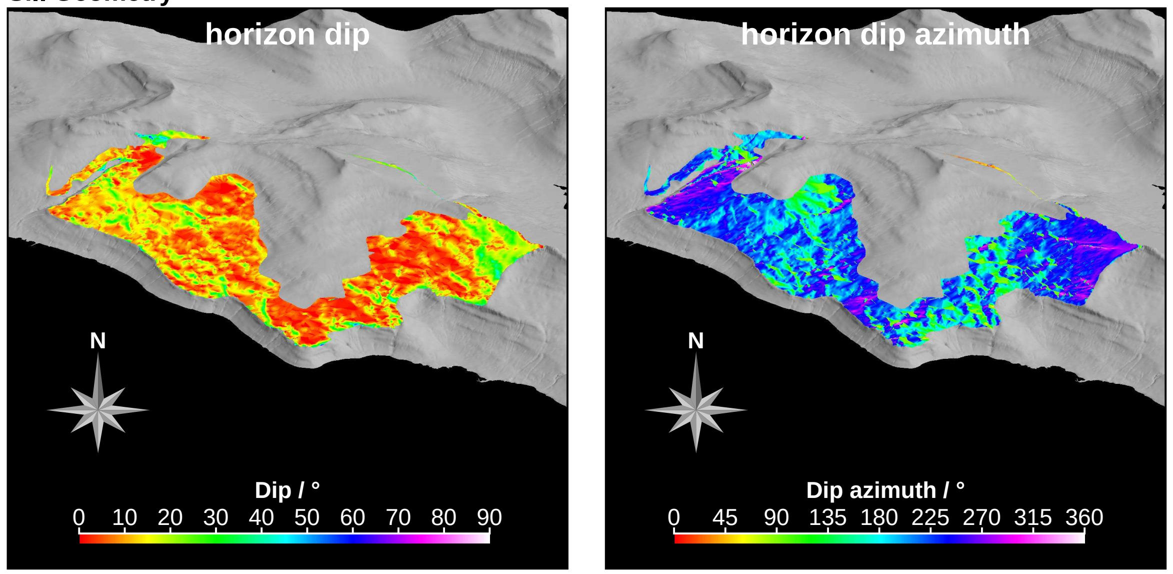

Cross-cutting relationships

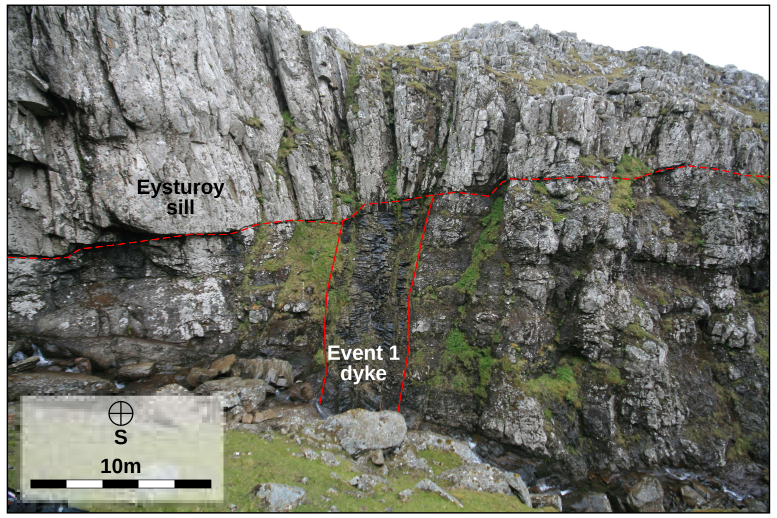

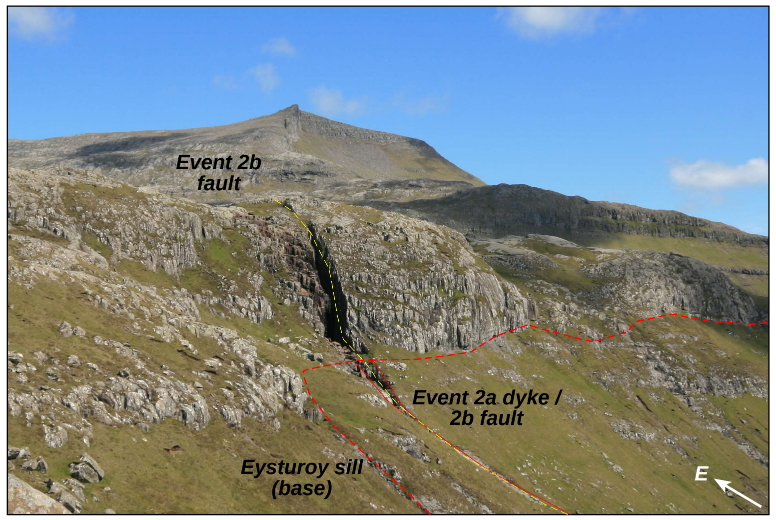

Overview

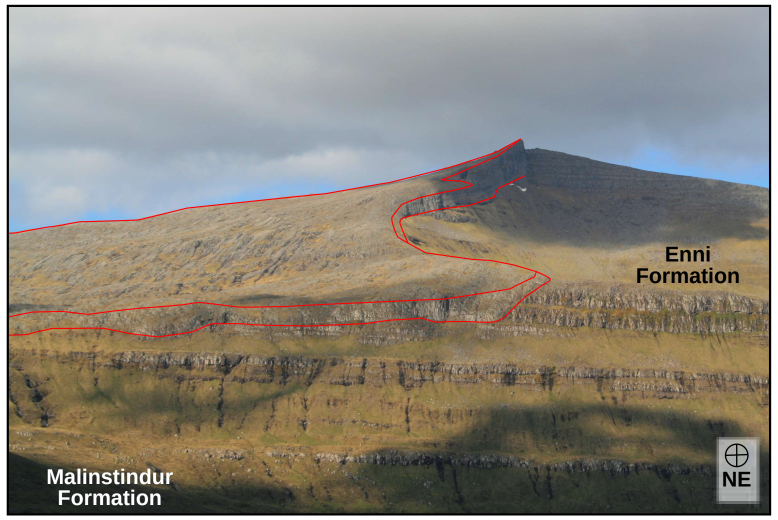

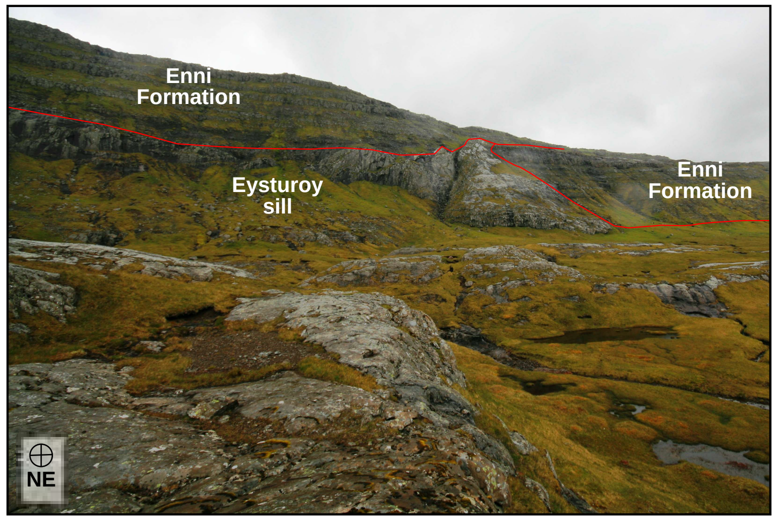

The Eysturoy sill is a transgressive intrusion on the western side of Eysturoy (*top left*), occupying an area of about 16km2, and ranging in thickness from 10-55m. Generally the sill dips SW, displaying a pronounced flat section at the level of the Sneis Formation (*top right*). Where observed, the sill clearly cuts Event 1 and 2 dykes, but is cut by Event 2 faults (*right*), most likely indicating its intrusion was towards the end of Event 2a, and therefore at a similar time to the Streymoy sill.

Streymoy Sill

Location

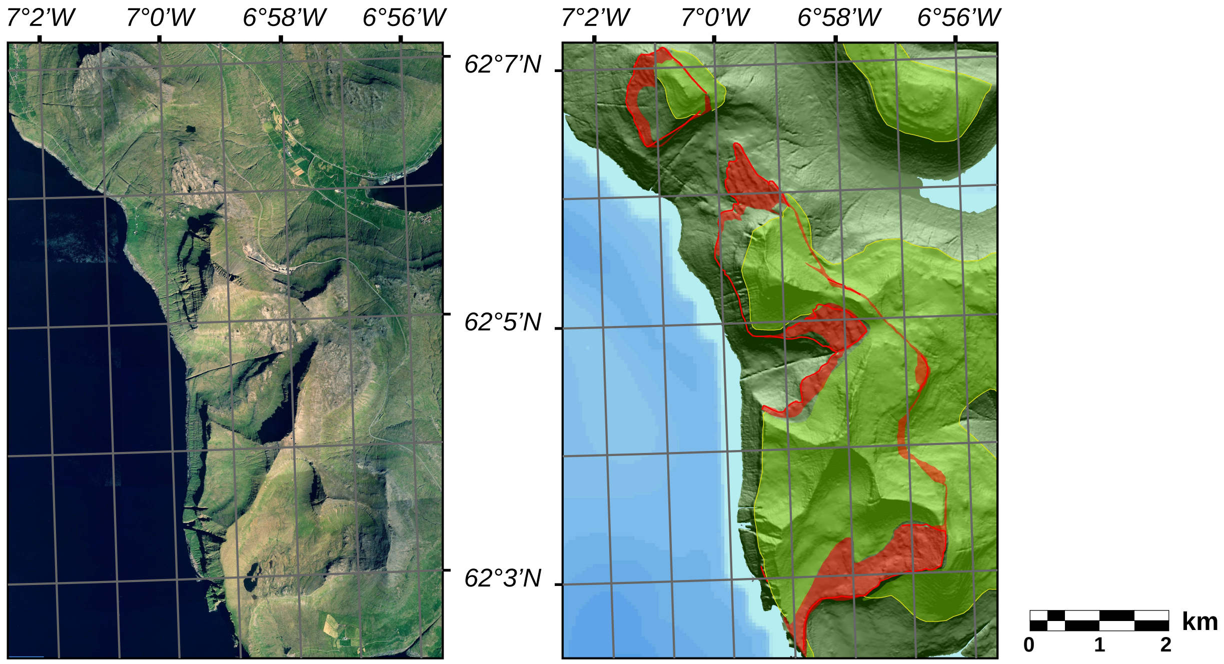

Sill Geometry

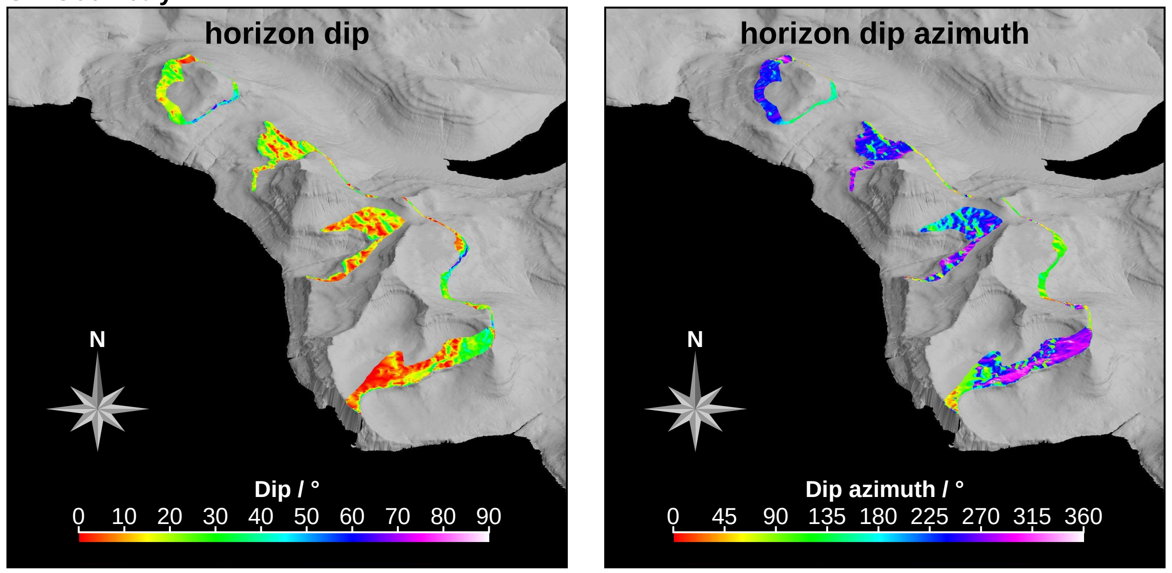

Overview

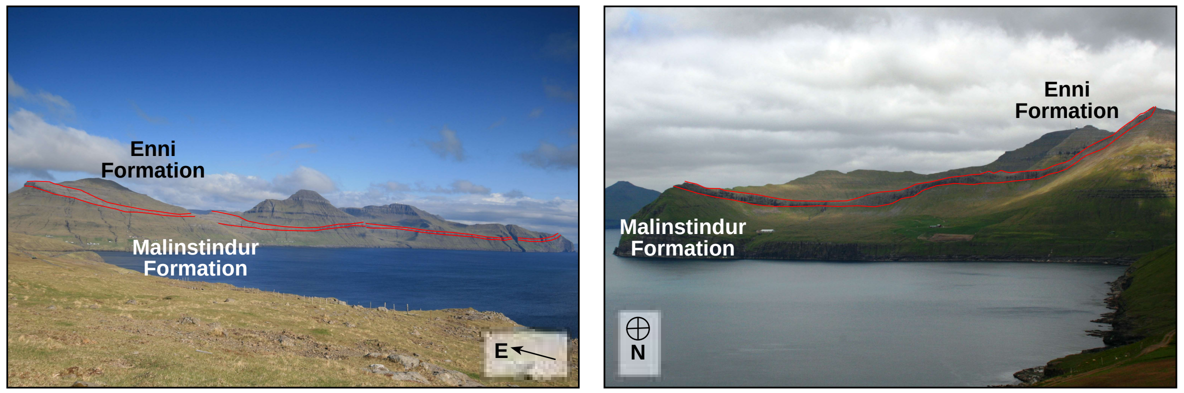

Cross-cutting relationships

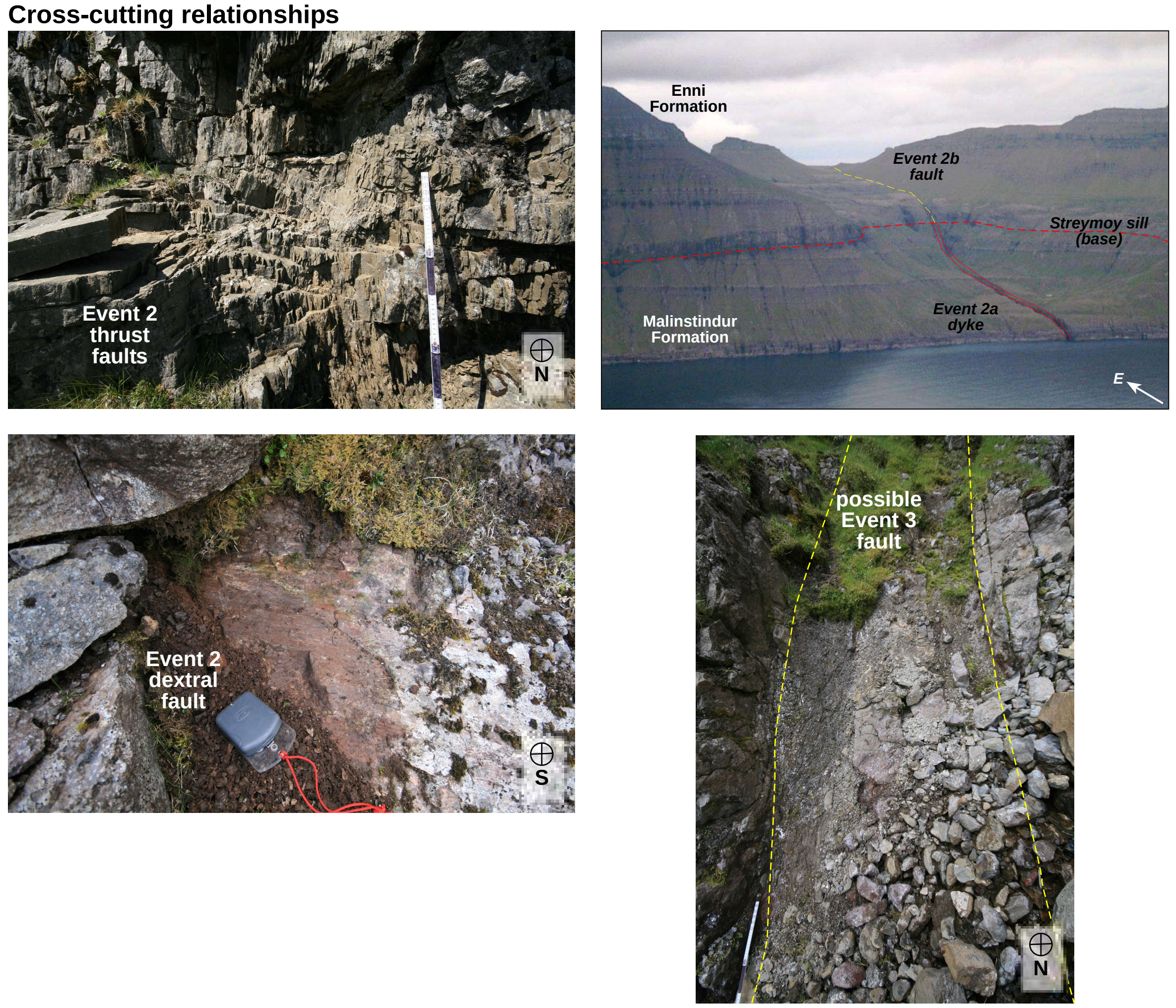

The Streymoy sill is located on the western side of central Streymoy (*above*), and like the Eysturoy is transgressive, rising from the west towards the east and northeast. The sill ranges from ~10-55m thickness, and covers an area of about 13km2, displaying a saucer-like geometry in 3-D (*top right*). Within this general trasngressive geometry are numerous ramp- and flat-sections, cutting upwards from within the top part of the Malinstindur Formation, becoming flat at the level of the Sneis Formation, and then ramping upwards again into the Enni Formation. More minor flat sections may therefore be a reflection of variations in the lithology of the country rock. Like the Eysturoy sill, the Streymoy sill cuts Event 1 and 2 dykes, but is cut by Event 2 faults, including numerous, minor thrusts (*right*). A poorly consolidated breccia-filled fault is also observed cutting the sill, which may be related to Event 3 (*bottom right*).

Tjornuvik, NE Streymoy

Location

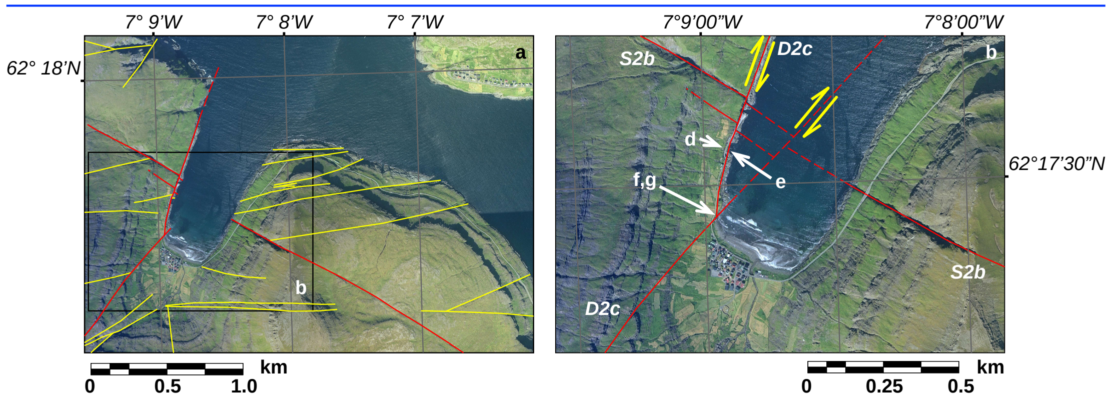

Overview

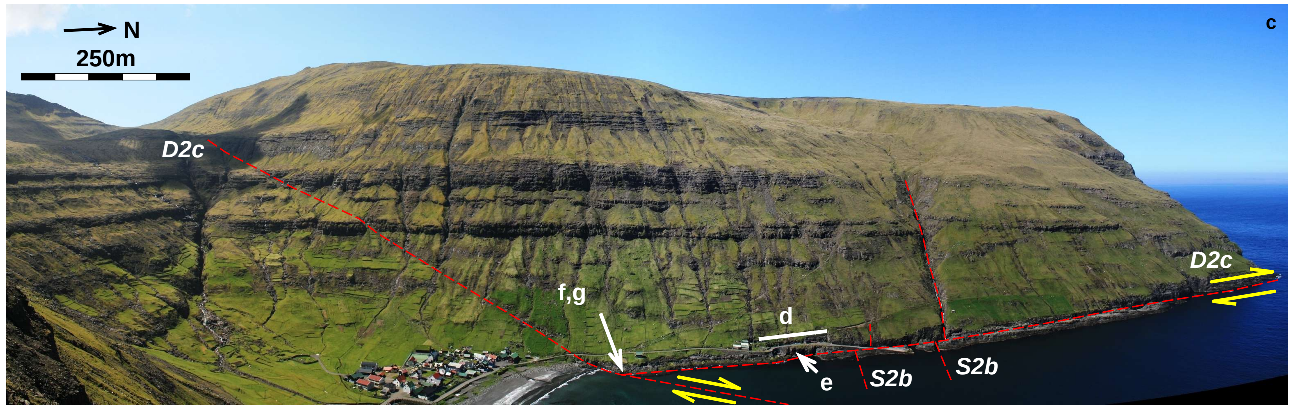

Event 2b: Structural characteristics

Structural log

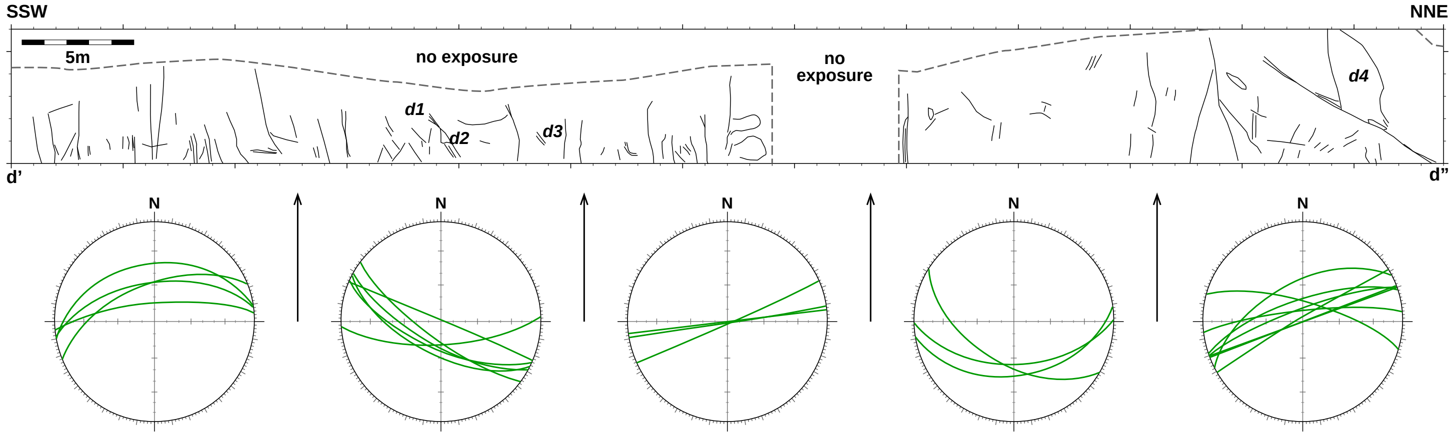

Tjornuvik is located in the NE of Streymoy, set in the middle third of the Malinstindur Formation. Structures in the area are predominantly ENE-WSW to ESE-WNW oriented, but with two notable dykes oriented NNE-SSW and NE-SW. The most prominent feature is an ESE-trending dyke that can be seen on both sides of the bay, across which it is apparently offset by 80-100m. At the pier section (e.g. *structural log*) numerous fault panels are exposed displaying strike-slip kinematics and tensile openings that record a N-S extension, and E-W compression. Displacements on these faults are negligible however, and do not appear to markedly offset the stratigraphy.

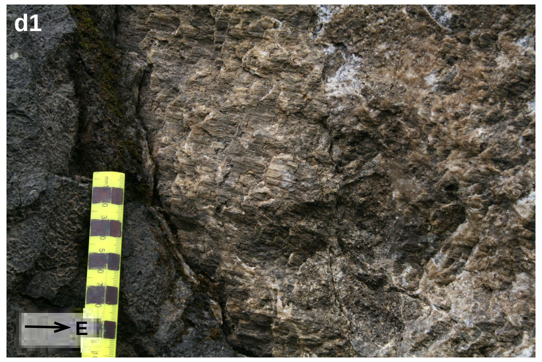

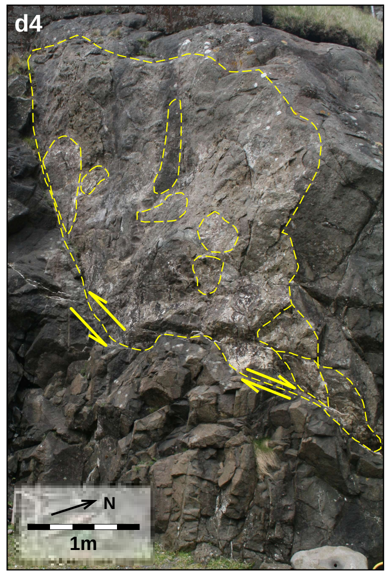

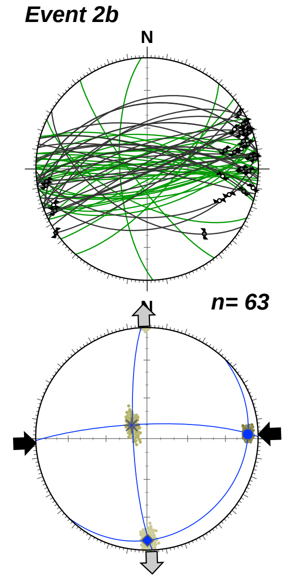

A gully marks the location of the NNE-trending dyke at the pier section, with sporadic outcrops where it comes on land, where it is clearly heavily mineralised with zeolite and calcite and brecciated. Across this dyke, structures and other dykes (including the prominent dyke across the bay) are offset by about 20m, with a dextral motion sense. Following the dyke to the SSW, it joins the NE-SW trending dyke, perhaps as a bifurcation of the same intrusion. Again this dyke is heavily mineralised (*right*), but cut by E-W trending veins. Upon entering the dyke, those veins become aligned along the jointing pattern. Examples of dilational jogs in mineral veins in the dyke indicate a dextral offset sense: this may therefore explain the large offset of the dyke across the bay (see *top left*).

Event 2c: Structural characteristics

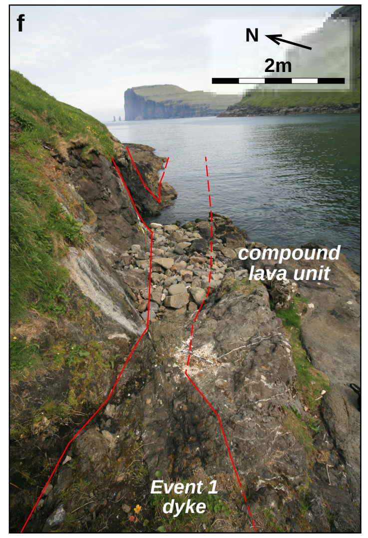

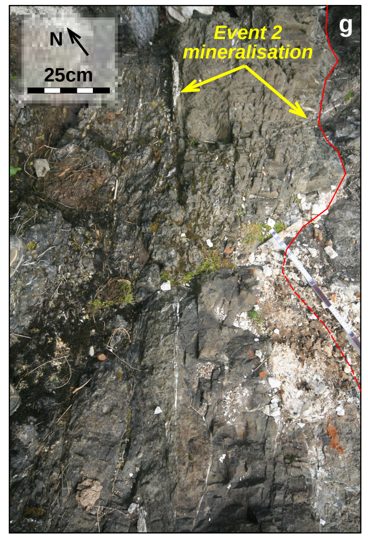

Vagseiði, Suðuroy

Suðuroy, Southern Faroe Islands

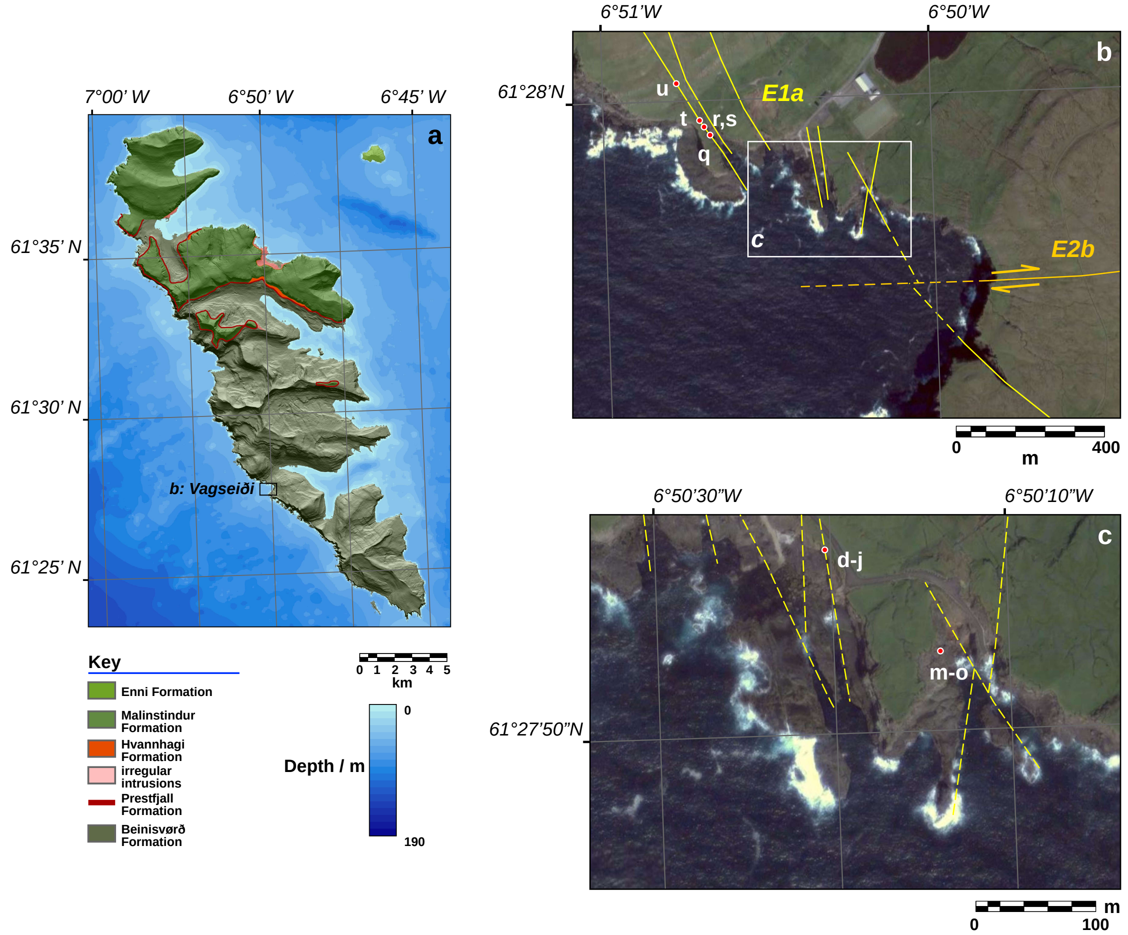

Vagseiði is located on the western coast of Suðuroy, and is set within the lower third of the exposed section of the Beinisvørð Formation. Structures in the area are typically NW-SE to N-S oriented dip-slip faults and dykes (recording a NE-SW extension), with a small proportion of E-W trending faults. Fault displacements range from cm-scale (e.g. *right, this page*) to dam-scale (e.g. *top, next page*). Damage zone widths vary depending on the scale and nature of the fault. Minor offset faults (e.g. *right, this page*: ~15cm) commonly display wide damage zones (~6m), reflecting the extensional failure mode (perhaps providing open conduits for hydrous fluids for a prolonged period of time), whereas larger offset extensional and shear hybrids (e.g. *top of next page*: 30m) display a similar damage zone width (i.e. ~6m). Small offset faults display increased damage towards the master fault, with either a reduction in grain size or increased brecciation (*right, this page*) depending on the magnitude of offset. For example, across the N-S trending fault on the right, the nature and intensity of deformation changes markedly towards the master fault, with (*left to right*) pure tensile veining at distances of 4-6m from the master fault, minor offset shear tensile faults 1-4m from the master fault and intense brecciation within a 1m wide zone from the master fault (i.e. the fault core).

Differences in fault style are noted between basalt and volcaniclastic horizons (e.g. *next page*). Faults and fractures typically exploit the existing cooling joints, hence are commonly vertical, whereas faults through volcaniclastic sediments, with no pre-existing structure, are more typically oriented (i.e. to within predicted Andersonian inclination ranges).

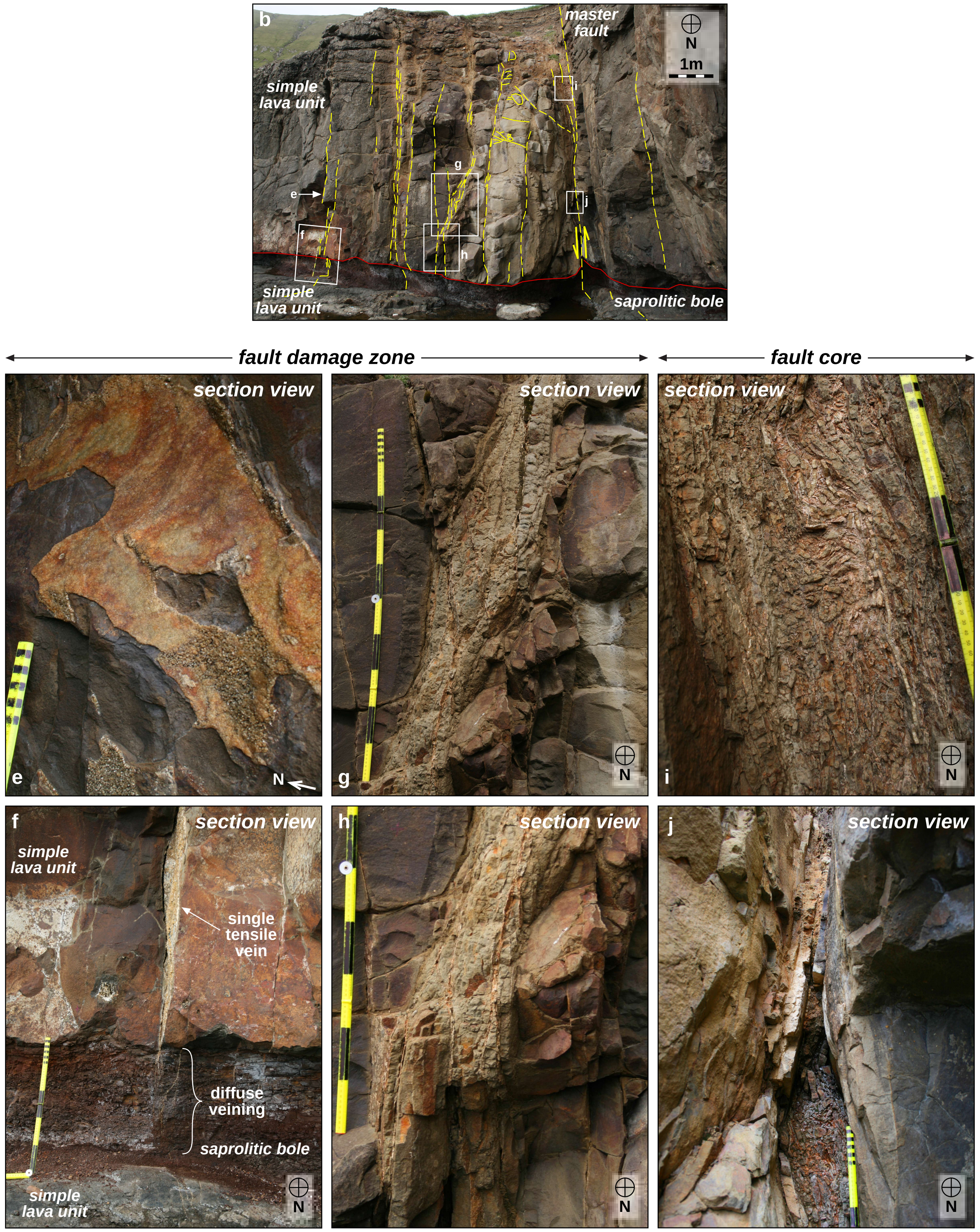

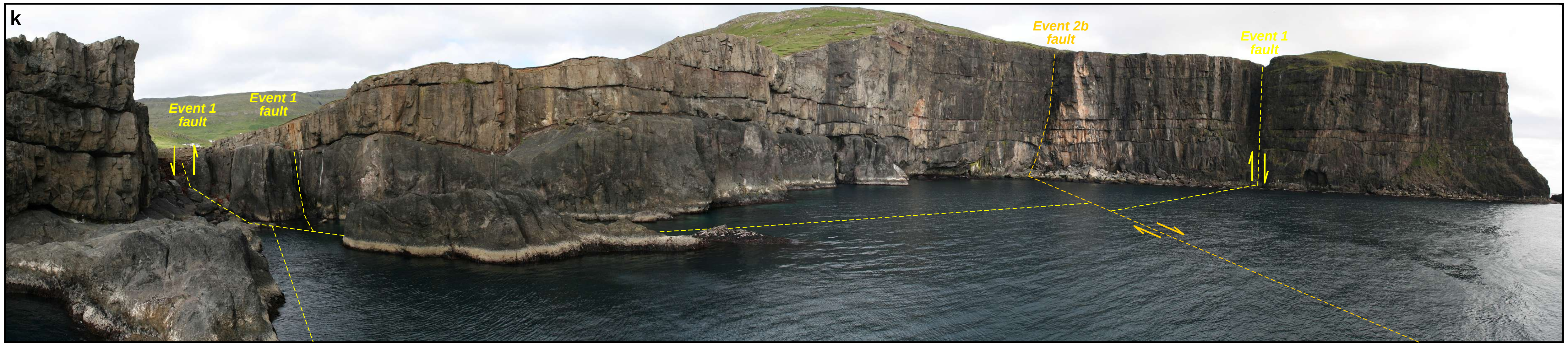

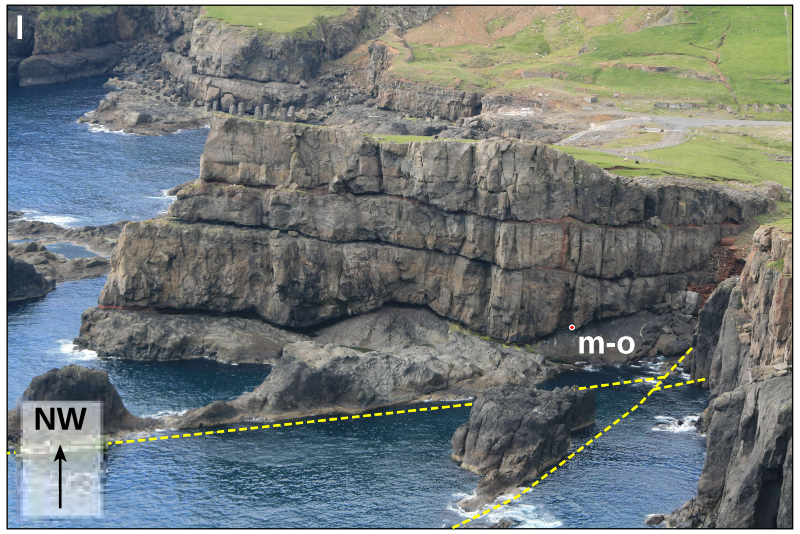

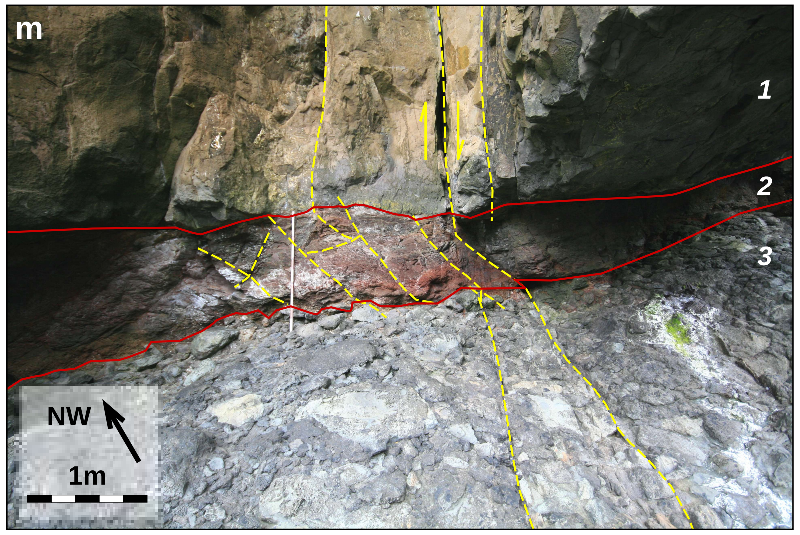

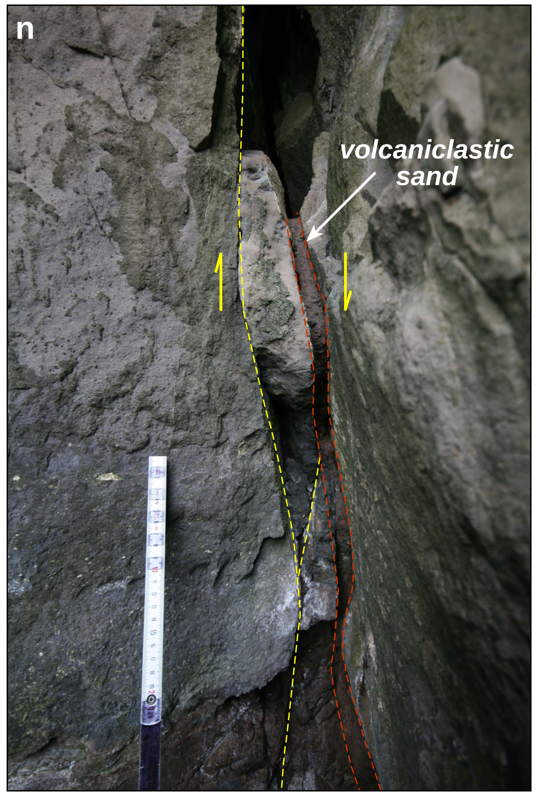

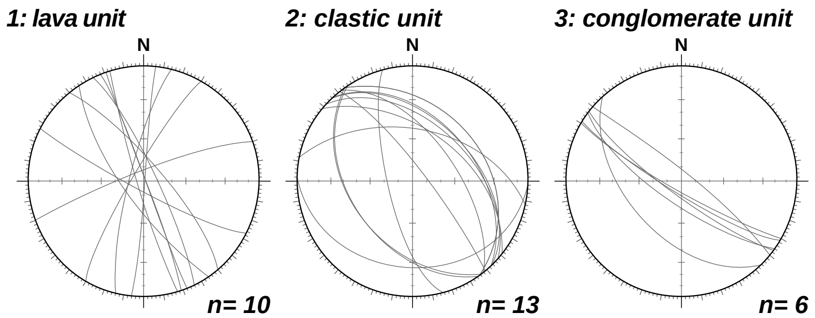

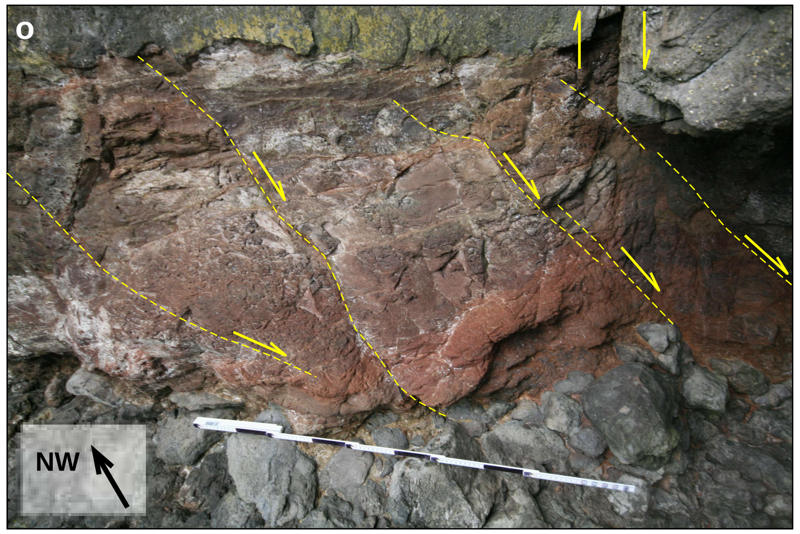

Where observed, N-S and NW-SE faults in the area are cut by E-W trending faults. E-W trending faults are strike-slip, and record a N-S extension and E-W compression. This cross-cutting relationship is observed Vagseiði (*top, this page*), where a NW-SE trending fault appears to be offset by some 20m or so across the bay, with a dextral sense.

Numerous examples of clastic materials entrained along faults are observed in this area. However, the most notable of these occurrences are observed along a single fault to the north of the bay (*see map*), where poorly to unlithified clastic materials are observed within lenses along a NW-SE trending fault (*next page*). The clastic materials in these faults clearly cut and therefore post-date mineralisation of the original fault. Furthermore, where observed, drag fabrics within the clastic material displays the opposite motion sense to the kinematics of the host fault, most likely indicating minor inversion of the structure.

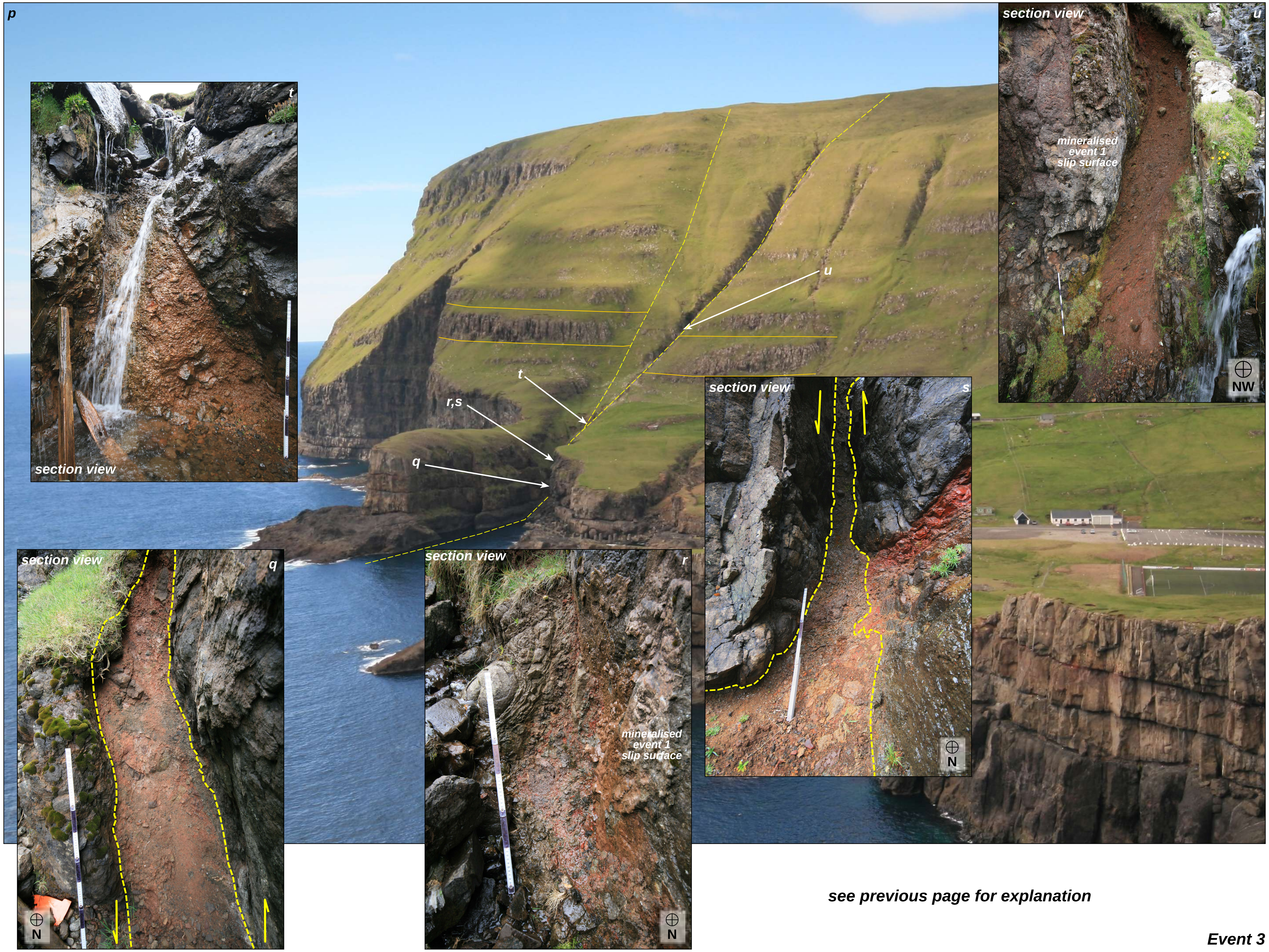

see previous page for explanation

Event 3

Viðareiði, N. Viðoy: Event 2b

Viðoy, NE Faroe Islands

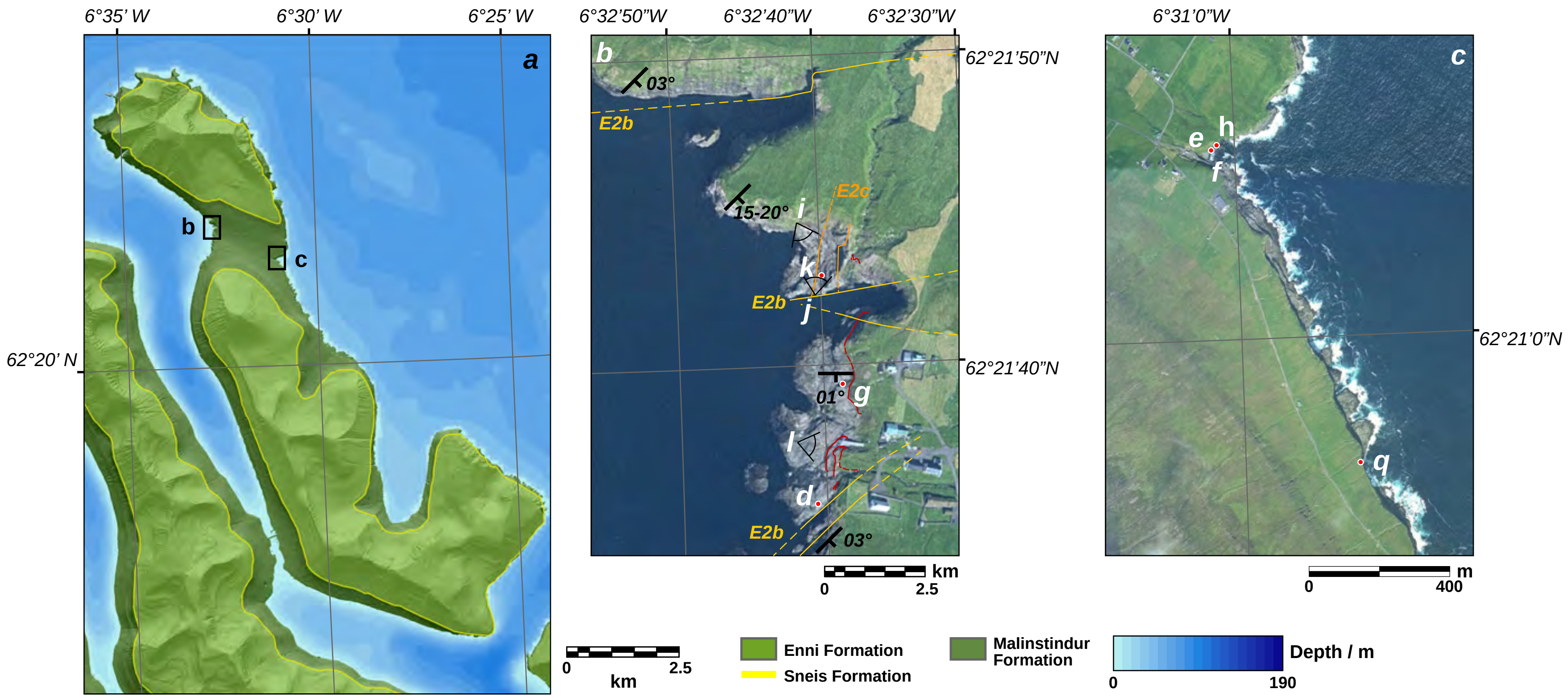

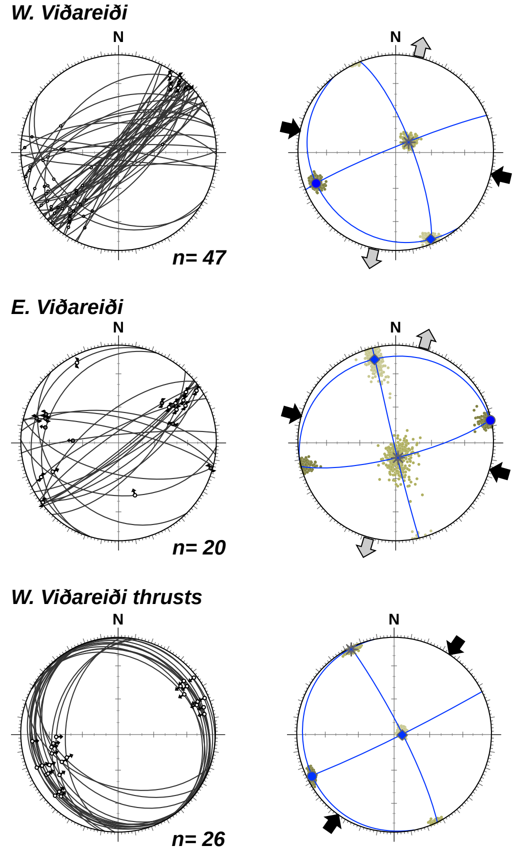

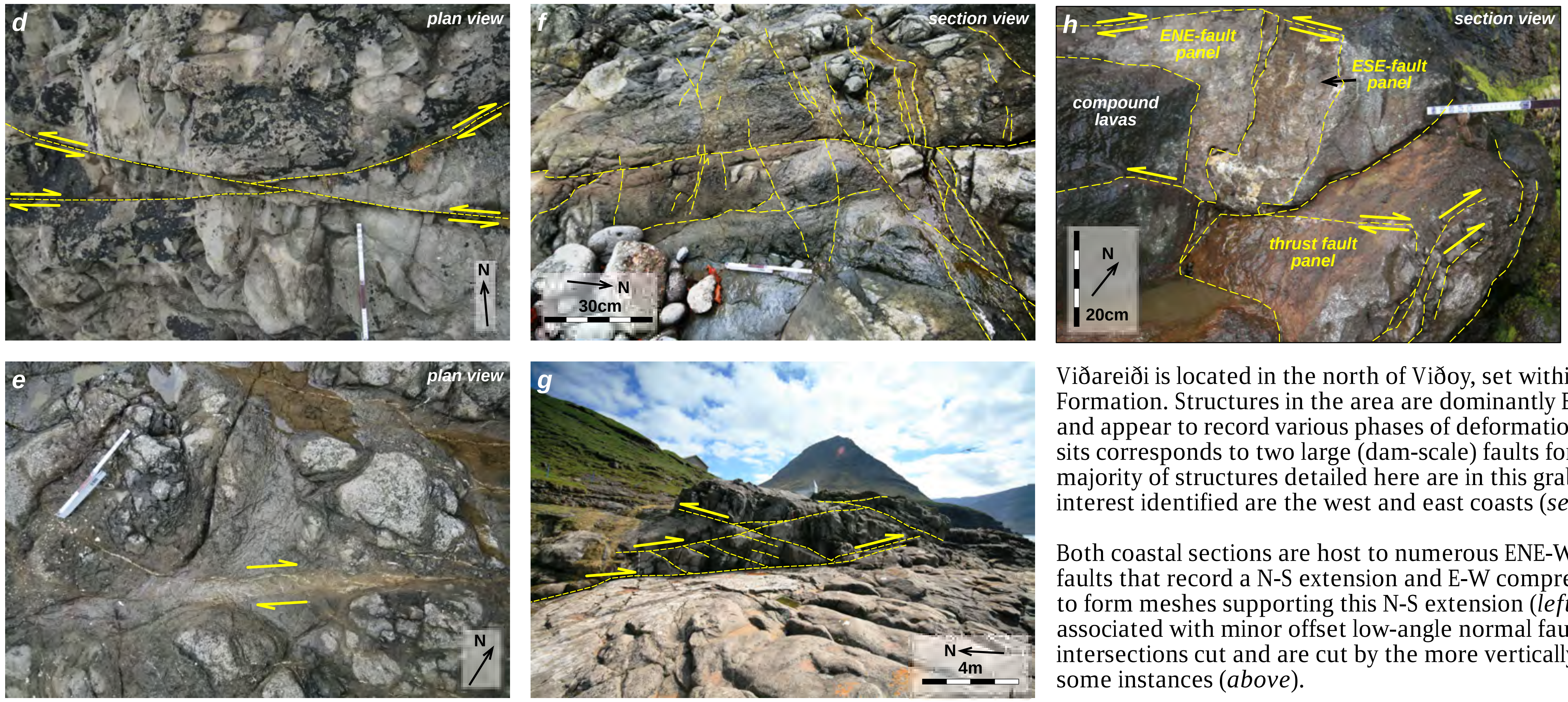

Viðareiði is located in the north of Viðoy, set within the upper third of the Malinstindur Formation. Structures in the area are dominantly E-W to NE-SW trending strike-slip faults and appear to record various phases of deformation. The low lying area in which Viðareiði sits corresponds to two large (dam-scale) faults forming an E-W trending graben. The majority of structures detailed here are in this graben, and the two particular areas of interest identified are the west and east coasts (*see maps above*).

Both coastal sections are host to numerous ENE-WSW to ESE-WNW trending strike slip faults that record a N-S extension and E-W compression. Where observed, vein sets link to form meshes supporting this N-S extension (*left*). The strike-slip faults are closely associated with minor offset low-angle normal faults and thrust faults, which in at intersections cut and are cut by the more vertically oriented faults, as well as linking in some instances (*above*).

Viðareiði, N. Viðoy: Event 2c

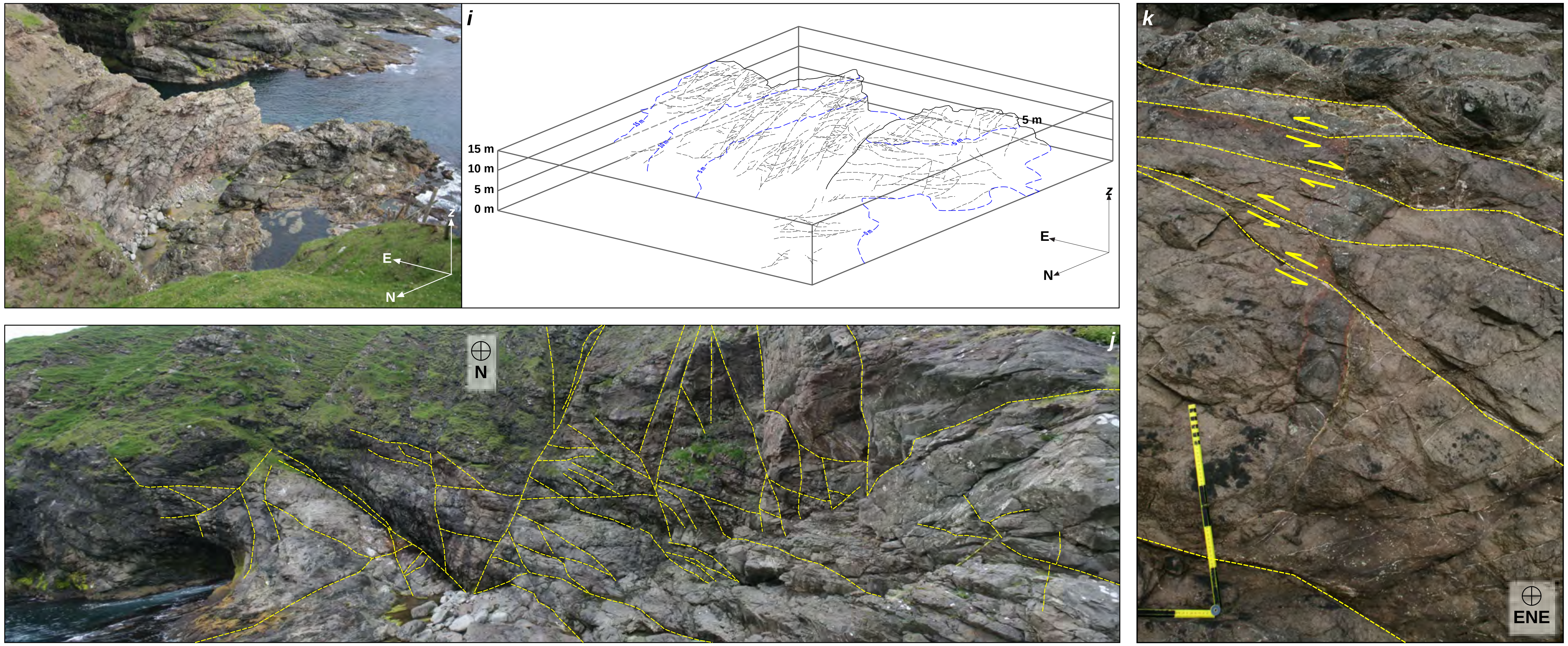

E-W trending structures are cut by more NE-SW to NNE-SSW trending faults (above right). These structures appear to dominate in an area on the west coast, to the north of the pier section (above left, see map). Faults in this orientation display only minor offsets, in the order of centimetres generally, however, strain is distributed across a zone in excess of 100m, and therefore may record a significant phase of deformation. Commonly offset sense is dextral, however in some instances, conjugate pairs are observed (above right).

Viðareiði, N. Viðoy: Event 3

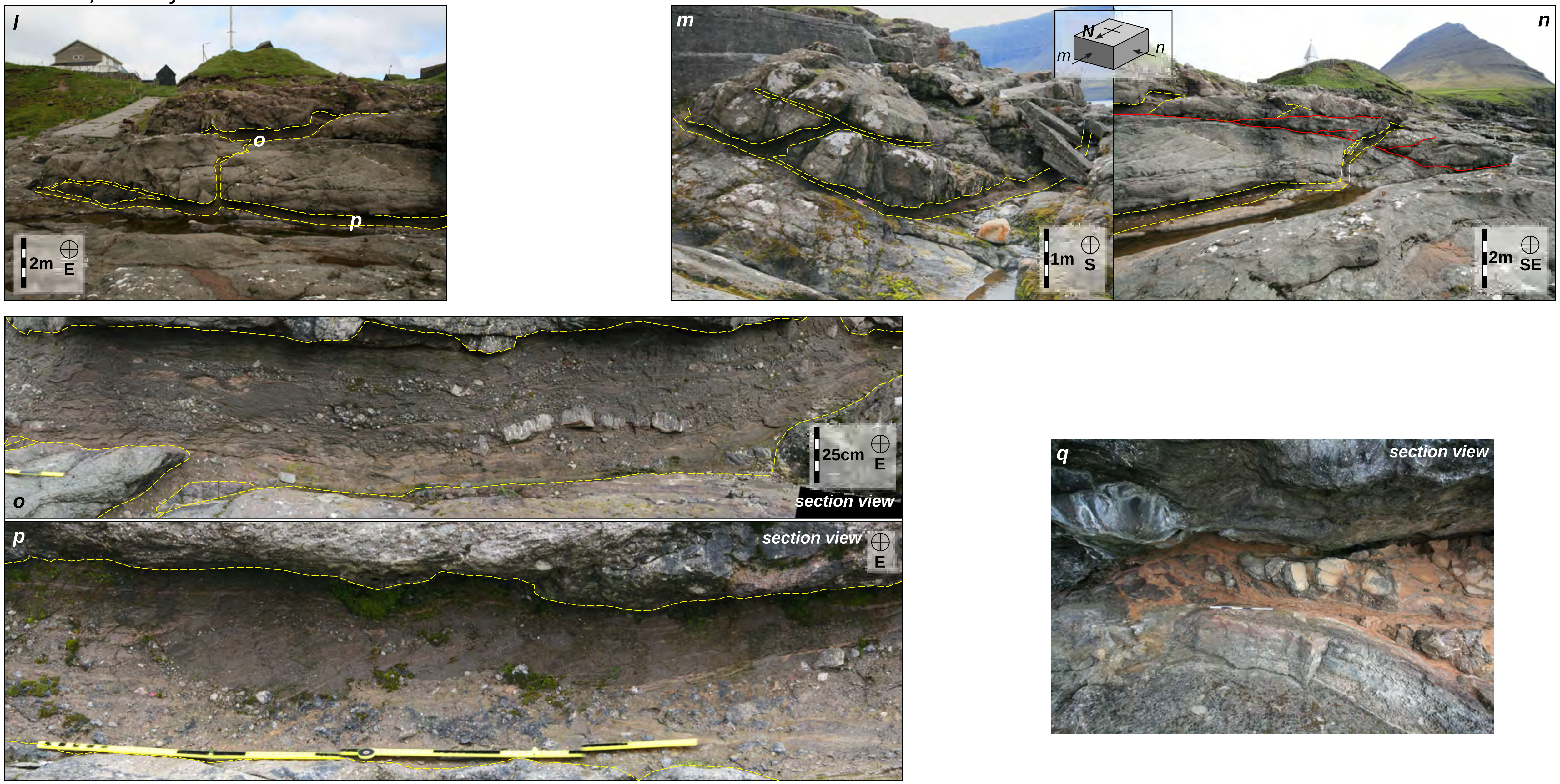

The pier section at Viðareiði is host to an overlapping succession of compound lavas, and lava tubes of the Malinstindur Formation, separated by numerous irregular saucer-shaped clastic horizons 0.3-0.6m thick. The lava units typically preserve a well developed lower crust, core, and upper crust. The lower crust is characterised by pipe amygdales that start a few centimetres from the base of the unit and are often curved in the palaeoflow direction. The core is generally a massive zone with more globular-shaped amygdales, and irregular joints ranging in orientation, from sub-horizontal to sub-vertical. In the upper crust, amygdales are spherical to globular, and the groundmass often exhibits a progressive reddening towards the top. Both the lower and upper crusts commonly exhibit classic rope-structures on the bounding surfaces that are characteristic of pahoehoe-type lavas.

The clastic horizons are typically sub-horizontal, but in some instances more steeply inclined (45-75°) ramp sections are observed. Mineralised Event 2 strike-slip faults are developed within the basalt units and are either cross-cut by, or sometimes filled with clastic material. The ramp sections are also discordant, cross-cutting solid-state lava unit features.. Ramps of this nature occur in three-dimensions, and overall give the clastic horizons a saucer-shaped geometry, akin to that of saucer-shaped intrusions. However, the sedimentary units preserve clear sedimentary structures on mm- to cm-scales, including planar and cross-laminations, bar structures and scour structures. These features are completely undeformed and show that the clastics were not emplaced by forceful injection, but rather were laid down as fluvial- to debris-flow-type deposits. Planar laminations at the top of the horizons appear to 'drape' the topography of the lava unit above, and are equivalent to gravitational settling laminae, implying that there was free space between the lava flows that became filled through time, followed by settling of the units above 'indenting' the sediment fills. In order to gravitationally deposit those materials, we infer that the free space must therefore have been larger than the thickness of the exposed remnants. Further evidence for a filling through time is provided by the clast-provenance. In some instances, fragments of the lava unit above have clearly fallen down into and become buried by the clastics below; the fragile lithofacies above such fragments are undisturbed and must therefore have been deposited afterwards. Collectively, the cross-cutting relationships with the lava flows and features observed within the clastic horizons indicate that there was an open cave network in the subsurface, which post-dates all other faulting in the area.

References

Acocella, V., Faccenna, C., Funiciello, R., Rossetti, F., 1999. Sand-box modelling of basement-controlled transfer zones in extensional domains. *Terra Nova,* **11***,* 149-156

Acocella, V., Korme, T., Salvini, F. 2003. Formation of normal faults along the axial zone of the Ethiopian Riift. *J. Struct. Geol.*, **25**, 503-513

Allen, P.A., Allen, J.R. 2005. *Basin Analysis: Principles and Applications, 2nd Edition*. Blackwell Publishing Ltd.

Antonellini, M., Aydin, A. 1994. Effect of faulting on fluid flow in porous sandstones: Petrophysical properties. *AAPG Bulletin*, **78**, 355-377

Anderson, E.M. 1936. The dynamics of the formation of cone-sheets, ring-dykes and cauldron-subsidences. *Proc. R. Soc. Edinburgh*, **56**, 128-157

Anderson, E.M. 1942. *The dynamics of faulting and dyke formation with application to Britain*. Oliver Boyd, Edinburgh.

Anderson, E.M. 1951. *The Dynamics of Faulting, 2nd edition*. Oliver and Boyd, Edinburgh.

Anderson, M.S., Boldreel, L.O. 1995. Tertiary compression structures in Faeroe-Rockall area. Geological Society, London, Special Publications, **90**, 215-216

Andersen, M.S., Sørensen, A.B., Boldreel, L.O., Nielsen, T. 2002. Cenozoic evolution of the Faroe Platform, comparing denudation and deposition. *In:* Doré, A.G., Cartwright, J.A., Stoker, M.S., Turner, J.P. & White, N. (eds) *Exhumation of the North Atlantic Margin: Timing,* *Mechanisms and Implications for Petroleum Exploration.* Geological Society, London, Special Publications, **196**, 291–311.

Angelier, J. 1984. Tectonic stress analysis of fault slip data sets. *J. Geophys. Res.*, **89**, 5835-5848

Angelier, J. 1990. Inversion of field data in fault tectonics to obtain the regional stress - III. A new rapid direct inversion method by analytical means. *Geophysical Journal International*, **103**, 363-376

Atkinson, B.K. 1987. Introduction to fracture mechanics and its geophysical applications. *In*: Atkinson, B.K. (*ed.*), Fracture Mechanics of Rock. *Academic Press, London*, 1-26

Aydin, A., Johnson, A.M. 1978. Development of faults as zones of deformation bands and as slip surfaces in sandstone. *Pure and Applied Geophysics*, **116**, 931-942

Baas, J.H. 2000. EZ-ROSE: a computer program for equal-area circular histograms and statistical analysis of two-dimensional vectorial data. *Computers and Geosciences*, **26**, 153-166

Badley, M.E., Price, J.D., Rambech-Dahl, C., Agdestein, T. 1988. The structural evolution of the northern Viking Graben and its bearing upon extensional modes of basin formation. *Journal of the Geological Society, London*, **145**, 455-472

Bai, T., Maerten, L., Gross, M.R., Aydin, A. 2002. Orthogonal cross joints: do they imply a regional stress rotation? *Journal of Structural Geology*, **24**, 77-88

Bartholomew, I.D., Peters, J.M., Powell, C.M., 1993. Regional structural evolution of the North Sea: oblique slip and the reactivation of basement lineaments. *In*: Parker, J. R. (ed.) *Petroleum Geology of Northwest Europe: Proceedings of the 4th Conference*. Geological Society, London, 1109-1122

Beacom, L.E., Anderson, T.B., Holdsworth, R.E. 1999. Using basement-hosted clastic dykes as syn-rifting palaeostress indicators: an example from the basal Stoer Group, morthwest Scotland. *Geol. Mag.*, **136**, 201-310

Berggren, W.A., Kent, D.V., Swisher, C.C., III, Aubry, M.-P. 1995. A revised Cenozoic geochronology and chronostratigraphy. *In*: Berggren, W. A. et al., (eds.) *Geochronology time scales and global stratigraphic correlations*. SEPM, Special Publications, **54**, 129-212

Billi, A., Salvini, F., Storti, F. 2003. The damage zone-fault core transition in carbonate rocks: implications for fault growth, structure and permeability. *Journal of Structural Geology*, **25**, 1779-1794

Blenkinsop, T.G. 2008. Relationships between faults, extension fractures and veins, and stress. Journal of Structural Geology, **30**, 622-632

Boldreel, L.O., Andersen, M.S. 1993. Late Paleocene to Miocene compression in the Faeroe–Rockall area. *In:* Parker, J.R. (ed.) *Petroleum Geology of Northwest Europe: Proceedings of the 4th Conference.* Geological Society, London, 1025–1034.

Boldreel, L.O., Anderson, M.S. 1998. Tertiary compressional structures on the Faeroe–Rockall Plateau in relation to northeast Atlantic ridge-push and Alpine foreland stresses. Tectonophysics, **300**, 13–28.

Bott, M.H.P., Gunnarsson, K. 1980. Crustal structure of the Iceland-Faeroe Ridge. *J. Geophys.*, **47**, 221-227

Bott, M. H. P. 1983. The crust beneath the Iceland-Faroe Ridge. *In:* Bott, M.H.P., Saxov, S., Talwani, M., Thiede, J. (eds) *Structure and development of the Greenland-Scotland Ridge: New Methods and Concepts.* Plenum Press, New York, 63-75

Brekke, H. 2000. The tectonic evolution of the Norwegian Sea continental margin, with emphasis on the Vøring and Møre basins. In: Nøttvedt, A. (ed.) *Dynamics of the Norwegian Margin*. Geological Society, London, Special Publications, **167**, 327-378.

Brock, W.G., Engelder, T. 1977. Deformation associated with the movement of the Muddy Mountain overthrust in the Buffington window, southeastern Nevada. *GSA Bulletin*, **88**, 1667-1677

Bücker, C.J., Delius, H., Wohlenberg, J., and ODP Leg 163 Shipboard Scientific Party. 1998. Comparison of core and downhole measurements of ODP Legs in basaltic volcanics in the NE Atlantic. *Geol. Soc. Special Publication.*

Burkhard, M. 1993. Calcite twins, their geometry, appearance and significance as stress-strain markers and indicators of tectonic regime: a review. *Journal of Structural Geology*, **15**, 351-368

Byerlee, J. 1978. Friction of rocks. *Pure and Applied Geophysics*, **116**, 615-626

Caine, J.S., Evans, J.P., Forster, C.B. 1996. Fault zone architecture and permeability structure. *Geology*, **24**, 1025-1028

Calassou S, Larroque C, and Malavieille , (1993). Transfer zones of deformation in thrust wedges: An experimental study. *Tectonophysics 221,* 325-344

Carr, A.D., Scotchman, I.C. 2003. Thermal modelling in the southern Faroe-Shetland Basin. *Petroleum Geoscience*, **9**, 333-345

Chester, F.M., Logan, J.M. 1987. Composite planar fabric of gouge from the Punchbowl Fault, California. *Journal of Structural Geology*, **9**, 621-634

Chester, F.M., Friedman, M., Logan, J.M. 1985, Foliated cataclasites. *Tectonophysics*, **111**, 139-146

Childs, C., Nicol., A, Walsh, J.J., Watterson, J. 1996. Growth of vertically segmented normal faults. *Journal of Structural Geology*, **18**, 1389-1397

Childs, C., Nicol, A., Walsh, J.J., Watterson, J. 2003. The growth and propagation of synsedimentary faults. *Journal of Structural Geology*, **25**, 633-648

Cloetingh, S., Beekman, F., Ziegler, P.A., Van Wees, J-D., Sokouts, D. 2008. Post-rift compressional reactivation potential of passive margins and extensional basins. *In*: Johnson, H., Doré, A. G., Gatliff, R.W., Holdsworth, R., Lundin, E.R. & Ritchie, J.D. (eds) The nature and origin of compression in passive margins. *Geological Society, London, Special Publications*, **306**, 27-70

Cloos, H. 1955. Experimental analysis of fracture patterns. *Geol. Soc. Am. Bull.*, **66**, 241-256

Coffin, M.F., Rabinowitz, P.D. 1987. Reconstruction of Madagascar and Africa: evidence from the Davie Fracture Zone and Western Somali Basin. *Journal of Geophysical Research*, **92**, 9385-9406

Coffin, M.F., Rabinowitz, P.D. 1988. Evolution of the conjugate East African-Madagascan margins and Western Somali Basin. *Geol. Soc. Am. Spec. Pap*., **226**, 78

Colletini, C., De Paola, N., Goulty, N.R. 2006. Switches in the minimum compressive stress direction induced by the overpressure beneath a low-permeability fault zone. *Terra Nova*, **18**, 224-231

Cosgrove, J.W., Ameen, M.S. 2000. A comparison of the geometry, spatial organization and fracture patterns associated with forced folds and buckle folds. *In*: Cosgrove, J.W., Ameen, M.S. (eds) Forced Folds and Fractures. *Geological Society, London, Special Publications*, **169**, 7-21

Cowan, D.S. 1999. Do faults preserve a record of seismic slip? A field geologist's opinion. *Journal of Structural Geology*, **21**, 995–1001.

Coward, M.P. 1990. The Precambrian, Caledonian and Variscan framework to NW Europe. *In*: Hardman, R.F.P., Brooks, J. (eds) *Tectonic Events Responsible for Britain's Oil and Gas Reserves*. Geological Society, London, Special Publications, **55**, 1–34.

Cox, S.J.D., Sholz, C.H. 1988. On the formation and growth of faults: an experimental study. *Journal of Structural Geology*, **10**, 413-430

Dahlstrom, C.D.A. 1970. Structural geology in the eastern margin of the Canadian Rocky Mountains. *Bulletin of Canadian Petroleum Geology,* **18***,* 332-406

De Paola, N., Holdsworth, R.E., McCaffrey, K.J.W., Barchi, M.R. 2005. Partitioned transtension: An alternative to basin inversion models. *J. Struct. Geol.*, **27**, 607-625.

Delaney, P.T., Pollard, D.D., Zioney, J.I., McKee, E.H. 1986. Field relations between dikes and joints: Emplacement processes and palaeostress analysis. *Journal of Geophysical Research*, **91**, 4920-4938

Dewey, J.F. 2002. Transtension in arcs and orogens. *International Geology Review*, **44**, 402-439.

Dickson, J.A.D. 1993. Crystal growth diagrams as an aid to interpreting fabrics of calcite aggregates. *Journal of Sedimentary Petrology*, **63**, 1-17.

Doré, A.G., Lundin, E.R. 1996. Cenozoic compressional structures on the NE Atlantic margin: Nature, origin and potential significance for hydrocarbon exploration. *Petroleum Geoscience,* **2**, 299–311.

Doré, A.G., Lundin, E.R., Fichler, C., Olesen, O. 1997. Patterns of basement structure and reactivation along the NE Atlantic margin. Journal of the Geological Society, 154, 85-92

Doré, A.G., Lundin, E.R., Jensen, L.N., Birkeland, Ø., Eliassen, P.E., Fichler, C. 1999. Principal tectonic events in the evolution of the northwest European Atlantic margin. *In*: Fleet A.J. & Boldy, S.A.R. (eds.) Petroleum Geology of Northwest Europe: Proceedings of the Fifth Conference. *Geol. Soc. London, London*. 41-61

Doré, A.G., Lundin, E.R., Kusznir, N.J., Pascal, C. 2008. Potential mechanisms for the genesis of Cenozoic domal structures on the NE Atlantic margin: pros, cons and some new ideas. *In*: Johnson, H., Doré, A. G., Gatliff, R.W., Holdsworth, R., Lundin, E.R. & Ritchie, J.D. (eds) The nature and origin of compression in passive margins. *Geological Society, London, Special Publications*, **306**, 1-26

Eldholm, O., Grue, K. 1994. North Atlantic volcanic margins: Dimensions and production rates. *Journal of Geophysical Research*, **99**, 2955-2968

Ellis, D., Bell, B.R., Jolley, D.W., O'Callaghan, M. 2002. The stratigraphy, environment of eruption and age of the Faroes Lava Group, NE Atlantic Ocean. *Geological Society of London, Special Publication*, **197**, 253-270.

Ellis, D., Passey, S.R., Jolley, D.W., Bell, B.R. 2009. Transfer zones: The application of new geological information from the Faroe Islands applied to the offshore exploration of intra basalt and sub-basalt strata. *In*: Faroe Islands Exploration Conference: Proceedings of the 2nd Conference. Annales Societatis Scientiarum Færoensis

Evans, J.P. 1988. Deformation mechanisms in granitic rocks at shallow crustal levels. *Journal of Structural Geology*, **10**, 437-443

Færseth, R.B., Gabrielsen, R.H., Hurich, C.A. 1995. Influence of basement in structuring of the North Sea Basin, offshore southwest Norway. *Norsk Geologisk Tidsskerift*, **75**, 105-119

Faulds, J.E., Varga, R.J. 1998. The role of accommodation zones and transfer zones in the regional segmentation of extended terranes. I*n:* Faulds, J.E., Stewart, J.H. (*eds*.). Accommodation zones and Transfer zones: The regional segmentation of the Basin and Range Province: Boulder, Colorado, *Geol. Soc. America Spec. Paper,* **323***,* 1-45

Ferrill, D.A., Morris, P.A., Evans, M.A., Burkhard, M., Groshong Jr., R.H., Onasch, C.M. 2004. Calcite twin morphology: a low-temperature deformation geothermometer. *Journal of Structural Geology*, **26**, 1521-1529

Fry, N. 1999. Striated faults: visual appreciation of their constraint on possible paleostress tensors. *J. Struct. Geo*., **21**, 7-21.

Fry, N. 2001. Stress space: straited faults, deformation twins, and their constraints on paleostress. *J. Struct. Geo.*, **23**, 1-9.

Gaina, C., Gernigon, L., Ball, P. 2009. Palaeocene-Recent plate boundaries in the NE Atlantic and the formation of the Jan Mayen microcontinent. *Journal of the Geological Society, London,* **166**, 601-616

Geoffroy, L., Bergerat, F., Angelier, J. 1994. Tectonic evolution of the Greenland-Scotland ridge during the Palaogene: new constraints. *Geology*, **22**, 653-656

Gernigon, L., Olesen, O., Gaina, C. 2009. The Norway Basin revisited: New aeromagnetic survey and implications for early spreading development in the Norwegian-Greenland Sea. *Faroe Islands Exploration Conference 2009*.

Gibbs, A.D. 1984. Structural evolution of extensional basin margins. *J. Geol. Soc. London,* **141***,* 609-620

Gillespie, P.A., Walsh, J.J., Watterson, J., Bonson, C. G., Manzocchi, T. 2001. Scaling relationships of joint and vein arrays from The Burren, Co. Clare, Ireland. *Journal of Structural Geology* **23**, 183-201.

Glassley, W.E. 2006. Mineralogical and thermodynamic constraints on Palaeogene palaeotemperature conditions during low-grade metamorphism of basaltic lavas recovered from the Lopra-1/1A deep hole, Faroe Islands. *Geological Survey of Denmark and Greenland Bulletin*, **9**, 109-118

Goździk, J., van Loon, A.J. 2007. The origin of a giant downward directed clastic dyke in a kame (Bełchatów mine, central Poland). *Sedimentary Geology*, **193**, 71-79

Grant, J.V., Kattenhorn, S.A. 2004. Evolution of vertical faults at an extensional plate boundary, southwest Iceland. *Journal of Structural Geology,* **26**, 537–557

Groshong Jr, R.H., Teufel, L.W., Gasteiger, C. 1984. Precision and accuracy of the calcite stain-guage technique. *Geol. Soc. Am. Bulletin*, **95**, 357-363

Gudmundsson, A. 1992. Formation and growth of normal faults at the divergent plate boundary in Iceland, *Terra Nova*, **4**, 464-471

Gudmundsson, A. 1995. Infrastructure and mechanics of volcanic systems in Iceland. *Journal of Volcanology and Geothermal Research*, **64**, 1-22

Gudmundsson, A. 2000. Fracture dimensions, displacements and fluid transport. Journal of Structural Geology, **22**, 1221–1231

Gudmundsson, A., Brenner, S.L. 2004. Local stresses, dyke arrest and surface deformation in volcanic edifices and rift zones. *Annals of Geophys.*, **47**, 1433-1454

Hald, N., Waagstein, R. 1984. Lithology and chemistry of a 2-km sequence of lower Tertiary tholeiitic lavas drilled on Suðuroy, Faeroe Islands (Lopra-1). *In*: Berthelsen, O., Noe-Nygaard, A., Rasmussen, J. (eds). The deep drilling project 1980–1981 in the Faeroe Islands. Ann Soc Sci Fær Suppl, IX: 15-38

Hancock, P.L. 1985. Brittle microtectonics: principles and practice. *Journal of Structural Geology*, **7**, 437-457

Hansen, J., Jerram, D.A., McCaffrey, K.J.W., Passey, S.R. 2009. The onset of the Naorth Atlantic Igneous Province in a rifting perspective. *Geol. Mag.*, **146**, 309-325

Holdsworth, R.E., Butler, C.A. Roberts A.M. 1997. The recognition of reactivation during continental deformation, J. Geol. Soc. London, 154, 73-78

Holland, M., Urai, J.L., Martel S. 2006 The internal structure of fault zones in basaltic sequences. *Earth and Planetary Science Letters*, **248**, 301-315

Hubbert, M.K. Rubey, W.W. 1959. Role of fluid pressure in mechanics of overthrust faulting. *Geol. Soc. Am. Bull.*, **70**, 115-166

Jamison, W.R., Spang, J.H. 1976. Use of calcite twin lamellae to infer differential stress. *Geol. Soc. Am.*, **87**, 868-872

Jerram, D.A. 2002. Volcanology and facies architecture of flood basalts. In: Menzies, M.A., Klemperer, S.L., Ebinger, C.J., Baker, J. (eds.). Volcanic Rifted Margins: Boulder Colorado. GSA Special Paper, 362, 119-132

Jerram, D.A., Single, R.T., Hobbs, R.W., Nelson, C.E. 2009. Understanding the offshore flood basalt sequence using onshore volcanic facies analogues: an example from the Faroe-Shetland basin. *Geol. Mag.*, **00**, 1-15

Johnson, H., Ritchie, J.D., Hitchen, K., McInroy, D.B., Kimbell, G.S. 2005. Aspects of the Cenozoic deformational history of the Northeast Faroe–Shetland Basin, Wyville-Thomson Ridge and Hatton Bank areas. *In*: Doré, A.G., Vining, B.A. (eds) *Petroleum Geology: North-West Europe and Global Perspectives. Proceedings of the 6th Petroleum Geology Conference*. Geological Society, London, 993–1008.

Jolley, D.W., Morton, A. 2007. Understanding basin sedimentary provenance: evidence from allied phytogeographic and heavy mineral analysis of the Paleocene of the NE Atlantic. *Journal of the Geological Society, London*, **164**, 553-563.

Jolly, R.J.H., Cosgrove, J.W., Dewhurst, D.N. 1998. Thickness and spatial distributions of clastic dykes, northwest Sacramento valley, California. *Journal of Structural Geology,* **20**, 1163-1672

Jones, S.M., White, N. 2003. *Shape and size of the starting Iceland plume swell. Earth and Planetary Science Letters*, **216**, 271-282

Jonk R., Duranti, D, Parnell, J., Hurst, A., Fallick, A.E. 2004. The structural and diagenetic evolution of injected sandstones: examples from the Kimmeridgian of NE Scotland. *Journal of the Geological Society, London*, **160**, 881-894

Jorgensen, O. 1984. Zeolite zones in the basaltic lavas of the Faroe Islands – a quantitative description of the secondary minerals in the deep wells of Vestmanna-1 and Lopra-1. *In*: Berthelsen, O., Noe-Nygaard, A., Rasmussen, J. (eds). *The deep drilling project 1980-1981 in the Faroe Islands.* Føroya Froðskaparfelag, Torshavn, 71-91

Kavanagh, J.L., Menand, T., Sparks, R.S.J. 2006. An experimental investigation of sill formation and propagation in layered elastic media. *Earth and Planetary Science Letter*, **245**, 799-813.

Kim, Y.-S., Peacock, D.C.P., Sanderson, D.J. 2004. Fault damage zones. *Journal of Structural Geology*, **26**, 503-517

Kimbell, G.S., Ritchie, J.D., Johnson, H., Gatliff, R.W. 2005. Controls on the structure and evolution of the NE Atlantic margin revealed by regional potential field imaging and 3D modelling. *In*: Doré, A.G., Vining, B.A. (eds) *Petroleum Geology: North-West Europe and Global Perspectives*, Proceedings of the 6th Petroleum Geology Conference. Geological Society, London, 933–945.

Kokelaar, B.P. 1982. Fluidization of wet sediments during the emplacement and cooling of various igneous bodies. *Journal of the Geological Society*, **139**, 21-33

Kusznir, N.J., Park, R.G. 1987. The extensional strength of the continental lithosphere: its dependence on geothermal gradient, and crustal composition and thickness. *In*: Coward, M.P., Dewey, J.F., Hancock, P.L. (eds.) *Continental Extensional Tectonics*, Geol. Soc. Spec. Pub., **28**, 35-52

Lacombe, O., Laurent, P. 1996. Determination of deviatoric stress tensors based on inversion of calcite twin data from experimentally deformaed monophase samples. Preliminary results. *Tectonophyics*, **355**, 189-202

Larsen, H.C., Saunders, A.D. 1998. Tectonism and volcanism at the southeast Greenland rifted margin: a record of plume impact and later continental rupture. *In*: Saunders, A.D., Larsen, H.C., Clift, P.D., Wise, S.W. (*eds*.). Proceedings of the Ocean Drilling Program Scientific Results. **152**, 503–533.

Larsen, M., Whitham, A.G. 2005. Evidence for a major sediment input point into the Faroe-Shetland Basin from the Kangerlussuaq region of southern East Greenland. *In*: Doré, A.G., Vining, B.A. (eds) *Petroleum Geology: North-West Europe and Global Perspectives - Proceedings of the 6th Petroleum Geology Conference*, 912-922.

Laurent, P., Tourneret, C., Laborde, O. 1990. Determining deviatoric stress tensors from calcite twins: applications to monophased synthetic and natural poycrystals. *Tectonophysics*, **9**, 379-389

Laurent, P., Kern, H., Lacombe, O. 2000. Determination of deviatoric stress tensors based on inversion of calcite twin data from experimentally deformaed monophase samples. Part II. Axial and triaxial stress experiments. *Tectonophyics*, **327**, 131-148

Larsen, L.M., Waagstein, R., Pedersen, A.K., Storey, M. 1999. Trans-Atlantic correlation of the Palaeogene volcanic successions in the Faeroe Islands and East Greenland. *Journal of the Geological Society, London*, **156**, 1081-1095

Le Heron, D.P., Etienne, J.L. 2005. A complex sub-glacial clastic dyke swarm, Sólheimajökull, southern Iceland. *Sedimentary Geology*, **181**, 25-37

Lenoir, X., Feraud, G., Geoffroy, L. 2003. High-rate flexure of the East Greenland volcanic margin: constraints from 40Ar/39Ar dating of basaltic dykes. *Earth and Planetary Science Letters*, **6773**, 1-14

Loucks, R.G. 1999. Paleocave carbonate reservoirs: origins, burial-depth modifications, spatial complexity, and reservoir implications. *American Association of Petroleum Geologists Bulletin,* **83**, 1795-1834.

Lund, J. 1983. Biostratigraphy of interbasaltic coals from the Faeroe Islands. In: Bott, M.H.P., Saxov, S., Talwani, M. & Theide, J. (eds). *Structure and Development of the Greenland-Scotland Ridge, New Methods and Concepts.* Plenum Press, New York: 417-423

Lund, J. 1989. A late Palaeocene non-marine microflora from the interbasaltic coals of the Faeroe Islands, North Atlantic. *Bulletin of the Geological Society of Denmark*, **37**, 191-203

Lundin, E.R. 2002. Atlantic-Arctic seafloor spreading history. *In*: Eide, E.A. (coord.), *BATLAS-mid Norway plate reconstructions atlas with global and Atlantic perspectives*. Nor. Geol. Unders., 40–47.

Lundin, E.R., Doré, A.G. 1997. A tectonic model for the Norwegian passive margin with implications for the NE Atlantic: Early Cretaceous to break-up. *Journal of the Geological Society, London*, **154**, 545-550

Maclennan, J., Jones, S.M. 2006. Regional uplift, gas hydrate dissociation and the origins of the Palaeocene-Eocene Thermal Maximum. *EPSL*, **245**, 65-80

Martel, S.J., Langley, J.S. 2006. Propagation of normal faults to the surface in basalt, Koae fault system, Hawaii. *Journal of Structural Geology*, **28**, 2123-2143

McClay, K.R. 1987. *The Mapping of Geological Structures*. Geol. Soc. London Handbook Series, Open University Press, Milton Keynes.

McClay, K.R., White, M.J. 1995, analogue modelling of orthogonal oblique rifting. *Marine and Petroleum Geology*, **12**, 137-151

Menand, T. 2008. The mechanics and dynamics of sills in layered elastic rocks and their implications for the growth of laccoliths and other igneous complexes. *Earth and Planetary Science Letters*, **267**, 93-99.

Menand, T., Tait, 2002. The propagation of a buoyant liquid-filled fissure from a source under constant pressure: an experimental approach. *J. Geophys. Res.*, **107**, B11, doi: 10.1029/2001JB000589

Michael, A.J. 1984. Determination of stress from slip data: faults and folds. *J. Geophys. Res.*, **89**, 11517-11526

Michael, A.J. 1987a. Use of focal mechanisms to determine stress: a control study. *J. Geophys. Res.*, **92**, 357-368

Michael, A.J. 1987b. Stress rotation during the Coalinga aftershock sequence. *J. Geophys. Res.*, **92**, 7963-7979

Michael, A.J. 1991. Spatial variations in stress within the 1987 Whittier Narrows, California, aftershock sequence: new techniques and results *J. Geophys. Res.*, **96**, 6303-6319.

Morley, C.K., Nelson, R.A., Patton, T.L., Munn, S.G. 1990. Transfer zones in the East African Rift system and their relevance to hydrocarbon exploration in rifts. *American Assoc. Petroleum Geologists Bull.,* **74***,* 1234-1253

Mosar, J., Torsvik, T.H., the BAT team. 2002. Opening of the Norwegian and Greenland Seas: Plate tectonics in Mid Norway since the Late Permian. *In:* Eide, E.A. (*coord.*). BATLAS – Mid Norway plate reconstructions atlas with global and Atlantic perspectives. Geological Survey of Norway, 48-59.

Moy, D.J., Imber, J. 2009. A critical analysis of the structure and tectonic significance of rift-oblique1 lineaments (‘transfer zones’) in the Mesozoic–Cenozoic succession of the2 Faeroe–Shetland Basin, NE Atlantic margin. *Journal of the Geological Society, London*, **166**, 1-14

Naylor, P.H., Bell, B.R., Jolley, D.W., Durnall, P., Fredstead, R. 1999. Palaeogene magmatism in the Faeroe-Shetland Basin : influences on uplift history and sedimentation. *In*: Fleet and Boldy (eds), Petroleum Geology of the Northwest Europe, Proceedings of the 5th Conference, Geological Society of London, 545-558.

Nelson, C.E., Jerram, D.A. Single, R.T., Hobbs, R.W. 2009. Understanding the facies architecture of flood basalts and volcanic rifted margins and its effect on geophysical properties. *Faroe Islands Exploration Conference: Procceedings of the 2nd Conference. Annales Societatis Scientiarum Faeroenis, Supplementum,* **50**, 84-103

Neuhoff, P.S., Watt, W.S., Bird, D.K., Pedersen, A.K. 1997. Timing and structural relations of regional zeolite zones in basalts of the East Greenland continental margin. *Geology*, **25**, 803-806

Nisbet, E.G., Jones, S.M., Maclennan, J., Eagles, G., Moed, J., Warwick, N., Bekki, S., Braesicke, P., Pyle, J.A., Fowler, C.M.R. 2009. Kick0starting ancient warming. *Nature Geoscience*, **2**, 156-159

O'Keefe, F.X., Stearns, D.W. 1982. Characteristics of displacement transfer zones associated with thrust faults. *In*: Powers, R.B. (*ed.*). Geologic studies of the Cordilleran thrust belt: Denver, Colorado, *Rocky Mountain Association of Geologists*, 219-233

Oliver, N.H.S., Bons, P.D. 2001. Mechanisms of fluid flow and fluid-rock interaction in fossil metamorphic hydrothermal systems inferred from vein-wallrock patterns, geometry and microstructure. *Geofluids*, **1**, 137-162.

Pascal, C. 2006. On the role of heat flow, lithosphere thickness and lithosphere density on gravitational potential stresses. Tectonophysics, 425, 83-99.

Pascal, C., Cloetingh, S.A.P.L. 2008. Gravitational potential stresses and stress field of passive continental margins: Insights from the south-Norway shelf. *Earth and Planetary Science Letters,* doi:10.1016/j.epsl.2008.11.014

Passchier, C.W., Trouw, R.A.J. 2005. *Micro-tectonics. Second Edition*. Springer-Verlag, Berlin.

Passey, S.R. 2009. Recognition of a faulted basalt lava flow sequence through the correlation of stratigraphic marker units, Skopunarfjørður, Faroe Islands. In: Faroe Islands Exploration Conference: Proceedings of the 2nd Conference. Annales Societatis Scientiarum Færoensis

Passey, S.R., Bell, B.R. 2007. Morphologies and emplacement mechanisms of the lava flows of the Faroe Islands Basalt Group, Faroe Islands, NE Atlantic Ocean. Bulletin of Volcanology.

Passey S.R., Jolley, D.W., Bell B.R. (2006). Lithostratigraphic framework for the Faroe Islands Basalt Group, NE Atlantic. *A George P.L. Walker symposium on advances in volcanology, 12–17 June. Reykholt, Iceland*

Peacock, D.C.P. 2002. Propagation, interaction and linkage of normal fault systems. *Earth Science Reviews*, **58**, 121-142

Peacock, D.C.P., Knipe, R.J., Sanderson, D.J., 2000. Glossary of normal faults. *Journal of Structural Geology,* **22**, 291–305

Petit, J.P. 1987. Criteria for the sense of movement on fault surfaces in brittle rocks. *Journal of Structural Geology*, **9**, 597-608

Petit, J-P., Wibberley, C.A.J., Ruiz, G. 1999. 'Crack-seal' slip: a new fault valve mechanism? *Journal of Structural Geology*, **21**, 1199-1207

Phillips, C.A., Alsop, G.I. 2000. Post-tectonic clastic dykes in the Dalradian of Scotland and Ireland: implications for delayed lithification and deformation of sediments. *Geological Journal,* **35**, 99-110

Pitman, W.C., Talwani, M. 1972. Seafloor spreading in the North Atlantic. *Geological Society of America Bulletin*, **83**, 619-646

Planke, S. 1994. Geophysical response of flood basalts from analysis of wire line logs: Ocean Drilling Program Site 642, Vøring volcanic margin. *Journal of Geophysical Research*, **99**, 9279-9296

Pollard, D.D. 1973. Derivation and evaluation of a mechanical model of sheet intrusions, *Tectonophysics*, **19**, 233-269.

Pollard, D.D., Johnson, A.M. 1973. Mechanics of growth of some laccolithic intrusions in the Henry Mountains, Utah, II. *Tectonophysics*, **18**, 311-354.

Pollard, D.D. Muller, O.H., Dockstader, D.R. 1975. The form and growth of fingered sheet intrusions. *Geol. Soc. Am. Bull.*, **86**, 351-363.

Potts, G.J., Reddy, S.M. 1999. Construction and systematic assessment of relative deformation histories. *Journal of Structural Geology*, **21**, 1245-1253

Price, N.J., Cosgrove, J.W. 1990. *Analysis of Geological Structures*. Cambridge University Press, Cambridge

Rabinowitz, P.D., Coffin, M.F., Falvey, D.A. 1983. The separation of Madagascar and Africa. *Science*, **220**, 67-69

Ramsay, J.G. 1980. The crack-seal mechanism of rock deformation. *Nature* **284**, 135-139.

Ramsay, J.G. Huber, M.I. 1983 The Techniques of Modern Structural Geology, Volume 1: Strain Analysis. Academic Press, London.

Ramsay, J.G., Huber, M.I. 1987. *The Techniques of Modern Structural Geology, Volume 2: Folds and Fractures.* Elsevier Ltd. London

Rasmussen, J. 1990. *The origin of the Faroe Islands, in text, pictures and on maps.* Geological Survey of Denmark

Rasmussen, J., Noe-Nygaard, A. 1969. *Beskrivelse til Geologisk Kort over Færøerne I Målestok 1:50 000.* G. Danmarks Geologiske Undersøgelse, København, 1/24

Rasmussen, J., Noe-Nygaard, A. 1970 (1969). *Geology of the Faeroe Islands (Pre-Quaternary)*. *Trans*. Henderson, G. Danmarks Geological survey of Denmark, Copenhagen 1/25.

Reches, Z. 1987. Determination of the tectonic stress tensor from slip along faults that obey the Coulomb yield condition. *Tectonics*, **6**, 849-861

Richter, D. 1966. On the New Red Sandstone Neptunian Dykes of the Tor Bay Area (Devonshire). *Proceedings of the Geological Association,* **77***,* 173-186

Rijsdijk, K.F., Owen, G., Warren, W.P., McCarroll, D., van der Meer, J.J.M. 1999. Clastic dykes in over-consolidated tills: evidence for sub-glacial hydrofracturing at Killiney Bay, eastern Ireland. *Sedimentary Geology*, **129**, 111-126

Ritchie, J.D., Johnson, H., Kimbell, G. S. 2003. The nature and age of Cenozoic contractional dating within the NE Faroe-Shetland Basin. *Marine Geology*, **20**, 399–409.

Ritchie, J.D., Johnson, H., Quinn, M.F., Gatliff, R.W. 2008. The effects of Cenozoic compression within the Faroe-Shetland Basin and adjacent areas. *In*: Johnson, H., Doré, A. G., Gatliff, R.W., Holdsworth, R., Lundin, E.R., Ritchie, J.D. (eds) The nature and origin of compression in passive margins. *Geological Society, London, Special Publications*, **306**, 137-152

Roberts, D.G., Thompson, M., Mitchener, B., Hossack, J., Carmichael, S.M.M., Bjørnseth, H.M. 1999. Palaeozoic to Tertiary rift and basin dynamics: mid-Norway to the Bay of Biscay—a new context for hydrocarbon prospectivity in the deep water frontier. *In:* Fleet, A.J., Boldy, S.A.R. *(eds) Petroleum Geology of Northwest Europe: Proceedings of the 5th Conference.* Geological Society*, London, 7–40.*

Roberts, G.P. 1994. Displacement localization and palaeo-seismicity of the Rencurel Thrust Zone, French Sub-Alpine Chains. *Journal of Structural Geology*, **16**, 633–646.

Rowe, K.J., Rutter, E.H. 1990. Palaeostress estimation using calcite twinning: experimental calibration and application to nature. *Journal of Structural Geology*, **12**, 1-18

Rubin, A.M. 1995. Propagation of magma-filled cracks. *Annu. Rev. Earth Planet. Sci.*, **23**, 287-236

Rumph, B., Reaves, C.M., Orange, V.G., Robinson, D.L. 1993. Structuring and transfer zones in the Faeroe basin in a regional tectonic context. *In* : Parker, J.R. (ed) Petroleum Geology of Northwest Europe : Proceedings of the 4th Conference. Geological Society, London, 999-1010.

Saunders, A. D., Fitton, J. G., Kerr, A. C., Norry, M. J., Kent, R. W. 1997. The North Atlantic Igneous Province. *In*: Mahoney, J. J. & Coffin, M. L. (eds). Large Igneous Provinces: Continental, Oceanic, and Planetary Flood Volcanism. American Geophysical Union. Geophysical Monographs **100**, 45-93

Saunders, A. D., Jones, S. M., Morgan, L. A., Pierce, K. L., Woddowon, M., Xu, Y. G. 2007. Regional uplift associated with continental large igneous provinces: The roles of mantle plumes and the lithosphere. *Chemical Geology*, **241**, 282-318

Schmid, S.M., Handy, M.R. 1991. Towards a genetic classification of fault rocks: Geological usage and tectonophysical implications. *In*: Müller, D.W.,McKenzie, J.A., Weissert, H. (*eds.*). Controversies in Modern Geology, *Academic Press, London*, 339-361

Secor, D.T. 1965. Role of fluid pressure in jointing. *Am. J. Sci.*, **263**, 633-646

Shipton, Z.K., Cowie, P.A., 2001. Damage zone and slip-surface evolution over mm to km scales in high-porosity Navajo sandstone, Utah. *Journal of Structural Geology,* **23**, 1825-1844.

Sibson, R.H. 1981. Fluid flow accompanying faulting: field evidence and models. *In*: Simpson, D. Richards, P.G. (*eds.*) Earthquake prediction: an International Review. *American Geophysical Union, Maurice Ewing Series*, **4**, 593-603.

Sibson, R.H. 1985. A note on fault reactivation. *Journal of Structural Geology*, **7**, 751-754

Sibson, R.H. 1986. Brecciation processes in fault zones: inferences from earthquake rupturing. *Pure and Applied Geophysics*, **124**, 159–175

Sibson, R.H. 1987. Earthquake rupturing as a mineralizing agent in hydrothermal systems. *Geology*, **15**, 701-704

Sibson, R.H. 1989. Earthquake faulting as a structural process. *Journal of Structural Geology*, **11**, 1–14.

Sibson, R.H. 1996. Structural permeability of fluid-driven fault-fracture meshes. *Journal of Structural Geology*, **18**, 1031-1042

Sibson, R.H. 1998. Brittle failure mode plots for compressional and extensional tectonic regimes. *Journal of Structural Geology*, **20**, 655-660

Sibson, R.H. 2000. Fluid involvement on normal faulting. *J. Geodyn*., **29**, 469-499

Sibson, R.H. 2004. Controls on maximum fluid pressure defining conditions of mesozonal mineralisation. *Journal of Structural Geology*, **26**, 1127-1136

Simpson, C. 1985. Deformation of granitic rocks across the brittle-ductilw transition. *Journal of Structural Geology*, **7**, 503-511

Simpson, G.D.H. 2000. Synmetamorphic vein spacing distributions: characterisation and origin of a distribution of veins from NW Sardinia, Italy. *Journal of Structural Geology,* **22**, 335-348.

Smallwood, J.R. 2004. Tertiary inversion in the Faroe-Shetland Channel and the development of major erosional scarps. *In*: Davies, R.J., Stewart, S.A., Cartwright, J.A., Lappin, M. & Underhill, J.R. (eds) *3D Seismic Technology: Application to the Exploration of Sedimentary Basins*. Geological Society, London, Memoirs, **29**, 187-198

Smallwood, J.R. 2008. Uplift, compression and the Cenozoic Faroe-Shetland sediment budget. *In*: Johnson, H., Doré, A. G., Gatliff, R.W., Holdsworth, R., Lundin, E.R. & Ritchie, J.D. (eds) The nature and origin of compression in passive margins. *Geological Society, London, Special Publications*, **306**, 137-152

Smallwood, J.R., Gill, C.E. 2002. The rise and fall of the Faroe-Shetland Basin: evidence from seismic mapping of the Balder Formation. *Geological Society, London,* **159**, 627-630.

Sørensen, A.B. 2003. Cenozoic basin development and stratigraphy of the Faroes area. *Petroleum Geoscience*, **9**, 189-207

Speight, J., Skelhorn, R., Sloan, T., Knaap, R. 1982. The dyke swarms of Scotland. *In*: Sutherland, D.S. (ed.) *Igneous Rocks of the British Isles*. John Wiley, New York, 449-621

Sperner, B., Ratschbacher L., Ott, R. 1993. Fault-Striae analysis: a Turbo Pascal program package for graphical presentation and reduced stress tensor calculation. *Comp. & Geosci.*, **19(9)**, 1361-1388.

Srivastava, S.P., Tapscott, C.R. 1986. Plate kinematics of the North Atlantic. *In:* Vogt, P. R. & Tucholke, B. E. (eds) *The Western North Atlantic Region, The Geology of North America*, **M**, 379-405

Stoker, M.S., Hitchen, K., Graham, C.C. 1993. *The Geology of the Hebrides and West Shetland Shelves, and adjacent deep-water areas.* United Kingdom Offshore Regional Report. British Geological Survey/HMSO, London.

Talwani, M., Eldholm, O. 1977. Evolution of the Norwegian-Greenland Sea. *GSA Bulletin*, **88**, 969-999

Torsvik, T.H., Mosar, J., Eide, E.A. 2001. Cretaceous-Tertiary geodynamics: a North Atlantic exercise. *Geophysical Journal International*, **146**, 850–866.

Torsvik, T.H., Carlos, D., Mosar, J., Cocks, L.R.M., Malme, T. 2002. Global reconstructions and North Atlantic palaeogeography 400 Ma to Recent. *In*: Eide, E.A. (*coord.*). BATLAS – Mid Norway plate reconstructions atlas with global and Atlantic perspectives. Geological Survey of Norway, 18-39.

Touret, J.L.R., 2001. Fluids in metamorphic rocks. *Lithos*, **55**, 1-25

Twiss, R.J., Moores, E.M. 1992. *Structural Geology*. W. H. Freeman &Co., New York.

Tullis, J., Yund, R.A. 1977. Experimental deformation of dry Westerley Granite. *Journal of Geophysical Research*, **82**, 5705-5718

Waagstein, R. 1988. Structure, composition and age of the Faeroe basalt plateau. *In*: Morton AC, Parson LM (eds) Early Tertiary volcanism and the opening of the NE Atlantic. Geol. Soc. Lond. Spec. Pub. **39**, 225–238

Waagstein, R., Guise, P.D Rex, D. 2002. K/Ar and Ar/ Ar whole-rock dating of zeolite facies metamorphosed flood basalts; the upper Paleocene basalts of the Faroe Islands, NE Atlantic. *Geological Society of London, Special Publication*, **197**, 219-252.

Walker, G.P.L. 1960. Zeolite zones and dike distribution in relation to the structure of basalts of eastern Iceland. *The Journal of Geology*, **68**, 515-528

Walker, G.P.L. 1987. The dyke complex of Koolau Volcano, Oahu; Internal structure of a Hawaiian rift zone. *In*: Decker, R.W., Wright, T.L., Stauffer, P.H. (eds.) *U.S.G.S. Prof. Paper*. 1350, 961-993.

Walker, R.J., Holdsworth, R.E., Imber, J. 2009. Clastic shear-fabrics and intrastratal-flow in basalt provinces: Uplift-related fault classifications on the NE Atlantic Margin. *Tectonic Studies Group AGM*

Walsh, J.J., Nicol, A., Childs, C. 2002. An alternative model for the growth of faults. *Journal of Structural Geology*, **24**, 1669-1675

Walsh, J.J., Bailey, W.R., Child,s C., Nicol, A., Bonson, C.G. 2003. Formation of segmented normal faults: a 3-D perspective. *Journal of Structural Geology*, **25**, 1251-1262

Weber, K.J., Mandl, G., Pilaar, W.F., Lehner, F., Precious, R.G. 1978. The role of faults in hydrocarbon migration and trapping in Nigerian growth fault structures. 10th Annual Offshore Technology Conference Proceedings 4, 2643-2653

White, R.S. 1988. A hot-spot model for the early Tertiary volcanism in the N. Atlantic. *In*: Morton, A.C., Parson, L.M. (eds) *Early Tertiary Volcanism and the Opening of the NE Atlantic*. Geological Society Special Publication, **39**, 3-13

White R.S., Smallwood, J.R., Fliedner, M.M., Boslaugh, B., Maresh, J., Fruehn, J. 2003. Imaging and regional distribution of basalt flows in the Faroe-Shetland Basin. *Geophysical Prospecting*, **51**, 215-231.

Wilson, R.W., McCaffrey, K.J.W., Holdsworth, R.E., Imber, J., Jones, R.R., Welbon, A.I.F., Roberts, D. 2006. Complex fault patterns, transtension and structural segmentation of the Lofoten Ridge, Norwegian margin: using digital mapping to link onshore and offshore geology. *Tectonics*, **25**, TC4018.

Wilson, R.W., Holdsworth, R.E., Wild, L.E., McCaffrey K.J.W., England, R.W., Imber, J., Strachan, R.A. 2009. Basement influenced rifting and basin development: a reappraisal of post-Caledonian faulting patterns from across the North Coast Transfer Zones, Scotland.

Woodcock, N.H., Mort, K. 2008. Classification of fault breccias and related fault rocks. *Geol. Mag.*, **145**, 435-440

Woodcock, N.H., Omma, J.E., Dickson, J.A.D. 2006. Chaotic breccia along the Dent Fault, NW England: implosion or collapse of a fault void? *J. Geol. Soc. Lond.*, **163**, 431-446

Woodcock, N.H., Dickson, J.A.D., Tarasewicz, J.P.T. 2007. Transient fracture permeability and reseal hardening in fault zones: evidence from dilation breccia textures. *In*: Sanderson, D.J., Lonergan, L., Jolly, R.J.H. & Rawnsley, K. (eds) *Fractured Reservoirs*. Geological Society, London, Special Publications, **270**, 43-53

Wright, V., Woodcock, N.H., Dickson, J.A.D. 2009. Fissure fills along faults: Variscan examples from Gower, South Wales. *Geological Magazine, Cambridge*

Ziegler, P.A. 1988. *Evolution of the Arctic-North Atlantic and Western Tethys.* American Association of Petroleum Geologists, Memoirs, **43**